MASS. INST. OF TECHNOLOGY
OCT 25 1967
LIBRARIES

LIGHT MIXING SPECTROSCOPY AND THE SPECTRUM OF LIGHT SCATTERED BY THERMAL FLUCTUATIONS IN LIQUIDS

by

JOSEPH BENEDICT LASTOVKA

B.S., John Carroll University

(1962)

SUBMITTED IN PARTIAL FULFILLMENT OF THE
REQUIREMENTS FOR THE DEGREE OF
DOCTOR OF PHILOSOPHY
at the
MASSACHUSETTS INSTITUTE OF TECHNOLOGY
July, 1967

Signature of Author...
Department of Physics, July, 1967

Certified by..
Thesis Supervisor

Accepted by..... ....
Chairman, Departmental Committee
on Graduate Students

FICHE

THESIS
PHYS
1967
Ph.D

LIGHT MIXING SPECTROSCOPY AND THE SPECTRUM OF LIGHT SCATTERED BY THERMAL FLUCTUATIONS IN LIQUIDS

by

JOSEPH BENEDICT LASTOVKA

Submitted to the Department of Physics on July 1, 1967 in partial fulfillment of the requirements for the degree of Doctor of Philosophy.

ABSTRACT

This thesis presents the results of ultrahigh resolution measurements of the spectrum of light scattered from toluene liquid at room temperature and atmospheric pressure. These data were taken using a low power (≃ 50 mW) helium-neon laser and an optical superheterodyne spectrometer.

Two features of the spectrum were investigated; the first, the inelastic part corresponding to the interaction of the incident light beam with the thermally excited sound waves (phonons). At a fixed scattering angle this part consists of a doublet, called the Brillouin doublet, split symmetrically about the exciting frequency; the magnitude of the splitting gives the frequency of the phonons responsible for the scattering. The Brillouin components in toluene were detected at a scattering angle of $\Theta = (0.547 \pm 0.002)°$ where the expected* splitting was $\Delta\nu = 30.00$ Mc/sec. The experimental determination of the splitting, made using a superheterodyne optical mixing spectrometer with a resolving power $(\nu/\delta\nu)$ of about 2×10^8, gave $\Delta\nu = (30.0 \pm 0.2)$ Mc/sec. This result demonstrated for the first time the applicability of high resolution optical beating techniques to small cross section scattering processes. **

The second feature of the spectrum to be examined was the so-called quasi-elastic component.§ At a given scattering angle this component consists of a single broadened line centered at the exciting frequency. This light is scattered as a result of the interaction of the incident light beam and thermally generated isobaric fluctuations in entropy. The spectral shape and characteristic width of this line (sometimes called the Rayleigh line) were carefully studied as a function of the scattering angle over the range $(0.3° \leq \Theta \leq 2.8°)$. In every case the spectrum was found to be quite accurately Lorentzian as predicted by theory[†] with a half-width at half-height varying from 75 cps to 7500 cps. The resolving powers of the superheterodyne spectrometer used in these measurements varied from 5×10^{11} to 5×10^{13}. The angular dependence of the half-width was found to be in substantial agreement with available theories.[†] These theories predict a linear dependence of half-width on the square of the magnitude of the wave vector of the scattering entropy fluctuation.

Since optical mixing has only very recently been applied to the problems of spectroscopy, a detailed theoretical analysis is given of the operation, resolution, and sensitivity of the two main types of mixing spectrometers. Equivalent results for resolution and sensitivity are also presented for the Fabry-Pérot etalon spectrometer. This allows a direct comparison to be made between conventional and optical mixing spectroscopy.

The theory of the light scattering by thermal fluctuations in liquids is outlined and results presented on the intensity, the spectrum, and the spatial coherence properties of the scattered field. These results are used to calculate the theoretical signal-to-noise ratios to be expected for heterodyne detection of the Brillouin and Rayleigh components of the spectrum. A comparison is made between these values and the experimentally determined quantities for scattering from toluene. This comparison verifies the essential features of the theory.

---

[*] L. Brillouin, Ann. Phys. (Paris) 17, 88 (1922).

[**] J. B. Lastovka and G. B. Benedek, in Physics of Quantum Electronics, edited by P. L. Kelly, B. Lax, and P. E. Tannenwald (McGraw-Hill Book Company, Inc., New York, 1966), p. 231.

[§] J. B. Lastovka and G. B. Benedek, Phys. Rev. Letters 17, 1039 (1966).

[†] R. D. Mountain, Rev. Mod. Phys. 38, 205 (1966).

Thesis supervisor: George B. Benedek

Title: Professor of Physics

TABLE OF CONTENTS

Chapter 1: INTRODUCTION. 25

Bibliography. 37

Chapter 2: THE THEORY OF LIGHT SCATTERING FROM THERMAL FLUCTUATIONS IN LIQUIDS 41

- A. Introduction. 41
- B. The General Characteristics of the Scattered Field 41
  - 1. The General Solution for the Scattered Field in Terms of the Fluctuating Part of the Optical Susceptibility. 44
    - a. Notation. 48
    - b. The Scattering from a Plane Wave Fluctuation. 48
    - c. Two Physical Interpretations of the Scattering Integral. . . . 53
  - 2. The Solution for the Scattered Field in the Limit of Small Frequency Shifts. 55
  - 3. The Spatial Fourier Series Expansion of the Susceptibility Fluctuations. 57
- C. The Intensity of the Scattered Light. . . 63
  - 1. Thermal Fluctuations. 63
  - 2. The General Expression for the Scattered Intensity 64
  - 3. The Spatial Correlation Functions and Mean-Square Amplitudes for Pressure and Entropy Fluctuations . . 66
  - 4. The Total Scattering Cross Section— The Rayleigh Ratio. 71
- D. The Spectrum of the Scattered Light . . . 76
  - 1. Definitions of the Time Correlation Function and the Power Spectral Density 78

2. The Correlation Function for the Scattered Field 79

3. Transformation of the Correlation Functions to Statistical Averages . . 81

4. The Correlation Function and Power Spectral Density for Isobaric Entropy Fluctuations. 84

5. The Correlation Function and Power Spectral Density for Adiabatic Pressure Fluctuations 90

E. The Spatial Coherence Properties of the Scattered Field 100

1. Introduction. 100

2. The Definition and General Properties of the Spatial Correlation Function. 102

3. The Origin of the Finite Range of Spatial Coherence. 106

4. The Spatial Correlation Function for the Scattered Field 109

a. The Description of the Scattered Field by Analogy with Diffraction 109

b. The General Expression for $T_Q(\vec{r},\vec{\rho})$ in Terms of the Interference or Diffraction Integral. 113

c. The Relationship between the Spatial Correlation Function and the Diffraction Pattern of the Scattering Volume. 119

d. The Averaged Properties of $T_Q(\vec{r},\vec{\rho})$ which are Important in Light Mixing Spectroscopy. . . 122

e. The Properties of $I(\vec{r},\vec{K})$ for a Rectangular Parallelopiped Scattering Volume 123

5. Calculation of the Coherence Solid Angle 130

a. The Direct Approach 132

b. A Simple Diffraction Approach . . 140

c. The Shell Approach. 143

6. The Behavior of Ω_{COH} and the Optimization of the Scattered Power per Coherence Solid Angle . . . 147

Bibliography. 153

Chapter 3: THE THEORY OF LIGHT MIXING SPECTROMETERS. . . 156

A. Introduction. 156

B. The Relationship between the Spectrum of the Current Output of a Photodetector and the Spectrum of the Incident Optical Field. 165

1. The Classical Description 166

2. The Stochastic Description. 170

3. The Spectrum of the Photocurrent— The Time Correlation Function for the Photocurrent Density. 173

4. The Effects of Spatial Coherence— The Time Correlation Function for the Total Current 183

C. The Self-Beating Optical Spectrometer . . 191

1. The Observed Photocurrent Power Spectrum for the Case of a Lorentzian Input Field. 192

2. The Processing of the Photocurrent Signal. 197

a. The Pre-Detection Signal-to-Noise Ratio 197

(1) Definition 197

(2) Effects of Spatial Coherence. 198

b. The Electronic System 201

(1) The Tuned Filter 201

(2) The Detector 205

(3) The Post-Detection Signal-to-Noise Ratio. . . . 207

(4) Post-Detection Filtering . . 210

c. The Output Signal-to-Noise Ratio 211

D. The Superheterodyne Optical Spectrometer. 213

  1. The Temporal, Spatial, and Statistical Coherence Properties of the Local Oscillator Field 214

  2. The Correlation Function for the Total Photocurrent. 220

  3. The Spatial Characteristics of the Mixing Process. 225

    a. The Effects of Spatial Coherence 225

    b. Collinearity of the Mixing Fields. 227

      (1) Angular Misalignment 227

      (2) Wavefront Radius Mismatch. . 233

      (3) Wavefront Distortion 234

    c. The Heterodyning Efficiency . . . 235

  4. The Spectrum of the Photocurrent. . . 237

  5. The Processing of the Photocurrent Signal. 240

    a. The Pre-Detection Signal-to-Noise Ratio. 240

    b. The Output Signal-to-Noise Ratio 242

E. The Detection Capabilities of Optical Mixing Spectrometers—The Ideal Case. . . 243

  1. Introduction. 243

  2. The Effects of Spatial Coherence on the Output Signal-to-Noise Ratio . 244

  3. The Limiting Behaviors of $(S/N)_{OUT}$. . 246

    a. Large Values of $(S/N)_{PRE}$— $(S/N)_{PRE} >> 1$ 246

    b. Small Values of $(S/N)_{PRE}$— $(S/N)_{PRE} << 1$ 249

  4. The Isones. 251

  5. An Example. 257

F. The Detection Capabilities of Optical Mixing Spectrometers—The Practical State-of-the-Art. 259
  1. General Discussion. 259
  2. Relevant Properties of State-of-the-Art Photomixers 264
  3. The Effects of Dark Current Shot-Noise. 269
    a. The Self-Beat Spectrometer. . . . 271
    b. The Superheterodyne Spectrometer. 275
    c. Summary 281
  4. The Effects of Johnson Noise. 281
    a. The Case of Zero Intermediate Frequency and Unity Internal Photodetector Gain. 285
    b. The Case of Zero Intermediate Frequency and Arbitrary Internal Photodetector Gain. 300
    c. The Case of Non-Zero Intermediate Frequency and Arbitrary Gain. 311
  5. The Effects of Excess Amplifier Noise 333
  6. Summary
G. A Comparison between Optical Mixing and Conventional Spectrometers. 341
  1. The Fabry-Pérot Etalon Spectrometer. 342
    a. The Signal Processing 342
    b. The Output Signal-to-Noise Ratio 346
    c. The Effects of Spatial Coherence 347
  2. The Intrinsic Difference between Conventional and Light Mixing Spectroscopy. 347
Bibliography. 357

Chapter 4: THE EXPERIMENTAL APPARATUS EMPLOYED IN THE STUDY OF THE BRILLOUIN-MANDEL'SHTAM AND CENTRAL COMPONENTS IN THE LIGHT SCATTERED FROM TOLUENE LIQUID 361

A. Introduction. 361

B. The Laser 363

  1. General Features. 363

  2. The Phase and Intensity Profiles of the Laser Electric Field 366

  3. Amplitude Modulation Effects. 376

    a. Mechanical Stability. 376

    b. Discharge Current Noise 377

    c. Dust. 377

    d. Axial Mode Locking. 378

    e. Importance of the Modulation Effects 385

C. The Scattering Cell 386

  1. Physical Description. 387

    a. Reflection Losses 387

    b. Wedge Angle 389

    c. Optical Thickness Distortion. . . 391

  2. The Thermal Lens Effect 392

  3. Refractive Corrections to the Scattering Angle. 394

  4. The Dimensions of the Illuminated Region. 399

  5. Measurement of the Scattering Angle 401

  6. Sample Preparation. 406

D. The Optical and Electronic System for Detection of the Brillouin Components. 406

  1. The Optical System. 406

  2. The Alignment Procedure 414

3. The Electronic Detection System . . . 418
    a. General Discussion. 418
    b. The Photodetector 421
    c. The Tunable Filter and Photomixer Load Circuit 423
    d. The Pre-Amplifier and Main Amplifier. 427
    e. The Detector. 427
4. The Resolution and Sensitivity of the Spectrometer 432
E. The Optical and Electronic System for Superheterodyne Detection of the Central Component 438
1. General Discussion. 438
2. The Optical System. 444
    a. General Features. 444
    b. The Wavefront Radius Mismatch Heterodyning Efficiency 447
    c. The Angular Misalignment Heterodyning Efficiency 454
    d. Determining the Scattering Angle and the Instrumental Acceptance Angle. 462
3. The Alignment Procedure 463
4. The Electronic System 466
    a. The Photomixer. 468
    b. The Mixer Load Circuits 470
    c. Wave Analyzers. 475
    d. The Squarer 478
    e. The Effect of a Finite Bandwidth on the Recorded Heterodyne Spectrum 480
5. Operating Characteristics of the Spectrometer. 481
Bibliography. 485

Chapter 5: EXPERIMENTAL RESULTS. 488
- A. Introduction. 488
- B. The Brillouin-Mandel'shtam Components . . 490
  - 1. The Frequency Shift 490
  - 2. The Line Width. 493
    - a. The Natural Broadening. 499
    - b. The Effect of Finite Sample Dimensions. 495
    - c. The Acceptance Angle Contribution. 497
    - d. The Observed Half-Width 504
  - 3. The Signal-to-Noise Ratios. 506
- C. The Central (Rayleigh) Component. 510
  - 1. The Line Shape. 511
  - 2. The Line Width. 515
  - 3. Discussion of the Results 521
  - 4. The Observed Signal-to-Noise Ratios . 528
    - a. The Pre-Detection (S/N) Ratio. . . 530
    - b. The Output (S/N) Ratio. 534
- Bibliography. 537

Appendix A: THE GENERAL EXPRESSION FOR THE SCATTERED ELECTRIC FIELD. 539

Appendix B: THE EVALUATION OF THE SUSCEPTIBILITY DERIVATIVES $(\partial\chi/\partial s)_P$ and $(\partial\chi/\partial P)_s$ IN TERMS OF THE PRESSURE AND TEMPERATURE DEPENDENCES OF THE INDEX OF REFRACTION. . . . 546

Appendix C: THE PROBABILITY DISTRIBUTIONS FOR THE ENTROPY AND PRESSURE FLUCTUATIONS OF WAVE VECTOR K 550

Appendix D: THE EFFECT OF WAVEFRONT CURVATURE MISMATCH ON THE HETERODYNING EFFICIENCY. 555

Appendix E: THE EFFECT OF THE FINITE SIZE OF THE ILLUMINATED REGION ON THE SPECTRUM OF THE SCATTERED LIGHT 561

BIOGRAPHICAL NOTE 568

ACKNOWLEDGEMENTS 569

LIST OF ILLUSTRATIONS

Figure 2-1 p.42	The assumed shape of the illuminated region and its position relative to the observer at Q.
Figure 2-2 p.46	The position of the observer in the far field of the scattering volume.
Figure 2-3 p.52	The orientation of the two wave vectors, $\vec{q}^{\,+} = (\vec{k}_s^{\,+} - \vec{k}_o)$ and $\vec{q}^{\,-} = -(\vec{k}_s^{\,-} - \vec{k}_o)$.
Figure 2-4 p.62	The scattering angles Θ and Φ.
Figure 2-5 p.62	The wave vector conservation triangle in the limit of small frequency shifts.
Figure 2-6 p.98	The theoretical spectrum for the light scattered by thermal fluctuations in liquids.
Figure 2-7 p.107	The change of path length between two points in the scattering volume and the observer's position as a function of the observation direction.
Figure 2-8 p.112	Equivalent illumination of the volume V for a diffraction interpretation of the scattering process.
Figure 2-9 p.115	The spherical surface Q used in the computation of the spatial correlation function.
Figure 2-10 p.124.	The shape and orientation of the scattering volume for an example calculation of the coherence solid angle.
Figure 2-11 p.126	A plot of the function $g(w) = \sin w/w$.

Figure 2-12 p.131 The reciprocal space associated with the Fourier series expansion of the susceptibility fluctuations.

Figure 2-13 p.135 A pictorial illustration of the coherence solid angle as fixed by the area of the sphere Q_K contained within a single ξ cell of reciprocal space.

Figure 2-14 p.137 A pictorial representation of the coherence angle in the (x,k_s) plane of the scattering volume.

Figure 2-15 p.138 A pictorial representation of the coherence angle in the (y,z) plane of the scattering volume.

Figure 2-16 p.139 Illustration of the coherence angles $\overline{\Delta\Theta}$ and $\overline{\Delta\Phi}$.

Figure 2-17 p.141 The extremal source dimensions in the (x,k_s) plane of the scattering volume.

Figure 2-18 p.142 The extremal source dimensions in the (z,y) plane of the scattering volume.

Figure 2-19 p.145 The shell swept out by a single ξ cell in allowing $\vec{k}_s$ to assume all allowed positions on Q_K.

Figure 2-20 p.151 The coherence angles and coherence solid angle for the scattering geometry described in Chapter 4 versus the scattering angle Θ.

Figure 2-21 p.152 The ratio of power per coherence area to incident power for scattering from entropy fluctuations in toluene.

Figure 3-1 p.158 Radio frequency and optical analogs of a tuned radio receiver.

Figure 3-2 p.158 Radio frequency and optical analogs of a superheterodyne receiver.

Figure 3-3 p.161 Radio frequency and optical analogs of a crystal video or self-beating receiver.

Figure 3-4 p.161 The power spectral density of a monochromatic wave which is weakly amplitude modulated at the frequency ω_m.

Figure 3-5 p.167 Two monochromatic light waves incident collinearly on a photodetector.

Figure 3-6 p.178 Illustration of the dc, shot-noise, and signal components of the photocurrent density corresponding to mixing between two monochromatic optical fields.

Figure 3-7 p.179 The power spectral density of the photocurrent corresponding to mixing between two monochromatic optical fields.

Figure 3-8 p.187 Illustration of the beat note phase variation as a function of position on the photomixer when the photosurface is not coplanar with the wavefronts of the mixing fields.

Figure 3-9 p.193 Block diagram of a self-beating optical spectrometer.

Figure 3-10 p.196 The power spectral density of the current output of a photodetector illuminated with an optical field having a Lorentzian spectrum with a half-width at half-height of Γ rad/sec.

Figure 3-11 p.203	Assumed system function for the tuned filter used to examine the photocurrent spectrum.
Figure 3-12 p.203	The power spectral density of the filtered photocurrent.
Figure 3-13 p.208	The power spectral density of the detector output.
Figure 3-14 p.208	The power spectral density of the detector output after post-filtering.
Figure 3-15 p.215	Block diagram of a superheterodyne optical spectrometer.
Figure 3-16 p.228	Two plane waves incident non-collinearly on a plane photosurface.
Figure 3-17 p.228	Two collinear, spherically spreading beams exhibiting wavefront radius mismatch.
Figure 3-18 p.239	The power spectral density of the photocurrent for the superheterodyne detection of an optical field having a Lorentzian spectrum with a half-width at half-height of Γ radians per second.
Figure 3-19 p.254	The signal-to-noise curves for optical mixing spectrometers.
Figure 3-20 p.262	Photocurrent power spectral density for a self-beat spectrometer including the effects of practical noise sources.
Figure 3-21 p.272	The power per coherence area required for $(S/N)_{OUT} = 1$ and the equivalent dark input power for three types of photodetectors.

Figure 3-22 p.274 The ratio of the power required to swamp the photomixer dark current to the power per coherence area necessary to achieve unity output signal-to-noise ratio.

Figure 3-23 p.279 Typical power spectral density of the output of a real laser.

Figure 3-24 p.284 The voltage generator equivalent circuit of a real impedance.

Figure 3-25 p.284 The current generator equivalent circuit of a real impedance.

Figure 3-26 p.287 The general equivalent circuit of a photodetector mixer with unity gain.

Figure 3-27 p.287 Simplified equivalent circuit for a photomixer operating into a pure resistance load.

Figure 3-28 p.295 The optimum load resistance for some typical unity gain detectors.

Figure 3-29 p.296 The total incident optical power required to overcome thermal noise in the photomixer load resistance of an optimally loaded unity gain detector.

Figure 3-30 p.298 The ratio of the total optical power required to overcome the Johnson noise in the photomixer load to the power per coherence area in the signal necessary to achieve $(S/N)_{OUT} = 1$.

Figure 3-31 p.301 The general equivalent circuit for a photodetector having arbitrary internal gain.

Figure 3-32 p.301 The general equivalent circuit for an arbitrary gain detector with coincident ac and dc units.

Figure 3-33 p.303 Simplified equivalent circuits for arbitrary gain photomixers having noiseless internal current amplification.

Figure 3-34 p.306 The optimum load resistance for some typical arbitrary gain photodetectors.

Figure 3-35 p.307 The total incident optical power required to swamp the thermal noise of an optimally loaded, arbitrary gain photodetector.

Figure 3-36 p.310 The ratio of the power required to swamp the Johnson noise in the photomixer load to the power per coherence area in the signal necessary to achieve $(S/N)_{OUT} = 1$.

Figure 3-37 p.313 General photomixer equivalent circuit with an arbitrary load.

Figure 3-38 p.313 Voltage generator series equivalent circuit for a photomixer with an arbitrary load impedance.

Figure 3-39 p.316 Series equivalent circuit of a photomixer terminated by a complex conjugate load.

Figure 3-40 p.316 Series equivalent circuit of a photomixer terminated by a modified complex conjugate load.

Figure 3-41 p.326 Equivalent resistive load for a photomixer terminated in a modified complex conjugate load.

Figure 3-42 p.329 The total incident optical power required to overcome the Johnson noise in the load of a photomixer terminated by a modified complex conjugate load.

Figure 3-43 p.331 The ratio of the total optical input power necessary to swamp thermal noise to the power per coherence area which gives $(S/N)_{OUT} = 1$.

Figure 3-44 p.337 Typical noise figures for radio frequency amplifiers useful in optical mixing spectrometers.

Figure 3-45 p.340 The power per coherence area required to achieve unity output signal-to-noise ratio for optical mixing spectrometers employing the best state-of-the-art photomixers.

Figure 3-46 p.343 Block diagram of a conventional Fabry-Pérot spectrometer.

Figure 3-47 p.349 A comparison of the sensitivity curves for a self-beat optical spectrometer and a conventional Fabry-Pérot etalon spectrometer.

Figure 3-48 p.352 The spectral information available at the photodetector output of a self-beating optical spectrometer.

Figure 4-1 p.364 Laser plasma tube and rf excitation geometry.

Figure 4-2 p.365 The schematic diagram of the rf laser exciter.

Figure 4-3 p.368 A comparison between the intensity profiles for the uni-phase modes of a spherical mirror and for the light focussed by an ideal lens.

Figure 4-4 p.371 The geometrical ray cone of the constant phase normal modes of a near-hemispherical resonator.

Figure 4-5 p.372 A model of the intensity and phase profiles in the focal region of a hemispherical resonator.

Figure 4-6 p.379 A typical laser power output spectrum.

Figure 4-7 p.382 Photodiode monitoring circuit used to observe changes in the axial mode beat pattern of the laser source.

Figure 4-8 p.384 Servo system used to control the laser cavity length.

Figure 4-9 p.388 A cross sectional view of the scattering cell.

Figure 4-10 p.390 The geometrical effects of an intracavity scattering cell on the laser axis orientation in a hemispherical system.

Figure 4-11 p.395 The relationship between the internal and external scattering angles, Θ and Θ', as measured in the (y,z) plane of the scattering volume.

Figure 4-12 p.398 The relationship between the internal and external scattering angles, Ψ and Ψ', as measured in the (x,z) plane of the scattering volume.

Figure 4-13 p.405 Pictorial and block diagram of the quartz transducer and associated electronics used to inject sound waves into the scattering cell.

Figure 4-14 p.407 Basic Mach-Zehnder optical system used as a superheterodyne mixing spectrometer.

Figure 4-15 p.410 The effect of a diverging lens on the apparent local oscillator source point and divergence angle.

Figure 4-16 p.413 Complete optical system of the superheterodyne spectrometer employed in measurements on the Brillouin components of the light scattered from toluene liquid.

Figure 4-17 p.419 Block diagram of the superheterodyne spectrometer used in detecting the Brillouin components.

Figure 4-18 p.422 The SD-100 photodiode load circuit.

Figure 4-19 p.424 Equivalent parallel circuit for the photomixer and its load impedance.

Figure 4-20 p.425 Equivalent series circuit of the photomixer and load as compared to the ideal complex conjugate load.

Figure 4-21 p.428 The schematic diagram of the 30 Mc/sec preamplifier.

Figure 4-22 p.429 The schematic diagram of the 30 Mc/sec main amplifier, detector, and dc detector output monitoring circuits.

Figure 4-23 p.434 The instrumental profile for the superheterodyne optical spectrometer used to detect the Brillouin doublet in the light scattered from toluene liquid.

Figure 4-24 p.445 Optical system for the superheterodyne spectrometer used to observe the central component line width.

Figure 4-25 p.450 The coherence angles for the experimental scattering geometry.

Figure 4-26 p.453 The Θ and Ψ dimensions of the scattered field coherence area at the beam splitter of the Mach-Zehnder spectrometer.

Figure 4-27 p.456 The geometrical positions of the local oscillator and effective signal source points in relation to the light collection waves.

Figure 4-28 p.456 The origin of the angular misalignment between the local oscillator and signal fields.

Figure 4-29 p.458 The angular misalignment contribution to the heterodyning efficiency for the superheterodyne spectrometer used to detect the width of the central component.

Figure 4-30 p.461 The two possible interpretations of the wavefront alignment criteria in terms of resolution limits.

Figure 4-31 p.461 Block diagram of the superheterodyne spectrometer used to observe the width of the central component.

Figure 4-32 p.471 Compensated photomixer load used with a General Radio 1900A wave analyzer.

Figure 4-33 p.474 Compensated photomixer load used with a Hewlett-Packard 310A wave analyzer.

Figure 4-34 p.479 Block and schematic diagram of the analog squaring device.

Figure 5-1 p.491 Typical Brillouin spectrum.

Figure 5-2 p.492 Typical Brillouin spectrum.

Figure 5-3 p.498 The geometry of the plane H used to calculate the instrumental acceptance angle of the superheterodyne Mach-Zehnder spectrometer.

Figure 5-4 p.505 Data trace showing the natural width of the photocurrent spectrum for the beat note between the laser local oscillator and the Brillouin components of the light scattered from toluene at $\Theta = 0.547^{\circ}$.

Figure 5-5 p.512 A typical central component spectrum obtained at $\Theta \simeq 0.31^{\circ}$.

Figure 5-6 p.513 A typical central component spectrum obtained at $\theta \approx 1.72^{\circ}$.

Figure 5-7 p.514 A typical central component spectrum obtained at $\theta \approx 2.8^{\circ}$.

Figure 5-8 p.516 The rms uncertainty of a Lorentzian fit to the central component spectrum.

Figure 5-9 p.520 Experimental results on the central component line width versus K^2.

Figure 5-10 p.532 The experimentally observed values of the pre-detection signal-to-noise ratio for the measurements on the central component in the light scattered from toluene.

Figure 5-11 p.535 Experimental results on the output signal-to-noise ratio for detection of the central component.

Figure D-1 p.556 Two spherically spreading waves of different radius of curvature incident collinearly on a circular, plane photocathode.

Figure D-2 p.558 The assumed photocathode geometry used to compute the wavefront radius mismatch heterodyning efficiency.

LIST OF TABLES

Table I The Rayleigh ratios $\mathbf{R}_p$ and $\mathbf{R}_s$ for some typical scatterers. 75

Table II Predicted central line width $(\Gamma_{max}/2\pi)$ for some typical scatterers. 91

Table III The predicted Brillouin splittings and line widths for some typical scatterers. . . . 99

Table IV Electrical properties of some useful photomixers. 265

Table V The uncertainties Δn and $\Delta\phi$ for various measurement techniques 356

Table VI Experimental results for the central component line width 519

Table B-1 Useful thermodynamic parameters for some typical scattering media. 548

Chapter 1

INTRODUCTION

The field of light scattering from thermal fluctuations in transparent media has had a rich theoretical and experimental development dating back to the last half of the nineteenth century. It was in 1871 that Lord Rayleigh[1] presented his now famous discussion of the "Light from the Sky, Its Colour and Polarization." In this paper he considered the problem of light scattering by a system of particles much smaller than the wavelength of light and calculated the magnitude and angular dependence of the scattered intensity, its variation with the frequency of the incident light, and the polarization characteristics of the scattered field. Using these results he successfully explained the observed color and polarization of the sunlight scattered in the atmosphere and the earlier results obtained by Tyndall[2] on light scattering by laboratory suspensions of small particles.

In 1910 Einstein[3] showed that one should expect light to be scattered even from a continuous and nominally homogeneous medium. He proved that scattering could also result from inhomogeneities in the optical properties of a medium brought about by local fluctuations in its density. He then calculated the expected magnitude of this effect by evaluating the mean-square amplitude of the density fluctuations from a statistical mechanics approach. This theory immediately provided an explanation of the intense scattering or opalescence that occurs in a fluid near its liquid-gas critical point in terms of the large density fluctuations that take place there.[4] By a spatial Fourier decomposition of these fluctuations, Einstein was also able to show that the light scattered away from the direction of the incident beam results essentially from a Bragg "reflection." This reflection takes place from that particular Fourier component of the fluctuations whose wavelength and orientation (i.e. whose wave vector) are just right to form a three dimensional diffraction grating that "reflects" the incident light into the direction of observation. In particular, if one allows monochromatic light of wave vector $\vec{k}_o$ to be incident on a transparent medium and observes the scattering in a direction specified by $\vec{k}_s$, the wave vector of the scattered light, then the fluctuations responsible for this scattering have a wave vector $\vec{K}$ given by

$$\vec{K} = \vec{k}_s - \vec{k}_o \tag{1-1}$$

Both $|\vec{k}_s|$ and $|\vec{k}_o|$ are measured in the scattering medium.

The exact nature of Einstein's density fluctuations went unexplained until 1912 when Debye[5] showed that the thermal energy content of an elastic medium could be regarded as being contained in thermally excited sound waves (phonons). In 1914 Brillouin[6] pointed out that the spontaneous density fluctuations described by Einstein could be interpreted as Debye's sound waves and he presented a calculation of the scattered intensity based on Debye's theory.

The first consideration of the spectrum of the light scattered from a homogeneous medium was reported by Brillouin[7] in 1922. In this paper, by retaining the time behavior of the thermal sound waves, Brillouin showed that, in addition to producing a Bragg reflection of the incident beam, the sound wave would also impose its time dependence on the scattered light in the form of a frequency shift. The magnitude of this frequency shift is equal to the frequency of the sound wave responsible for the scattering, i.e.

$$\Delta\omega = v_s|\vec{K}| \tag{1-2}$$

where v_s is the phase velocity of sound in the scattering medium. In Russia, Mandel'shtam[8] had independently calculated the spectral properties of the light scattered by the thermal phonons and had also obtained the frequency shift. His calculations show that if monochromatic light of frequency ω_o passes through a continuous elastic medium, then the light scattered at an angle Θ from the incident direction consists of two lines split symmetrically above and below ω_o by an amount

$$\Delta\omega = v_s|\vec{K}| = 2\omega_o(v_s/c_m) \sin(\Theta/2) \tag{1-3}$$

where

$$|\vec{K}| = |\vec{k}_s - \vec{k}_o| = 2|\vec{k}_o| \sin(\Theta/2) \tag{1-4}$$

is the wave vector of the sound wave responsible for the scattering into angle Θ, and c_m is the velocity of light in the scattering medium.

Equation (1-3) may be interpreted physically as showing that in addition to producing a Bragg reflection, the thermal sound wave "diffraction grating" also causes a Doppler shift because of its motion. Since this shift is of order $(v_s/c_m) \simeq 10^{-5}$, rather high resolution is required to observe the effect.

The first experimental observation of the Brillouin-Mandel'shtam (B-M) components was made by Gross[9,10,11,12,13] in 1930 at the Leningrad Optical Institute. Using the $\lambda = 4358$ Å line of a mercury arc discharge as a source and a thirty step echelon grating, he was able to resolve the doublet lines at $\Theta = 90°$ in seven liquids and show that the results agreed with the predicted splittings of the B-M theory. In a later paper[14] he also demonstrated that the angular dependence of the splitting and its variation with the frequency of the incident light were both in agreement with Eq. (1-3).

Gross also found that, in addition to the doublet, there was light scattered without a noticeable frequency shift in all seven liquids. In each case this unshifted or "central" component had an intensity comparable to that of the Brillouin lines. In 1934 Landau and Plačzek[15] proposed that this third component was due to scattering from thermally excited fluctuations in temperature. Since each Fourier spatial component of these fluctuations obeys a diffusion equation, rather than a wave equation, the temperature disturbances do not propagate and, therefore, no Doppler shift occurs. Indeed, using the fact that temperature fluctuations obey the heat flow equation, Mandel'shtam[8] and Leontovich[16] were able to show that the frequency spectrum of the spatial Fourier component of these fluctuations having wave vector $\vec{K}$ was a Lorentzian centered at $\omega = 0$ and having half-width at half-height of Γ rad/sec where

$$\Gamma = (\Lambda/\rho c_p)|\vec{K}|^2 \qquad (1\text{-}5)$$

Here Λ is the thermal conductivity of the scattering medium, ρ is its density, and c_p the specific heat at constant pressure per unit mass. It follows that the central component observed at a scattering angle Θ from an incident monochromatic beam is not infinitely sharp but has a Lorentzian spectrum centered at $\omega = \omega_o$ with a half-width

$$\Gamma = (\Lambda/\rho c_p)[2|\vec{k}_o|\sin(\theta/2)]^2 \qquad (1\text{-}6)$$

Therefore, the expected broadening goes to zero in the forward direction ($\theta = 0°$) and has its maximum value, Γ_{max}, for backscattering ($\theta = 180°$). Evaluating Γ_{max} for a number of liquids using an incident light wavelength $\lambda_{air} \simeq 6000$ Å and room temperature values of Λ, ρ, and c_p, we find typically $(\Gamma_{max}/2\pi) \simeq 10$ Mc/sec. This corresponds to a maximum fractional broadening of $(\Gamma_{max}/\omega_o) \simeq 2 \times 10^{-8}$. Because the narrowest available conventional light sources have fractional widths of $(\Delta\omega/\omega_o) \simeq 10^{-6}$ and fractional instrumental widths are generally about 10^{-6} it has been impossible to verify this prediction up until the present.

Another interesting feature of Gross' observations was pointed out by Leontovich.[16] Assuming that thermal sound waves obey the Navier-Stokes equation, they are damped. Therefore, the B-M components must also be broadened by an amount depending on the attenuation of the scattering phonons. Leontovich's calculation showed that the spectrum of each component of the doublet should be a Lorentzian with a half-width at half-height

$$\gamma = \alpha v_s \quad \text{rad/sec} \qquad (1\text{-}7)$$

where α is the amplitude attenuation coefficient for sound waves having the frequency $\Delta\omega$ given by Eq. (1-3). Since $\Delta\omega$ for ninety degree scattering is typically a few thousand megacycles per second, while conventional ultrasonic measurements of α extend only up to a few hundred megacycles per second, the attenuation of the scattering sound wave must be obtained by extrapolation from the low frequency results. This extrapolation is based on the fact that α is proportional to $(\Delta\omega)^2$ for viscous type losses. On doing this Leontovich found that for several of the liquids which Gross had studied the predicted width was greater than the splitting and, therefore, no discrete doublet spectrum should have been observed. The experiments and the theory were only to be reconciled later in terms of the relaxation theory of sound absorption.[17] Surprisingly, none of the materials that were investigated ever had a broadening sufficient to be detected above the natural source and instrumental widths.

The experimental situation regarding the spectrum of the Brillouin and central components remained essentially stagnant until 1964. Although the problem of measuring the doublet splitting was pursued vigorously in India, the difficulties of low intensity, sometimes requiring as long as 5 days of exposure, and the lack of intense monochromatic light sources and sufficiently high resolution spectrometers made accurate results extremely difficult to achieve.[18] As a result there are only a few noteworthy papers in this period.[19,20,21,22,23,24,25,26]

In 1964, with the availability of pulsed ruby and helium-neon lasers, interest in Brillouin scattering was revived and a number of papers were published showing that the laser was an ideal source for observing the effect.[27,28,29] The laser provided a light source of high power, extreme directivity, and exceptional monochromaticity. With fractional widths of $(\Delta\omega/\omega_o) \simeq 1 \times 10^{-8} - 2 \times 10^{-6}$ the laser source allowed accurate measurements to be made on the doublet splitting, thereby yielding important information on the velocity of hypersonic acoustic waves.

The laser ultimately led to the first observation of the natural width of the Brillouin-Mandel'shtam lines.

Using a helium-neon gas laser operating at $\lambda_{air} = 6328$ Å, Fabelinskii[30] and his co-workers measured the line width for 90° scattering in benzene

$$\frac{\Delta\omega}{2\pi} = 4800 \text{ Mc/sec} \qquad \frac{\gamma}{2\pi} = 150 \text{ Mc/sec}$$

and CCl_4

$$\frac{\Delta\omega}{2\pi} = 3200 \text{ Mc/sec} \qquad \frac{\gamma}{2\pi} = 300 \text{ Mc/sec},$$

while Chiao and Fleury[31] determined the natural broadening in a series of liquids for $\Theta = 180°$.

Lasers coupled with ultrahigh resolution Fabry-Pérot etalon and grating spectrometers and sensitive photomultipliers have brought about a very rapid renewal of interest in the field. The Brillouin components have been studied in liquids,[32,33,34,35] solids,[36,37] and gases[38]; and the basic light scattering technique is now being applied to observe the presence of other thermal excitations such as magnons,[39] polaritons,[40] and plasmons.[41,42,43,44,45]

However, even the highest resolving power Fabry-Pérot etalons fall short of providing sufficient resolution to obtain all of the useful information present in the spectrum. For typical sound velocities in liquids ($v_s \simeq 1.5 \times 10^5$ cm/sec) the maximum fractional Brillouin shift is approximately $(\Delta\omega/\omega_o) \simeq 10^{-5}$; with a helium-neon laser source ($\lambda_{air} = 6328$ Å) this corresponds to a splitting of $(\Delta\omega/2\pi) \simeq 7000$ Mc/sec. The attenuation of such sound waves may produce a line broadening of about $(\gamma/\omega_o) \simeq 10^{-8} - 10^{-6}$. However, extending the light scattering data down to the upper limit of conventional ultrasonic experiments requires going to scattering angles where $(\Delta\omega/\omega_o) \simeq 5 \times 10^{-7}$ and

$(\gamma/\omega_o) \simeq 10^{-11}$ — 10^{-9}. A study of such splittings and line widths would demand the ability to resolve details as fine as 10^{-12} of the incident frequency. Furthermore, a measurement of the broadening of the central component even in the most favorable situation ($\Theta = 180°$) requires a fractional resolution of $(\Gamma/\omega_o) \simeq 2 \times 10^{-8}$. A study of the angular dependence of the line width and line shape of this component would demand resolutions approaching $(\delta\omega/\omega_o) \simeq 10^{-14}$. That is, out of an optical frequency of approximately 5×10^{14} cps, one must detect spectral features on the scale of cycles per second. This is impossible by conventional spectroscopic techniques.

To study such narrow lines it is necessary to employ laser light sources combined with optical mixing spectrometers. These devices are exact analogs for the optical region of the spectrum of the ultrahigh resolution receivers that are common in the radio frequency regime.[47] In all cases the objective is to translate the desired spectral information from the "high" optical frequency ω_o, where a specified resolvable width $\delta\omega$ may be difficult to achieve, down to a "lower" frequency ω_1 where the necessary width may be attained easily. This frequency translation process can be carried out using two alternate instruments. In the first, referred to as the superheterodyne[46] spectrometer, the light whose spectrum is to be analyzed is mixed with an intense monochromatic beam called the local oscillator on a non-linear element—a photoelectric surface. By a proper choice of the frequency of the local oscillator, the optical signal spectrum can be shifted down to any desired frequency; the "mixer" output appears as an ac component in the photocurrent with a spectrum centered about the difference frequency between the local oscillator and the optical signal.

In the second type of instrument, referred to as a low-level,[46] square-law,[48] or self-beat[49] spectrometer, only the signal is allowed to fall on the photosurface. However, because of the non-linear current versus optical electric field characteristic of the photoelectric effect, mixing takes place between the various spectral components of the signal itself. The result is that the photocurrent spectrum contains, in a somewhat modified form, the spectral information that was originally present in the optical signal. However, this information is now centered around $\omega = 0$ rather than around the optical frequency $\omega = \omega_o$.

The resolving power capabilities of these two types of optical mixing spectrometers have been well demonstrated in light scattering experiments. Both have been applied to the problem of obtaining the spectrum of the central component from a pure fluid in the vicinity of its liquid-gas critical point[49,50,51] and determining from these measurements the temperature behavior of the thermal diffusivity $(\Lambda/\rho c_p)$. The superheterodyne technique has also been used to study the spectrum of concentration fluctuations in a binary mixture near its critical solution temperature.[52] Both methods have also been used successfully in detecting the spectral width of the light scattered from dilute solutions of large molecules.[53,54,55] In all these experiments the scattering cross section is from 10^3 to 10^6 times greater than that expected for the Brillouin and central components in the light scattered from pure liquids at room temperature.

This thesis presents experimental results on the application of ultrahigh resolution optical mixing spectroscopy to the problem of determining the spectrum of the light scattered from toluene liquid at room temperature and atmospheric pressure. Both the Brillouin[48] and central[56] components of the spectrum were studied using a low power (≃50 mW) helium-neon laser source (λ_{air} = 6328 Å) in conjunction with an optical superheterodyne spectrometer.

The Brillouin-Mandel'shtam doublet was observed at a scattering angle of $\Theta = (0.547 \pm 0.005)°$ where the predicted splitting was $(\Delta\omega/2\pi) = 30.0$ Mc/sec. The experimentally determined value of $(\Delta\omega/2\pi) = (30.0 \pm 0.2)$ Mc/sec was obtained with a resolving power of $(\omega_o/\delta\omega) \simeq 2 \times 10^8$.

Both the spectral shape and characteristic width of the central component were studied as a function of the scattering angle Θ over the range $(0.31° \leq \Theta \leq 2.83°)$. For this range in Θ the spectrum was found to be accurately Lorentzian, as predicted by the Landau-Plačzek theory, with a half-width at half-height $(\Gamma/2\pi)$ varying from 75 cps to 7500 cps. The fraction resolutions achieved in these measurements varied from $(\delta\omega/\omega_o) \simeq 2 \times 10^{-12}$ to $(\delta\omega/\omega_o) \simeq 2 \times 10^{-14}$. The angular dependence of the half-width was found to be in good agreement with the K^2 prediction of Eq. (1-5). A fit between Eq. (1-5) and the data yielded the thermal diffusivity as

$$(1/2\pi)(\Lambda/\rho c_P)_{experimental} = (1.38 \pm 0.05) \times 10^{-4} \text{ cm}^2/\text{sec}$$

The equivalent quantity calculated from the thermodynamically measured values of Λ[57] and c_P[58] is

$$(1/2\pi)(\Lambda/\rho c_P)_{static} = (1.52 \pm 0.09) \times 10^{-4} \text{ cm}^2/\text{sec}$$

which is in quantitative agreement with the present result.

Since optical mixing has only very recently been applied to the problems of spectroscopy, a detailed analysis is given of the operation, resolution, and sensitivity of the superheterodyne and self-beat spectrometers. Equivalent results are also presented for the Fabry-Pérot etalon spectrometer allowing a direct comparison to be made between conventional optical spectroscopy and optical mixing spectroscopy. In connection with this comparison, practical considerations are presented on the state-of-the-art of the essential components of mixing spectrometers. From these data, limits are set on the resolutions and sensitivities which may be achieved by an optical mixing receiver using present day devices.

Chapter 2 of this thesis presents the theory of light scattering by thermal fluctuations in liquids and gives results on the intensity, the spectrum, and the spatial coherence properties of the scattered field. In this review special attention is given to those aspects that bear directly on the applicability of optical mixing spectroscopy. The results are used in Chapter 5 to calculate the theoretical "signal-to-noise ratios" to be expected for heterodyne detection of the Brillouin and central components of the light scattered from toluene. A comparison between these calculated quantities and the experimentally observed values verifies the essential features of the theory.

The significant contributions of this work may be summarized as follows: (1) it clearly demonstrates the applicability of ultrahigh resolution optical mixing spectroscopy to small cross section scattering processes, (2) the measurements on the Brillouin components show that light scattering can yield data on sound velocity and absorption well into the present ultrasonic regime, (3) it presents the first measurements of the natural line width of the central component of the spectrum in the light scattered from a normal fluid, (4) this central component data provides the first accurate quantitative test of the Landau-Plačzek theory, (5) it clarifies the theoretical understanding of the applicability of optical mixing methods to spectroscopy, and (6) it delineates the capabilities of these methods in terms of present day technology.

BIBLIOGRAPHY: Chapter 1

1. Hon. J. W. Strutt (Lord Rayleigh), Phil. Mag. XLI, 107 (1871).

2. John Tyndall, Phil. Mag. XXXVIII, 384 (1869).

3. A. Einstein, Ann. Physik 33, 1275 (1910).

4. M. von Smolochowski, Ann. Physik 25, 205 (1908).

5. P. Debye, Ann. Physik 39, 789 (1922).

6. L. Brillouin, Compt. Rend. 158, 1331 (1914).

7. L. Brillouin, Ann. Phys. (Paris) 17, 88 (1922).

8. L. I. Mandel'shtam, Zhurnal Russkogo Fiziko Khimicheskogo Obshchestva 58, 381 (1926).

9. E. F. Gross, Nature 126, 201 (1930).

10. E. F. Gross, Nature 126, 400 (1930).

11. E. F. Gross, Z. Physik 63, 685 (1930).

12. E. F. Gross, Nature 126, 603 (1930).

13. E. F. Gross, Naturwiss. 18, 718 (1930).

14. E. Gross and J. Khvostikov, Phys. Rev. 42, 579 (1932).

15. L. Landau and G. Plačzek, Physikalische Zeitschrift der Sowjetunion 5, 172 (1934).

16. M. Leontovich, Z. Physik 72, 247 (1931).

17. L. I. Mandel'shtam and M. Leontovich, Comptes Rendus de l'Académie des Sciences de l'URSS 3, 111 (1936).

18. See for example the excellent review by Fabelinskii in reference 19.

19. I. L. Fabelinskii, Usp. Fiz. Nauk 63, 355 (1957) [English transl.: AEC Translation 3973, Part I, Advan. Phys. Sci. 63, 474 (1957)].

20. I. L. Fabelinskii and O. A. Shustin, Dokl. Akad. Nauk SSSR 92, 285 (1953) [English transl.: U. S. National Science Foundation translation NSF-tr-194].

21. P. Flubacher, A. J. Leadbetter, J. A. Morrison, and B. P Stoicheff, J. Phys. Chem. Solids 12, 53 (1960).

22. R. S. Krishnan, Proc. Indian. Acad. Sci. A26, 399 (1947).

23. R. S. Krishnan, Nature 159, 740 (1947).

24. R. S. Krishnan, Proc. Indian Acad. Sci. A41, 91 (1955).

25. M. S. Pesin and I. L. Fabelinskii, Dokl. Akad. Nauk SSSR 129, 299 (1959) [English transl.: Soviet Phys.—Doklady 4, 1264 (1960)].

26. M. S. Pesin and I. L. Fabelinskii, Dokl. Akad. Nauk SSSR 135, 1114 (1960) [English transl.: Soviet Phys.—Doklady 5, 1290 (1961)].

27. R. Y. Chiao, C. H. Townes, and B. P. Stoicheff, Phys. Rev. Letters 12, 592 (1964).

28. G. B. Benedek, J. B. Lastovka, K. Fritsch, and T. Greytak, J. Opt. Soc. Am. 54, 1284 (1964).

29. R. Y. Chiao and B. P. Stoicheff, J. Opt. Soc. Am. 54, 1286 (1964).

30. D. I. Mash, V. S. Starunov, and I. L. Fabelinskii, Zh. Eksperim. i Teor. Fiz. 47, 783 (1964) [English transl.: Soviet Phys.—JETP 20, 523 (1965)].

31. R. Y. Chiao and P. A. Fleury, in Physics of Quantum Electronics, edited by P. L. Kelly, B. Lax, and P. E. Tannenwald (McGraw-Hill Book Company, Inc., New York, 1966), p. 241.

32. G. Benedek and T. Greytak, Proc. IEEE 53, 1623 (1965).

33. E. Garmire and C. H. Townes, Applied Physics Letters 5, 84 (1964).

34. R. G. Brewer and K. E. Rieckhoff, Phys. Rev. Letters 13, 334 (1964).

35. D. I. Mash, V. S. Starunov, E. V. Tiganov, and I. L. Fabelinskii, Zh. Eksperim. i Teor. Fiz. 49, 1764 (1965) [English transl.: Soviet Phys.—JETP 22, 1205 (1966)].

36. G. B. Benedek and K. Fritsch, Phys. Rev. 149, 647 (1966).

37. S. M. Shapiro, R. W. Gammon, and H. Z. Cummins, Applied Physics Letters 9, 157 (1966).

38. T. J. Greytak and G. B. Benedek, Phys. Rev. Letters 17, 179 (1966).

39. P. A. Fleury, S. P. S. Porto, L. E. Cheesman, and H. J. Guggenheim, Phys. Rev. Letters 17, 84 (1966).

40. S. P. S. Porto, B. Tell, and T. C. Damon, Phys. Rev. Letters 16, 450 (1966).

41. B. Kronast, H. Röhr, H. Zwicker, and E. Fünfer, Phys. Rev. Letters 16, 1082 (1966).

42. P. W. Chan and R. A. Nodwell, Phys. Rev. Letters 16, 122 (1966).

43. S. A. Ramsden and W. E. R. Davies, Phys. Rev. Letters 16, 303 (1966).

44. O. A. Anderson, Phys. Rev. Letters 16, 978 (1966).

45. A. Mooradian and G. B. Wright, Phys. Rev. Letters 16, 999 (1966).

46. A. T. Forrester, J. Opt. Soc. Am. 51, 253 (1961).

47. Monte Ross, *Laser Receivers* (John Wiley and Sons, Inc., New York, 1966).

48. J. B. Lastovka and G. B. Benedek, in *Physics of Quantum Electronics*, edited by P. L. Kelly, B. Lax, and P. E. Tannenwald (McGraw-Hill Book Company, Inc., New York, 1966), p. 231.

49. N. C. Ford, Jr., and G. B. Benedek, in *Critical Phenomena*, edited by M. S. Green and J. V. Sengers (U. S. Government Printing Office, Washington, D. C., 1966), p. 150.

50. N. C. Ford, Jr., and G. B. Benedek, Phys. Rev. Letters 15, 649 (1965).

51. S. S. Alpert, D. Balzarini, R. Novick, L. Seigel, and Y. Yeh, in Physics of Quantum Electronics, edited by P. L. Kelly, B. Lax, and P. E. Tannenwald (McGraw-Hill Book Company, Inc., New York, 1966), p. 253.

52. S. S. Alpert, Y. Yeh, and E. Lipworth, Phys. Rev. Letters **14**, 486 (1965).

53. H. Z. Cummins, N. Knable, and Y. Yeh, Phys. Rev. Letters **12**, 150 (1964).

54. J. A. White, J. S. Osmundson, and B. H. Ahn, Phys. Rev. Letters **16**, 639 (1966).

55. J. H. Lunacek, S. B. Dubin, and G. B. Benedek, Bull. Am. Phys. Soc. **12**, 544 (1967).

56. J. B. Lastovka and G. B. Benedek, Phys. Rev. Letters **17**, 1039 (1966).

57. American Institute of Physics Handbook, edited by D. E. Gray (McGraw-Hill Book Company, Inc., New York, 1963), 2nd ed., p. **4**-86.

58. International Critical Tables, E. W. Washburn editor-in-chief (McGraw-Hill Book Company, Inc., New York, 1929), 1st ed., Volume 5.

Chapter 2

THE THEORY OF LIGHT SCATTERING FROM THERMAL FLUCTUATIONS IN LIQUIDS

A. Introduction

This chapter presents a brief analysis of the theory of light scattering from thermal fluctuations in transparent, homogeneous media. Specifically, we will consider those scattering processes which can be described in terms of a modulation in the index of refraction of the scattering medium produced by statistical fluctuations in its thermodynamic coordinates. The objective is to determine the following features of the scattered light: (1) its absolute intensity and angular distribution, (2) its spectrum, and (3) the spatial coherence properties of the scattered electric field.

B. The General Characteristics of the Scattered Field

Consider a linearly polarized, monochromatic, collimated light beam passing through a homogeneous, transparent medium as illustrated in Fig. 2-1. We would like to calculate the electric field scattered in the direction of the point $\mathbf{Q}$ due to the interaction of this incoming wave with the material in the cylindrical volume V.

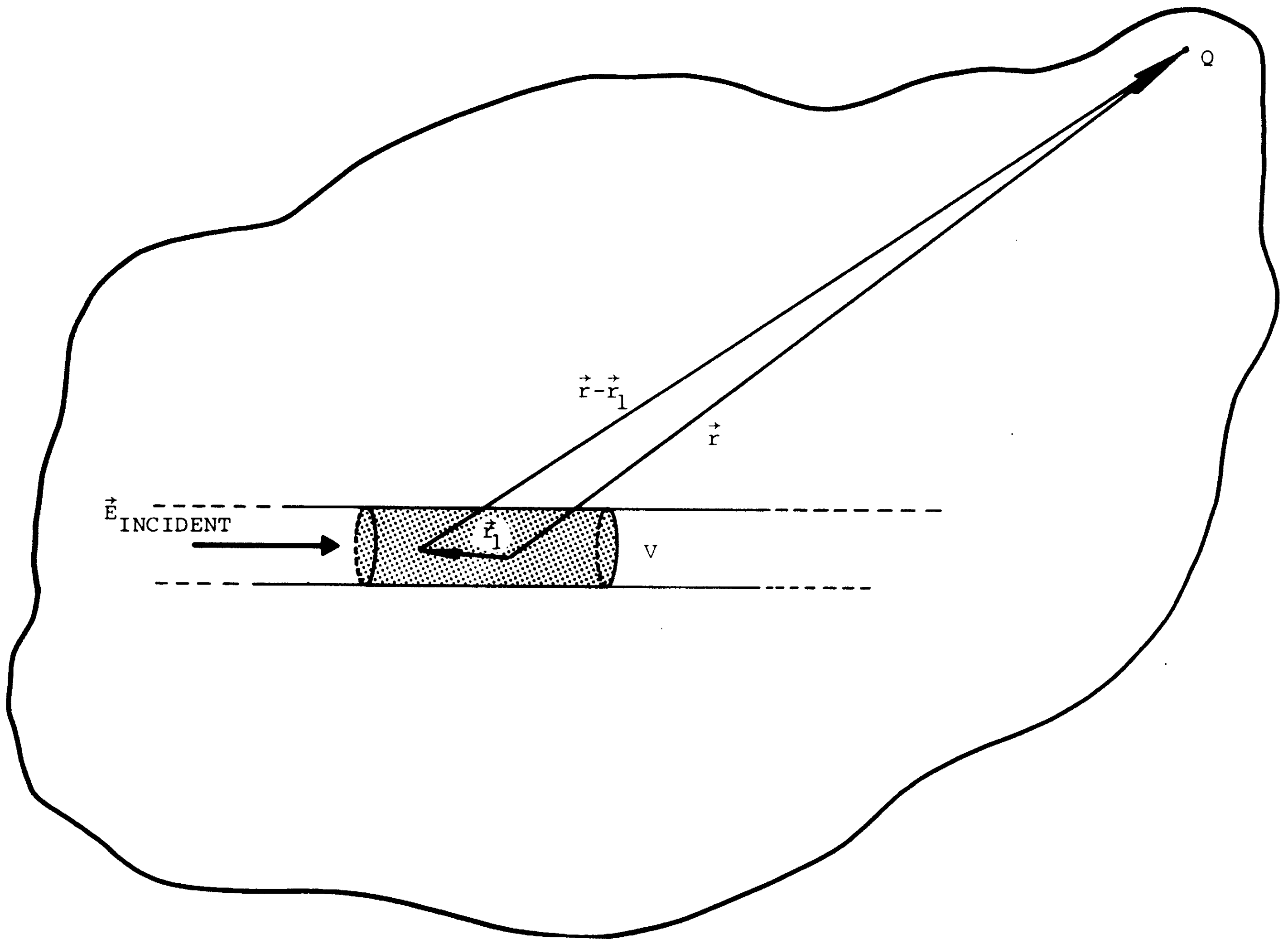

Q
$\vec{r}-\vec{r}_1$
$\vec{r}$
$\vec{E}_{INCIDENT}$
$\vec{r}_1$
V

Figure 2-1 The assumed shape of the illuminated region and its position relative to the observer at Q.

We assume that, as far as its optical properties are concerned, the scattering medium can be; (1) regarded as a *continuum*, and (2) characterized completely by a *scalar* electric susceptibility $\chi(\vec{r},t)$ at the optical frequencies of interest. In this case the effect of the incident field $\vec{E}_{INC}(\vec{r},t)$ is to induce an oscillating dipole moment[1]

$$\vec{p}(\vec{r}_1,t) = \varepsilon_o\chi(\vec{r}_1,t)\vec{E}_{INC}(\vec{r}_1,t)d^3\vec{r}_1 \qquad (2\text{-}1)$$

in every volume element of V. This induced polarization field can subsequently radiate in the direction of the observer at **Q** . In fact, a calculation of the scattered field $\vec{E}_S(\vec{r},t)$ may be carried out directly by summing the dipole fields reaching the point $\vec{r}$ in such a way as to include the proper relative phase between waves originating from spatially separated points in V.[2]

An alternate approach, which is outlined in Appendix A, shows that $\vec{E}_S(\vec{r},t)$ can also be obtained by demanding that the sum of the *incident plus reradiated* fields satisfy Maxwell's equations throughout all space. This method is particularly useful in scattering problems since it automatically eliminates from direct consideration the uninteresting portion of the dipolar sum associated with the *time average* susceptibility. The effect of the time average susceptibility is simply to alter the velocity of light from its free space value c_o to its value in the scattering medium, $c_m = (c_o/n)$, where n is the index of refraction of the sample.

For the scattering processes considered here we take $\chi(\vec{r},t)$ to be a function of $(\vec{r},t)$ *only* because of its implicit dependence on the local "thermodynamic" coordinates* of the scattering medium, for example, its density and temperature. It follows that $\chi(\vec{r},t)$ may be decomposed into two parts.

---

* Chapter 2, Section C.1.

The first contribution is a time average[*] susceptibility, $\langle\chi\rangle$, related to the index of refraction by the result[**]

$$n^2 = 1 + \langle\chi\rangle$$

This average susceptibility is independent of $\vec{r}$ if the scattering medium is in a state of equilibrium in which the time average thermodynamic coordinates are independent of position in V. The second contribution to $\chi(\vec{r},t)$ is a random function[§] of both $\vec{r}$ and t and is associated with statistical fluctuations in the "thermodynamic" variables[3] about their average values.[†] This part, which we designate $\Delta\chi(\vec{r},t)$, is chosen such that

$$\chi(\vec{r},t) = \langle\chi\rangle + \Delta\chi(\vec{r},t) \qquad (2\text{-}2)$$

3. The General Solution for the Scattered Field in Terms of the Fluctuating Part of the Optical Susceptibility

If $\vec{E}(\vec{r},t)$ is the total electric field acting at a point $\vec{r}$ in the volume V then Appendix A gives the scattered field as

---

[*] Time averages will be denoted throughout by the symbol $\langle\ \rangle$ which we define as

$$\langle(\ldots.)\rangle = \lim_{T\to\infty} \frac{1}{2T} \int_{-T}^{T} (\ldots.)dt$$

[**] Appendix A.

[§] Chapter 2, Section C.3 and Chapter 5, Section C.3.

[†] Chapter 2, Section C.1.

$$\vec{E}_S(\vec{r},t) = \frac{1}{4\pi\varepsilon_o}\,\vec{\nabla}_r\times\left[\vec{\nabla}_r\times\int_V\int_{t_1=-\infty}^{\infty}\frac{\varepsilon_o}{1+\langle\chi\rangle}\;\frac{\Delta\chi(\vec{r}_1,t_1)\vec{E}(\vec{r}_1,t_1)\,\delta\left(t_1-t+\frac{|\vec{r}-\vec{r}_1|}{c_m}\right)d^3\vec{r}_1\,dt_1}{|\vec{r}-\vec{r}_1|}\right] \qquad (2\text{-}3)$$

The coordinates $\vec{r}$ and $\vec{r}_1$ are as shown in Fig. 2-1. Note that the observation point $\mathbf{Q}$ has been chosen to lie inside the sample in order to avoid refractive effects at the surface which may be accounted for at a later stage by simple geometrical optics.

Physically, Eq. (2-3) is simply a sum of the elementary dipole radiation fields produced by the effective dipole moment distribution $\varepsilon_o\Delta\chi(\vec{r}_1,t_1)\vec{E}(\vec{r}_1,t_1)$. Therefore, we find that in the absence of fluctuations in the susceptibility there is no light scattered out of the incident beam. Because the summing integral, $\int\ldots d^3\vec{r}_1$, attaches the proper relative phase to each of the fields reaching $\vec{r}$ it is sometimes referred to as the "interference" integral.[2]

The rigorously correct result in Eq. (2-3) can be simplified by the following considerations. If the point $\mathbf{Q}$ is sufficiently far from the illuminated volume V, we have in the usual far field approximation

$$|\vec{r}-\vec{r}_1| \simeq |\vec{r}| - \vec{r}_1\cdot\hat{r}$$

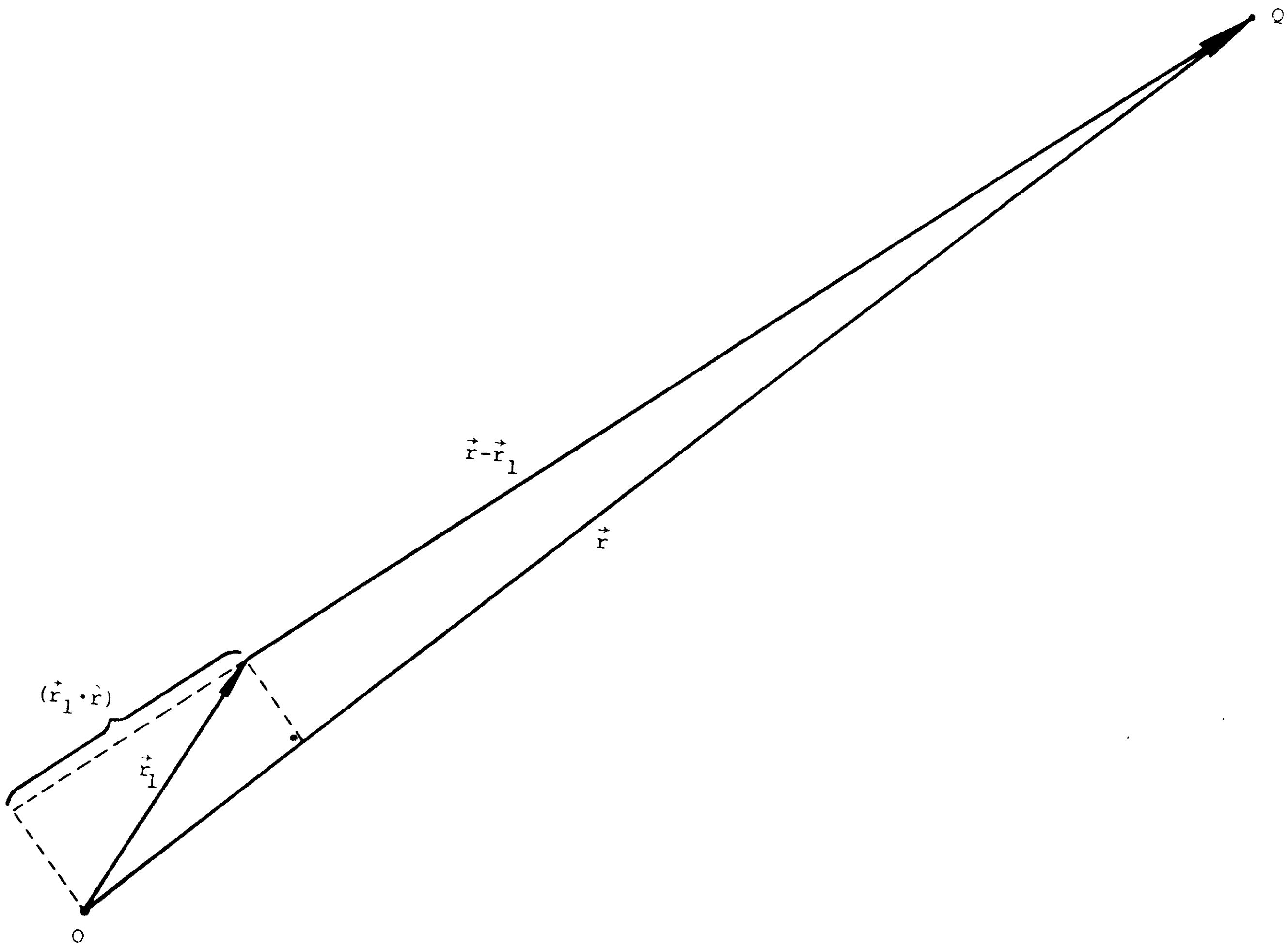
Q
$\vec{r}-\vec{r}_1$
$\vec{r}$
$(\vec{r}_1 \cdot \hat{r})$
$\vec{r}_1$
O

Figure 2-2 The position of the observer in the far field of the scattering volume.

as illustrated in Fig. 2-2. The vector $\hat{r}$ is a unit vector in the direction of $\vec{r}$. The zero order approximation can be made in the denominator of the integrand, taking $|\vec{r} - \vec{r}_1| \simeq |\vec{r}| \equiv r$. As it stands, Eq. (2-3) is an integral equation for the scattered field since $\vec{E}_T(\vec{r}_1,t_1)$ represents the total field, incident plus scattered, acting on the medium. In normal liquids, however, we find that the total power scattered out of the incoming beam by "thermal fluctuations" is approximately 10^{-5} of the incident power; therefore, to first order, we may take $\vec{E}_T(\vec{r}_1,t_1)$ as simply the incident field, $\vec{E}_{INC}(\vec{r}_1,t_1)$. This corresponds to the usual "first Born approximation" to the scattering process.[5]

With these modifications, and writing $\varepsilon_o(1 + \langle\chi\rangle) = \varepsilon$, where ε is the dielectric permittivity of the medium, we have $\vec{E}_S(\vec{r},t)$ in the form

$$\vec{E}_S(\vec{r},t) = \frac{1}{4\pi r}\left(\frac{\varepsilon_o}{\varepsilon}\right)\vec{\nabla}_r\times\left[\vec{\nabla}_r\times\int_V\int_{t_1=-\infty}^{\infty}\Delta\chi(\vec{r}_1,t_1)\vec{E}_{INC}(\vec{r}_1,t_1)\right.$$

$$\left.\times\delta[t_1-t+(1/c_m)(r-\vec{r}_1\cdot\hat{r})]d^3\vec{r}_1dt_1\right] \qquad (2\text{-}4)$$

This is the desired general solution for the scattered field.

a. Notation

Since it will be convenient to handle $\vec{E}_{INC}(\vec{r},t)$, $\vec{E}_S(\vec{r},t)$, and $\Delta\chi(\vec{r},t)$ in the form of complex exponentials it is useful to adopt the following conventions: complex quantities will be denoted by underlining e.g. $\underline{E}_S(\vec{r},t)$, $\underline{\Delta\chi}(\vec{r},t)$. Complex quantities decomposed into their real and imaginary components will be written as $\underline{\Delta\chi} = \Delta\chi + i\Delta\chi'$. In this notation Eq. (2-4) remains unchanged; $\vec{E}_S$, $\Delta\chi$, and $\vec{E}_{INC}$ in each case are the real parts of their respective complex representations.

b. The Scattering from a Plane Wave Fluctuation

In order to illustrate the important features of the solution for $\vec{E}_S(\vec{r},t)$ let us consider a specific example in which $\Delta\chi$ is a simple *sinusoidal traveling wave* of frequency ϖ traveling in a direction $\hat{q}$ with a phase velocity $v = (\varpi/|\vec{q}|)$, *viz*.

$$\underline{\Delta\chi}(\vec{r},t) = \Delta\chi_o \exp[i(\vec{q}\cdot\vec{r}) - \varpi t] \tag{2-5}$$

The amplitude $\Delta\chi_o$ is a real number.

We assume that the incident field is a monochromatic plane wave having a constant intensity over the cross section of the scattering volume,

$$\underline{\vec{E}}_{INC}(\vec{r},t) = \vec{E}_o \exp\,[i(\vec{k}_o\cdot\vec{r}) - \omega_o t] \tag{2-6}$$

where $\vec{E}_o$ is real and $(\omega_o/|\vec{k}_o|) = c_m$ is the phase velocity of light in the medium.

In this case Eq. (2-4) becomes

$$\vec{E}_S(\vec{r},t) = \frac{1}{4\pi r}\left(\frac{\varepsilon_o}{\varepsilon}\right)\vec{\nabla}_r\times(\vec{\nabla}_r\times\Delta\chi_o\vec{E}_o)$$

$$\times\int_V\int_{t_1=-\infty}^{\infty}\cos(\vec{q}\cdot\vec{r}_1 - \varpi t_1)\ \cos\ (\vec{k}_o\cdot\vec{r}_1 - \omega_o t_1)$$

$$\times\delta[t_1-t+(1/c_m)(r-\vec{r}_1\cdot\hat{r})]d^3\vec{r}_1 dt_1 \tag{2-7}$$

The product of the two sinusoidally oscillating factors, one corresponding to the incident field and one to the "fluctuations" in χ, shows that $\Delta\chi$ impresses its time dependence on $\vec{E}_{INC}$ by modulating the amplitude of the field scattered from every point in V. By decomposing the cos•cos product and performing the time integration we find $\vec{E}_S(\vec{r},t)$ in its complex form as

$$\underline{\vec{E}}_S(\vec{r},t) = \frac{1}{4\pi r}\left(\frac{\varepsilon_o}{\varepsilon}\right)\vec{\nabla}_r\times(\vec{\nabla}_r\times\Delta\vec{E}_o) \tag{2-8}$$

$$\times\left[\frac{1}{2}\exp\{i[\frac{\omega_o+\varpi}{c_m}r - (\omega_o+\varpi)t]\}\times\int_V \exp\{i[\vec{k}_o + \vec{q} - \frac{\omega_o+\varpi}{c_m}\vec{r}]\cdot\vec{r}_1\}d^3\vec{r}_1\right.$$

$$\left.+\frac{1}{2}\exp\{i[\frac{\omega_o-\varpi}{c_m}r - (\omega_o-\varpi)t]\}\times\int_V \exp\{i[\vec{k}_o - \vec{q} - \frac{\omega_o-\varpi}{c_m}\vec{r}]\cdot\vec{r}_1\}d^3\vec{r}_1\right]$$

As would be expected, the "modulation" phenomenon gives rise to dipole wavelets of two frequencies, $\omega^+ = \omega_o+\varpi$ and $\omega^- = \omega_o-\bar{\omega}$. One effect of the time retardation factor in Eq. (2-4) has been to assign the proper wavelength to each of these waves; that is, we find from Eq. (2-8)

$$k_s^+ = (2\pi/\lambda^+) = (\omega^+/c_m) = (\omega_o+\varpi)/c_m \qquad (2\text{-}9)$$

and

$$k_s^- = (2\pi/\lambda^-) = (\omega^-/c_m) = (\omega_o-\varpi)/c_m \qquad (2\text{-}10)$$

In terms of k_s^+ and k_s^- the scattered field observed at $\vec{r}$ has the form

$$\underline{\vec{E}}_S(\vec{r},t) = \frac{1}{4\pi r}\left(\frac{\varepsilon_o}{\varepsilon}\right)\vec{\nabla}_r\times(\vec{\nabla}_r\times\Delta\chi_o\vec{E}_o)$$

$$\times\left[\frac{1}{2}\,e^{i(k_s^+r\,-\,\omega^+t)}\int_V e^{i(\vec{k}_o+\vec{q}-\vec{k}_s^+)\cdot\vec{r}_1}\,d^3\vec{r}_1\right.$$

$$\left.+\,\frac{1}{2}\,e^{i(k_s^-r\,-\,\omega^-t)}\int_V e^{i(\vec{k}_o-\vec{q}-\vec{k}_s^-)\cdot\vec{r}_1}\,d^3\vec{r}_1\right] \qquad (2\text{-}11)$$

where the vectors $\vec{k}_s^+$ and $\vec{k}_s^-$ are defined as $\vec{k}_s^+ \equiv (\omega^+/c_m)\hat{r}$ and $\vec{k}_s^- \equiv (\omega^-/c_m)\hat{r}$. Both point in the direction of observation, $\vec{r}$.

The integrals that determine the amplitude of the scattered field

$$I[\vec{r},(\vec{q})] = \int_V e^{i(\vec{k}_o+\vec{q}-\vec{k}_s^+)\cdot\vec{r}_1}\,d^3\vec{r}_1 \qquad (2\text{-}12)$$

and

$$I[\vec{r},(-\vec{q})] = \int_V e^{i(\vec{k}_o-\vec{q}-\vec{k}_s{}^-)\cdot\vec{r}_1}\, d^3\vec{r}_1 \qquad (2\text{-}13)$$

describe the properly phased sum of the elementary dipole wavelets as they interfere at $\vec{r}$. If all the dimensions of V are large compared to the wavelength of light, we find* that these volume integrals will in general be vanishingly small. In fact, complete destructive interference occurs at $\vec{r}$ unless $\vec{q}$ satisfies one of the two conditions

$$\vec{q}^{\,+} = \vec{k}_s{}^+ - \vec{k}_o \qquad (2\text{-}14)$$

or

$$\vec{q}^{\,-} = -(\vec{k}_s{}^- - \vec{k}_o) \qquad (2\text{-}15)$$

Equations (2-14) and (2-15) represent conditions on the wavelength and the propagation direction of the "fluctuation" which insure that the scattered wavelets sum constructively in the direction $\vec{r}$. The two wave vectors, $\vec{q}^{\,+}$ and $\vec{q}^{\,-}$, are illustrated in Fig. 2-3; both are drawn for the case ($\overline{\omega} << \omega_o$) where we have $k_s{}^+ \simeq k_s{}^- \simeq k_o$. The sets of parallel lines indicate the surfaces of constant phase for the wave $\Delta\chi(\vec{r},t)$.

Equations (2-11), (2-14), and (2-15) also summarize the essential features of the scattering process.

(1) In the absence of susceptibility fluctuations in the medium there is no light scattered away from the direction of the incident beam.

(2) If such fluctuations do exist, and if $\Delta\chi(\vec{r},t)$ is decomposed into plane wave components of all possible wave vectors,

---

* Chapter 2, Section E.4.e.

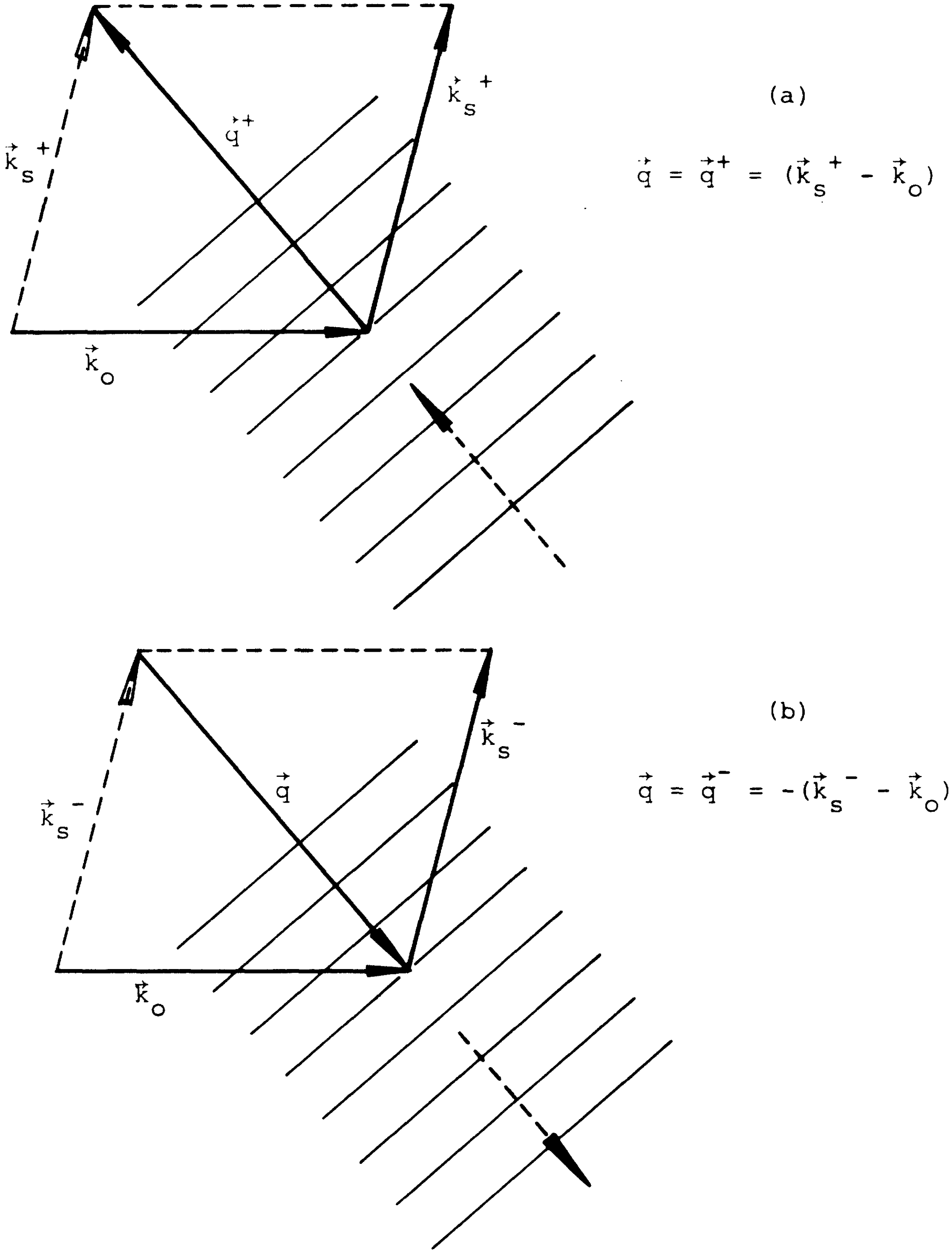
$\vec{k}_s^{\,+}$
$\vec{q}^{\,+}$
$\vec{k}_s^{\,+}$
$\vec{k}_o$
(a)
$\vec{q} = \vec{q}^{\,+} = (\vec{k}_s^{\,+} - \vec{k}_o)$
$\vec{k}_s^{\,-}$
$\vec{q}$
$\vec{k}_s^{\,-}$
$\vec{k}_o$
(b)
$\vec{q} = \vec{q}^{\,-} = -(\vec{k}_s^{\,-} - \vec{k}_o)$

Figure 2-3 The orientation of the two wave vectors, $\vec{q}^{\,+} = (\vec{k}_s^{\,+} - \vec{k}_o)$ and $\vec{q}^{\,-} = -(\vec{k}_s^{\,-} - \vec{k}_o)$.

then the light observed in a direction $\hat{k}_s^+ = \hat{k}_s^- = \hat{r}$ is scattered by two of these components with very specific wavelengths and propagation directions; namely those plane wave components whose wave vectors satisfy the conditions displayed in Eqs. (2-14) and (2-15).

(3) They show that the scattering fluctuation imposes its time dependence on $\vec{E}_S(\vec{r},t)$ in the form of a frequency shift. The magnitude of this frequency shift is equal to the frequency of the scattering plane wave.

c. Two Physical Interpretations of the Scattering Integral

The mathematical conditions on $\vec{q}$ which are displayed in Eqs. (2-14) and (2-15) can be given two physical interpretations. From a classical wave picture they pick out plane wave fluctuations whose directions and wavelengths will bring about constructive interference between the elementary dipole fields reaching some observation point $\vec{r}$. This situation is analagous to that encountered in x-ray scattering from crystals;[6] in fact, in the limit $\bar{\omega} << \omega_0$ the constructive interference phenomenon can be viewed as a simple Bragg reflection of the incoming beam from the three dimensional periodic "lattice" formed by $\Delta\chi(\vec{r},t) = \Delta\chi_0 \cos(\vec{q}\cdot\vec{r} - \bar{\omega}t)$. This picture also provides a physical interpretation of the frequency shift that accompanies the scattering process. It is a Doppler effect caused by the motion of the wavefronts of the scattering plane wave. A classical calculation of the Doppler shift to be expected in the Bragg reflected wave if the scattering wavefronts move at a phase velocity $v = [\bar{\omega}/|\vec{q}|]$ gives

$$\omega_{DOPPLER} = \pm \varpi \qquad (2\text{-}16)$$

in agreement with Eqs. (2-8), (2-9), and (2-10).

The allowable scattering processes, i.e. those satisfying Eq. (2-14) or Eq. (2-15), can also be described quantum mechanically[2] as a collision between two particles; the incident photon, which has an energy $\hbar\omega_o$ and a momentum $\hbar\vec{k}_o$, and a wavelike disturbance describable as a quasi-particle of energy $\hbar\varpi$ and quasi-momentum $\hbar\vec{q}$. In this case, the energy, $\hbar\omega$, and momentum, $\hbar\vec{k}_s$, of the scattered photon are obtained by demanding that momentum and energy be conserved in the collision process. From this viewpoint the conditions in Eqs. (2-14) and (2-15) are to be interpreted as follows. The situation $\vec{q} = \vec{k}_s{}^+ - \vec{k}_o$ represents a collision in which a single quasi-particle is annihilated; the scattered photon exits with its energy and momentum

$$\hbar\vec{k}_s = \hbar\vec{k}_o + \hbar\vec{q} = \hbar k_s{}^+$$

$$\hbar\omega = \hbar\omega_o + \hbar\varpi = \hbar\omega^+$$

The condition $\vec{q} = -(\vec{k}_s{}^- - \vec{k}_o)$ represents a collision in which a single quasi-particle is created; the incident photon gives up the required energy and momentum

$$\hbar\vec{k}_s = \hbar\vec{k}_o - \hbar\vec{q} = \hbar\vec{k}_s{}^-$$

$$\hbar\omega = \hbar\omega_o - \hbar\varpi = \hbar\omega^-$$

2. The Solution for the Scattered Field in the Limit of Small Frequency Shifts

Although Eq. (2-4) is useful in pointing out the detailed features of a simple scattering process, such as the example presented above, the intensity, spectrum, and spatial coherence properties of the light scattered from fluids are more easily calculated in the limit of small frequency shifts, $\varpi << \omega_o$. The latter condition is well satisfied for the contributions to $\Delta\chi(\vec{r},t)$ which are considered here, namely, statistical fluctuations in the local entropy and pressure of the scattering medium.* In this limit Eqs. (2-4) and (2-6) combine to give

$$\underline{\vec{E}}_S(\vec{r},t) = \frac{1}{4\pi r}\left(\frac{\varepsilon_o}{\varepsilon}\right)\vec{\nabla}_r\times(\vec{\nabla}_r\times\vec{E}_o) \tag{2-17}$$

$$\times\int_V \Delta\chi(\vec{r}_1,t)\, e^{i(\vec{k}_o\cdot\vec{r}_1)}\, e^{-i\omega_o[t-(1/c_m)(r-\vec{r}_1\cdot\hat{r})]}\, d^3\vec{r}_1$$

with the time retardation kept only in the rapidly oscillating incident field term. To this approximation the magnitude of the wave vectors and, therefore, the wavelengths, of the incident and scattered fields are the same, and we have

---

* Chapter 2, Section C.1.

$$\vec{\underline{E}}_S(\vec{r},t) = \frac{1}{4\pi r}\left(\frac{\varepsilon_o}{\varepsilon}\right)\vec{\nabla}_r \times \vec{\nabla}_r \times \vec{E}_o e^{i(k_s r - \omega_o t)}$$

$$\int_V \Delta\chi(\vec{r}_1,t)\, e^{i(\vec{k}_o-\vec{k}_s)\cdot\vec{r}_1}\, d^3\vec{r}_1 \tag{2-18}$$

where

$$\vec{k}_s = (\omega_o/c_m)\hat{r} \tag{2-19}$$

The double curl operation can be carried out explicitly to give $\vec{\underline{E}}_S(\vec{r},t)$ as

$$\vec{\underline{E}}_S(\vec{r},t) = \vec{k}_s \times (\vec{k}_s \times \vec{E}_o)\, \frac{e^{i(k_s r - \omega_o t)}}{4\pi r}\, \left(\frac{\varepsilon_o}{\varepsilon}\right)$$

$$\int_V \Delta\chi(\vec{r}_1,t)\; e^{i(\vec{k}_o-\vec{k}_s)\cdot\vec{r}_1}\, d^3\vec{r}_1 \tag{2-20}$$

This result shows that the scattered field is a spherically spreading wave* with a polarization determined by the ordinary dipole radiation rules,[7] and with an amplitude and time dependence which is a function of the direction of observation through the integral

---

* This result follows automatically from the assumption that $|\vec{r}|$ is in the far field region of the scattering volume V.

$$\underline{J}(\vec{r},t) = \int_V \Delta\chi(\vec{r}_1,t)\, e^{i(\vec{k}_o-\vec{k}_s)\cdot\vec{r}_1}\, d^3\vec{r}_1 \qquad (2\text{-}21)$$

3. The Spatial Fourier Series Expansion of the Susceptibility Fluctuations

Although the intensity of the scattered light can be calculated[*] directly from Eq. (2-20) in terms of the total fluctuations $\Delta\chi(\vec{r},t)$, the spectrum is obtained more readily[**] by considering only specific wave vector components in a plane wave expansion of $\Delta\chi$. Such an expansion brings about a number of important simplifications in the physical description of the scattering process.

(1) The example given in Section B.1.b illustrated the point that a plane wave fluctuation can cause scattering only in a single direction away from the incident beam. This result is verified in Eq. (2-21) which shows that the "interference" integral is simply the finite domain spatial Fourier transform of the susceptibility fluctuations $\Delta\chi(\vec{r},t)$. The field observed at the point $\vec{r}$ arises from the plane wave components of $\Delta\chi$ having a wave vector $\vec{K} = \pm(\vec{k}_o-\vec{k}_s)$ where $\vec{k}_s = (\omega_o/c_m)\hat{r}$.

(2) The plane wave components of the total entropy and pressure fluctuations responsible[§] for $\Delta\chi$ are homogeneous solutions of their respective thermodynamic equations of motion.[†] As a result, the time dependence of the scattered

---

[*] Chapter 2, Section C.

[**] Chapter 2, Section D.

[§] Chapter 2, Section C.1.

[†] Chapter 2, Sections D.4 and D.5.

field reaching $\vec{r}$ may be obtained in a straightforward manner from the time evolution of thermal fluctuations having wave vector $\vec{K} = \pm(\vec{k}_o - \vec{k}_s)$.

(3) The plane wave expansion of the adiabatic pressure fluctuations gives a description of these disturbances in terms of ordinary sound waves.

In order to take advantage of these simplifications, we make a Fourier decomposition of $\Delta\chi(\vec{r},t)$ using a complete set of orthonormal plane waves as the basis functions. Since the evaluation of the interference integral $\underline{J}(\vec{r},t)$ requires knowing $\Delta\chi(\vec{r},t)$ only in the finite volume V, a particularly useful basis set are the plane wave eigenfunctions or "normal modes" of the closed region V. In this case we have $\Delta\chi$ in terms of a Fourier series expansion as

$$\Delta\chi(\vec{r},t) = \sum_{K} \underline{\Delta\chi_K}(t)\, e^{i\vec{K}\cdot\vec{r}} \tag{2-22}$$

where the allowed $\vec{K}$ values are found by applying the usual cyclic boundary conditions[8] on the surface bounding V.* These conditions lead to an orthogonality relation between waves of different $\vec{K}$ given by

$$\int_V e^{i(\vec{K}-\vec{K}')\cdot\vec{r}}\, d^3\vec{r} = V\delta_{\vec{K},\vec{K}'} \tag{2-23}$$

where $\delta_{\vec{K},\vec{K}'}$ is the Kronecker delta.

---

* Chapter 2, Section E.4.e.

The Fourier amplitudes $\underline{\Delta\chi_K}(t)$ can be expressed in terms of $\Delta\chi(\vec{r},t)$ by inverting Eq. (2-22). With the help of Eq. (2-23) we find easily

$$\underline{\Delta\chi_K}(t) = \frac{1}{V}\int_V \Delta\chi(\vec{r},t)\, e^{-i\vec{K}\cdot\vec{r}}\, d^3\vec{r} \qquad (2\text{-}24)$$

Before evaluating $\underline{J}(\vec{r},t)$ in terms of the $\underline{\Delta\chi_K}(t)$ we note that the right hand side of Eq. (2-22) may be rewritten to make it a sum of explicitly real terms. Since $\Delta\chi(\vec{r},t)$ is real we have

$$\Delta\chi(\vec{r},t) = \frac{1}{2}\,[\Delta\chi(\vec{r},t) + \Delta\chi^*(\vec{r},t)]$$

$$= \frac{1}{2}\left[\sum_K \underline{\Delta\chi_K}(t)e^{i\vec{K}\cdot\vec{r}} + \sum_K \underline{\Delta\chi_K}^*(t)e^{-i\vec{K}\cdot\vec{r}}\right]$$

Grouping terms of the same $\vec{K}$ value gives

$$\Delta\chi(\vec{r},t) = \frac{1}{2}\sum_K \left[\underline{\Delta\chi_K}(t)\, e^{i\vec{K}\cdot\vec{r}} + \underline{\Delta\chi_K}^*(t)\, e^{-i\vec{K}\cdot\vec{r}}\right] \qquad (2\text{-}25)$$

which is the desired result.

With $\Delta\chi(\vec{r},t)$ expanded as in Eq. (2-25), Eq. (2-21) becomes

$$\underline{J}(\vec{r},t) = \frac{1}{2}\sum_{K} \underline{\Delta\chi_K}(t) \int_V e^{i(\vec{k}_o-\vec{k}_s+\vec{K})\cdot\vec{r}_1}\, d^3\vec{r}_1$$

$$+ \frac{1}{2}\sum_{K} \underline{\Delta\chi_K}^*(t) \int_V e^{i(\vec{k}_o-\vec{k}_s-\vec{K})\cdot\vec{r}_1}\, d^3\vec{r}_1 \qquad (2\text{-}26)$$

When all the dimensions of V are large compared to the wavelength of the incident beam, $\lambda = (2\pi/k_o)$, the interference integral

$$I(\vec{r},\vec{K}) = \int_V e^{i(\vec{k}_o-\vec{k}_s+\vec{K})\cdot\vec{r}_1}\, d^3\vec{r}_1 \qquad (2\text{-}27)$$

$$\vec{k}_s = (\omega_o/c_m)\hat{r}$$

vanishes unless $\vec{K}$ assumes the value $\vec{K} = (\vec{k}_o - \vec{k}_s)$.[§] Therefore, the scattered light observed at $\vec{r}$ is contributed by those plane wave components of $\Delta\chi(\vec{r},t)$ with wave vectors[†]

$$\vec{K} = \vec{k}_s - \vec{k}_o \qquad (2\text{-}28)$$

and

$$\vec{K} = -(\vec{k}_s - \vec{k}_o) \qquad (2\text{-}29)$$

[§] Chapter 2, Section E.4.e.

[†] Note that we allow K to be both positive and negative but confine the frequency of the wave to be positive, $\varpi > 0$. An alternate approach[2] is to assign two possible frequencies ($\pm\varpi$) to each wave vector; in this case, one of the conditions in Eqs. (2-28) and (2-29) is superfluous.

These conditions on $\vec{K}$ are simply restatements of Eqs. (2-14) and (2-15) for the case of small frequency shifts, i.e. $\vec{k}_s{}^{+} = \vec{k}_s{}^{-} = \vec{k}_s = (\omega_o/c_m)\hat{r}$.

If we assume that $\vec{K}$ takes on precisely the values $\pm(\vec{k}_s - \vec{k}_o)$, we have the scattered field in the simple form

$$\underline{\vec{E}}_S(\vec{r},t) = \vec{k}_s\times(\vec{k}_s\times\vec{E}_o)\ \frac{e^{i(k_s r-\omega_o t)}}{4\pi r}\ \left(\frac{\varepsilon_o}{\varepsilon}\right)$$

$$\times\frac{V}{2}\ [\underline{\Delta\chi}_{\vec{k}_s-\vec{k}_o}(t) + \underline{\Delta\chi}_{\vec{k}_o-\vec{k}_s}(t)] \qquad (2\text{-}30)$$

This result together with Eq. (2-20) represent the basic expressions for the scattered field which will be useful in analyzing the intensity, spectrum, and spatial coherence properties of the light scattered by entropy and pressure fluctuations in liquids.

If we take $|\vec{k}_o| = |\vec{k}_s|$, then the wave vector of the susceptibility fluctuation responsible for the observed scattering can be expressed in terms of the scattering angle Θ and the azimuthal angle Φ illustrated in Fig. 2-4. For isotropic scattering media like liquids, $|\vec{K}| = |\vec{k}_o-\vec{k}_s|$ is independent of Φ, and we find easily from Fig. 2-5

$$|\vec{K}| = 2k_o \sin(\Theta/2) \qquad (2\text{-}31)$$

$|\vec{K}|$ - the wave vector of the susceptibility fluctuation which causes scattering into an angle Θ away from the incident beam.

$k_o = n(2\pi/\lambda_{air})$ - the wave vector of the incident light as measured in the scattering medium

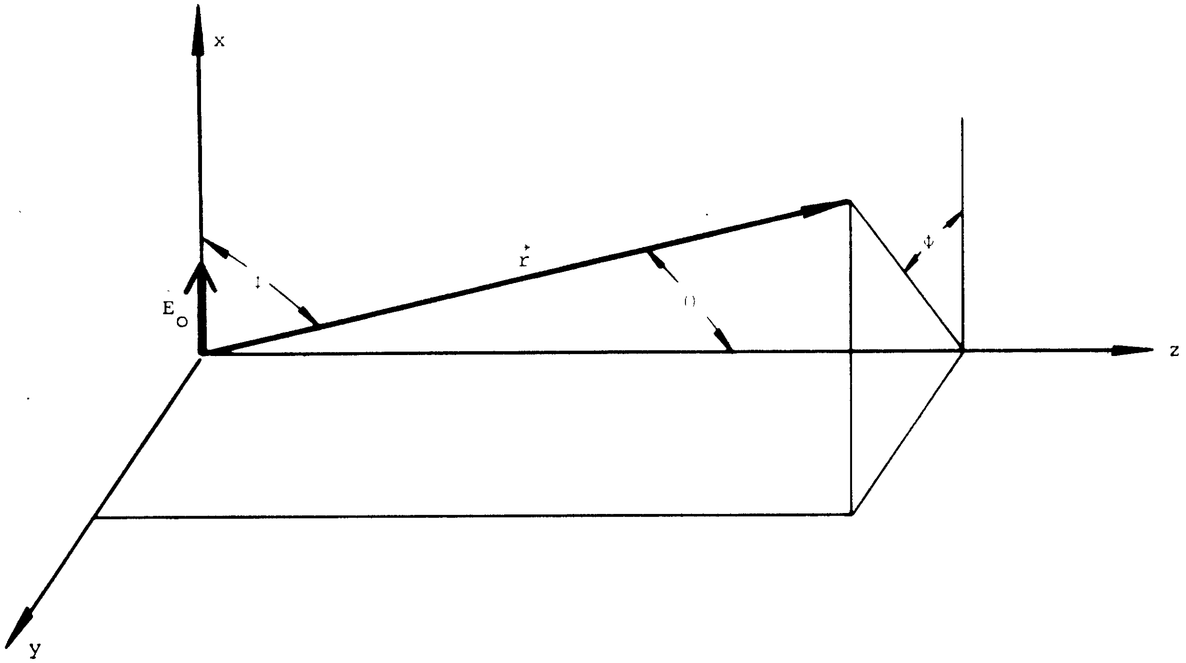
x
$\vec{r}$
E_o
Φ
Θ
z
y

Figure 2-4 The scattering angles Θ and Φ.

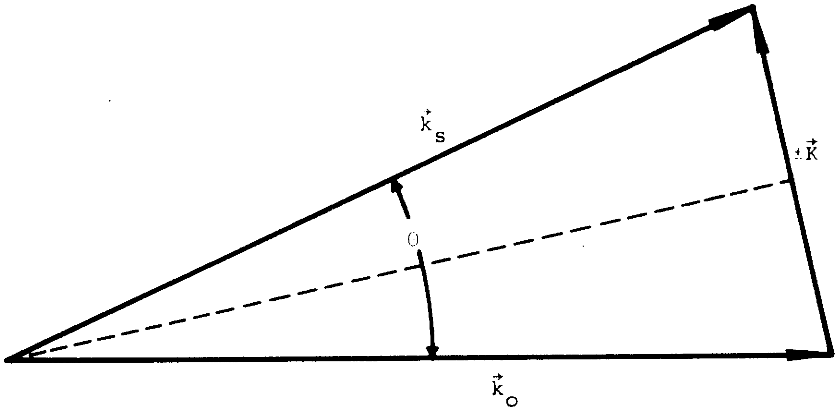
$\vec{k}_s$
$\vec{K}$
Θ
$\vec{k}_o$

Figure 2-5 The wave vector conservation triangle in the limit of small frequency shifts.

C. The Intensity of the Scattered Light

1. Thermal Fluctuations

In order to calculate the intensity of the scattered light we must now specify $\Delta\chi(\vec{r},t)$ in terms of the known properties of the scattering medium. We consider here only that time and position dependence of $\Delta\chi(\vec{r},t)$ which arises from so-called "thermal" fluctuations. These "thermal" disturbances are fluctuations in the "thermodynamic" coordinates of the system about their respective equilibrium values. More precisely, these disturbances represent the statistical fluctuations in local density, temperature, pressure, entropy, etc. which take place[3] in the medium viewed as a single member of a canonical ensemble of identical thermodynamic systems.

Of course, in general, $\chi(\vec{r},t)$ will depend not only on all the "thermodynamic" variables of the medium but also on the molecular orientation,[9] the molecular vibrational and electronic states,[10] and so on. Coupling between fluctuations in these quantities and the electromagnetic field (via $\Delta\chi$) result in additional light scattering phenomena, such as magnon scattering,[11] polariton scattering,[12] anisotropy scattering,[9] and Raman scattering,[10] which are not of direct interest here.

As usual, the exact state of a pure thermodynamic system can be specified completely[13] by giving any two of the thermodynamic coordinates, (ρ,T), (P,T), (V,T), and so on, together with the equation of state. However, since the thermal sound waves responsible for the Brillouin-Mandel'shtam components are adiabatic pressure disturbances, we choose a description in terms of the entropy and pressure. In this case, the fluctuations in the two independent thermodynamic variables of the system contribute separately to distinct features in the spectrum of the scattered light. For this choice of variables we have

$$\Delta\chi(\vec{r},t) = (\partial\chi/\partial s)_P[\Delta s_P(\vec{r},t)] + (\partial\chi/\partial P)_s[\Delta P_s(\vec{r},t)] \qquad (2\text{-}32)$$

Δs_P - the deviation in the entropy per unit volume from its equilibrium value at constant pressure.

ΔP_s - the deviation in the pressure from its equilibrium value at constant entropy.

2. The General Expression for the Scattered Intensity

The scattered intensity reaching the observation point $\vec{r}$ can be calculated from Eq. (2-20) in the form

$$I(\vec{r}) = \sqrt{\varepsilon\varepsilon_o/\mu_o}\left\langle \vec{E}_S(\vec{r},t)\cdot\vec{E}_S(\vec{r},t)\right\rangle$$

$$= \frac{1}{2}\sqrt{\varepsilon\varepsilon_o/\mu_o}\left\langle \underline{\vec{E}}_S(\vec{r},t)\cdot\underline{\vec{E}}_S^{*}(\vec{r},t)\right\rangle \qquad (2\text{-}33)$$

from which we find

$$I(\vec{r}) = I_o\,\frac{|\vec{k}_s\times(\vec{k}_s\times\vec{E}_o)|^2}{(4\pi r)^2}\left(\frac{\varepsilon_o}{\varepsilon}\right)^2 \qquad (2\text{-}34)$$

$$\times\left\langle \int_V\int_V \Delta\chi(\vec{r}_1,t)\,\Delta\chi(\vec{r}_2,t)\,e^{i(\vec{k}_o-\vec{k}_s)\cdot(\vec{r}_1-\vec{r}_2)}\,d^3\vec{r}_1\,d^3\vec{r}_2\right\rangle$$

where $I_o = (1/2)\sqrt{\varepsilon\varepsilon_o/\mu_o}\ |\vec{E}_o|^2$ is the intensity of the incident beam. On writing out the cross product in terms of k_s and ϕ, the angle between $\vec{k}_s$ and $\vec{E}_o$, and taking the time average inside the volume integrals, we obtain

$$I(\vec{r}) = I_o \frac{k_s^4 \sin^2 \phi}{(4\pi r)^2} \left(\frac{\varepsilon_o}{\varepsilon}\right)^2 \tag{2-35}$$

$$\int_V \int_V \left\langle \Delta\chi(\vec{r}_1,t)\Delta\chi(\vec{r}_2,t)\right\rangle e^{i(\vec{k}_o-\vec{k}_s)\cdot(\vec{r}_1-\vec{r}_2)} d^3\vec{r}_1 d^3\vec{r}_2$$

This result can be given in an alternate form by using the spatial plane wave expansion for $\Delta\chi(\vec{r},t)$ which was introduced in Section B.3, viz.

$$\Delta\chi(\vec{r},t) = \sum_K \underline{\Delta\chi_K}(t)\, e^{i\vec{K}\cdot\vec{r}} \tag{2-22}$$

In this case we find

$$I(\vec{r}) = I_o \frac{k_s^4 \sin^2 \phi}{(4\pi r)^2} \left(\frac{\varepsilon_o}{\varepsilon}\right)^2 \sum_K \sum_{K'} \left\langle \underline{\Delta\chi_K}(t)\underline{\Delta\chi_{K'}}^*(t)\right\rangle \tag{2-36}$$

$$\times \int_V \int_V e^{i(\vec{k}_o-\vec{k}_s+\vec{K})\cdot\vec{r}_1}\, e^{-i(\vec{k}_o-\vec{k}_s+\vec{K})\cdot\vec{r}_2}\, d^3\vec{r}_1 d^3\vec{r}_2$$

Equations (2-35) and (2-36) indicate two basic approaches to the problem of determining the intensity of the scattered light. The first, Eq. (2-35), proceeds via a calculation of the mean-square amplitude of the total susceptibility fluctuations $\Delta\chi(\vec{r},t)$ while the second, Eq. (2-36), relates the intensity to the plane-wave-component amplitudes of these fluctuations. The analysis given below follows the first approach, although the scattered intensity is also obtained in terms of $\langle \underline{\Delta\chi}_K(t)\underline{\Delta\chi}_{K'}^*(t)\rangle$ as a by-product of the spectrum calculations presented in Sections D.4 and D.5.

3. The Spatial Correlation Functions and Mean-Square Amplitudes for Pressure and Entropy Fluctuations

The time average $\langle\Delta\chi(\vec{r}_1,t)\Delta\chi(\vec{r}_2,t)\rangle$ required in Eq. (2-35) can be expressed in terms of the entropy and pressure fluctuations with the help of Eq. (2-32) as

$$\begin{aligned}\langle\Delta\chi(\vec{r}_1,t)\Delta\chi(\vec{r}_2,t)\rangle &= (\partial\chi/\partial s)_P{}^2\langle\Delta s_P(\vec{r}_1,t)\Delta s_P(\vec{r}_2,t)\rangle \\ &+ (\partial\chi/\partial P)_s(\partial\chi/\partial s)_P[\langle\Delta P_s(\vec{r}_1,t)\Delta s_P(\vec{r}_2,t)\rangle \\ &\qquad + \langle\Delta s_P(\vec{r}_1,t)\Delta P_s(\vec{r}_2,t)\rangle] \\ &+ (\partial\chi/\partial P)_s{}^2\langle\Delta P_s(\vec{r}_1,t)\Delta P_s(\vec{r}_2,t)\rangle \qquad (2\text{-}37)\end{aligned}$$

From the theory of statistical fluctuations[3] it is known that $\Delta s_P(\vec{r},t)$ and $\Delta P_s(\vec{r},t)$ are random functions of time; therefore, it is impossible to display the time behavior of either quantity in an explicit form.[14] However, since the process of random molecular motion which gives rise to Δs_P and ΔP_s satisfies the ergodic hypothesis,[15] the time averages appearing in the right hand side of Eq. (2-37) may be replaced by statistical averages, namely,

$$\overline{\Delta\chi(\vec{r}_1,t)\Delta\chi(\vec{r}_2,t)} = \left(\frac{\partial\chi}{\partial s}\right)_P^2 \cdot\overline{\Delta s_P(\vec{r}_1,t)\Delta s_P(\vec{r}_2,t)}$$

$$+ \left(\frac{\partial\chi}{\partial P}\right)_s \left(\frac{\partial\chi}{\partial s}\right)_P \left[\overline{\Delta P_s(\vec{r}_1,t)\Delta s_P(\vec{r}_2,t)} + \overline{\Delta s_P(\vec{r}_1,t)\Delta P_s(\vec{r}_2,t)}\right]$$

$$+ \left(\frac{\partial\chi}{\partial P}\right)_s \cdot\overline{\Delta P_s(\vec{r}_1,t)\Delta P_s(\vec{r}_2,t)}$$

The bar indicates a statistical or thermodynamic average over an ensemble of identical and similarly prepared systems. Since the variables P and s are statistically independent,[3] Eq. (2-38) immediately reduces to

$$\overline{\Delta\chi(\vec{r}_1,t)\Delta\chi(\vec{r}_2,t)} = \left(\frac{\partial\chi}{\partial s}\right)_P^2 \cdot\overline{\Delta s_P(\vec{r}_1,t)\Delta s_P(\vec{r}_2,t)}$$

$$+ \left(\frac{\partial\chi}{\partial P}\right)_s^2 \cdot\overline{\Delta P_s(\vec{r}_1,t)\Delta P_s(\vec{r}_2,t)}$$

For a liquid which is in uniform and isotropic equilibrium it is physically plausible to assume that the remaining statistical averages are independent of the origins of the time and space coordinates and are functions only of the separation $|\vec{r}_2 - \vec{r}_1|$. In face, comparing Eq. (2-37) to Eq. (2-105) of Section E.2 shows that the quantities

$$\overline{\Delta s_P(\vec{r}_1,t)\Delta s_P(\vec{r}_2,t)} = \overline{\Delta s_P(\vec{r}_1-\vec{r}_2,0)\Delta s_P(0,0)} = \delta(|\vec{r}_1-\vec{r}_2|) \qquad (2\text{-}40)$$

and

$$\overline{\Delta P_s(\vec{r}_1,t)\,\Delta P_s(\vec{r}_2,t)} = \overline{\Delta P_s(\vec{r}_1-r_2,0)\,\Delta P_s(0,0)} = g(|\vec{r}_1-\vec{r}_2|)$$

(2-41)

are spatial correlation functions for the total fluctuations Δs_P and ΔP_s respectively. From a statistical mechanical viewpoint, then, f and g describe the degree to which the thermal behavior of the medium at the position $\vec{r}_2$ is influenced by its behavior at $\vec{r}_1$.*

Let us define the normalized spatial correlation functions for entropy and pressure fluctuations as

$$\mathcal{F}(\rho) = \frac{\overline{\Delta s_P(\rho,0)\,\Delta s_P(0,0)}}{\overline{\Delta s_P{}^2(0,0)}} \qquad (2\text{-}42)$$

and

$$\mathcal{G}(\rho) = \frac{\overline{\Delta P_s(\rho,0)\,\Delta P_s(0,0)}}{\overline{\Delta P_s{}^2(0,0)}} \qquad (2\text{-}43)$$

respectively.

The important qualitative features of $\mathcal{F}(\rho)$ and $\mathcal{G}(\rho)$ can be given by direct analogy with the behavior of the spatial correlation function for the scattered field which is described in Section E.2. First, both $\mathcal{F}(\rho)$ and $\mathcal{G}(\rho)$ are normalized to give $\mathcal{F}(\rho) = 1$ or $\mathcal{G}(\rho) = 1$ when perfect correlation or linear dependence exists between the time evolutions of the fluctuations appearing at the two points $\vec{r}_1$ and $\vec{r}_2 = \vec{r}_1 + \vec{\rho}$. Perfect correlation is approached in the limit $|\vec{\rho}| \to 0$. Secondly, both functions will tend to zero when the separation ρ is such that the fluctuations at $\vec{r}_1$ and $\vec{r}_1 + \vec{\rho}$ are statistically independent. Thirdly, the separations for which $F(\rho)$ and $G(\rho)$ fall to some predetermined level can be called the entropy and pressure correlation ranges, r_s and r_P respectively. An attempt to raise the entropy at a point $\vec{r}$ results in an entropy increase throughout a volume $v \simeq r_s^3$ surrounding that point. A similar interpretation follows for r_P.

---

* Chapter 2, Section E.2.

On the basis of a molecular model the distances r_s and r_P are determined by the range of the molecular pair-correlation function.* It follows[16] that, in general, $F(\rho)$ and $G(\rho)$ will both decrease rapidly to zero as ρ increases beyond the value $r_s, r_P \simeq a$, where a is the intermolecular distance. This behavior has been verified in liquids on the basis of light and x-ray scattering experiments which examine the angular dependence of the scattered intensity.

The volume integrals in Eq. (2-35) can now be carried out easily. Because r_s and r_P are both small compared to the wavelength of the incident light, we may set

$$\exp\,[i(\vec{k}_o-\vec{k}_s)\cdot(\vec{r}_1-\vec{r}_2)] = \exp\,[i(\vec{k}_o-\vec{k}_s)\cdot\vec{\rho}] = 1$$

in the region of integration where $F(\rho)$ and $G(\rho)$ are nonvanishing. In this case we have

$$I(\vec{r}) = I_o \frac{k_s^4 \sin^2\phi}{(4\pi r)^2}\left(\frac{\varepsilon_o}{\varepsilon}\right)^2 V\left[\left(\frac{\partial\chi}{\partial s}\right)_P^2 \overline{\Delta s_P^2(0,0)}\; v_F^* + \left(\frac{\partial\chi}{\partial P}\right)_s^2 \overline{\Delta P_s^2(0,0)}\; v_G^*\right] \tag{2-44}$$

---

* Chapter 5, Section C.3.

where ν_F^* and ν_G^* are the correlation volumes given by

$$\nu_F^* = 4\pi \int_0 \rho^2 F(\rho)\,d\rho \qquad \nu_G^* = 4\pi \int_0 \rho^2 G(\rho)\,d\rho \qquad (2\text{-}45)$$

These "effective volume" factors determine the extent of the regions over which essentially uniform fluctuations in Δs_P and ΔP_s take place.

The ensemble average mean-square amplitudes $\overline{\Delta s_P^2(0,0)}$ and $\overline{\Delta P_s^2(0,0)}$ are easily obtained by calculating the thermodynamic free energy[3] required to generate an entropy or pressure disturbance at a single point in the medium. For example, an isobaric change in the entropy per unit volume by an amount Δs_P at some arbitrary point in the medium increases the free energy of the system by an amount

$$\overline{\Delta(\text{Free Energy})} = \frac{T}{\rho c_P} \int_V (\Delta s_P)^2 F(r)\,d^3\vec{r}$$

$$= \frac{T}{\rho c_P} (\Delta s_P)^2 \; \nu_F^*$$

c_P - the specific heat at constant pressure per unit mass

ρ - the density

T - the absolute temperature

Similarly, an adiabatic pressure change ΔP_s produces a free energy increase given by

$$\overline{\Delta(\text{Free Energy})} = \frac{1}{B_s}\int_V (\Delta P_s)^2 G(r)\, d^3\vec{r} = \frac{\Delta P_s^{\ 2} \nu_G^{\ *}}{B_s} \qquad (2\text{-}47)$$

B_s - the adiabatic bulk modulus

The required mean-square entropy and pressure fluctuations follow immediately from the methods of Appendix D as

$$\overline{\Delta P_s^{\ 2}(0,0)} = \frac{kTB_s}{\nu_G^{\ *}} \qquad \overline{\Delta s_P^{\ 2}(0,0)} = \frac{k\rho c_P}{\nu_F^{\ *}} \qquad (2\text{-}48)$$

where *k* is Boltzmann's constant.

4. The Total Scattering Cross Section—The Rayleigh Ratio

Equations (2-44) and (2-48) combine to give the scattered intensity as

$$I(\vec{r}) = I_o \frac{k_s^{\ 4} \sin^2 \phi}{(4\pi r)^2} \left(\frac{\varepsilon_o}{\varepsilon}\right) V \left[\left(\frac{\partial \chi}{\partial s}\right)_P^2 k\rho c_P + \left(\frac{\partial \chi}{\partial P}\right)_s^2 kTB_s\right] \qquad (2\text{-}49)$$

This result shows that $I(\vec{r})$ is *independent of the direction of observation* except for the dipole radiation factor $\sin^2 \phi$. However, the form of Eq. (2-49) follows directly from the assumption that both $\hbar_s$ and $\hbar_P$ are small compared to the wavelength of the incident light. In general, the double volume integral in Eq. (2-35), which determines the directional variation of the total intensity, can be written as a sum of two spatial Fourier transforms, namely,

$$\int_V \int_V \longrightarrow (\partial\chi/\partial s)_P V \int_V F(\rho)\, e^{i(\vec{k}_o-\vec{k}_s)\cdot\vec{\rho}}\, d^3\vec{\rho}$$

$$+\ (\partial\chi/\partial P)_s V \int_V G(\rho)\, e^{i(\vec{k}_o-\vec{k}_s)\cdot\vec{\rho}}\, d^3\vec{\rho} \qquad (2\text{-}50)$$

Therefore, the isotropy of the scattered intensity equivalently reflects the fact that the mean-square spatial Fourier amplitudes of entropy and pressure fluctuations are independent of $\vec{K}$ in the range

$$0 \leq |\vec{K}| \leq (1/\lambdabar_s),\ (1/\lambdabar_P)$$

Since the wave vectors of the fluctuations responsible for the scattered light observed at an angle Θ to the incident direction have the magnitude*

$$|\vec{K}| = 2k_o \sin(\Theta/2) = 2(2\pi/\lambda_{air})n \sin(\Theta/2),$$

$I(\vec{r})$ will be independent of Θ when the incident wavelength λ_{air} satisfies the inequalities

$$\lambda_{air} \geq \frac{1}{4\pi n \lambdabar_s},\ \frac{1}{4\pi n \lambdabar_P}$$

For wavelengths in the visible region of the spectrum, and liquid samples at room temperature and atmospheric pressure, we have $\lambda >> (1/\lambdabar_s),\ (1/\lambdabar_P)$ and $I(\vec{r})$ is experimentally found to be accurately independent of the scattering angle. However, in the case of x-ray scattering from a

---

[*] Chapter 2, Section B.3.

liquid we approach $\lambda \leq (1/r)$ and, therefore, obtain the short range behavior of the susceptibility correlation function $\overline{\Delta\chi(\rho,0)\Delta\chi(0,0)}$. Such x-ray measurements show that r for normal liquids, like toluene, is equal to the intermolecular distance $a \simeq 6$ Å within a factor of two.[17,18]

Using the relationships $\varepsilon = \varepsilon_o(1 + \langle\chi\rangle)$ and $1 + \langle\chi\rangle = n^2$, and writing $k_s{}^4 = (\omega_o/c_m)^4 = (\omega_o/c_o)^4 n^4$, we have the intensity in the form

$$I(\vec{r}) = I_o\left(\frac{\omega_o}{c_o}\right)^4 \frac{V}{(4\pi r)^2} \sin^2 \phi \left[\left(\frac{\partial\chi}{\partial s}\right)_P^2 \underline{k}\rho c_P + \left(\frac{\partial\chi}{\partial P}\right)_s^2 \underline{k}TB_s\right] \tag{2-51}$$

By convention we define the Rayleigh ratio as[4]

$$\mathbf{R} = \mathbf{R}_s + \mathbf{R}_P \equiv \frac{r^2}{V} \frac{1}{I_o} \left[\frac{1}{2\pi} \int_{\phi=0}^{2\pi} I(\Theta=90°,\Phi,\phi)\, d\phi\right] \tag{2-52}$$

where $\mathbf{R}_s$ and $\mathbf{R}_P$ are the contributions from entropy and pressure fluctuations respectively. From Eq. (2-51) one finds easily

$$\mathbf{R}_s = \frac{\omega_o^4}{c_o^4} \frac{1}{2(4\pi)^2}\left(\frac{\partial\chi}{\partial s}\right)_P^2 \underline{k}\rho c_P \qquad \text{entropy fluctuations}$$

$$\tag{2-53}$$

$$\mathbf{R}_P = \frac{\omega_o^4}{c_o^4} \frac{1}{2(4\pi)^2}\left(\frac{\partial\chi}{\partial P}\right)_s^2 \underline{k}TB_s \qquad \text{pressure fluctuations}$$

The scattered intensity may be given in terms of $\mathbf{R}$ as

$$I(\vec{r}) = \frac{2I_o V \mathbf{R}}{r^2} \sin^2 \phi \qquad (2\text{-}54)$$

By writing V, the volume of the illuminated region, as the product of a cross sectional area and a length L, we have for the power scattered into a solid angle Ω as

$$P = 2P_o \mathbf{R} L(\sin^2 \phi)\Omega \qquad (2\text{-}55)$$

Therefore, $\mathbf{R}$ represents the fraction of the incident power, P_o, scattered into unit solid angle per unit length of scattering volume.

Appendix B shows that the Rayleigh ratio can be calculated from the definitions of Eq. (2-53) by evaluating the susceptibility derivatives $(\partial\chi/\partial s)_P$ and $(\partial\chi/\partial P)_s$ in terms of the pressure and temperature dependences of the index of refraction. Table I gives values of $\mathbf{R}_s$ and $\mathbf{R}_P$ which are obtained at a temperature of T = 20.0°C from the known static measurements of these quantities and an assumed incident wavelength of λ_{air} = 6328 Å.

Fabelinskii[4] has reviewed the experimental measurements of $\mathbf{R}$ made prior to 1957 while Lundberg, Mooney, and Gardner[19] have presented new data taken with a laser light source. The general agreement with the static theory is good; however, because most of the experimental data were taken on spectrally unresolved light, it is usually impossible to verify the values of $\mathbf{R}_s$ and $\mathbf{R}_P$ separately.

The analysis of the intensity given in this section, based on the treatments of Einstein[20] and Ginzburg,[21] is one of two approaches to the problem. As stated in Section C.2, an alternative method is to calculate the intensity of the light scattered at a given angle Θ by computing the

Table I THE RAYLEIGH RATIOS $\mathbf{R}_p$ AND $\mathbf{R}_s$ FOR SOME TYPICAL SCATTERERS

Material	$\mathbf{R}_p$ - cm^{-1}	$\mathbf{R}_s$ - cm^{-1}
CS_2	2.9×10^{-6}	2.05×10^{-6}
Benzene	2.05×10^{-6}	0.95×10^{-6}
Toluene		0.79×10^{-6}
H_2O	0.45×10^{-6}	0.0040×10^{-6}
Glycerol	0.50×10^{-6}	0.046×10^{-6}
CCl_4		0.61×10^{-6}
Acetone		0.45×10^{-6}
Methanol		0.175×10^{-6}
Fused Quartz		0.00216×10^{-6}
KCl		0.003×10^{-6}
NaCl		0.0025×10^{-6}

Fourier amplitudes $|\underline{\Delta\chi_K}(t)|^2$ directly. Recently, Benedek[22] has carried through such a calculation for a representation of $\underline{\Delta\chi_K}$ in terms of the thermodynamic variables pressure and entropy, or density and temperature. He proves that each Fourier amplitude $\underline{\Delta\chi_K}$ is an independent random variable by showing that the probability for finding an ensemble member with a specified set of amplitudes, $\underline{\Delta\chi_K}$, factors into an extended product* of Gaussians, each depending only on a single amplitude. The variance of each Gaussian is the required mean-square amplitude of the corresponding plane wave fluctuation. The expression obtained for the intensity by this method** is identical to that given in Eq. (2-51).

D. The Spectrum of the Scattered Light

The spectrum of the scattered light is determined by the time dependence of the fluctuations in susceptibility, $\Delta\chi(\vec{r},t)$. If we go back to Eq. (2-20) for the scattered field and use the spatial plane wave expansion for $\Delta\chi$ given in Eq. (2-22), then $\underline{\vec{E}}_S(\vec{r},t)$ may be written in the form

$$\underline{\vec{E}}_S(\vec{r},t) = V\vec{f}(\vec{r})e^{i(k_s r - \omega_o t)}\{\underline{\Delta\chi}_{-K}(t)\} \tag{2-56}$$

where $\vec{K}$ is fixed by the direction of $\vec{r}$ through Eq. (2-31) and $\vec{f}(\vec{r})$ is the time independent factor

$$\vec{f}(\vec{r}) = \frac{\vec{k}_s\times(\vec{k}_s\times\vec{E}_o)}{4\pi r}\left(\frac{\varepsilon_o}{\varepsilon}\right) \tag{2-57}$$

---

* Appendix C.

** Chapter 2, Sections D.4 and D.5.

Assuming that $\Delta\chi$ arises from fluctuations in entropy and pressure we have from Eq. (2-32)

$$\underline{\vec{E}}_S(\vec{r},t) = V\vec{f}(\vec{r})e^{i(k_s r - \omega_o t)} \left\{\left(\frac{\partial\chi}{\partial s}\right)_P [\underline{\Delta s}_{-K}(t)] + \left(\frac{\partial\chi}{\partial P}\right)_s [\underline{\Delta P}_{-K}(t)]\right\} \tag{2-58}$$

In this section we show (1) that the spectrum of the entropy fluctuation term in Eq. (2-58) is a single Lorentzian line centered at the incident frequency ω_o and having an intrinsic width which is dependent on the value of K; and (2) that the quantity $\underline{\Delta P}_K(t)$ represents two sound waves having wave vector $|\vec{K}|$ and traveling in opposite directions. The spectrum of this part of $\vec{E}_S(\vec{r},t)$ gives the two Lorentzian B-M doublet components, each broadened by an amount determined by the sound wave attenuation coefficient.

The spectrum of the scattered light, or more precisely, its power spectral density, is by definition the scattered optical intensity per unit frequency interval. Clearly the spectrum is related to the ordinary Fourier time transform of $\underline{\vec{E}}_S(\vec{r},t)$, the desired power spectral density at any frequency ω being simply $\sqrt{\epsilon\epsilon_o/\mu_o}$ times the square of the Fourier amplitude of that particular frequency. However, $\underline{\vec{E}}_S(\vec{r},t)$ does not satisfy one of the fundamental existence theorems for the Fourier integral; it is not mean-square integrable over the infinite time domain.[23] Therefore, the ordinary Fourier integral does not exist. Even if we were willing to expand $\vec{E}_S$ in a large, but finite, time domain using a Fourier series representation, another problem still remains. Both $\underline{\Delta s}_K(t)$ and $\underline{\Delta P}_K(t)$ are random variables*;

---

* Chapter 2, Section C.

therefore, it is impossible to specify the exact time behavior of either quantity. However, we can get the desired spectral information on the fluctuations as follows.

1. Definitions of the Time Correlation Function and the Power Spectral Density

Suppose that x(t) is a real random variable and that the random process for which x(t) is a sample function is wide sense stationary.[24] Then we define the time correlation function of x(t) as

$$R_x(\tau) = \lim_{T\to\infty} \frac{1}{2T} \int_{-T}^{T} x(t)x(t+\tau)dt = \left\langle x(t)x(t+\tau)\right\rangle \qquad (2\text{-}59)$$

The indicated limit exists provided $R_x(0) = \left\langle x^2(t)\right\rangle$, which is the average "power" in x(t), is finite. This condition can be compared to the normal requirement on x(t) for the existence of the Fourier integral, namely, that x(t) be mean-square integrable in the limit $T\to\infty$. This latter condition demands that the total "energy" in x(t) be bounded.

If $R_x(\tau)$ exists and is absolutely integrable, the power spectral density of x(t) can be given as the Fourier cosine transform

$$S_x(\omega) = (1/2\pi) \int_{-\infty}^{+\infty} R_x(\tau) \cos \omega\tau \, d\tau \qquad (2\text{-}60)$$

The function $S_x(\omega)$ gives the "mean-square x" per unit time per unit frequency interval (or per unit bandwidth) as a function of the frequency ω. By combining Eqs. (2-59) and (2-60) we find that $S_x(\omega)$ is essentially the square of the cosine Fourier amplitudes of $x(t)$; however, the former is normalized in terms of "power" $\langle x^2(t)\rangle$ rather than "energy" $T\langle x^2(t)\rangle$. This normalization allows us to treat random variables, such as the scattered field, which are characterized by infinite total "energy" but finite average "power." In addition, a calculation of $R_x(\tau)$ does not require a knowledge of the precise time evolution of $x(t)$. If the associated random process satisfies the ergodic hypothesis then, as shown in the following section, we need only describe its ensemble average time evolution from some fixed instant.

As written in Eq. (2-59), $R_x(\tau)$ is a symmetric function of τ; therefore, it follows immediately from Eq. (2-60) that $S_x(\omega)$ is also symmetric. Although this symmetry convention is convenient in the mathematical treatment, it should be pointed out that the physical "mean-squared x" per unit bandwidth can exist only for $\omega \geq 0$. Applying Eqs. (2-59) and (2-60) to the simple example $x(t) = \cos \omega_o t$ shows that the physical power spectral density is simply

$$\underset{(\omega\geq 0)}{S(\omega)} = S(\omega) + S(-\omega)$$

2. The Correlation Function for the Scattered Field

The desired spectral information on the scattered field may be obtained from the correlation function

$$R_E(\tau) = R_E(\vec{r},\tau) \equiv \left\langle \vec{E}_S(\vec{r},t)\cdot\vec{E}_S(\vec{r},t+\tau)\right\rangle \tag{2-61}$$

Recalling that $\underline{\Delta s}_{-K}(t) = \underline{\Delta s}_K^{\,*}(t)$ and $\underline{\Delta P}_{-K}(t) = \underline{\Delta P}_K^{\,*}(t)$, we have from Eq. (2-58)

$$R_E(\tau) = \frac{V^2}{4}\,|\vec{f}(\vec{r})|^2 \Bigg[\Bigg\langle e^{i\omega_o\tau}\left(\frac{\partial\chi}{\partial s}\right)_P^2 \underline{\Delta s}_{-K}(t)\,\underline{\Delta s}_{-K}^{\,*}(t+\tau)$$

$$+\, e^{i[2k_s r\,-\,\omega_o(2t+\tau)]}\left(\frac{\partial\chi}{\partial s}\right)_P^2 \underline{\Delta s}_{-K}(t)\,\underline{\Delta s}_{-K}(t+\tau)$$

$$+\, e^{i\omega_o\tau}\left(\frac{\partial\chi}{\partial P}\right)_s \underline{\Delta P}_{-K}(t)\,\underline{\Delta P}_{-K}^{\,*}(t+\tau)$$

$$+\, e^{i[2k_s r\,-\,\omega_o(2t+\tau)]}\left(\frac{\partial\chi}{\partial P}\right)_s^2 \underline{\Delta P}_{-K}(t)\,\underline{\Delta P}_{-K}(t+\tau)$$

$$+ \text{ the complex conjugates of all terms}\Bigg\rangle\Bigg] \tag{2-62}$$

If the characteristic frequencies in $\underline{\Delta s}_K(t)$ and $\underline{\Delta P}_K(t)$ are small compared to the optical frequency ω_o this result becomes

$$R_E(\tau) = \frac{V^2}{4}\,|\vec{f}(\vec{r})|^2 \left(\frac{\partial\chi}{\partial s}\right)_P^2 e^{-i\omega_o\tau}\Big[\left\langle\underline{\Delta s}_K(t)\,\underline{\Delta s}_K^{\,*}(t+\tau)\right\rangle + \text{c.c.}$$

$$+ \left(\frac{\partial\chi}{\partial P}\right)_s e^{-i\omega_o\tau}\left\langle\underline{\Delta P}_K(t)\,\underline{\Delta P}_K^{\,*}(t+\tau)\right\rangle + \text{c.c}\Big] \tag{2-63}$$

In both Eq. (2-62) and Eq. (2-63) we have assumed that cross products such as $\langle \underline{\Delta s}_K(t)\,\underline{\Delta P}_K(t+\tau) \rangle$ vanish identically. A more exact treatment[22] which retains these terms shows that this assumption is valid in the limit in which the spectrum $S_E(\omega)$ consists of three non-overlapping lines corresponding to the Brillouin and central components respectively. For all measurements reported in this thesis, the no-overlap condition is satisfied to excellent approximation.[§]

3. Transformation of the Correlation Functions to Statistical Averages

The correlation functions for the entropy and pressure fluctuations,

$$\underline{R}_{\Delta s}(K,\tau) = \langle \underline{\Delta s}_K(t)\,\underline{\Delta s}_K^{\,*}(t+\tau) \rangle$$

and

$$\underline{R}_{\Delta P}(K,\tau) = \langle \underline{\Delta P}_K(t)\,\underline{\Delta P}_K^{\,*}(t+\tau) \rangle ,$$

are most easily evaluated by expressing them in terms of statistical rather than time averages.

Suppose that the process describing a random variable x(t) is ergodic and stationary in the strict sense.[24] Then we have immediately

$$\langle x(t)x(t+\tau) \rangle = \overline{x(t)x(t+\tau)} = \overline{x(0)x(\tau)} \qquad (2\text{-}64)$$

[§] Chapter 5, Sections B.1, B.2, and C.2.

where the bar denotes an average over an ensemble of identical, similarly prepared systems, for example, an ensemble of identical light scattering experiments. The stationary character of the process guarantees that the ensemble average is independent of the time origin and hence we have chosen t=0 arbitrarily.

Physically, the ensemble average would be performed by measuring x(t) and x(t+τ) on each of the members of the ensemble, multiplying, adding the results, and dividing by the number of members.[25] In the limit as this number approaches infinity the result is the required average

$$\overline{x(t)x(t+\tau)} = \lim_{N\to\infty} \frac{1}{N} \sum_{N} x_i(t)x_i(t+\tau) \tag{2-65}$$

where i labels a particular ensemble member. The counting, however, may be ordered in a different way. Suppose we group together all terms in Σ(N) which have the same values of x(t) and x(t+τ), say x(t) = x_1 and x(t+τ) = x_2 respectively, and write the number of times this particular product appears in Σ(N) as $n(x_1,x_2)$. In this case Eq. (2-65) may be rewritten as

$$\overline{x(t)x(t+\tau)} = \lim_{N\to\infty} \frac{1}{N} \sum_{x_1,x_2} n(x_1,x_2)x_1x_2 \tag{2-66}$$

where $\Sigma(x_1,x_2)$ is to be carried out over all occurring values of x_1 and x_2. Now in the limit N→∞

$$\lim_{N\to\infty} \{n(x_1,x_2)/N\}$$

is just the ensemble average joint probability $\mathbf{p}(x_1,x_2)$ that x(t) has the value x_1 and that x(t+τ) has the value x_2. If x(t) is a continuous random variable, then $\mathbf{p}(x_1,x_2)$

is zero in the limit $N \to \infty$, and it is convenient to introduce the joint probability density

$$\mathbf{P}[x_1 x_2] \equiv \lim_{\substack{N\to\infty \\ dx_1 \to 0 \\ dx_2 \to 0}} \sum_{x_1, x_2} \frac{n(x_1,x_2)}{dx_1 dx_2} \tag{2-67}$$

$\mathbf{P}[x_1,x_2]$ gives the ensemble average probability that in a measurement on any particular member of the ensemble we will find $x_1 \leq x(t) \leq x_1+dx_1$ and $x_2 \leq x(t+\tau) \leq x_2+dx_2$. As $N \to \infty$ we have then

$$\overline{x(t)x(t+\tau)} = \int_{x'=-\infty}^{\infty} \int_{x''=-\infty}^{\infty} x'x'' \; \mathbf{P}[x'(t),x''(t+\tau)]dx'dx'' \tag{2-68}$$

The correlation function can be written in another useful form by factoring the joint probability density $\mathbf{P}[\;\;]$ into a conditional probability density and a simple probability density[27] as

$$\mathbf{P}[x'(t),x''(t+\tau)] = \mathbf{P}[x''(t+\tau)|x'(t)] \; \mathbf{P}[x'(t)] \tag{2-69}$$

$\mathbf{P}[x''(t+\tau)|x'(t)]dx''$ specifies the probability that a single measurement of $x(t+\tau)$ on any member of the ensemble will give $x'' \leq x(t+\tau) \leq x'' + dx''$ if it is known that $x(t)$ had the value x' for that member. $\mathbf{P}[x'(t)]dx'$ gives the simple probability of finding an ensemble member with $x' \leq x(t) \leq x'+dx'$. Equation (2-69) is merely another way of ordering the basic counting process described in Eq. (2-65). In terms of $\mathbf{P}[\;|\;]$ the correlation function $R_x(\tau)$ may be expressed as

$$R_x(\tau) = \overline{x(0)x(\tau)}$$

$$= \int\limits_{x'=-\infty}^{+\infty} \int\limits_{x''=-\infty}^{+\infty} x'x'' \, \mathbf{P}[x''(\tau)\,|x'(0)] \; \mathbf{P}[x'(0)]\,dx'dx'' \tag{2-70}$$

This result is the relationship between the time averaged and ensemble averaged behavior of a random variable which is needed to compute the pressure and entropy correlation functions.

4. The Correlation Function and Power Spectral Density for Isobaric Entropy Fluctuations

Let us first consider the entropy fluctuation term in Eq. (2-63), namely,

$$\underline{R}_{\Delta s}(K,\tau) = \left\langle \underline{\Delta s}_K(t)\,\underline{\Delta s}_K(t+\tau) \right\rangle$$

According to Eq. (2-70) we need the two probability densities $\mathbf{P}[\underline{\Delta s}_K{}''^*(\tau)\ \underline{\Delta s}_K{}'(0)]$ and $\mathbf{P}[\underline{\Delta s}_K{}'(0)]$ in order to evaluate this correlation function using an ensemble averaging technique. However, an explicit calculation of the conditional probability density $\mathbf{P}[\ |\ ]$ implies that we exactly specify the time evolution of the *canonical ensemble* entropy $s(\vec{r},t)$ in every member of the ensemble. In reality we are only able to give the equations of motion for the *thermodynamic* or *ensemble average* entropy of the system $\overline{s(\vec{r},t)}$. Fortunately, $R_{\Delta s}(K,\tau)$ depends only on averaged properties of $\mathbf{P}[\ |\ ]$ which can be obtained directly from thermodynamic considerations.

In order to decide what features of $\mathbf{P}[\underline{\Delta s}_K{}^{\prime\prime *}(t)\,|\,\underline{\Delta s}_K{}^{\prime}(0)]$ are required to evaluate $R_{\Delta s}(K,\tau)$, let us first describe its interpretation in physical terms. This probability density asks that we prepare an ensemble of identical systems all having $\underline{\Delta s}_K = \underline{\Delta s}_K{}^{\prime}$ at the time t=0. This is a very unusual state. First of all, it is not in thermodynamic equilibrium since the statistical average $\overline{\underline{\Delta s}_K(t)}$ is non-zero; rather we have $\overline{\underline{\Delta s}_K(0)} = \underline{\Delta s}_K{}^{\prime}$. However, if we release such an ensemble at t=0, then we expect at some later time t to find that its members have reached thermodynamic equilibrium, i.e.

$$\overline{\underline{\Delta s}_K(t)} = \int \underline{\Delta s}_K{}^{\prime\prime}\, \mathbf{P}[\underline{\Delta s}_K{}^{\prime\prime}(t)\,|\,\underline{\Delta s}_K{}^{\prime}(0)]\, d\underline{\Delta s}_K{}^{\prime\prime} = 0$$

In fact, the ensemble average or thermodynamic entropy $\overline{s}(\vec{r},t)$ relaxes to equilibrium under constant pressure conditions according to the heat diffusion equation[28]

$$\frac{\Lambda}{\rho c_P} \nabla^2 \overline{s(\vec{r},t)} = \frac{\partial \overline{s(\vec{r},t)}}{\partial t} \tag{2-71}$$

where Λ is the thermal conductivity and c_P the specific heat at constant pressure per unit mass. By taking the spatial Fourier transform of this equation we find that the Fourier amplitude $\overline{\underline{s}_K(t)}$ obeys the equation

$$\frac{\Lambda K^2}{\rho c_P} \overline{\underline{s}_K(t)} = - \frac{\partial \overline{\underline{s}_K(t)}}{\partial t} \tag{2-72}$$

Therefore, assuming the initial condition $\overline{\underline{\Delta s}_K(0)} = \underline{\Delta s}_K{}^{\prime}$ we find the solution

$$\overline{\underline{\Delta s}_K(t)} = \underline{\Delta s}_K{}^{\prime}\, e^{-\Gamma t} \tag{2-73}$$

where

$$\Gamma = (\Lambda/\rho c_p)K^2 \tag{2-74}$$

That is, the ensemble average entropy disturbance $\overline{\underline{\Delta s}_K}$ relaxes back to equilibrium exponentially at a characteristic rate Γ. In fact, it is this average time behavior that determines the spectrum of the fluctuations and, hence, of the scattered light. Therefore, we have one of the important properties of $\mathbf{P}[\underline{\Delta s}_K''^*(\tau)|\underline{\Delta s}_K'(0)]$, namely

$$\overline{\underline{\Delta s}_K^*(\tau)} = \int \underline{\Delta s}_K''^* \, \mathbf{P}[\underline{\Delta s}_K''^*(\tau)|\underline{\Delta s}_K'(0)]\, d\underline{\Delta s}_K''^* = \underline{\Delta s}_K'^* e^{-\Gamma\tau} \tag{2-75}$$

We can now show that the average $\overline{\underline{\Delta s}_K^*(\tau)}$ is sufficient information to compute the desired correlation function $\underline{R}_{\Delta s}(K,\tau)$. Writing out $\underline{R}_{\Delta s}(K,\tau)$ explicitly in terms of the conditional probability density $\mathbf{P}[\ |\ ]$ yields

$$\underline{R}_{\Delta s}(K,\tau) = \int \int (\underline{\Delta s}_K''^*)(\underline{\Delta s}_K')\, \mathbf{P}[\underline{\Delta s}_K''^*(\tau)|\underline{\Delta s}_K'(0)]$$

$$\times \quad [\underline{\Delta s}_K'(0)]\; d\underline{\Delta s}_K''^* \; d\underline{\Delta s}_K' \tag{2-76}$$

The $\underline{\Delta s}_K''^*(\tau)$ integral is identically $\overline{\underline{\Delta s}_K^*(\tau)}$ as given in Eq. (2-75). Therefore, Eq. (2-76) simplifies to the form

$$\underline{R}_{\Delta s}(K,\tau) = e^{-\Gamma\tau} \int \underline{\Delta s}_K'(0)\,\underline{\Delta s}_K'^*(0)\; \mathbf{P}[\underline{\Delta s}_K'(0)]\; d[\underline{\Delta s}_K'(0)] \tag{2-77}$$

The remaining integral over $\underline{\Delta s}_K(0)$ is just the ensemble average mean-square amplitude of the entropy fluctuation with wave vector K. Using the assumed equivalence of time and ensemble averaging we have

$$R_{\Delta s}(K,\tau) = e^{-\Gamma\tau}\,\overline{|\underline{\Delta s}_K(0)|^2} = e^{-\Gamma\tau}\left\langle|\underline{\Delta s}_K(t)|^2\right\rangle \qquad (2\text{-}78)$$

This result points out the two pieces of information which are contained in the correlation function $R_{\Delta s}(K,\tau)$. The first is its τ behavior which, via Eqs. (2-60) and (2-63) determines the power spectral density of both $\underline{\Delta s}_K(t)$ and the scattered field. The derivation leading to Eq. (2-77) shows that this τ dependence is fixed completely by the equations of motion for the thermodynamic variables of the system. Secondly, the correlation function evaluated at $\tau=0$ gives the mean-square amplitude of the corresponding entropy fluctuation and, therefore, is proportional to the intensity[§] in the central component of the scattered light observed at an angle Θ $[K = 2k_o \sin(\Theta/2)]$ to the incident beam.

The calculation of the probability density $\mathbf{P}[\underline{\Delta s}_K(0)]$ which is outlined in Appendix C yields the result

$$\mathbf{P}[\underline{\Delta s}_K(0)] = \sqrt{\frac{V}{2\pi\underline{k}\rho c_p}}\;\exp\left[-\frac{V|\underline{\Delta s}_K(0)|^2}{2\underline{k}\rho c_p}\right] \qquad (2\text{-}79)$$

from which we find

[§] Chapter 2, Section C.

$$\overline{|\underline{\Delta s}_K(0)|^2} = \left\langle |\underline{\Delta s}_K(t)|^2 \right\rangle = \frac{\underline{k}\rho c_P}{V} \qquad (2\text{-}80)$$

Therefore, the entropy fluctuation time correlation function has the form

$$R_{\Delta s}(K,\tau) = \frac{\underline{k}\rho c_P}{V} e^{-\Gamma\tau} \qquad (2\text{-}81)$$

where

$$\Gamma = (\Lambda/\rho c_P)K^2 \qquad (2\text{-}82)$$

From the derivation of Eq. (2-81) it follows that $R_X(K,\tau)$ for any thermodynamic variable X can be evaluated by the simple two steps of (1) computing the mean-square amplitude of the corresponding fluctuation $\Delta X_K(t)$ and (2) multiplying by the normalized solution of the differential equation that governs the time evolution of $\overline{X}_K$.

The power spectral density of $\underline{\Delta s}_K(t)$ can now be found by taking the Fourier cosine transform of the correlation function. Using Eq. (2-60) we have

$$S_{\Delta s}(\omega,K) \equiv \frac{1}{2\pi}\int_{-\infty}^{\infty} R_{\Delta s}(K,\tau)\cos\omega\tau\, d\tau$$

from which it follows that

$$\underset{(\omega\geq 0)}{S_{\Delta s}(\omega,K)} = \left(\frac{\underline{k}\rho c_P}{V}\right)\frac{(2\Gamma/\pi)}{\omega^2+\Gamma^2} \qquad (2\text{-}83)$$

Thus the spatial plane wave component of the entropy fluctuations with wave vector K has a Lorentzian power spectral density with its maximum value at $\omega=0$ and a width at half-height of Γ rad/sec.

Let us now go back and calculate the entropy contribution to the correlation function of the scattered field, $[R_E(\vec{r},\tau)]_{\Delta s}$, and its associated power spectral density. From Eqs. (2-63) and (2-81) we have

$$[R_E(\vec{r},\tau)]_{\Delta s} = \frac{V}{2} |\vec{f}(\vec{r})|^2 \left(\frac{\partial \chi}{\partial s}\right)_P \cdot (\underline{k}\rho c_P) e^{-\Gamma\tau} \cos \omega_o \tau$$

where[§]

$$|\vec{f}(\vec{r})|^2 = \frac{k_s^4 \sin^2 \phi}{(4\pi r)^2} \left(\frac{\varepsilon_o}{\varepsilon}\right)^2 E_o^2$$

Evaluated at $\tau=0$, $[R_E(\vec{r},\tau)]_{\Delta s}$ gives $\sqrt{\mu_o/\varepsilon\varepsilon_o}$ times the total intensity observed at the point $\vec{r}$ as a result of scattering from entropy fluctuations. This expression may be compared with the calculations of Section C as summarized in Eq. (2-49).

For the power spectral density of the scattered field we have

$$[S_E(\omega)]_{\Delta s} = \frac{1}{2\pi} \int_{-\infty}^{\infty} [R_E(\vec{r},0)]_{\Delta s} e^{-\Gamma\tau} \cos(\omega_o\tau) \cos(\omega\tau)\, d\tau$$

The integration is straightforward and yields

$$\underset{(\omega\geq 0)}{[S_E(\omega)]_{\Delta s}} = [R_E(\vec{r},0)]_{\Delta s} \frac{(\Gamma/\pi)}{(\omega-\omega_o)^2 + \Gamma^2} \tag{2-85}$$

or equivalently

$$\underset{(\omega\geq 0)}{[S_E(\omega)]_{\Delta s}} = \left\langle |\vec{E}_S(\vec{r},t)|^2 \right\rangle_{\Delta s} \frac{(\Gamma/\pi)}{(\omega-\omega_o)^2 + \Gamma^2} \tag{2-86}$$

[§] Chapter 2, Section B, Eq. (2-57)

The factor Γ depends on the direction of observation, $\hat{r}$, through the relations $\Gamma = (\Lambda/\rho c_p)K^2$ and $K = 2k_o \sin(\Theta/2)$, where Θ is the scattering angle.

Equation (2-86) shows that if we illuminate a medium with monochromatic light of frequency ω_o and observe the light scattered at an angle Θ to the incident beam, then this light has a component with a Lorentzian spectrum centered at the incoming frequency ω_o. The natural breadth of this "unshifted" component varies with the scattering angle Θ, its half-width at half-height being given by

$$\Gamma = (\Lambda/\rho c_p)[2k_o \sin(\Theta/2)]^2 \qquad (2\text{-}87)$$

The line width assumes its maximum value, Γ_{max}, for backscattering ($\Theta = 180°$) and goes to zero in the forward direction ($\Theta = 0°$). Table II gives values of $(\Gamma_{max}/2\pi)$ computed for a number of liquids and a few isotroptic solids assuming an incident wavelength $\lambda_{air} = 6328$ Å. The values of Λ, ρ, and c_p used in these calculations were those corresponding to room temperature and atmospheric pressure.

5. The Correlation Function and Power Spectral Density for Adiabatic Pressure Fluctuations

In this section we consider the pressure term in the correlation function for the scattered field, namely,

$$\underline{R}_{\Delta P}(K,\tau) = \left\langle \underline{\Delta P}_K(t)\,\underline{\Delta P}_K^*(t+\tau) \right\rangle$$

The pressure fluctuation correlation function may be evaluated by the same statistical ensemble averaging technique

Table II PREDICTED CENTRAL LINE WIDTH ($\Gamma_{max}/2\pi$) FOR SOME TYPICAL SCATTERERS

Material	Λ watts/cm°C	$(\Gamma_{max}/2\pi)$ Mc/sec	n, ρ, c_p
CS_2	1.61×10^{-3}	21.2	
Benzene	1.32×10^{-3}	12.4	
Toluene	1.38×10^{-3}	13.3	
H_2O	6.18×10^{-3}	16.4	
Glycerol	2.9×10^{-3}	13.6	
CCl_4	1.06×10^{-3}	10.5	*
Acetone	1.6×10^{-3}	10.6	
Methanol	2.09×10^{-3}	11.6	
KCl	69.6×10^{-3}	712	
NaCl	69.7×10^{-3}	556	

---

[*] The required values of n, ρ, and c_p are given in Table BI, Appendix B.

presented in the preceding section for entropy fluctuations. Because the methods employed in both cases are identical, we will here proceed by the simple two-step technique suggested there; namely, $\left\langle \underline{\Delta P}_K(t)\, \underline{\Delta P}_K^{*}(t+\tau) \right\rangle$ is given by the product of the mean-square amplitude $\left\langle |\underline{\Delta P}_K(t)|^2 \right\rangle$ and the normalized solution of the governing differential equation.

We can immediately calculate $\left\langle |\underline{\Delta P}_K(t)|^2 \right\rangle$ from the probability density $\mathbf{P}[\underline{\Delta P}_K(0)]$ derived in Appendix C as

$$\left\langle |\underline{\Delta P}_K(t)|^2 \right\rangle = \overline{|\underline{\Delta P}_K(0)|^2} = \frac{kTB_s}{V} \qquad (2\text{-}88)$$

where B_s is the adiabatic bulk modulus, and V is the illuminated volume.

The description of the elastic behavior of a compressible continuum which is needed to determine the time evolution of the pressure fluctuation, is in its complete generality given by the solutions of the hydrodynamic equations.[29] However, several important simplifying assumptions can be made in the present instance. For example, if we evaluate the root-mean-square amplitude of $\underline{\Delta P}_K(t)$ from Eq. (2-88), using $V = 0.1\ \mathrm{cm}^3$ and $T = 300°\mathrm{K}$, we find for a typical liquid

$$[\overline{|\underline{\Delta P}_K(t)|^2}] \simeq 10^{-7}\ \mathrm{atm}$$

Under these conditions the hydrodynamic equations may be linearized[30] in terms of small deviations of the pressure and fluid velocity from their equilibrium values. Secondly, by confining our attention to liquids or solids, we find that the effects of heat conduction on the propagation of the thermal sound waves responsible for the Brillouin-Mandel'shtam doublet may be neglected. Therefore, terms in the linearized equations of motion involving gradients of the temperature can be dropped. Liquids exhibit the additional simplifying feature of having zero shear rigidity. This leads to purely longitudinal disturbances for which we can write a simple one dimensional differential equation.

These assumptions lead to the usual Navier-Stokes equation

$$\rho\left(\frac{\partial u}{\partial t}\right) = -\frac{\partial P}{\partial x_1} + \left(\frac{4}{3}\eta + \eta'\right)\frac{\partial^2 u}{\partial x^2} \qquad (2\text{-}89)$$

where u is the fluid velocity in the direction x_1, which we choose to be the direction of $\vec{K}$. The quantities η and η' are the shear and compressional viscosities respectively.[31] The required equation of motion for the adiabatic pressure can now be obtained by specifying the adiabatic equation of state for the medium. In terms of the pressure and fluid velocity we have for a liquid[32]

$$(1/B_s)(\partial P_s/\partial t) = -(\partial u/\partial x_1) \qquad (2\text{-}90)$$

Taking the partial derivative of the Navier-Stokes equation with respect to x_1, and using Eq. (2-90), gives

$$\frac{\rho}{B_s}\frac{\partial^2 P_s}{\partial t^2} = \frac{\partial^2 P_s}{\partial x_1{}^2} + \frac{1}{B_s}\left(\frac{4}{3}\eta + \eta'\right)\frac{\partial^3 P_s}{\partial x_1{}^2\partial t} \qquad (2\text{-}91)$$

which is a damped wave equation for P. The desired differential equation for $\underline{\Delta P}_K(t)$ is simply the spatial Fourier transform of this result

$$\frac{\rho}{B_s}\frac{\partial^2[\underline{\Delta P}_K(t)]}{\partial t^2} = -K^2[\underline{\Delta P}_K(t)] - \frac{K^2}{B_s}\left(\frac{4}{3}\eta + \eta'\right)\frac{\partial[\underline{\Delta P}_K(t)]}{\partial t} \qquad (2\text{-}92)$$

To calculate the pressure correlation function $\underline{R}_{\Delta P}$ we need the general solution to this equation which is unity at time t=0. This is most easily found by assuming a solution of the form $\underline{\Delta P}_K(t) = \exp(\xi t)$. Substitution of this proposed solution into Eq. (2-92) yields a quadratic algebraic equation in ξ whose roots in the limit of small damping are

$$\xi_{\pm} = -\frac{K^2}{2\rho}\left(\frac{4}{3}\eta + \eta'\right) \pm i\sqrt{\frac{B_s}{\rho}}\ K \tag{2-93}$$

The corresponding solutions for $\underline{\Delta P}_K(t)$

$$\underline{\Delta P}_K(t) = \exp\left[-\frac{K^2}{2\rho}\left(\frac{4}{3}\eta + \eta'\right)t\right]\exp\left[\pm i\sqrt{\frac{B_s}{\rho}}\ Kt\right] \tag{2-94}$$

show that the adiabatic pressure fluctuations with wave vector $\vec{K}$ are damped propagating waves with a frequency

$$\varpi_K = (B_s/\rho)^{\frac{1}{2}}K$$

traveling in opposite directions with a phase velocity

$$v_s = (\varpi/K) = (B_s/\rho)^{\frac{1}{2}}$$

Of course, this velocity v_s is just the velocity of ordinary sound in the medium.

According to Eq. (2-94) the thermally excited sound waves exhibit a characteristic damping rate, γ_K, given by

$$\gamma_K = \frac{K^2}{2\rho}\left(\frac{4}{3}\eta + \eta'\right) = \frac{\varpi_K^{\ 2}}{2\rho v_s^{\ 2}}\left(\frac{4}{3}\eta + \eta'\right) \tag{2-95}$$

and showing the classic ϖ^2 dependence.[33] This damping rate is related to the spatial decay constant, α, normally measured in ordinary ultrasonic experiments, by the identity

$$\alpha_K = \frac{\gamma_K}{v_s} = \frac{\varpi_K{}^2}{2\rho v_s{}^3}\left(\frac{4}{3}\eta + \eta'\right) \tag{2-96}$$

The approximation used in obtaining the roots $\xi_\pm$ displayed in Eq. (2-93) involved assuming that $\gamma_K << \varpi_K$; it follows from Eq. (2-96) that this approach is equivalent to assuming that the sound wave in question is not appreciably damped in a distance of one acoustic wavelength.

The general normalized solution to the Navier-Stokes equation can now be written as

$$e^{-\gamma_K\tau}[ae^{i\varpi_K\tau} + be^{-i\varpi_K\tau}]$$

where (a + b) = 1. Combined with the mean-square amplitude factor given in Eq. (2-88) this result leads immediately to the correlation function $\underline{R}_{\Delta P}(K,\tau)$ as

$$\underline{R}_{\Delta P}(K,\tau) = \left\langle \underline{\Delta P}_K(t)\underline{\Delta P}_K{}^*(t+\tau)\right\rangle$$

$$= \frac{k\underline{T}B_s}{V} e^{-\gamma_K\tau}[ae^{i\varpi_K\tau} + be^{-i\varpi_k\tau}] \tag{2-97}$$

Calculating the power spectral density of $\underline{\Delta P}_K(t)$ according to Eq. (2-60) gives

$$\underset{(\omega\geq 0)}{S_{\Delta P}(\omega,K)} = \frac{k\underline{T}B_s}{V} \frac{(\gamma_K/\omega)}{(\omega-\omega_K)^2 + \gamma_K{}^2} \tag{2-98}$$

That is, the pressure fluctuations of wave vector K have a Lorentzian spectrum centered at the sound wave frequency ϖ_K and with a half-width at half-height of γ_K rad/sec.

The pressure part of the correlation function for the scattered field follows directly from Eqs. (2-97) and (2-63) as

$$[R_E(\vec{r},\tau)]_{\Delta P} = \frac{V}{2}\,|\vec{f}(\vec{r})|^2\left(\frac{\partial\chi}{\partial P}\right)_s\cdot(\underline{k}TB_s)e^{-\gamma_K\tau}$$

$$\times[a\cos(\omega_o-\varpi_K)\tau + b\cos(\omega_o+\varpi_K)\tau] \qquad (2\text{-}99)$$

Evaluated at $\tau=0$, $[R_E(\vec{r},\tau)]_{\Delta P}$ gives the total mean-square field $\left\langle|\vec{E}_S(\vec{r},t)|^2\right\rangle_{\Delta P}$ observed at $\vec{r}$ due to scattering from spontaneous pressure fluctuations in the sample. The wave vector of the fluctuation responsible for this scattering is given in Eq. (2-31).

The power spectral density of the scattered field follows from Eq. (2-99) as

$$\underset{(\omega\geq 0)}{[S_E(\omega)]_{\Delta P}} = \frac{2}{\pi}\int_0^\infty \left\langle|\vec{E}_S(\vec{r},t)|^2\right\rangle_{\Delta P} e^{-\gamma_K\tau} \qquad (2\text{-}100)$$

$$\times[a\cos(\omega_o-\varpi_K)\tau + b\cos(\omega_o+\varpi_K)\tau]\cos\omega\tau\, d\tau$$

from which we obtain

$$\underset{(\omega\geq 0)}{[S_E(\omega)]_{\Delta P}} = \left\langle|\vec{E}_S(\vec{r},t)|^2\right\rangle_{\Delta P}\left[\frac{a(\gamma_K/\pi)}{[\omega-(\omega_o+\varpi_K)]^2+\gamma_K{}^2}\right.$$

$$\left.+\frac{b(\gamma_K/\pi)}{[\omega-(\omega_o-\varpi_K)]^2+\gamma_K{}^2}\right] \qquad (2\text{-}101)$$

Therefore, we find that the light scattered from pressure fluctuations of wave vector K has a spectrum consisting of two Lorentzian components, one centered above the incident frequency ω_o by an amount ϖ_K and the other below ω_o by the same amount. Besides being shifted by the sound wave frequency ϖ_K, both components are broadened because of the acoustic attenuation so that each Lorentzian exhibits a half-width at half-height of γ_K rad/sec. Figure 2-6 illustrates the spectrum of the light observed at an angle Θ to the incident beam, $K = 2k_o \sin(\Theta/2)$, including both the doublet components and the unshifted line.

As was stated in Section B of this chapter, the splitting of the doublet corresponds classically to the Doppler shift imposed on the incident light because of the motion of the scattering fluctuation, in this case, a thermally excited sound wave. Quantum mechanically, the two terms in Eq. (2-101) represent respectively the annihilation and creation of a single thermal phonon. This interpretation also fixes the values of a and b; at room temperature ($\underline{k}T \gg \hbar\varpi_K$) the transition probabilities for annihilation and creation are equal[2] and we have a = b = 1/2. It follows that the total scattered intensity contained in the "pressure fluctuations" term in Eq. (2-51) actually represents the total power in both of the Brillouin-Mandel'shtam components.

With the help of Eq. (2-31) the frequency shift ϖ_K and the line width γ_K can be expressed as a function of the scattering angle Θ as

$$\varpi_K = v_s K = 2k_o v_s \sin(\Theta/2) \qquad (2\text{-}102)$$

$$\gamma_K = \frac{\varpi_K^2}{2\rho v_s^2}\left(\frac{4}{3}\eta + \eta'\right) = \alpha_K v_s \qquad (2\text{-}103)$$

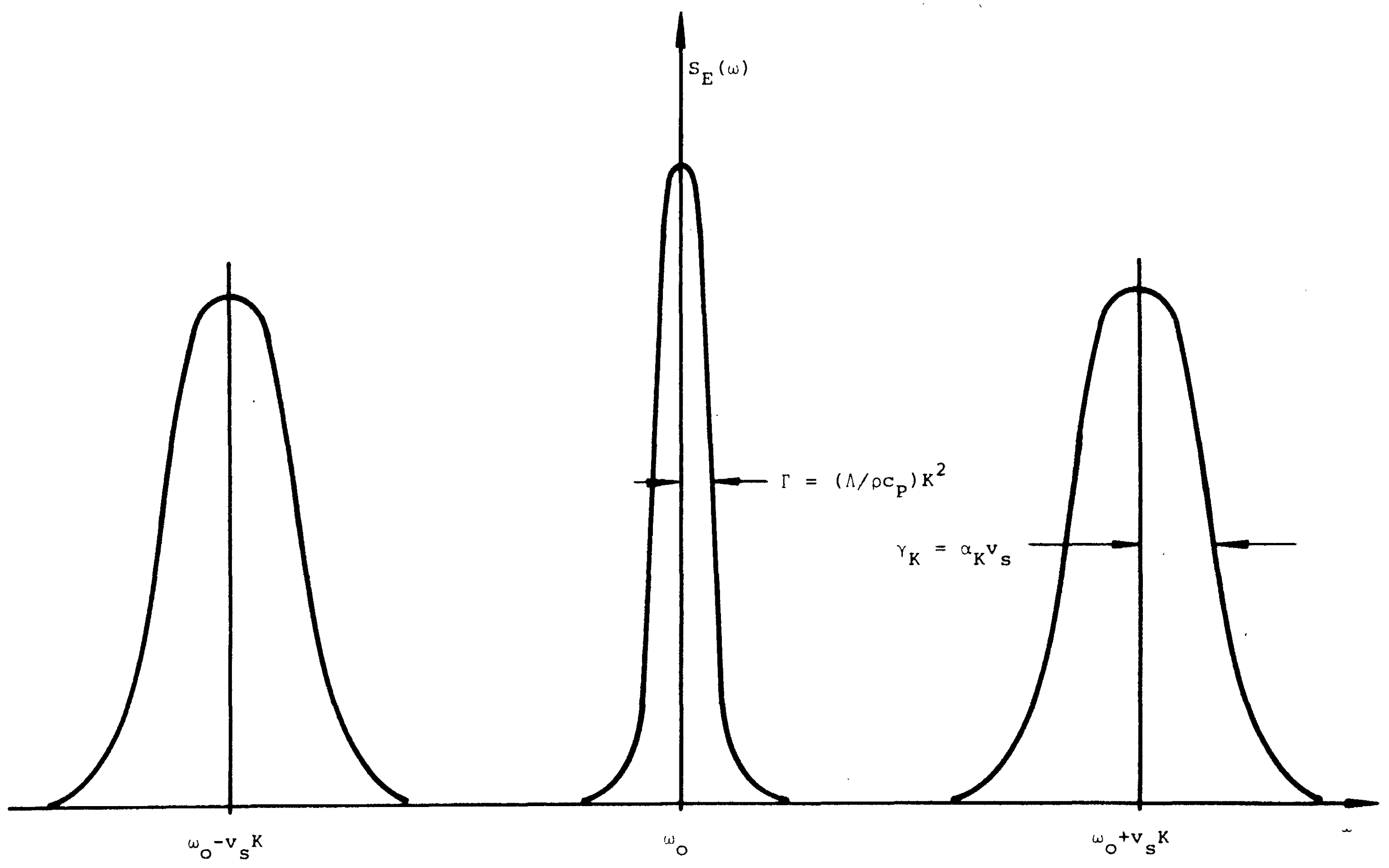
$S_E(\omega)$
$\Gamma = (\Lambda/\rho c_P)K^2$
$\gamma_K = \alpha_K v_s$
$\omega_o - v_s K$
ω_o
$\omega_o + v_s K$

Figure 2-6 The theoretical spectrum for the light scattered by thermal fluctuations in liquids.

Table III THE PREDICTED SPLITTINGS AND LINE WIDTHS FOR SOME TYPICAL SCATTERERS

	v_s	$\frac{\alpha}{v^2}$	$\Theta = 1°$		$\Theta = 10°$		$\Theta = 180°$	
	cm/sec ($\times 10^5$)	sec^2/cm ($\times 10^{-17}$)	$\varpi/2\pi$ Mc/sec	$\gamma/2\pi$ Mc/sec	$\varpi/2\pi$ Mc/sec	$\gamma/2\pi$ Mc/sec	$\varpi/2\pi$ Mc/sec	$\gamma/2\pi$ Mc/sec
CS_2	1.158	5800	51.9	2.88	517	286	5940	37,720
Benzene	1.317	800	54.4	0.49	543	49.4	6233	6515
Toluene	1.317	85	54.2	0.052	541	5.2	6212	687
H_2O	1.492	25.3	54.8	0.018	547	1.8	6280	237
Glycerol	1.915		77.8		777		8910	
CCl_4	0.940	533	37.8	0.114	377	11.3	4331	1495
Acetone	1.190	54.2	44.6	0.020	445	2.0	5106	267
Methanol	1.114	37	40.8	0.011	407	1.1	4675	143
Fused Quartz	5.968	0.025	240	0.0014	2395	0.14	27,480	18
KCl	4.470	1.1	183	0.026	1832	2.6	21,022	345
NaCl	4.744	0.5	202	0.015	2015	1.5	23,120	202

or with k_o written in terms of the incident wavelength, λ_{air}, and the index of refraction of the scattering medium, n, as

$$\varpi_K = 2(2\pi/\lambda_{air})nv_s \sin(\Theta/2) \qquad (2\text{-}104)$$

Table III gives values of $(\varpi_K/2\pi)$ and $(\gamma_K/2\pi)$ in some typical materials for the three angles, $\Theta = 1°$, $\Theta = 10°$, and $\Theta = 180°$. These results were calculated on the basis of low frequency ultrasonic values of v_s and α and an incident wavelength $\lambda_{air} = 6328$ Å. In each case γ_K was determined by an extrapolation of α based on an assumed ϖ^2 dependence. Such a procedure is known to fail in some liquids where B_s, η and η' are, in fact, functions of the frequency of the sound wave.[34] In general this frequency dependence takes the form of a relaxation, the usual result being an increase in v_s with increasing frequency and an attenuation which falls below the ϖ^2 extrapolated result. Surprisingly enough in view of the predictions of Table III, no liquid whose Brillouin spectrum has been studied has ever shown a broadening comparable to the frequency shift.

E. The Spatial Coherence Properties of the Scattered Field

1. Introduction

Having calculated both the total intensity and the spectral distribution of the scattered light, we turn in this section to a description of two additional characteristics of the scattered electric field. These are: (1) the geometrical shape of its constant phase surfaces, i.e. its wavefronts, and (2) the range of spatial coherence on each of these wavefronts.

As it is used here the term spatial coherence refers to a mutual dependence or correlation[35] between the time behaviors of the instantaneous electric field amplitudes observed at two spatially separated points $\vec{r}_1$ and $\vec{r}_2$. To describe this correlation quantitatively we introduce the spatial correlation function, a suitably normalized ensemble average of the product of the electric fields $\vec{E}_S(\vec{r}_1,t)$ and $\vec{E}_S(\vec{r}_2,t)$. The desired information on the range of spatial coherence is contained in the variation in the magnitude of this average as a function of the separation $(\vec{r}_2 - \vec{r}_1)$.

In this section we will determine the general behavior and average range of this correlation function when both $\vec{r}_1$ and $\vec{r}_2$ lie on the surface of a sphere Q centered on the scattering volume V and having a radius much larger then the maximum dimension of V. This calculation demonstrates an unusually close relationship between spatial coherence properties and simple diffraction theory; the total scattered field reaching Q can be expressed as the sum of a set of far field diffraction or antenna patterns of the three-dimensional "source" V. We find that there is no time average correlation between the electric fields of two different diffracted beams while perfect correlation exists at all separations $(\vec{r}_2 - \vec{r}_1)$ for the field of a single diffracted beam. As a result the behavior of the spatial correlation function versus $(\vec{r}_2 - \vec{r}_1)$ is determined completely by the electric field amplitude distribution in the ordinary diffraction pattern of the scattering volume.

The motivation for studying the spatial coherence characteristics of the scattered field is provided by the calculations given in Sections C.2.a.2 and D.3.a of Chapter 3. These results show that the usefulness of an optical mixing spectrometer is determined _not_ by the total available scattered power, but rather by the amount of power scattered into the solid angle of a single _diffracted beam_. The size of this "coherence solid angle" depends on three factors; (1) the shape of the scattering volume V, (2) the scattering angles Θ and Φ, and (3) the variation of the incident light intensity in a plane normal to the direction of the incoming beam, $\vec{k}_o$.

For purposes of presenting some explicit calculations of tpyical coherence properties we consider a rectangular parallelopiped scattering volume and an incident intensity profile which corresponds to a laser light source operating in the so-called uni-phase* or fundamental transverse modes, TEM_{ooq}. For this type of source, a semiquantitative description of the spatial coherence function can be obtained easily from the geometrical properties of the reciprocal or K-space lattice of points representing the wave vectors K_j used in the Fourier series expansion** of the susceptibility fluctuations $\Delta\chi(\vec{r},t)$.

2. The Definition and General Properties of the Spatial Correlation Function

To measure the degree of coherence between the scattered fields observed at the two separated points $\vec{r}$ and $\vec{r}+\vec{\rho}$ we define the spatial correlation function $\underline{T}(\vec{r},\vec{\rho})$ as follows:

---

* Chapter 4, Section B.2.

** Chapter 2, Section B.

$$\underline{T}(\vec{r},\vec{\rho}) \equiv \frac{\overline{\underline{\vec{E}}_S{}^*(\vec{r}+\vec{\rho},t)\cdot\underline{\vec{E}}_S(\vec{r},t)}}{[\overline{\underline{\vec{E}}_S{}^*(\vec{r},t)\cdot\underline{\vec{E}}_S(\vec{r},t)}]^{\frac{1}{2}}[\overline{\underline{\vec{E}}_S(\vec{r}+\vec{\rho},t)\cdot\underline{\vec{E}}_S(\vec{r}+\vec{\rho},t)}]^{\frac{1}{2}}} \tag{2-105}$$

The bar denotes a statistical average taken over an ensemble of identical light scattering experiments generating all possible behaviors of the random variable $\underline{\vec{E}}_S(\vec{r},t)$. Since we assume that $\underline{\vec{E}}_S(\vec{r},t)$ is strict sense stationary, and also satisfies the ergodic hypothesis, $\underline{T}(\vec{r},\vec{\rho})$ is independent of t and may be written[36] in an equivalent time averaged form as

$$\underline{T}(\vec{r},\vec{\rho}) = \frac{\left\langle\underline{\vec{E}}_S{}^*(\vec{r}+\vec{\rho},t)\cdot\underline{\vec{E}}_S(\vec{r},t)\right\rangle}{[\langle|\underline{\vec{E}}_S(\vec{r},t)|^2\rangle]^{\frac{1}{2}}[\langle|\underline{\vec{E}}_S(\vec{r}+\vec{\rho},t)|^2\rangle]^{\frac{1}{2}}} \tag{2-106}$$

Equation (2-106) shows that $\underline{T}(\vec{r},\vec{\rho})$ measures the degree to which the time behavior of the field at $\vec{r}+\vec{\rho}$ is influenced by, i.e. is correlated with, its behavior at $\vec{r}$.

The general properties of $T(\vec{r},\vec{\rho})$ can be examined by writing out the numerator of Eq. (2-105) explicitly in terms of its ensemble average, namely,[§]

$$\begin{aligned}\overline{\underline{\vec{E}}_S(\vec{r}+\vec{\rho},t)\cdot\underline{\vec{E}}_S(\vec{r},t)} &= \overline{\underline{\vec{E}}_S{}^*(\vec{r}+\vec{\rho},0)\cdot\underline{\vec{E}}_S(\vec{r},0)}\\ &= \int_{E_S(\vec{r}+\vec{\rho})}\int_{E_S(\vec{r})} \underline{\vec{E}}_S(\vec{r}+\vec{\rho},0)\cdot\underline{\vec{E}}_S(\vec{r},0)\\ &\quad\times \mathbf{P}[\underline{\vec{E}}_S{}^*(\vec{r}+\vec{\rho},0),\underline{\vec{E}}_S(\vec{r},0)]\; d[\underline{\vec{E}}_S{}^*(\vec{r}+\vec{\rho},0)]\; d[\underline{\vec{E}}_S(\vec{r},0)]\end{aligned} \tag{2-107}$$

[§] Chapter 2, Section D.3.

where $\mathbf{P}[\ ,\ ]$ is the joint probability density that the field at $\vec{r}$ has the value $\vec{\underline{E}}_S(\vec{r},0)$ and that the field at $\vec{r}+\vec{\rho}$ has the value $\vec{\underline{E}}_S(\vec{r}+\vec{\rho},0)$. As usual[§] the joint probability may be factored into a product

$$\mathbf{P}[\ ,\ ] = \mathbf{P}[\vec{\underline{E}}_S^{\,*}(\vec{r}+\vec{\rho},0)\,|\,\vec{\underline{E}}_S(\vec{r},0)]\ \mathbf{P}[\vec{\underline{E}}_S(\vec{r},0)] \qquad (2\text{-}108)$$

in which $\mathbf{P}[\ |\ ]$ is the conditional probability density that the field at $\vec{r}+\vec{\rho}$ has the value $\vec{\underline{E}}_S(\vec{r}+\vec{\rho},0)$ given that the field at $\vec{r}$ has the value $\vec{\underline{E}}_S(\vec{r},0)$.

First, suppose that the fields detected at $\vec{r}$ and $\vec{r}+\vec{\rho}$ are completely independent of one another. Then $\mathbf{P}[\ |\ ]$ becomes simply $\mathbf{P}[\vec{\underline{E}}_S^{\,*}(\vec{r}+\vec{\rho},0)]$ and Eq. (2-107) yields

$$\overline{\vec{\underline{E}}_S(\vec{r}+\vec{\rho},0)\cdot\vec{\underline{E}}_S(\vec{r},0)} = \overline{\vec{\underline{E}}_S(\vec{r}+\vec{\rho},0)}\cdot\overline{\vec{\underline{E}}_S(\vec{r},0)} = 0 \qquad (2\text{-}109)$$

The zero result follows from the fact that $\vec{\underline{E}}_S(\vec{r},t)$ has a zero mean for all $\vec{r}$. Since the denominator in Eq. (2-105) measures the mean-square fields at $\vec{r}$ and $\vec{r}+\vec{\rho}$, it is nonvanishing; therefore, Eq. (2-109) implies that $\underline{T}(\vec{r},\vec{\rho}) \to 0$ in the absence of correlation.

On the other hand, suppose that the fields at $\vec{r}$ and $\vec{r}+\vec{\rho}$ are completely linearly dependent, so that $\vec{\underline{E}}_S(\vec{r}+\vec{\rho},0)$ is simply some complex function $\underline{\beta}(\vec{\rho})$ times $\vec{\underline{E}}_S(\vec{r},0)$. Then we have

$$\mathbf{P}[\ |\ ] = \delta[\vec{\underline{E}}_S^{\,*}(\vec{r}+\vec{\rho},0) - \underline{\beta}^*(\vec{\rho})\vec{\underline{E}}_S^{\,*}(\vec{r},0)] \qquad (2\text{-}110)$$

and Eq. (2-107) yields

[§] Chapter 2, Section D.3.

$$\overline{\vec{\underline{E}}_S^{\,*}(\vec{r}+\vec{\rho},0)\cdot\vec{\underline{E}}_S(\vec{r},0)} = \underline{\beta}^*(\vec{\rho})\ \overline{\vec{\underline{E}}_S^{\,*}(\vec{r},0)\cdot\vec{\underline{E}}_S(\vec{r},0)} \tag{2-111}$$

Therefore, in the case of perfect correlation $\underline{T}(\vec{r},\vec{\rho})$ becomes

$$\underline{T}(\vec{r},\vec{\rho}) = \frac{\underline{\beta}^*(\vec{\rho})}{|\underline{\beta}(\vec{\rho})|}\ , \tag{2-112}$$

a normalized description of the phase and amplitude of the field at $\vec{r}+\vec{\rho}$ relative to the field at $\vec{r}$.

The behavior of $\underline{T}(\vec{r},\vec{\rho})$ in the intermediate range of partial correlation can best be described by expressing $\vec{\underline{E}}_S(\vec{r}+\vec{\rho},0)$ in terms of a completely uncorrelated component $\vec{\underline{E}}_S^{\,un}(\vec{r}+\vec{\rho},0)$ and a perfectly correlated part $\underline{\beta}(\vec{\rho})\vec{\underline{E}}_S(\vec{r},0)$. In this case we find

$$\underline{T}(\vec{r},\vec{\rho}) = \frac{\underline{\beta}^*(\vec{\rho})}{|\underline{\beta}(\vec{\rho})|[1+\mathbf{r}]^{\frac{1}{2}}} \tag{2-113}$$

The quantity $\mathbf{r}$

$$\mathbf{r} = \frac{\left\langle|\vec{\underline{E}}_S^{\,un}(\vec{r}+\vec{\rho},t)|^2\right\rangle}{|\underline{\beta}(\vec{\rho})|^2\left\langle|\vec{\underline{E}}_S(\vec{r}+\vec{\rho},t)|^2\right\rangle} \tag{2-114}$$

is the ratio of the intensities in the uncorrelated and correlated components of $\vec{\underline{E}}_S(\vec{r}+\vec{\rho},0)$.

With this result and Eqs. (2-105), (2-109) and (2-112) the qualitative dependence of $\underline{T}(\vec{r},\vec{\rho})$ on the separation may be given as follows:

(1) The magnitude of $\underline{T}(\vec{r},\vec{\rho})$ reflects the degree of coherence existing between the fields reaching the two observation points $\vec{r}$ and $\vec{r}+\vec{\rho}$; $|\underline{T}(\vec{r},\vec{\rho})|$ has a maximum value of one, representing perfect correlation, a minimum value of zero, corresponding to no correlation, and intermediate

values for the case of partial coherence. The case of zero separation, $\vec{\rho}=0$, by definition gives $|\underline{T}(\vec{r},\vec{\rho})| = 1$, while the separation for which $|\underline{T}(\vec{r},\vec{\rho})|$ falls to some pre-set value may be termed the coherence distance.

(2) The actual value of $\underline{T}(\vec{r},\vec{\rho})$ describes the phase and amplitude of the fully correlated component of $\vec{\underline{E}}_S(\vec{r}+\vec{\rho},0)$ as measured relative to $\vec{\underline{E}}_S(\vec{r},0)$.

3. The Origin of the Finite Range of Spatial Coherence

In computing $\underline{T}(\vec{r},\vec{\rho})$ for the field of some arbitrary source, we find that two basic phenomena can combine to destroy coherence between the fields reaching the points $\vec{r}$ and $\vec{r}+\vec{\rho}$. The first enters whenever $\vec{r}$ and $\vec{r}+\vec{\rho}$ are situated at different retarded times

$$t_{ret} = t - \frac{|\vec{r} - \vec{r}_o|}{c_m}$$

from the source, and represents an uninteresting effect of the temporal coherence characteristics, $R_E(\tau)$, of the emitted radiation.

The second mechanism enters whenever $\vec{r}$ and $\vec{r}+\vec{\rho}$ point in different directions. In this situation we find from Fig. 2-7 that the wavelets originating from any two volume elements in the source will, in general, interfere with somewhat different relative phases at the two observation points. For our purposes we may regard the field leaving ΔV_i as having an arbitrary and random phase[§] with respect to that leaving any other ΔV_j, $j \neq i$. It follows that the total fields at $\vec{r}$ and $\vec{r}+\vec{\rho}$,

---

[§] It follows that ΔV_i must be large compared to the cube of the range of the pair-correlation function which is described in Section C.3 of Chapter 5.

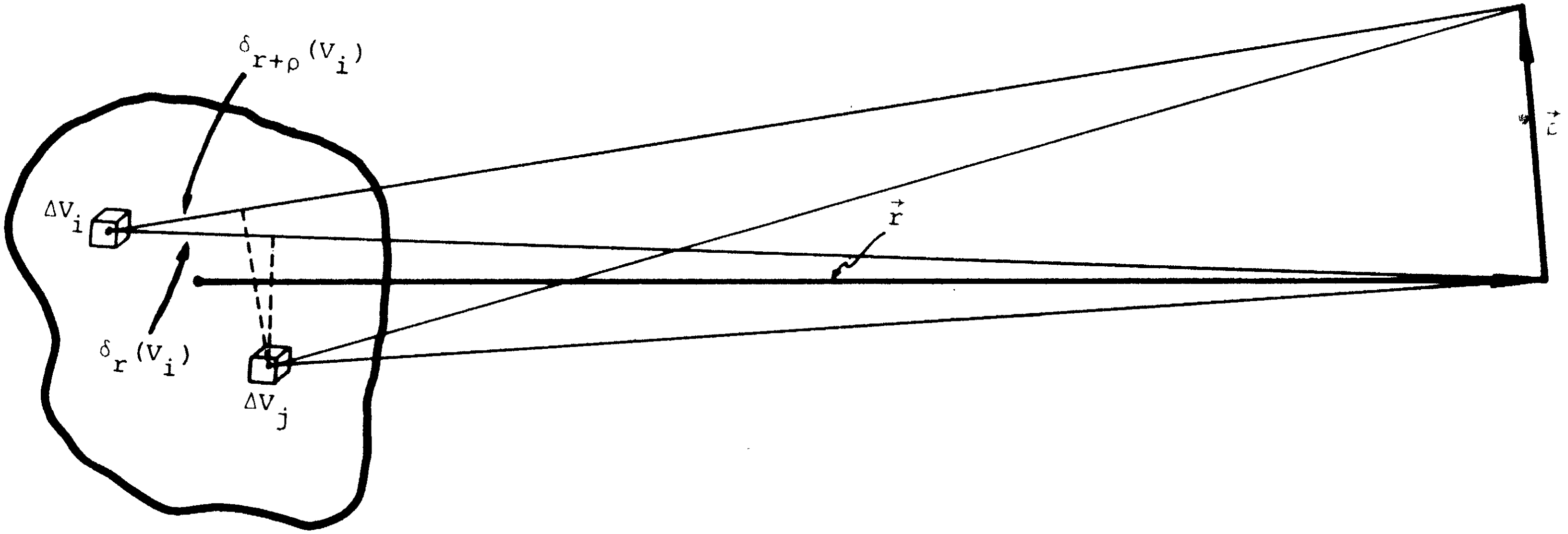
$\delta_{r+\rho}(V_i)$
ΔV_i
$\delta_r(V_i)$
ΔV_j
$\vec{r}$
$\vec{\rho}$

Figure 2-7 The change of path length between two points in the scattering volume and the observer's position as a function of the observation direction.

$$E^*(\vec{r}+\vec{\rho},t) = \sum_{\Delta V_i} E^*(\Delta v_i,t)e^{-i(2\pi/\lambda)\delta_{r+\rho}(V_i)}$$

and

$$E(\vec{r},t) = \sum_{\Delta V_i} E(\Delta V_i,t)e^{i(2\pi/\lambda)\delta_r(V_i)} ,$$

will have a time average product which vanishes unless the sum of the "diagonal" terms

$$\left\langle E^*(\vec{r}+\vec{\rho},t)E(\vec{r},t)\right\rangle = \sum_{\Delta V_i} \left\langle |E(\Delta V_i,t)|^2\right\rangle e^{i(2\pi/\lambda)[\delta_r(V_i) - \delta_{r+\rho}(V_i)]} \tag{2-115}$$

is a non-zero. Correlation between the two fields is destroyed when the original phase factors $(2\pi/\lambda)\delta_r(V_i)$ are replaced by a new set of values $(2\pi/\lambda)\delta_{r+\rho}(V_i)$ for which the differences

$$\frac{2\pi}{\lambda}[\delta_r(V_i) - \delta_{r+\rho}(V_i)]$$

are distributed between $-\pi$ and π. Clearly this second mechanism for destroying spatial coherence is a purely geometric effect, depending only on the shape of the source and its intensity distribution $|E(\Delta V_i,t)|^2$. We will prove below[§] that these factors enter the calculation of $\underline{T}(\vec{r},\vec{\rho})$ and the ordinary diffraction pattern of the source in identical manners.

[§] Chapter 2, Section E.4.c.

4. The Spatial Correlation Function for the Scattered Field

a. The Description of the Scattered Field by Analogy with Diffraction

In Section B we obtained a general expression for the field scattered by a volume V of nominally homogeneous material exhibiting fluctuations in its optical susceptibility. This result was based on three simplifying assumptions. First, the distance between the observer and the scattering volume was assumed to be large compared to the maximum dimension of V, thereby placing the observer in the far field region of the source. Secondly, the incident beam was taken to have a constant amplitude E_o over its cross section; this intensity distribution approximates the focal region of a laser light source operating in its uni-phase modes.* Third, the change in wavelength on scattering was neglected so that

$$|\vec{k}_o| = |\vec{k}_s| = (\omega_o/c_m)$$

where $\vec{k}_o$ and $\vec{k}_s$ are the wave vectors of the incident and scattered fields respectively.

In this case, by expanding the susceptibility fluctuations $\Delta\chi(\vec{r},t)$ in terms of a spatial Fourier series, we obtained the scattered field as a sum of terms $[\underline{\vec{E}}_S(\vec{r},t)]_K$ each of the form

---

* Chapter 4, Section B.2.

$$[\underline{\vec{E}}_S(\vec{r},t)]_K = \vec{k}_s\times(\vec{k}_s\times\vec{E}_o)\frac{e^{i(k_s r - \omega_o t)}}{4\ r}\left(\frac{\varepsilon_o}{\varepsilon}\right)\underline{\Delta\chi}_K(t)$$

$$\times \int_V e^{i(\vec{k}_o-\vec{k}_s+\vec{K})\cdot\vec{r}_1}\, d^3\vec{r}_1 \tag{2-116}$$

giving a total field

$$\underline{\vec{E}}_S(\vec{r},t) = \sum_K [\underline{\vec{E}}_S(\vec{r},t)]_K \tag{2-117}$$

Note that the explicit variation of $[\underline{\vec{E}}_S(\vec{r},t)]_K$ with the direction of $\vec{r}$ is described in the right hand side of Eq. (2-116) entirely through the wave vector $\vec{k}_s$

$$\vec{k}_s = (\omega_o/c_m)\hat{r} \tag{2-118}$$

which points in the direction of observation.

For purposes of comparing this expression for the scattered field to ordinary diffraction, consider the vector diffraction integral generalized to a three-dimensional diffracting region V, namely[37]

$$\vec{E}_D(\vec{r},t) = \frac{1}{4\pi\varepsilon}\,\vec{\nabla}\times\left[\vec{\nabla}\times\int_V \frac{\vec{E}(\vec{r}_1,t_1)\,\delta\left(t_1 - t + \frac{|\vec{r}-\vec{r}_1|}{c_m}\right)d^3\vec{r}_1 dt_1}{|\vec{r}-\vec{r}_1|}\right] \tag{2-119}$$

where $\vec{E}(\vec{r}_1,t_1)$ is the total field acting in V.

Equation (2-119) has been written for a medium in which the velocity of light is $c_m = (c_o/n)$ and the permittivity is $\varepsilon = n^2\varepsilon_o$, where n is the index of refraction. In actual diffraction calculations the Kirchhoff approximation is made by taking $\vec{E}(\vec{r}_1,\vec{t}_1)$ as being the incident field rather than the sum of incident and diffracted fields.

Suppose the incoming beam corresponds to a uni-phase laser source

$$E_{INC}(\vec{r},t) = E_o{}' \; e^{i(\vec{k}_o{}'\cdot\vec{r} - \omega_o t)}$$

Then with the Kirchhoff assumption and the usual[*] far field approximations we find for the diffracted field

$$\vec{E}_D(\vec{r},t) = \vec{k}_d\times(\vec{k}_d\times\vec{E}_o{}') \; \frac{e^{i(k_d r - \omega_o t)}}{4\pi r} \; \left(\frac{1}{\varepsilon}\right) \int_V e^{i(\vec{k}_o{}'-\vec{k}_d)\cdot\vec{r}_1} \, d^3\vec{r}_1 \tag{2-120}$$

where

$$\vec{k}_d = (\omega_o/c_m)\,\hat{r} \tag{2-121}$$

A comparison of Eqs. (2-116), (2-118), (2-120) and (2-121) shows that the field scattered by a single spatial Fourier component of the fluctuations can be regarded as the diffraction pattern of the scattering volume V, as illuminated with an effective incident field

$$\vec{E}_{INC}(\vec{r},t) = \varepsilon_o \underline{\Delta\chi_K}(t)\vec{E}_o e^{i[(\vec{k}_o+\vec{K})\cdot\vec{r} - \omega_o t]} \tag{2-122}$$

The orientation of this beam is illustrated in Fig. 2-8.

---

[*] Chapter 2, Section B.1.

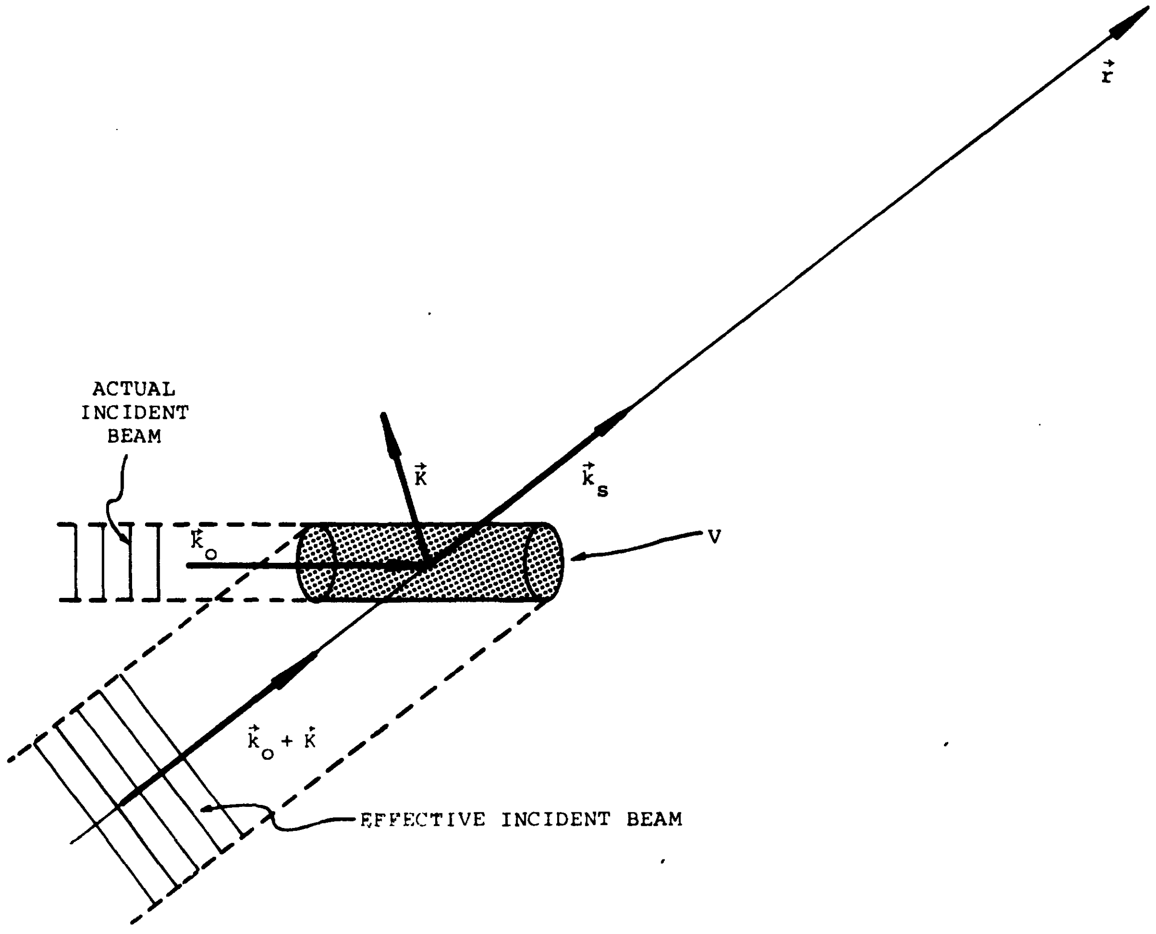
$\vec{r}$
ACTUAL INCIDENT BEAM
$\vec{K}$
$\vec{k}_s$
$\vec{k}_o$
V
$\vec{k}_o + \vec{K}$
EFFECTIVE INCIDENT BEAM

Figure 2-8 Equivalent illumination of the volume V for a diffraction interpretation of the scattering process.

An even stronger statement of the analogy can be made by contrasting Eqs. (2-119) and (2-3) for the diffracted and scattered fields respectively. On the basis of this comparison it can be shown that the diffraction interpretation of the scattering process is valid (1) in both the near _and_ far field regions of the source volume, (2) for an arbitrary intensity profile for the incident electric field, and (3) for the _exact_ field integrals without Kirchhoff-like approximations as to the ratio of incident and diffracted intensities.

It follows that the total scattered field can be described as the superposition of a series of diffraction or antenna patterns, each one characterizing the geometrical shape of the illuminated volume V and an effective incident beam of the form displayed in Eq. (2-122).

b. The General Expression for $T(\vec{r},\vec{\rho})$ in Terms of the Interference or Diffraction Integral

In calculating $\underline{T}(\vec{r},\vec{\rho})$ for the scattered field $\vec{E}_S(\vec{r},t)$ we will be interested only in the lack of spatial coherence that is due to the finite geometrical size of the illuminated region.* Therefore, to avoid the effects of the temporal coherence characteristics of the scattered light we compute $\underline{T}(\vec{r},\vec{\rho})$ for the case where $\vec{r}$ and $\vec{r}+\vec{\rho}$ are located at identical retarded times from the scattering volume V. The points $\vec{r}$ and $\vec{r}+\vec{\rho}$ are taken to lie on a single wavefront of the scattered field.

Equation (2-116) shows that in the far field each "diffracted beam," $[\vec{E}_S(\vec{r},t)]_K$ represents a spherically spreading wave whose amplitude in a particular direction $\vec{r}$ is determined by the interference integral

---

* Chapter 2, Section E.3.

$$I(\vec{r},\vec{K}) \equiv \int_V e^{i(\vec{k}_o-\vec{k}_s+\vec{K})\cdot\vec{r}_1}\, d^3\vec{r}_1 \qquad (2\text{-}123)$$

and the definition

$$\vec{k}_s = (\omega_o/c_m)\hat{r} \qquad (2\text{-}124)$$

Therefore, we will assume that the two observation points $\vec{r}$ and $\vec{r}+\vec{\rho}$ lie on the surface of a sphere, Q, centered on V and having a radius r_o much larger than the largest dimension of V. On Q the field scattered by a susceptibility fluctuation of wave vector $\vec{K}$ has* an average amplitude and phase fixed by the factor

$$\vec{k}_s\times(\vec{k}_s\times\vec{E}_o)\ \frac{e^{i(k_o r_o\ -\ \omega_o t)}}{4\pi r_o}\ \left(\frac{\varepsilon_o}{\varepsilon}\right)\underline{\Delta\chi_K}(t)$$

and modulated by the interference integral $I(\vec{r},\vec{K})$ given in Eq. (2-123). The orientation of the vectors $\vec{r}$ and $\vec{r}+\vec{\rho}$ and their associated wave vectors $\vec{k}_s(\vec{r})$ and $\vec{k}_s(\vec{r}+\vec{\rho})$ are illustrated in Fig. 2-9.

Writing $\underline{\vec{E}}_S(\vec{r},t)$ in terms of $I(\vec{r},\vec{K})$ with the help of Eqs. (2-116), (2-117), and (2-123) gives $T(\vec{r},\vec{\rho})$ on the surface of Q as

---

* Chapter 2, Section B.3.

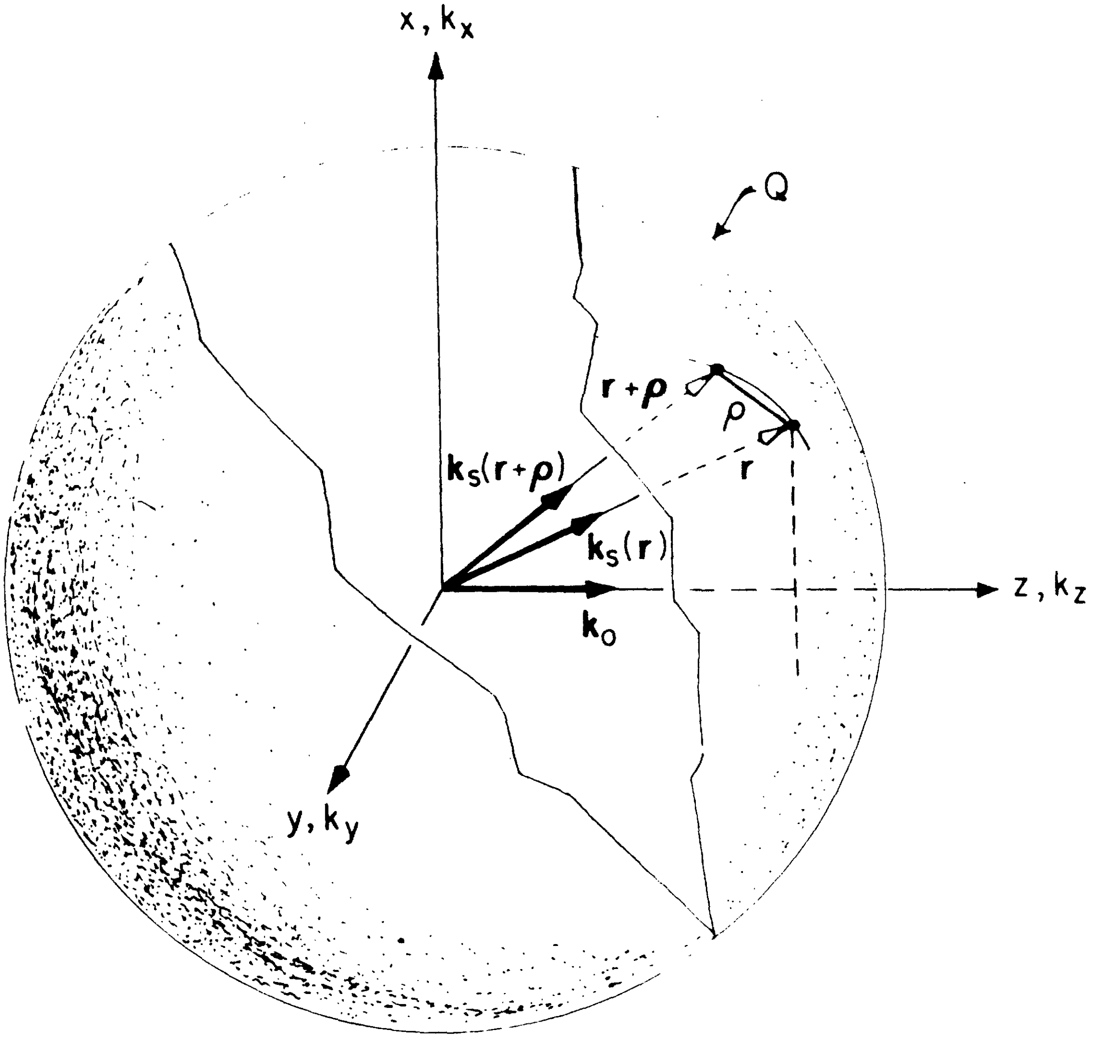
x, k_x
Q
$\mathbf{r}+\boldsymbol{\rho}$
ρ
$\mathbf{r}$
$\mathbf{k}_s(\mathbf{r}+\boldsymbol{\rho})$
$\mathbf{k}_s(\mathbf{r})$
z, k_z
$\mathbf{k}_0$
y, k_y

Figure 2-9 The spherical surface Q used in the computation of the spatial correlation function.

$$\underline{T}_Q(\vec{r},\vec{\rho}) = \frac{\sum\limits_{K}\ \sum\limits_{K'}\ \overline{\underline{\Delta\chi}_K(t)\,\underline{\Delta\chi}^{*}_{K'}(t)}\ I(\vec{r},\vec{K})\,I^{*}(\vec{r}+\vec{\rho},\vec{K}')}{\left[\sum\limits_{K}\ \sum\limits_{K'}\ \overline{\underline{\Delta\chi}_K(t)\,\underline{\Delta\chi}^{*}_{K'}(t)}\ I(\vec{r},\vec{K})\,I^{*}(\vec{r},\vec{K}') \times \sum\limits_{K}\ \sum\limits_{K'}\ \underline{\Delta\chi}_K(t)\,\underline{\Delta\chi}^{*}_{K'}(t)\ I(\vec{r}+\vec{\rho},\vec{K})\,I^{*}(\vec{r}+\vec{\rho},\vec{K}')\right]^{\frac{1}{2}}} \qquad (2\text{-}125)$$

The maximum value of K that need be considered in the double summation corresponds to scattering in the backward direction ($\Theta = 180°$) where

$$K_{\max} = 2k_o = 2n(2\pi/\lambda_{\mathrm{air}})$$

For larger K, $I(\vec{r},\vec{K})$ is zero[§] for all possible $\vec{r}$. Furthermore, under normal circumstances the range of the pair-correlation function[†] in the scattering medium is small compared to $(1/K_{\max})$ and $\Delta\chi(\vec{r}_1,t_1)$ may be regarded as a random function of the position coordinate $\vec{r}_1$ as well as of the time t_1. In this limit, the set of Fourier amplitudes

$$\underset{K\leq K_{\max}}{\underline{\Delta\chi}_K(t)} = \frac{1}{V}\int_V \Delta\chi(\vec{r}_1,t)\, e^{-i\vec{K}\cdot\vec{r}_1}\, d^3\vec{r}_1$$

form a sequence of statistically independent random functions of time, and the ensemble average

$$\overline{\underline{\Delta\chi}_K(t)\,\underline{\Delta\chi}_{K'}^{*}(t)}$$

vanishes unless $\vec{K} = \vec{K}'$. Therefore, $T_Q(\vec{r},\vec{\rho})$ immediately reduces to the simpler form

$$\underline{T}_Q(\vec{r},\vec{\rho}) = \tag{2-126}$$

$$\frac{\sum\limits_K \overline{\underline{\Delta\chi}_K(t)\,\underline{\Delta\chi}_K^{*}(t)}\; I(\vec{r},\vec{K})\,I^{*}(\vec{r}+\vec{\rho},\vec{K})}{\left[\sum\limits_K \overline{\underline{\Delta\chi}_K(t)\,\underline{\Delta\chi}_K^{*}(t)}\;\left|I(\vec{r},\vec{K})\right|^2 \times \sum\limits_K \overline{\underline{\Delta\chi}_K(t)\,\underline{\Delta\chi}_K^{*}(t)}\;\left|I(\vec{r}+\vec{\rho},\vec{K})\right|^2\right]^{\frac{1}{2}}}$$

[§] Chapter 2, Section E.4.e.

[†] Chapter 5, Section C.3.

The product $I(\vec{r},\vec{K})I^*(\vec{r}+\vec{\rho},\vec{K})$ appearing in the numerator of Eq. (2-126) shows that correlation will occur between the fields observed at $\vec{r}$ and $\vec{r}+\vec{\rho}$ only if at least one of the "diffracted beams" has a non-vanishing intensity at both $\vec{r}$ and $\vec{r}+\vec{\rho}$. This result may be interpreted as showing that perfect correlation exists at all $\vec{\rho}$ in the field scattered by a single $\underline{\Delta\chi}_K(t)$ while the fields associated with different values of $\vec{K}$ are completely uncorrelated.

In fact, the spatial correlation function for one of the field components $[E_S(\vec{r},t)]_K$ can be computed from Eq. (2-116) as

$$[\underline{T}_Q(\vec{r},\vec{\rho})]_K = \frac{\left\langle [\underline{\vec{E}}_S(\vec{r},t)]_K \ [\underline{\vec{E}}_S^{\,*}(\vec{r}+\vec{\rho},t)]_K \right\rangle}{\left\{\left\langle |[\underline{\vec{E}}_S(\vec{r},t)]_K|^2\right\rangle\left\langle |[\underline{\vec{E}}_S(\vec{r}+\vec{\rho},t)]_K|^2\right\rangle\right\}^{\frac{1}{2}}} \qquad (2\text{-}127)$$

$$= \frac{\beta^*}{|\beta|}$$

where

$$\beta = \int_V \int_V e^{-i(\vec{k}_o-\vec{k}_s+\vec{K})\cdot\vec{r}_1} \, e^{+i(\vec{k}_o-\vec{k}_s{}'+\vec{K})\cdot\vec{r}_2} \, d^3\vec{r}_1 d^3\vec{r}_2$$

$$(2\text{-}128)$$

The wave vectors $\vec{k}_s$ and $\vec{k}_s{}'$ point in the directions of $\vec{r}$ and $\vec{r}+\vec{\rho}$ respectively. Since $[\underline{T}_Q(\vec{r},\vec{\rho})]_K$ has unit magnitude for all $\vec{\rho}$, it follows[§] that the field of a single diffracted beam is spatially coherent over the entire sphere Q. On the other hand, the statistical independence of $\underline{\Delta\chi}_K(t)$ and $\underline{\Delta\chi}_{K'}(t)$ guarantees that the average

---

[§] Chapter 2, Section E.2.

$$\overline{[\vec{\underline{E}}_S(\vec{r},t)]_K\;[\vec{\underline{E}}_S^*(\vec{r}+\vec{\rho},t)]_{K'}} \propto \overline{\underline{\Delta\chi}_K(t)\underline{\Delta\chi}_{K'}^*(t)}$$

vanishes for $\vec{K} \neq \vec{K}'$ and, hence, there is no correlation between the fields scattered from fluctuations of different $\vec{K}$.

In a qualitative fashion, then, the desired information on the range of spatial correlation in the scattered field is determined entirely by the $\hat{r}$ behavior of a single interference integral $I(\vec{r},\vec{K})$. However, as is clear from a comparison of Eqs. (2-120) and (2-123), $I(\vec{r},\vec{K})$ is simply the ordinary diffraction integral for the region V.

c. The Relationship Between the Spatial Correlation Function for the Scattered Field and the Diffraction Pattern of the Scattering Volume

A rigorous equivalence between the diffraction pattern and the spatial correlation function may be established as follows. Let $\vec{r}$, the principal direction of observation, be fixed, and consider first of all the diffraction pattern of V. Suppose that V is illuminated with a plane wave incident beam traveling in the direction $\vec{r}$, as in Fig. 2-8, so that the observer at $\vec{r}$ is at the position of maximum intensity of the diffracted beam. Then if $\vec{r}$ and $\vec{r}+\vec{\rho}$ lie on a spherical surface Q, we have

$$|\vec{r}| = |\vec{r}+\vec{\rho}|$$

and Eq. (2-120) gives the ratio of the fields observed at $\vec{r}+\vec{\rho}$ and $\vec{r}$ as

$$\frac{E_D^*(\vec{r}+\vec{\rho},t)}{E_D(\vec{r},t)} = \frac{1}{V}\int_V e^{i\frac{\omega_o}{c_m}\frac{1}{|\vec{r}|}\vec{\rho}\cdot\vec{r}_1}\, d^3\vec{r}_1 \tag{2-129}$$

Next, consider Eq. (2-126) for $\underline{T}_Q(\vec{r},\vec{\rho})$ in the usual situation in which $\overline{\underline{\Delta\chi}_K(t)\underline{\Delta\chi}_K^*(t)}$ is independent[*] of K over the range

$$0 \le |\vec{K}| \le \overline{K}$$

$$\overline{K} >> k_o$$

In this case the sums over $\vec{K}$ may be performed explicitly and we find

$$\underline{T}_Q(\vec{r},\vec{\rho}) = \frac{1}{V}\int_V e^{i\frac{\omega_o}{c_m}\frac{1}{|\vec{r}|}\vec{\rho}\cdot\vec{r}_1}\, d^3\vec{r}_1 \tag{2-130}$$

Comparing Eqs. (2-129) and (2-130) shows that $\underline{T}_Q(\vec{r},\vec{\rho})$ for the scattered field identically describes the amplitude distribution in that particular diffraction pattern of V whose center lies in the direction $\vec{r}$.

Finally, consider the field scattered by the susceptibility fluctuation whose wave vector K satisfies the condition

$$\vec{k}_o - \vec{k}_s + \vec{K} = \vec{k}_o - |\vec{k}_o|\hat{r} + \vec{K} = 0 \tag{2-131}$$

---

[*] Chapter 2, Section D.3; Chapter 5, Section C.3; this K independence is a direct result of assuming that the range of the pair correlation function is small compared to the wavelength of a fluctuation having $K=K_{max}=2k_o$. Equation (2-130) can be obtained directly from this assumption by evaluating $T_Q(\vec{r},\vec{\rho})$ in terms of $\Delta\chi(\vec{r},t)$ rather than $\underline{\Delta\chi}_K(t)$.

The corresponding interference integrals

$$I^{*}(\vec{r}+\vec{\rho},\vec{k}_s{}'-\vec{k}_o) = \int_V e^{i\frac{\omega_o}{c_m}\frac{1}{|\vec{r}|}\vec{\rho}\cdot\vec{r}_1} d^3\vec{r}_1 \tag{2-132}$$

$$I(\vec{r},\vec{k}_s-\vec{k}_o) = V \tag{2-133}$$

show that the spatial correlation function may be written in the form

$$\underline{T}_Q(\vec{r},\vec{\rho}) = \frac{1}{V} I^{*}(\vec{r}+\vec{\rho},\vec{k}_s{}'-\vec{k}_o) \tag{2-134}$$

From Eqs. (2-129), (2-130), (2-134), and the properties of $\underline{T}(\vec{r},\vec{\rho})$ described in Section E.2 we may draw the following conclusions.

(1) The range of spatial correlation in the scattered field is the extent of the ordinary diffraction pattern of the illuminated volume.

(2) Distinct regions of spatial coherence on the spherical surface Q can be interpreted as the diffraction patterns or scattered beams originating from susceptibility fluctuations of different wave vectors.

d. The Averaged Properties of $T_Q(\vec{r},\vec{\rho})$ Which Are Important in Light Mixing Spectroscopy

Although the behavior of $I(\vec{r},\vec{K})$ and, therefore, of $\underline{T}_Q(\vec{r},\vec{\rho})$ can be displayed explicitly for certain simple geometrical shapes of the illuminated region, the calculations given in Sections C and D of Chapter 3 indicate that only certain averaged properties of $\underline{T}_Q$ enter into determining the effects of spatial coherence on the operation of an optical mixing spectrometer. Specifically, we encounter the following surface integrals,

$$A_{COH} = \int_Q T_Q(\vec{r}_o,\vec{\rho})\,d^2\vec{\rho} \qquad (2\text{-}135)$$

and

$$A^*_{COH} = \int_Q T_Q{}^2(\vec{r}_o,\vec{\rho})\,d^2\vec{\rho} \qquad (2\text{-}136$$

Since the maximum value of $\underline{T}_Q(\vec{r},\vec{\rho})$ is $\underline{T}(\vec{r},0) = 1$, both of these expressions determine an effective area on Q over which there is complete spatial coherence. Both are designated as coherence areas of the scattered field. The desired integrals can be put in a form which is independent of the choice of Q by computing the corresponding coherence solid angles

$$\Omega_{COH} = (A_{COH}/r_o{}^2) \qquad (2\text{-}137)$$

and

$$\Omega^*_{COH} = (A^*_{COH}/r_o{}^2) \qquad (2\text{-}138)$$

respectively. The usefulness of a light mixing spectrometer is determined by the amount of scattered power available in a single coherence solid angle.

e. The Properties of $I(\vec{r},\vec{K})$ for a Rectangular Parallelopiped Scattering Volume

The calculations and discussions of this section are directed toward investigating the important properties of the diffraction integral $I(\vec{r},\vec{K})$. First, we consider its exact behavior with the direction of observation, $\vec{r}$, using a specific choice for the shape of the scattering region and a single value of $\vec{K}$. This behavior describes the intensity distribution in the field scattered from a single fluctuation $\underline{\Delta\chi}_K(t)$ and also, via Eq. (2-134), gives a qualitative picture of the spatial correlation function $\underline{T}_Q(\vec{r},\vec{\rho})$. Secondly, we obtain an approximate form for $\underline{T}_Q(\vec{r},\vec{\rho})$ which allows the integrals defining the coherence solid angles Ω_{COH} and Ω^*_{COH} to be carried out explicitly. Finally, we investigate the relative spatial orientation of the "diffracted beams" $I(\vec{r},\vec{K})$ corresponding to the entire set of allowed $\vec{K}$ values.

Let us first consider the exact evaluation of $I(\vec{r},\vec{K})$ with a particular choice for the shape of the illuminated volume V; specifically, let V be a rectangular parallelopiped with dimensions L_x, L_y, and L_z along the x, y, and z axes respectively. The z axis is oriented along the direction of the incoming beam, $\vec{k}_o$, as illustrated in Fig. 2-10. With this choice for V Eq. (2-123) has the form

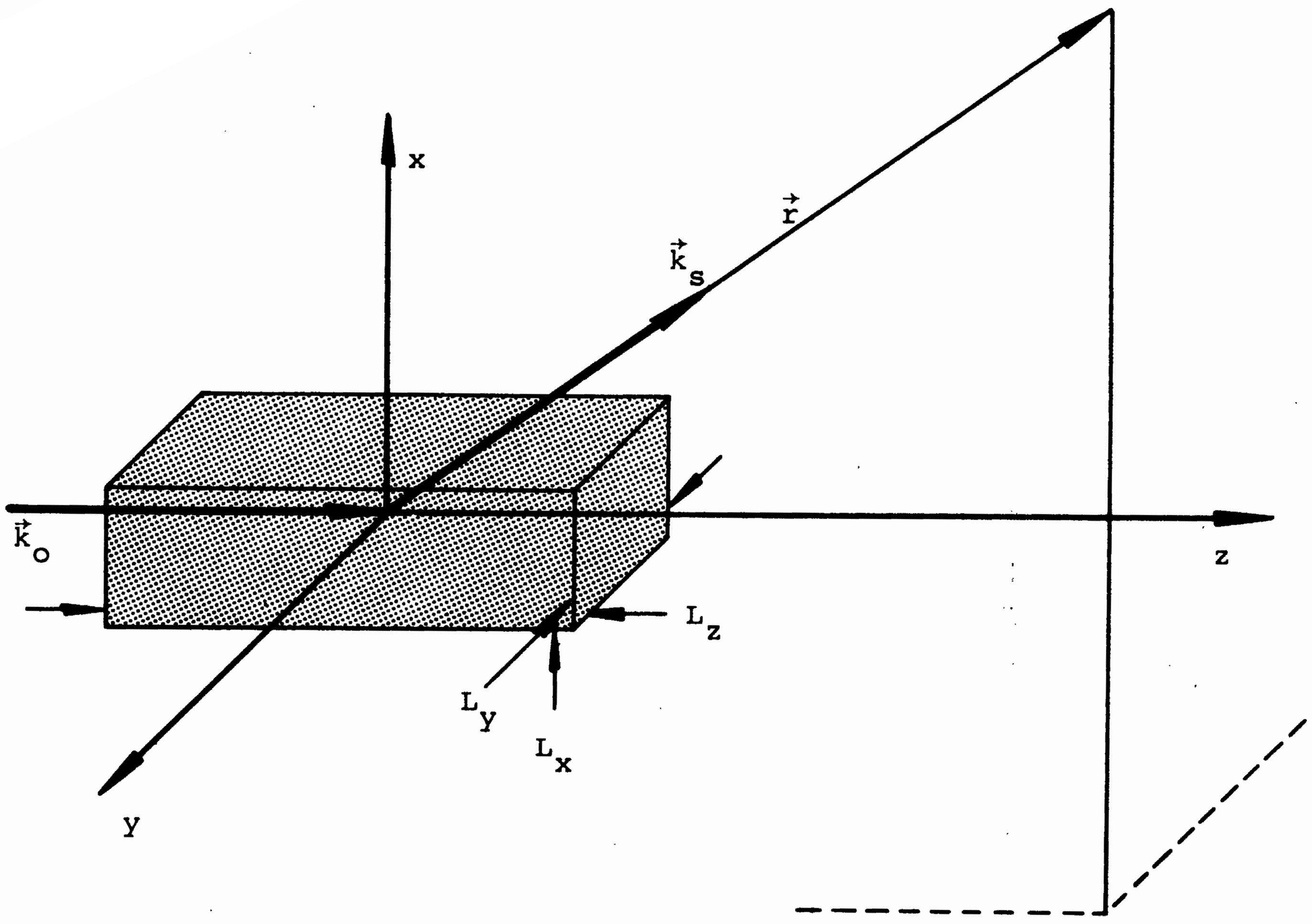
x
$\vec{r}$
$\vec{k}_s$
$\vec{k}_o$
z
L_z
L_y
L_x
y

Figure 2-10 The shape and orientation of the scattering volume for an excalculation of the coherence solid angle.

$$I(\vec{r},\vec{K}) = \int_{-\frac{L_x}{2}}^{\frac{L_x}{2}} e^{i(K_x-q_x)x'}\,dx' \int_{-\frac{L_y}{2}}^{\frac{L_y}{2}} e^{i(K_y-q_y)y'}\,dy'$$

$$\times \int_{-\frac{L_z}{2}}^{\frac{L_z}{2}} e^{i(K_z-q_z)z'}\,dz' \qquad (2\text{-}139)$$

where

$$\vec{q} \equiv \vec{k}_s - \vec{k}_o = (\omega_o/c_m)\hat{r} - \vec{k}_o \qquad (2\text{-}140)$$

The integrations are straightforward and we find for $I(\vec{r},\vec{K})$

$$I(\vec{r},\vec{K}) = V \frac{\sin\,(K_x-q_x)(L_x/2)}{(K_x-q_x)(L_x/2)} \cdot \frac{\sin(K_y-q_y)(L_y/2)}{(K_y-q_y)(L_y/2)}$$

$$\cdot \frac{\sin\,(K_z-q_z)(L_z/2)}{(K_z-q_z)(L_z/2)} \qquad (2\text{-}141)$$

Each of the three cartesian factors in this result is of the general form

$$g(w) = [(\sin w)/w]\ .$$

The function $g(w)$ peaks sharply at $w = 0$, going to unity in the limit $(w \to 0)$, and then dies off in an oscillatory manner for large w with an envelope $(w)^{-1}$. Figure 2-11 illustrates this behavior for the range $-4\pi \leq w \leq 4\pi$.

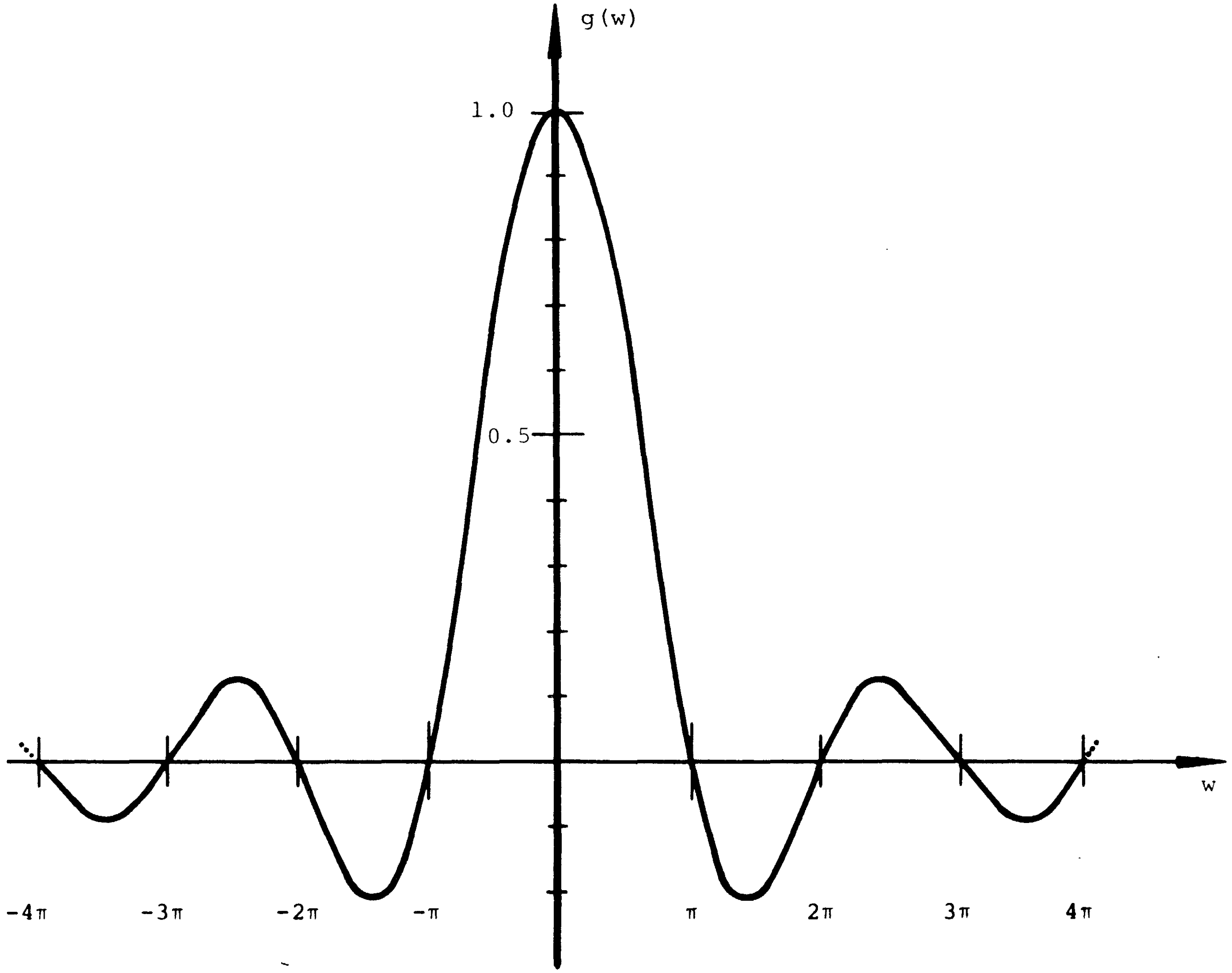

Figure 2-11 A plot of the function g(w) = (sin w)/w.

Equation (2-141) shows that the diffraction integral $I(\vec{r},\vec{K})$ contains two interesting pieces of information. One, for a fixed direction of observation, $\vec{k}_s$, it demonstrates that the fluctuations which contribute to the observed scattering have a wave vector that satisfies the condition

$$\vec{K} - \vec{q} = \vec{k}_o - \vec{k}_s + \vec{K} = 0 \qquad (2\text{-}142)$$

This is simply the constructive interference or momentum transfer requirement stated without proof in Section B.

Two, for a fixed value of $\vec{K}$, $I(\vec{r},\vec{K})$ describes the angular range of $\vec{r}$ (or $\vec{k}_s$) over which the fluctuation $\underline{\Delta\chi_K}(t)$ will contribute a non-negligible scattered intensity. This angle is the opening angle of a single "diffracted beam" $[\vec{E}_S(\vec{r},t)]_K$ and, hence, from Eq. (2-134), measures the desired coherence solid angle of the scattered light.

For the purpose of calculating the coherence solid angles Ω_{COH} and Ω^*_{COH} from $I(\vec{r},\vec{K})$ and Eqs. (2-135) through (2-138), we may approximate the factors $g(w) = (\sin w)/w$ by a step function $g^*(w)$ which is unity in the range $-\Delta w \leq w \leq \Delta w$, and zero otherwise. The increment Δw is chosen by equating the areas under $g(w)$ and $g^*(w)$ respectively. As an example, for the x component of $\vec{q}$ we find

$$\int_{-\infty}^{\infty} \frac{\sin\,(K_x-q_x)(L_x/2)}{K_x-q_x)(L_x/2)}\, d(\vec{k}_s)_x = \int_{-(\Delta k_s)_x}^{(\Delta k_s)_x} d(\vec{k}_s)_x = \frac{2\pi}{L_x}$$

(2-143)

The corresponding result for $I(\vec{r},\vec{K})$ is

$$I(\vec{r},\vec{K}) = \begin{cases} V \;; & \begin{bmatrix} -(\pi/L_x) \le (k_o - k_s + K)_x \le (\pi/L_x) \\ -(\pi/L_y) \le (k_o - k_s + K)_y \le (\pi/L_y) \\ -(\pi/L_z) \le (k_o - k_s + K)_z \le (\pi/L_z) \end{bmatrix} \\ 0 \;; & \text{otherwise} \end{cases} \tag{2-144}$$

From the form of Eq. (2-144) we may state two conclusions.

(1) The fluctuations that will produce scattering in the direction $\vec{r} = \vec{k}_s$ must have wave vectors $\vec{K}$ such that $\vec{k}_o + \vec{K}$ falls inside a rectangular parallelopiped cell ξ which is centered on the wave vector $\vec{k}_s$ and has dimensions $(\Delta k_x, \Delta k_y, \Delta k_z) = [(2\pi/L_x), (2\pi/L_y), (2\pi/L_z)]$. That is, $\vec{K}$ comes within an amount $(\Delta k_x, \Delta k_y, \Delta k_z)$ of satisfying the condition $\vec{k}_o - \vec{k}_s + \vec{K} = 0$ given in Eq. (2-142). This allowed deviation from exact momentum conservation§ can be explained semi-classically in terms of the uncertainty relation $\Delta p \Delta x \simeq \hbar$ and the finite dimensions of the scattering volume.

(2) For a fluctuation $\vec{K}_j$ which satisfies the above requirement, it follows that $I(\vec{r},\vec{K})$ is non-zero only if $\vec{r}$ remains within the diffraction pattern of $\vec{K}_j$ by taking

---

§ Chapter 2, Section B.

on only those orientations on Q around the direction $\vec{k}_o + \vec{K}$ for which $\vec{k}_s$ falls in the same cell ξ now centered on the vector $\vec{k}_o + \vec{K}$.

The possibility of interpreting the interference integral in these two ways follows directly from its symmetrical dependence on the wave vectors $\vec{k}_s$ and $\vec{K}$. We will show in Section 5 below that both interpretations lead to identical results for the coherence solid angles.

We now determine the spatial relationship between the ξ cells corresponding to different $\vec{K}_j$ by specifying the values of $\vec{K}_j$ which are to be used in the plane wave expansion of the susceptibility fluctuations $\Delta\chi(\vec{r},t)$. Equation (2-22) gives $\Delta\chi(\vec{r},t)$ as

$$\Delta\chi(\vec{r},t) = \sum_K \underline{\Delta\chi}_K(t) e^{i\vec{K}\cdot\vec{r}} \qquad (2\text{-}22)$$

where the $e^{i\vec{K}\cdot\vec{r}}$ terms are a set of plane wave functions which are complete and orthonormal on the scattering volume V. Applying the usual[8] Born-von-Kármán boundary conditions on the faces of the rectangular parallelopiped volume V yields

$$\vec{K}_j = \vec{K}_{\bar{\ell}\bar{m}\bar{n}} = (2\pi\bar{\ell}/L_x)x + (2\pi\bar{m}/L_y)y + (2\pi\bar{n}/L_z)z \qquad (2\text{-}145)$$

where $\bar{\ell}$, $\bar{m}$, and $\bar{n}$ are the integers

$$(\bar{\ell}, \bar{m}, \bar{n}) = 0, \pm 1, \pm 2, \ldots \qquad (2\text{-}146)$$

The lattice of points $K_{\bar{\ell}\bar{m}\bar{n}}$ may be conveniently plotted in a cartesian $\vec{k}$-space or reciprocal space whose k_x, k_y, and k_z axes are exactly coincident with the x, y, and z axes of Fig. 2-4. As shown in Fig. 2-9, the use of this dual coordinate system allows the wave vectors $\vec{k}_s$ and $\vec{k}_o$ and the position coordinate $\vec{r}$ to be displayed simultaneously on the same set of axes.

From the spacing of the points $\vec{K}_{\bar{\ell}\bar{m}\bar{n}}$ and the approximate form for $I(\vec{r},\vec{K})$ given in Eq. (2-144), we notice first that only a single $\vec{K}_{\bar{\ell}\bar{m}\bar{n}}$ can fall inside the cell ξ; therefore the light scattered in the direction $\vec{r}$ is produced by a single Fourier component of the fluctuations. This Fourier component will have a wave vector $\vec{K}_{\bar{\ell}\bar{m}\bar{n}}$ which is within an amount $(\Delta k_x, \Delta k_y, \Delta k_z) = [(\pi/L_x),(\pi/L_y),(\pi/L_z)]$ of satisfying the condition $\vec{k}_o - \vec{k}_s + \vec{K} = 0$. Secondly, we find that since the spacing of the allowed $\vec{K}_{\bar{\ell}\bar{m}\bar{n}}$ are identically the dimensions of ξ, the cells attached to all possible vectors $\vec{k}_o + \vec{K}_{\bar{\ell}\bar{m}\bar{n}}$ form a non-overlapping net which fills all $\vec{k}$-space. Figure 2-12 shows a projection of this net onto the (x,z) plane of Fig 2-10. There is no overlap between adjacent diffracted beams.

5. Calculation of the Coherence Solid Angle

In this section we calculate Ω_{COH} as a function of the direction of observation $\vec{r}$ and the dimensions of the rectangular parallelopiped scattering volume V which was described above. These results are obtained by synthesizing three alternate viewpoints. First, we consider an explicit calculation of the coherence solid angle based on the definitions given in Eqs. (2-135) through (2-138). For the simplified form of $I(\vec{r},\vec{K})$ given in Eq. (2-144) this method yields the average angular range open to $\vec{r}$ for which $\vec{k}_s$ remains within one ξ cell in $\vec{k}$ space, i.e. within a single diffraction pattern of the scattering

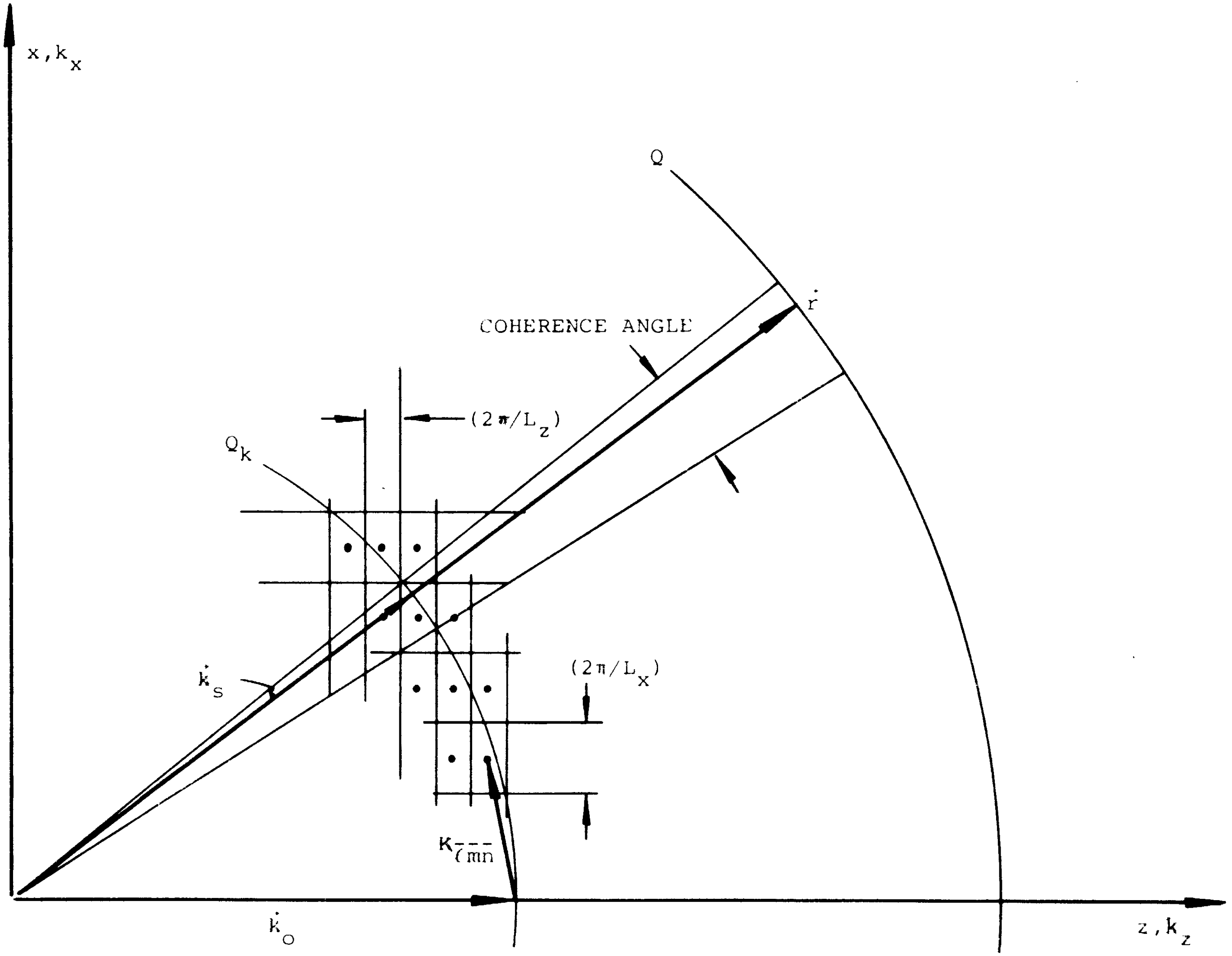
x, k_x
Q
$\dot{r}$
COHERENCE ANGLE
$(2\pi/L_z)$
Q_k
$\dot{k}_s$
$(2\pi/L_x)$
$K_{\bar{\ell}\bar{m}\bar{n}}$
$\dot{k}_o$
z, k_z

Figure 2-12 The reciprocal space associated with the Fourier series expansion of the susceptibility fluctuations.

volume V. This direct approach proves to be tractable only when $\vec{k}_s$ lies in one of the high symmetry planes of V. Secondly, for the same high symmetry planes we verify the results of the direct approach by applying a simplified diffraction angle technique suggested by the discussion of spatial coherence presented in Section E.3. Thirdly, we derive a general expression for Ω_{COH} which is valid for an arbitrary direction of observation, $\vec{k}_s$. This last calculation proceeds by evaluating the number of $\vec{K}_{\bar{\ell}\bar{m}\bar{n}}$ per unit solid angle which contribute to light scattered into the desired direction.

a. The Direct Approach

In the approximation that $I_Q(\vec{r},\vec{K})$ and, therefore, $T_Q(\vec{r},\vec{\rho})$ have the simple step function form given in Eq. (2-144), the two coherence solid angles Ω_{COH} and Ω^*_{COH} defined via Eqs. (2-135), (2-136), (2-137), and (2-138) become identical

$$\Omega_{COH}(\Theta,\Phi) = \Omega^*_{COH}(\Theta,\Phi) = \frac{1}{r_o^2}\int_Q T_Q(\vec{r}_o,\vec{\rho})\,d^2\vec{\rho} \qquad (2\text{-}147)$$

where $\vec{r}_o$ points in the principal direction of observation (Θ,Φ). From Eq. (2-134) we have

$$\Omega_{COH}(\Theta,\Phi) = \frac{1}{Vr_o^2}\int_Q I_Q^*\,(\vec{r}_1+\vec{\rho},\vec{K}_{\bar{\ell}\bar{m}\bar{n}})\,d^2\vec{\rho} \qquad (2\text{-}148)$$

where

$$\vec{k}_o - \vec{k}_s(\vec{r}_o) + \vec{K}_{\bar{\ell}\bar{m}\bar{n}} = 0$$

The required diffraction integral $I_Q^*(\vec{r}_o+\vec{\rho},\vec{K}_{\bar{\ell}\bar{m}\bar{n}})$ is given in Eq. (2-144) as

$$I_Q^*(\vec{r}_o+\vec{\rho},\vec{K}_{\bar{\ell}\bar{m}\bar{n}}) = \begin{cases} V; & \left[\begin{array}{l} -(\pi/L_x) \leq [\vec{k}_o - \vec{k}_s(\vec{r}_o+\vec{\rho}) + \vec{K}_{\bar{\ell}\bar{m}\bar{n}}]_x \leq (\pi/L_x) \\ -(\pi/L_y) \leq [\vec{k}_o - \vec{k}_s(\vec{r}_o+\vec{\rho}) + \vec{K}_{\bar{\ell}\bar{m}\bar{n}}]_y \leq (\pi/L_y) \\ -(\pi/L_z) \leq [\vec{k}_o - \vec{k}_s(\vec{r}_o+\vec{\rho}) + \vec{K}_{\bar{\ell}\bar{m}\bar{n}}]_z \leq (\pi/L_z) \end{array}\right. \\ 0; & \text{otherwise} \end{cases} \tag{2-149}$$

Equation (2-148) can be put in a somewhat more transparent form by recalling that $\vec{k}_s$ points in the direction $\vec{r}$ and is confined to the surface of a sphere Q_k having a radius $|\vec{k}_o| = (\omega_o/c_m)$. With this simplification $\vec{k}_s(\vec{r}_o+\vec{\rho})$ becomes

$$\vec{k}_s(\vec{r}_o+\vec{\rho}) = \frac{\vec{r}_o+\vec{\rho}}{|\vec{r}_o|} \frac{\omega_o}{c_m}$$

and $\Omega_{COH}(\Theta,\Phi)$ can be rewritten as an integral over Q_k using Eq. (2-134), namely,

$$\Omega_{COH}(\Theta,\Phi) = \frac{1}{|\vec{k}_o|^2} \int_{Q_k} \mathbf{T}_Q\ (\vec{k}_s,\vec{K}_{\bar{\ell}\bar{m}\bar{n}})\ d^2\vec{k}_s \tag{2-150}$$

where

$$\mathbf{T}_Q(\vec{k}_s,\vec{K}_{\bar{\ell}\bar{m}\bar{n}}) = \begin{cases} 1\ ; & \left[\begin{array}{l} -(\pi/L_x) \leq [\vec{k}_o - \vec{k}_s + \vec{K}_{\bar{\ell}\bar{m}\bar{n}}]_x \leq (\pi/L_x) \\ \cdots\cdots\cdots\cdots\cdots\cdots \\ \cdots\cdots\cdots\cdots\cdots\cdots \end{array}\right. \\ 0\ ; & \text{otherwise} \end{cases}$$

(2-151)

The function $\mathbf{T}_Q$ vanishes if $\vec{k}_s$ falls outside the cell ξ of dimensions

$$[\Delta k_x,\Delta k_y,\Delta k_z] = [(2\pi/L_x,(2\pi/L_y),(2\pi/L_z)]$$

centered at $(\vec{k}_o + \vec{K}_{\bar{\ell}\bar{m}\bar{n}})$; thus the integral in Eq. (2-150) is identically the surface area of Q_k contained inside ξ. It follows that the coherence solid angle Ω_{COH} is the angular range open to $\vec{r}$ (or $\vec{k}_s$) for which $\vec{k}_s$ terminates within a single ξ cell in reciprocal space. A pictorial representation of this coherence solid angle is illustrated in Fig. 2-13.

Under normal circumstances all three dimensions of V will be large compared to the wavelength of the incident light and we may take the dimensions of ξ, $[(2\pi/L_x),(2\pi/L_y),(2\pi/L_z)]$, to be small compared to the magnitudes of $\vec{k}_s$ and $\vec{k}_o$, $|\vec{k}_s| = |\vec{k}_o| = (2\pi/\lambda)$. In this limit the surface of Q_k is essentially planar in the immediate vicinity of any particular $\xi_{\bar{\ell}\bar{m}\bar{n}}$.

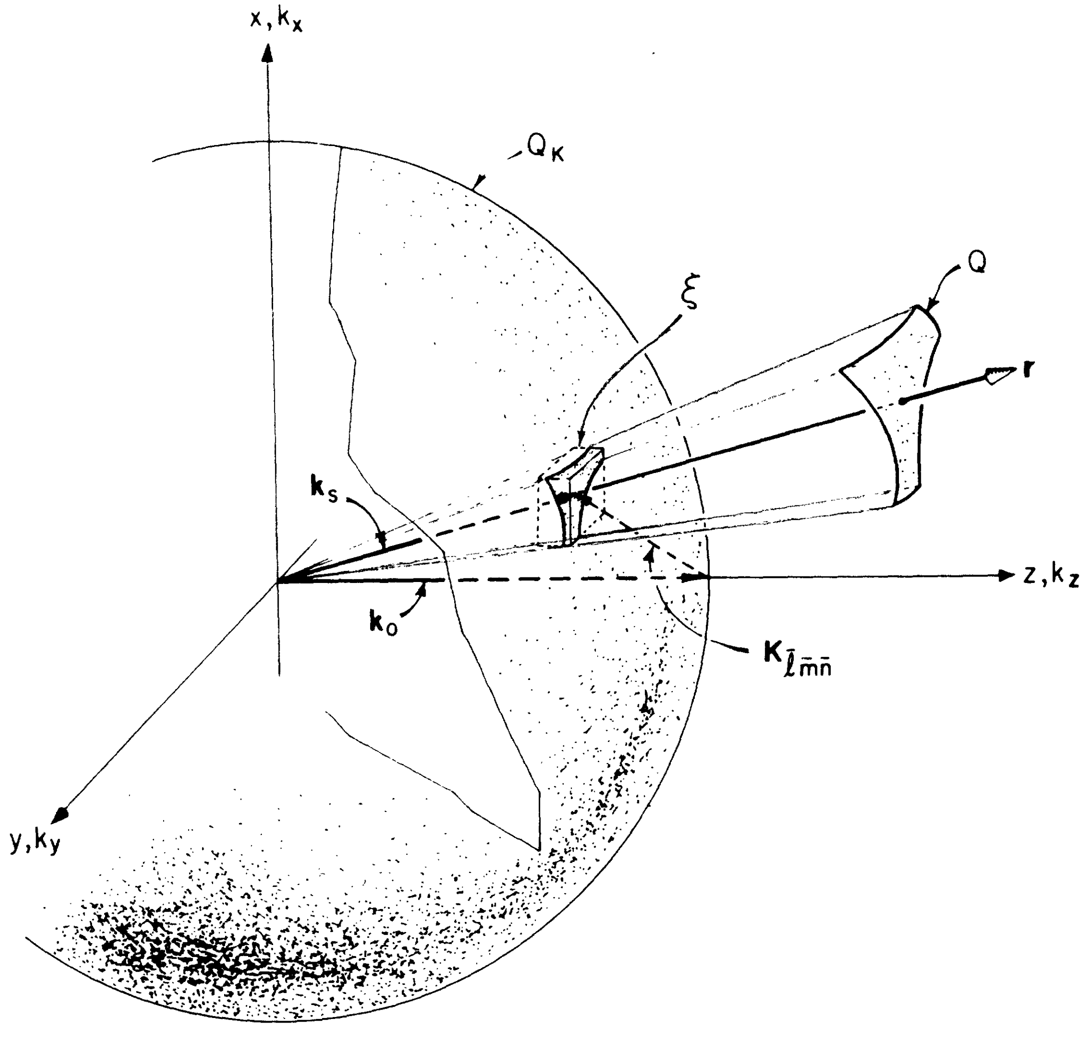
x, k_x
Q_K
Q
ξ
r
k_s
z, k_z
k_o
$K_{\bar{l}\bar{m}\bar{n}}$
y, k_y

Figure 2-13 A pictorial illustration of the coherence solid angle as fixed by the area of the sphere Q_K contained within a single ξ cell of reciprocal space.

Suppose that the direction of $\vec{k}_s$ is given in terms of the scattering angle Θ and the azimuthal angle Φ shown in Fig. 2-4, and we consider the special case $\Phi = 90°$ so that $\vec{k}_s$ lies in the (y,z) plane. Then the solid angle open to $\vec{k}_s$ within one cell in $\vec{k}$-space can be obtained by inspection from Figs. 2-14 and 2-15. These figures illustrate the intersection between Q_k and the ξ cells as seen in two particular orthogonal directions around the point $(\Theta, \Phi = 90°)$.

Figure 2-14 represents the (x,k_s) plane of Fig. 2-4. The half-angle of coherence in this plane is simply

$$\overline{\Delta\Psi} = \frac{1}{2}\left(\frac{2\pi}{L_x}\right)\frac{1}{|\vec{k}_s|} = \frac{\lambda}{2L_x} \tag{2-152}$$

where λ is the wavelength of the incident light in the medium.

Figure 2-15 illustrates the situation in the (y,z) plane of Fig. 2-4. In this direction the opening angle of a particular diffraction pattern depends on the precise location at which Q_k intersects the cell ξ. Performing an average over all possible locations based on an equal probability for each we find

$$\overline{\Delta\Theta} = \frac{1}{2}\,\frac{\lambda}{L_z \sin\Theta + L_y \cos\Theta} \tag{2-153}$$

The orientations of $\overline{\Delta\Theta}$ and $\overline{\Delta\Psi}$ in relation to $\vec{k}_s$ are shown in Fig. 2-16. From the two orthogonal full-opening angles, $2\overline{\Delta\Theta}$ and $2\overline{\Delta\Psi}$, we find the desired coherence solid angle as

$$\Omega_{COH}(\Theta, \Phi = 90°) = 4\overline{\Delta\Theta}\cdot\overline{\Delta\Psi} = \frac{\lambda^2}{L_x(L_z \sin\Theta + L_y \cos\Theta)} \tag{2-154}$$

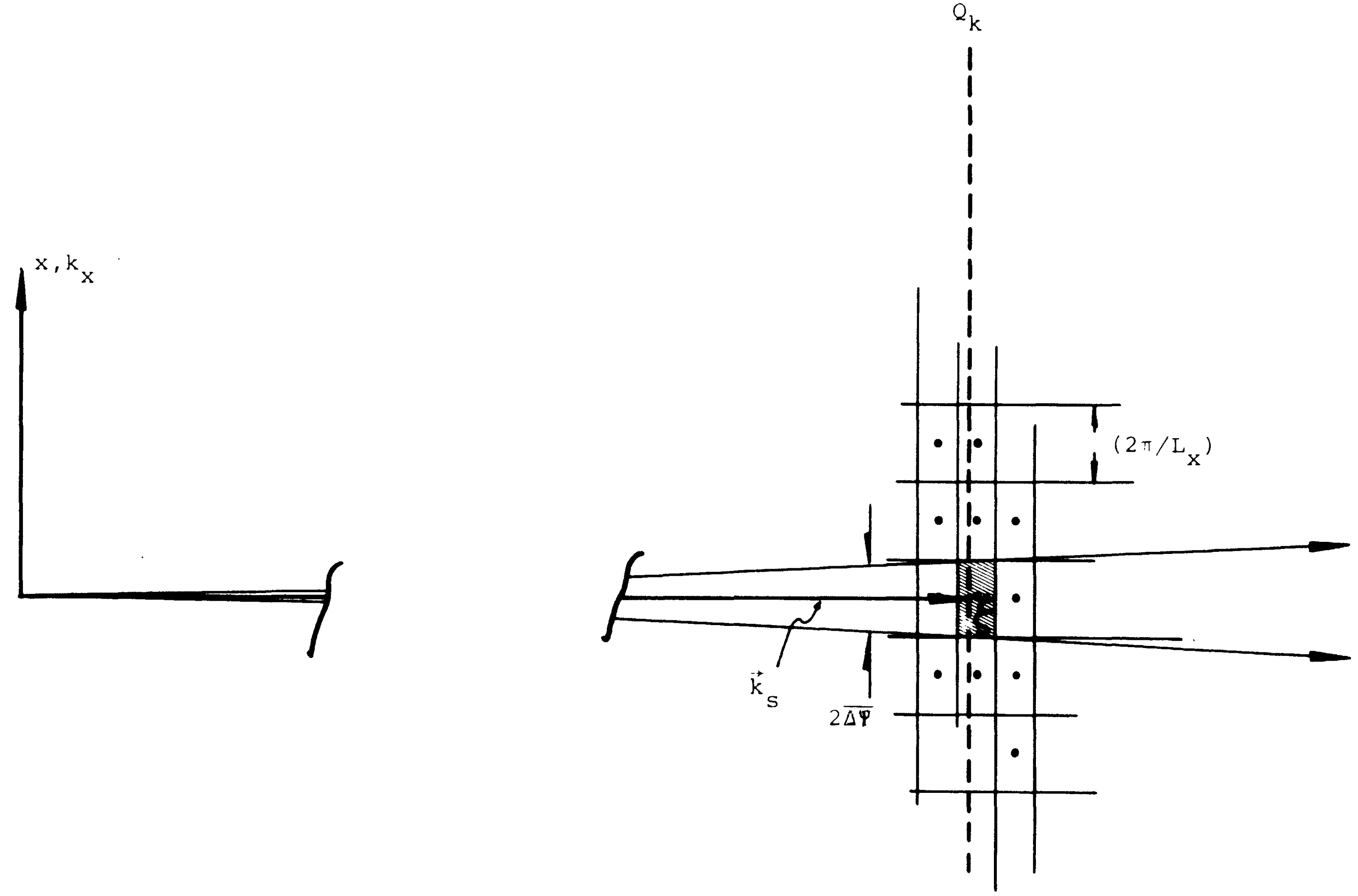
Q_k
x, k_x
$(2\pi/L_x)$
$\vec{k}_s$
$2\overline{\Delta\Psi}$

Figure 2-14 A pictorial representation of the coherence angle in the (x,k_s) plane of the scattering volume.

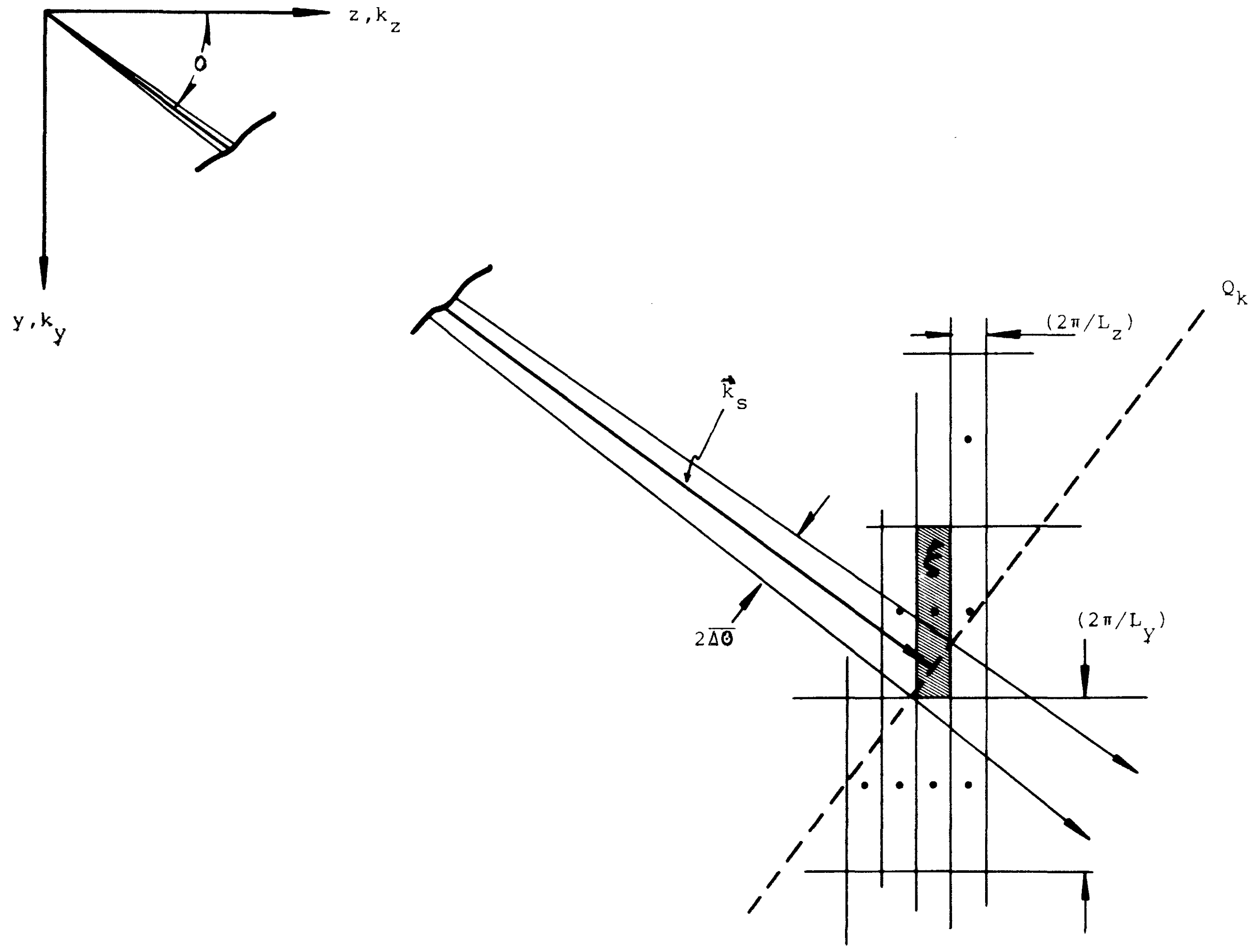
z,k_z
θ
y,k_y
$\vec{k}_s$
$2\overline{\Delta\theta}$
$(2\pi/L_z)$
$(2\pi/L_y)$
Q_k

Figure 2-15 A pictorial representation of the coherence angle in the (y,z) plane of the scattering volume.

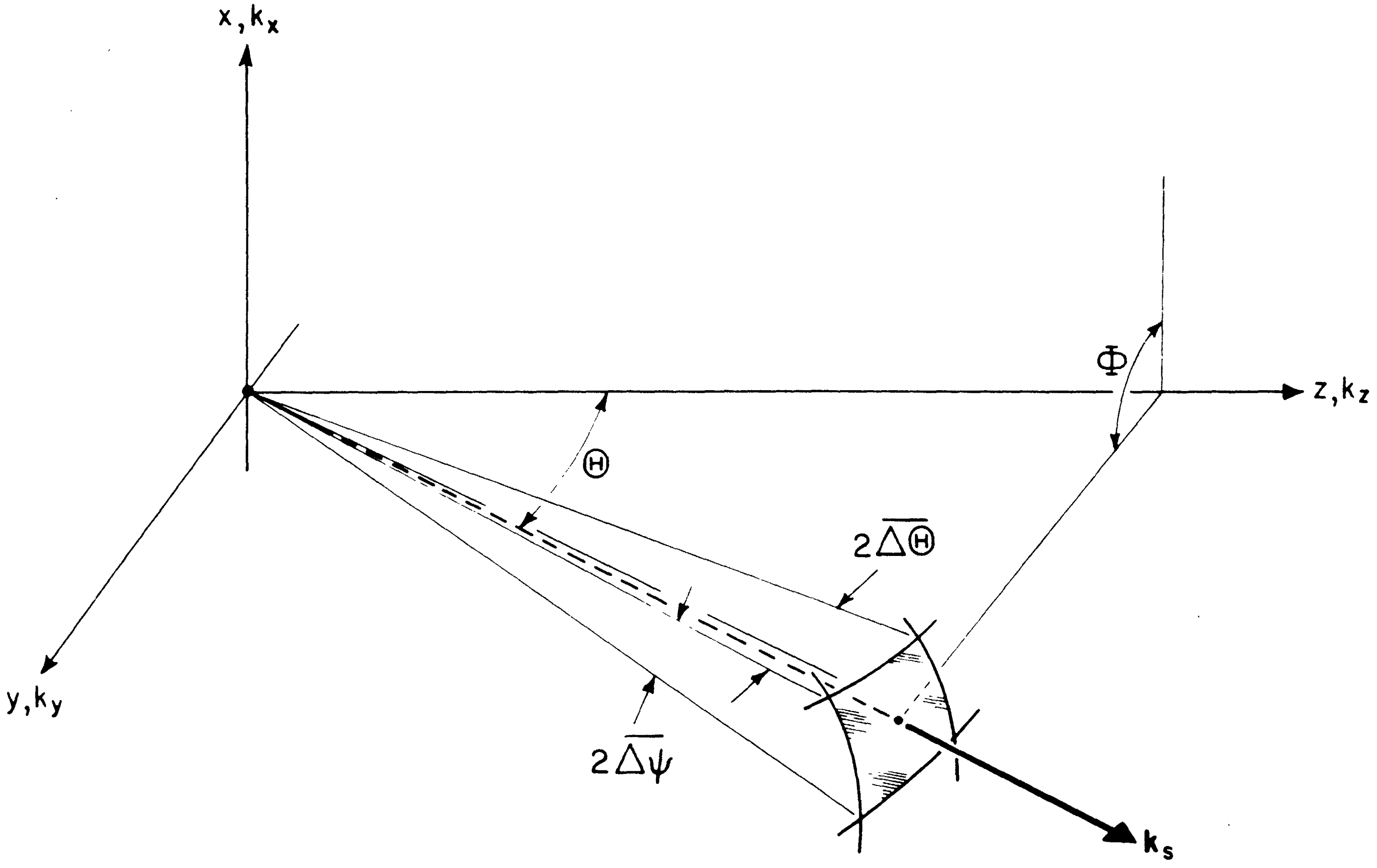
x, k_x
z, k_z
y, k_y
Φ
Θ
$2\overline{\Delta\Theta}$
$2\overline{\Delta\psi}$
k_s

Figure 2-16 Illustration of the coherence angles $\overline{\Delta\Theta}$ and $\overline{\Delta\Phi}$.

b. A Simple Diffraction Approach

In the interest of estimating Ω_{COH} by some simple technique it is useful to point out that $\overline{\Delta\Theta}$ and $\overline{\Delta\Psi}$ can often be derived directly by using the basic description of the spatial coherence phenomenon as given in Section E.3; namely, coherence vanishes when the relative phases of the waves reaching $\vec{r}$ from any two points on the source change by an amount $\pm\pi$ as we proceed to $\vec{r}+\vec{\rho}$. The source points that produce the maximum relative phase change are determined by the extremal dimensions of the source as seen by the observer at $\vec{r}$.

Figure 2-17 shows that the maximum dimension of V in the (x,k_s) plane of Fig. 2-4. is just L_x. The relative phase at the observer's position **Q** between waves originating at the two extremal points A and B changes with the angle Ψ at a rate

$$\frac{d(\text{relative phase})}{d\Psi} = \frac{2\pi}{\lambda}\frac{d(\Delta)}{d\Psi} = \frac{2\pi}{\lambda}(L_x \sin\Theta) \qquad (3\text{-}155)$$

For a maximum phase change of π at $\Psi = 0$ we have

$$\overline{\Delta\Psi} = (\lambda/2L_x) \qquad (2\text{-}156)$$

which is in agreement with Eq. (2-152).

In the (y,z) plane shown in Fig. 2-18 the extremal path length increments

$$\Delta_1 = L_z \cos\Theta$$

and (2-157)

$$\Delta_2 = L_y \sin\Theta$$

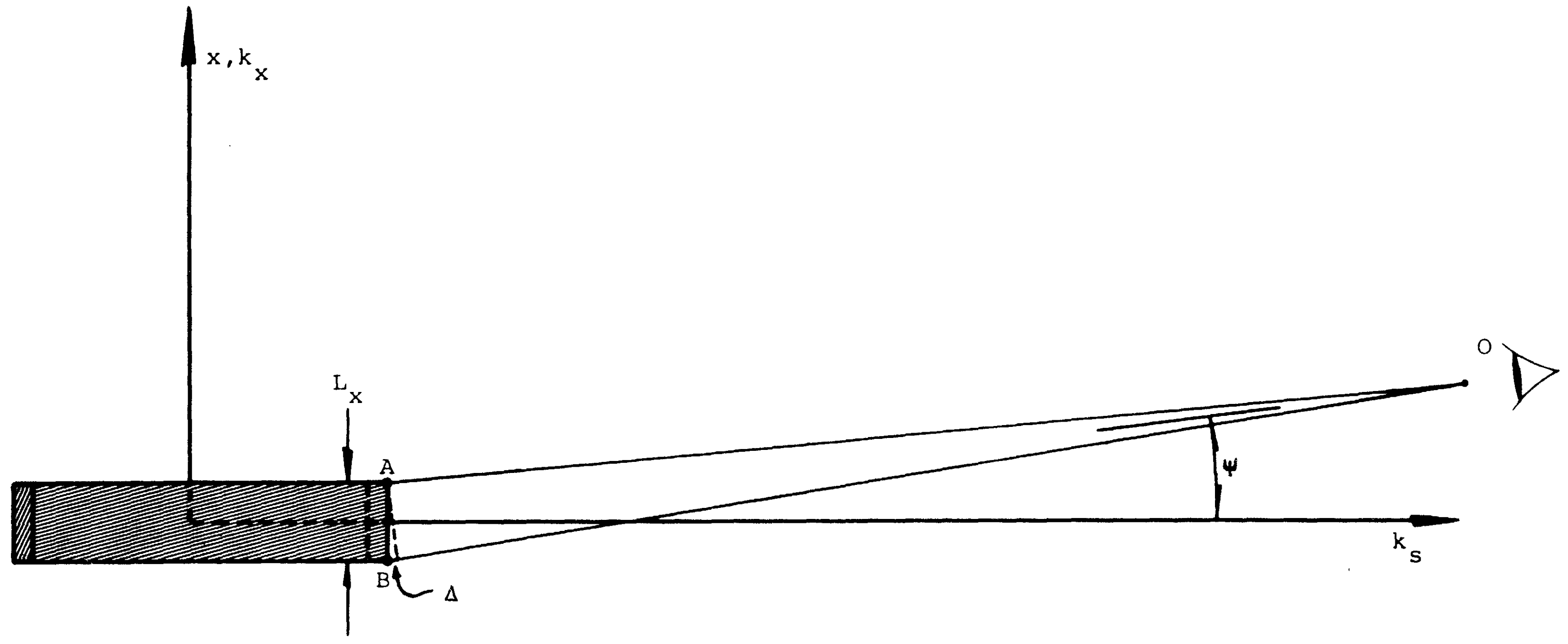
x,k_x
L_x
A
B
Δ
O
ψ
k_s

Figure 2-17 The extremal source dimensions in the (x,k_s) plane of the scattering volume.

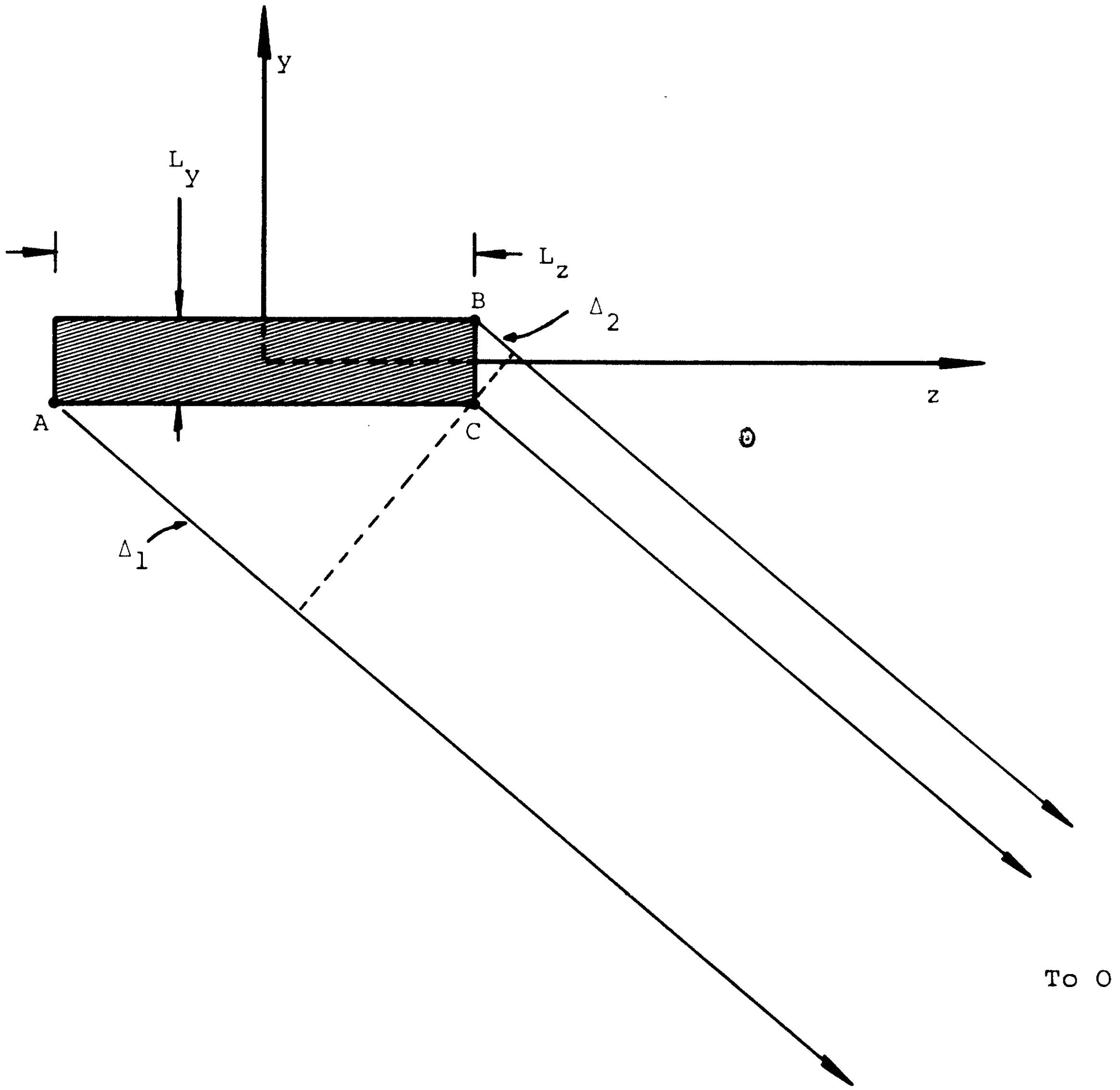
y
L_y
L_z
B
Δ_2
z
A
C
Θ
Δ_1
To O

Figure 2-18 The extremal source dimensions in the (z,y) plane of the scattering volume.

both change with the scattering angle Θ. The relative phase measured at $\mathbf{Q}$ for waves originating at points A and B changes with a rate which is related to the variation in the difference $(\Delta_2 - \Delta_1)$ by the derivative

$$\frac{d(\text{relative phase})}{d\Theta} = \frac{2\pi}{\lambda}\frac{d(\Delta_2-\Delta_1)}{d\Theta} = \frac{2\pi}{\lambda}(L_y \cos\Theta + L_z \sin\Theta) \tag{2-158}$$

Therefore, a variation of π in relative phase occurs when Θ changes by an amount

$$\overline{\Delta\Theta} = \frac{\lambda}{2[L_z \sin\Theta + L_y \cos\Theta]} \tag{2-159}$$

A comparison with Eq. (2-153) shows that this result is precisely the half-angle of coherence in the plane $(\Theta,\Phi=90°)$.

This simple technique based on phase changes and the extremal source dimensions is generally the most straightforward method for obtaining Ω_{COH}.

c. The Shell Approach

Although the computation of the angular size of a single diffracted beam is straightforward for the symmetry planes of V, the general result $\Omega_{COH}(\Theta,\Phi)$ is more easily obtained from an entirely different approach. The analysis of Section E.4.f indicated that the form of the interference integral $I(\vec{r},\vec{K})$ may be interpreted from two equally valid points of view; the first, in which we regard $\vec{K}$ as fixed and $\vec{k}_s$ as free to assume all allowed positions in the $\vec{k}$ space cell $\xi_{\bar{\ell}\bar{m}\bar{n}}$, leads to the calculation of Ω_{COH} by the direct method given above. However, Eq. (2-144) can also be taken to mean that *if* a fluctuation of wave vector $\vec{K}$ is to scatter light into the direction $\vec{k}_s = (\omega_o/c_m)\hat{r}$, then the *wave vector* $\vec{k}_o + \vec{K}$ must fall inside a rectangular parallelopiped volume *centered on the wave vector* $\vec{k}_s$ and having dimensions $(\Delta k_x, \Delta k_y, \Delta k_z) = [(2\pi/L_x), (2\pi/L_y), (2\pi/L_z)]$. In this interpretation, the cell ξ is attached to the direction of observation and not to the lattice of points $\vec{K}_{\bar{\ell}\bar{m}\bar{n}}$.

If $\vec{k}_s$ is allowed to assume *all* possible positions on the sphere Q_k, then the motion of the attached cell ξ sweeps out a shell-like volume whose thickness is determined by the dimensions of ξ and the orientation of $\vec{k}_s$. If a fluctuation with wave vector $\vec{K}_{\bar{\ell}\bar{m}\bar{n}}$ is to contribute to scattering then the vector $\vec{k}_o + \vec{K}_{\bar{\ell}\bar{m}\bar{n}}$ must terminate somewhere inside the shell. Figure 2-19 shows a cut through the shell taken in the (x,z) plane of Fig. 2-4.

The shell thickness in the general direction (Θ,Φ) is simply the maximum dimension of ξ, its diagonal, projected onto the vector $\vec{k}_s$. Expressing the length and orientation of this diagonal by the vector notation

$$\Delta\vec{k} = (2\pi/L_x)\hat{x} + (2\pi/L_y)\hat{y} + (2\pi/L_z)\hat{z} \qquad (2\text{-}160)$$

we find for the shell thickness in spherical coordinates

$$\Delta\vec{k}\cdot\hat{k}_s = 2\pi\left[\frac{\sin\Theta\cos\Phi}{L_x} + \frac{\sin\Theta\sin\Phi}{L_y} + \frac{\cos\Theta}{L_z}\right] \qquad (2\text{-}161)$$

It follows that the *volume* of $\vec{k}$-space occupied by the shell in allowing $\vec{k}_s$ to take any position on Q_k within a solid angle Ω is simply

$$V_k = |\vec{k}_o|^2(\Delta\vec{k}\cdot\hat{k}_s)\Omega \qquad (2\text{-}162)$$

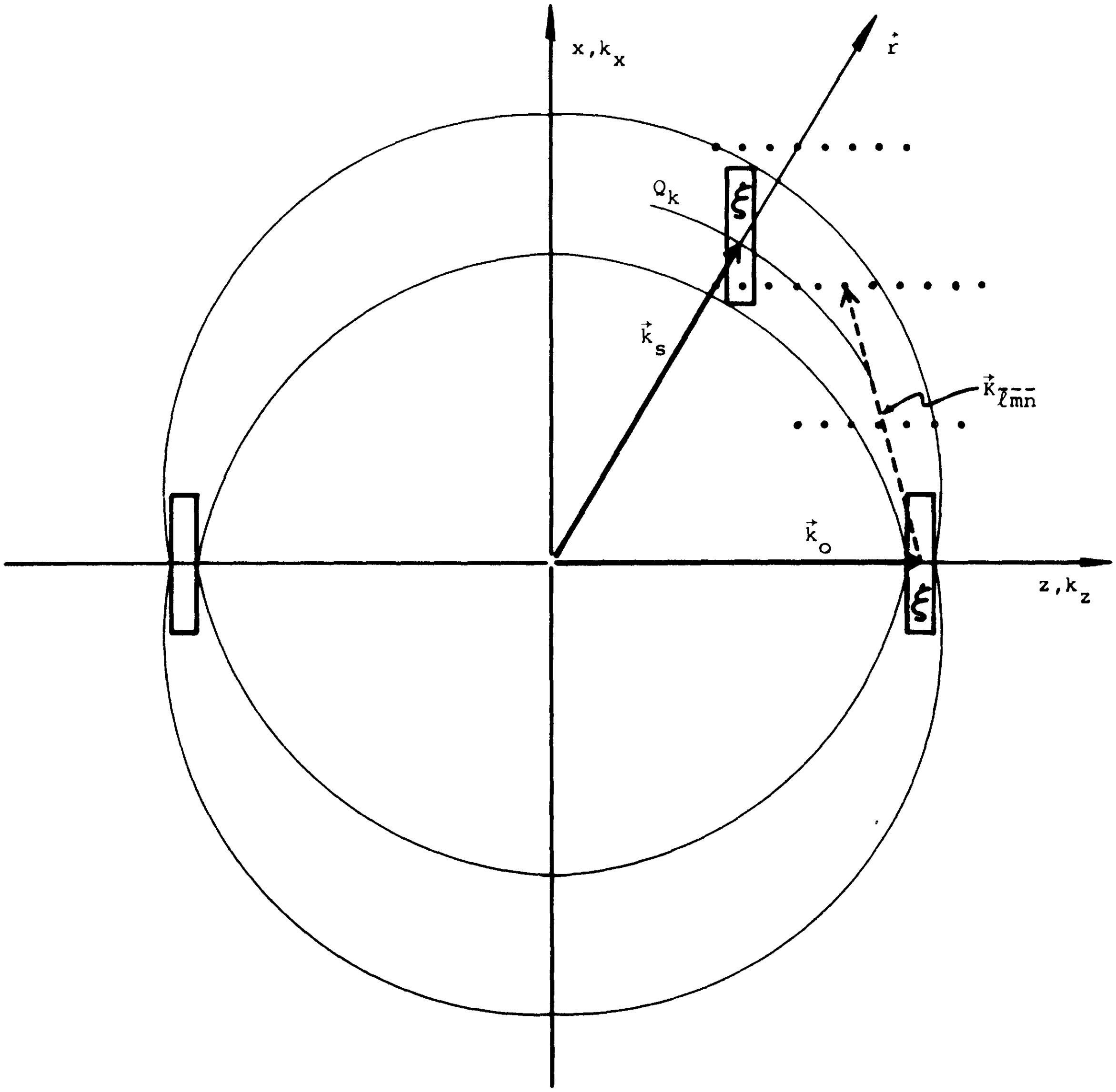
x,k_x
$\vec{r}$
Q_K
ξ
$\vec{k}_s$
$\vec{K}_{\bar{\ell}\bar{m}\bar{n}}$
$\vec{k}_o$
z,k_z
ξ

Figure 2-19 The shell swept out by a single ξ cell in allowing $\vec{k}_s$ to assume all allowed positions on Q_K.

With this result and the volume density of $\vec{K}_{\bar{\ell}\bar{m}\bar{n}}$ points in k-space, namely,*

$$\rho_k = \frac{1}{\Delta k_x \Delta k_y \Delta k_z} = \frac{V}{8\pi^3} , \tag{2-163}$$

we have for the number of $\vec{K}_{\bar{\ell}\bar{m}\bar{n}}$ contributing to the scattered field in a small solid angle $d\Omega$ as

$$\frac{dN}{d\Omega} = \frac{V}{\lambda^2}\left[\frac{\sin\Theta\cos\Phi}{L_x} + \frac{\sin\Theta\sin\Phi}{L_y} + \frac{\cos\Theta}{L_z}\right] \tag{2-164}$$

or, writing $V = L_x L_y L_z$, in the more useful form

$$\frac{dN}{d\Omega} = \frac{1}{\lambda^2}\,[L_y L_z \sin\Theta\cos\Phi + L_x L_z \sin\Theta\sin\Phi + L_x L_y \cos\Theta] \tag{2-165}$$

Inverting Eq. (2-165) yields an average solid angle per contributing $\vec{K}_{\bar{\ell}\bar{m}\bar{n}}$ and, therefore, a coherence solid angle of the form

$$\Omega_{COH}(\Theta,\Phi) = \frac{\lambda^2}{L_y L_z \sin\Theta\cos\Phi + L_x L_z \sin\Theta\sin\Phi + L_x L_y \cos\Theta} \tag{2-166}$$

This result represents the desired generalization of the calculation made via the direct approach in Section E.5.a. Setting $\Phi = 90°$ shows that Eq. (2-166) is in agreement with the previously derived expression given in Eq. (2-154).

---

* Chapter 2, Section E.4.

6. The Behavior of Ω_{COH} and the Optimization of the Scattered Power per Coherence Solid Angle

The manner in which the coherence solid angle varies with the direction of observation (Θ,Φ) and the sample dimensions (L_x,L_y,L_z) can be summarized easily in terms of the simple diffraction approach of Section 5.b. The diffraction or coherence angles at some particular (Θ,Φ) are inversely proportional to the sample dimensions projected on a plane perpendicular to the direction of observation.

Although the behavior of Ω_{COH} itself is of some interest from the viewpoint of analyzing the light collection system of an optical mixing spectrometer,[*] the quantity which determines the detection capability of such an instrument is the available scattered power per coherence solid angle, P_{COH}. Since the amount of scattered power per unit solid angle is itself a function of the sample dimensions, it is more useful to investigate the properties of P_{COH} directly rather than Ω_{COH}.

For the case $\Phi = 90°$, we find from Eq. (2-154) and (2-55)

$$P_{COH} = 2P_o \mathbf{R} L_z (\sin^2 \phi) \cdot \frac{\lambda^2}{L_x(L_z \sin \Theta + L_y \cos \Theta)} \qquad \text{(2-167)}$$

P_o - the incident power

$\mathbf{R}$ - the Rayleigh coefficient

ϕ - the angle between the polarization vector of the incident beam and the direction of observation

---

[*] Chapter 4, Sections E.2.b and E.2.c.

λ - the wavelength of the incident light in the scattering medium

Equation (2-167) shows that P_{COH} depends on the geometrical shape of the illuminated region through the factor

$$P_{COH} \propto \frac{1}{L_x[\sin\Theta + (L_y/L_z)\cos\Theta]} \qquad (2\text{-}168)$$

In attempting to maximize P_{COH} by changing L_x, L_y, and L_z we may note the following points from Eq. (2-168).

First, it is advantageous to have L_x, the dimension of the scattering volume V in the direction normal to the scattering plane, as small as possible. This procedure maximizes the coherence angle $\overline{\Delta\Psi} = (\lambda/2L_x)$.

Second, only the ratio of L_y to L_z appears in P_{COH}, L_z being the length of V in the direction of the incident beam, and L_y its width in the scattering plane. The largest values of P_{COH} occur for the smallest values of (L_y/L_z) independent of the scattering angle Θ.

Third, the dependence of P_{COH} on the sample length L_z exhibits two distinct limiting behaviors depending on whether the ratio (L_y/L_z) is larger or smaller than the tangent of the scattering angle.

Starting from small values of L_z, $(L_y/L_z) >> \tan\Theta$, P_{COH} grows linearly with increasing L_z. In this limit the coherence angle $\overline{\Delta\Theta}$ is controlled by the L_y dimension of the source

$$\overline{\Delta\Theta} \simeq \frac{\lambda}{2L_y\cos\Theta} \qquad (L_y/L_z) >> \tan\Theta$$

while the scattered power per unit solid angle is proportional to L_z.

If L_z is increased until $(L_y/L_z) << \tan\Theta$ the available power per coherence area becomes independent of L_z, an increase in the total scattered power $P \propto L_z$ being exactly offset by a decrease in the coherence angle $\overline{\Delta\Theta}$

$$\overline{\Delta\Theta} \simeq \frac{\lambda}{2L_z \sin\Theta} \qquad (L_y/L_z) << \tan\Theta$$

It follows from Eq. (2-168) that in optimizing P_{COH} for a fixed value of Θ, it is essentially unnecessary to lengthen L_z beyond the value which gives $(L_y/L_z) = \tan\Theta$. In this case P_{COH} is one-half of its maximum possible value

$$[P_{COH}]_{MAX} = 2P_o \mathbf{R} (\sin^2 \phi) \frac{\lambda^2}{L_x \sin\Theta} \tag{2-169}$$

For fixed dimensions L_x, L_y, and L_z, P_{COH} shows two types of behavior as a function of the scattering angle. At values of Θ much larger than $\Theta_c = \tan^{-1}(L_y/L_z)$ the length L_z is sufficiently large to yield the optimum value of P_{COH} and we find

$$P_{COH} \propto \frac{1}{L_x \sin\Theta} \qquad \tan\Theta >> (L_y/L_z)$$

as in Eq. (2-169). The power per coherence solid angle dips below its maximum value when Θ approaches Θ_c, while for $\Theta << \Theta_c$ we have

$$P_{COH} \propto \frac{L_z}{L_x L_y \cos\Theta} \qquad \tan\Theta << (L_y/L_z)$$

which levels off as $\Theta \to 0$. The ratio of the actual to the optimum value of P_{COH} at an arbitrary scattering angle Θ can be written in the useful form

$$\frac{P_{COH}}{[P_{COH}]_{MAX}} = \frac{1}{1 + (\tan \Theta_c / \tan \Theta)} \qquad (2\text{-}170)$$

$$\Theta_c \equiv \tan^{-1} (L_y/L_z) \qquad (2\text{-}171)$$

For the laser source and scattering cell geometry used in this thesis the dimensions of the illuminated region are[*]

$$\begin{aligned} L_x &= 0.019 \text{ cm} \\ L_y &= 0.028 \text{ cm} \\ L_z &= 2.54 \text{ cm} \end{aligned} \qquad (2\text{-}172)$$

yielding $\Theta_c = 0.636°$. Figure 2-20 shows a plot of the corresponding coherence angles $\overline{\Delta\Theta}$ and $\overline{\Delta\Psi}$ calculated from Eqs. (2-152) and (2-153) using the numerical quantities

$$\begin{aligned} \lambda_{air} &= 6328 \text{ Å} \\ n &= 1.49 \end{aligned} \qquad (2\text{-}173)$$

This same figure also displays the behavior of the coherence solid angle $\Omega_{COH} = 4\overline{\Delta\Theta}\cdot\overline{\Delta\Psi}$. To illustrate the Θ variation of P_{COH} and $[P_{COH}]_{MAX}$ for this example, we show in Fig. 2-21 the ratios P_{COH}/P_o and $[P_{COH}]_{MAX}/P_o$ obtained from Eqs. (2-167), (2-172) and (2-173) for the case of scattering from entropy fluctuations in toluene where $\mathbf{R}_{\Delta s} \simeq 10^{-6}$ /cm.[**]

---

[*] Chapter 4, Section C.4.

[**] Chapter 5, Section C.4.a.

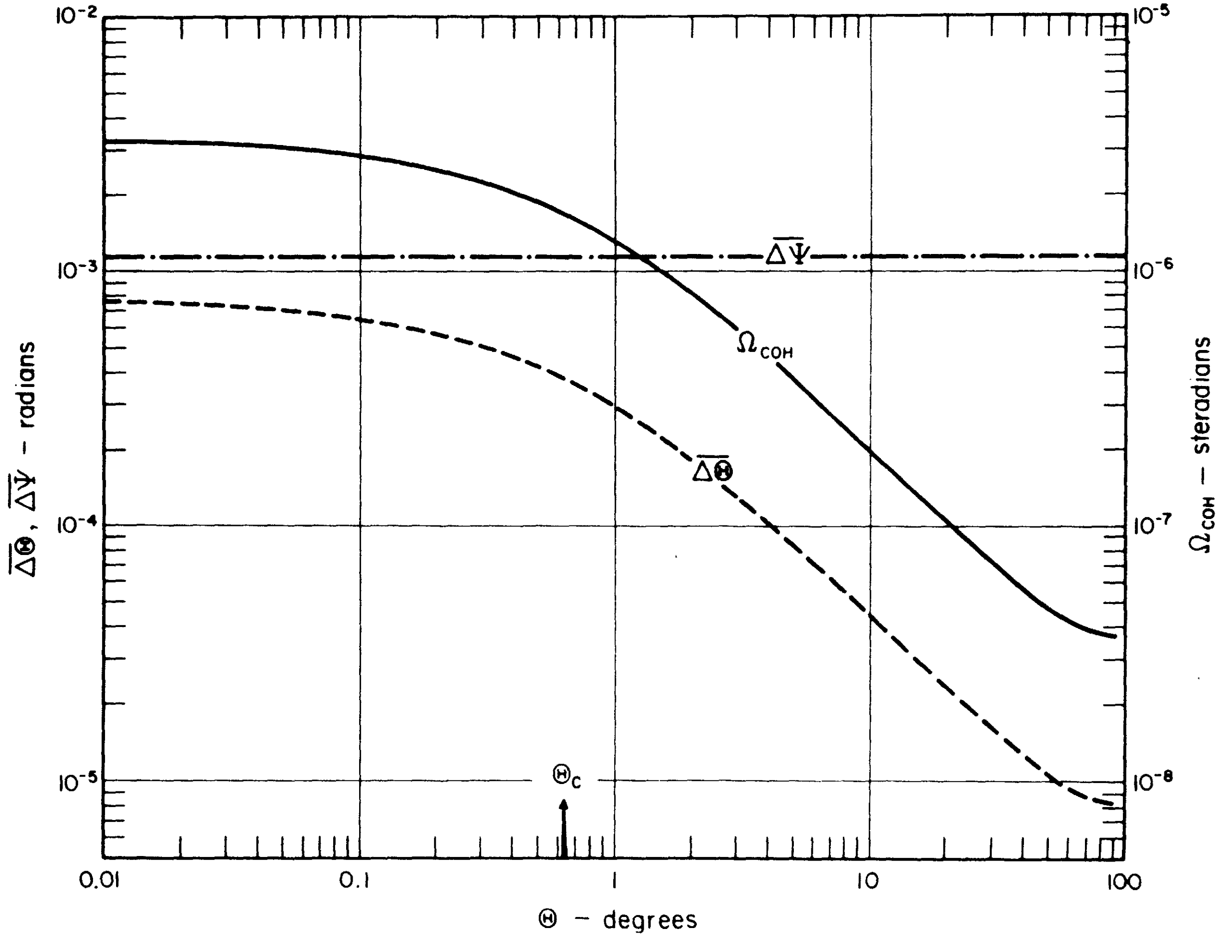

Figure 2-20 The coherence angles and coherence solid angle for the scattering geometry described in Chapter 4 versus the scattering angle Θ. The critical angle Θ_c is defined as $\Theta_c \equiv \tan^{-1} (L_y/L_z)$.

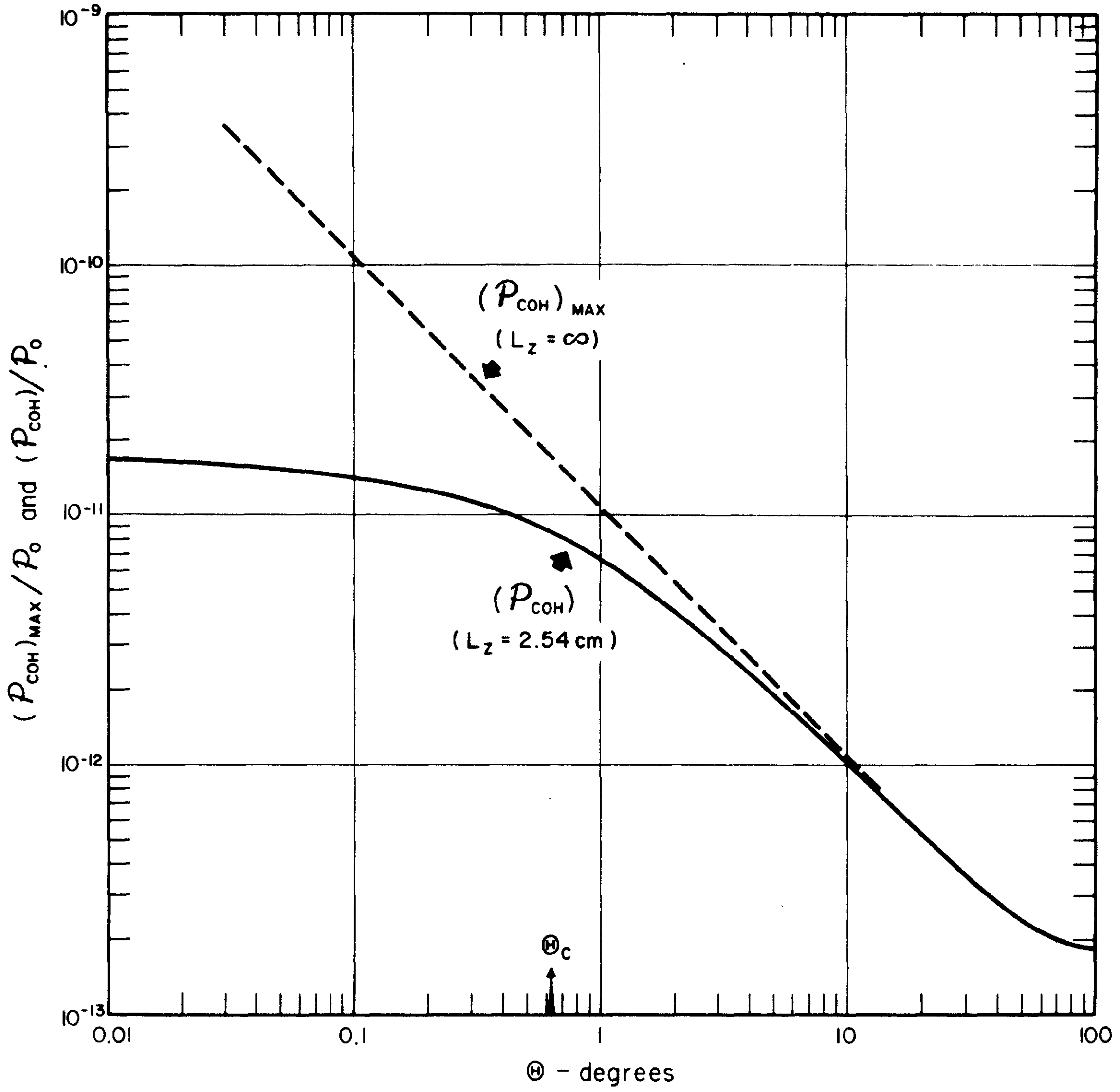

Figure 2-21 The ratio of power per coherence area to incident power for scattering from entropy fluctuations in toluene. The results are given as a function of the scattering angle Θ for two geometries, (1) the illuminated region described in Section C.4 of Chapter 4, and (2) the same volume extended to infinite length, $L_z = \infty$.

BIBLIOGRAPHY: Chapter 2

1. W. K. H. Panofsky and M. Phillips, *Classical Electricity and Magnetism* (Addison-Wesley Publishing Company, Inc., Reading, Massachusetts, 1955), Chapter 2.

2. G. Benedek and T. Greytak, Proc. IEEE **53**, 1623 (1965).

3. L. D. Landau and E. M. Lifshitz, *Statistical Physics* (Addison-Wesley Publishing Company, Inc., Reading, Massachusetts, 1958), Chapter 12.

4. I. L. Fabelinskii, Usp. Fiz. Nauk **63**, 355 (1957) [English transl.: AEC Translation 3973, Part I, Advan. Phys. Sci. **63**, 474 (1957)].

5. L. I. Schiff, *Quantum Mechanics* (McGraw-Hill Book Company, Inc., New York, 1955), pp. 161 ff.

6. C. Kittel, *Introduction to Solid State Physics* (John Wiley and Sons, Inc., New York, 1956), 2nd ed., Chapter 2.

7. Reference 1, pp. 222 ff.

8. J. M. Ziman, *Principles of the Theory of Solids* (Cambridge University Press, Cambridge, England, 1964), pp. 23-25.

9. V. S. Starunov, Opt. i Spektroskopiya **18**, 300 (1965) [English transl.: Opt. Spectry. (USSR) **18**, 165 (1965)].

10. R. Loudon, Adv. Phys. **13**, 423 (1964).

11. P. A. Fleury, S. P. S. Porto, L. E. Cheesman, and H. J. Guggenheim, Phys. Rev. Letters **17**, 84 (1966).

12. S. P. S. Porto, B. Tell, and T. C. Damon, Phys. Rev. Letters **16**, 450 (1966).

13. M. W. Zemansky, *Heat and Thermodynamics* (McGraw-Hill Book Company, Inc., New York, 1957), Chapter 2.

14. W. B. Davenport, Jr., and W. L. Root, *An Introduction to the Theory of Random Signals and Noise* (McGraw-Hill Book Company, Inc., New York, 1958), Chapters 2 and 3.

15. W. Yourgrau, A. van der Merwe, G. Raw, Treatise on Irreversible and Statistical Thermophysics (The Macmillan Company, New York, 1966), Sections 2-3 and 1-4.

16. B. U. Felderhof, J. Chem. Phys. 44, 602 (1966).

17. C. M. Sogani, Indian J. Phys. 1, 357 (1927).

18. C. M. Sogani, Indian J. Phys. 2, 97 (1927).

19. J. L. Lundberg, E. J. Mooney, and K. R. Gardner, Science 145, 1308 (1964).

20. A. Einstein, Ann. Physik 25, 205 (1908).

21. V. L. Ginzburg, Izv. AN SSSR, seriya fizicheskaya (Bulletin of the USSR Academy of Sciences, physical series), 9, 174 (1945).

22. G. B. Benedek, Lectures on the Theory of the Scattering of Light from Thermal Fluctuations, Brandeis Summer Institute for Theoretical Physics, 1966 (to be published).

23. H. Margenau and G. M. Murphy, The Mathematics of Physics and Chemistry (D. Van Nostrand Company, Inc., Princeton, New Jersey, 1956), pp. 247 ff.

24. Reference 14, pp. 59 ff.

25. G. P. Wadsworth and J. G. Bryan, Introduction to Probability and Random Variables (McGraw-Hill Book Company, Inc., New York, 1960), Chapter 4.

26. Reference 25, Chapter 5.

27. E. Parzen, Modern Probability Theory and Its Applications (John Wiley and Sons, Inc., New York, 1960), p. 339.

28. L. A. Pipes, Applied Mathematics for Engineers and Physicists (McGraw-Hill Book Company, Inc., New York), Chapter 18.

29. R. D. Mountain, Rev. Mod. Phys. 38, 205 (1966).

30. K. F. Herzfeld and T. A. Litovitz, Absorption and Dispersion of Ultrasonic Waves (Academic Press, Inc., New York, 1959), pp. 28 ff.

31. Reference 30, Section 6.

32. Reference 30, Section 5.

33. Reference 30, Section 7.

34. Reference 30, Section 31.

35. M. J. Beran and G. B. Parrent, Jr., *Theory of Partial Coherence* (Prentice-Hall, Inc., Englewood Cliffs, New Jersey, 1964).

36. Reference 14, pp. 66 ff.

37. J. D. Jackson, *Classical Electrodynamics* (John Wiley and Sons, Inc., New York, 1962), pp. 268 ff.

Chapter 3

THE THEORY OF LIGHT MIXING SPECTROMETERS

A. Introduction

From the calculations and numerical results presented in Section D of Chapter 2 it becomes apparent that in many cases an investigation of the spectrum of light scattered from thermal fluctuations in liquids requires spectroscopic techniques whose fractional resolutions $(\delta\omega/\omega_o)$ are far beyond those obtainable by classic methods. The three main features, the splitting and natural width of the Brillouin-Mandel'shtam components, and the natural width of the central component, indicate that desirable resolutions are respectively $(\delta\omega/\omega_o) \simeq 10^{-5} - 10^{-7}$, $(\delta\omega/\omega_o) \simeq 10^{-7} - 10^{-11}$, and $(\delta\omega/\omega_o) \simeq 10^{-8} - 10^{-14}$. In comparison, the best available grating spectrometers[1] achieve $(\delta\omega/\omega_o) \simeq 10^{-6}$ while ultrahigh resolution Fabry-Pérot etalons [2,3] can approach $(\delta\omega/\omega_o) \simeq 5 \times 10^{-8}$.

The problem of obtaining extremely high resolving powers in the optical region of the electromagnetic spectrum has its exact analog in the difficulties of sufficient selectivity faced by the radio frequency (rf) engineer. Since the latter have been solved by very effective methods, it is instructive to approach the problem from the viewpoint of conventional rf practices. In particular, the relevance of this approach stems from the availability of an optical "oscillator," the laser, which makes possible the actual realization of optical equivalents to well known rf systems.

Figure 3-1 shows a block diagram representation of the simplest rf receiver[4] along with its optical analog; an example of a typical optical spectrometer. The function of both receivers (or spectrometers) is to examine the power per unit frequency interval, $S_E(\omega)$, in the electric field at their respective inputs. In the rf case the signal is amplified and then passed through a tunable filter whose bandwidth is chosen to be narrow compared to the spectral width of $S_E(\omega)$. The output of the filter contains those frequencies in $S_E(\omega)$ which fall within this bandpass. The filtered rf signal is then rectified and the resulting dc level displayed as the output. A recording of this output as the rf filter is tuned through its range yields a plot whose amplitude reflects the input power spectral density. This elementary system is referred to in electrical engineering terms as a tuned-radio-frequency or crystal receiver.

Although at present there are no optical amplifiers equivalent to their low noise, high gain rf counterparts, the operation of the optical spectrometer analog shown in Fig. 3-1 is identical to that of the crystal receiver. The tunable optical filter may represent a scanning Fabry-Pérot etalon, a diffraction grating, or any of the common optical dispersing instruments. The "optical rectifier" is a photodetector, which has the advantage over the rf rectifier diode of being a perfect square-law device; its output current is linearly related to the square of the amplitude of the incident electric field. Thus a plot of the output of the optical receiver as the filter is tuned is exactly proportional to the desired power spectral density at the input, $S_E(\omega)$.

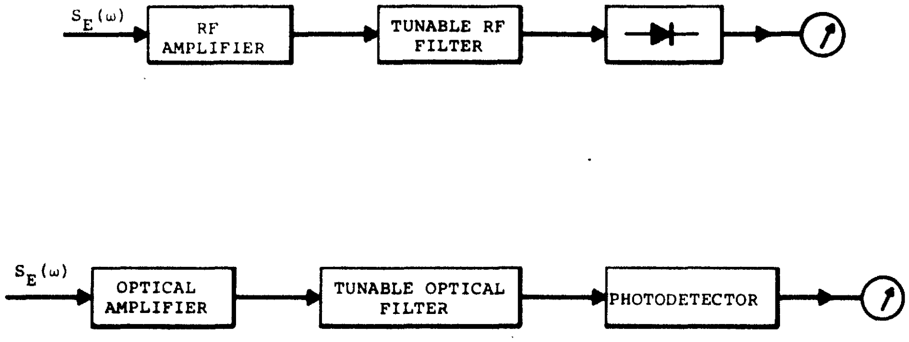
$S_E(\omega)$
RF AMPLIFIER
TUNABLE RF FILTER
$S_E(\omega)$
OPTICAL AMPLIFIER
TUNABLE OPTICAL FILTER
PHOTODETECTOR

Figure 3-1 Radio frequency and optical analogs of a tuned radio frequency receiver.

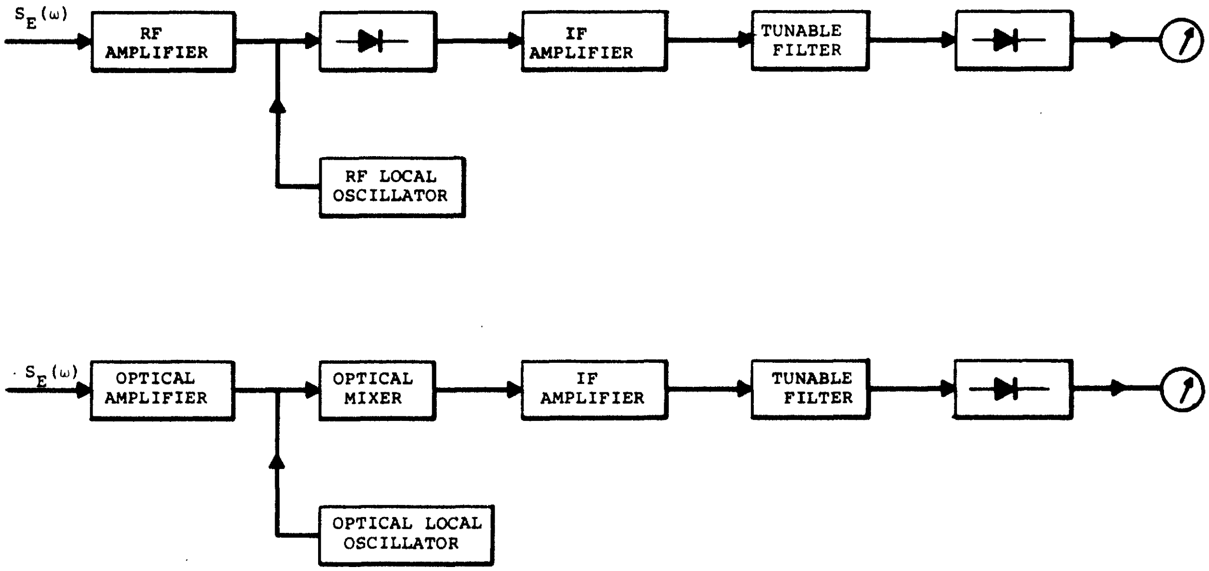
$S_E(\omega)$
RF AMPLIFIER
IF AMPLIFIER
TUNABLE FILTER
RF LOCAL OSCILLATOR
$S_E(\omega)$
OPTICAL AMPLIFIER
OPTICAL MIXER
IF AMPLIFIER
TUNABLE FILTER
OPTICAL LOCAL OSCILLATOR

Figure 3-2 Radio frequency and optical analogs of a superheterodyne receiver.

Both the optical and rf versions of this type of receiver exhibit limited resolution because the associated tunable filter cannot be made with an arbitrarily small bandwidth. In the rf case $(\delta\omega/\omega_o)$ is typically 10^{-5} minimum. In the optical case if the dispersing element is chosen as a Fabry-Pérot etalon then we can approach $(\delta\omega/\omega_o) \simeq 10^{-8}$. The basic difficulty in obtaining any specific bandpass $\delta\omega$ lies in the requirement of achieving this bandpass at the incoming frequency ω_o. However, if the information in $S_E(\omega)$ centered at the frequency ω_o could be translated down to a sufficiently low frequency prior to filtering it would be possible to achieve the desired bandwidth at this new center frequency. This chapter is in essence a detailed analysis of how such a frequency translation may be accomplished in the optical domain.

The most common rf technique used to shift the center frequency of the incoming signal is encountered in the superheterodyne receiver[5] shown in Fig. 3-2 along with its optical analog. After amplification the incoming rf signal is "mixed" in a non-linear element with a pure sinusoidal signal produced by the rf local oscillator. Because the mixer is non-linear, its output signal as a function of time involves a sum of various products of the incident and local oscillator signals. These product terms represent "beats" between the two mixer inputs. In particular, if the mixer is assumed to be a square-law device and the local oscillator has a frequency ω_{LO}, then the beat signals between each frequency component of the input signal and the local oscillator give rise to a mixer output whose spectrum is identical to the spectrum of the input signal, $S_E(\omega)$, except for a shift in center frequency to $\omega_1 = (\omega_o - \omega_{LO})$. The spectrum of this intermediate frequency (i.f.) signal is examined with a tuned filter in a manner identical to that used in the crystal receiver. In practice the fractional resolution $(\delta\omega/\omega_o)$ of the tuned filter is approximately independent of its center frequency ω_o; therefore, the heterodyning or mixing procedure results in an overall decrease of the fractional resolution by a factor (ω_1/ω_o). That is, the effective resolution is given by

$$(\delta\omega/\omega_o) = (\omega_1/\omega_o)(\delta\omega/\omega_1).$$

The optical superheterodyne spectrometer achieves its resolving power in a fashion identical to its rf counterpart.[6,7,8,9,10,11] In this case the local oscillator is a laser light source whose frequency differs from the center frequency of the signal, ω_o, by the desired amount, ω_1. Although, in principle, the intermediate frequency ω_1 may be selected to be anywhere between low audio and optical frequencies, the lack of suitable optical mixers limits the choice at present to the microwave regime and below, in which case photosensitive detectors can be used as the mixing elements. Because photodetectors are perfect square law devices the spectrum of the optical signal, $S_E(\omega)$, is faithfully preserved in the frequency translation process. The spectrum of the i.f. signal and, therefore, the optical signal can then be determined by the standard rf methods being outlined here. With this technique it is possible to achieve effective fractional resolutions from $(\delta\omega/\omega_o) \simeq 10^{-5}$ to $(\delta\omega/\omega_o) \simeq 10^{-15}$. These resolutions encompass the specific range of particular interest in light scattering experiments.

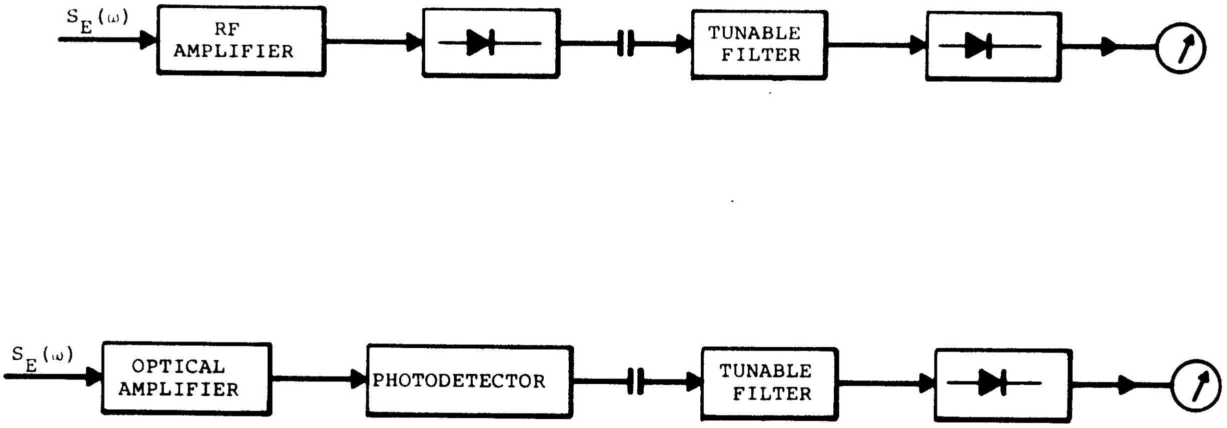
$S_E(\omega)$
RF AMPLIFIER
TUNABLE FILTER
$S_E(\omega)$
OPTICAL AMPLIFIER
PHOTODETECTOR
TUNABLE FILTER

Figure 3-3 Radio frequency and optical analogs of a crystal video or self-beating receiver.

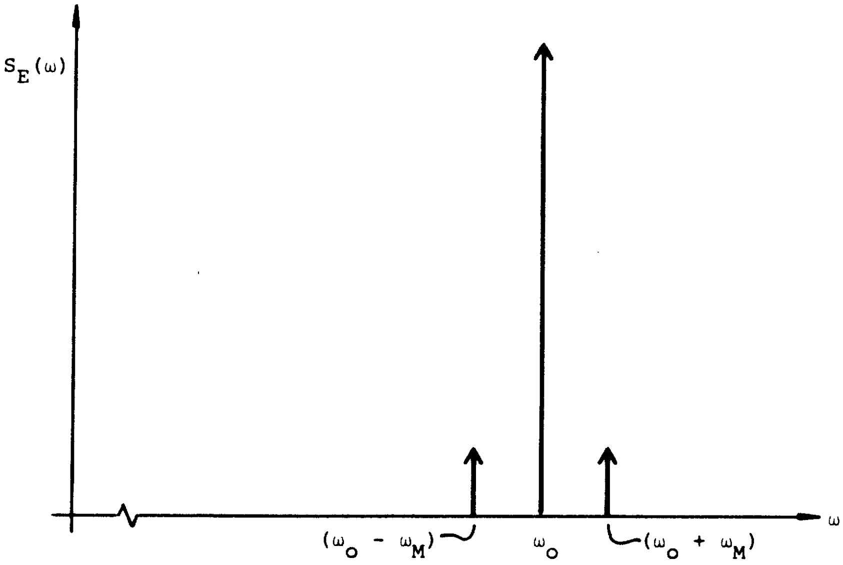

Figure 3-4 The power spectral density of a monochromatic wave which is weakly amplitude modulated at the frequency ω_m.

A second frequency translating receiver used in the rf domain is diagrammed in Fig. 3-3. The amplified incoming signal is again fed to a mixer; however, unlike the superheterodyne spectrometer, this receiver has no local oscillator. The beat signals observed at the mixer output are simply the result of beating between the various frequency components of the input signal itself. For a square-law mixer the beat signals observed at some frequency ω_1 are produced by all pairs of components in the input signal which are separated by an amount ω_1. As an example, consider the input spectrum shown in Fig. 3-4 which corresponds to a carrier weakly amplitude modulated at the frequency ω_M. Mixing between the carrier at the frequency ω_o and the upper and lower side bands produces a mixer output at the modulation frequency ω_M, while mixing between sidebands gives an output at a frequency $2\omega_M$. When the percentage of modulation is small the latter signal may be neglected and the mixer output simply reproduces the original modulation signal impressed on the carrier. For this reason the system is often referred to as a crystal video[12] receiver.

From the viewpoint of application to rf spectroscopy the important feature of the crystal video receiver is that its mixer output consists of frequencies between zero and roughly the spectral width of the input, $S_E(\omega)$. That is, the self-mixing or self-beating of the signal with itself accomplishes a frequency translation of the signal information from the original center frequency ω_o down to dc. A rigorous calculation shows that the power spectral density of the output of a square-law mixer is the convolution of the power spectral density of the input, $S_E(\omega)$, with itself. Therefore, a measurement of the spectrum of the mixer output does not give the input spectrum directly; however, if $S_E(\omega)$ has certain common forms (Lorentzian, Gaussian, rectangular, and so on) its line shape and line width can be derived easily from the mixer output spectrum. In particular, if $S_E(\omega)$ is a Lorentzian of half-width at half-height γ, then the mixer output spectrum is also a Lorentzian with its maximum at $\omega = 0$ and with a width at half-height of 2γ. Since the spectral information at the input has been shifted down to ($\omega \simeq \gamma$) the crystal video receiver is capable of fractional resolutions given by

$$(\delta\omega/\omega_o)_{\text{effective}} = (\gamma/\omega_o)(\delta\omega/\gamma).$$

This represents a decrease over the tuned rf case of (γ/ω_o). Furthermore, since the center frequency of the tunable filter is ($\omega_1 \simeq \gamma$), it is, in theory, always possible to achieve the condition $(\delta\omega/\gamma) << 1$ and, therefore, to examine the i.f. spectrum in detail.

The optical "self-beating" spectrometer shown in Fig. 3-3 is identical in operation to its rf analog.[13,14,15] The self-mixing takes place at a photo-sensitive detector and the mixer output signal is the electrical current output of this detector. The spectrum of this current is then examined by an appropriate filter. In theory the self-mixing spectrometer has no lower limit to its fractional resolution and has an upper limit dictated only by the maximum beat frequency to which a photodetector mixer can respond. In practice, resolutions of $(\delta\omega/\omega_o) \simeq 10^{-8}$ to $(\delta\omega/\omega_o) \simeq 10^{-14}$ are readily achievable.[14,15,16,17]

In this chapter we will examine in detail the operation of optical superheterodyne and optical self-beating spectrometers. We start with the relationship between the power spectral density of the incoming field and the spectrum of the current which this field produces from a photodetector, and proceed through the signal-processing operations to derive the final signal-to-noise (S/N) ratios to be expected from each spectrometer. The results are presented in terms of a set of parameterized universal curves from which the sensitivity of the spectrometer can be deduced, given the spectral width of the incident field and the characteristic features of the instrument. One of the most striking results of this analysis is that while both light-mixing methods are capable of exceedingly good resolution they both exhibit a minimum detectable power which is critically dependent on the spatial coherence properties of the incident optical field. In contrast to the conventional optical spectrometer, the optical mixing spectrometer does not have an output signal-to-noise ratio determined by the total available input power. Rather, its sensitivity is fixed by the available power per coherence area. For this reason it is interesting to compare the minimum optical powers that can be detected by an optical mixing spectrometer and a conventional Fabry-Pérot etalon instrument. This comparison shows that the two light-mixing methods secure their resolutions at the cost of available sensitivity. Moreover, it becomes strikingly apparent that this limited sensitivity is not simply a result of the effects of spatial coherence, but is, in fact, due to a fundamental difference in the nature of the "measuring" processes that distinguish a mixing spectrometer from a "crystal" receiver.

Finally, in order to delineate the resolution and sensitivity limits which can be approached by a practical light-mixing spectrometer, it is necessary to describe the present state-of-the-art in regard to the components which form the optical mixing and detection system. In this analysis particular attention is given to the properties of available photomixers and their associated electronics.

B. The Relationship Between the Spectrum of the Current Output of a Photodetector and the Spectrum of the Incident Optical Field

In this section we derive the basic relation which describes the heterodyning or mixing action that occurs between optical fields of different frequencies which are coincident on a photosensitive surface. We consider first a simple classical picture of the mixing that pinpoints the physical origin of the production of beat signals but which neglects the essentially stochastic nature of the photoemission process. We then proceed to a more rigorous theory which accounts for the fact that the relationship between the incident field and the photocurrent it generates is a statistical one. Further, we examine the generalization of this theory to the case where the incident field itself is a Gaussian random variable as is the situation for the light scattered from thermal fluctuations. These considerations are used to obtain the time correlation function of the photodetector output current in terms of the time correlation function of the incident field. The Fourier transform of this result yields the desired relationship between the spectrum of the incident field and the spectrum of the mixer output.

1. The Classical Description

Consider two light waves, one of frequency ω_1 and one of frequency ω_2, which are incident on a photosensitive surface designated the photocathode. We suppose that the wavefronts of the two beams are identical and collinear* as shown in Fig. 3-5. Let us compute the time variation of the resulting photocurrent.

In the usual description[18] of the photoelectric effect the current density $j(\vec{r},t)$ produced by the total electric field acting at the point $\vec{r}$ on the photocathode is written as being simply proportional to the instantaneous intensity or Poynting vector evaluated at $(\vec{r},t)$. If the constant of proportionality is expressed in terms of the quantum efficiency, ε, which gives the ratio of the number of emitted photoelectrons to the number of incident photons then we have

$$j(\vec{r},t) = \frac{\varepsilon e}{\hbar\omega_o}\left(\frac{1}{\mu_o c_m}\right)|\vec{E}(\vec{r},t)|^2 \qquad (3\text{-}1)$$

e - the electronic charge
μ_o - the permeability of free space
c_m - the velocity of light in the medium surrounding the photocathode

In Eq. (3-1) ω_o is the center frequency of the spectrum of the total field $\vec{E}(\vec{r},t)$. We will always assume this spectrum to be sufficiently narrow that the variation in $\hbar\omega$ is negligible over the range of interest. Since $\hbar\omega_o$ is the incident photon energy and $[(1/\mu_o c_m)\langle|\vec{E}(\vec{r},t)|^2\rangle]$ is the incident power per unit area, the ratio

---

* The lack of collinearity is treated in Section D.3.b of this chapter.

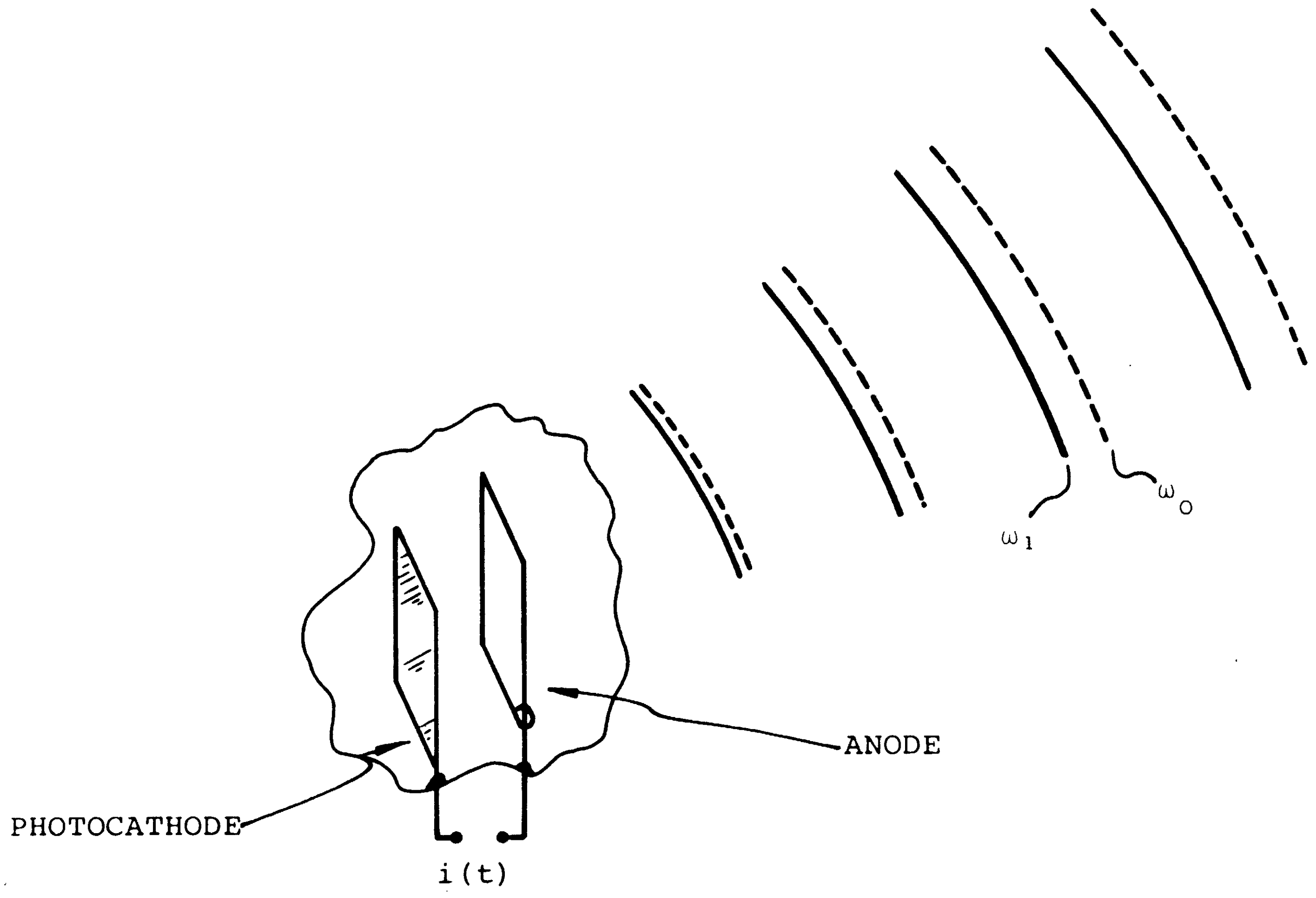
ω_o
ω_1
ANODE
PHOTOCATHODE
i(t)

Figure 3-5 Two monochromatic light waves incident collinearly on a photodetector.

$(1/\hbar\omega_o)(1/\mu_o c_m)|\vec{E}(\vec{r},t)|^2$ is the number of photons arriving at the photocathode per unit time and per unit area.

Writing the two incident fields in our example as $\vec{E}_1(\vec{r},t) = \vec{E}_1(\vec{r})\cos\omega_1 t$ and $\vec{E}_2(\vec{r},t) = \vec{E}_2(\vec{r})\cos\omega_2 t$ we have for the square of the total incident field

$$\begin{aligned}|\vec{E}(\vec{r},t)|^2 &= |\vec{E}_1(\vec{r},t) + \vec{E}_2(\vec{r},t)|^2 \\ &= (1/2)|\vec{E}_1(\vec{r})|^2 + (1/2)|\vec{E}_2(\vec{r})|^2 \\ &\quad + (1/2)|\vec{E}_1(\vec{r})|^2\cos 2\omega_1 t \\ &\quad + (1/2)|\vec{E}_2(\vec{r})|^2\cos 2\omega_2 t \\ &\quad + 2[\vec{E}_1(\vec{r})\cdot\vec{E}_2(\vec{r})]\cos\omega_1 t\cos\omega_2 t \qquad (3\text{-}2)\end{aligned}$$

Neglecting the double frequency terms and the sum frequency term from the expansion of the cosine product, since photodetectors cannot produce such optical frequency currents, we find for the current density $j(\vec{r},t)$

$$\begin{aligned}j(\vec{r},t) &= \alpha[(1/2)|\vec{E}_1(\vec{r})|^2 + (1/2)|\vec{E}_2(\vec{r})|^2 \\ &\quad + \vec{E}_1(\vec{r})\cdot\vec{E}_2(\vec{r})\cos(\omega_2 - \omega_1)t] \qquad (3\text{-}3)\end{aligned}$$

where α is defined as

$$\alpha \equiv \frac{\varepsilon e}{\hbar\omega_o}\left(\frac{1}{\mu_o c_m}\right) . \qquad (3\text{-}4)$$

This current density can be interpreted as follows. The two time independent dc terms represent the time average photocurrents that would flow if either $\vec{E}_1(\vec{r},t)$ or $\vec{E}_2(\vec{r},t)$ were present on the photocathode alone. In fact, from the definitions of $\vec{E}_1(\vec{r},t)$ and $\vec{E}_2(\vec{r},t)$ we can write $(1/2)|\vec{E}_1(\vec{r})|^2 = \langle|\vec{E}_1(\vec{r},t)|^2\rangle$ and $(1/2)|\vec{E}_2(\vec{r})|^2 = \langle|\vec{E}_2(\vec{r},t)|^2\rangle$, so that the dc terms are the photoelectric response to the time average incident power per unit area in each beam.

The factor of real interest in Eq. (3-3), however, is the term which oscillates at the frequency $(\omega_2 - \omega_1)$ and has an amplitude which is proportional to the product of the amplitudes of the two incident fields. This contribution to the photocurrent output represents a beat note due to the heterodyning or mixing between the two input optical signals. The appearance of the beat note results physically from the non-linear response of the photodetector to the incident electric field as expressed by Eq. (3-1). Because of this relationship the photodetector can be called a perfect square-law mixer.

Having found that a photo-sensitive detector can act as an optical mixing element we now proceed to derive a general relationship between the spectrum of the photo current and the spectrum of the total incident field. Since we will be interested in fields which are in essence random noise and hence which cannot be decomposed into sinusoidal frequency components by ordinary Fourier analysis,[19] we attack the problem by computing the correlation function of the total photocurrent, $R_i(\tau)$

$$R_i(\tau) = \langle i(t+\tau)i(t)\rangle = \overline{i(t+\tau)i(t)}$$

The bar indicates an average over an ensemble of identical processes which generate the random incident field; for example, an ensemble of identical light scattering experiments. The total photocurrent i(t) is given by the surface integral of the current density over the photocathode as

$$i(t) = \int_A j(\vec{r},t)\,dS \tag{3-5}$$

Once we have computed $R_i(\tau)$, the power spectral density[§] of the current, $S_i(\omega)$, is found by evaluating the Fourier cosine transform

$$S_i(\omega) = (1/2\pi) \int_{-\infty}^{\infty} R_i(\tau)\cos\,\omega\tau d\tau \tag{3-6}$$

2. The Stochastic Description

Before performing the average over the ensemble of incident fields we must first account for the purely statistical relationship that obtains between the photocurrent and the square of the incident field. Suppose we illuminate a photosensitive surface with an exactly defined incident field $\vec{E}(\vec{r},t)$. Then we know that although Eq. (3-1) predicts a well defined continuous current density, in actuality this current is composed of a series of pulses in time corresponding to the ejection of single photoelectrons from the photocathode. Moreover, the emission process itself is a random one.[20,21,22] Thus the appropriate description of $j(\vec{r},t)$ is the specification of the probability that the current density has a given value, $j(\vec{r},t)$, if the photosurface is illuminated with the field $\vec{E}(\vec{r},t)$. We designate this probability as $\mathbf{P}[j(\vec{r},t)]$.

[§] Chapter 2, Section D.

$\mathbf{P}[j(\vec{r},t)]$ is computed by considering an ensemble of identical photocathodes, all illuminated with the same incident field $\vec{E}(\vec{r},t)$ and represents the "photocathode ensemble" average probability of finding the specified $j(\vec{r},t)$. Knowing $\mathbf{P}[j(\vec{r},t)]$ we may calculate the "photocathode ensemble" average value of $j(\vec{r},t)$, designated $\overline{j(\vec{r},t)}$, by the usual definition

$$\overline{j(\vec{r},t)} = \int j(\vec{r},t) \; \mathbf{P}[j(\vec{r},t)] \; d[j(\vec{r},t)] \tag{3-7}$$

From a consideration of the quantum mechanical problem of the interaction between the electromagnetic field and the atoms of the photocathode[20, 21, 22] one can calculate the "photocathode ensemble" average probability that a single photoelectron will be emitted at a time t within an interval δt from a unit area at $\vec{r}$ as

$$\mathbf{P}(1,t,\vec{r})\,\delta t = \frac{\varepsilon}{\hbar\omega_o}\left(\frac{1}{\mu_o c_m}\right) \; |\vec{E}(\vec{r},t)|^2 \delta t \tag{3-8}$$

Since the photoelectron carries charge e this is the probability that $j(\vec{r},t)$ has the value $(e/\delta t)$. In the derivation of Eq. (3-8) it is assumed that δt is chosen so short that either zero or one photoelectron is observed. Therefore, Eq. (3-8) actually specifies the probability distribution that n photoelectrons are observed in δt as

$$\mathbf{P}(n,t,\vec{r}) = \begin{cases} 1 - \mathbf{P}(1,t,\vec{r}) & ;\ n=0 \\ \mathbf{P}(1,t,\vec{r}) & ;\ n=1 \\ 0 & ;\ n\geq 2 \end{cases} \tag{3-9}$$

Since the possible values of the current density are discrete, the integral in Eq. (3-7) becomes a sum and we have

$$\overline{j(\vec{r},t)} = \sum_{n=0}^{\infty} \left(\frac{ne}{\delta t}\right) \mathbf{P}(n,t,\vec{r})\,\delta t \tag{3-10}$$

which yields

$$\overline{j(\vec{r},t)} = \frac{\varepsilon e}{\hbar\omega_o}\left(\frac{1}{\mu_o c_m}\right)|\vec{E}(\vec{r},t)|^2 = \alpha|\vec{E}(\vec{r},t)|^2 \tag{3-11}$$

Thus the expression given in Eq. (3-1) actually represents the "photocathode ensemble" average response of a photosurface. However, in addition to describing this average behavior, $\mathbf{P}(n,t,\vec{r})$ also contains information on fluctuations about the average. We will see that these fluctuations correspond to the so-called "shot-noise" associated with the time average photocurrent.

The measured current i(t) whose correlation function we want to calculate is, in fact, the "photocathode ensemble" average current. That is, the statement of Eq. (3-5) is more rigorously written as

$$\overline{i(t)} = \int_A \overline{j(\vec{r},t)}\,dS \tag{3-12}$$

It follows that the photocurrent correlation function has the form

$$R_i(\tau) = \left\langle \overline{i(t+\tau)i(t)} \right\rangle = \int_A \int_{A'} \left\langle \overline{j(\vec{r},t+\tau)j(\vec{r},t)} \right\rangle dS dS' \tag{3-13}$$

Equation (3-13) contains information on the two fundamental properties of the mixing process.

(1) The time behavior of $R_i(\tau)$ and, therefore, the photocurrent spectrum is described completely by the

correlation function of the current density $\overline{\langle j(\vec{r},t+\tau)j(\vec{r},t)\rangle}$.

(2) The *spatial characteristics* of the mixing process are contained in the double surface integral which describes the *properly phased* addition of the currents produced at different points on the photocathode to yield the total current i(t).

3. The Spectrum of the Photocurrent—The Time Correlation Function for the Photocurrent Density

We first consider the current density correlation function $R_j(\tau) = \overline{\langle j(\vec{r},t+\tau)j(\vec{r},t)\rangle}$ and the corresponding spectral features of the photocurrent.

In order to evaluate $R_j(\tau)$ we need the ensemble average behavior of the product of the current densities at two distinct times, namely, $\overline{j(\vec{r},t_2)j(\vec{r},t_1)}$. This average may be calculated if we know the joint probability distribution $\mathbf{P}[(n,t_2,\vec{r}),(m,t_1,\vec{r})]\delta t_1 \delta t_2$ which specifies the probability that m photoelectrons are emitted at time t_1 in the interval δt_1 per unit area at $\vec{r}$ *and* that n photoelectrons are emitted at time t_2 in the interval δt_2 per unit area at $\vec{r}$. In terms of $\mathbf{P}[(\ ),(\ )]$ we have

$$\overline{j(\vec{r},t_2 j(\vec{r},t_1)} = \sum_{n=0}^{\infty}\sum_{m=0}^{\infty}\left(\frac{ne}{\delta t_2}\right)\left(\frac{me}{\delta t_1}\right)\mathbf{P}[(n,t_2,\vec{r}),(m,t_1,\vec{r})]\delta t_{.}\delta t_2 \tag{3-14}$$

where $j(\vec{r},t_2) = (ne/\delta t_2)$ and $j(\vec{r},t_1) = (me/\delta t_1)$. The required distribution has been calculated by Mandel, Sudarshan, and Wolf[20] as

$$\mathbf{P}[(n,t_2,\vec{r}),\ (m,t_1,\vec{r})] = (\alpha^2/e^2)\,|\vec{E}(\vec{r},t_2)|^2|\vec{E}(\vec{r},t_1)|^2 \tag{3-15}$$

for $t_1 \neq t_2$. For $t_1 = t_2$ we have simply

$$\mathbf{P}[(1,t_1,\vec{r}),(1,t_1,\vec{r})] = (\alpha/e)\,|\vec{E}(\vec{r},t_1)|^2 \tag{3-16}$$

Implicit in Eqs. (3-15) and (3-16) is the assumption that δt_1 and δt_2 are both sufficiently small that one count at most is recorded in either interval. The physical meaning of these distributions may be explained by expressing $\mathbf{P}[(1,t_2,\vec{r}),(1,t_1,\vec{r})]$ in terms of a conditional probability[§] as

$$\mathbf{P}[(1,t_2,\vec{r}),(1,t_1,\vec{r})] = \mathbf{P}[(1,t_2,\vec{r})\,|\,(1,t_1,\vec{r})]\ \mathbf{P}(1,t_1,\vec{r}) \tag{3-17}$$

Comparing Eqs. (3-8), (3-15), and (3-16) gives for $\mathbf{P}[(1,t_2,\vec{r})\,|\,(1,t_1,\vec{r})]$

$$\mathbf{P}[(1,t_2,\vec{r})\,|\,(1,t_1,\vec{r})] = \begin{cases} (\alpha/e)\,|\vec{E}(\vec{r},t_2)|^2 = \quad (1,t_2,\vec{r}); & t_1 \neq t_2 \\ 1 & ;\ t_1 = t_2 \end{cases} \tag{3-18}$$

This result implies that the photo-events at times t_1 and t_2 are completely correlated for $t_1 = t_2$, as must be the case; but that the events at different times ($t_2 \neq t_1$) are completely random and uncorrelated even for arbitrarily small $|t_2 - t_1|$. This randomness is a result of the complete independence of the emission process on the past history of the photocathode; the probability of photoemission depends only on the instantaneous light flux.

[§] Chapter 2, Section D.

Combining Eqs. (3-14), (3-15), and (3-16) yields the desired ensemble average

$$\overline{j(\vec{r},t_2)j(\vec{r},t_1)} = \begin{cases} \alpha^2|\vec{E}(\vec{r},t_2)|^2|\vec{E}(\vec{r},t_1)|^2 & t_2 \neq t_1 \\ \\ \alpha e|\vec{E}(\vec{r},t_1)|^2 & t_2 = t_1 \end{cases} \tag{3-19}$$

Setting $t_1 = t$ and $t_2 = t + \tau$ in Eq. (3-19), and performing a time average, we have the current density correlation function as

$$R_j(\tau) = \alpha^2\left\langle|E(\vec{r},t+\tau)|^2|\vec{E}(\vec{r},t)|^2\right\rangle + \alpha e\left\langle|\vec{E}(\vec{r},t)|^2\right\rangle\delta(\tau) \tag{3-20}$$

or in terms of Eq. (3-11)

$$R_j(\tau) = \alpha^2\left\langle|\vec{E}(\vec{r}_1 t+\tau)|^2|\vec{E}(\vec{r},t)|^2\right\rangle + e\left\langle\overline{j(\vec{r},t)}\right\rangle\delta(\tau) \tag{3-21}$$

The first factor of this result would have followed directly from the classical expression for $j(\vec{r},t)$ given in Eq. (3-1). By analogy with the simple analysis given above it must, therefore, describe both the dc current produced by $\vec{E}(\vec{r},t)$ and the beat notes between its spectral components. The second factor represents a "shot-effect" due to the noncontinuous nature of the photocurrent.

To examine the features of $R_j(\tau)$ let us consider the simple example of an incident field composed of only two frequencies ω_1 and ω_2. Using $|\vec{E}(\vec{r},t)|^2$ as given in Eq. (3-2) we find:

$$\begin{aligned} R_j(\tau) = {} & [\overline{\langle j_1(\vec{r},t)\rangle} + \overline{\langle j_2(\vec{r},t)\rangle}]^2 + \tfrac{1}{2}[\overline{\langle j_1(\vec{r},t)\rangle}]^2 \cos 2\omega_1\tau \\ & + \tfrac{1}{2}[\overline{\langle j_2(\vec{r},t)\rangle}]^2 \cos 2\omega_2\tau \\ & + (\alpha^2/2)[\vec{E}_1(\vec{r})\cdot\vec{E}_2(\vec{r})]^2 \cos (\omega_1+\omega_2)\tau \\ & + (\alpha^2/2)[\vec{E}_1(\vec{r})\cdot\vec{E}_2(\vec{r})]^2 \cos (\omega_2-\omega_1)\tau \\ & + e[\overline{\langle j_1(\vec{r},t)\rangle} + \overline{\langle j_2(\vec{r},t)\rangle}]\,\delta(\tau) \end{aligned} \qquad (3\text{-}22)$$

where $\overline{\langle j_1(\vec{r},t)\rangle} = (\alpha^2/2)|\vec{E}_1(\vec{r})|^2$ is the dc photocurrent density produced by $\vec{E}_1(\vec{r},t)$ and $\overline{\langle j_2(\vec{r},t)\rangle}$ the dc current density produced by $\vec{E}_2(\vec{r},t)$. Utilizing the τ dependence to recognize the time behavior of the various factors we find that the first term in Eq. (3-22) represents the square of the total dc photocurrent density. The next three factors correspond respectively to two second harmonic ac currents and to a sum frequency beat note at $(\omega_1+\omega_2)$. The fifth term represents a beat note at frequency $(\omega_2-\omega_1)$. All these contributions come from the first term in Eq. (3-21) and correspond to the results of the classical analysis given before. The remaining term is more easily interpreted from the power spectral density of $j(\vec{r},t)$ defined by

$$S_j(\omega) = (1/2\pi)\int_{-\infty}^{\infty} R_j(\tau) \cos \omega\tau \, d\tau \qquad (3\text{-}23)$$

Neglecting the optical frequency currents we find from Eq. (3-22)

$$S_j(\omega) = [\overline{\langle j_1(\vec{r},t)\rangle} + \overline{\langle j_2(\vec{r},t)\rangle}]^2\delta(\omega)$$

$$(\omega \geq 0) \qquad + (\alpha^2/2)[\vec{E}_1(\vec{r})\cdot\vec{E}_2(\vec{r})]^2\delta[(\omega_2 - \omega_1) - \omega]$$

$$(e/\pi)[\overline{\langle j_1(\vec{r},t)\rangle} + \overline{\langle j_2(\vec{r},t)\rangle}] \tag{3-24}$$

Thus the delta function part of $R_i(\tau)$ produces a uniform contribution to the spectrum, the last term of Eq. (3-24), which on examination is just the shot-noise current power per unit bandwidth to be expected[23] from an emission limited diode carrying a dc current $[\overline{\langle j_1(\vec{r},t)\rangle} + \overline{\langle j_2(\vec{r},t)\rangle}]$. Figures (3-6) and (3-7) illustrate the components of $R_j(\tau)$ and their corresponding power spectra together with the total spectrum $S_j(\omega)$.

As expressed in Eq. (3-21), $R_j(\tau)$ is valid for a specified incident field $\vec{E}(\vec{r},t)$. Suppose, however, that $\vec{E}(\vec{r},t)$ is taken to represent a single member of an ensemble of possible fields generated by some random process, e.g. light scattering. Then the measured correlation function is found by averaging Eq. (3-21) over all members of this ensemble, i.e.

$$\overline{\overline{\langle j(\vec{r},t+\tau)j(\vec{r},t)\rangle}} \equiv \langle\langle j(\vec{r},t+\tau)j(\vec{r},t)\rangle\rangle =$$

$$\alpha^2\langle\overline{|\vec{E}(\vec{r},t+\tau)|^2|\vec{E}(\vec{r},t)|^2}\rangle + e\langle\langle j(\vec{r},t)\rangle\rangle\delta(\tau) \tag{3-25}$$

Since in all cases of interest here $\vec{E}(\vec{r},t)$ will be a strict sense stationary random variable and will satisfy the ergodic hypothesis, the time and ensemble averages on the quantity $\overline{\langle |\vec{E}(\vec{r} \ldots\ldots \rangle}$ are redundant. Therefore, we may write $R_j(\tau)$ as simply

$$R_j(\tau) = \alpha^2\langle|\vec{E}(\vec{r},t+\tau)|^2|\vec{E}(\vec{r},t)|^2\rangle + e\langle\langle j(\vec{r},t)\rangle\rangle\delta(\tau) \tag{3-26}$$

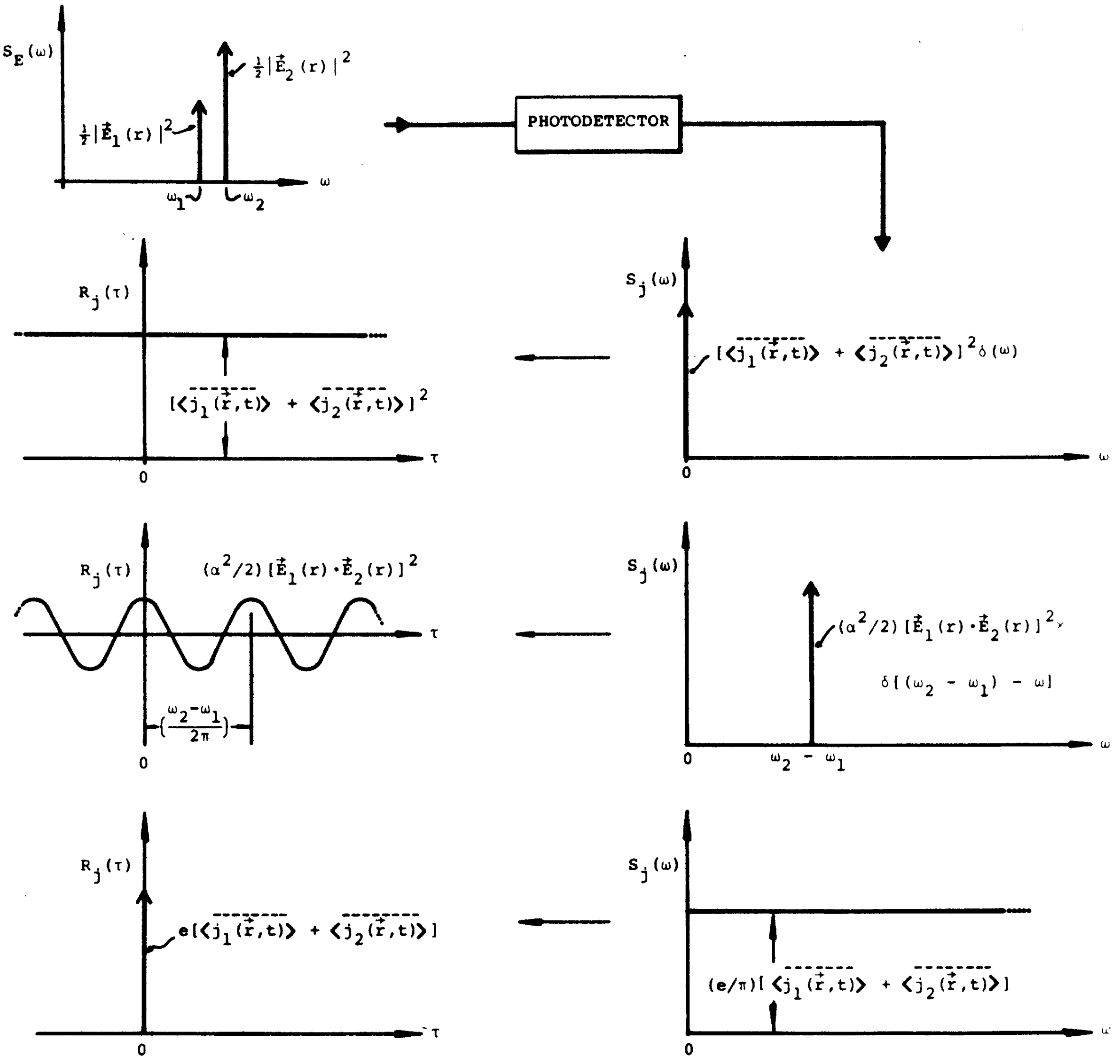
$S_E(\omega)$
$\frac{1}{2}|\vec{E}_1(r)|^2$
$\frac{1}{2}|\vec{E}_2(r)|^2$
ω_1
ω_2
ω
PHOTODETECTOR
$R_j(\tau)$
$[\langle \overline{j_1(\vec{r},t)}\rangle + \langle \overline{j_2(\vec{r},t)}\rangle]^2$
0
τ
$S_j(\omega)$
$[\langle \overline{j_1(\vec{r},t)}\rangle + \langle \overline{j_2(\vec{r},t)}\rangle]^2 \delta(\omega)$
$(\alpha^2/2)[\vec{E}_1(r)\cdot\vec{E}_2(r)]^2$
$(\frac{\omega_2-\omega_1}{2\pi})$
$(\alpha^2/2)[\vec{E}_1(r)\cdot\vec{E}_2(r)]^2 \times$
$\delta[(\omega_2 - \omega_1) - \omega]$
$\omega_2 - \omega_1$
$e[\langle \overline{j_1(\vec{r},t)}\rangle + \langle \overline{j_2(\vec{r},t)}\rangle]$
$(e/\pi)[\langle \overline{j_1(\vec{r},t)}\rangle + \langle \overline{j_2(\vec{r},t)}\rangle]$

Figure 3-6 Illustration of the dc, shot-noise, and signal components of the photocurrent density corresponding to mixing between two monochromatic optical fields.

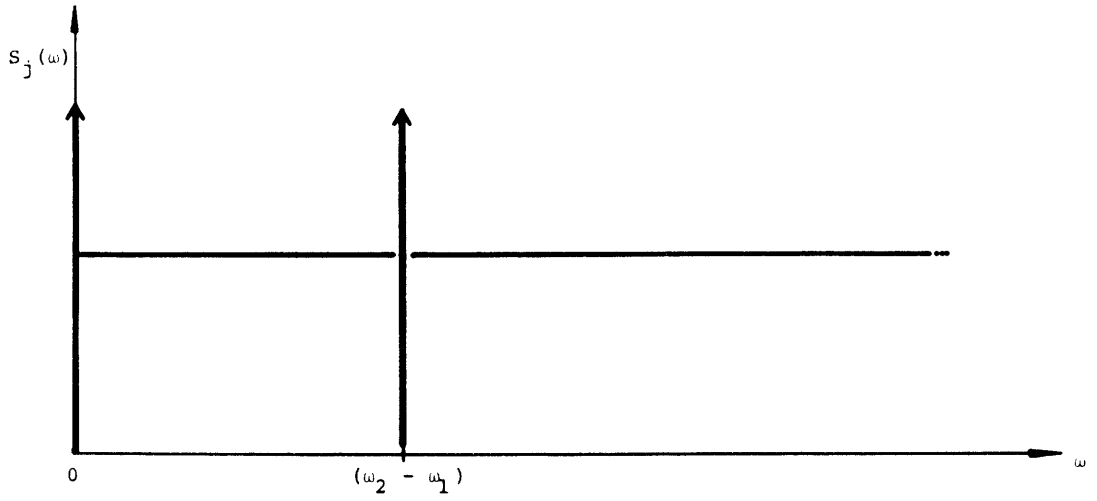

Figure 3-7 The power spectral density of the photocurrent corresponding to mixing between two monochromati optical fields.

This result is the fundamental relationship that describes the spectral output of an optical photodetector-mixer.

We must now attempt to express the correlation function for the square of the field in terms of the correlation function of the field itself in order to write the spectrum $S_j(\omega)$ in terms of the spectrum of the incident field, $S_E(\omega)$. This step can be accomplished only if $\vec{E}(\vec{r},t)$ is an exactly defined non-stochastic function or if it is a Gaussian random variable. In the latter case we may utilize the following theorem[25] to factor the first term of Eq. (3-26).

If x_1, x_2, x_3, and x_4 are real random variables with a Gaussian joint probability density function and if all have zero mean, then the ensemble average $\overline{x_1x_2x_3x_4}$ may be factored according to the rule

$$\overline{x_1x_2x_3x_4} = (\overline{x_1x_2})(\overline{x_3x_4}) + (\overline{x_1x_3})(\overline{x_2x_4}) + (\overline{x_1x_4})(\overline{x_2x_3}) \tag{3-27}$$

As we saw in Chapter 2 the scattered field $\vec{E}_S(\vec{r},t)$ is distributed according to a Gaussian distribution and has a zero mean-value for all times, t. Therefore, if $\vec{E}(\vec{r},t)$ represents the scattered field we have immediately

$$\begin{aligned} R_j(\tau) = \alpha^2\{ & \overline{[\vec{E}(\vec{r},t+\tau)\cdot\vec{E}(\vec{r},t+\tau)]}\ \overline{[\vec{E}(\vec{r},t)\cdot\vec{E}(\vec{r},t)]} \\ & + 2\overline{[\vec{E}(\vec{r},t+\tau)\cdot\vec{E}(\vec{r},t)]}\ \overline{[\vec{E}(\vec{r},t)\cdot\vec{E}(\vec{r},t+\tau)]}\} \\ & + e\langle\langle j(\vec{r},t)\rangle\rangle\,\delta(\tau) \end{aligned} \tag{3-28}$$

Using the fact that $\vec{E}(\vec{r},t)$ is strict sense stationary and employing the definition of the correlation function $R_E(\vec{r},\tau) = \langle\vec{E}(\vec{r},t+\tau)\cdot\vec{E}(\vec{r},t)\rangle$ gives

$$R_j(\tau) = \alpha^2\{[\langle|\vec{E}(\vec{r},t)|^2\rangle]^2 + 2R_E{}^2(\vec{r},\tau)\}$$

$$+ e\langle\langle j(\vec{r},t)\rangle\rangle\delta(\tau) \qquad (3\text{-}29)$$

Since $\langle\langle j(\vec{r},t)\rangle\rangle = \alpha\langle|\vec{E}(\vec{r},t)|^2\rangle$ this result can also be written as

$$R_j(\tau) = [\langle\langle j(\vec{r},t)\rangle\rangle]^2 + 2\alpha^2 R_E{}^2(\vec{r},\tau) + e\langle\langle j(\vec{r},t)\rangle\rangle\delta(\tau) \qquad (3\text{-}30)$$

The three terms in Eq. (3-30) represent the three essential features of the photocurrent that emerged in the simple example given above; namely, the square of the dc photocurrent, the beat terms between different frequency components of the light, and the shot-noise.

Equation (3-30) allows the spectrum of the photocurrent density to be obtained easily in terms of the spectrum of the incident field, i.e.

$$S_E(\omega) = (1/2\pi)\int_{-\infty}^{\infty} R_E(\tau)\cos\omega\tau\, d\tau \qquad (3\text{-}31)$$

Multiplying both sides of this expression by cos $\omega\tau'$ and integrating over all ω gives the inversion relation

$$R_E(\tau) = \int_{-\infty}^{\infty} S_E(\omega)\cos\omega\tau\, d\omega \qquad (3\text{-}32)$$

If $R_E(\tau)$ in Eq. (3-30) is written in terms of its power spectrum, $R_j(\tau)$ takes the form

$$R_j(\tau) = [\langle\langle j(\vec{r},t)\rangle\rangle]^2$$

$$+ 2\alpha^2\int_{-\infty}^{\infty}\int_{-\infty}^{\infty} S_E(\omega')S_E(\omega'')\cos\omega'\tau\cos\omega''\tau\, d\omega' d\omega''$$

$$+ e\langle\langle j(\vec{r},t)\rangle\rangle\,\delta(\tau) \qquad (3\text{-}33)$$

This correlation function has a power spectrum given by

$$S_j(\omega) = [\langle\langle j(\vec{r},t)\rangle\rangle]^2\delta(\omega) + (e/2\pi)\langle\langle j(\vec{r},t)\rangle\rangle$$
$$+ (\alpha^2/2)\int_{-\infty}^{\infty} S_E(\omega')\{S_E(-\omega'+\omega) + S_E(\omega'+\omega)$$
$$+ S_E(-\omega'-\omega) + S_E(\omega'-\omega)\}d\omega' \qquad (3\text{-}34)$$

Since $S_E(\omega)$ is a symmetric function,[§] the terms corresponding to the frequencies $\pm(\omega'+\omega)$ and $\pm(\omega'-\omega)$ can be grouped to give

$$S_j(\omega) = [\langle\langle j(\vec{r},t)\rangle\rangle]^2\delta(\omega) + (e/2\pi)\langle\langle j(\vec{r},t)\rangle\rangle$$
$$+ \alpha^2\int_{-\infty}^{\infty} S_E(\omega')[S_E(\omega'+\omega) + S_E(\omega'-\omega)]d\omega' \qquad (3\text{-}35)$$

Thus we find that the optical mixing action that produces the signal part of the spectrum can be interpreted in the simple manner suggested at the beginning of this section; the beat note observed at a frequency ω is generated by the mixing of all pairs of frequencies in the incident light wave which are separated by an amount ω, i.e. $[\omega',\omega'+\omega]$ and $[\omega',\omega'-\omega]$. The sum of all these beat notes is expressed mathematically by the convolution integral appearing in Eq. (3-35) which gives the desired spectral properties of the mixer output.

[§] Chapter 2, Section D.

4. The Effects of Spatial Coherence—The Time Correlation Function for the Total Current

Having found the ac and dc current signals generated at a single point on the photocathode we now ask how these signals add to produce the total current i(t). The "photocathode ensemble" average current is simply the surface integral of Eq. (3-11), *viz*.

$$\overline{i(t)} = \int_A \overline{j(\vec{r},t)}\,dS = \alpha \int_A |\vec{E}(\vec{r},t)|^2 dS \tag{3-36}$$

It follows that the total *dc* current is

$$\begin{aligned}\langle\langle i(t)\rangle\rangle = \langle\overline{i(t)}\rangle &= \alpha \int_A \langle|\vec{E}(\vec{r},t)|^2\rangle dS \\ &= \alpha A\langle|\vec{E}(\vec{r}_o,t)|^2\rangle \end{aligned} \tag{3-37}$$

the last equality being valid if the time average intensity is uniform over the photocathode. We designate this time average current as i_p, thus

$$i_p = \langle\langle i(t)\rangle\rangle = \alpha A\langle|\vec{E}(\vec{r}_o,t)|^2\rangle \tag{3-38}$$

Since $(A/\mu_o c_m)\langle|\vec{E}(\vec{r}_o,t)|^2\rangle$ is the total average power, $\mathcal{P}_o$ falling on the photocathode, i_p can also be written in the more useful form

$$i_p = (\varepsilon e/\hbar\omega_o)\mathcal{P} \ . \tag{3-39}$$

The ensemble averaged correlation function for i(t), $R_i(\tau) = \langle\langle i(t+\tau)\,i(t)\rangle\rangle$, is given by the double integral

$$\langle\langle i(t_2)\,i(t_1)\rangle\rangle = \int_A\int_A \langle\overline{j(\vec{r}_2,t_2)\,j(\vec{r}_1,t_1)}\rangle dS_1 dS_2 \tag{3-40}$$

To compute $\overline{j(\vec{r}_2,t_2)j(\vec{r}_1,t_1)}$ we need the joint distribution specifying the probability that n photoelectrons are emitted at time t_2 in the interval δt_2 per unit area at $\vec{r}_2$ and that m photoelectrons are emitted at time t_1 in the interval δt_1 per unit area at $\vec{r}_1$. Making the assumption that the points of emission as well as the emission times of two distinct photoelectrons are completely uncorrelated we have

$$\mathbf{P}[(n,t_2,\vec{r}_2),(m,t_1,\vec{r}_1)] = \begin{cases} (\alpha^2/e^2)\,|\vec{E}(\vec{r}_2,t_2)|^2|\vec{E}(\vec{r}_1,t_1)|^2; & t_1 \neq t_2 \ \underline{\text{or}}\ \vec{r}_1 \neq \vec{r}_2 \\ (\alpha/e)\,|\vec{E}(\vec{r}_1,t)|^2\ ; & t_1 = t_2 \ \underline{\text{and}}\ \vec{r}_1 = \vec{r}_2 \end{cases} \tag{3-41}$$

by analogy with Eq. (3-15). Applying Eq. (3-14) gives the desired average

$$\overline{j(\vec{r}_2,t_2)j(\vec{r}_1,t_1)} = \begin{cases} \alpha^2|\vec{E}(\vec{r}_2,t_2)|^2|\vec{E}(\vec{r}_1,t_1)|^2\ ; & t_2 \neq t_1 \text{ or } \vec{r}_2 \neq \vec{r}_1 \\ \alpha|\vec{E}(\vec{r}_1,t_1)|^2\ ; & t_2 = t_1 \text{ and } \vec{r}_2 = \vec{r}_1 \end{cases} \tag{3-42}$$

Finally, on taking the time average of this expression and performing an ensemble average over all possible incident fields we find:

$$\langle\langle j(\vec{r}_2,t_2)j(\vec{r}_1,t_1)\rangle\rangle = \alpha^2\langle|\vec{E}(\vec{r}_2,t_2)|^2|\vec{E}(\vec{r}_1,t_1)|^2\rangle + e\langle\langle j(\vec{r}_1,t_1)\rangle\rangle\delta(\vec{r}_2-\vec{r}_1)\delta(t_2-t_1) \tag{3-43}$$

This result represents a generalization of Eq. (3-25) to include the effects of both the temporal and the spatial coherence properties of the incident field. Let us set $t_1 = t$, $t_2 = t + \tau$, $\vec{r}_1 = \vec{r}$, and $\vec{r}_2 = \vec{r} + \vec{\rho}$ in Eq. (3-43) and perform both surface integrals over the photocathode area A. This gives $R_i(\tau)$ in the form

$$\begin{aligned} R_i(\tau) &= \langle\langle i(t+\tau)i(t)\rangle\rangle \\ &= \alpha^2\int_A\int_A \langle|\vec{E}(\vec{r}+\vec{\rho},t+\tau)|^2|\vec{E}(\vec{r},t)|^2\rangle d^2\vec{r}\, d^2\vec{\rho} \\ &\quad + ei_p\delta(\tau) \end{aligned} \tag{3-44}$$

with i_p as defined in Eq. (3-38). This result for $R_i(\tau)$ expresses the fundamental description of the photomixing operation as seen via the output current of the detector. Again, it is valid either for a specifically defined field $\vec{E}(\vec{r},t)$, or for a random field that satisfies the ergodic hypothesis and is strict sense stationary.

To simplify $R_i(\tau)$ further requires assuming that $\vec{E}(\vec{r},t)$ is either a well defined, non-stochastic field or a random field with Gaussian statistics. In the latter case, the correlation function $\langle|\vec{E}(\vec{r}+\vec{\rho},t+\tau)|^2|\vec{E}(\vec{r},t)|^2\rangle$ can be expanded with the help of Eq. (3-27) as

$$\langle|\vec{E}(\vec{r}+\vec{\rho},t+\tau)|^2|\vec{E}(\vec{r},t)|^2\rangle = \langle|\vec{E}(\vec{r}+\vec{\rho},t+\tau)|^2\rangle\langle|\vec{E}(\vec{r},t)|^2\rangle + 2[\langle\vec{E}(\vec{r}+\vec{\rho},t+\tau)\cdot\vec{E}(\vec{r},t)\rangle]^2 \tag{3-45}$$

The surface integrals can be performed on the first term to give

$$R_i(\tau) = i_p^2 + ei_p\delta(\tau) + 2\alpha^2 \int_A \int_A [\langle\vec{E}(\vec{r}+\vec{\rho},t+\tau)\cdot\vec{E}(\vec{r},t)\rangle]^2 \, d^2\vec{r} \, d^2\vec{\rho} \qquad (3\text{-}46)$$

As we found for $R_j(\tau)$ the Gaussian assumption results in the separation of the correlation function into three terms representing the dc current, the shot-noise, and the beat signals respectively. The dc and shot-noise current terms scale in proportion to the detector area in a manner which would be expected intuitively from Eq. (3-30). However, the beat note term in $R_i(\tau)$ no longer depends only on the temporal correlation function of the incident field, $R_E(\tau)$; but, in fact, now contains the effects of spatial coherence between the fields at the points $(\vec{r})$ and $(\vec{r}+\vec{\rho})$.

In general, the correlation function $\langle\vec{E}(\vec{r}+\vec{\rho},t+\tau)\cdot\vec{E}(\vec{r},t)\rangle$ cannot be factored into separate time and space parts. However, under certain restrictions that are easily satisfied in all practical optical photomixing applications this decomposition can be made.[26] The conditions are as follows: (1) the largest dimension of the photosensitive surface, A, must be small compared to the wavelength of an electromagnetic wave with a frequency equal to that of the highest frequency beat signal; (2) the optical frequency currents must be neglected. The physical interpretation of these statements can be seen by reference to Fig. 3-8 which shows two collinear light beams with frequencies ω_1 and ω_2 incident on a photocathode surface, A. At any instant, t, the phase of the beat note $(\omega_1-\omega_2)$ varies with position along the direction of propagation. This is represented by the relative spacing of the wavefronts

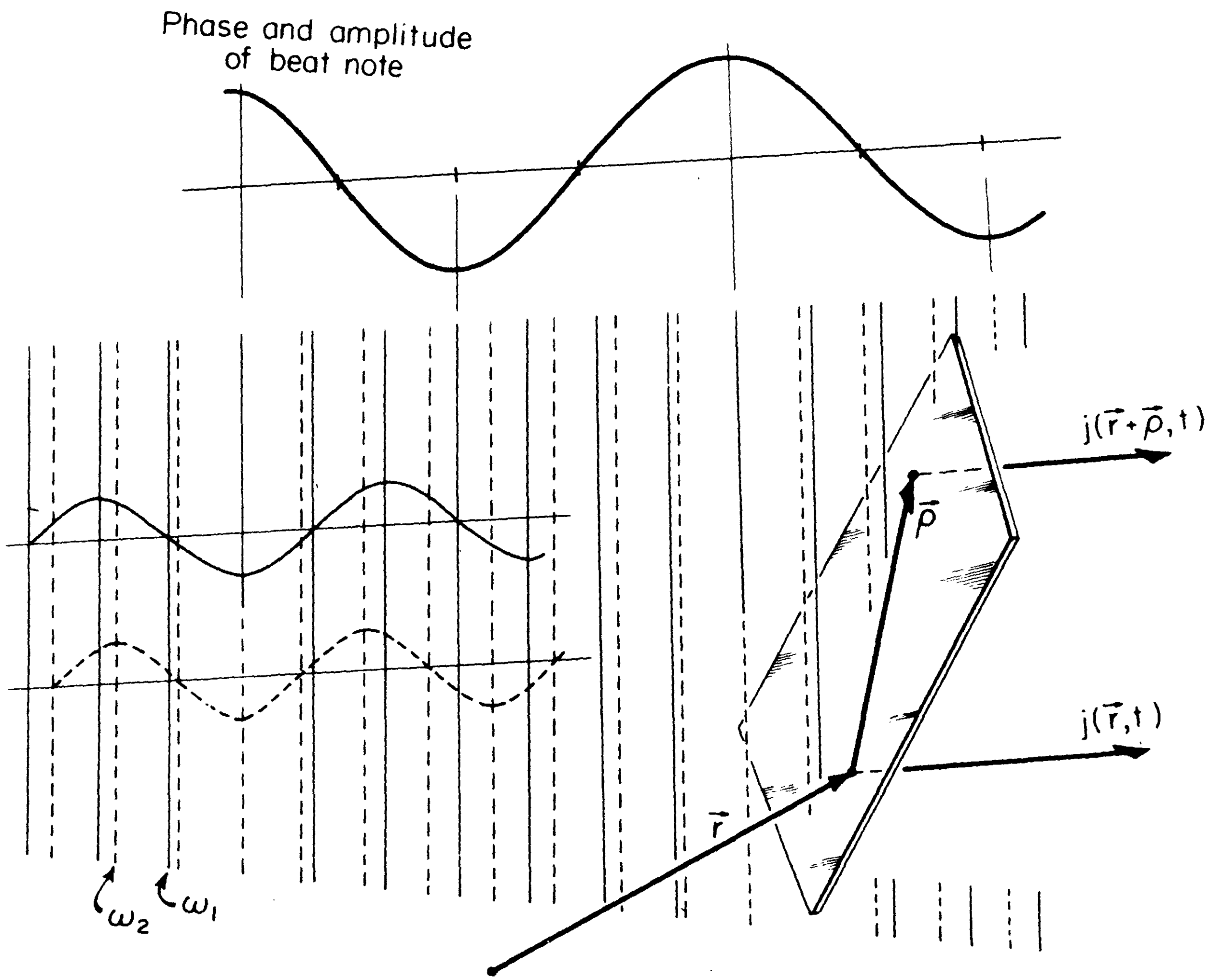
Phase and amplitude
of beat note
$j(\vec{r}+\vec{\rho},t)$
$\vec{\rho}$
$j(\vec{r},t)$
$\vec{r}$
ω_2
ω_1

Figure 3-8 Illustration of the beat note phase variation as a function of position on the photomixer when the photosurface is not coplanar with the wavefronts of the mixing fields.

of the two incident fields. The result is a phase difference between the current densities produced at the points $\vec{r}$ and $(\vec{r}+\vec{\rho})$ which is due not to the spatial coherence properties of the incident wave but to the equivalent time delay between the arrival of a given phase front at the two points. However, in the limit in which the maximum time delay becomes small with respect to the period of the beat signal, the correlation of $j(\vec{r}+\vec{\rho},t)$ and $j(\vec{r},t)$ is determined entirely by the spatial correlation function of the incident field. Condition (1) given above is an alternate description of that limit.

With these assumptions Beran and Parrent[26] have shown that we can write

$$\langle \vec{E}(\vec{r}+\vec{\rho},t+\tau)\cdot\vec{E}(\vec{r},t)\rangle = \frac{\langle \vec{E}(\vec{r}+\vec{\rho},t)\cdot\vec{E}(\vec{r},t)\rangle}{\langle \vec{E}(\vec{r},t)\cdot\vec{E}(\vec{r},t)\rangle}\langle \vec{E}(\vec{r},t+\tau)\cdot\vec{E}(\vec{r},t)\rangle \tag{3-47}$$

If the intensities at $\vec{r}$ and $\vec{r}+\vec{\rho}$ are equal, the quotient term in Eq. (3-47) is the real part of the spatial correlation function $\underline{T}(\vec{r},\vec{\rho})$ defined in Section E.2 of Chapter 2. In this case we have the desired factoring

$$\langle \vec{E}(\vec{r}+\vec{\rho},t+\tau)\cdot\vec{E}(\vec{r},t)\rangle = T(\vec{r},\vec{\rho})R_E(\tau) \tag{3-48}$$

Substituting this result into Eq. (3-46) gives for the total current correlation function

$$R_i(\tau) = i_p^{\,2} + ei_p\delta(\tau) + 2\alpha^2 R_E^{\,2}(\tau)\int_A\int_A T^2(\vec{r},\vec{\rho})\,d^2\vec{r}\;d^2\vec{\rho} \tag{3-49}$$

A comparison between Eqs. (3-49) and (3-30) shows that the total current and the current density have identical spectral features: a dc term representing the time average photocurrent, a frequency independent shot-noise term that results from the non-continuous and stochastic nature of the photoemission process, and a beat note term that describes the optical mixing action at the photocathode. However, the magnitude of the beat note term in $R_i(\tau)$ does not simply increase with A^2 as might be expected from Eq. (3-30). Rather, the strength of the beat note observed in the total current i(t) depends both on the size of the detector and the range of spatial correlation in the incident field.

If the time average intensity is uniform over the photosurface, $T(\vec{r},\vec{\rho})$ is independent of $\vec{r}$ on A and we have

$$\int_A \int_A T^2(\vec{r},\vec{\rho})\, d^2\vec{r}\, d^2\vec{\rho} = A \int_A T^2(\vec{r}_o,\vec{\rho})\, d^2\vec{\rho} \tag{3-50}$$

where $\vec{r}_o$ gives the reference position of the photodetector in the field $\vec{E}(\vec{r},t)$. The integral

$$\int_{\text{all } \vec{\rho}} T^2(\vec{r}_o,\vec{\rho})\, d^2\vec{\rho}$$

is a measure of the area surrounding a given point on the photosurface over which the incident field and hence the beat note photocurrent densities $j(\vec{r},t)$ are all in phase. We designate this area as the coherence area, A_{COH},

$$A_{COH} = \int_{\text{all } \vec{\rho}} T^2(\vec{r}_o,\vec{\rho})\, d^2\vec{\rho} \tag{3-51}$$

It follows that the double integral in Eq. (3-50) has two limiting behaviors. If the size of the photocathode is large compared to the range[†] of $T(\vec{r}_o,\vec{\rho})$, then the integrals give

$$\int_A \int_A = A\, A_{COH} \;;$$

[†] Chapter 2, Section E.

on the other hand, if the photocathode is small compared to the size of a coherence area, then we have

$$\int_A \int_A = A^2 \,.$$

This yields $R_i(\tau)$ in the form

$$R_i(\tau) = i_p^2 + ei_p\delta(\tau) + 2\alpha^2 R_E^2(\tau) A^2 \begin{cases} 1 & ; \quad A \ll A_{COH} \\ (A_{COH}/A) & ; \quad A \gg A_{COH} \end{cases} \tag{3-52}$$

The effects of spatial coherence on the operation of an optical mixing spectrometer are described completely by the quantity A_{COH}. A detailed discussion of these effects and their physical origin is presented in the following two sections which analyze the self-beat and superheterodyne optical mixing spectrometers respectively.

The correlation function given in Eq. (3-52) represents the desired generalization to i(t) of the result found in Eq. (3-30) for the current density. The power spectral density of the total current, $S_i(\omega)$, can be calculated by the same method used to compute $S_j(\omega)$, with the result

$$\begin{aligned} S_i(\omega) = {} & i_p^2\delta(\omega) + (e/2\pi)i_p \\ & + \alpha^2A^2 \left\{ \begin{matrix} 1 \\ (A_{COH}/A) \end{matrix} \right\} \int_{-\infty}^{\infty} S_E(\omega')[S_E(\omega'+\omega) + S_E(\omega'-\omega)]d\omega' \end{aligned} \tag{3-53}$$

C. The Self-Beating Optical Spectrometer

In the preceding section we considered in detail the operation of a photomixer and derived the basic relationship between the spectrum of the photocurrent and the spectrum of the incident field. We are now in a position to analyze the two optical mixing spectrometers that were described in the introduction to this chapter. Here we will consider the self-beat or self-mixing spectrometer in which a frequency translation of the spectral information in the incident field is accomplished by simply allowing the light to fall on a photosurface. In this case mixing takes place between the different frequency components of the field itself and generates a photocurrent beat note spectrum located around $\omega = 0$.

In this section we will assume that the spectrum of the incoming field is Lorentzian and determine the spectrum of the resulting photocurrent. We find that if $S_E(\omega)$ is Lorentzian then $S_i(\omega)$ is also Lorentzian, but that the latter has its maximum at $\omega = 0$ and has a width at half-height equal to twice the half-width at half-height of $S_E(\omega)$. We then consider the step-by-step processing of the current signal i(t): the examination of its spectrum with a narrow band tunable filter, the rectification of the filtered current, and the display of the output. The objective is to calculate the sensitivity of the spectrometer by determining a "signal-to-noise ratio" at the output for a given amount of input optical power. The choice of a suitable definition for this (S/N) ratio will emerge in the course of the calculation. The sensitivity results are presented in the form of a set of parameterized curves called isones which represent lines of constant output (S/N) ratio. From these curves it is possible to predict easily how a specific change in input optical power, filter bandwidth, photomixer quantum efficiency, and so on will affect the detection capabilities of the instrument.

A very striking feature that emerges from the analysis is that increasing the size of the detector area in order to accept more light does not increase the output (S/N) ratio once the area of the photosurface exceeds the coherence area† A_{COH}. This result is explained in terms of the randomness in phase between beat frequency currents generated at two different coherence areas on the photocathode surface.

1. The Observed Photocurrent Power Spectrum for the Case of a Lorentzian Input Field

Let us consider the self-beating spectrometer shown in Fig. 3-9. We assume that the incident field can be described as Gaussian random noise, perhaps the light scattered from thermal fluctuations in a liquid. The power spectrum of this field is taken to be a Lorentzian centered at the optical frequency ω_o and having a half-width at half-height of Γ rad/sec, that is

$$S_E(\omega) = \left\langle |\vec{E}(\vec{r}_o,t)|^2 \right\rangle \frac{(\Gamma/2\pi)}{(\omega-\omega_o)^2 + \Gamma^2} + \frac{(\Gamma/2\pi)}{(\omega+\omega_o)^2 + \Gamma^2} \qquad (3\text{-}54)$$

Equation (3-54) expresses $S_E(\omega)$ in its symmetric form§; the actual power per unit spectral interval at any frequency $\omega \geq 0$ is found by adding $S_E(-\omega)$ to $S_E(\omega)$. The

---

† Chapter 3, Section B.4.

§ Chapter 2, Section D.

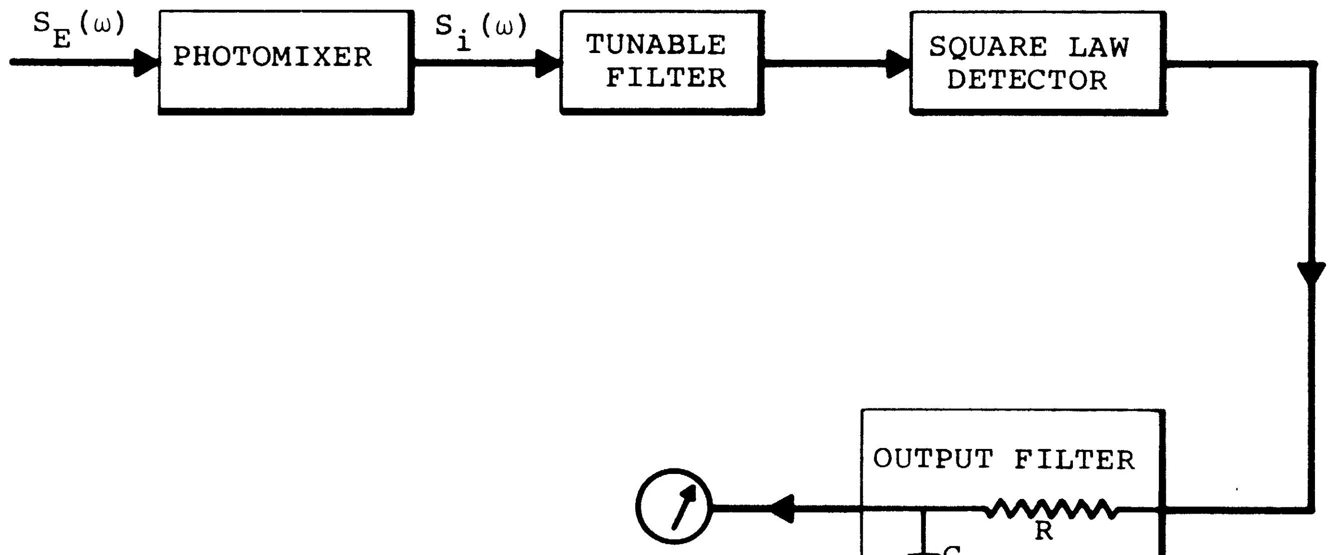
$S_E(\omega)$
PHOTOMIXER
$S_i(\omega)$
TUNABLE FILTER
SQUARE LAW DETECTOR
OUTPUT FILTER
R
C

Figure 3-9 Block diagram of a self-beating optical spectrometer.

intensity of the incoming beam $(1/\mu_o c_m)\langle|\vec{E}(\vec{r},t)|^2\rangle$ has been assumed to be constant over the photosurface.

Suppose we let the field described by Eq. (3-54) be incident on a photodetector. The power spectrum of the resulting photocurrent then follows directly from Eq. (3-53) as

$$S_i(\omega) = i_p{}^2\delta(\omega) + (e/2\pi)\, i_p + \alpha^2 A^2 \left\{\begin{matrix} 1 \\ \\ (A_{COH}/A) \end{matrix}\right\} [\langle|\vec{E}(\vec{r}_o,t)|^2\rangle]^2 \, \frac{(2\Gamma/\pi)}{\omega^2 + (2\Gamma)^2} \tag{3-55}$$

the upper line in the braces corresponding to $A << A_{COH}$, the lower line to $A >> A_{COH}$. Writing[§]

$$i_p = \alpha A\langle|\vec{E}(\vec{r}_o,t)|^2\rangle \, .$$

gives Eq. (3-55) in the more useful form

$$S_i(\omega) = i_p{}^2\delta(\omega) + (e/2\pi) i_p + \left\{\begin{matrix} 1 \\ \\ (A_{COH}/A) \end{matrix}\right\} i_p{}^2 \left[\frac{(2\Gamma/\pi)}{\omega^2 + (2\Gamma)^2}\right] \tag{3-56}$$

This result shows that for a Lorentzian optical spectrum the beat note term in $S_i(\omega)$ is also a Lorentzian; however, rather than being centered at $\omega = \omega_o$, the spectral information has been translated down to $\omega=0$. In addition, the half-width at half-height of the self-beat spectrum is twice that of the incoming light. The calculation of $S_i(\omega)$ can also be carried through by employing the correlation function corresponding to the assumed incident field, viz.

[§] Chapter 3, Section B.4, Eq. (3-38).

$$R_E(\tau) = \langle|\vec{E}(\vec{r}_o,t)|^2\rangle e^{-\Gamma\tau}\cos\omega_o\tau \tag{3-57}$$

The correlation function of the photocurrent is then computed using Eq. (3-52) with the result

$$R_i(\tau) = i_p^{\,2} + ei_p\delta(\tau) + \alpha^2A^2 \left\{\begin{matrix} 1 \\ \\ (A_{COH}/A) \end{matrix}\right\} \langle|\vec{E}(\vec{r}_o,t)|^2\rangle e^{-2\Gamma\tau} \tag{3-58}$$

Equation (3-56) follows directly on taking the Fourier cosine transform

$$S_i(\omega) = (1/2\pi) \int_{-\infty}^{\infty} R_i(\tau) \cos(\omega\tau)\, d\tau \ .$$

The total current spectrum including the signal, the dc, and the shot-noise components is illustrated in Fig. 3-10.

Clearly the self-beating process does accomplish the desired frequency translation of the spectral information present in the optical field, with the exception of the value of the original center frequency ω_o which is lost. Furthermore, although the spectral distribution of the light is not preserved exactly in the photocurrent spectrum, if the incident light wave does have a Lorentzian power spectrum then the two are related in a trivial manner.

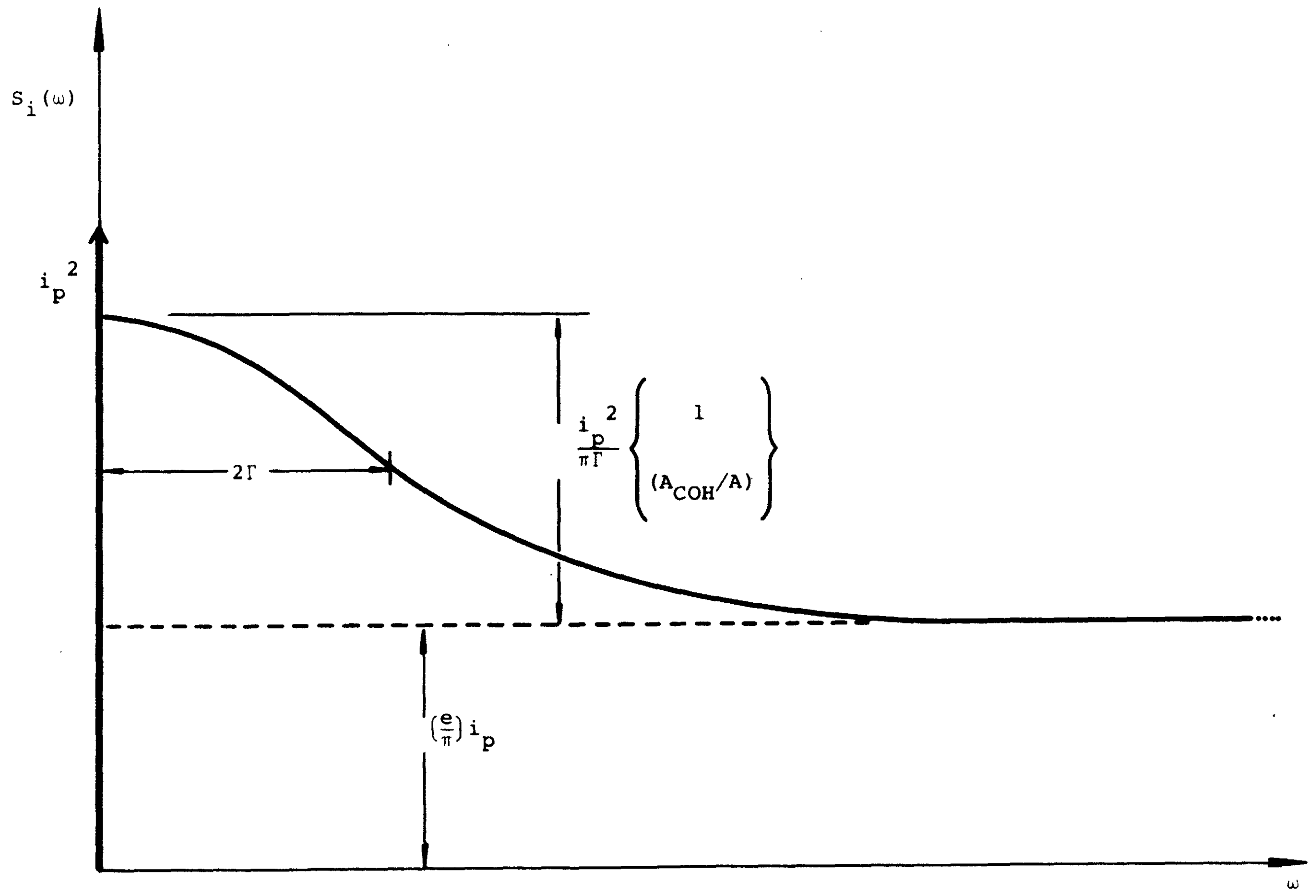

Figure 3-10 The power spectral density of the current output of a photodetector illuminated with an optical field having a Lorentzian spectrum with a half-width at half-height of Γ rad/sec.

2. The Processing of the Photocurrent Signal

We turn now to the problem of *measuring* the self-beat part of $S_i(\omega)$ and determining the possible sources of noise that make this measurement uncertain. For handling the processing of the current it is convenient to label each of the three components of $S_i(\omega)$ separately; therefore, we define the signal, the shot-noise, and the dc terms respectively as

$$I_S^2(\omega) = \left[\frac{1}{(A_{COH}/A)}\right] i_p^2 \left[\frac{(4\Gamma/\pi)}{\omega^2 + (2\Gamma)^2}\right] \qquad (\omega \geq 0)$$

$$I_N^2(\omega) = (e/\pi) i_p \qquad (\omega \geq 0) \qquad (3\text{-}59)$$

$$I_o^2 = i_p^2$$

a. The Pre-Detection Signal-to-Noise Ratio

(1) Definition

As is evident from Fig. 3-10, one measure of the detectability of the *signal* current spectrum is its power per unit bandwidth (power spectral density) as compared to that of the shot-noise. We define the pre-detection signal-to-noise ratio, $(S/N)_{PRE}$, as

$$(S/N)_{PRE} \equiv [I_S{}^2(0)/I_N{}^2(0)] = \left\{ \begin{matrix} 1 \\ \\ (A_{COH}/A) \end{matrix} \right\} \frac{i_p}{e\Gamma} \qquad (3\text{-}60)$$

or using Eq. (3-39) to write i_p in terms of the total optical power falling on the photocathode by

$$(S/N)_{PRE} = \left(\frac{\varepsilon}{\hbar\omega_o}\right) \left\{ \begin{matrix} 1 \\ \\ (A_{COH}/A) \end{matrix} \right\} \frac{P_o}{\Gamma} \qquad (3\text{-}61)$$

The ratio (P_o/Γ) measures the incident optical power per unit frequency interval while $(A_{COH}/A)P_o$ is just the optical power falling on a single coherence area of the photosurface. The behavior of $(S/N)_{PRE}$ with Γ is easily understood by noting that the total power in the signal part of the current spectrum,

$$\int_o^\infty I_S{}^2(\omega)\,d\omega,$$

is independent of Γ and depends only on the incident light intensity and the area of the detector. Therefore, a decrease in Γ must cause an increase in the available signal power per unit bandwidth at $\omega=0$.

(2) Effects of Spatial Coherence

The really interesting feature of $(S/N)_{PRE}$ is its behavior with increasing photodetector area, A. Writing i_p in terms of a uniform incident light intensity $(1/\mu_o c_m)\langle|\vec{E}(\vec{r}_o,t)|^2\rangle$ and analyzing the cases $A >> A_{COH}$ and $A << A_{COH}$ separately we find

$$\underline{A \gg A_{COH}}$$

$$I_S{}^2(\omega) = AA_{COH} \cdot \alpha^2 [\langle |\vec{E}(\vec{r}_o,t)|^2 \rangle]^2 \frac{(4\Gamma/\pi)}{\omega^2 + (2\Gamma)^2} \qquad \omega \geq 0$$

$$I_N{}^2(\omega) = A \cdot \alpha [\langle |\vec{E}(\vec{r}_o,t)|^2 \rangle] (e/\pi) \qquad \omega \geq 0$$

$$I_o{}^2 = A^2 \cdot \alpha^2 [\langle |\vec{E}(\vec{r}_o,t)|^2 \rangle]^2$$

$$(S/N)_{PRE} = A_{COH} \cdot (\alpha/e\Gamma) [\langle |\vec{E}(\vec{r}_o,t)|^2 \rangle]$$

(3-62)

$$\underline{A \ll A_{COH}}$$

$$I_S{}^2(\omega) = A^2 \cdot \alpha^2 [\langle |\vec{E}(\vec{r}_o,t)|^2 \rangle]^2 \frac{(4\Gamma/\pi)}{\omega^2 + (2\Gamma)^2} \qquad \omega \geq 0$$

$$I_N{}^2(\omega) = A \cdot \alpha [\langle |\vec{E}(\vec{r}_o,t)|^2 \rangle] (e/\pi) \qquad \omega \geq 0$$

$$I_o{}^2 = A^2 \cdot \alpha^2 [\langle |\vec{E}(\vec{r}_o,t)|^2 \rangle]^2$$

$$(S/N)_{PRE} = A \cdot (\alpha/e\Gamma) [\langle |\vec{E}(\vec{r}_o,t)|^2 \rangle]$$

Consider the shot noise terms, $I_N{}^2(\omega)$, for each limit first. Although the dc photocurrent power goes up as the square of the photocathode area, the shot-noise power spectral density increases only linearly with A. This is a direct result of the random character[§] of the photoemission process which demands that the phases of the shot-noise currents generated at separated points on the photodetector be completely uncorrelated. These randomly phased currents can add only linearly to the total shot-noise power. A similar argument applies to the beat signal currents, $I_S^2(\omega)$, where the phases are determined by the spatial coherence properties of the incident field.[*] In the case $A << A_{COH}$, in which $\vec{E}(\vec{r},t)$ is spatially coherent over the detector, the beat signal currents produced at all points on the photosurface are in phase. Therefore, they add linearly to the total beat current and quadratically to its power spectrum. In this case we find $I_S^2(\omega) \propto A^2$. In the opposite limit, $A >> A_{COH}$, the photosurface must be divided up into a large number of areas equal in size to A_{COH}. The beat signal current generated in each of these regions is randomly phased relative to that generated in any other coherence area. These randomly phased currents add to produce a signal power spectrum that increases only linearly with A.

The behavior of the pre-detection signal-to-noise ratio with increasing A can be summarized as follows. For $A << A_{COH}$, $(S/N)_{PRE}$ increases with A since $I_S^2(0)$ grows faster than $I_N^2(0)$; but, when $A = A_{COH}$, $(S/N)_{PRE}$ limits at the value

$$(S/N)_{PRE} = A_{COH}(\alpha/e\Gamma)\langle|\vec{E}(\vec{r}_o,t)|^2\rangle$$

and is unchanged by further increases in A. This analysis suggests a conclusion that is verified by the final calculations, namely, that the sensitivity of an optical mixing spectrometer is dependent not on the total available optical power but on the optical power per area of spatial coherence in the incident field.

[§] Chapter 3, Section B.4

[*] Chapter 2, Section E, and Chapter 3, Section B.4, Eq.(3-48)

If we define the power per coherence area as $\mathcal{P}_{\mathrm{COH}} = (A_{\mathrm{COH}}/A)\,\mathcal{P}_o$, the limiting value of $(S/N)_{\mathrm{PRE}}$ is

$$(S/N)_{\mathrm{PRE}} = \frac{\varepsilon}{\hbar\omega_o}\left(\frac{\mathcal{P}_{\mathrm{COH}}}{\Gamma}\right) \qquad A \geq A_{\mathrm{COH}} \qquad (3\text{-}63)$$

For incident light with a wavelength $\lambda_{\mathrm{air}} = 6328$ Å and for a quantum efficiency of 100% we find that the power per unit coherence area, per unit bandwidth necessary to give $(S/N)_{\mathrm{PRE}} = 1$ is

$$\left.\left(\frac{\mathcal{P}_{\mathrm{COH}}}{\Gamma}\right)\right|_{(S/N)_{\mathrm{PRE}} = 1} = 3.1 \times 10^{-19} \frac{\text{watts}}{\text{radian/sec}}$$

$$= 2.0 \times 10^{-18} \frac{\text{watts}}{\text{cps}}$$

Although this ratio is one measure of the sensitivity of the self-beating spectrometer it neither specifies how accurately we can measure the spectrum of $I_S^2(\omega)$, nor what the source of noise in the measurement will be. It is an indication simply that the shot-noise spectrum provides a uniform background against which $I_S^2(\omega)$ must be determined.

b. The Electronic System

(1) The Tuned Filter

We now proceed to examine the effects of the tunable filter. The result of passing a signal through such a linear element is usually specified in terms of the so called system or filter function[27] $H(\omega)$ as

$$S_f(\omega) = |H(\omega)|^2 S_i(\omega) \tag{3-64}$$

where $S_f(\omega)$ is the power spectral density of the filtered current. An equivalent relation can be given between the output correlation function $R_f(\tau)$ and the input correlation function $R_i(\tau)$ in terms of the unit impulse response of the filter[27] $h(t_2-t_1)$, viz.

$$R_f(\tau) = \int_{-\infty}^{\infty} h(\tau')d\tau' \int_{-\infty}^{\infty} h(\tau'')d\tau'' \, R_i(\tau+\tau''-\tau') \tag{3-65}$$

The unit impulse response of the network and the network system function are related as Fourier cosine transform pairs, that is

$$h(\tau) = (1/2\pi) \int_{-\infty}^{\infty} H(\omega) \cos \omega\tau \, d\omega$$

Here the action of the filter is specified in terms of $|H(\omega)|^2$ which we assume to have the rectangular form shown in Fig. 3-11 . This filter passes perfectly all frequencies in $S_i(\omega)$ between $[\omega_f - (\Delta\omega_f/2)]$ and $[\omega_f + (\Delta\omega_f/2)]$ and stops all others. If we also block the dc photocurrent from getting to the filter (e.g., with a capacitor) then the spectrum of the filtered shot-noise and beat signal components of $S_i(\omega)$ is given by

$$S_f(\omega) = I_S{}^2(\omega)\,|H(\omega)|^2 + I_N{}^2(\omega)\,|H(\omega)|^2 \tag{3-66}$$

$(\omega \geq 0)$

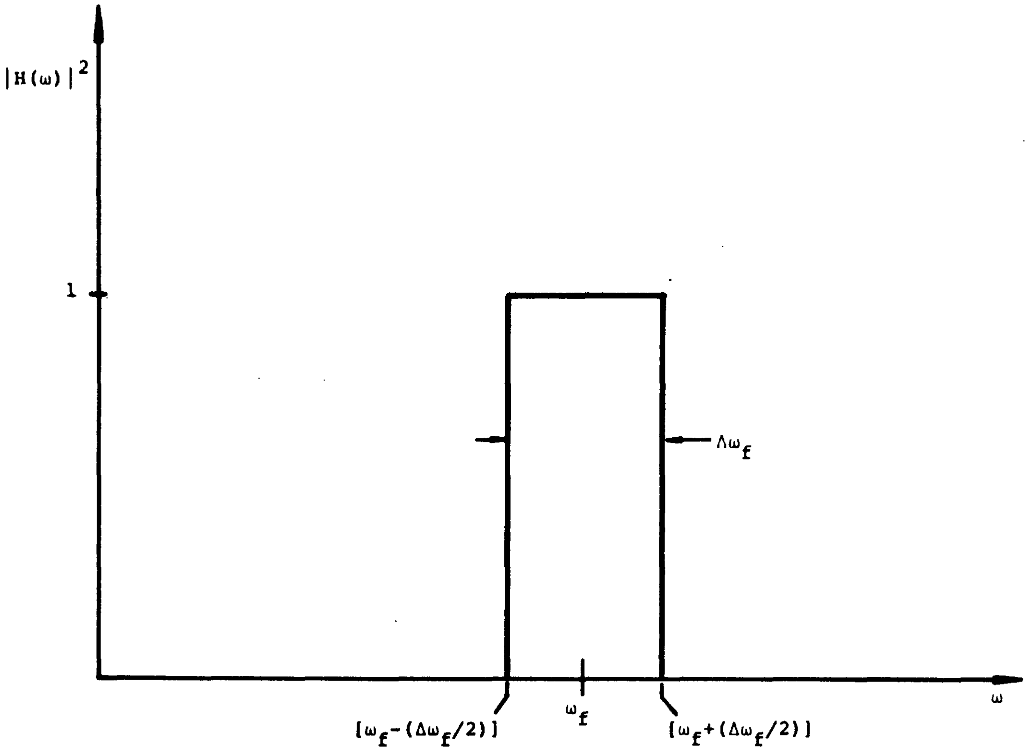
$|H(\omega)|^2$
1
$\Delta\omega_f$
$[\omega_f-(\Delta\omega_f/2)]$
ω_f
$[\omega_f+(\Delta\omega_f/2)]$
ω

Figure 3-11 Assumed system function for the tuned filter used to examine the photocurrent spectrum.

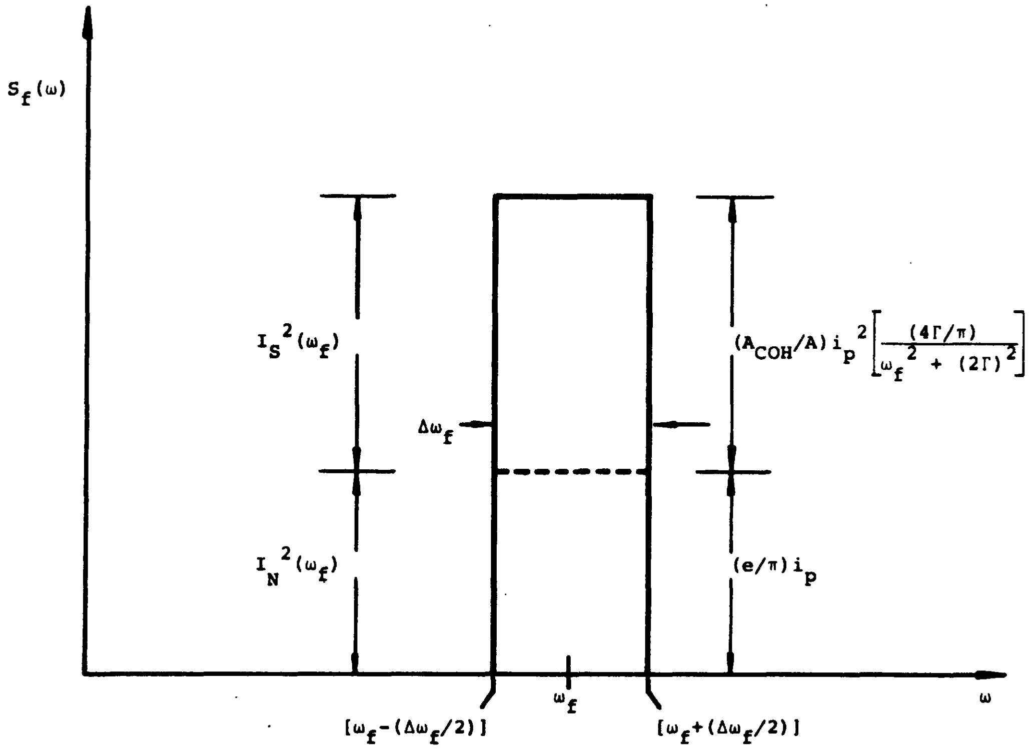
$S_f(\omega)$
$I_S^2(\omega_f)$
$I_N^2(\omega_f)$
$\Delta\omega_f$
$(A_{COH}/A)\, i_p^2 \left[\frac{(4\Gamma/\pi)}{\omega_f^2 + (2\Gamma)^2}\right]$
$(e/\pi)\, i_p$
$[\omega_f-(\Delta\omega_f/2)]$
ω_f
$[\omega_f+(\Delta\omega_f/2)]$
ω

Figure 3-12 The power spectral density of the filtered photocurrent.

$$\underset{(\omega\geq 0)}{S_f(\omega)} = \begin{cases} (A_{COH}/A)\ i_p^{\,2}\left[\dfrac{(4\Gamma/\pi)}{\omega^2 + (2\Gamma)^2}\right] + (e/\pi)i_p \ ; \\ \qquad [\omega_f - (\Delta\omega_f/2)] \leq \omega \leq [\omega_f + (\Delta\omega_f/2)] \\ 0 \qquad ; \text{ otherwise} \end{cases}$$

Under normal circumstances the bandwidth of the filter, $\Delta\omega_f$, is chosen to be small compared to the line width of the signal spectrum, 2Γ. The variation in the amplitude of $I_S^{\,2}(\omega)$ over the range of frequencies passed by the filter is then negligible and we have $S_f(\omega)$ in the simple form

$$\underset{(\omega\geq 0)}{S_f(\omega)} = \begin{cases} I_S^{\,2}(\omega_f) + I_N^{\,2}(\omega_f) \ ; \ [\omega_f - (\Delta\omega_f/2)] \leq \omega \leq [\omega_f + (\Delta\omega_f/2)] \\ 0 \qquad ; \text{ otherwise} \end{cases} \tag{3-67}$$

This filtered spectrum is shown in Fig. 3-12. It consists of two uniform contributions, one from the signal and one from the shot-noise. The quantity of interest, $I_S^{\,2}(\omega)$, is now reflected in the total power output of the filter. That is, as the filter is tuned, its power output traces out the value of $[I_S^{\,2}(\omega) + I_N^{\,2}(\omega)]$; furthermore, the constant* $I_N^{\,2}(\omega)$ may be determined by tuning to a frequency $\omega \gg 2\Gamma$ where $I_S^{\,2}(\omega) \simeq 0$.

---

* Eq. (3-59)

(2) The Detector

To measure this output power we must put the filtered current into some sort of detector or bolometer. As indicated in Fig. 3-9 we choose a detector with a square-law response, e.g. a diode biased into its quadratic current regime. The properties of such a detector can be described as follows. If the instantaneous filtered current is called $i_f(t)$ and the instantaneous output voltage of the detector $v_D(t)$, then $i_f(t)$ and $v_D(t)$ are related by

$$v_D(t) = Mi_f^2(t) \tag{3-68}$$

where M is called the transfer constant. However, the current $i_f(t)$ is, in fact, a random noise current;[28] therefore, the appropriate description of the detector output is found by calculating the power spectral density of $v_D(t)$, designated $S_V(\omega)$, in terms of the spectrum of the filtered current, $S_f(\omega)$. The desired result can be obtained easily by noting the formal similarity between the relation of $v_D(t)$ and $i_f(t)$ given in Eq. (3-68) and the relation between the photocurrent density and the electric field as given in Eq. (3-1). Both of these equations describe the operation of a "square-law" device. Equation (3-35) can immediately be adapted to the present case in the form

$$S_V(\omega) = [\langle\langle v_D(t)\rangle\rangle]^2\delta(\omega) + M^2\int_{-\infty}^{\infty} S_f(\omega')[S_f(\omega'+\omega) + S_f(\omega'-\omega)]d\omega' \tag{3-69}$$

The dc detector output voltage $\langle\langle v_D(t)\rangle\rangle$ is given by

$$\langle\langle v_D(t)\rangle\rangle = M\langle\langle i_f^2(t)\rangle\rangle \tag{3-70}$$

Equation (3-70) can be rewritten in a more useful form by noting that the mean square amplitude $\langle\langle i_f^2(t)\rangle\rangle$ is equal to the integral under the power spectrum $S_f(\omega)$ by Parseval's theorem

$$\langle\langle i_f^2(t)\rangle\rangle = \int_{-\infty}^{\infty} S_f(\omega')d\omega' \tag{3-71}$$

so that we also have the result

$$\langle\langle v_D(t)\rangle\rangle = M\int_{-\infty}^{\infty} S_f(\omega')d\omega' \tag{3-72}$$

Equations (3-69) and (3-72) completely specify the action of the detector. The features of the detected spectrum are identical to those found in the output current spectrum of a "photo" square-law detector; a dc term which measures the average total input power, an ac part representing beats between all pairs of frequency components present in the input signal, and a shot-noise term that has been neglected in Eq. (3-69). The shot-noise contribution, although actually present in a real detector, can always be made as small as desired relative to the ac beat signals by suitably amplifying the filtered current prior to detection.

If the detector input is the filtered self-beat and shot-noise current whose spectrum is given in Eq. (3-67) and shown in Fig. 3-12, then the dc detector output is

$$\langle\langle v_D(t)\rangle\rangle = M[I_S^2(\omega_f) + I_N^2(\omega_f)]\Delta\omega_f \tag{3-73}$$

part of which is the desired signal term $I_S^2(\omega_f)$. The total power spectrum has the form

$$S_V(\omega) = M^2(\Delta\omega_f)^2[I_S{}^2(\omega_f) + I_N{}^2(\omega_f)]^2\delta(\omega)$$

$$+ 2M^2[I_S{}^2(\omega_f) + I_N{}^2(\omega_f)]^2(\Delta\omega_f)\left[\frac{(\Delta\omega_f) - \omega}{(\Delta\omega_f)}\right] \qquad (3\text{-}74)$$

$$0 \le \omega \le \Delta\omega_f$$

in which the terms at frequencies $\omega \simeq 2\omega_f$ have been neglected. The ac part of $S_V(\omega)$ represents a triangularly shaped spectrum as shown in Fig. 3-13.

The source of noise encountered in measuring $I_S{}^2(\omega)$ now becomes evident. The desired information, $I_S{}^2(\omega_f)$, is present at the detector output as a dc voltage which can be measured, for example, by a meter. However, the detector output also contains ac noise voltages which will cause the meter reading to fluctuate, thus making the determination of $I_S{}^2(\omega_f)$ uncertain. Moreover these "noise" voltages are simply "beat notes" between all pairs of frequency components present in the filtered current; both in the signal $I_S{}^2(\omega_f)$ and shot-noise $I_N{}^2(\omega_f)$ contributions. These "noise beats" which interfere with the measurement are produced through the non-linearity of the detection process.

(3) The Post-Detection Signal-to-Noise Ratio

Suppose we define a post-detection (S/N) ratio as the ratio of the dc detector output produced by the signal $I_S{}^2(\omega_f)$ to the root-mean-square ac component, namely,

$$(S/N)_{POST} \equiv \frac{\langle\langle v_o(t)\rangle\rangle\Big|_{SIGNAL}}{\sqrt{\langle|[v_D(t)]_{ac}|^2\rangle}} \qquad (3\text{-}75)$$

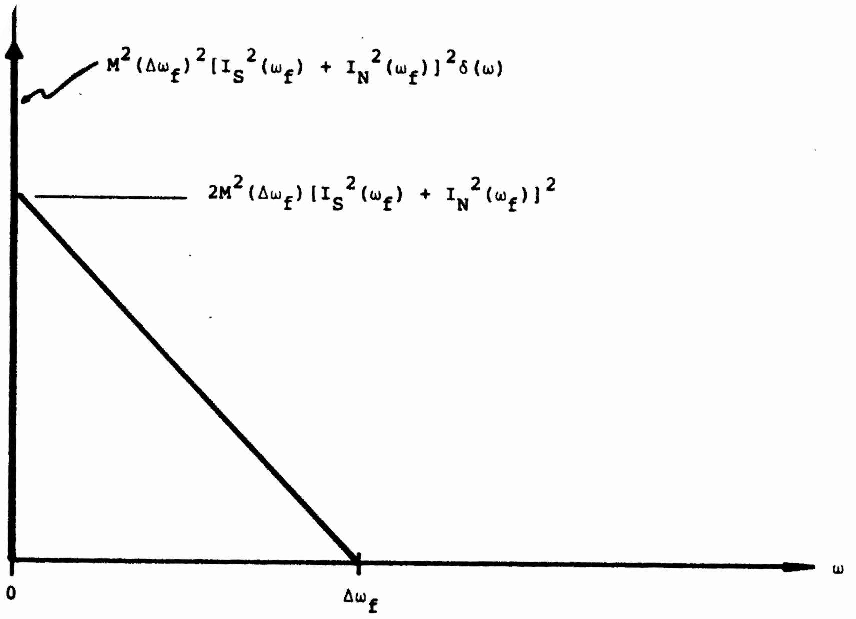

Figure 3-13 The power spectral density of the detector output.

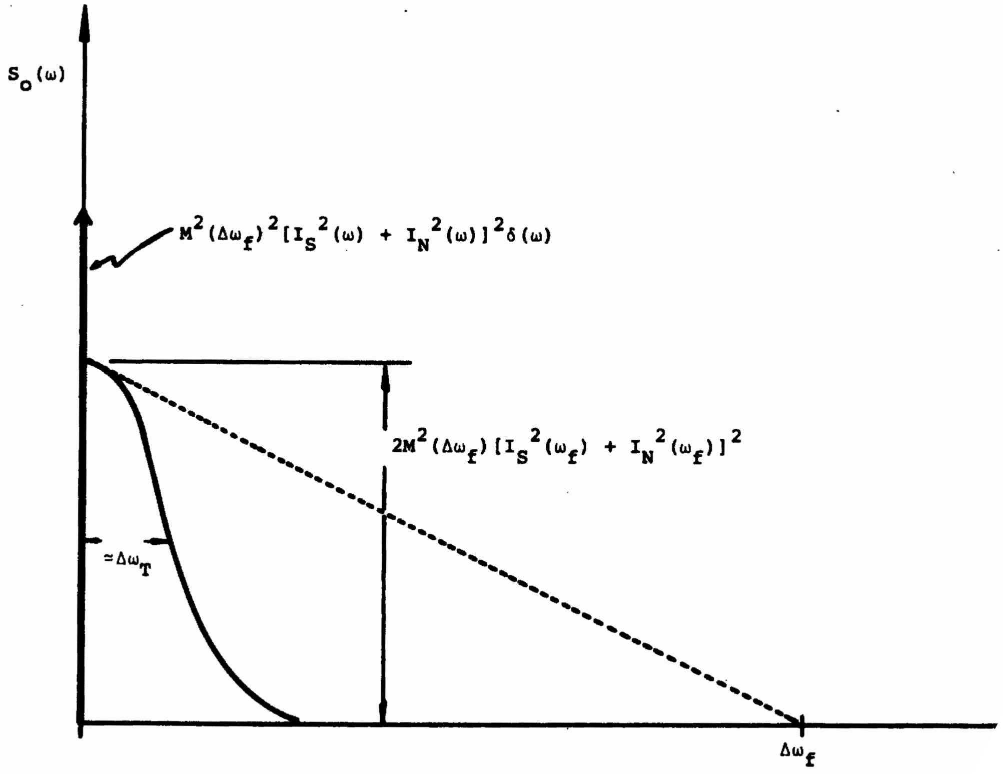

Figure 3-14 The power spectral density of the de
output after post-filtering.

the average $\langle | [v_D(t)]_{ac} |^2 \rangle$ simply measures the mean-square fluctuations in detector output around its average value $\langle\langle v_D(t) \rangle\rangle$ and is defined by

$$\langle | [v_D(t)]_{ac} |^2 \rangle = \langle | v_D(t) - \langle v_D(t) \rangle |^2 \rangle$$

Because $[v_D(t)]_{ac}$ has a zero time average, Parseval's theorem[29] can be applied to yield

$$\langle | [v_D(t)]_{ac} |^2 \rangle = \int_{-\infty}^{\infty} S_V^{\,*}(\omega')\, d\omega' \qquad (3\text{-}76)$$

The spectrum $S_V^{\,*}(\omega)$ is identical to $S_V(\omega)$ excluding the dc term.

The definition of $(S/N)_{POST}$ implies that for a signal-to-noise ratio of unity the rms fluctuation in meter reading is equal to the meter deflection due to the signal. Suppose, for example, that the meter can respond equally well to all ac frequencies present in the detector output ($0 \leq \omega \leq \Delta\omega_f$). Then the post-detection signal-to-noise ratio in the self-beating spectrometer follows from Eqs. (3-75), (3-76), and (3-74) as

$$(S/N)_{POST} = \frac{M(\Delta\omega_f)[I_S^{\,2}(\omega_f)]}{\sqrt{M^2(\Delta\omega_f)^2[I_S^{\,2}(\omega_f) + I_N^{\,2}(\omega_f)]^2}}$$

$$= \frac{I_S^{\,2}(\omega_f)}{I_S^{\,2}(\omega_f) + I_N^{\,2}(\omega_f)} \qquad (3\text{-}77)$$

This result shows that both the shot-noise and the signal parts of the filtered current beat with themselves and each other in the detector to produce the observed meter fluctuations. Moreover, even in the absence of the shot-noise contribution, the signal term alone will produce sufficient meter noise to completely mask the desired dc deflection. Clearly some method of "filtering" or "averaging" out these ac noise currents must be employed prior to recording.

(4) Post-Detection Filtering

The simplest such averaging scheme is the RC filter or "time constant circuit" shown in Fig. 3-9. This network passes the entire dc detector output to the meter but bypasses some of the undesired ac output voltage through the capacitor C. As was the case for the tunable filter, the effect of such a network is most easily specified in terms of its system function, $H(\omega)$. For the RC filter we find $|H(\omega)|^2$ as

$$|H(\omega)|^2 = \frac{(1/RC)^2}{\omega^2 + (1/RC)^2} \qquad (\omega \geq 0) \qquad (3\text{-}78)$$

a Lorentzian having a maximum response at $\omega = 0$ and a width at half-height equal to $(1/RC)$. Therefore, this filter will pass on to the output indicator only those frequencies in the detector output spectrum which lie within a bandwidth $(\Delta\omega_T) = (1/RC)$ of zero frequency.

The product RC is generally referred to as the time constant of the circuit since the RC network impulse response

$$h(\tau) = e^{-\tau/RC}$$

shows that the output of this circuit requires a time $\tau_c = RC$ to respond to any change made at the input terminals.

Calling the filtered detector output voltage $v_o(t)$ and its power spectral density $S_o(\omega)$ we have easily from Eqs. (3-64), (3-74), and (3-78)

$$S_o(\omega) = S_v(\omega)\,|H(\omega)|^2 \tag{3-79}$$

$$= M^2(\Delta\omega_f)^2[I_S{}^2(\omega_f) + I_N{}^2(\omega_f)]^2\delta(\omega)$$

$$+ 2M^2[I_S{}^2(\omega_f) + I_N{}^2(\omega_f)]^2(\Delta\omega_f)\left[\frac{(\Delta\omega_f) - \omega}{(\Delta\omega_f)}\right]\left[\frac{(\Delta\omega_T)^2}{(\Delta\omega_T)^2 + \omega^2}\right.$$

$(0 \le \omega \le \Delta\omega_f)$

The filtered output spectrum is shown in Fig. 3-14 for the case $(\Delta\omega_T) << (\Delta\omega_f)$.

c. The Output Signal-to-Noise Ratio

We now define the output signal-to-noise ratio of the spectrometer in analogy with $(S/N)_{POST}$ as

$$(S/N)_{OUT} \equiv \frac{\langle\!\langle v_o(t) \rangle\!\rangle \Big|_{SIGNAL}}{\sqrt{\langle |[v_o(t)]_{ac}|^2 \rangle}} \tag{3-80}$$

The physical interpretation of $(S/N)_{OUT}$ completely parallels that given $(S/N)_{POST}$: $(S/N)_{OUT}$ measures the ratio of the signal deflection of the output device to the rms fluctuation in deflection.

The total mean-square ac output voltage can again be calculated by using Parseval's theorem

$$\left\langle \left| [v_o(t)]_{ac} \right|^2 \right\rangle = \int_{-\infty}^{\infty} S_o^{*}(\omega')\,d\omega'$$

where the spectrum $S_o^{*}(\omega)$ is identical to the ac part of $S_o(\omega)$ as given in Eq. (3-79). Evaluating

$$\int_{-\infty}^{\infty} S_o^{*}(\omega')\,d\omega'$$

we find easily

$$\left\langle \left| [v_o(t)]_{ac} \right|^2 \right\rangle = 2M^2[I_S{}^2(\omega_f) + I_N{}^2(\omega_f)]^2(\Delta\omega_f) \times$$

$$(\Delta\omega_T)\tan^{-1}\left(\frac{\Delta\omega_f}{\Delta\omega_T}\right) - \frac{(\Delta\omega_T)^2}{(\Delta\omega_f)^2}\,\ell n\left[\frac{(\Delta\omega_f)^2 + (\Delta\omega_T)^2}{(\Delta\omega_T)^2}\right]$$

In the usual limit $(\Delta\omega_T) << (\Delta\omega_f)$ this result becomes simply

$$\left\langle \left| [v_o(t)]_{ac} \right|^2 \right\rangle = \pi M^2[I_S{}^2(\omega_f) + I_N{}^2(\omega_f)]^2(\Delta\omega_f)(\Delta\omega_T) \qquad (3\text{-}81)$$

In determining $(S/N)_{OUT}$ using Eqs. (3-80), (3-81), and (3-79) we arbitrarily choose $\omega_f = 0$; at this point $I_S{}^2(\omega_f)$ takes on its maximum value and, therefore, $(S/N)_{OUT}$ is also a maximum. This choise yields as the final result

$$(S/N)_{OUT} = \frac{1}{(\pi)^{\frac{1}{2}}}\sqrt{\frac{\Delta\omega_f}{\Delta\omega_T}} \cdot \frac{I_S{}^2(0)}{I_S{}^2(0) + I_N{}^2(0)} \qquad (3\text{-}82)$$

Equation (3-82) together with Eqs. (3-59) and (3-39) represent the desired expressions for the detection capability of a self-beating optical spectrometer. They specify in terms of a signal-to-noise ratio the accuracy with which one can measure the spectrum of the self-beat current, and hence that of the incident light. An almost identical result is found for the superheterodyne optical spectrometer. For this reason, and since the discussions of the sensitivities of each of these light mixing spectrometers would be practically identical, we postpone the detailed analysis of Eq. (3-82) to Section E of this chapter.

D. The Superheterodyne Optical Spectrometer

In this section we consider the detailed operation of the typical optical superheterodyne spectrometer whose basic features were outlined in Section A. The superheterodyne mixing spectrometer achieves its ultrahigh resolving powers by translating the spectral information present in the incident electric field from an optical frequency ω_o down to a lower intermediate frequency ω_1. The frequency shift is accomplished by mixing the light beam whose spectrum is to be analyzed with a monochromatic optical "local oscillator" beam. The mixing process is carried out by superimposing these two beams on a photodetector; the desired beat signal at the intermediate frequency is observed in the resulting photocurrent.[6,30,31,32]

We find that unlike the self-beat system the superheterodyne spectrometer preserves the spectrum of the incident light exactly in the process of frequency translation, including information on the center frequency ω_o. In fact, the spectral shape of the signal part of the photocurrent power spectrum is identical to the spectrum of the incident field, the latter being centered at $\omega = 0$ and the former at $\omega_1 = \omega_o - \omega_{LO}$, where ω_{LO} is the local oscillator frequency.[31,32]

The processing of this photocurrent proceeds exactly as in the self-beating case. The desired final result for the output signal-to-noise ratio may be taken over directly from the calculations presented in the previous section. Furthermore, most of the arguments presented there regarding the role of the spatial coherence properties of the incident field apply equally well to the present case. In particular, we again find a pre-detection signal-to-noise ratio which is limited by the available optical signal power per coherence area.

The analysis of the superheterodyne spectrometer also points out a very important feature of optical mixing which did not appear in the self-beat case: the necessity of interferometric alignment between the wavefronts of the mixing fields. We examine here how the amplitude of the observed beat signal depends on the angular misalignment and radius of curvature mismatch between these wavefronts.

Let us consider then the optical mixing receiver shown in Fig. 3-15. There are two fields incident on the photodetector-mixer, a local oscillator field $\vec{E}_{LO}(\vec{r},t)$ and a signal field $\vec{E}_S(\vec{r},t)$.

1. The Temporal, Spatial, and Statistical Coherence Properties of the Local Oscillator Field

The local oscillator field will be assumed to be a monochromatic wave of frequency ω_{LO} and of a uniform intensity $(1/\mu_o c_m)\langle|\vec{E}_{LO}(\vec{r}_o,t)|^2\rangle$ over the surface of the mixer. Its spectral properties can be specified in terms of a correlation function, $R_{LO}(\tau)$, and a power spectrum, $S_{LO}(\omega)$, given by

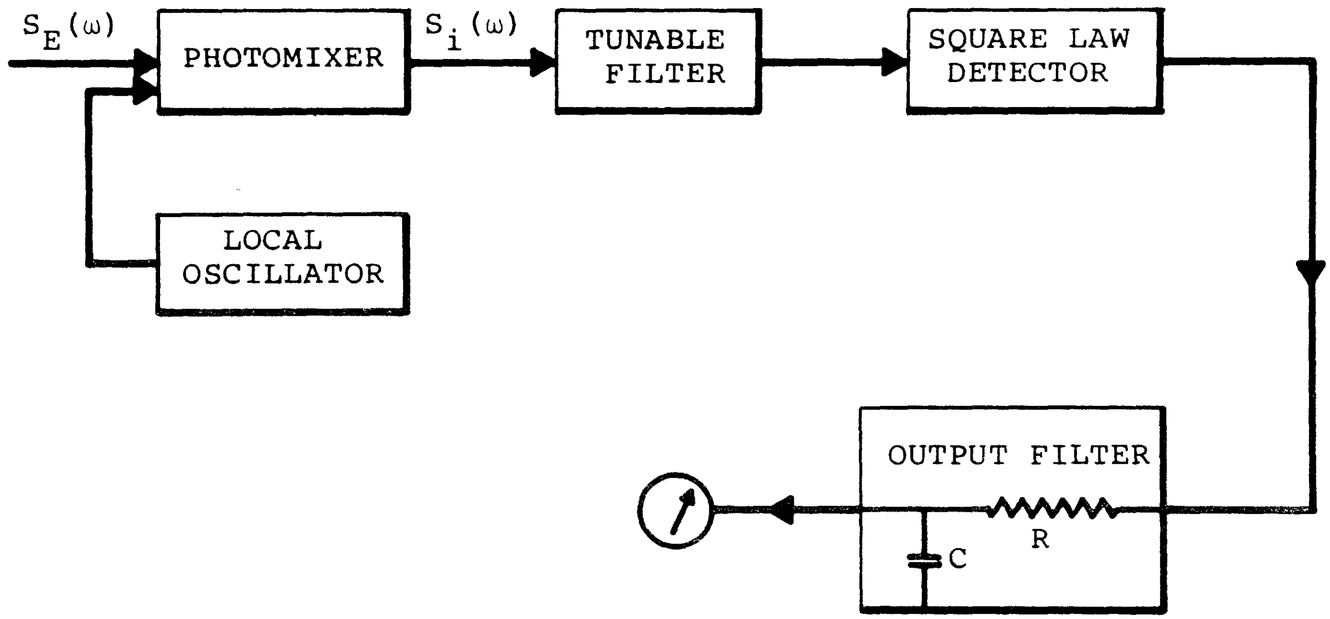
$S_E(\omega)$
PHOTOMIXER
$S_i(\omega)$
TUNABLE FILTER
SQUARE LAW DETECTOR
LOCAL OSCILLATOR
OUTPUT FILTER
R
C

Figure 3-15 Block diagram of a superheterodyne optical spectrometer.

$$R_{LO}(\tau) = \left\langle|\vec{E}_{LO}(\vec{r}_o,t)|^2\right\rangle \cos \omega_{LO}\tau \qquad (3\text{-}83)$$

$$S_{LO}(\omega) = \left\langle|\vec{E}_{LO}(\vec{r}_o,t)|^2\right\rangle \{\tfrac{1}{2}\delta(\omega+\omega_{LO}) + \tfrac{1}{2}\delta(\omega-\omega_{LO})\}$$

where $S_{LO}(\omega)$ es expressed in its symmetric form.[†]

It is appropriate to comment at this point on the definition of the term "coherent" as applied to an oscillator such as a laser. Two meanings of the word coherence have already been introduced in previous sections in reference to the properties of an optical field; namely, temporal coherence[†] or correlation, which is a measure of the spectral purity of the field, and spatial coherence[§] which measures the time average correlation between the temporal behaviors at two distinct points in the field. A comparison between lasers and ordinary black body sources shows the laser to be a superior light source from the standpoint of both temporal and spatial coherence properties; although, as Forrester[32] has pointed out, the temporal coherence of ordinary atomic spectral lines extends over many periods of the optical oscillation. In fact, such a discharge line may have a relative spectral purity ($\delta\omega/\omega_o$) that would correspond to a frequency stability of 0.1 cps in a 600 kc/sec "oscillator." However, the use of the word "oscillator" in describing a particular source of electromagnetic radiation implies still a third definition of coherence. Coherence in this last sense is a statement concerning the statistical properties of the electric field amplitude. A useful definition of this coherence characteristic can be formulated as follows.

[†] Chapter 2, Section D.

[§] Chapter 2, Section E.

Suppose we express the time evolution of the electric field from a spectrally narrow band source in its most general form as

$$E(t) = [E_o + \delta E_o(t)] \cos [\omega_o t + \phi(t)] \qquad (3\text{-}84)$$

where E_o is a constant. The quantities $\delta E_o(t)$ and $\phi(t)$ are random variables characterizing that portion of the time behavior of $E(t)$ which can be given only in terms of a correlation function; as such they are not specifically defined functions of the time.

The source of the electric field given in Eq. (3-84) is said to be statistically coherent or amplitude stabilized when the envelope function or amplitude defined by

$$\mathcal{E}(t) = E_o + \delta E_o(t)$$

is a constant, $\mathcal{E}(t) = E_o$, independent of time. On the other hand, the source may be designated statistically incoherent for the case

$$\mathcal{E}(t) = \delta E_o(t)$$

so that $\mathcal{E}(t)$ is a random variable.

If we neglect phase fluctuations then the time dependence of the field from a statistically coherent source, for example an ideal oscillator, may be displayed explicitly. The time behavior of the field from a statistically incoherent source can be given only in terms of a correlation function.

The degree of statistical coherence may be specified for the general field by the quantity W

$$W = \frac{\langle | E(t) - \langle E(t) \rangle |^2 \rangle}{(1 - \pi/4) \langle | E(t) |^2 \rangle} \tag{3-85}$$

which measures the mean-square fluctuations in the envelope function. If the random component of E(t)

$$E_R(t) = \delta E_o(t) \cos [\omega_o t + \phi(t)] \tag{3-86}$$

has the usual Gaussian probability distribution, i.e.

$$\mathbf{P}(E_R) = \frac{1}{\sqrt{2 \langle | E_R(t) |^2 \rangle}} \exp - \frac{E_R{}^2}{2 \langle | E_R(t) |^2 \rangle} \tag{3-87}$$

then the corresponding probability distributions for δE_o and ϕ are

$$\mathbf{P}(\delta E_o) = \begin{cases} \dfrac{2 \delta E_o}{\langle | \delta E_o(t) |^2 \rangle} \exp \left[- \dfrac{\delta E_o{}^2}{\langle | \delta E_o(t) |^2 \rangle} \right] & ; \ \delta E_o > 0 \\ 0 & ; \ \text{otherwise} \end{cases} \tag{3-88}$$

and

$$\mathbf{P}(\phi) = \begin{cases} \dfrac{1}{2\pi} & ; \quad 0 \leq \phi \leq 2\pi \\ 0 & ; \quad \text{otherwise} \end{cases} \tag{3-89}$$

as given by Davenport and Root.[34] Assuming the equivalence of time and statistical averages[24] we find for the field given in Eq. (3-84)

$$W = \frac{\langle |\delta E_o(t)|^2 \rangle}{\langle |E_o + \delta E_o(t)|^2 \rangle} \tag{3-90}$$

Thus a source with full statistical coherence, such as an ideal oscillator, has (W = 0) while a narrow band Gaussian noise source, such as a spectral line, has (W = 1).

The importance of the degree of amplitude stabilization for the present purposes is that for W = 0 and neglecting phase fluctuations we can describe the corresponding field using a well defined time function in addition to the usual temporal and spatial correlation functions.

Measurements by Freed and Haus[35] and by Smith and Armstrong[36] of $\langle |\delta E_o(t)|^2 \rangle$ and E_o for laser light have shown that except very near oscillation threshold, a laser light source, in fact, is characterized by W = 0 to excellent approximation.

We will assume here that our local oscillator is both temporally and statistically fully coherent. Thus its time dependence may be given explicitly, viz.

$$\vec{E}_{LO}(\vec{r},t) = \vec{E}_{LO}(\vec{r}) \cos \omega_{LO} t \tag{3-91}$$

We will assume, however, that the optical signal field $\vec{E}_S(\vec{r},t)$ is Gaussian random noise.

2. The Correlation Function for the Total Photocurrent

Since one component of the total incident field has a non-Gaussian amplitude distribution, the factoring process which led to Eq. (3-49) for $R_i(\tau)$ is no longer valid. In this case we must refer back to the general form of the photocurrent correlation function given in Eq. (3-44) in order to calculate the spectrum of the photomixer output. Equation (3-44) gives $R_i(\tau)$ as

$$\begin{aligned} R_i(\tau) &= \langle i(t+\tau)i(t)\rangle \\ &= \alpha^2 \int_A \int_A \langle|\vec{E}(\vec{r}+\vec{\rho},t+\tau)|^2|\vec{E}(\vec{r},t)|^2\rangle d^2\vec{r}\ d^2\vec{\rho} + ei_p\delta(\tau) \end{aligned} \tag{3-92}$$

In a superheterodyne spectrometer the dc photocurrent i_p is produced by contributions from the signal and local oscillator intensities and has the form

$$i_p = \alpha A[\langle|\vec{E}_S(\vec{r}_o,t)|^2\rangle + (1/2)|\vec{E}_{LO}(\vec{r}_o)|^2] \tag{3-93}$$

where A is the photocathode area and $\vec{r}_o$ is some convenient reference point on A. Here we will assume the local oscillator intensity to be much greater than the intensity of the signal beam and take i_p as simply

$$i_p = (\alpha A/2)|\vec{E}_{LO}(\vec{r}_o)|^2 = (\varepsilon e/\hbar\omega_o)P_{LO} \tag{3-94}$$

where P_{LO} is the total local oscillator power incident on A.

Writing $\vec{E}(\vec{r},t)$ as the sum of the two incident fields, $\vec{E}_{LO}(\vec{r},t)$ and $\vec{E}_S(\vec{r},t)$ and using Eq. (3-91) we find easily

$$|\vec{E}(\vec{r},t)|^2 = |\vec{E}_{LO}(\vec{r})|^2 \cos^2 \omega_{LO}t + 2[\vec{E}_{LO}(\vec{r})\cdot\vec{E}_S(\vec{r},t)] \cos \omega_{LO}t + |\vec{E}_S(\vec{r},t)|^2 \tag{3-95}$$

and a similar result for $|\vec{E}(\vec{r}+\vec{\rho},t+\tau)|^2$. Taking the product of these expressions and performing the required time average indicated in Eq. (3-92) yields the result

$$\begin{aligned}\left\langle|\vec{E}(\vec{r}+\vec{\rho},t+\tau)|^2|\vec{E}(\vec{r},t)|^2\right\rangle &= [(1/2)|\vec{E}_{LO}(\vec{r})|^2]^2 \\ &+ 2[(1/2)|\vec{E}_{LO}(\vec{r})|^2]\left\langle|\vec{E}_S(\vec{r}+\vec{\rho},t+\tau)|^2\right\rangle \\ &+ \left\langle|\vec{E}_S(\vec{r}+\vec{\rho},t+\tau)|^2|\vec{E}_S(\vec{r},t)|^2\right\rangle \\ &+ (1/2)[(1/2)|\vec{E}_{LO}(\vec{r})|^2]^2 \cos 2\omega_{LO}\tau \\ &+ 2\left\langle[\vec{E}_{LO}(\vec{r}+\vec{\rho})\cdot\vec{E}_S(\vec{r}+\vec{\rho},t+\tau)][\vec{E}_{LO}(\vec{r})\cdot\vec{E}_S(\vec{r},t)]\right\rangle \cos \omega_{LO}\tau\end{aligned} \tag{3-96}$$

The first two terms of this result represent contributions to the square of the exact total dc photocurrent as given in Eq. (3-93). The missing factor $[\langle|\vec{E}_S(\vec{r},t)|^2\rangle]^2$ is contained in the third term which is just a self-beat correlation function of the type examined in the preceding section. As would be expected, the signal field incident on a superheterodyne spectrometer still produces its self-beat contribution to the photocurrent spectrum. Equation (3-45) shows that the time average $\langle|\vec{E}_S(\vec{r}+\vec{\rho},t+\tau)|^2|\vec{E}_S(\vec{r},t)|^2\rangle$ may be broken down into the missing dc term and an ac term describing the correlation function of the signal part of the self-beat current spectrum. The fourth factor in Eq. (3-96) represents an uninteresting second harmonic term. Finally, the fifth and last term describes the mixing between the two incident fields.

If we assume that the local oscillator intensity greatly exceeds the intensity in the signal beam, we may safely ignore the self-beat contribution to $R_i(\tau)$ and write

$$R_i(\tau) = i_p^2 + ei_p\delta(\tau) + 2\alpha^2 \int_A \int_A \left\langle [\vec{E}_{LO}(\vec{r}+\vec{\rho})\cdot\vec{E}_S(\vec{r}+\vec{\rho},t+\tau)][\vec{E}_{LO}(\vec{r})\cdot\vec{E}_S(\vec{r},t)] \right\rangle \times \cos \omega_{LO}\tau \, d^2\vec{\rho} \, d^2\vec{r} \qquad (3\text{-}97)$$

Let us consider some of the features of the signal part of this result and determine if it can be simplified to a more useful form.

From the integrand of the double surface integral it becomes apparent that the beat signal term will vanish if the polarizations of the two incoming beams are at right angles. For simplicity we will assume that the directions of polarization are identical and write

$$\left\langle [\vec{E}_{LO}(\vec{r}+\vec{\rho})\cdot\vec{E}_S(\vec{r}+\vec{\rho},t+\tau)][\vec{E}_{LO}(\vec{r})\cdot\vec{E}_S(\vec{r},t)] \right\rangle = E_{LO}(\vec{r}+\vec{\rho})E_{LO}(\vec{r}) \left\langle E_S(\vec{r}+\vec{\rho},t+\tau)E_S(\vec{r},t) \right\rangle \qquad (3\text{-}98)$$

where $E_{LO}(\vec{r})$ and $E_S(\vec{r},t)$ are the scalar amplitudes of the respective vector fields. The remaining time average is the two point, two time correlation function encountered in Section B.4. As described there, we may, under suitable conditions, factor this average into separate time and spatial parts as

$$\left\langle \vec{E}_S(\vec{r}+\vec{\rho},t+\tau)\vec{E}_S(\vec{r},t) \right\rangle = T_E(\vec{r},\vec{\rho})R_E(\tau) \qquad (3\text{-}99)$$

In this case the spatial[*] and time correlation[**] functions $T_E(\vec{r},\vec{\rho})$ and $R_E(\tau)$ are given by

$$\underline{T}_E(\vec{r},\vec{\rho}) = \frac{\left\langle \underline{\vec{E}}(\vec{r}+\vec{\rho},t)\cdot\underline{\vec{E}}^*(\vec{r},t)\right\rangle}{\left\langle \underline{\vec{E}}(\vec{r},t)\cdot\underline{\vec{E}}^*(\vec{r},t)\right\rangle} \tag{3-100}$$

and

$$R_E(\tau) = \left\langle \vec{E}(\vec{r},t+\tau)\cdot\vec{E}(\vec{r},t)\right\rangle \tag{3-101}$$

The primary restriction that insures the validity of Eq. (3-99) can be stated as follows: the largest dimension of the photosurface, A, must be small compared to the wavelength of an electromagnetic wave with a frequency equal to that of the highest frequency beat signal. An examination of the cutoff frequency and active photosurface dimensions of present day photomixers shows that the condition is well satisfied in all cases.

We may also define a spatial correlation function for the local oscillator field as

$$\underline{T}_{LO}(\vec{r},\vec{\rho}) = \frac{\left\langle \underline{\vec{E}}_{LO}(\vec{r}+\vec{\rho},t)\cdot\underline{\vec{E}}_{LO}^{\,*}(\vec{r},t)\right\rangle}{\left\langle \underline{\vec{E}}_{LO}(\vec{r},t)\cdot\underline{\vec{E}}_{LO}^{\,*}(\vec{r},t)\right\rangle} \tag{3-102}$$

For the form of $E_{LO}(\vec{r},t)$ given in Eq. (3-91) we find easily

$$\underline{T}_{LO}(\vec{r},\vec{\rho}) = \frac{E_{LO}(\vec{r}+\vec{\rho})}{E_{LO}(\vec{r})} \tag{3-103}$$

---

[*] Chapter 2, Section E.

[**] Chapter 2, Section D.

Thus the function $T_{LO}(\vec{r},\vec{\rho})$ is simply a normalized description of the amplitude and phase behavior of the local oscillator field as a function of position $\vec{\rho}$ relative to the fixed reference point $\vec{r}$.

Combining Eqs. (3-97), (3-98), (3-99), (3-103), and (3-83) we have $R_i(\tau)$ in the form

$$R_i(\tau) = i_p^2 + ei_p\delta(\tau) + 4\alpha^2A^2R_{LO}(\tau)R_E(\tau)\int_A\int_A T_{LO}(\vec{r},\vec{\rho})T_E(\vec{r},\vec{\rho})d^2\vec{r}\ d^2\vec{\rho} \qquad (3\text{-}104)$$

where Eq. (3-83) was used to identify $R_{LO}(\tau)$. Equation (3-104) is the desired simplification of Eq. (3-97); it represents a factoring of the two important characteristics of the superheterodyne spectrometer, namely, the spectral and spatial features of the mixing process itself. Before proceding to analyze each of these we note that the double surface integral in Eq. (3-104) has a maximum value of A^2 and define the spatial factor [B] as

$$\frac{1}{A^2}\int_A\int_A T_{LO}(\vec{r},\vec{\rho})\ T_E(\vec{r},\vec{\rho})\ d^2\vec{r}\ d^2\vec{\rho} \equiv [B] \qquad (3\text{-}105)$$

This puts the correlation function in the form

$$R_i(\tau) = i_p^2 + ei_p\delta(\tau) + 4\alpha^2A^2R_{LO}(\tau)R_E(\tau)[B] \qquad (3\text{-}106)$$

When [B] has its maximum value [B] = 1 Eq. (3-106) takes the form that would be obtained in an intuitive manner from $R_j(\tau)$ in Eq. (3-30). The [B] factor describes what might be called the spatial efficiency of the mixing process.

3. The Spatial Characteristics of the Mixing Process

Let us first examine the spatial factor [B]. If we assume that the intensities of both the local oscillator and signal beams are uniform on A, then $T_{LO}(\vec{r},\vec{\rho})$ and $T_E(\vec{r},\vec{\rho})$ are both independent of $\vec{r}$ on A and we have

$$[B] = (1/A) \int_A T_{LO}(\vec{r}_o,\vec{\rho})\, T_E(\vec{r}_o,\vec{\rho})\, d^2\vec{\rho} \qquad (3\text{-}107)$$

The remaining integral describes an interference pattern between the wavefronts of the local oscillator and signal fields. It contains two pieces of information. The first is the effect of the spatial coherence properties of the field $\vec{E}_S(\vec{r},t)$.

a. The Effects of Spatial Coherence

Suppose, as an example, that the shape of the surface A corresponds exactly to the shape of the wavefronts of the local oscillator so that $T_{LO}(\vec{r}_o,\vec{\rho}) = 1$ on A. Further, suppose that the nominal surfaces of constant phase of $\vec{E}_S(\vec{r},t)$ are identical in shape and orientation (i.e., are collinear) with those of $\vec{E}_{LO}(\vec{r},t)$. Then as $\vec{\rho}$ assumes different points on A, $T_E(\vec{r}_o,\vec{\rho})$ will vary, but only[§] due to the finite range of spatial correlation in the field since $\vec{\rho}$ remains on a single wavefront of $\vec{E}_S(\vec{r},t)$. In this case the expression for [B] can take on two values depending on the ratio of the size of the photosurface to the range of the correlation function $T_E(\vec{r}_o,\vec{\rho})$. If we define the coherence area A^*_{COH} as

---

[§] Chapter 2, Section E.2

$$A^*_{COH} = \int_{\text{all } \vec{\rho}} T_E(\vec{r},\vec{\rho})\, d^2\vec{\rho} \tag{3-108}$$

then [B] has the limiting values

$$[B] = \begin{cases} 1 & ; \quad A << A^*_{COH} \\ (A^*_{COH}/A) & ; \quad A >> A^*_{COH} \end{cases} \tag{3-109}$$

A simple analysis shows that this result is valid even if the surface A does not have the exact shape of the incoming wavefronts as long as these wavefronts are exactly collinear.

By comparing Eq. (3-58) to Eqs. (3-106) and (3-109) for the case of perfect collinearity we find that a finite range of spatial correlation in the signal field has identical effects on both superheterodyne and self-beating spectrometers. In this regard it is interesting to note that the collinearity condition is automatically satisfied in a self-beating spectrometer since the signal field is mixing only with itself.

The physical explanation of Eq. (3-109) in terms of the phasing of the beat signal currents generated in different coherence areas on the photocathode exactly parallels that given in the preceding section.

The efficiency factor [B] also describes the effect of a finite range of correlation in the local oscillator field. Clearly, since $T_E(\vec{r},\vec{\rho})$ and, therefore, the integrand in Eq. (3-107) goes to zero as $|\vec{\rho}|$ approaches the correlation range in the signal field, it is unnecessary to have the local oscillator spatially coherent over the entire photocathode area in order to maximize [B]. The local oscillator need be coherent only over an area corresponding to one coherence area of the signal field. Under some circumstances it may be impossible to achieve this condition and the coherence area of the local oscillator may, in fact, be smaller than that of the signal beam. In this case, in evaluating Eq. (3-107) for assumed collinearity, we may set $T_E(\vec{r}_o,\vec{\rho}) = 1$ over the range of integration. The term A^*_{COH} is then to be interpreted as

$$A^*_{COH} = \int_A T_{LO}(\vec{r}_o,\vec{\rho})\, d^2\vec{\rho}$$

the coherence area of the local oscillator field.

The above results may be summarized as follows: if the nominal surfaces of constant phase of the signal and the local oscillator fields are identical in shape and orientation over the photomixer, then the spatial factor [B] takes the value unity for $A << A^*_{COH}$ and the value (A^*_{COH}/A) for $A >> A^*_{COH}$. Further, A^*_{COH} is to be identified as the smaller of the coherence areas describing the local oscillator and signal beams.

b. Collinearity of the Mixing Fields

(1) Angular Misalignment

The second piece of information contained in [B] concerns the effect on the mixing process of a lack of collinearity between the two input fields. To illustrate this point suppose that the two input fields are plane waves incident on the photosurface shown in Fig. 3-16. The photocathode is a rectangular surface in the (y,z) plane with dimensions d_y and d_z. Both incoming beams are assumed to be non-stochastic, well defined fields with coherence areas much larger than the size of the photosurface.

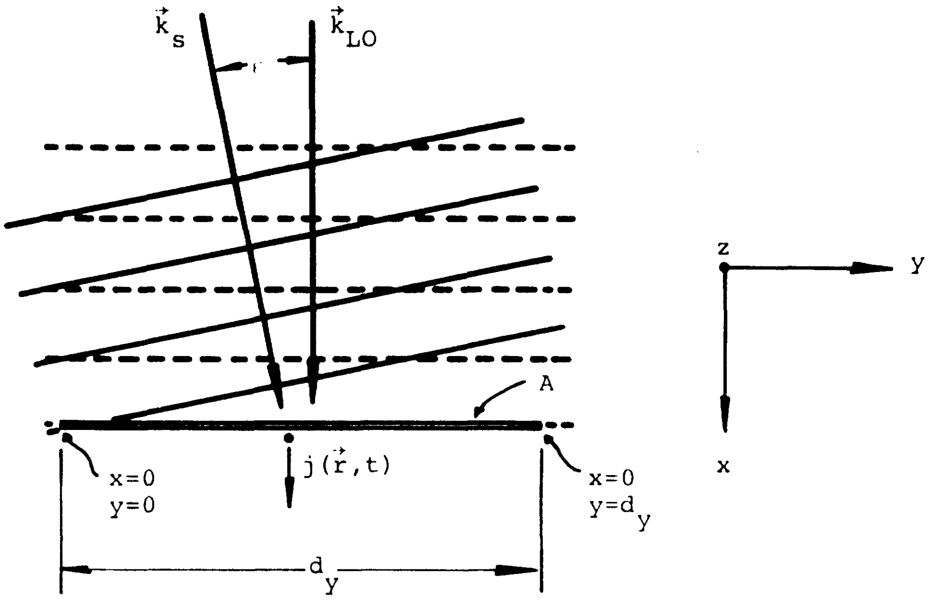
$\vec{k}_s$
$\vec{k}_{LO}$
ϵ
A
x=0
y=0
$j(\vec{r},t)$
x=0
y=d_y
d_y
z
y
x

Figure 3-16 Two plane waves incident non-collinearly on a plane photosurface.

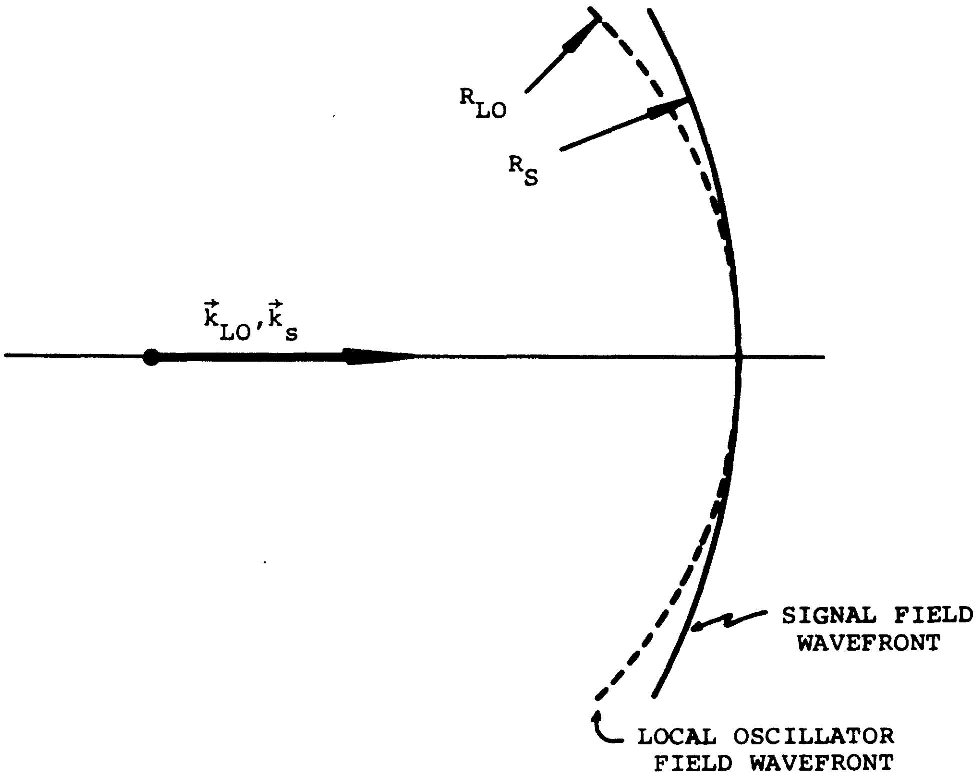
R_{LO}
R_S
$\vec{k}_{LO}, \vec{k}_s$
SIGNAL FIELD WAVEFRONT
LOCAL OSCILLATOR FIELD WAVEFRONT

Figure 3-17 Two collinear, spherically spreading beams exhibiting wavefront radius mismatch.

The local oscillator field $\vec{E}_{LO}(\vec{r},t)$ is incident normal to the photocathode and may be written as

$$\underline{E}_{LO}(\vec{r},t) = \underline{E}_{LO} \exp [i(\vec{k}_{LO}\cdot\vec{r} - \omega_{LO}t)] \tag{3-110}$$

with

$$\vec{k}_{LO} = (\omega_{LO}/c)\hat{x} \tag{3-111}$$

The signal beam is incident at an angle ε to the surface normal in the (x,y) plane; its electric field has the form

$$\underline{E}_S(\vec{r},t) = E_S \exp [i(\vec{k}_S\cdot\vec{r}) - \omega t)] \tag{3-112}$$

where

$$\vec{k}_s = (\omega/c)[(\cos \varepsilon)\hat{x} + (\sin \varepsilon)\hat{y}] \tag{3-113}$$

For this example the spatial correlation functions for the two fields can be evaluated easily from Eq. (3-102) as

$$\begin{aligned} T_{LO}(0,\vec{\rho}) &= \cos (k_{LO}\cdot\vec{\rho}) \\ T_E\ (0,\vec{\rho}) &= \cos (k_s\cdot\vec{\rho}) \end{aligned} \tag{3-114}$$

with $\vec{r}_o$ chosen as the point $(x,y,z) = (0,0,0)$. Since $\vec{\rho}$ has the form $\vec{\rho} = y(\hat{y}) + z(\hat{z})$ on the surface A, we have on the photocathode

$$\begin{aligned} T_{LO}(0,\vec{\rho}) &= 1 \\ T_E\ (0,\vec{\rho}) &= \cos [(\omega/c)y \sin \varepsilon] \end{aligned} \tag{3-115}$$

The general expressions in Eq. (3-114) give us the normalized behavior of the amplitudes of the two electric fields as a function of some arbitrary position $\vec{\rho}$ relative to the point $\vec{r}_o = 0$. On the photocathode we find $T_{LO}(0,\vec{\rho}) = 1$ since all points on A lie on a single wavefront of the local oscillator field. However, because the signal field makes an angle with the photosurface normal, we advance from one of its wavefronts to another as we change the y coordinate on A. This phase advance is described by the sinusoidal variation of $T_E(0,\vec{\rho})$ with y.

The integral for [B] indicated in Eq. (3-107) can now be carried out easily as

$$[B] = \frac{1}{(d_z)(d_y)} \int_{y=0}^{d_y} \int_{z=0}^{d_z} (1) \cos[(\omega/c)y \sin \varepsilon] dy\, dz \qquad (3\text{-}116)$$

with the result

$$[B] = \frac{\sin[(\omega/c)d_y \sin \varepsilon]}{[(\omega/c)\ dy \sin \varepsilon]} \qquad (3\text{-}117)$$

Let us examine the salient features of this expression in terms of the relative amplitude and phase of the beat note currents generated at different points on A. As was apparent in the general description of $R_i(\tau)$, the role of the area integral appearing in [B] is to sum, with appropriate phases, the beat signal current contributions from various parts of the photocathode.* Of course the instantaneous amplitude of the beat signal current produced at the position $(\vec{r},t)$ is simply proportional to the local product of the amplitudes[§] of the two mixing fields, $\vec{E}_{LO}(\vec{r},t)$ and $\vec{E}_S(\vec{r},t)$. Therefore, the product $[T_{LO}(0,\vec{\rho})T_E(0,\vec{\rho})]$ describes the spatial variation of the beat note amplitude as a function of position on A. In the present example, the phase and amplitude of this product is constant over A only for $(\varepsilon=0)$, i.e. for exact collinearity between the two incident beams. In this limit then the beat note phase and amplitude are also constant over A; the current contributions from various portions of the photocathode must add in phase to produce a beat note power that increases as A^2. This result follows by setting [B] = 1 in Eq. (3-106).

---

* Chapter 3, Section C.2.

For $(\varepsilon\neq0)$, according to Eq. (3-115) the product of the field amplitudes and, therefore, the amplitude of the heterodyne signal varies sinusoidally with y. The result is a destructive interference between currents generated at two points on A. The net effect of this interference in reducing the beat note amplitude is determined by the expression for [B] given in Eq. (3-117). It is worthwhile to point out that the interference being described here is not the addition of randomly phased currents which would result in a beat note power that increased as A, but is the addition of currents with exactly specified phases which can sum to identically zero.

The result for [B] is of the functional form $g = (\sin w)/w$ which was examined in Section E of Chapter 2. The interesting features of g are that it is a function highly peaked about $(w = 0)$, going to one in the limit $(w \to 0)$; that it is effectively non-zero only in the range $[(-\pi/2) \leq w \leq (\pi/2)]$; and that it has zeros at $w = \pm\bar{n}\pi$ where $\bar{n}$ is integral and not equal to zero. These characteristics determine the angle ε which can be tolerated between the $\vec{k}$ vectors of the two mixing fields before we incur a serious loss in beat note signal power.

[§] Chapter 3, Section B.1.

According to Eq. (3-117) the condition for the first zero of [B] at $[(\omega/c)\, d_y \sin\varepsilon] = \pi$, occurs when there is a relative phase advance of π radians between the two incident beams over the range $(y = 0)$ to $y = d_y)$. In this case the beat note amplitude goes through exactly one-half of a complete period of the cosine function as we traverse the photo-cathode and total destructive interference takes place. With the relation $(\omega/c) = (2\pi/\lambda)$, where λ is the wavelength of the signal beam, this first zero occurs at an angle ε^* given by $\sin\varepsilon^* = (\lambda/2d_y)$. In general d_y is much larger than λ and we have approximately

$$\varepsilon^* = (\lambda/2d_y)$$

For $(\varepsilon = \varepsilon^*)$ the wavefronts that overlap at $(y = 0)$ are separated or "misaligned" by a distance of $(\lambda/2)$ at $(y = d_y)$. As ε becomes larger than ε^* the beat note amplitude goes through additional oscillations as we move across A and for all practical purposes the destructive interference can be regarded as complete.

On the other hand, the condition $[(-\pi/2) \leq w \leq (\pi/2)]$ on w and, therefore, the condition

$$\{-(\pi/2) \leq [(\omega/c)\, d_y \sin\varepsilon] \leq (\pi/2)\}$$

yields $B \geq 0.637$ and implies a misalignment between the surfaces of the two incident wavefronts which is less than $(\lambda/4)$ over the photomixer area. This extremely stringent requirement

$$|\varepsilon| \leq (\lambda/4d_y) \qquad (3\text{-}118)$$

is, of course, the characteristic condition for "interference" between the two beams.[37]

(2) Wavefront Radius Mismatch

For the example used above to demonstrate the effects of non-collinearity, in which both beams are perfect plane waves, the condition [B] = 1 can always be assured by having the directions of propagation $\vec{k}_S$ and $\vec{k}_{LO}$ be parallel. However, in practice the signal and local oscillator fields generally will have a finite radius of curvature. In this case, as shown in Fig. 3-17, there may still be a relative phase advance between the two beams even if the vectors $\vec{k}_S$ and $\vec{k}_{LO}$ are collinear. Let R_{LO} and R_S be the radii of curvature of the local oscillator and signal wavefronts, respectively, as measured at the photodetector, and d be a characteristic dimension of the photocathode. Then an analysis* similar to the example presented above yields the two conditions

$$|\varepsilon| \leq (\lambda/8d) \qquad (3\text{-}119)$$

and

$$|R_{LO} - R_S| \leq (\lambda)(R_{LO}R_S/d^2) \qquad (3\text{-}120)$$

---

* Appendix D.

for $[B] \geq 0.81$. These conditions guarantee that the total wavefront misalignment from both causes, i.e. non-collinearity of the $\vec{k}$ vectors and wavefront radius mismatch, is less than $(\lambda/4)$ over A. Taking $d = 1$ cm and $R_{LO} \simeq R_S \simeq 100$ cm as being typical values we find the numerical limits

$$|\varepsilon| \leq 10^{-5} \text{ radians} \simeq 5 \times 10^{-4} \text{ degrees}$$

$$|R_{LO} - R_S| \leq 10^{-1} \text{ cm}$$

(3) Wavefront Distortion

A third possible cause of misalignment that is always present to some extent in a heterodyne spectrometer is the inevitable distortion of the wavefronts of the signal and local oscillator fields that occurs in the light gathering and focussing optics. This factor cannot be removed by suitable alignment of the beams and must be curtailed by the use of high quality Schlieren free[38] lenses, preferably with surface figure tolerances of better than $(\lambda/4)$ over the beam width, and reflecting optics of similar tolerance. The total wavefront distortion over the detector should be kept below $(\lambda/10)$, if possible, to ease the requirements on alignment accuracy.

The quantitative effect of distortion is difficult to evaluate in practice but an order of magnitude estimate may usually be obtained by determining the approximate total wavefront distortion λ^* over the distance d and calculating a value of $[B]_{\text{DISTORTION}}$ using the relation

$$[B]_{\text{DISTORTION}} = \frac{\sin\,[2\pi(\lambda^*/\lambda)]}{2\pi(\lambda^*/\lambda)} \tag{3-121}$$

Equation (3-121) represents only the effect of wavefront distortion and must be multiplied by a misalignment factor, if necessary, to get the value of [B].

c. The Heterodyning Efficiency

It is useful to symbolically combine the effects of angular misalignment, wavefront curvature mismatch, spatial coherence, and wavefront distortion in referring to the factor [B] as the heterodyning efficiency. This efficiency has a theoretical maximum value of unity and a practical upper limit set by the quality of the optical system used to combine the two input beams.

The analysis of [B] given above is valid for $A << A^*_{COH}$ and yields the current correlation function in the form

$$R_i(\tau) = i_p^2 + ei_p\delta(\tau) + 4\alpha^2A^2R_{LO}(\tau)R_E(\tau)[B] \tag{3-122}$$

where

$$[B] = [B]_{\text{DISTORTION}}[B]_{\Delta\text{-ANGLE}}[B]_{\Delta\text{-RADIUS}} \tag{3-123}$$

$[B]_{\text{DISTORTION}}$ - the wavefront distortion factor; Eq. (3-121)

$[B]_{\Delta\text{-ANGLE}}$ - the angular misalignment factor; Eq. (3-117)

$[B]_{\Delta\text{-RADIUS}}$ - the wavefront radius mismatch factor; Appendix D.

In the case $A >> A^*_{COH}$ the heterodyne signal current changes phase randomly outside an area A^*_{COH} due to the finite spatial correlation range in one of the incident fields. Thus the alignment and distortion criteria need be satisfied only over A^*_{COH} rather than over the entire photocathode area. The heterodyning efficiency factor for this area is designated $[B_{COH}]$ and is defined by

$$[B_{COH}] = \frac{1}{A^*_{COH}} \int_{A^*_{COH}} T_E(\vec{r}_o,\vec{\rho})T_{LO}(\vec{r}_o,\vec{\rho})d^2\vec{\rho} \tag{3-124}$$

The behavior of $[B_{COH}]$ with the angle ε, the radius mismatch $|R_{LO} - R_S|$, and the wavefront distortion λ^* is identical to that of [B] with the detector dimension d replaced by the appropriate coherence distance. Since the integrand in Eq. (3-124) vanishes for $|\vec{\rho}|$ greater than this coherence distance, we have for [B] from Eq. (3-107)

$$[B] = (A^*_{COH}/A)[B_{COH}] \tag{3-125}$$

where $A >> A^*_{COH}$. Equation (3-125) combines the effects of both misalignment and spatial coherence and gives $R_i(\tau)$ in the form

$$R_i(\tau) = i_p^{\,2} + ei_p\delta(\tau) + 4\alpha^2A^2(A^*_{COH}/A)[B_{COH}]R_{LO}(\tau)R_E(\tau) \tag{3-126}$$

where

$$[B_{COH}] = [B_{COH}]_{DISTORTION}[B_{COH}]_{\Delta\text{-ANGLE}}[B_{COH}]_{\Delta\text{-RADIUS}} \tag{3-127}$$

4. The Spectrum of the Photocurrent

Having examined the spatial factor [B], let us now turn to a calculation of the spectrum of the mixer current,

$$S_i(\omega) = (1/2\pi) \int_{-\infty}^{\infty} R_i(\tau) \cos \omega\tau \, d\tau.$$

Using Eq. (3-83) for $R_{LO}(\tau)$, Eqs. (3-122) and (3-126) for $R_i(\tau)$, and the definition of $S_E(\omega)$ gives immediately

$$S_i(\omega) = i_p{}^2\delta(\omega) + (e/2\pi)i_p \qquad (3\text{-}128)$$

$$+ 2i_p\alpha A[S_E(\omega+\omega_{LO}) + S_E(\omega-\omega_{LO})] \begin{cases} [B] & ; A << A^*_{COH} \\ \\ (A^*_{COH}/A)[B_{COH}] & ; A >> A^*_{COH} \end{cases}$$

where $S_i(\omega)$ is expressed in its symmetric[†] form.

The current spectrum contains the usual three components; a dc term produced here primarily by the local oscillator beam, a uniform shot-noise part, also due principally to the local oscillator, and the heterodyne beat signal. Equation (3-128) shows that the spectral information in the incident field around the optical frequency ω_o is present in the photocurrent around the intermediate frequency $\omega_1 = \omega_o - \omega_{LO}$. Furthermore, the shape of the optical spectrum has been preserved exactly in the frequency translation. Therefore, regardless of the structure of $S_E(\omega)$, a measurement of the spectrum of the mixer output of a superheterodyne spectrometer yields directly the spectrum of the incident light beam.

[†] Chapter 2, Section D.1.

Let us assume that the signal field incident on the superheterodyne spectrometer is the same one used to describe the operation of the self-beat spectrometer; namely, a field having a Lorentzian spectrum centered at $\omega = \omega_o$ and a half-width at half-height of Γ rad/sec. The power spectral density of this field was expressed in Eq. (3-54) as

$$S_E(\omega) = \left\langle |\vec{E}(\vec{r}_o,t)|^2 \right\rangle \left[\frac{(\Gamma/2\pi)}{(\omega-\omega_o)^2 + \Gamma^2} + \frac{(\Gamma/2\pi)}{(\omega+\omega_o)^2 + \Gamma^2} \right] \qquad (3\text{-}54)$$

Putting this spectrum into Eq. (3-128) and neglecting the sum frequency beat terms yields, for $\omega \geq 0$,

$$\underset{(\omega\geq 0)}{S_i(\omega)} = i_p{}^2\delta(\omega) + (e/\pi)i_p \qquad (3\text{-}129)$$

$$+ 2i_p i_s \frac{(\Gamma/\pi)}{[\omega - (\omega_o-\omega_{LO})]^2 + \Gamma^2} \begin{cases} [B] & ; A \ll A^*_{COH} \\ & \omega\geq 0 \\ (A^*_{COH}/A)[B_{COH}] & ; A \gg A^*_{COH} \end{cases}$$

where we have defined the dc photocurrent produced by the signal beam as

$$\alpha A \left\langle |\vec{E}_S(\vec{r}_o,t)|^2 \right\rangle \equiv i_s \qquad (3\text{-}130)$$

The resulting photocurrent spectrum is shown in Fig. 3-18. As expected, the beat signal term in $S_i(\omega)$ is also Lorentzian with a half-width at half-height of Γ rad/sec, and now centered at the intermediate frequency $\omega_1 = (\omega_o-\omega_{LO})$.

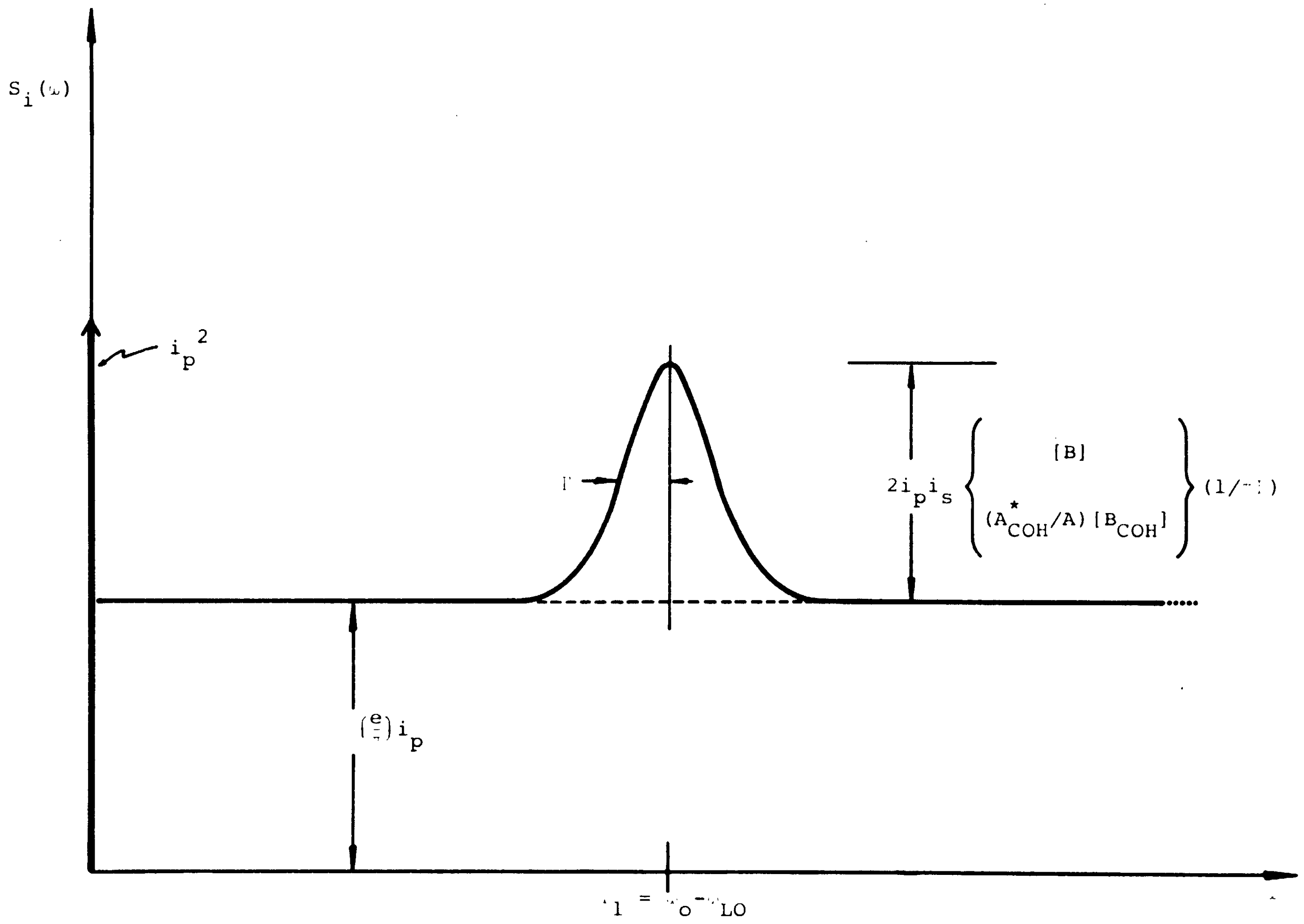

Figure 3-18 The power spectral density of the photocurrent for the superheterodyne detection of an optical field having a Lorentzian spectrum with a half-width at half-height of Γ radians per second.

5. The Processing of the Photocurrent Signal

a. The Pre-Detection Signal-to-Noise Ratio

The processing of the photomixer output, as diagrammed schematically in Fig. 3-15, proceeds exactly as it did for the self-beat spectrometer except that the tuned filter now operates about the intermediate frequency ω_1, rather than around $\omega = 0$. It is again useful to separate $S_i(\omega)$ into its dc, shot-noise, and signal components as

$$\underset{(\omega\geq 0)}{I_S{}^2(\omega)} = 2i_p i_s \frac{(\Gamma/\pi)}{(\omega-\omega_1)^2 + \Gamma^2} \begin{cases} [B] & ;\ A \ll A^*_{COH} \\ \\ (A^*_{COH}/A)\,[B_{COH}] & ;\ A \gg A^*_{COH} \end{cases}$$

$$\underset{(\omega\geq 0)}{I_N{}^2(\omega)} = (e/\pi)\, i_p \tag{3-131}$$

$$I_o{}^2 = i_p{}^2$$

respectively.

We may define the pre-detection signal-to-noise ratio, $(S/N)_{PRE}$, in analogy with that of the self-beat spectrometer,[§] as the ratio of the signal to the shot-noise current power per unit bandwidth evaluated at the peak of the signal, here $\omega = \omega_1$. This yields

---

[§] Chapter 3, Section C.2.a.

$$(S/N)_{PRE} = \frac{I_S^2(\omega_1)}{I_N^2(\omega_1)} = \left(\frac{\varepsilon}{\hbar\omega_o}\right)\frac{P_o}{\Gamma}\begin{cases} A[B] & ;\ A \ll A^*_{COH} \\ \\ A^*_{COH}[B_{COH}] & ;\ A \gg A^*_{COH} \end{cases} \qquad (3\text{-}132)$$

where P_o is the total optical signal power reaching the detector. Surprisingly, we find that the pre-detection signal-to-noise ratio for the heterodyne spectrometer is completely independent of the local oscillator power. This situation results from the fact that the magnitude of both the signal and the shot-noise terms increases linearly with $i_p = (\varepsilon e/\hbar\omega_o)P_{LO}$.

Comparing Eq. (3-132) with the equivalent result for the self-beat spectrometer given in Eq. (3-61) we find that for unity heterodyning efficiency the two expressions for $(S/N)_{PRE}$ are identical except for a factor of two advantage to the superheterodyne instrument. Moreover, this factor of two appears simply because the total beat note power is distributed in a Lorentzian line of half-width 2Γ in the self-beat spectrometer versus a half-width of Γ in the heterodyne instrument.

The discussion and physical interpretation of the behavior of $(S/N)_{PRE}$ as we vary the area of the mixer is also identical to that presented for the self-beat case.* In particular, we again find a pre-detection signal-to-noise ratio limited by the available signal power per coherence area on the detector; now with the modification that A^*_{COH} may be attributed to lack of spatial coherence in either the local oscillator or the signal field. If we define the power per coherence area as $\mathcal{P}_{COH} = (A^*_{COH}/A)\mathcal{P}_o$, where $\mathcal{P}_o$ is the total signal power reaching the mixer, then this limiting value of $(S/N)_{PRE}$ is

---

* Chapter 3, Section C.2.a.

$$(S/N)_{PRE} = 2\left(\frac{\varepsilon}{\hbar\omega_o}\right)\left(\frac{\mathcal{P}_{COH}}{\Gamma}\right)[B_{COH}] \qquad (3\text{-}133)$$

This result is the analog of Eq. (3-63) in the preceding section.

b. The Output Signal-to-Noise Ratio

The pre-filtering, detection, and post-filtering of the photocurrent is carried out exactly as before[†] and leads to an output signal-to-noise ratio given by

$$(S/N)_{OUT} = \frac{1}{(\pi)^{\frac{1}{2}}}\sqrt{\frac{\Delta\omega_f}{\Delta\omega_T}} \cdot \frac{I_S{}^2(\omega_1)}{I_S{}^2(\omega_1) + I_N{}^2(\omega_1)} \qquad (3\text{-}134)$$

A discussion of the physical significance of this quantity may be found by reference to Section C.2.b of this chapter.

Having found essentially identical expressions for $(S/N)_{OUT}$ for both light mixing spectrometers we turn in the next section to a detailed analysis of these results.

[†] Chapter 3, Section C.2.b.

E. The Detection Capabilities of Optical Mixing Spectrometers—The Ideal Case

1. Introduction

In this and the following section we present a detailed analysis and discussion of the output signal-to-noise ratios of self-beating and superheterodyne optical spectrometers. This analysis is broken down into two parts. In the first we examine the mathematical results for $(S/N)_{OUT}$ as derived in the two preceding sections. We determine how $(S/N)_{OUT}$ for a light mixing spectrometer depends on the available optical power, the spatial coherence of the incident electric field, the spectral width of the input field, and the parameters characteristic of the spectrometer itself, for example, the photomixer quantum efficiency, ε. The results are expressed in a set of parametrized curves, called isones, which are simply lines of constant output signal-to-noise ratio. From these curves it is possible to predict easily how a specific change in input optical power, tunable filter bandwidth, photomixer quantum efficiency, and so on will affect the noise properties of either spectrometer. The isones also form a convenient representation of the minimum optical signal power that can be detected by either method in terms of a choice of a lower limit on $(S/N)_{OUT}$. We will refer to this minimum signal power as the sensitivity of the spectrometer for the condition $(S/N)_{OUT} = 1$.

Because the expressions for $(S/N)_{OUT}$ that are used in the above discussion were calculated neglecting such factors as photomixer dark current, Johnson noise, and extraneous noise inherent in the processing electronics, they describe what may be called the ideal light mixing spectrometer. The following section analyzes these added practical complications in terms of the state-of-the-art characteristics of present day photomixers and their associated electronics. Fortunately the effects of all these additional noise sources can be taken into account through a simple modification of the original signal-to-noise expressions. Furthermore, the reinterpretation of the isones can also be handled in a straightforward manner.

2. The Effects of Spatial Coherence on the Output Signal-to-Noise Ratio

The expressions for $(S/N)_{OUT}$ to be analyzed here are given by Eqs. (3-134) and (3-82) for the superheterodyne and self-beat cases respectively as

superheterodyne

$$(S/N)_{OUT} = \frac{1}{(\pi)^{\frac{1}{2}}} \sqrt{\frac{\Delta\omega_f}{\Delta\omega_T}} \; \frac{I_S^{\,2}(\omega_1)}{I_S^{\,2}(\omega_1) + I_N^{\,2}(\omega_1)} \tag{3-134}$$

self-beat

$$(S/N)_{OUT} = \frac{1}{(\pi)^{\frac{1}{2}}} \sqrt{\frac{\Delta\omega_f}{\Delta\omega_T}} \; \frac{I_S^{\,2}(0)}{I_S^{\,2}(0) + I_N^{\,2}(0)} \tag{3-82}$$

In actuality these two results are much more closely related than simply the formal similarity of their mathematical statements. This can be seen by dividing through in each equation by the appropriate $I_N^{\,2}(\;)$ and identifying the definition of the pre-detection signal-to-noise ratio. We have then

$$(S/N)_{OUT} = \frac{1}{(\pi)^{\frac{1}{2}}} \sqrt{\frac{\Delta\omega_f}{\Delta\omega_T}} \cdot \frac{(S/N)_{PRE}}{1 + (S/N)_{PRE}} \quad \text{superheterodyne}$$

$$(S/N)_{OUT} = \frac{1}{(\pi)^{\frac{1}{2}}} \sqrt{\frac{\Delta\omega_f}{\Delta\omega_T}} \cdot \frac{(S/N)_{PRE}}{1 + (S/N)_{PRE}} \quad \text{self-beat} \tag{3-135}$$

If the same Lorentzian input optical field is incident on both spectrometers, and we assume a unity heterodyning efficiency for the superheterodyne instrument, then

$$(S/N)_{PRE}^{\text{superheterodyne}} = 2(S/N)_{PRE}^{\text{self-beat}} \tag{3-136}$$

follows from Eqs. (3-133) and (3-63). Furthermore, because the pre-detection (S/N) ratio is proportional to the optical signal power per coherence area we conclude that the behavior of $(S/N)_{OUT}$ for a superheterodyne spectrometer is identical to that of a self-beating spectrometer receiving twice the incident signal power per coherence area.

The expressions for $(S/N)_{OUT}$ as given in Eq. (3-135) do not depent explicitly on the incident signal power. Therefore, they must exhibit a saturation phenomenon* with increasing detector area as does $(S/N)_{PRE}$. That is, increasing the detector area A beyond the coherence area does not increase $(S/N)_{PRE}$ and, therefore, $(S/N)_{OUT}$ will also remain constant. Thus we find that the ultimate sensitivity of an ideal light mixing spectrometer is not

---

[*] Chapter 3, Sections C.2.a and D.3.a.

specified in terms of total available optical signal power but by the available power per coherence area on the detector.

3. The Limiting Behaviors of $(S/N)_{OUT}$

a. Large Values of $(S/N)_{PRE}$—$(S/N)_{PRE} >> 1$

The output signal-to-noise ratio shows two distinct limiting behaviors in the regions $(S/N)_{PRE} >> 1$ and $(S/N)_{PRE} << 1$ respectively. Let us consider first $(S/N)_{PRE} >> 1$, where we have approximately

$$(S/N)_{OUT} \simeq \frac{1}{(\pi)^{\frac{1}{2}}} \sqrt{\frac{\Delta\omega_f}{\Delta\omega_T}} \qquad (S/N)_{PRE} >> 1 \qquad (3\text{-}137)$$

This result is completely independent of both the input signal power per coherence area and the spectral line width. Physically this behavior represents a situation in which the beat signal power per unit bandwidth, $I_S^2(\omega)$, is sufficient to completely overwhelm the shot-noise contribution $I_N^2(\omega)$. In this case the filtered photocurrent consists essentially of a signal part only[†] and the source of noise in the measurement is the ac component of the detector output generated by this filtered signal itself.[§] Because the signal is acting as its own source of noise, increasing the incident power per coherence area causes no change in $(S/N)_{OUT}$.

[†] Chapter 3, Section C.2.b.1.

[§] Chapter 3, Section C.2.b.2.

This rather startling situation would also occur in a conventional optical spectrometer, such as that shown in Fig. 3-1, if the power spectral density in the self-beat part of the detector output exceeded that in the shot-noise. This self-beat spectrum arises simply from mixing at the photodetector between the various spectral components of the filtered optical signal itself and aids the shot-noise in obscuring the desired measurement of the dc photocurrent. This "signal" contribution to the noise, which is normally[39] neglected in calculating $(S/N)_{OUT}$ for a conventional instrument, is discussed in more detail in Section G of this chapter.

The limiting form of $(S/N)_{OUT}$ in Eq. (3-137) may be explained as follows. Parseval's theorem applied to the filtered current states that the total ac power output of the detector is equal to the total dc power output, where both are now due entirely to the signal. That is, from Eqs. (3-76), (3-69), (3-72), and (3-67) we have

$$\left\langle \left| [v_D(t)]_{ac} \right|^2 \right\rangle = [\langle\langle v_D(t) \rangle\rangle]^2 = \{M(\Delta\omega_f) I_S{}^2(\omega_f)\}^2 \qquad (3\text{-}138)$$

including only frequencies in $[v_D(t)]_{ac}$ below $(2\Delta\omega_f)$. In this "large signal" limit then it follows from Eq. (3-75) that the signal-to-noise ratio in the absence of a post-detection RC filter is unity. With the output filter, $(S/N)_{OUT}$ defined in Eq. (3-80) is simply the square root of one over the fraction of the ac power that gets to the output meter. This fraction is* $[\pi\Delta\omega_T/\Delta\omega_f]$ for the RC output filter, from which Eq. (3-137) follows immediately.

---

* Eq. (3-81).

Therefore, we find the important conclusion that even with unlimited input power the output (S/N) ratio of a light mixing spectrometer is bounded by the value given in Eq. (3-137).

Equation (3-63) gives $(S/N)_{PRE}$ for the self-beat spectrometer as

$$(S/N)^{\text{self-beat}}_{\text{PRE}} = \frac{\varepsilon}{\hbar\omega_o}\left(\frac{P_{COH}}{\Gamma}\right) \tag{3-63}$$

This result indicates that a likely situation for finding $(S/N)_{PRE} >> 1$ occurs in measurements on very narrow spectral lines. However, Eq. (3-137) shows that it is precisely these measurements that are the most difficult from the standpoint of sufficient output signal-to-noise ratio because of the requirements they impose on $(\Delta\omega_f)$ and $(\Delta\omega_T)$. To illustrate this point suppose the optical signal has a line width of $(\Gamma/2\pi) = 10$ cps and we wish to examine the resulting current spectrum with a tunable filter whose bandwidth is (1/10) of the optical line width, i.e., $(\Delta\omega_f/2\pi) = 1$ cps. Then to achieve $(S/N)_{OUT} = 10$ we require an RC post-detection filter whose time constant is at least $\tau = (1/\Delta\omega_T) = 50$ sec. If $(\Gamma/2\pi) = 1$ cps and $(\Delta\omega_f/2\pi) = 0.1$ cps then we need $\tau = 500$ sec for the same output signal-to-noise ratio. Therefore, although narrow lines may yield large pre-detection signal-to-noise ratios, they can require post-detection filters having excessive time constants to achieve reasonable output signal-to-noise ratios.

The conclusion is that large values of the pre-detection signal-to-noise ratio do not necessarily imply ease of detectability, i.e. large $(S/N)_{OUT}$.

b. Small Values of $(S/N)_{PRE}$—$(S/N)_{PRE} << 1$

In the second limiting region, $(S/N)_{PRE} << 1$, we have the output signal-to-noise ratio as

$$(S/N)_{OUT} \simeq \frac{1}{(\pi)^{\frac{1}{2}}} \sqrt{\frac{\Delta\omega_f}{\Delta\omega_T}} \cdot (S/N)_{PRE} \qquad (3\text{-}139)$$

which is now implicitly dependent on P_{COH} and Γ through the quantity $(S/N)_{PRE}$ as given in Eqs. (3-61) and (3-132).

The detector noise in the regime $(S/N)_{PRE} << 1$ is entirely due to the filtered shot-noise since the condition

$$(S/N)_{PRE} = I_S{}^2(0)/I_N{}^2(0) \; << 1$$

implies that the shot-noise power per unit bandwidth greatly exceeds that in the signal. Therefore, the filtered current and, hence, the ac portion of the detector output is primarily the product of the shot-noise part of the photocurrent. In fact, the total ac noise power at the detector output will be $[(S/N)_{PRE}]^{-2}$ times the dc detector power in the signal.* Therefore, in the absence of an output filter we would have

$$(S/N)_{OUT} = \left[\frac{P_{DC}}{P_{DC}[(S/N)_{PRE}]^{-2}}\right]^{\frac{1}{2}} = (S/N)_{PRE}$$

The post-detection filter passes only the fraction $[\pi\Delta\omega_T/\Delta\omega_f]$ of the ac noise power to the meter, and we find

---

* Figure 3-13.

$$(S/N)_{OUT} = \left\{\frac{P_{DC}}{[\pi\Delta\omega_T/\Delta\omega_f]\,[(S/N)_{PRE}]^{-2}P_{DC}}\right\}^{\frac{1}{2}}$$

$$= \frac{1}{(\pi)^{\frac{1}{2}}}\sqrt{\frac{\Delta\omega_f}{\Delta\omega_T}}\cdot(S/N)_{PRE}$$

in agreement with Eq. (3-139).

Equation (3-139) is often interpreted[6,40,41] as meaning that a wide input bandwidth ($\Delta\omega_f$) and a narrow output bandwidth ($\Delta\omega_T$) "results in an increase of the signal-to-noise ratio by the factor $[\Delta\omega_f/\pi\Delta\omega_T]$." Such an interpretation does not properly distinguish between pre- and post-detection signal-to-noise ratio and is valid only for $(S/N)_{PRE} << 1$. In fact, as implied above, $(S/N)_{OUT}$ can become smaller than $(S/N)_{PRE}$ in the regime $(S/N)_{PRE} >> 1$.

By using Eq. (3-63) for $(S/N)_{PRE}$ in Eq. (3-139) we have $(S/N)_{OUT}$ in a form that displays its dependence on Γ, ε, and P_{COH}, namely

$$(S/N)_{OUT} = \frac{1}{(\pi)^{\frac{1}{2}}}\sqrt{\frac{\Delta\omega_f}{\Delta\omega_T}}\left(\frac{\varepsilon}{\hbar\omega_o}\right)\frac{P_{COH}}{\Gamma} \qquad \text{self-beat} \qquad (3\text{-}140)$$

$[(S/N)_{PRE} << 1]$

Therefore, in the region of small pre-detection signal-to-noise ratio the output (S/N) ratio varies linearly with the photomixer quantum efficiency and the input optical power per coherence area. Ordinarily the tunable filter bandwidth ($\Delta\omega_f$) will be chosen as some fixed fraction of the optical line width so that $(S/N)_{OUT}$ will be proportional to $\Gamma^{-\frac{1}{2}}$.

We may summarize the important characteristics of $(S/N)_{OUT}$ as follows:

(1) It depends on the input optical power per coherence area, not the total input power.

(2) In the limit of small pre-detection signal-to-noise ratios, $(S/N)_{PRE} << 1$, we have

$$(S/N)_{OUT} \propto (\varepsilon P_{COH}/\Gamma^{\frac{1}{2}})$$

(3) In the limit of large $(S/N)_{PRE}$, which may occur for large P_{COH} or small Γ, $(S/N)_{OUT}$ approaches a maximum value

$$(S/N)_{OUT} = [\Delta\omega_f/(\pi\Delta\omega_T)]^{\frac{1}{2}}.$$

4. The Isones

Although Eq. (3-135) does describe the general behavior of the output signal-to-noise ratio for arbitrary $(S/N)_{PRE}$, it is not particularly useful in its present form. In general, the quantities which are the readily available and independently specified variables are the power per coherence area, P_{COH}, and the half-width at half-height, Γ, of the input optical spectrum. The bandwidth $(\Delta\omega_f)$ is normally fixed at some fraction of this line width

$$(\Delta\omega_f/\Gamma) \equiv a \qquad (3\text{-}141)$$

where a is the "normalized resolution." The photomixer quantum efficiency, ε, is a fixed parameter; the output filter time constant, τ, and hence the filter bandwidth ($\Delta\omega_T$), is limited by long term instrumental stability and can also be regarded as a fixed parameter. Under these conditions a more useful expression for the relation in Eq. (3-135) would have the functional form

$$\mathcal{P}_{COH} = \mathfrak{f}[\Gamma;(S/N)_{OUT}] \tag{3-142}$$

in which Γ is the independent variable, $(S/N)_{OUT}$ is a "variable parameter," and $\mathcal{P}_{COH}$ is the dependent variable. A plot of the function in Eq. (3-142) gives the power per coherence area required to achieve a given $(S/N)_{OUT}$ as a function of the optical line width, Γ. A family of such curves drawn for various values of $(S/N)_{OUT}$ forms a two dimensional plot of $\mathcal{P}_{COH}$ versus Γ which displays lines of constant output signal-to-noise ratio. Therefore, given $\mathcal{P}_{COH}$ and Γ, we may find $(S/N)_{OUT}$ by determining which member of the family of curves passes through the point $(\mathcal{P}_{COH},\Gamma)$. Furthermore, since the relation for $(S/N)_{PRE}$ as given in Eq. (3-63) can also be expressed in the form

$$\mathcal{P}_{COH} = g[\Gamma;(S/N)_{PRE}] \tag{3-143}$$

the lines of constant pre-detection signal-to-noise ratio may be drawn on this same plot. In this case the point $(\mathcal{P}_{COH},\Gamma)$ intersects two curves that specify $(S/N)_{OUT}$ and $(S/N)_{PRE}$ respectively. Such a set of curves, which we call isones, predict the usefulness of a light mixing spectrometer in examining the spectrum of a given field when we know $\mathcal{P}_{COH}$ and Γ.

For the self-beat spectrometer the required functions (f) and (g) are found by solving Eqs. (3-135) and (3-63) respectively for P_{COH}. This procedure gives

$$P_{COH} = \frac{\hbar\omega_o}{\varepsilon} \frac{\Gamma}{\frac{1}{(\pi)^{\frac{1}{2}}} \sqrt{\frac{a\Gamma}{\Delta\omega_T (S/N)^2_{OUT}} - 1}} \qquad \text{self-beat} \qquad (3\text{-}144)$$

and

$$P_{COH} = \frac{\hbar\omega_o}{\varepsilon} \Gamma (S/N)_{PRE} \qquad \text{self-beat} \qquad (3\text{-}145)$$

Figure 3-19 shows these two functions plotted for the following choice of fixed parameters.

$\lambda_{air} = 6328$ Å

$\varepsilon = 0.05$ (S-20 photosurface at $\lambda_{air} = 6328$ Å)

$a = (\Delta\omega_f/\Gamma) = 0.1$

$\tau = (1/\Delta\omega_T) = 1$ sec

The lines of constant output signal-to-noise ratio are labeled by the value of $(S/N)^2_{OUT}$ since Eq. (3-144) shows that this quantity can be easily corrected for changes in the fixed parameters (a) and ($\Delta\omega_T$).

The isones illustrate in a quantitative fashion the qualitative features of $(S/N)_{OUT}$ that we have been describing. Above the line $(S/N)_{PRE} = 1$ the curves of constant $(S/N)_{OUT}$ quickly become vertical as $(S/N)^2_{OUT}$ approaches its asymptotic value

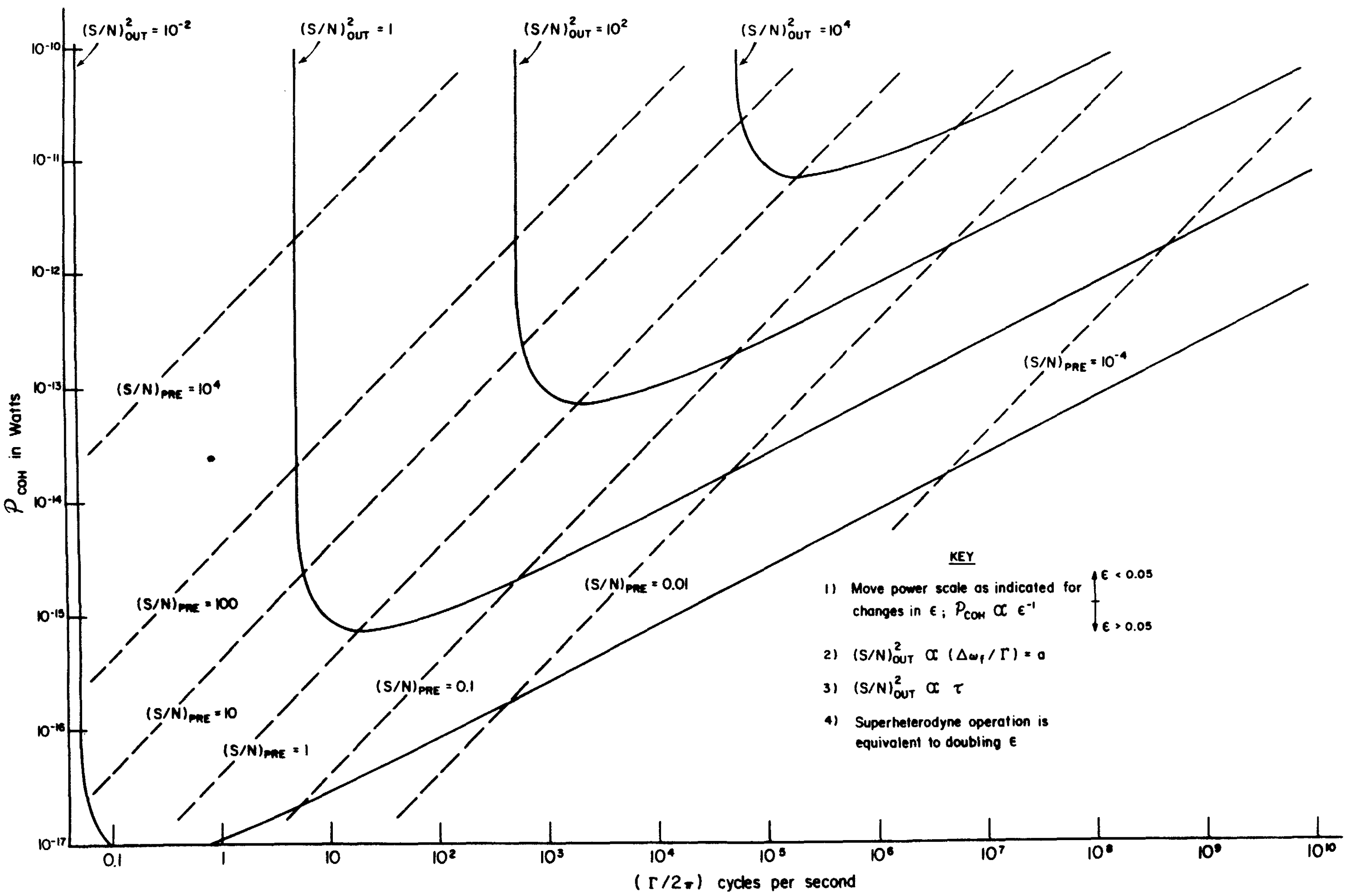

Figure 3-19 The signal-to-noise curves for optical mixing spectrometers.

$$(S/N)^2_{\mathrm{OUT}} = [\Delta\omega_f/\pi\Delta\omega_T] = [a\Gamma/\pi\Delta\omega_T]$$

$$[(S/N)_{\mathrm{PRE}} >> 1]$$

and becomes independent of P_{COH}. In the region $(S/N)_{\mathrm{PRE}} >> 1$ the isones are simply lines of constant Γ. Below the line $(S/N)_{\mathrm{PRE}} = 1$ we go over rapidly into the limiting behavior for $(S/N)_{\mathrm{PRE}} << 1$ where Eq. (3-140) gives

$$(S/N)_{\mathrm{OUT}} \propto (P_{\mathrm{COH}}/\Gamma^{\frac{1}{2}})$$

In this case the power required to maintain a constant output (S/N) ratio increases as the square-root of the optical linewidth.

Although the curves given in Fig. 3-19 correspond to a self-beat spectrometer with definite values of the fixed parameters ε, a, and $\Delta\omega_T$ they are easily corrected for changes in these parameters and generalized to the superheterodyne spectrometer.

We first note from Eq. (3-144) that the curves of constant $(S/N)_{\mathrm{OUT}}$ have a universal shape namely

$$P_{\mathrm{COH}}[c\Gamma; c(S/N)^2_{\mathrm{OUT}}] = cP_{\mathrm{COH}}[\Gamma; (S/N)^2_{\mathrm{OUT}}] \qquad (3\text{-}146)$$

Therefore these curves can simply be translated relative to one another in order to generate lines corresponding to arbitrary values of $(S/N)^2_{\mathrm{OUT}}$. Furthermore, Eqs. (3-144) and (3-145) indicate that changes in the quantities ε, a, and $\Delta\omega_T$ are easily accounted for by the following set of rules:

(1) A change in ε from ε_1 to ε_2 corresponds to a shift in the power scale; the new values of $(S/N)_{PRE}$ and $(S/N)_{OUT}$ are found by changing the ordinate P_{COH} at constant Γ by the factor $(\varepsilon_2/\varepsilon_1)$.

(2) For constant P_{COH} and Γ we have $(S/N)^2_{OUT} \propto a$; but, changes in a do not affect $(S/N)_{PRE}$.

(3) For constant P_{COH} and Γ we have $(S/N)^2_{OUT} \propto \tau$; but changes in τ do not affect $(S/N)_{PRE}$.

Thus a given set of isones apply universally for an arbitrary choice of all the quantities that characterize the spectrometer.

Secondly, with a slight modification the signal-to-noise curves given for the self-beat case can be used equally well for the superheterodyne spectrometer. It was noted in Eq. (3-135) and the accompanying text that $(S/N)_{OUT}$ for the superheterodyne and self-beat spectrometers are identical functions of their respective predetection (S/N) ratios. Furthermore, Eqs. (3-132) and (3-61) give the general relationship between the two values of $(S/N)_{PRE}$ as

$$(S/N)^{\text{superheterodyne}}_{PRE} = 2[B_{COH}]\,(S/N)^{\text{self-beat}}_{PRE} \qquad (3\text{-}147)$$

for $A \gg A_{COH}$. It follows that the desired values of $(S/N)_{PRE}$ and $(S/N)_{OUT}$ for the superheterodyne instrument are found by using Fig. 3-19 and plotting the known power per coherence area and half-width as the point $\{2[B_{COH}]P_{COH},\Gamma\}$ instead of (P_{COH},Γ). Corrections to the resulting value of $(S/N)^2_{OUT}$ because of changed fixed parameters follow exactly the same rules prescribed above for the self-beat case.

In applying Fig. 3-19 we should note that these curves reflect three implicit assumptions. First, they are drawn for a mixing spectrometer in which the photomixer area A satisfies the condition $A >> A_{COH}$. If instead we have $A < A_{COH}$ the power to be used on the ordinate scale is the total optical signal power falling on the photocathode. Secondly, the approximations $(\Delta\omega_T << \Delta\omega_f << \Gamma)$ that were utilized in the process of calculating $(S/N)_{OUT}$ in Section C.2.b have been incorporated into the results given here; therefore, the isones are only approximately correct when these conditions are not satisfied. Thirdly, in deriving the output (S/N) ratios given in Eq. (3-135) we neglected the effects of such factors as photomixer dark current and inherent noise in the processing electronics. Therefore, the curves of Fig. 3-19 refer to an "ideal" light mixing spectrometer.

5. An Example

A superheterodyne spectrometer is to be used to examine the spectrum of an optical field with a center frequency $\omega_o = (2\pi c/\lambda_{air})$, where $\lambda_{air} = 6328$ Å, and a Lorentzian spectrum with a half-width at half-height of $(\Gamma/2\pi) = 10^5$ cps. A total of 10^{-9} watts of signal power falls on the photocathode which contains 100 coherence areas. The photomixer has a quantum efficiency of $\varepsilon = 0.2$ at $\lambda_{air} = 6328$ Å. The total misalignment between the signal and local oscillator wavefronts and the wavefront warp are such that $[B_{COH}] = 0.1$. The spectrum of the photomixer output current is measured by a tuned filter whose bandwidth is 1000 cps. This filtered current is rectified by a square-law detector and the output is post-filtered by an RC network with a time constant of RC = 10 sec. What are the pre- and post-detection (S/N) ratios?

Labeling the fixed parameters used in Fig. 3-19 by the subscript (1) and those of the present example by (2) we have

$\varepsilon_2 = 0.2 \qquad (\varepsilon_2/\varepsilon_1) = 4$

$a_2 = 10^{-2} \qquad (a_2/a_1) = 10^{-1}$

$\tau_2 = 10$ sec $\qquad (\tau_2/\tau_1) = 10$

$2[B_{COH}] = 0.2$

$P_{COH} = 10^{-11}$ watts

$(\Gamma/2\pi) = 10^5$ cps

The ordinate used for P_{COH} must be corrected for the difference in quantum efficiencies, the factor of two appropriate to the superheterodyne instrument, and the heterodyning efficiency. The value to be plotted in Fig. 3-19 is

$$2P_{COH}(\varepsilon_2/\varepsilon_1)[B_{COH}] = 0.8 \times 10^{-11} \text{ watts}$$

This gives

$$(S/N)_{PRE} \simeq 2$$

$$(S/N)^2_{OUT} \simeq 2 \times 10^4 \qquad (S/N)_{OUT} \simeq 140$$

The corrections to $(S/N)_{OUT}$ because of the altered values of a and τ cancel one another so that we have as the answer

$$(S/N)_{PRE} \simeq 2 \qquad (S/N)_{OUT} \simeq 140$$

F. The Detection Capabilities of Optical Mixing Spectrometers—The Practical State of the Art

1. General Discussion

Although we have found a mathematical result that expresses the sensitivity of light mixing optical spectrometers, the significance of this result remains rather doubtful without the answers to the following questions. Can a practical instrument achieve this theoretical sensitivity, and how does the actual attainable sensitivity compare with that of other optical spectrometers? Is the light mixing spectrometer inherently any different than any other optical spectroscopic instrument? In this and the following section we discuss the answers to these questions.

To analyze the problem of practical sensitivities we must account, in particular, for the effects of three sources of noise which were neglected entirely in the calculation of $(S/N)_{OUT}$ as presented above. These are (1) the inevitable dark current in the photodetector and its associated shot-noise, (2) the thermal or "Johnson" noise in the load impedance presented to the output of the photomixer and (3) the internal noise inherent in the processing electronics, particularly the amplifiers immediately following the photomixer. Fortunately all three of these added noise voltages or currents have a common feature that simplifies their inclusion in the expressions for $(S/N)_{PRE}$ and $(S/N)_{OUT}$. They all have power spectral densities, i.e., power per unit bandwidths, that are constant with frequency; as a result, each acts as a uniform background against which the beat note spectrum is to be measured. These background contributions to the current spectrum have an effect on the noise properties of the spectrometer which is identical to the effect of the photomixer shot-noise.

The photocurrent shot-noise power spectral density is[*]

$$I_N^{\,2}(\omega) = (e/\pi) i_p = (\varepsilon e/\hbar\omega_o) \mathcal{P}_o \qquad (\omega \geq 0) \tag{3-148}$$

where i_p is the dc photocathode current and $\mathcal{P}_o$ is the total optical power incident on the photomixer. Since $I_N^{\,2}(\omega)$ is measured at the photocathode it is convenient to also refer to each of the three additional noise sources in terms of an equivalent current power per unit bandwidth generated at the photocathode. We denote these equivalent contributions as $I_D^{\,2}(\omega)$, the dark current shot-noise, $I_R^{\,2}(\omega)$, the

---

[*] Eqs. (3-59) and (3-131).

Johnson noise in the photomixer load, and $I_{RA}^2(\omega)$, the equivalent input amplifier noise. Using these definitions we may describe the photocathode current spectrum as having a frequency independent part, an effective shot-noise power per unit bandwidth, of the form

$$[I_N^2(\omega)]_{\text{effective}} = I_N^2(\omega) + I_D^2(\omega) + I_R^2(\omega) + I_{RA}^2(\omega) \tag{3-149}$$

Figure 3-20 shows the self-beat photocurrent spectrum $S_i(\omega)$ of Fig. 3-10 modified to include the three new noise contributions.

The filtering, detection, and post-filtering processes of both mixing spectrometers are carried out exactly as before; the only effect of the additional background terms is to replace $I_N^2(\omega)$ at each step by the effective shot-noise term $[I_N^2(\omega)]_{\text{eff}}$. In particular, we again find $(S/N)_{\text{OUT}}$ as

$$(S/N)_{\text{OUT}} = \frac{1}{(\pi)^{1/2}} \sqrt{\frac{\Delta\omega_f}{\Delta\omega_T}} \cdot \frac{(S/N)_{\text{PRE}}}{1 + (S/N)_{\text{PRE}}} \tag{3-150}$$

however, $(S/N)_{\text{PRE}}$ is now given by

$$(S/N)^*_{\text{PRE}} = \frac{I_S^2(\omega)}{[I_N^2(\omega)]_{\text{eff}}} = \frac{I_S^2(\omega)}{I_N^2(\omega) + I_D^2(\omega) + I_R^2(\omega) + I_{RA}^2(\omega)} \tag{3-151}$$

Therefore, the detection capabilities of a practical light mixing spectrometer can be completely specified by modifying

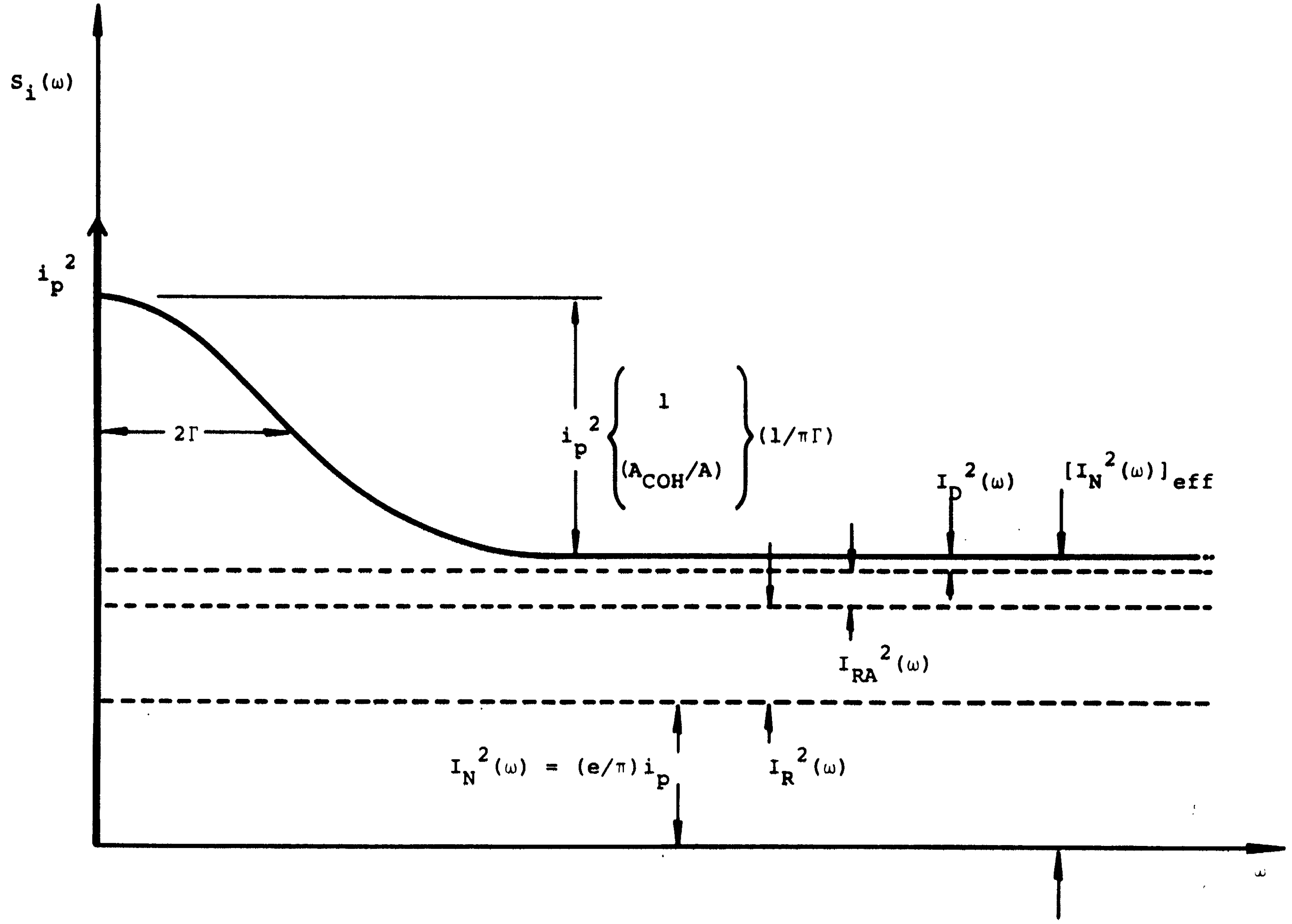
$S_i(\omega)$
i_p^2
2Γ
$i_p^2 \left\{ \begin{matrix} 1 \\ (A_{COH}/A) \end{matrix} \right\} (1/\pi\Gamma)$
$I_D^2(\omega)$
$[I_N^2(\omega)]_{eff}$
$I_{RA}^2(\omega)$
$I_N^2(\omega) = (e/\pi) i_p$
$I_R^2(\omega)$
ω

Figure 3-20 Photocurrent power spectral density for a self-beat spectrometer including the effects of practical noise sources.

the interpretation of the pre-detection signal-to-noise ratio. The actual pre-detection (S/N) ratio, $(S/N)^*_{PRE}$, is related to the "ideal" result, $(S/N)_{PRE}$, by

$$(S/N)^*_{PRE} = \frac{(S/N)_{PRE}}{1 + F} \tag{3-152}$$

where

$$F = \frac{I_D^{\,2}(\omega) + I_R^{\,2}(\omega) + I_{RA}^{\,2}(\omega)}{I_N^{\,2}(\omega)} \tag{3-153}$$

The description of the limiting behaviors of the output signal-to-noise ratio and the quantitative results expressed by the isones are still valid if we now simply interpret $(S/N)_{PRE}$ in Eq. (3-150) to be its appropriately modified value, $(S/N)^*_{PRE}$. In particular, by writing $(S/N)_{PRE}$ in terms of the signal power per coherence area, P_{COH}, and the optical line width, Γ, we have from Eq. (3-63)

$$(S/N)^*_{PRE} = \frac{1}{\Gamma}\left(\frac{\varepsilon}{\hbar\omega_o}\right) \cdot \frac{P_{COH}}{1 + F} \qquad A >> A_{COH} \tag{3-154}$$

for the self-beat spectrometer and a similar result for the superheterodyne instrument. Thus the original isones may be used to predict both $(S/N)^*_{PRE}$ and $(S/N)_{OUT}$ by plotting the effective signal power per coherence area $P_{COH}/(1 + F)$ as the ordinate in Fig. 3-19. Since Eq. (3-153) gives $F \geq 0$ this procedure always results in a decrease in the predicted pre- and post-detection signal-to-noise ratios.

In order to calculate the typical reduction in sensitivity we must now determine the individual contributions to the factor F due to dark current shot-noise, Johnson noise, and amplifier noise respectively. We will examine each of these contributions in terms of the relevant properties of state-of-the-art photomixers and their associated electronics. The objective is to delineate quantitatively the limits of sensitivity and resolution that can be achieved by a practical light mixing spectrometer utilizing present day techniques.

2. Relevant Properties of State-of-the-Art Photomixers

Table IV lists the important characteristics of some typical photodetectors that are useful as optical photomixers. These devices fall into two basic categories: (1) those in which the photocurrent is generated by the ejection of electrons from a suitable "photosurface" material into a surrounding vacuum, i.e. the photo-equivalent of the vacuum tube, and (2) solid state junction devices in which the photocurrent carriers are electron-hole pairs produced by the incident photons. The basic operation of these photodetectors will not be described here and the interested reader is referred to the bibliography accompanying the table. A detailed explanation of the quantities that appear in this table is given below in the process of calculating the dark current and thermal noise contributions to F.

Table IV ELECTRICAL PROPERTIES OF SOME USEFUL PHOTOMIXERS

	Device	I	II
		ε (λ_{air} = 6328Å)	P_{DARK} - Watts
1	RCA-7265 Photomultiplier tube S-20 photosurface	0.05	2.5×10^{-13}
2	Vacuum photodiode S-20 photosurface	0.05	1.2×10^{-14} cm^{-2}
3	Bi-planar vacuum photodiode S-20 photosurface	0.05	1.2×10^{-14} cm^{-2}
4	Dynamic crossed-field electron multiplier S-1 photosurface	0.004	4.65×10^{-10} cm^{-2}
5	Bell Labs static crossed-field photomultiplier S-1 photosurface	0.004	4.65×10^{-10} cm^{-2}
6	Sylvania traveling wave phototube S-1 photosurface	0.004	4.65×10^{-10} cm^{-2}
7	EG&G SD-100 silicon photodiode	> 0.5	10^{-5}
8	Philco L4501 silicon photodiode	> 0.5	N.S.
9	Bell Labs point contact germanium photodiode	> 0.5	3×10^{-5}
10	Bell Labs silicon epitaxial photodiode with avalanche gain	> 0.5	N.S.

Table IV (continued)

	III	IV	V	VI
	$(\omega/2\pi)$ - cutoff	G_{DC}	G_{AC}	I_{OUT} - MAX
1	200 Mc/sec (transit time)	10^6	10^6	100 μamps
2	500 Mc/sec (transit time)	1	1	100 μamps
3	1 Gc/sec (transit time)	1	1	100 μamps
4	3-9 Gc/sec (transit time)	10^6	10^6	100 μamps
5	4 Gc/sec (transit time)	10^5	10^5	100 μamps
6	Covers octave intervals 1-2 Gc/sec; 2-4 Gc/sec; 4-8 Gc/sec.	1	10^2	100 μamps
7	130 Mc/sec - RC	1	1	1 ma
8	15 Gc/sec - transit time 40 Gc/sec - RC	1	1	10 ma
9	100 Gc/sec - RC	2-6	2-6	3 ma
10	10 Gc/sec - transit time 8 Gc/sec - RC	10	10	3 ma

Table IV (continued)

	VII	VIII	IX	X	
	R_{LOAD}	R_{SHUNT}	R_{SERIES}	C_{SHUNT}	Bibliography
1	arbitrary	∞	N.S.	6 pf	a,b
2	arbitrary	∞	N.S.	0.3 pf	a
3	arbitrary	∞	N.S.	1.0 pf	a
4	50 Ω	∞	N.S.	N.S.	b,c,d,e
5	50 Ω	∞	N.S.	N.S.	f,b
6	50 Ω	∞	N.S.	N.S.	b
7	arbitrary	10^7 Ω	150 Ω	8 pf	g
8	arbitrary	N.S	5 Ω	0.8 pf	h
9	arbitrary	N.S.	11.5 Ω	0.15 pf	i
10	arbitrary	N.S.	15-25 Ω	1.0 pf	j

Table IV (continued)

Bibliography

a. RCA Phototubes and Photocells, Technical Manual PT-60 (Radio Corporation of America, Lancaster, Pa., 1963), p. 165 ff.

b. Monte Ross, Laser Receivers (John Wiley and Sons, Inc., New York, 1966), Chapter 5.

c. O. L. Gaddy and D. F. Holshouser, Proc. IEEE 51, 153 (1963).

d. O. L. Gaddy and D. F. Holshouser, Proc. IEEE 52, 412 (1964).

e. R. B. Hankin, E. Dallafior, and B. Alpiner, Proc. IEEE 52, 412 (1964).

f. R. C. Miller and N. C. Witwer, IEEE Journal of Quantum Electronics QE-1, 62 (1965).

g. SD-100 Data Sheet; Edgerton, Germeshausen, and Grier, Inc.

h. L4501 Data Sheet; Philco Corp.

i. M. DiDomenico, Jr., W. M. Sharpless, and J. J. McNicol, Applied Optics 4, 677 (1965).

j. L. K. Anderson, P. G. McMullin, L. A. D'Asaro, and A. Goetzberger, Applied Physics Letters 6, 62 (1965).

N.S. - Not Specified

3. The Effects of Dark Current Shot-Noise

We first investigate the contribution to the signal-to-noise reduction factor F from shot-noise associated with the photomixer dark current. Designating this factor as F_D, we have from Eq. (3-153)

$$F_D = [I_D{}^2(\omega)/I_N{}^2(\omega)] \qquad (3\text{-}155)$$

Ideally $I_D{}^2(\omega) = 0$ and Eq. (3-152) shows that favorable values of F_D correspond to the region $F_D << 1$.

The power spectral density $I_D{}^2(\omega)$ is the equivalent current power per unit bandwidth in the dark current shot-noise as seen at the photocathode. If i_{pd} is the dc photocathode dark current then we have

$$I_D{}^2(\omega) = (e/\pi)i_{pd} \qquad (\omega\geq 0) \qquad (3\text{-}156)$$

while the photocurrent shot-noise term $I_N{}^2(\omega)$ is given by

$$I_N{}^2(\omega) = (e/\pi)i_p \qquad (\omega\geq 0) \qquad (3\text{-}157)$$

The dc photocurrent, i_p, is produced by the signal itself in the self beat spectrometer and by the local oscillator beam in the superheterodyne instrument. In terms of the total power, P, on the photocathode we have

$$i_p = (\varepsilon e/\hbar\omega_o)P \qquad (3\text{-}158)$$

It is convenient to also represent the dark current i_{pd} in terms of an equivalent optical input power which would generate the specified current. This quantity, denoted by P_{DARK}, is defined by the relation

$$i_{pd} = (\varepsilon e/\hbar\omega_o)\mathcal{P}_{DARK} \qquad (3\text{-}159)$$

Equations (3-155) through (3-159) yield the value of F_D as simply

$$F_D = [\mathcal{P}_{DARK}/\mathcal{P}] \qquad (3\text{-}160)$$

Column II of Table IV gives $\mathcal{P}_{DARK}$ in watts or in watts per square centimeter of photocathode area for some useful photomixers. The values fall into three groups according to the active photomaterial: the S-1 photosurface, the S-20 photosurface, and the solid state junction. Taking a minimum useful photocathode diameter as 1 mm we have

$$\mathcal{P}_{DARK} \simeq \begin{cases} 1 \times 10^{-16} \text{ watts} & \text{(S-20)} \\ 3.5 \times 10^{-12} \text{ watts} & \text{(S-1)} \\ 1 \times 10^{-5} \text{ watts} & \text{(solid state junction)} \end{cases} \qquad (3\text{-}161)$$

The values of $\mathcal{P}_{DARK}$ given in Table IV and in Eq. (3-161) are appropriate to a photocathode temperature of T = 25°C. The dark currents of the photosurface devices may be decreased by cooling with an apparent lower limit for both S-20 and S-1 surfaces of about one electron per second per square centimeter of active area.[42] For a 1 mm diameter photocathode this corresponds to

$$\mathcal{P}_{DARK} \simeq \begin{cases} 6 \times 10^{-18} \text{ watts} & \text{(S-20)} \\ 8 \times 10^{-17} \text{ watts} & \text{(S-1)} \end{cases} \quad \text{cooled} \qquad (3\text{-}162)$$

at λ = 6328 Å. The above values of P_{DARK} are now to be compared with the total optical power available at the photocathode.

a. The Self-Beat Spectrometer

Consider the self-beat spectrometer first. Figure 3-21 shows the ideal sensitivity curves, i.e. the isone $(S/N)_{OUT} = 1$, for the three different types of active photoemitters. These curves were obtained from Eq. (3-144) and the values of ε given in column I of Table IV. By comparing the minimum optical power $P = P_{COH}$ required to achieve $(S/N)_{OUT} = 1$ with the values of P_{DARK} given above we may draw the following conclusions:

(1) The S-20 surface photodetectors have sufficiently low dark emission at room temperature to achieve $F_D << 1$ for all values of Γ even with the minimum optical signal.

(2) The S-1 surface photodetectors at room temperature yield values of F_D between $F_D \simeq 100$ and $F_D \simeq 0.3$ in the range of line widths from $(\Gamma/2\pi) \simeq 10$ cps to $(\Gamma/2\pi) \simeq 100$ Mc/sec. On the other hand a cooled S-1 surface device can maintain $F_D << 1$ for all Γ.

(3) The solid state junction detectors have large dark currents which when coupled with their good quantum efficiencies lead to values of F_D between 2×10^{11} and 5×10^7 as $(\Gamma/2\pi)$ varies from 10 cps to 10^9 cps.

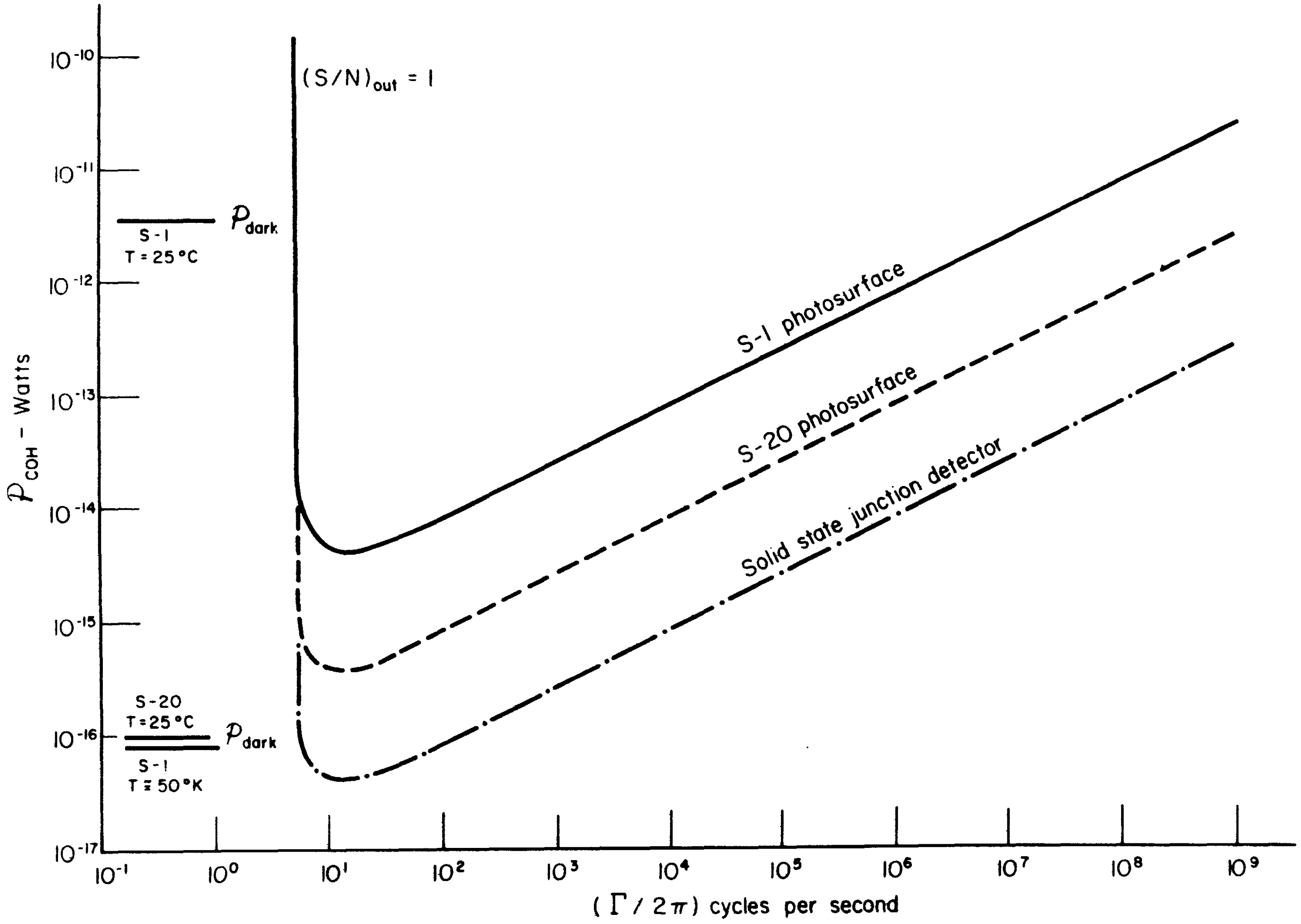

Figure 3-21 The power per coherence area required for $(S/N)_{OUT} = 1$ and the equivalent dark input power for three types of photodetectors.

These conclusions are valid when the total power incident on the photomixer is the minimum required to obtain $(S/N)_{OUT} = 1$. This will be the case when we have $A \leq A_{COH}$ and the ordinate in Fig. 3-21 is to be interpreted* as the total power falling on A.

The condition $(S/N)_{OUT} = 1$ requires a certain minimum optical power per coherence area; however, the result $F_D << 1$ depends only on the total available power. Therefore, a significant reduction in F_D from the values found for $A \leq A_{COH}$ can be obtained by arranging to collect light from a large number of coherence areas in the incoming field, thereby increasing the total power incident on the photomixer. Of course, this process does not alter P_{COH} and, therefore, the basic sensitivity of the instrument remains unchanged. This result points out that although $(S/N)_{PRE}$ for the ideal light mixing spectrometer depends only on P_{COH} the modified result for a practical spectrometer, $(S/N)^*_{PRE}$, also depends explicitly on the total input power P through the factor F.

The quantity of interest then in deciding the merit of a particular detector in regards to its dark current is the ratio $[P/P_{COH}]$. Here P_{COH} is the power per coherence area in the incident field necessary to achieve $(S/N)_{OUT} = 1$ for some particular value of Γ, and P is the total incident power that will make F_D negligible. For a self-beat spectrometer, $[P/P_{COH}]$ is just the number of coherence areas from which the spectrometer must gather light in order to override the effects of dark current and achieve its maximum sensitivity.

---

* Chapter 3, Section E.4.

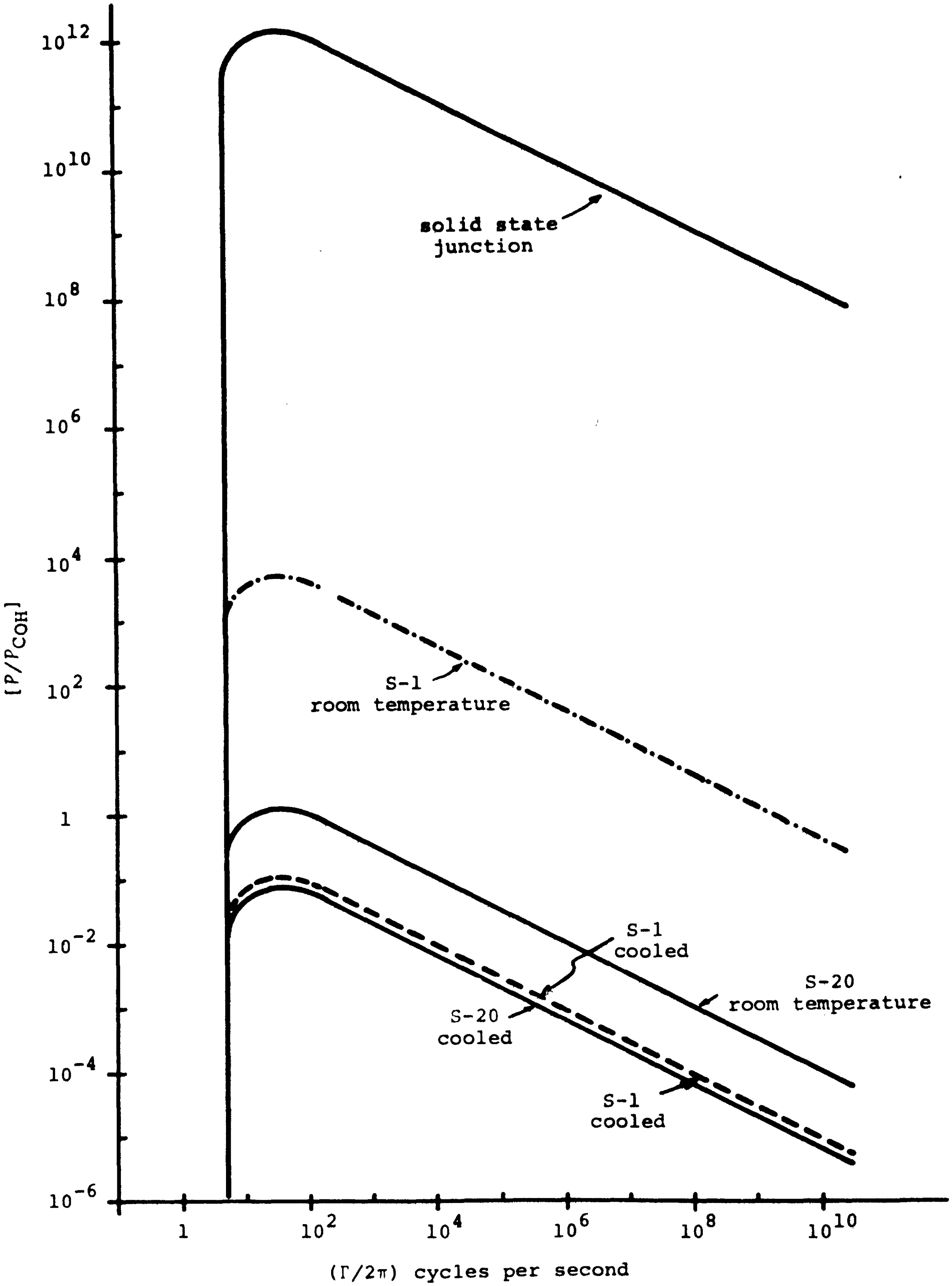

Figure 3-22 The ratio of the power required to swamp the photomixer dark current to the power per coherence area necessary to achieve unity output signal-to-noise ratio. The ratio is plotted versus the half-width at half-height of the Lorentzian spectrum under investigation.

Figure 3-22 shows this ratio, $[P/P_{COH}]$, plotted for the three types of photoemitters; the condition on F_D was taken as ($F_D = 0.1$). The curves drawn for the photosurface detectors correspond to a photocathode diameter of 1 mm, and are given for both room temperature and for the optimum cooled temperature.

From a dark current standpoint then the photomixers that are most useful in self-beat spectrometers are the S-20 photosurface detectors, and the S-1 photosurface detectors, in that order. For both types it is generally possible to insure that $(S/N)^*_{PRE}$ does not deviate from its ideal value due to dark current shot-noise. This situation may be realized either by cooling the photosurface to reduce the dark current or by gathering light from a reasonable number of coherence areas in order to overcome the equivalent dark input power. Although the solid-state junction devices offer the attractive advantage of high quantum efficiency, their dark currents are so high as to make them useless except in very unusual cases.

b. The Superheterodyne Spectrometer

For the superheterodyne spectrometer the total power on the photomixer is essentially just the local oscillator power, P_{LO}; therefore, in this case we have

$$F_D = [P_{DARK}/P_{LO}] \tag{3-163}$$

However, the values of $(S/N)_{PRE}$ and $(S/N)_{OUT}$ for the ideal instrument are completely independent* of P_{LO}. Therefore, we can in theory always make ($F_D << 1$) without affecting the operation of the spectrometer by suitably increasing the local oscillator power. Moreover, since F_D no longer depends on the total available signal power, we need gather light only from a single coherence area in the signal field in order to achieve the maximum values of $(S/N)^*_{PRE}$ and $(S/N)_{OUT}$. Under these circumstances the usefulness of a photomixer is related only to its quantum efficiency and the preferred mixers in order of increasing sensitivity would be; the S-1 photosurface detector, the S-20 photosurface detector, and the solid state junction detector respectively.

---

* Chapter 3, Sections D.5.a and D.5.b.

One of the operating characteristics assumed for the superheterodyne spectrometer* was that $P_{LO} >> P_S$, where P_S is the total signal power reaching the photocathode. This condition guarantees that the self-beat part of the photomixer current spectrum is negligible compared with the heterodyne beat signal. If the photomixer contains a single coherence area then a satisfactory ratio would be $P_{LO} \simeq 100\ P_{COH}$. If, in addition, P_{LO} must satisfy the inequality $P_{LO} >> P_{DARK}$ in order to achieve $F_D << 1$, then we have from Fig. 3-21 and the values of P_{DARK} given in Eq. (3-161)

$$P_{LO} \geq \begin{cases} 100\ P_{COH} & \text{S-1 photosurface} \\ 100\ P_{COH} & \text{S-20 photosurface} \\ (10^{10} - 10^{13})\,P_{COH} & \text{solid state junction} \end{cases} \tag{3-164}$$

---

* Chapter 3, Section D.2.

These values were chosen to simultaneously satisfy the two conditions; $P \geq 100\ P_{COH}$ and $(F_D \leq 0.1)$. When the photomixer contains N coherence areas the equivalent results are:

$$P_{LO} \geq \begin{cases} 100(N)P_{COH} & \text{S-1 photosurface} \\ 100(N)P_{COH} & \text{S-20 photosurface} \\ (10^{10} - 10^{13})P_{COH} & \text{solid state junction} \end{cases} \qquad (3\text{-}165)$$

The number of coherence areas appears in the first two conditions since for the photosurface type detectors the minimum value of P_{LO} is set by the requirement $P_{LO} \geq 100\ P_S$. The value of N does not appear in the condition on P_{LO} for the solid state junction detector as in this case P_{LO} is fixed by the much stronger requirement $P_{LO} >> P_{DARK}$.

The importance of the inequalities given in Eqs. (3-164) and (3-165) lie in the rather stringent limits which they impose on the allowable amplitude modulation of the local oscillator. Such a modulation generates a pair of "sidebands" on the local oscillator spectrum which are separated from ω_{LO} by the modulation frequency ω_M. The result is a self-beat signal in the photomixer output current at the modulation frequency which is due to the mixing between the local oscillator carrier at $\omega = \omega_{LO}$ and these sidebands. If ω_M is near the i.f. frequency ω_1 then this spurious beat note can interfere with the observation of the desired heterodyne beat signal.

In general the serious amplitude modulation present on a well designed laser is confined to low audio frequencies, generally less than a few hundred cycles per second. Furthermore, its strength is a rapidly decreasing function of increasing modulation frequency. For example, a possible local oscillator spectrum including the effects of modulation is shown in Fig. 3-23. The half-width at half-height of the sideband spectrum is typically $(\omega_c/2\pi) \simeq 100$ cps and the tails of the spectrum fall off at least as fast as $(\omega-\omega_{LO})^{-2}$. Therefore, it is usually possible to make modulation effects negligible by appropriately raising the intermediate frequency ω_1.

A quantitative analysis of the problem may be formulated as follows. Suppose that the optical power per unit bandwidth in the local oscillator modulation spectrum is taken as

$$S_{LO}(\omega) = m(\omega-\omega_{LO})\left\langle|\vec{E}_{LO}(\vec{r}_o,t)|^2\right\rangle \qquad (3\text{-}166)$$

$$(\omega\neq\omega_{LO})$$
$$(\omega\geq 0)$$

That is, $m(\omega)$ is a modulation index giving the fraction of the total local oscillator power present in the sideband spectrum per unit bandwidth. Then the spurious self-beat note in the photocurrent at the i.f. frequency has a power spectral density

$$\begin{aligned} I_M^2(\omega_1) &= \alpha^2 A^2 m(\omega_1)\left[\left\langle|\vec{E}_{LO}(\vec{r}_o,t)|^2\right\rangle\right]^2 \qquad (3\text{-}167)\\ (\omega\geq 0)\qquad & \\ &= 2m(\omega_1)\,i_p^2 \end{aligned}$$

as calculated from Eq. (3-53). Taking the ratio of $I_M^2(\omega_1)$ to the power spectral density of the heterodyne signal $I_S^2(\omega_1)$ we have from Eq. (3-129)

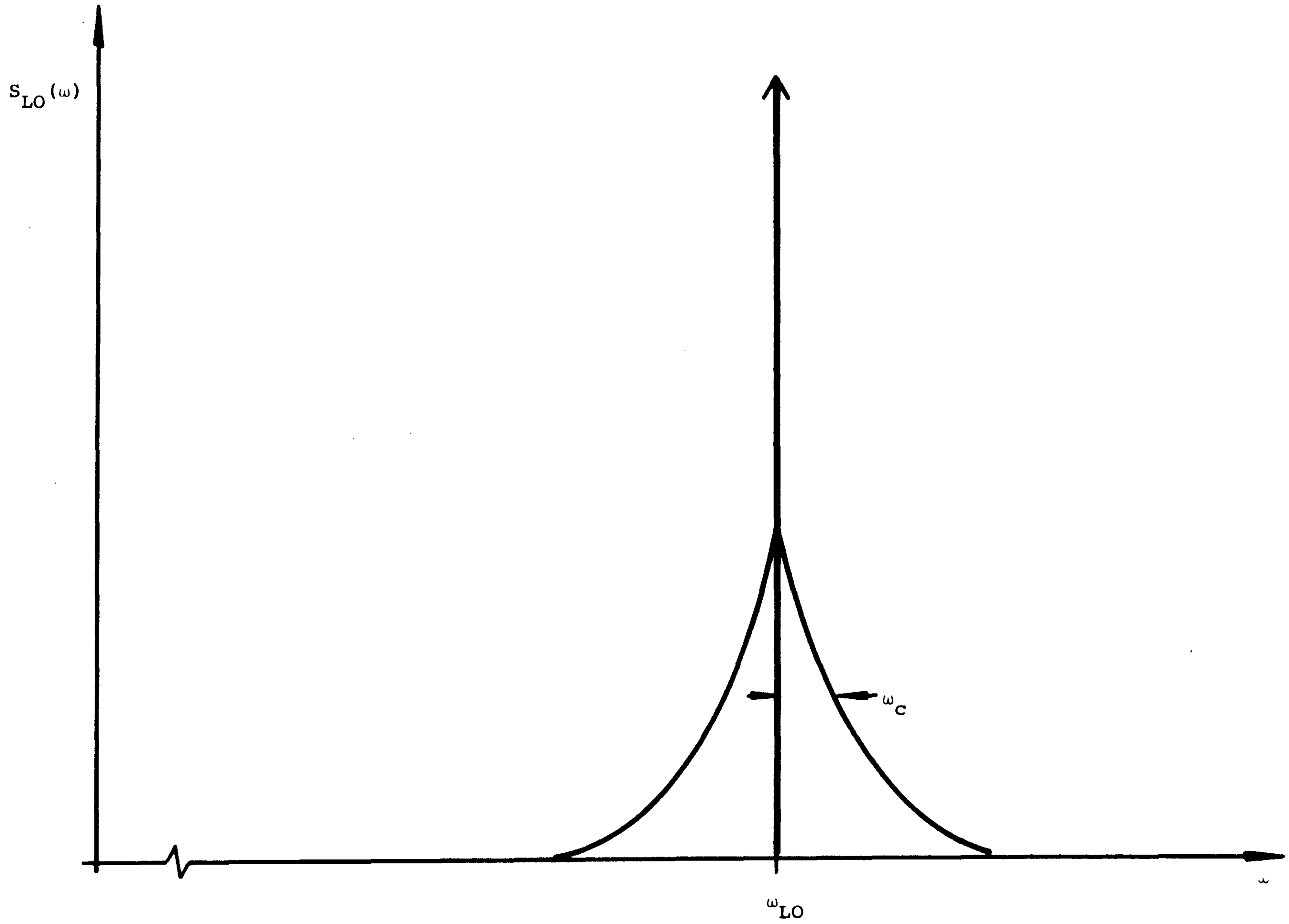
$S_{LO}(\omega)$
ω_c
ω_{LO}
ω

Figure 3-23 Typical power spectral density of the output of a real laser. The wing portion of the spectrum is the result of amplitude modulation.

$$\frac{I_M^{\ 2}(\omega_1)}{I_S^{\ 2}(\omega_1)} = \frac{m(\omega_1)\, i_p^{\ 2}}{i_p i_s (1/\pi\Gamma)(A^*_{COH}/A)[B_{COH}]} \tag{3-168}$$

With $[B_{COH} = 1]$ and the currents i_p and i_s written in terms of the local oscillator and signal powers respectively, Eq. (3-168) becomes simply

$$\frac{I_M^{\ 2}(\omega_1)}{I_S^{\ 2}(\omega_1)} = m(\omega_1)\left(\frac{\Gamma}{\pi}\right)\cdot\frac{P_{LO}}{P_{COH}} \tag{3-169}$$

This result combined with the minimum required ratios of (P_{LO}/P_{COH}) given in Eq. (3-165) and a choice as to the maximum allowable ratio of spurious to actual signal strengths will yield a numerical condition on $m(\omega_1)$. For the case $[I_M^{\ 2}(\omega_1)/I_S^{\ 2}(\omega_1)] \leq 0.01$ we find

$$m(\omega_1) \leq \begin{cases} \left(\frac{\pi}{\Gamma}\right)\frac{1}{10^4 N} & \text{S-1 photosurface} \\ \left(\frac{\pi}{\Gamma}\right)\frac{1}{10^4 N} & \text{S-20 photosurface} \\ \left(\frac{\pi}{\Gamma}\right)\frac{1}{(10^{12} - 10^{15})} & \text{solid state junction} \end{cases} \tag{3-170}$$

Equation (3-170) points out two important conclusions: (1) a superheterodyne spectrometer using a photosurface type mixer should gather light from only a single coherence area in order to ease the requirement on amplitude modulation, (2) although attractive because of its quantum efficiency the solid state junction detector imposes such severe restrictions on $m(\omega_1)$ that it is useful only for rather high (> 10 Mc/sec) intermediate frequencies.

c. Summary

We may summarize the preceding analysis as follows. In a self-beat spectrometer using an S-1 or S-20 photosurface type mixer the effects of dark current can be made negligible. The S-20 surface devices achieve this with the minimum optical power required to obtain $(S/N)_{OUT} = 1$. The S-1 surface has a higher dark current than the S-20 surface, but this current can be reduced by cooling or overcome by suitably increasing the total signal power accepted by the mixer. The solid state junction detector is not useful in a self-beat instrument because of a large dark equivalent input power. In a superheterodyne spectrometer we can always make the effects of dark current negligible by suitable increasing the local oscillator power. However, large values of P_{DARK} place severe restrictions on the amplitude stability of the local oscillator source.

4. The Effects of Johnson Noise

Equation (3-153) gives the thermal noise contribution to the factor F as

$$F_R = [I_R^2(\omega)/I_N^2(\omega)] \qquad (3\text{-}171)$$

where $I_R^2(\omega)$ is the equivalent current power per unit bandwidth in the thermal noise as referred to the photocathode. In order to quantitatively analyze this result we will investigate the four possible configurations in which a photomixer can be operated, their associated values of F_R, and the specific methods peculiar to each one by which F_R can be minimized.

The four basic operating situations can be grouped into two categories according to the characteristics of the photomixer: (1) the photomixer has no internal current gain of its own so that the output current is simply the photocurrent, or (2) the detector does have such an internal gain. For each of these categories there are two distinct possibilities for the type of operation: (1) the beat note spectrum is centered at $\omega = 0$, or (2) the beat note spectrum is centered at an i.f. frequency $\omega_1 \neq 0$. Each of these four configurations has its own characteristic thermal noise features.

The thermal noise referred to in Eq. (3-171) has its origin in the resistive part of the load impedance presented to the photomixer.[43] Calling this impedance $\underline{Z}_L$ and adopting the usual complex plane notation[44] we have

$$\underline{Z}_L = R + jX \qquad (3\text{-}172)$$

where R and X are respectively the resistive and reactive components of the load. The thermal noise properties of such an impedance can be described in a number of ways. The most common[45] is to represent the resistance R and its inherent thermal noise by a noiseless resistor R and an appropriate series voltage generator. From the central limit theorem[46] this voltage source is a Gaussian random noise generator whose voltage power spectral density, $V_r^2(\omega)$, is given by

$$V_r^2(\omega) = \frac{2\underline{k}T}{\pi}\cdot R \qquad (3\text{-}173)$$

$$(\omega \geq 0)$$

where $\underline{k}$ is Boltzmann's constant and T is the absolute temperature. For the purpose of noise analysis then, the corresponding lumped circuit schematic of the impedance $\underline{Z}_L$ is drawn as in Fig. 3-24. An equally valid description that will be useful here represents $\underline{Z}_L$ as a noiseless impedance, $\underline{Z}_L = (R + jX)$, in parallel with a suitable current generator.[45] This generator is also a source of Gaussian noise and has a current power spectal density, $I_r^2(\omega)$, which is

$$I_r^2(\omega) = \frac{2\underline{k}T}{\pi}\cdot\frac{1}{R} \qquad (3\text{-}174)$$

$$(\omega \geq 0)$$

Figure 3-25 illustrates the corresponding lumped circuit schematic of $\underline{Z}_L$.

Both Eqs. (3-173) and (3-174) reflect the fact that a circuit element at a finite temperature T has associated with it a thermal noise power per unit bandwidth $P_r(\omega)$

$$P_r(\omega) = \frac{2\underline{k}T}{\pi} \qquad (3\text{-}175)$$

$$(\omega \geq 0)$$

that is independent of the electrical nature of the element. This fact can be used to give a simple explanation of the objective in choosing the value of $\underline{Z}_L$; the photomixer should be terminated by a load into which it will deliver the maximum amount of power. This condition will guarantee the minimum possible value of F_R.

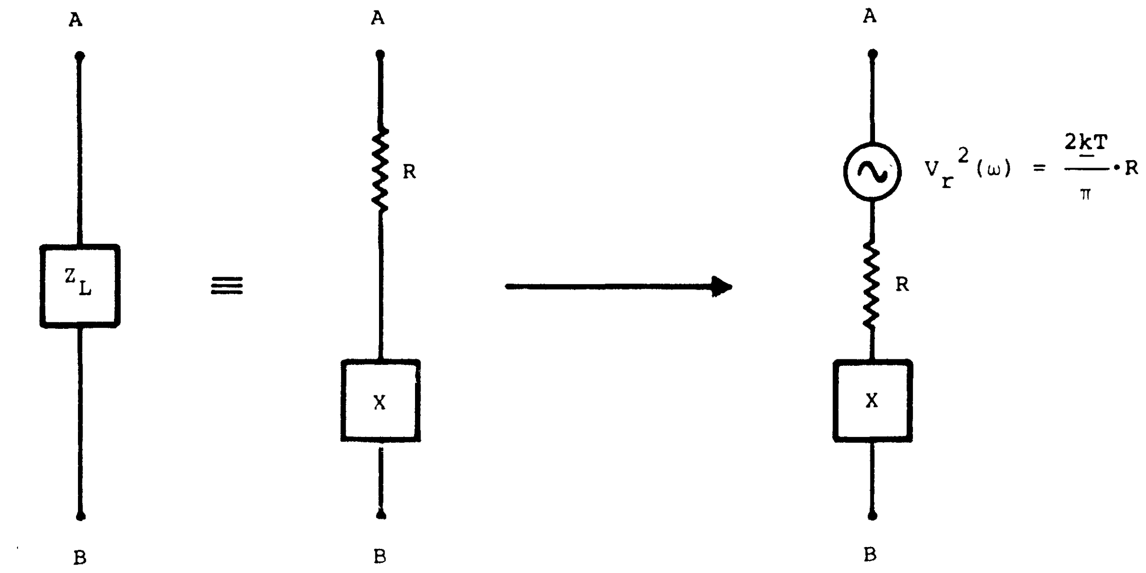
A
A
A
R
R
$V_r^2(\omega) = \frac{2kT}{\pi} \cdot R$
Z_L
≡
X
X
B
B
B

Figure 3-24 The voltage generator equivalent circuit of a real impedance.

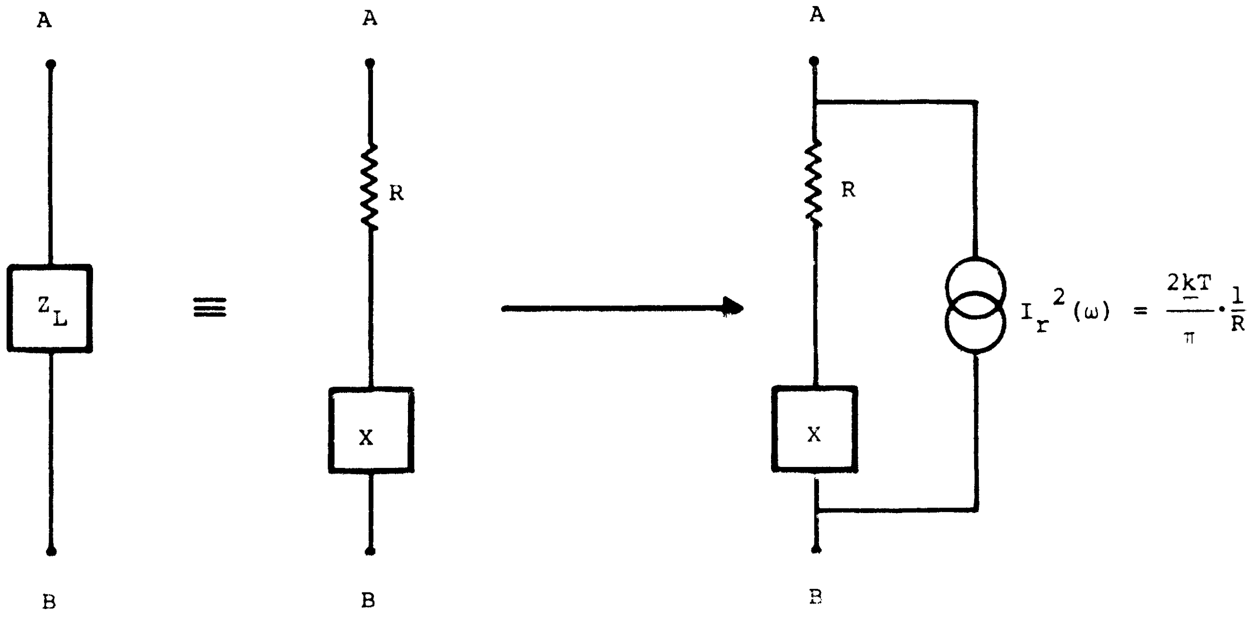
A
A
A
R
R
$I_r^2(\omega) = \frac{2kT}{\pi} \cdot \frac{1}{R}$
Z_L
≡
X
X
B
B
B

Figure 3-25 The current generator equivalent circuit of a real impedance.

Equation (3-174) specified $I_r^2(\omega)$ as referred to the load, $\underline{Z}_L$. From this point the evaluation of F_R can proceed in two equivalent directions; starting from $I_r^2(\omega)$ we may calculate the thermal noise as seen at the photocathode and then use Eq. (3-171) or given $I_N^2(\omega)$ we can determine the shot-noise current power as delivered to the load, $I_n^2(\omega)$, and make use of a corresponding result for F_R, namely

$$F_R = [I_r^2(\omega)/I_n^2(\omega)] \tag{3-176}$$

The calculations presented here will follow this second course.

a. The Case of Zero Intermediate Frequency and Unity Internal Photodetector Gain

Let us begin by analyzing the simplest of the four possible photomixer configurations. We assume that the mixer has no internal gain so that the maximum current available at its output terminals is just the photocurrent, i(t). Furthermore, we consider the case in which the signal part of the photocurrent spectrum is centered at $\omega = 0$. The latter will be true either for a self-beat spectrometer or for a superheterodyne spectrometer in which the intermediate frequency is chosen as ($\omega_1 = 0$). The objective of the following discussion is to determine the load impedance which will optimize the shot-noise current power delivered to the load by the photomixer.

By its nature the photoemission process is the source of a current whose magnitude is determined solely by the incident optical field and is independent of the details of the load into which this current is delivered. That is, the photocurrent can be regarded as originating in an ideal current generator whose current power spectral density is simply $S_i(\omega)$. The actual output of the photomixer, on the other hand, must also reflect the effects of the internal electrical characteristics of the device. One simple example of such an internal property is the unavoidable stray capacitance associated with the physical construction of the detector. For the purposes of an electrical analysis these characteristics can be represented by a so-called lumped equivalent circuit of the photomixer.[43]

Figure 3-26 shows the schematic diagram of a rather general equivalent circuit that is appropriate to the class of photodetectors being considered here, namely, those with no internal current gain.[43] This basic equivalent circuit contains four components: (1) an ideal current generator having a power spectral density $S_i(\omega)$; (2) a leakage or junction resistance R_j which describes the bypassing of that portion of the dc photocurrent which flows inside the detector; (3) a stray or junction capacitance C_j that reflects the size and proximity of the two electrodes that serve as the current generating and current gathering elements; and (4) a dynamic series resistance R_s which represents the finite conductance between these electrodes and the output terminals. Typical values of R_j, R_s, and C_j are given in columns VIII, IX, and X of Table IV as R_{SHUNT}, R_{SERIES}, and C_{SHUNT} respectively.

Figure 3-26 applies equally well both to photosurface type mixers and to solid state junction devices having no internal current gain. The photodetectors that fall into

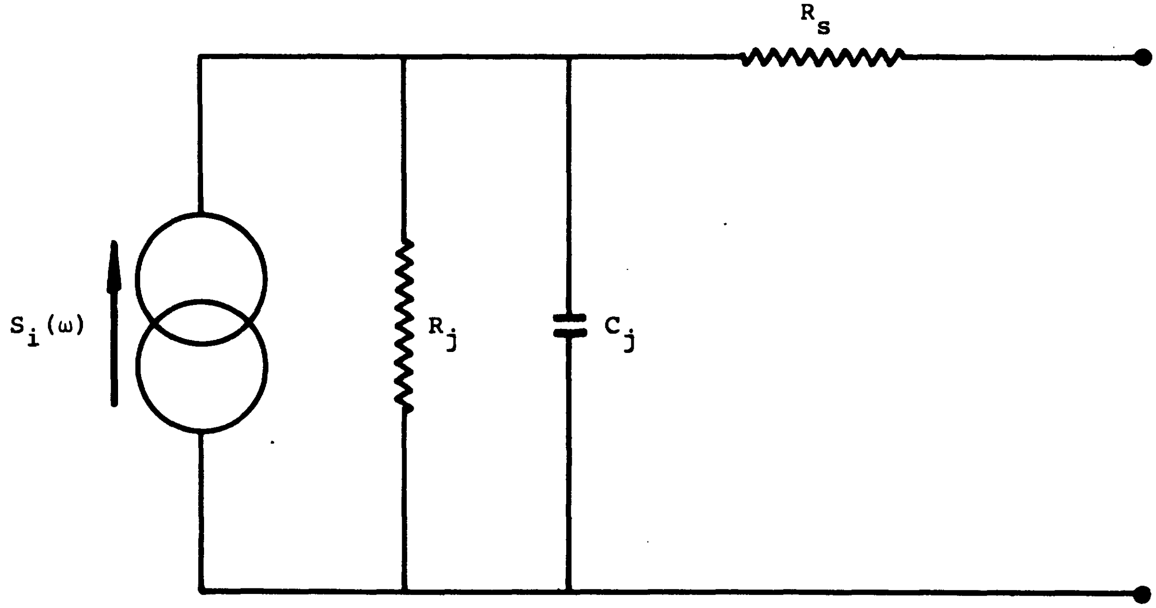
R_s
$S_i(\omega)$
R_j
C_j

Figure 3-26 The general equivalent circuit of a photodetector mixer with unity gain.

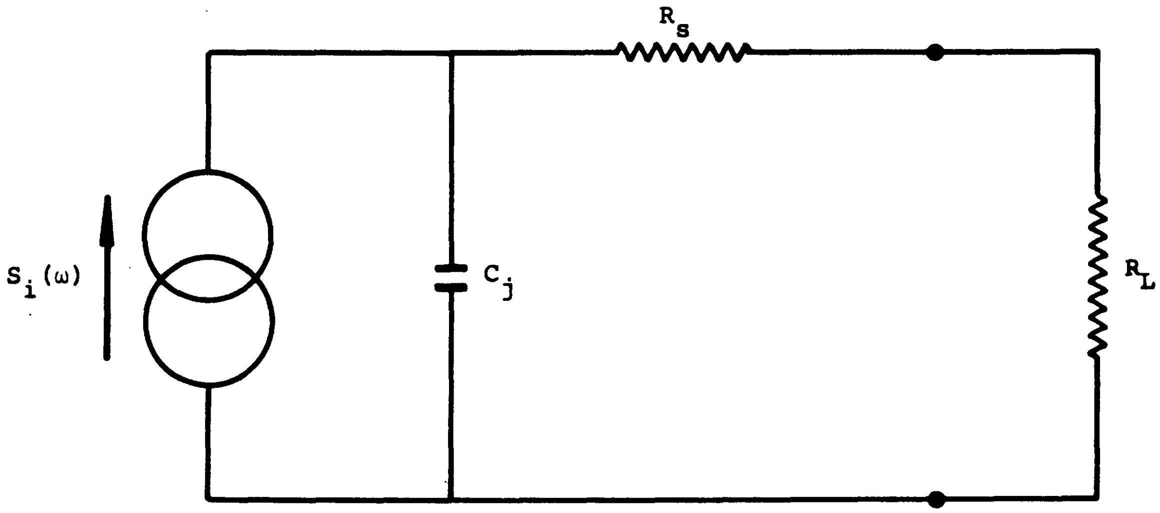
R_s
$S_i(\omega)$
C_j
R_L

Figure 3-27 Simplified equivalent circuit for a photomixer operating into a pure resistance load.

this category can be identified from Table IV by the values of the internal ac and dc current gains quoted in columns IV and V; these gain factors have been designated G_{AC} and G_{DC} respectively. Figure 3-26 is appropriate to the case ($G_{AC} = G_{DC} = 1$).

Let us determine the optimum load impedance for a photomixer having such an equivalent circuit. We take the incident optical field to be the usual Lorentzian of half-width Γ and assume that the signal part of the photocurrent arises either from a self-beat detection process or from a superheterodyne arrangement with $\omega_1 = 0$. In either case the frequencies of interest in the mixer current spectrum extend from $\omega = 0$ to $\omega \simeq 10\Gamma$. Ideally, the frequency response of the combined photodetector-load circuit should be uniform over this interval in order to avoid distorting the observed shape of the photocurrent spectrum. At the same time, in order to minimize F_R, the mixer should deliver to the load at each frequency the maximum amount of power which is theoretically consistent with its own internal circuit characteristics. However, if the detector has an equivalent circuit of the sort shown in Fig. 3-26 then there is no load impedance which can simultaneously achieve both of these conditions. In reality, the choice of the optimum load impedance, $\underline{Z}_L$, represents a compromise between efficient power transfer and a tolerable amount of non-uniformity in the frequency response. The appropriate form for $\underline{Z}_L$ can be deduced from the following arguments.

For very low frequencies, where X_{C_j}, the reactance of C_j, is essentially infinite, $X_{C_j} >> R_j + R_s$, the ideal load is a simple resistor R_L whose value is

$$R_L = R_j + R_s \qquad (3\text{-}177)$$

"Ideal" here signifies that the condition $\underline{Z}_L = R_L = (R_j + R_s)$ results in the theoretical maximum power transfer between mixer and load.[47] For all practical purposes R_j may be regarded as infinite, as is evident from Table IV; therefore, in the limit of zero frequency the ideal load impedance is that associated with a simple current generator, namely, an infinite resistance. In that limit the power per unit bandwidth dissipated in the load takes the form

$$P_L(\omega) = S_i(\omega)R_L \begin{cases} X_{C_j} >> R_L \\ \\ R_j >> R_L \end{cases} \tag{3-178}$$

and can be increased to an arbitrarily large value by suitably increasing R_L. In particular, since the thermal noise power spectral density of any load is independent of its impedance, it follows that the load that yields the minimum value of F_R at very low frequencies is a simple resistor with the largest possible resistance.

Equation (3-178) also shows that a resistive load will result in a uniform frequency response for that range of frequencies where $X_C >> R_L$. In this case the power per unit bandwidth seen across the load is simply proportional to $S_i(\omega)$. It follows that the optimum load from the standpoint of both uniform frequency response around $\omega = 0$ and maximum power transfer if a pure resistance, $\underline{Z}_L = R_L$. The magnitude of R_L should be as large as possible with a maximum value limited only by the finite reactance of C_j at the highest frequency of interest in the photocurrent spectrum.

These results may be expressed quantitatively by reference to the photodetector and load circuit illustrated in Fig. 3-27. A simple calculation shows that the current power spectral density produced in the load resistance R_L is

$$I_{LOAD}^2(\omega) = \frac{S_i(\omega)}{1 + \omega^2(R_s+R_L)^2C_j^2} \qquad (3\text{-}179)$$

Since the reactance of C_j at the frequency ω is given by

$$X_{C_j}(\omega) = (1/\omega C_j) \qquad (3\text{-}180)$$

We may also write $I_{LOAD}^2(\omega)$ as

$$I_{LOAD}^2(\omega) = \frac{S_i(\omega)}{1 + \left[\dfrac{R_s + R_L}{X_{C_j}(\omega)}\right]^2} \qquad (3\text{-}181)$$

Clearly the condition of uniform frequency response from ($\omega = 0$) up to a specified frequency ω_{max} requires that we have

$$\omega_{max}(R_s+R_L)C_j = \frac{R_s + R_L}{X_{C_j}(\omega_{max})} << 1 \qquad (3\text{-}182)$$

thus placing an upper limit on R_L. When Eq. (3-182) is satisfied the power per unit bandwidth dissipated in the load becomes simply

$$P_L(\omega) = I_{LOAD}^2(\omega)R_L = S_i(\omega)R_L \qquad (3\text{-}183)$$

the result given in Eq. (3-178).

The limiting frequency that satisfies the equality ($\omega R_sC_j = 1$) is called the RC cutoff frequency, ω_{RC}, of the detector. Equation (3-179) shows that at this point at least one half of the available current power produced by the generator flows internally through C_j even for $R_L = 0$. Therefore, ω_{RC} represents an absolute upper limit on the highest frequency which a mixer can produce in a resistive load simply because of its internal circuit parameters. Numerical values of this cutoff frequency appear in column III of Table IV. Column II also gives a maximum usable mixer frequency which is traceable to a dispersion of the times required for photocarriers to travel from their generation point to the collecting electrode. For most mixers this transit time cutoff frequency is smaller than the RC cutoff frequency, thus we may take $(\omega R_s C_j) << 1$ for all ω at which a specific detector will be useful. With this assumption Eq. (3-182) reduces to

$$\omega_{max} R_L C_j << 1$$

In actual practice by using a slightly more sophisticated load network we can usually achieve a load current response versus frequency which is uniform within approximately 1% up to the frequency ω_{max} even if R_L satisfies the less stringent requirement

$$\omega_{max} R_L C_j \leq 1 \qquad (3\text{-}184)$$

The required load network[48] is basically a resistance R_L having inductive compensation to increase the apparent load impedance at high frequencies, i.e. $\omega \simeq \omega_{max}$. In this case R_L represents the resistive component of $\underline{Z}_L$.

If ω_{max} is taken as 10Γ then choosing R_L as its maximum value

$$R_L = \frac{1}{\omega_{max} C_j} = \frac{1}{10\Gamma C_j} \tag{3-185}$$

guarantees an essentially flat frequency response over the entire region of interest in the signal part of the photocurrent spectrum. This choice also represents the desired optimum compromise between uniform response and maximum power delivery. When R_L satisfies Eq. (3-185) the relation between $I_{LOAD}^2(\omega)$ and $S_i(\omega)$ for $\omega \leq 10\Gamma$ becomes simply

$$I_{LOAD}^2(\omega) = S_i(\omega) \tag{3-186}$$

and we have from Eqs. (3-176) and (3-174)

$$F_R = \frac{I_R{}^2(\omega)}{I_N{}^2(\omega)} = \frac{I_r{}^2(\omega)}{I_n{}^2(\omega)} = \frac{\left(\frac{2\underline{k}T}{\pi}\right)\cdot\frac{1}{R_L}}{\left(\frac{e}{\pi}\right)\cdot i_p} = \frac{2\underline{k}T}{eR_L i_p} \tag{3-187}$$

where i_p is the total dc photocurrent. Equation (3-187) shows explicitly how the ratio of thermal to shot-noise powers at the load is degraded by an upper limit on R_L. The thermal noise power $(2\underline{k}T/\pi)$ is independent of the choice of Z_L while the amount of available shot-noise power $(e/\pi)i_pR_L$ depends linearly on R_L.

Writing i_p in terms of the total optical power falling on the photomixer gives F_R as

$$F_R = \left(\frac{2\underline{k}T}{\varepsilon e^2}\right)\frac{\hbar\omega_o}{\mathcal{P}}\cdot\frac{1}{R_L} \tag{3-188}$$

If we demand that F_R satisfy the condition $(F_R \leq 0.1)$, then Eq. (3-188) yields a requirement on $\mathcal{P}$ of the form

$$\mathcal{P} \geq 10\left(\frac{2\underline{k}T}{\varepsilon e^2}\right)\hbar\omega_o\cdot\frac{1}{R_L} \tag{3-189}$$

Finally, taking R_L as the optimum load impedance given by Eq. (3-185), we have

$$P \geq 100\left(\frac{2kT}{\varepsilon e^2}\right)\hbar\omega_o \cdot (\Gamma C_j) \qquad (3\text{-}190)$$

Formally speaking, Eq. (3-188) and the inequalities in Eqs. (3-189) and (3-190) are identical to the equivalent results presented in the discussion of dark current shot-noise. That is, the appropriate F factors, F_D and F_R, both depend solely on the total power incident on the detector. The analysis given in Section F.3 showed that the usefulness of a given photodetector operating under these circumstances can be measured by the ratio $[P/P_{COH}]$. The quantity P_{COH} is the power per coherence area needed in the signal beam of an ideal mixing spectrometer in order to obtain $(S/N)_{OUT} = 1$, and P is the minimum total incident power required to achieve shot-noise limited operation, in this case $(F_R \leq 0.1)$. The salient points of that analysis can be restated here briefly as follows.

(1) Moderate or small values of $[P/P_{COH}]$, for example, $[P/P_{COH}] \leq 10^3$, imply that the detector under consideration will achieve ideal sensitivity in a self-beat spectrometer which is capable of gathering incident light from a sufficiently large number of coherence areas, namely, $N \geq [P/P_{COH}]$. This same detector used in a superheterodyne spectrometer will also exhibit the ideal sensitivity while imposing only the minimum restriction on local oscillator amplitude modulation.

(2) Large values of $[P/P_{COH}]$, for example, $[P/P_{COH}] \geq 10^7$, characterize detectors that are unsuitable for use in self-beat detection. Although such detectors can in theory

operate with ideal sensitivity in a superheterodyne instrument the larger values of $[P/P_{COH}]$ lead to severe requirements on local oscillator amplitude stability.

Figures 3-28, 3-29, and 3-30 present the data necessary to determine the usefulness of the four detectors listed in Table IV as satisfying the condition ($G_{AC} = G_{DC} = 1$). Two of these are solid state junction photodiodes and two are S-20 photosurface type devices. In each case, the data corresponds to operation with the desired beat signal spectrum, either self-beat or superheterodyne, centered around $\omega = 0$.

The resistive part of the optimum load impedance was calculated for each of these detectors using Eq. (3-185) and the stray capacitance values listed in column X of Table IV. The results are presented in Fig. 3-28 as a plot of R_L versus the line width of the incident optical field. The data on R_L for a particular mixer extend up to a maximum value of Γ related to the transit time cutoff frequency, ω_{tr}, by

$$10\Gamma = \omega_{tr}$$

For larger half-widths the highest frequency of interest in the photocurrent spectrum exceeds the ultimate usable mixer frequency. Each curve is also terminated for small values of Γ at that half-width Γ_L where the optimum load resistance becomes $R_L = 10^7\Omega$. We assume that $10^7\Omega$ is a maximum permissible value of R_L set by leakage resistance in the circuitry external to the mixer.

Combining the values of R_L shown in Fig. 3-28 and the inequality given in Eq. (3-189) yields the total optical power which must be received by the detector

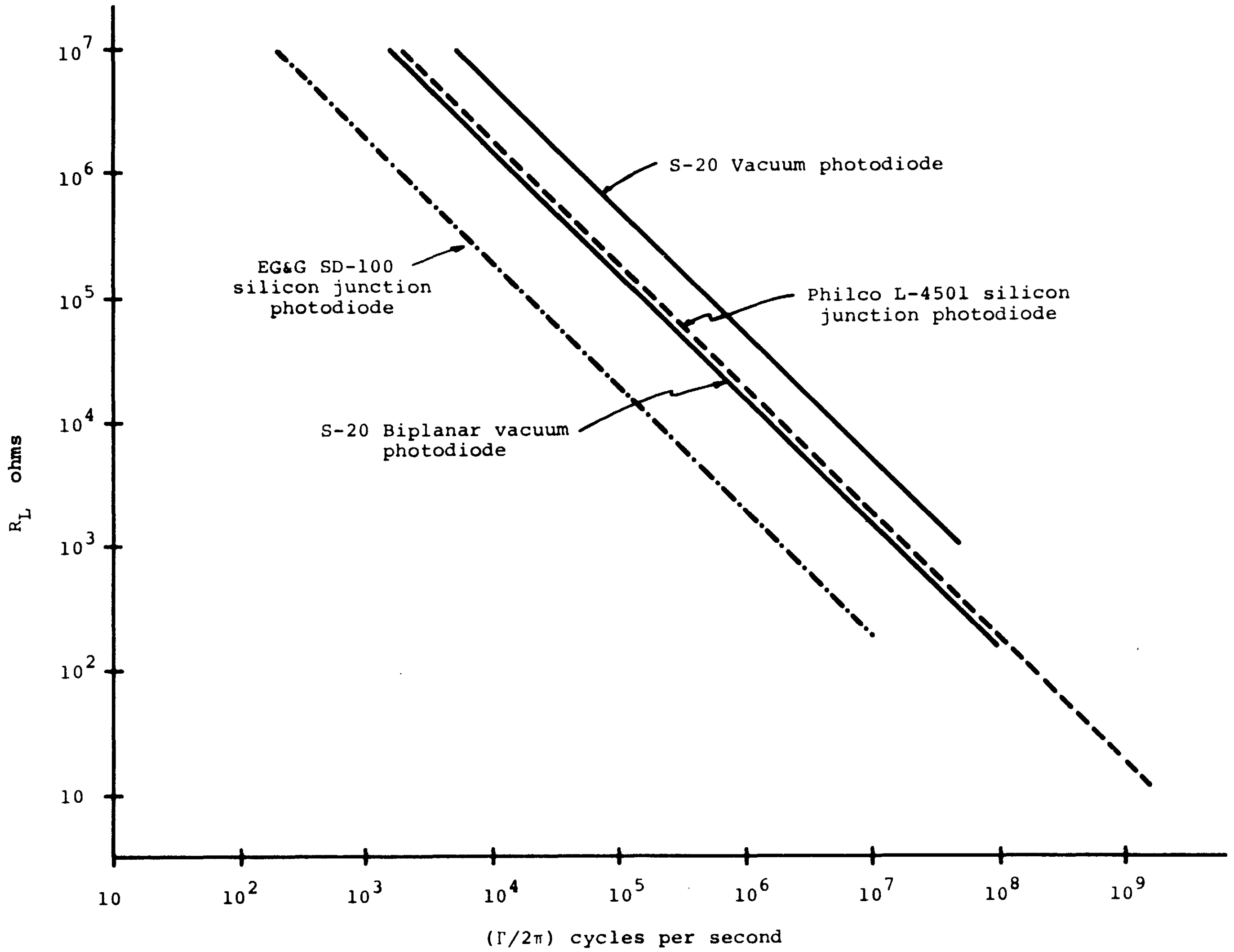

Figure 3-28 The optimum load resistance for some typical unity gain detectors. The load resistance is given versus the half-width at half-height of the Lorentzian optical spectrum under investigation.

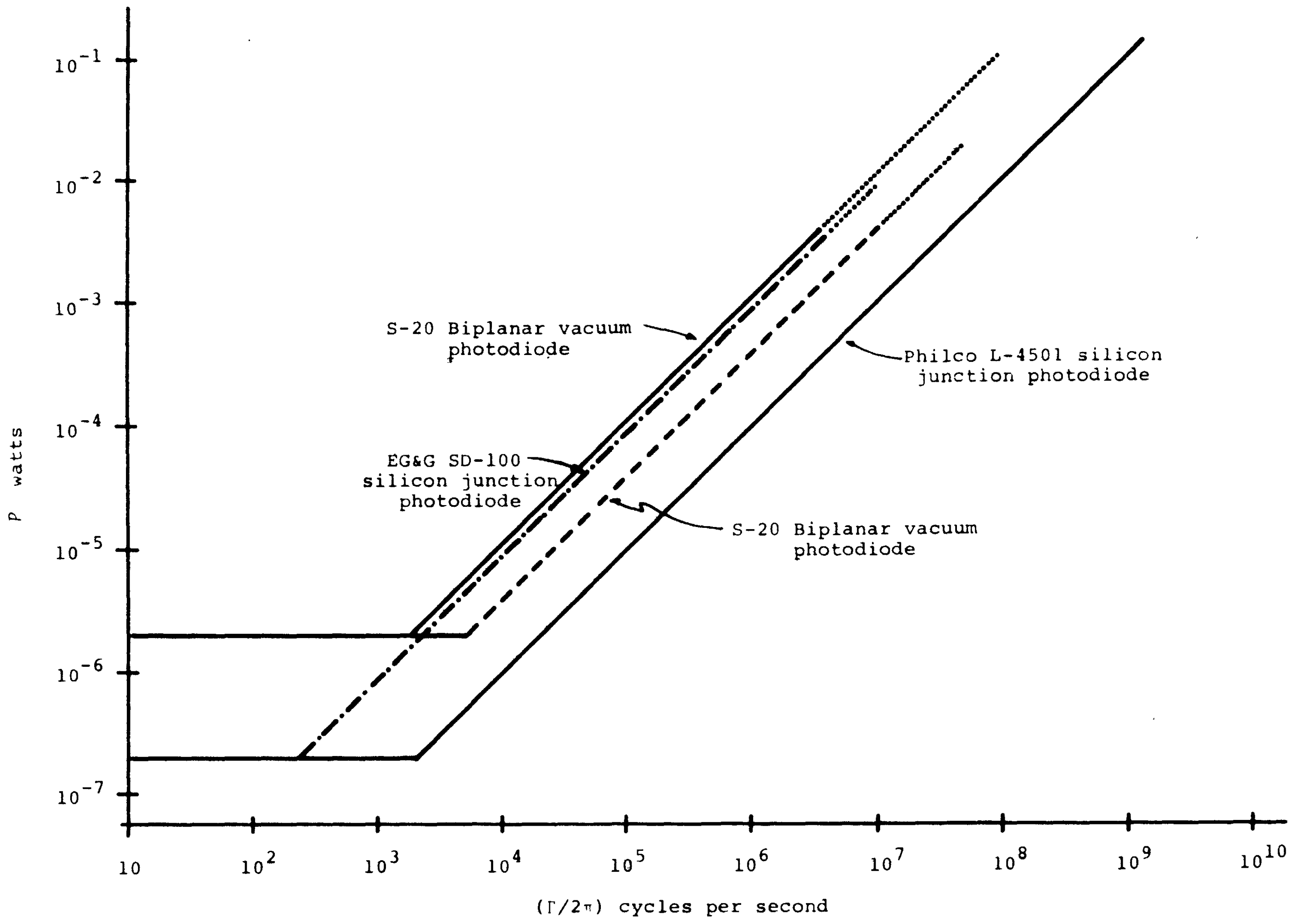

Figure 3-29 The total incident optical power required to overcome thermal noise in the photomixer load resistance of an optimally loaded unity gain detector.

in order to bring about shot-noise limited operation, ($F_R \leq 0.1$). The results, based on a load temperature of T = 300°K, are shown in Fig. 3-29. For small Γ, where we take $R_L = 10^7\Omega$ independent of Γ, the required power is also constant at a value determined only by the quantum efficiency ε; the curves break at $\Gamma = \Gamma_L$ and for larger widths P is proportional to Γ as in Eq. (3-190). The data on each detector again extends up to a maximum line width limited by the transit time cutoff frequency and the condition $10\Gamma < \omega_{tr}$. However, the dashed portions of the curve indicate that the necessary total incident power would exceed the maximum power rating of the detector, P_{MAX}.

The appropriate values of P_{MAX} were determined from column VI of Table IV which specifies the maximum allowable dc photodetector output current $(I_{OUT})_{MAX}$. For the unity gain detector, ($G_{AC} = G_{DC} = 1$), $(I_{OUT})_{MAX}$ is related to P_{MAX} by

$$(I_{OUT})_{MAX} = (\varepsilon e/\hbar\omega_o)P_{MAX} \tag{3-191}$$

Combining the results given in Fig. 3-29 with the ideal sensitivity curves of Fig. 3-21 yields the values of $[P/P_{COH}]$ plotted in Fig. 3-30. As in Fig. 3-29 the dotted extensions of the curves indicate regions accessible from the standpoint of frequency response but in which P exceeds P_{MAX}. On the basis of these results and the discussion of Section F.3 we can state the following conclusions:

(1) A unity gain detector is not useful in a self-beat spectrometer because of the effects of Johnson noise.

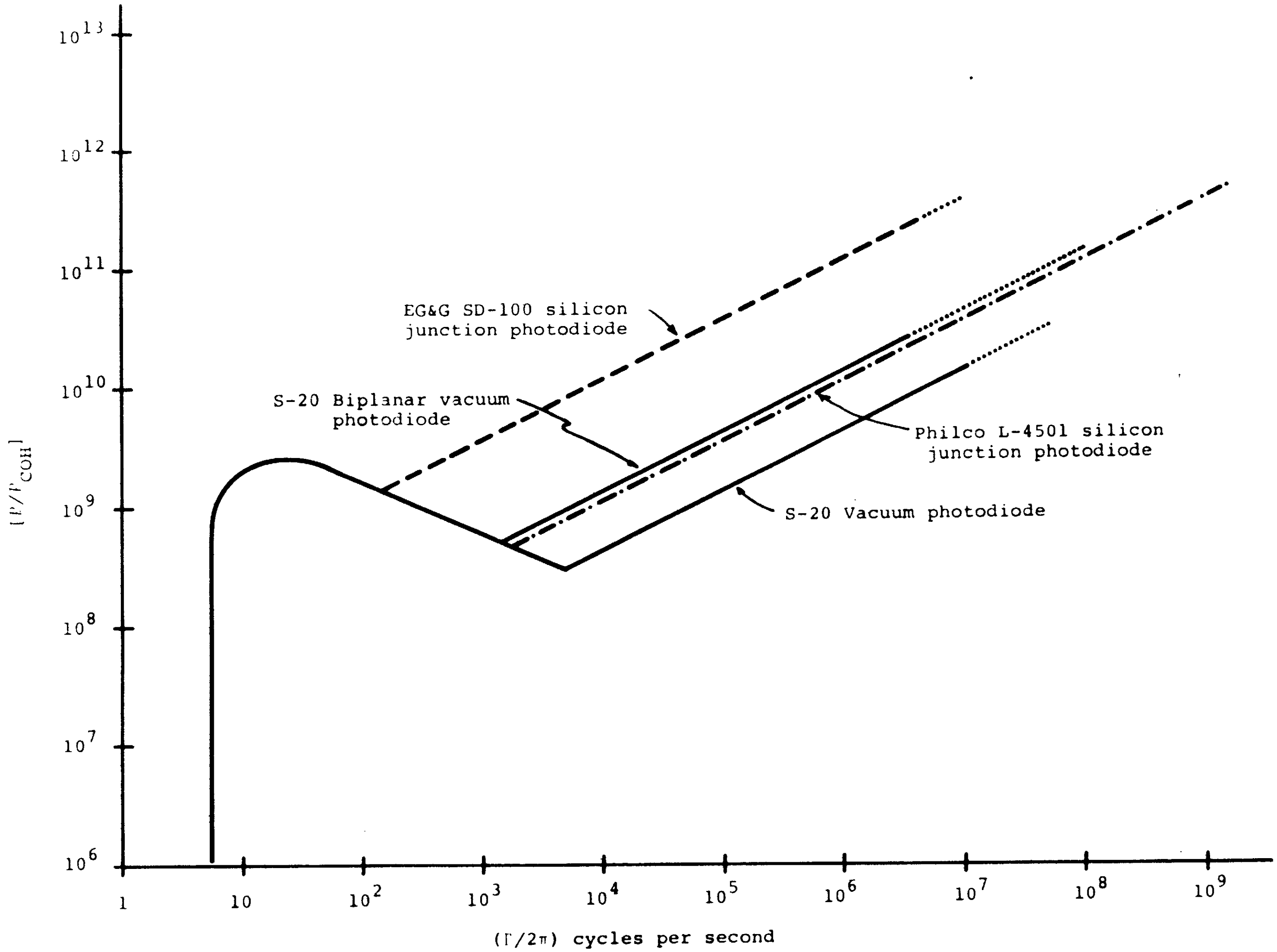

Figure 3-30 The ratio of the total optical power required to overcome the Johnson noise in the photomixer load to the power per coherence area in the signal necessary to achieve $(S/N)_{OUT} = 1$.

(2) A superheterodyne optical receiver employing a unity gain detector and operating at an i.f. frequency $\omega_1 = 0$ can achieve ideal sensitivity. However, this mode of operation would impose severe limits on the local oscillator modulation index*, $m(\omega)$.

It is also interesting to compare the relative importance of dark current noise and thermal noise to unity gain detectors. Comparing Figs. 3-29 and 3-22 we find that with an S-20 type photosurface detector the optical input power necessary to swamp the thermal noise is from 9 to 12 orders of magnitude larger than that required to overcome the equivalent dark input power. On the other hand, the solid state junction devices have such large values of P_{DARK} that in this case the two constraints are of comparable orders of magnitude.

The important features of the thermal noise analysis can be summarized as follows. The choice of a load impedance for any photomixer involves four basic considerations: (1) a realistic equivalent circuit for the detector, (2) the necessary frequency response characteristics of the combined mixer and load circuit, (3) maximum transfer of power between the mixer and load consistent with this required frequency response, and (4) the relationship between the photocurrent and the load current under these optimum conditions.

---

* Chapter 3, Section F.3.b.

b. The Case of Zero Intermediate Frequency and Arbitrary Internal Photodetector Gain

Let us now consider how the thermal noise situation changes when the mixer has an internal current gain other than unity. We will still assume that the signal part of the photocurrent spectrum is centered around ($\omega = 0$) and that it represents the self-beat or superheterodyne detection of a Lorentzian optical spectrum with half-width Γ. This case represents the second of the four possible photomixer configurations.

The lumped equivalent circuit for a photodetector with an ac current gain G_{AC} and a dc current gain G_{DC} is shown in schematic form by Fig. 3-31. Although the ac and dc gain processes and corresponding outputs are drawn as being distinct, they will actually coincide for most detectors. In the latter case we have $G_{AC} = G_{DC} = G$ and the simplified equivalent circuit schematic of Fig. 3-32. The components of both equivalent circuits are identical to those of the unity gain detector circuit shown in Fig. 3-26 and have the same functions as were described there. In fact, the only new features in Figs. 3-31 and 3-32 are the amplifiers that act on the photocurrent prior to delivering it to the remainder of the equivalent circuit. We will assume that these "black box" amplifiers are ideal, noiseless, current multipliers; that is, if $i_{ac}(t)$ and i_{dc} are the ac and dc parts of the photocurrent respectively, then the output of the ac amplifier is

$$[i_{ac}(t)]_{out} = G_{AC} i_{ac}(t)$$

and the output of the dc amplifier is

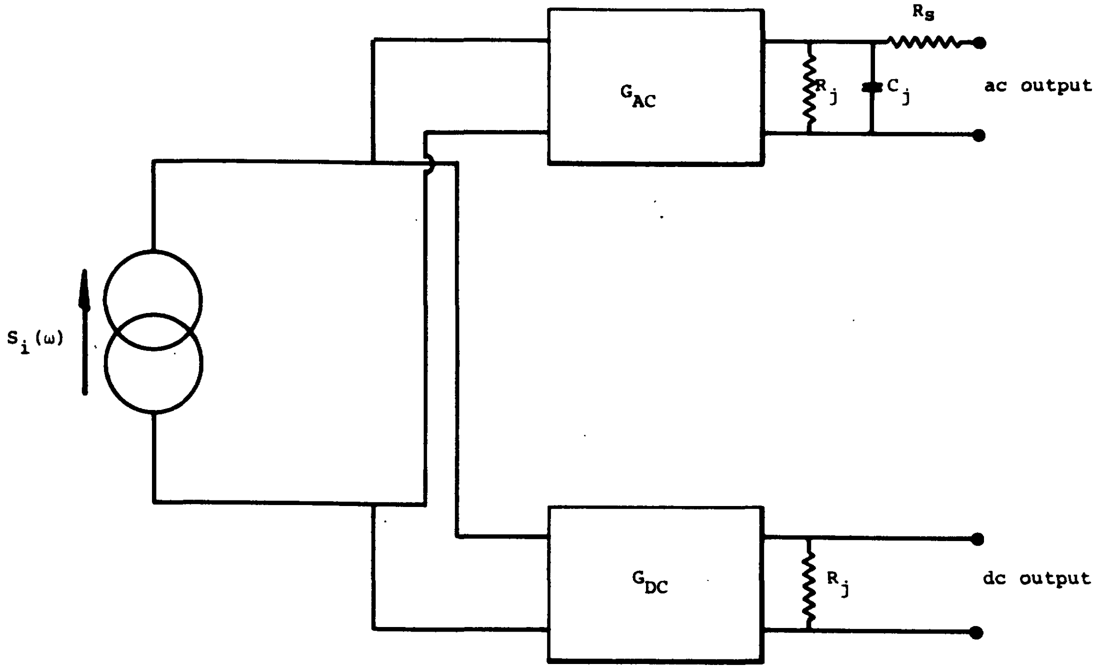
R_s
G_{AC}
R_j
C_j
ac output
$S_i(\omega)$
G_{DC}
R_j
dc output

Figure 3-31 The general equivalent circuit for a photodetector having arbitrary internal gain.

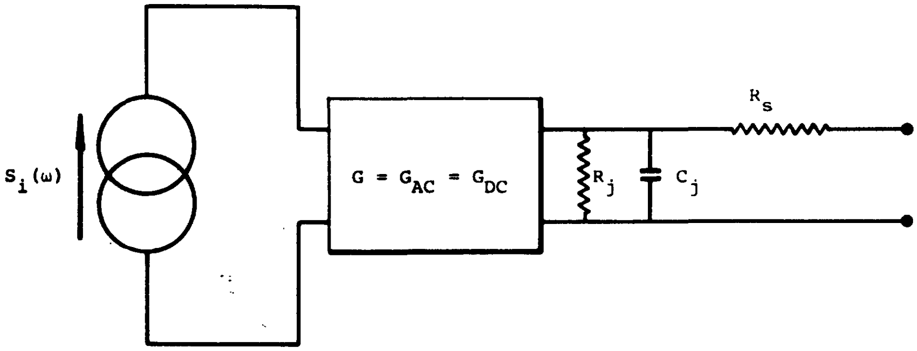
R_s
$S_i(\omega)$
$G = G_{AC} = G_{DC}$
R_j
C_j

Figure 3-32 The general equivalent circuit for an arbitrary gain detector with coincident ac and dc outputs.

$$[i_{dc}]_{out} = G_{DC} i_{dc}$$

where G_{DC} and G_{AC} are constants. The usual gain mechanisms, namely, electron multiplication by secondary emission and avalanche carrier multiplication, are indeed pure current gain phenomena. Moreover, the small amount of data available on the inherent noise of the multiplication process supports the assumption of an essentially noiseless amplification.[49,50] Under these circumstances the equivalent circuits presented in Figs. 3-31 and 3-32 may be redrawn as in Fig. 3-33.

For the purposes of an ac analysis then, the characteristics of a photomixer with a gain G_{AC} are identical to those of a unity gain detector with a photocurrent power spectral density $G_{AC}^2 S_i(\omega)$. In particular, the optimum load, $\underline{Z}_L$, for maximum power transfer and uniform frequency response is again an inductively compensated resistance R_L whose value is given by Eq. (3-185). Equation (3-186), the desired relationship between the load current and the photocurrent, now becomes

$$I_{LOAD}^2(\omega) = G_{AC}^2 S_i(\omega) \tag{3-192}$$

for the range of frequencies $(0 \leq \omega \leq 10\Gamma)$. Finally, considering only the shot-noise term of $S_i(\omega)$, we have F_R from Eq. (3-187) as

$$F_R = \frac{2\underline{k}T}{G_{AC}^2 e R_L i_p} \tag{3-193}$$

Since F_R is the ratio of thermal to shot-noise power as seen either at the load or at the photocathode, the effect of an internal gain can be described in two equivalent ways. In the first, the gain process can be viewed

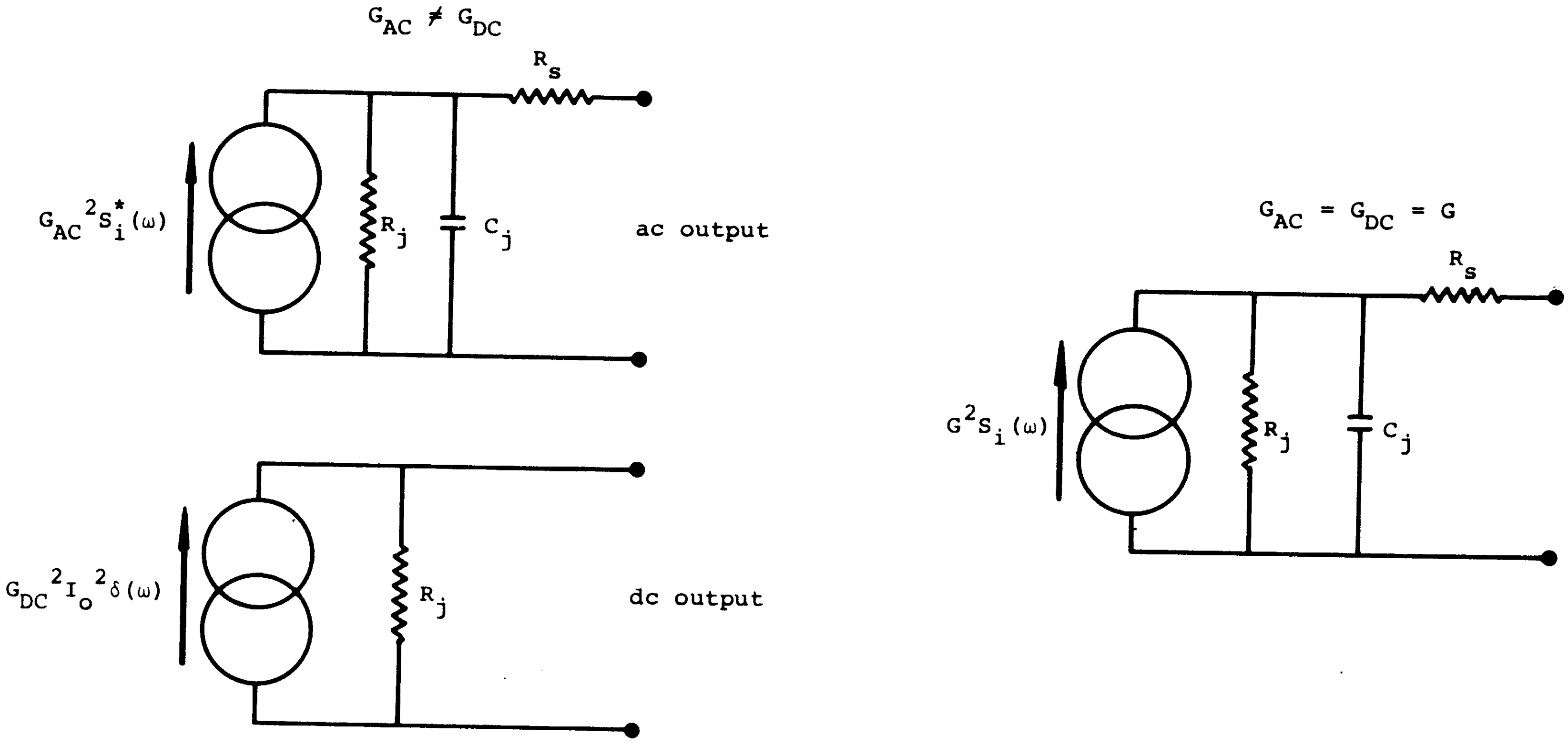

$G_{AC} \neq G_{DC}$
R_s
$G_{AC}^2 S_i^*(\omega)$
R_j
C_j
ac output
$G_{DC}^2 I_o^2 \delta(\omega)$
R_j
dc output
$G_{AC} = G_{DC} = G$
R_s
$G^2 S_i(\omega)$
R_j
C_j

Figure 3-33 Simplified equivalent circuits for arbitrary gain photomixers having noiseless internal current amplification.

as enhancing the photocurrent shot-noise power which is dissipated in the load relative to a fixed thermal noise power. In the second the effect of the gain may be taken as an apparent decrease in the thermal noise power of the load as seen by the photocurrent. In either case the result is a reduction in F_R by the factor G_{AC}^2.

Writing the dc photocurrent, i_p, in terms of the total optical power, P, incident on the detector gives F_R as

$$F_R = \left(\frac{2kT}{\varepsilon e^2}\right)\frac{\hbar\omega_o}{P G_{AC}^2}\cdot\frac{1}{R_L} \tag{3-194}$$

If we demand that F_R satisfy the condition ($F_R \leq 0.1$) in order to make the effects of thermal noise negligible then Eq. (3-194) yields a requirement on P of the form

$$P \geq 10\left(\frac{2kT}{\varepsilon e^2}\right)\frac{\hbar\omega_o}{G_{AC}^2}\cdot\frac{1}{R_L} \tag{3-195}$$

For the case $G_{AC} = 1$ this inequality reduces to the result derived in the preceding section. The typical values of G_{AC} quoted in column V of Table IV range from $G_{AC} = 2$ for the Bell Labs point contact germanium photodiode up to $G_{AC} = 10^6$ for the RCA 7265 photomultiplier. Therefore, on the basis of Eq. (3-195), the presence of an internal gain will represent a reduction of from 4 to 10^{12} in the minimum total incident power necessary to achieve shot-noise limited operation as compared to the result for an otherwise identical unity gain mixer. This reduction is extremely important in view of the conclusions given in the preceding section concerning the usefulness of unity gain detectors.

The importance of thermal noise problems for the photodetectors listed in Table IV as having ($G_{AC} \neq 1$)

can be decided on the basis of the data presented in Figs. 3-34, 3-35, and 3-36. Figure 3-34 shows the optimum load resistance, R_L, for each of these detectors plotted versus the half-width of the spectrum of the incident optical field. For two of the devices, the two crossed field photomultipliers, the value of R_L is fixed at $R_L = 50\Omega$ by the inherent design of the mixer output coupling and is therefore independent of Γ. This fact is noted in column VIII of Table IV. The remaining three mixers are capable of operating into an arbitrary load impedance and for each of these the optimum value of R_L was calculated using Eq. (3-185) and the values of C_j listed in Table IV. As in Fig. 3-28 the data on R_L for a given detector extends up to a maximum half-width determined by the transit time cutoff frequency, ω_{tr}, and the relation $(10\Gamma = \omega_{tr})$. In addition we again assume that R_L has a maximum permissible value of $R_L = 10^7\Omega$ and also terminate the curves at this point.

Combining the values of R_L given in Fig. 3-34 with Eq. (3-195) yields the minimum total optical input power necessary to achieve the condition $(F_R \leq 0.1)$ as a function of Γ. The results of this calculation are shown in Fig. 3-35 for the case of $T = 300°K$ and an incident wavelength $\lambda_{air} = (2\pi c/\omega_o)$, of $\lambda_{air} = 6328$ Å. As before the high frequency limits correspond to the condition $(10\Gamma = \omega_{tr})$.

Consider the crossed-field PMT's first. Since the optimum load resistance for both of these detectors is independent of Γ, the total optical power required to swamp the thermal noise is a constant fixed only by the gain, G_{AC}; the quantum efficiency, ε; and the load resistance $R_L = 50\Omega$. In spite of the small value of R_L the large internal gains that are characteristic of photomultipliers are sufficient to yield a condition on

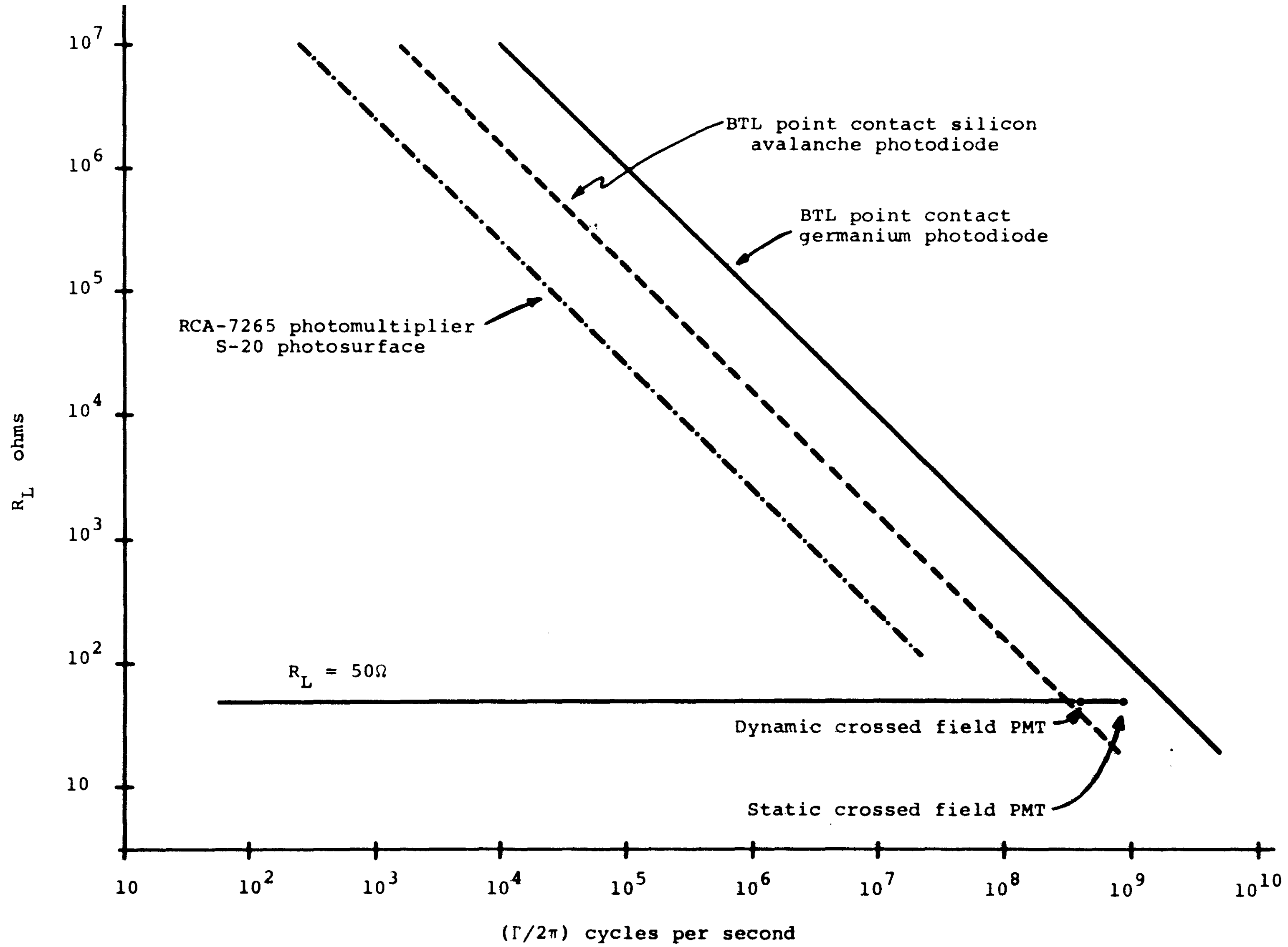

Figure 3-34 The optimum load resistance for some typical arbitrary gain photodetectors.

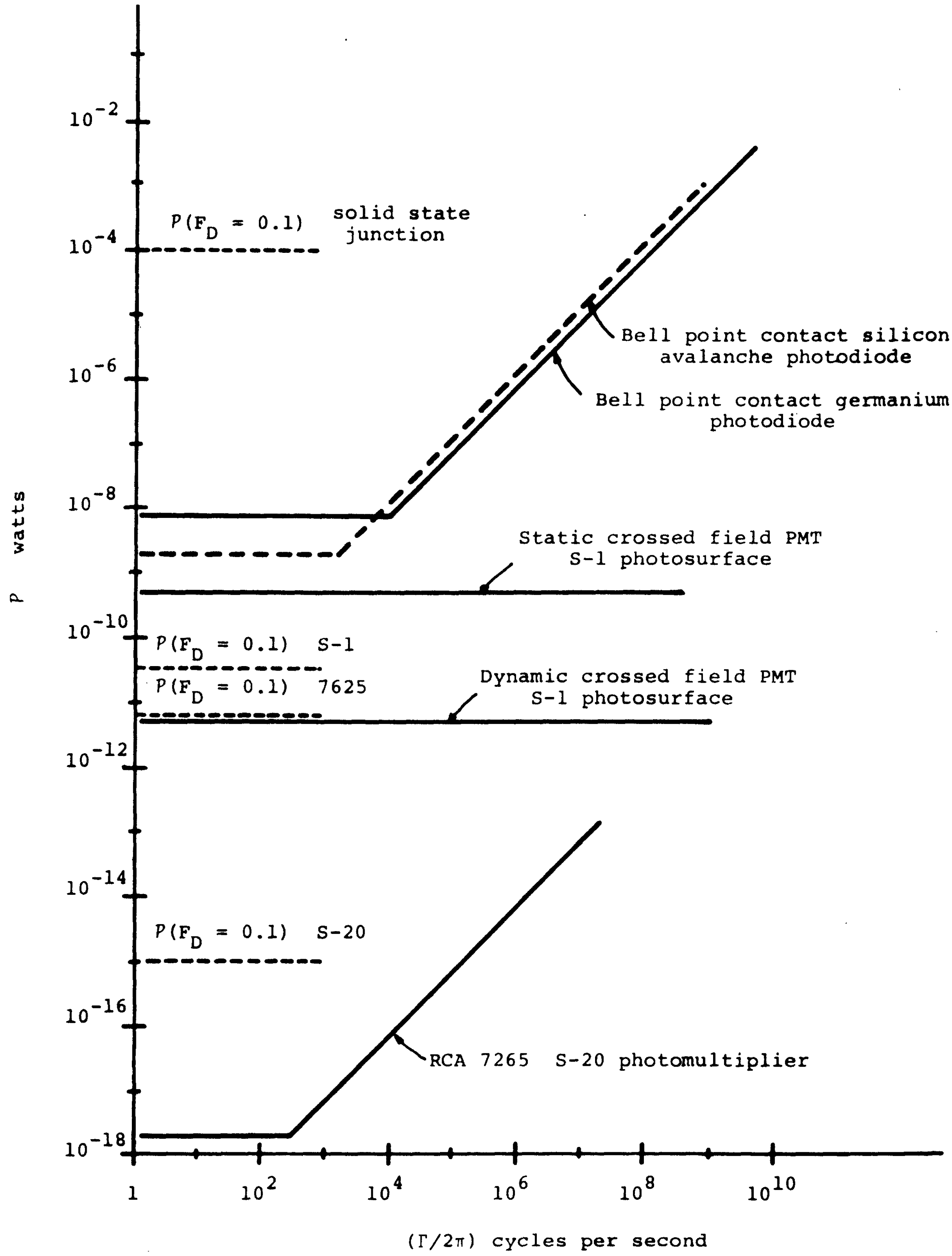

Figure 3-35 The total incident optical power required to swamp the thermal noise of an optimally loaded, arbitrary gain photodetector .

$\mathcal{P}$ which in both cases is comparable to the requirement on $\mathcal{P}$ set by dark current. For comparison the power necessary to override the room temperature dark equivalent input power of a 1 mm diameter S-1 photocathode is also indicated in Fig. (3-35) with the label $[\mathcal{P}(F_D=0.1)$ S-1].

The remaining curves of $\mathcal{P}$ versus Γ show the same two step behavior encountered in Fig. 3-29; a horizontal section corresponding to the range of half-widths where R_L has its limiting value $R_L = 10^7\Omega$ and a region in which $\mathcal{P}$ is proportional to Γ as per Eq. (3-190). Of particular interest is the RCA 7265 photomultiplier whose enormous gain capability results in values of $\mathcal{P}$ which are at least an order of magnitude below those required to overcome the room temperature dark current. However, this is, in part, due to the rather large dark current associated with this detector because of its 2" diameter photocathode. For example, compare the two conditions on $\mathcal{P}$ that yield $(F_D=0.1)$ which are given in Fig. 3-35 as $[\mathcal{P}(F_D=0.1)$ 7265] and $[\mathcal{P}(F_D=0.1)$ S-20]. The latter value corresponds to a 1 mm diameter active photosurface.

A second advantage of internal gain is evident in Fig. 3-35 from the fact that in no case does the total power necessary to swamp the thermal noise exceed the maximum input capability of the mixer, $\mathcal{P}_{MAX}$. For the detectors of interest here, $G_{DC} \neq 1$, $\mathcal{P}_{MAX}$ is related to the maximum allowed dc output current, $(I_{OUT})_{MAX}$, by the relation

$$(I_{OUT})_{MAX} = G_{DC}(\varepsilon e/\hbar\omega_o)\mathcal{P}_{MAX} \qquad (3\text{-}196)$$

For the usual situation $G_{DC} = G_{AC} = G$, and a fixed value of $(I_{OUT})_{MAX}$, Eq. (3-195) shows that the ratio $[\mathcal{P}/\mathcal{P}_{MAX}]$

will decrease as (1/G). Therefore, although an increasing gain does produce a corresponding decrease in allowable input power, the total power required to give (F_R=0.1) decreases at a more rapid rate.

Finally on using the results given in Fig. 3-35 and the ideal sensitivity curves of Fig. 3-21 we can calculate the desired ratio, $[\mathcal{P}/\mathcal{P}_{COH}]$, which is plotted in Fig. 3-36 versus the optical line width, Γ. From these curves and the discussion of Sections F.3.a and F.3.b we may draw the following conclusions:

(1) From the standpoint of both thermal noise and dark current the three photomultiplier detectors can all achieve ideal sensitivity in a self-beat spectrometer capable of accepting incident light from a reasonable number of coherence areas $\mathcal{N} \geq [\mathcal{P}/\mathcal{P}_{COH}]$. The worst case corresponds to $\mathcal{N} \simeq 5 \times 10^4$. These same detectors can also yield ideal sensitivity in a superheterodyne spectrometer with a local oscillator power that exceeds the minimum requirement[§] $[\mathcal{P}/\mathcal{P}_{COH}] = 100$ by less than a factor of 10^3.

(2) Although the gain avilable in solid state junction devices does decrease the ratio of $[\mathcal{P}/\mathcal{P}_{COH}]$ which is necessary to maintain the condition ($F_R \leq 0.1$), the dark current of these mixers already imposes[†] the constraint $[\mathcal{P}/\mathcal{P}_{COH}] > 10^9$ for all Γ even in the limit of infinite gain. Therefore, these detectors are unsatisfactory mixers for self-beat spectrometers. Moreover, because of the severe restrictions which large values of $[\mathcal{P}/\mathcal{P}_{COH}]$ place on local oscillator amplitude modulation they are also unsuitable for use in optical superheterodyne receivers which have an intermediate frequency near $\omega_1 = 0$.

[§] Chapter 3, Section D.2.

[†] Chapter 3, Section F.3.

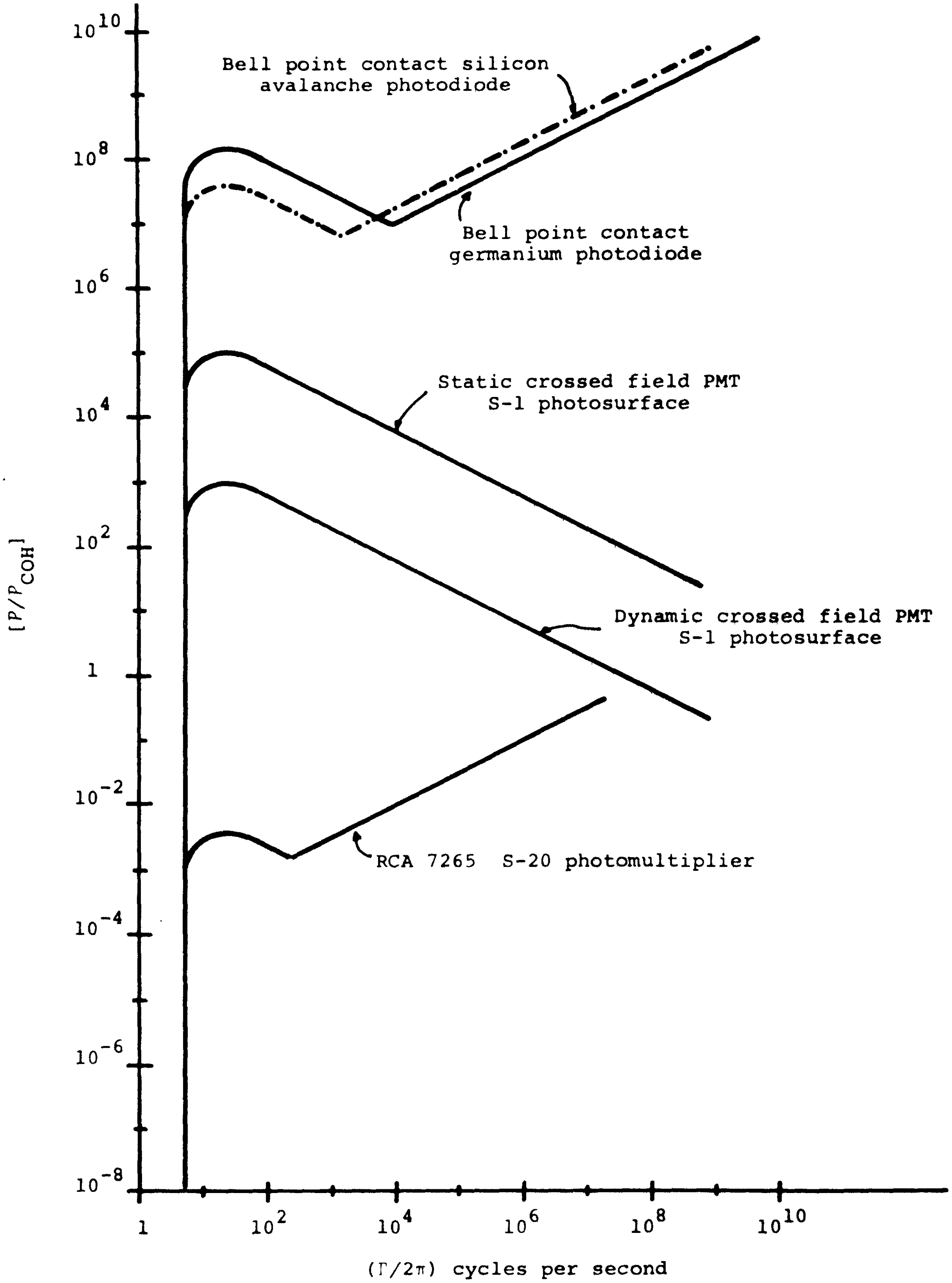

Figure 3-36 The ratio of the power required to swamp the Johnson noise in the photomixer load to the power per coherence area in the signal necessary to achieve $(S/N)_{OUT} = 1$.

c. The Case of a Non-Zero Intermediate Frequency and Arbitrary Gain

Having considered both photomixer configurations that operate with the beat note spectrum centered at $(\omega=0)$, we now examine the case of the optical superheterodyne spectrometer utilizing a non-zero intermediate frequency. As was discussed in Section F.3.b this latter situation will tend to ease the requirements imposed on local oscillator amplitude stability by large values of $[\mathcal{P}/\mathcal{P}_{COH}]$; however, in order to determine the nature of this advantage, if any, we must decide how the thermal noise properties of the optimum load circuit differ from those characteristic of the case $(\omega_1=0)$. In particular we must ask if the less severe conditions on local oscillator stability are not partially or totally offset by increases in the value of $[\mathcal{P}/\mathcal{P}_{COH}]$. In the present analysis we will attempt to answer the following questions:

(1) Is there an optimum choice for the intermediate frequency, ω_1, when the optical spectrum under investigation is a Lorentzian with a half-width of Γ radians per second?

(2) What is the optimum load impedance, $\underline{Z}_L$, for a given i.f. frequency from the standpoint of power transfer?

(3) Is the frequency response of this load circuit consistent with that required to unambiguously examine the signal part of the photocurrent spectrum?

(4) What are the values of $[\mathcal{P}/\mathcal{P}_{COH}]$ that characterize the load which is the best compromise between frequency response and maximum power transfer?

(5) How do these values compare with those obtained for the case $(\omega_1=0)$?

Section F.4.b showed that the electrical characteristics of a unity gain detector are described by the same results that apply to a detector with arbitrary gain; therefore, we will immediately adopt the equivalent circuits shown in Fig. 3-33 as the basis for the present discussion. However, the choice of the optimum load for these circuits now depends critically on the i.f. frequency, ω_1, and the ratio of the i.f. frequency to the line width of the current spectrum under investigation, (ω_1/Γ). Under normal circumstances we have $(\omega_1 >> \Gamma)$ so that in actuality the load need only achieve maximum power transfer over the relatively narrow band of interesting frequencies near $(\omega = \omega_1)$. The appropriate form of $\underline{Z}_L$ for this situation can be found from the circuit analysis outlined below.

Suppose we represent the equivalent circuits of Fig. 3-33 together with an arbitrary load impedance, $\underline{Z}_L$, as shown in Fig. 3-37. The impedance $\underline{Z}$ is in general complex since it corresponds to the parallel combination of R_j and C_j. If this circuit is driven from an ideal current generator whose rms output at a frequency ω is designated as $I(\omega)$, then the rms voltage between points A and B, $\underline{V}_{AB}(\omega)$, is simply

$$\underline{V}_{AB}(\omega) = I(\omega) \frac{\underline{Z}(R_s + \underline{Z}_L)}{(R_s + \underline{Z}_L) + \underline{Z}} \tag{3-197}$$

and the rms current in the load branch is

$$I_{LOAD}(\omega) = \frac{\underline{V}_{AB}(\omega)}{R_s + \underline{Z}_L} = \frac{I(\omega)\underline{Z}}{\underline{Z} + \underline{Z}_L + R_s} \tag{3-198}$$

From this result it follows that the current in the load impedance $\underline{Z}_L$ of Fig. 3-37 is identical to that which would be produced by an ideal voltage generator having an rms output $\underline{V}(\omega) = I(\omega)\underline{Z}$ in the series circuit drawn in Fig.

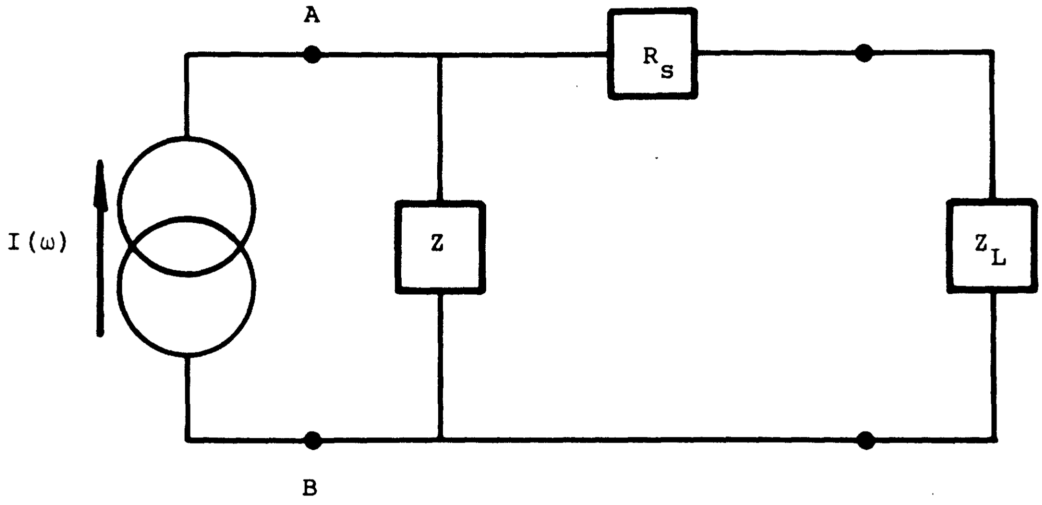

Figure 3-37 General photomixer equivalent circuit with an arbitrary load.

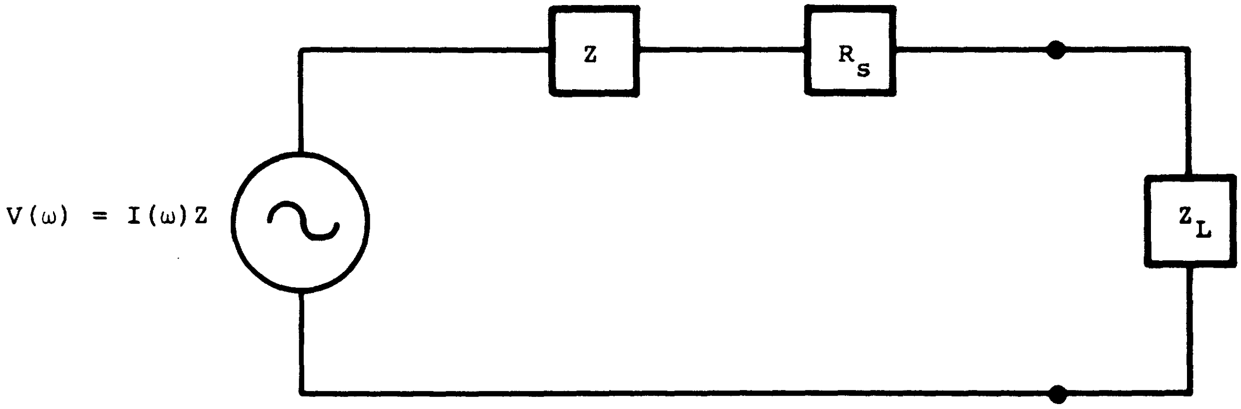
V(ω) = I(ω)Z
Z
R_s
Z_L

Figure 3-38 Voltage generator series equivalent circuit for a photomixer with an arbitrary load impedance.

3-38. That is, the current generator equivalent circuit representation of a photomixer can be transformed to a voltage generator equivalent circuit involving only series elements. This step is an important simplification in the determination of the optimum load impedance. In fact, the fundamental power transfer theorem[47] of electrical engineering states that a circuit of the type shown in Fig. 3-38 will deliver the theoretical maximum power to the load at the frequency ω when $\underline{Z}_L$ satisfies the condition

$$\underline{Z}_L = (\underline{Z} + R_s)^* = \underline{Z}^* + R_s \tag{3-199}$$

This optimum impedance is called a complex conjugate load. If we neglect R_j so that $\underline{Z}$ is the impedance of the junction capacitance, C_j, then we have

$$\underline{Z} = \frac{1}{j\omega C_j}$$

and

$$\underline{Z}^* = \frac{j}{\omega C_j}$$

The positive imaginary impedance $\underline{Z}^*$ represents an inductance, L, whose impedance is

$$\underline{Z}_\ell = j\omega L = \frac{j}{\omega C_j} \tag{3-200}$$

Therefore, the ideal load from the standpoint of power transfer at a single frequency ω is a series combination of a resistance, R_s, and an inductance, L, where the latter satisfies the requirement

$$\omega^2 L C_j = 1 \tag{3-201}$$

This is precisely the condition of series resonance between the load inductance and the internal capacitance of the mixer.

Let us examine the frequency response and power transfer characteristics of the complex conjugate load when L is chosen to resonate with C_j at the intermediate frequency ω_1. The appropriate circuit schematic is drawn in Fig. 3-39. The impedance, $\underline{Z}_1$, presented to the generator is

$$\underline{Z}_1 = \frac{1}{j\omega C_j} + 2R_s + j\omega L = \frac{(1 - \omega^2 LC_j) + j2\omega C_j R_s}{j\omega C_j}$$

leading to a current in the load branch given by

$$I_{LOAD}(\omega) = \frac{V(\omega)}{\underline{Z}_1} = \frac{I(\omega)}{j\omega C_j} \frac{j\omega C_j}{(1 - \omega^2 LC_j) + j2\omega C_j R_s}$$

$$= \frac{I(\omega)}{(1 - \omega^2 LC_j) + j2\omega C_j R_s} \qquad (3\text{-}202)$$

Knowing the load current, $I_{LOAD}(\omega)$, we may calculate the power delivered to the load, $P_L(\omega)$, by using the relation

$$P_L(\omega) = I_{LOAD}(\omega) I^*_{LOAD}(\omega) R_s = \frac{I^2(\omega) R_s}{(1 - \omega^2 LC_j) + (2\omega C_j R_s)^2} \qquad (3\text{-}203)$$

Although $I^2(\omega)$, as written in Eq. (3-203), represents the mean-square generator output current at the frequency ω it is equally valid to interpret this quantity as a current power spectral density. In this case $P_L(\omega)$ is the power per unit bandwidth dissipated in the load at the frequency ω. It follows that $I^2(\omega)$ can be taken to be the photo-

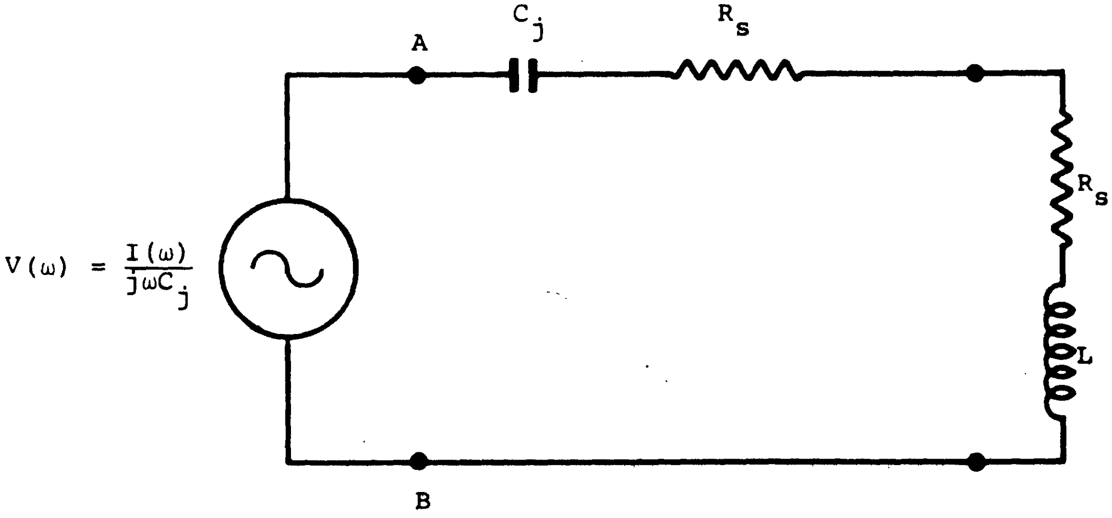
A
C_j
R_s
R_s
$V(\omega) = \frac{I(\omega)}{j\omega C_j}$
L
B

Figure 3-39 Series equivalent circuit of a photomixer terminated by a complex conjugate load.

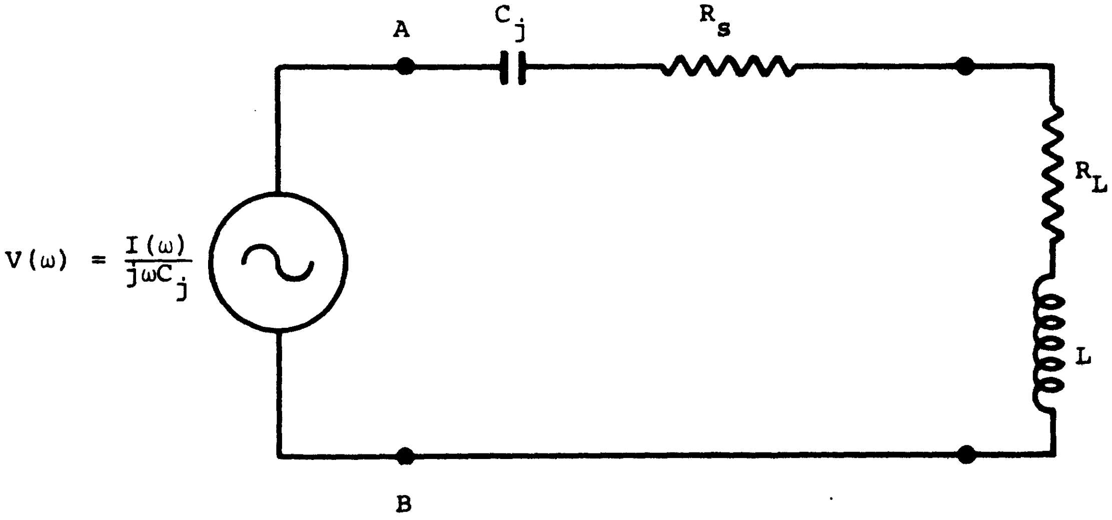
A
C_j
R_s
R_L
$V(\omega) = \frac{I(\omega)}{j\omega C_j}$
L
B

Figure 3-40 Series equivalent circuit of a photomixer terminated by a modified complex conjugate load. The resistive component of the load is allowed to take on an arbitrary value.

current power spectral density as seen after internal amplification in the mixer. Writing the product (LC_j) in terms of ω_1 with the help of the resonance condition $(\omega_1{}^2 LC_j = 1)$ we have $P_L(\omega)$ as

$$P_L(\omega) = \frac{G^2 S_i(\omega)}{\left(1 - \frac{\omega^2}{\omega_1{}^2}\right) + (2\omega C_j R_s)^2} \quad (3\text{-}204)$$

Thus the power delivered to the load at the i.f. frequency is

$$P_L(\omega_1) = \frac{G^2 S_i(\omega)}{(2\omega C_j)^2 R_s} = \frac{G^2 S_i(\omega)\ X_{C_j}(\omega_1)}{4R_s} \quad (3\text{-}205)$$

where $X_{C_j}(\omega_1)$ is the reactance of C_j. By comparing this result with Eqs. (3-183) and (3-192) we find that the complex conjugate load is equivalent to a pure resistive load $(R_L)_{eq}$ whose resistance is a function of the i.f. frequency and given by

$$(R_L)_{eq} = \frac{1}{4(\omega C_j)^2 R_s} = \frac{X_{C_j}(\omega_1)}{4R_s} \quad (3\text{-}206)$$

The ratio of this equivalent load resistance to the optimum value of R_L found for $\omega_1 = 0$, that is the ratio of the powers delivered to the load in each case, clearly hinge directly on the choice of the intermediate frequency. Although Eq. (3-205) would indicate that the most favorable situation corresponds to the lowest possible value of ω_1 there are two additional features of the resonant load yet to be considered. The first is the question of uniformity in its frequency response in relation to the line width of the signal part of the photocurrent spectrum.

If we make the reasonable assumption that ω_1 must be much less than the RC cutoff frequency of the detector it follows that $(\omega_1 R_s C_j)$ satisfies the condition $(\omega_1 R_s C_j << 1)$. In this case Eq. (3-204) shows that the load response function defined by

$$|H(\omega)|^2 = [P_L(\omega)/G^2 S_i(\omega)] \qquad (3\text{-}207)$$

has the form

$$|H(\omega)|^2 = \frac{(\omega_1{}^2/4)}{(\omega-\omega_1)^2 + \omega_1{}^4 C_j{}^2 R_s{}^2} \qquad (3\text{-}208)$$

That is, the efficiency of power transfer between the photodetector and a tuned load is a Lorentzian peaked at the i.f. frequency and having a half-width at half-response given by

$$\Delta\omega_{\frac{1}{2}} = \omega_1{}^2 C_j R_s \qquad (3\text{-}209)$$

The ratio $[\omega_1/(\Delta\omega_{\frac{1}{2}})]$ is normally defined as the Q of the load resonance, i.e.

$$Q = \frac{\omega_1}{\Delta\omega_{\frac{1}{2}}} = \frac{1}{\omega_1 C_j R_s} = \frac{X_{C_j}}{R_s} \qquad (3\text{-}210)$$

Equation (3-208) shows that the resonant load acts essentially as a filter; only those frequencies that lie inside the filter bandwidth $\Delta\omega_f' = 2\Delta\omega_{\frac{1}{2}}$ are passed on to the spectrometer electronic system. In order to achieve a uniform response over the entire frequency range of interest in the beat signal spectrum we would then require $\Delta\omega_f' \geq 10\Gamma$. However, the inductance L may be tuned in such a way that the center of the load response tracks the tunable filter used to examine the photocurrent spectrum; in this case $\Delta\omega_f'$ need only satisfy the weaker inequality $(\Delta\omega_f' \geq \Delta\omega_f)$. Since the tunable filter bandwidth $\Delta\omega_f$ is ordinarily taken as some fraction a of the line width Γ ($\Delta\omega_f = a\Gamma$, where typically $a \simeq 0.1$) we derive a condition relating $\Delta\omega_{\frac{1}{2}}$ and Γ, namely

$$\Delta\omega_{\frac{1}{2}} \geq (a/2)\Gamma \tag{3-211}$$

This result combined with Eq. (3-209) yields a minimum allowable value for ω_1 in terms of the line width Γ as

$$\omega_1{}^2 R_s C_j \geq (a/2)\Gamma \tag{3-212}$$

This condition will guarantee the desired frequency response when $\underline{Z}_L$ is taken as a complex conjugate load.

A second consideration also places a lower limit on the intermediate frequency. In order to avoid a distortion in the shape of the signal part of the photocurrent spectrum all the frequencies of interest in this signal must lie in the region $\omega > 0$. This point can be understood as follows. If the beat note spectrum overlaps the point $\omega = 0$ then the local oscillator frequency must lie within that range of optical frequencies in which the incoming signal has a significant power spectral density. But in this situation the beat-note observed at a frequency ω actually consists of two contributions, namely, a mixing between the local oscillator at the frequency ω_{LO} and the signal power at the two frequencies $(\omega_{LO}+\omega)$ and $(\omega_{LO}-\omega)$. This "overlap" distorts the shape of the optical spectrum as seen via the photocurrent.

Of course, one of these two beat notes can always be made negligible by choosing ω_{LO} to be sufficiently removed from the center frequency of the optical signal. This is equivalent to demanding that ω_1 be large enough such that the tail of the signal part of the current spectrum is insignificantly small at $(\omega = 0)$. Assuming that the heterodyne beat signal can be disregarded when it falls to 1% of its peak value we obtain a numerical condition on ω_1 given by

$$\omega_1 \geq 10\Gamma \qquad (3\text{-}213)$$

Let us consider the three results presented in Eqs. (3-205), (3-212), and (3-213). Equation (3-205) states that the most favorable intermediate frequency from the standpoint of power transfer alone is the lowest possible value. Equation (3-213) places a fundamental lower limit on the choice of ω_1 which must be satisfied if we wish to obtain an unambiguous measure of the spectrum of the incident optical field. This condition must always be satisfied. Equation (3-212) represents a secondary limit on ω_1 which is necessary in order to achieve the required frequency response if we use a complex conjugate load. We can decide on the importance of this secondary limit from the following analysis.

Suppose that the fractional resolution $a = (\Delta\omega_f/\Gamma)$ used to examine the photocurrent spectrum is $a = (0.1)$. Then Eq. (3-212) can be restated as

$$\omega_1^2 \geq (0.05)\Gamma\omega_{RC} \qquad (3\text{-}214)$$

where $\omega_{RC} = (1/R_sC_j)$ is the RC cutoff frequency of the mixer. Designating this limit on ω_1^2 as $(\omega_1^2)_2$ and taking the ratio of this result to the square of the inequality in Eq. (3-213) we have

$$\frac{(\omega_1{}^2)_2}{(\omega_1{}^2)} \simeq \frac{(0.05)\Gamma\omega_{RC}}{100\Gamma^2} \simeq 5 \times 10^{-4}(\omega_{RC}/\Gamma) \qquad (3\text{-}215)$$

Now the largest value of Γ which can be handled by a particular photodetector is determined by its transit time cutoff frequency, ω_{tr}. If ω_1 is its minimum allowed value ($\omega_1 = 10\Gamma$) then the highest frequency of interest in the signal part of the photocurrent spectrum is $(\omega_1 + 10\Gamma) = 20\Gamma$. Therefore, the maximum permissible half-width, Γ_m, is simply $\Gamma_m = (\omega_{tr}/20)$. In practical photomixers ω_{tr} is smaller than ω_{RC}, a typical ratio being $(\omega_{RC}/\omega_{tr}) \simeq 3$. Using these relationships we can give Eq. (3-215) in terms of Γ and Γ_m as

$$\frac{(\omega_1{}^2)_2}{(\omega_1{}^2)} \simeq 0.03\left(\frac{\Gamma_m}{\Gamma}\right) \qquad (3\text{-}216)$$

That is, for half-widths greater than approximately 3% of the maximum useful value the condition ($\omega_1 = 10\Gamma$) is dominant. Under these circumstances the resonance width of the complex conjugate load is always sufficient to give the desired frequency response. On the other hand for $\Gamma < (0.03)\Gamma_m$ the secondary limit on ω_1 imposed by Eq. (3-212) is dominant. In this case if we choose ($\omega_1 = 10\Gamma$) and use a complex conjugate load then the Q of the resulting resonant circuit formed by the load and the internal circuit elements of the mixer is too high to permit all the frequencies of interest to be delivered to the remaining electronics of the spectrometer. In the latter situation the Q must be decreased.

From the analysis leading to Eq. (3-212) we find that one method for reducing the Q of the load resonance is simply to increase the intermediate frequency beyond the value $\omega_1 = 10\Gamma$ until Eq. (3-212) is satisfied. However a second possible approach is to keep ω_1 fixed at $\omega_1 = 10\Gamma$ and decrease Q by making the resistive component of the load larger than the value R_s. Naturally, both of these methods lead to a decrease in the amount of power delivered to the load at the i.f. frequency. To decide on an optimum load impedance we must therefore determine which case yields the maximum power transfer consistent with the desired value of Q.

When the resistive component of $\underline{Z}_L$ has an arbitrary value R_L, as shown in Fig. 3-40, the impedance, $\underline{Z}_1$, presented to the voltage generator $\underline{V}(\omega)$ is

$$\underline{Z}_1 = \frac{1}{j\omega C_j} + (R_s+R_L) + j\omega L = \frac{(1-\omega^2 LC_j) + j\omega C_j(R_s+R_L)}{j\omega C_j} \qquad (3\text{-}217)$$

If the inductance L resonates with C_j at the intermediate frequency, then we find that the power dissipated in the load at the frequency ω is given by

$$\begin{aligned} P_L(\omega) &= I_{LOAD}(\omega)\, I^*_{LOAD}(\omega)\, R_L \\ &= \frac{G^2 S_i(\omega) R_L}{\left(1-\frac{\omega^2}{\omega_1^2}\right)^2 + \omega^2 C_j^2 (R_s+R_L)^2} \qquad (3\text{-}218) \end{aligned}$$

In particular the power delivered to the load at the i.f. frequency takes the form

$$P_L(\omega_1) = \frac{G^2 S_i(\omega_1) R_L}{\omega_1^2 C_j^2 (R_s + R_L)^2} \tag{3-219}$$

It is easily verified by direct differentiation that $P_L(\omega_1)$ has its maximum value for $R_L = R_s$, i.e. for the complex conjugate load.

The Q of the photomixer-load circuit now has the form

$$Q = \frac{\omega_1}{\Delta\omega_{\frac{1}{2}}} = \frac{2}{(R_L + R_s)\omega_1 C_j} \tag{3-220}$$

For $R_L = R_s$ we recover the result given in Eq. (3-210). Clearly Q may be decreased by increasing either ω_1 or R_L, or possibly both. To determine the best approach we will write $P_L(\omega_1)$ in terms of the single variable ω_1 in such a way that the expression always satisfies the desired constraint on Q, namely

$$\Delta\omega_{\frac{1}{2}} = \frac{\omega_1}{Q} = \left(\frac{a}{2}\right)\Gamma \tag{3-221}$$

In this case the optimum i.f. frequency can be found by inspection.

Combining Eqs. (3-219), (3-220), and (3-221) yields $P_L(\omega_1)$ at fixed Γ and $\Delta\omega_{\frac{1}{2}}$ in the form

$$[P_L(\omega_1)]_Q = \frac{G^2 S_i(\omega_1) R_L Q^2}{4} = G^2 S_i(\omega_1) R_L (\omega_1/a\Gamma)^2 \tag{3-222}$$

while Eqs. (3-220) and (3-221) combine to give R_L as

$$R_L = \frac{a\Gamma}{\omega_1{}^2 C_j} - R_s \tag{3-223}$$

This last expression specifies the value of R_L required to maintain the desired Q for an arbitrary choice of the i.f. frequency. From Eqs. (3-222) and (3-223) we find the power dissipated in the load at a given intermediate frequency subject to the constraint of a minimum permissible resonance width in the load circuit as

$$[P_L(\omega)]_Q = G^2 S_i(\omega_1) \left\{\frac{1}{a\Gamma C_j} - \left(\frac{\omega_1}{a\Gamma}\right)^2 R_s\right\} \tag{3-224}$$

Since $S_i(\omega_1)$ is independent of the choice of ω_1 the i.f. frequency which yields the condition of maximum power transfer is ($\omega_1 = 0$). Therefore, if the Q of the load must be reduced to obtain the desired frequency response then the condition of optimum power delivery is always obtained by increasing the resistive component of the load at the lowest possible intermediate frequency.

The results which we have found may be summarized in terms of the answers to the first three questions posed at the beginning of the discussion.

(1) There is an optimum choice for the intermediate frequency. When the optical spectrum to be investigated is a Lorentzian with a half-width of Γ rad/sec the choice is ($\omega_1 = 10\Gamma$).

(2) The load impedance which gives the condition of maximum possible power transfer is a complex conjugate load. This load forms a resonant circuit at the operating frequency in conjunction with the internal impedance of the photomixer.

(3) The frequency response of this load is consistent with that required to examine the signal part of the photocurrent spectrum for large values of Γ, i.e. ($\Gamma \geq 0.03\ \Gamma_m$). For smaller values of the half-width the resonance width of the load must be increased by employing a modified complex conjugate load in which the resistive component is larger than the optimum value ($R_L = R_s$).

Having quantitatively fixed the form of the impedance $\underline{Z}_L$ and the i.f. frequency we may now proceed to determine the values of $[P/P_{COH}]$ which are necessary to overcome the Johnson noise. This is most easily done in terms of the apparent resistance presented to the mixer,

$$(R_L)_{eq} \equiv [P_L(\omega_1)/G^2 S_i(\omega_1)]$$

and the formulae of Section F.4.b. Equations (3-224) and (3-205) yield $(R_L)_{eq}$ as

$$(R_L)_{eq} = \begin{cases} \dfrac{1}{a\Gamma C_j} - \left(\dfrac{\omega_1}{a\Gamma}\right)^2 R_s & : \ R_L \geq R_s \\ \\ \dfrac{1}{4\omega_1^{\,2} C_j^{\,2} R_s} & : \ R_L = R_s \end{cases} \qquad (3\text{-}225)$$

This quantity was calculated for some typical detectors using the data presented in Table IV. The results are plotted in Fig. 3-41 versus the line width of the incident optical spectrum. The following assumptions were employed in constructing these curves.

(1) The intermediate frequency is taken as ($\omega_1 = 10\Gamma$).

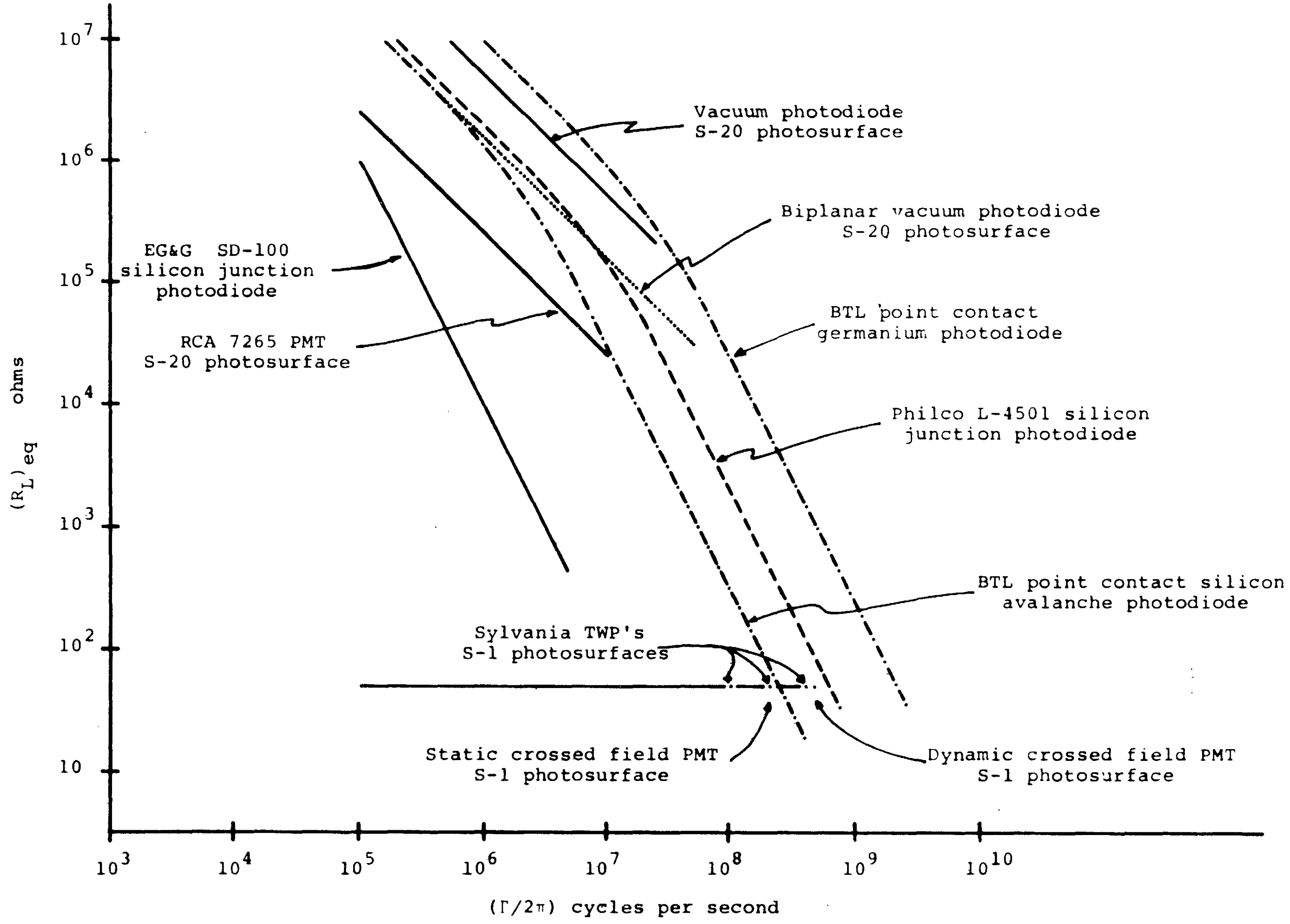

Figure 3-41 Equivalent resistive load for a photomixer terminated in a modified complex conjugate load.

(2) The maximum usable mixer frequency is the transit time cutoff frequency, ω_{tr}. Assuming that the tunable filter used to examine the signal part of the photocurrent spectrum operates between $\omega = \omega_1 = 10\Gamma$ and $\omega = \omega_1 + 10\Gamma = 20\Gamma$ we terminate the curves at $\Gamma = (\omega_{tr}/20)$.

(3) The fractional resolution used in examining the spectrum of the beat signal is $a = (\Delta\omega_f/\Gamma) = (0.1)$.

(4) The maximum permissible value of $(R_L)_{eq}$ is set by circuit leakage at $(R_L)_{eq} = 10^7\Omega$.

(5) The lower limit on intermediate frequency ω_1, fixed by the properties of practical inductors available to resonate with C_j, is $(\omega_1/2\pi) = 10^6$ cps, corresponding to a value of Γ given by $(\Gamma/2\pi) = 10^5$ cps.

The resulting curves for $(R_L)_{eq}$ show three distinct types of behavior, the first being simply $(R_L)_{eq}$ = constant which characterizes those devices limited to operating into a 50Ω termination. A second behavior which is typical of those detectors that have $(R_s \neq 0)$ is seen at large values of Γ, near the maximum permissible half-width. In this regime the appropriate form for $\underline{Z}_L$ is the exact complex conjugate load impedance and $(R_L)_{eq}$ increases with decreasing Γ as $(R_L)_{eq} \propto \Gamma^{-2}$. This corresponds to the case of theoretical maximum power transfer described in Eq. (3-206). For these same detectors we find a break in $(R_L)_{eq}$ when Γ is decreased through that point where R_L is forced to become greater than R_s. For smaller values of Γ power transfer is sacrificed for proper load Q and $(R_L)_{eq}$ increases only as Γ^{-1}. The photosurface devices, which were assumed to have $R_s = 0$, exhibit this latter behavior over their entire useful range.

The importance of the data in Fig. 3-41 lies in its comparison with the results given previously for the case ($\omega_1 = 0$) in Figs. 3-28 and 3-34. This comparison shows that although a superheterodyne spectrometer with a non-zero intermediate frequency must operate at somewhat higher beat frequencies than its ($\omega_1 = 0$) counterparts, there is an enhancement in power transfer obtainable with a resonant circuit load which yields a net advantage at any specific half-width to the case ($\omega_1 \neq 0$). This advantage appears as an increased value of the apparent load resistance presented to the amplified photocurrent. The ratio of the resistances in the two situations, $\omega_1 \neq 0$ and $\omega_1 = 0$, is between two for $\Gamma \simeq \Gamma_m$ to 100 for $\Gamma < (0.03)\Gamma_m$. It is easy to show that, in fact, the greater portion of this gain is achieved simply because of the relaxing of the requirement on the frequency response of the load from $\Delta\omega_{\frac{1}{2}} = 10\Gamma$ to $\Delta\omega_{\frac{1}{2}} = (a\Gamma/2)$. The resonance properties of the circuit merely serve as a means of shifting the point of maximum load response from ($\omega = 0$) to ($\omega = \omega_1$). Of course, it is the fact that this resonance frequency may be changed at will that makes possible the use of a less stringent condition on $\Delta\omega_{\frac{1}{2}}$.

The total incident optical power, P, required to swamp the thermal noise of $(R_L)_{eq}$ for the mixers listed in Table IV was calculated from the data presented in Fig. 3-41 and the condition given in Eq. (3-195), namely

$$P \geq 10\left(\frac{2kT}{\varepsilon e^2}\right) \frac{\hbar\omega_o}{G_{AC}^2} \frac{1}{(R_L)_{eq}} \tag{3-226}$$

This inequality corresponds to the situation ($F_R \leq 0.1$). The results, which are shown in Fig. 3-42, exhibit an improvement over the similar results for $\omega_1 = 0$ in terms of

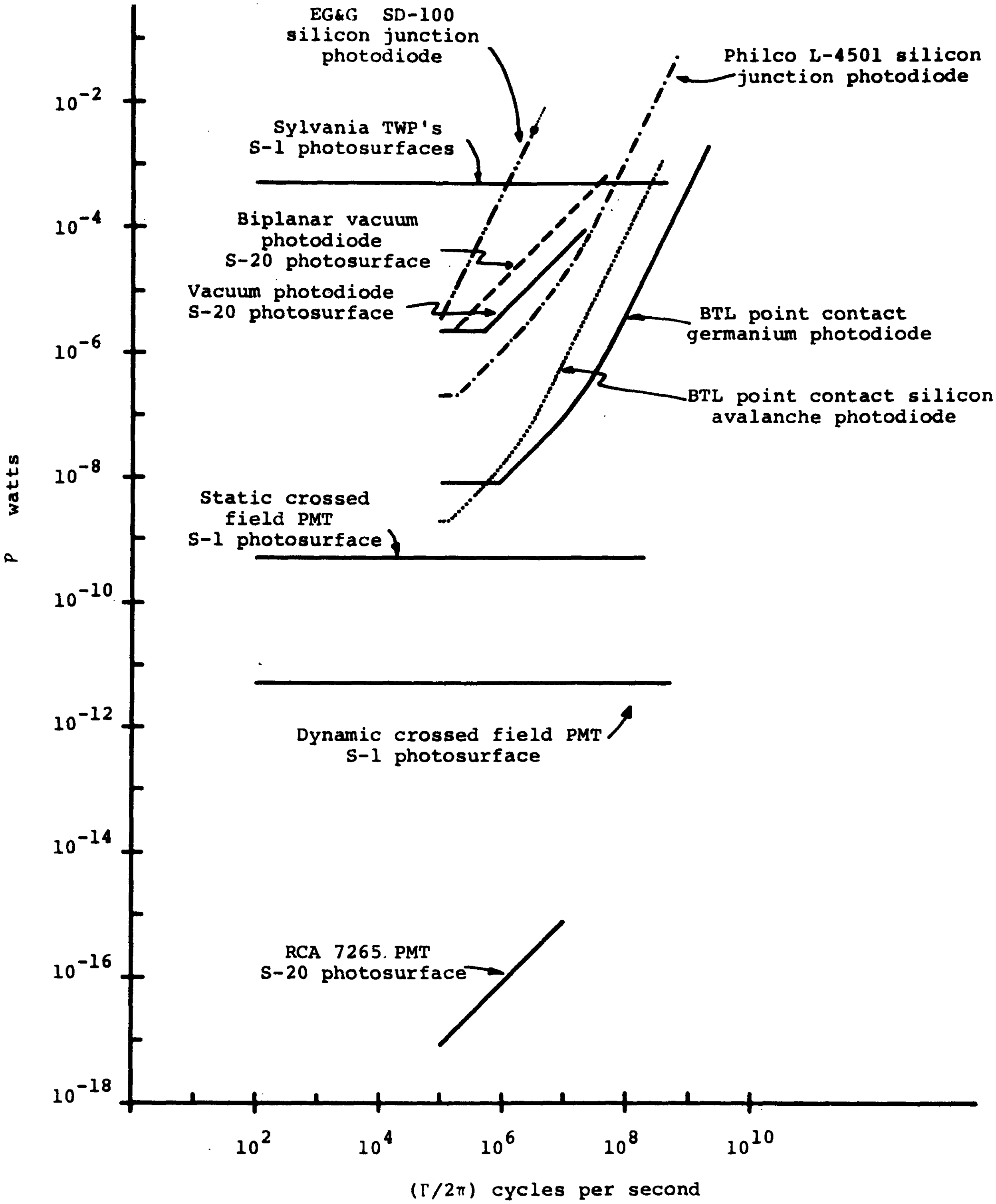

Figure 3-42 The total incident optical power required to overcome the Johnson noise in the load of a photomixer terminated by a modified complex conjugate load.

a reduction in the amount of local oscillator power needed to obtain shot-noise limited operation. This reduction has two immediate consequences. First, all the detectors except the EG&G (SD-100) silicon photodiode now operate well within their maximum power ratings at all allowed values of Γ. Secondly, in the case of the solid state detectors the dark current requirement on P now exceeds the value set by Eq. (3-226) over a rather large fraction of the accessible range in Γ. Therefore, these mixers are ordinarily operating under dark current limited conditions and the effects of Johnson noise may be neglected.

Of particular interest among the detectors represented in Fig. 3-42 are the RCA 7265 photomultiplier tube and the Bell Telephone Laboratories point contact germanium photodiode. As discussed previously the 7265 achieves shot-noise limited operation quite easily because of its large internal gain; however, we note that the Bell Labs diode also requires considerably less incident power than the other solid state mixers. This is not an effect of internal gain but the result of especially small values of both R_s and C_j.

The usefulness of each of the above mixers can be deduced from the plots of the ratio $[P/P_{COH}]$ shown in Fig. 3-43. The data for these curves were obtained from the results of Fig. 3-21. On the basis of previous discussions[§] of the relevance of $[P/P_{COH}]$ we may draw the following conclusions concerning the applicability of the various detectors as mixers in a superheterodyne spectrometer:

[§] Chapter 3, Section F.3.

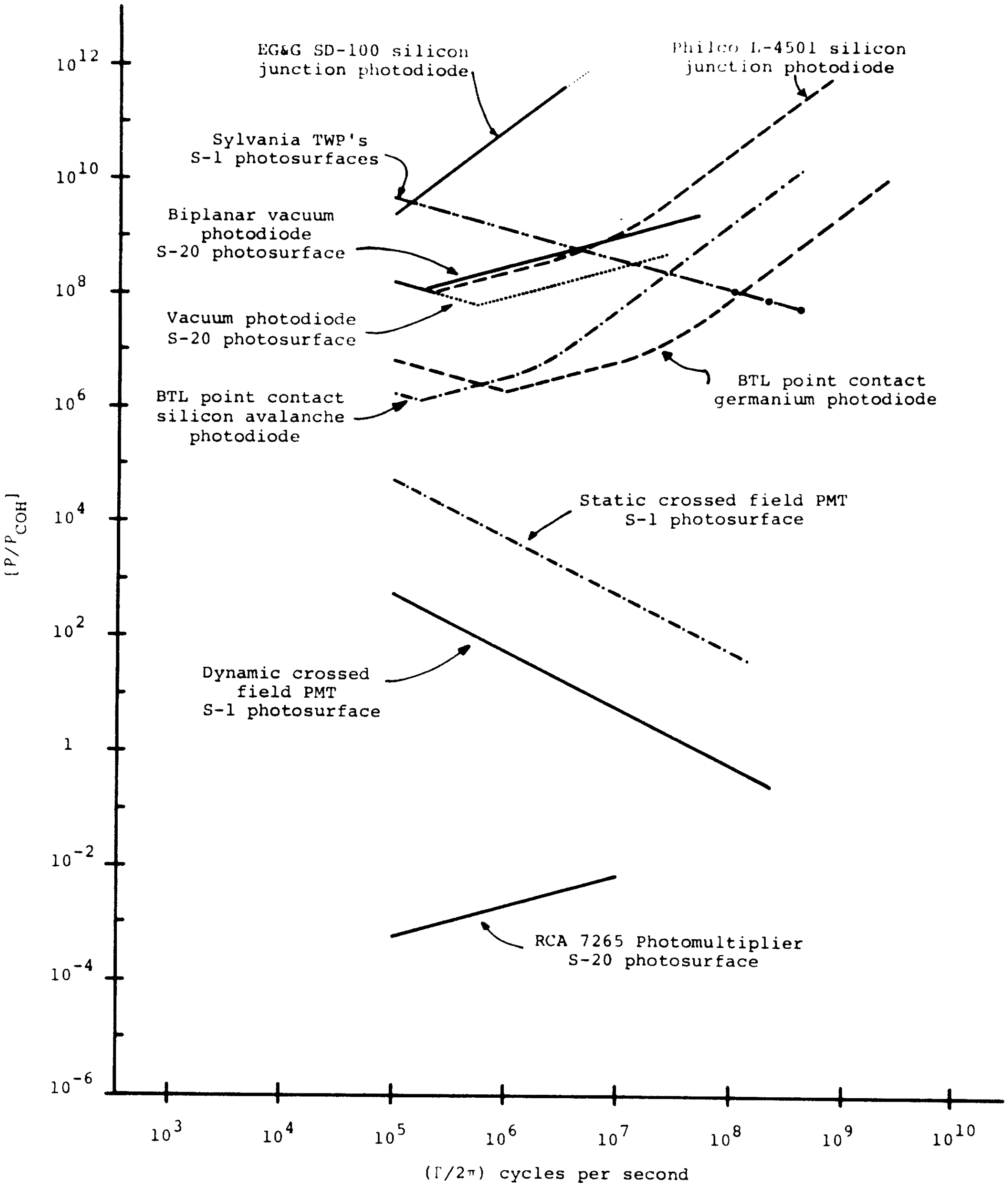

Figure 3-43 The ratio of the total optical input power necessary to swamp thermal noise to the power per coherence area which gives $(S/N)_{OUT} = 1$. The results are given versus the half-width of the incident spectrum $(\Gamma/2\pi)$.

(1) For line widths less than $(\Gamma/2\pi) \simeq 10^7$ cps and in situations where the additional quantum efficiency of a solid state mixer is not crucial, the RCA 7265 photomultiplier is the ideal detector. Its high gain guarantees that shot-noise limited operation can be obtained with the minimum permissible local oscillator power. Therefore, this mixer imposes only slight restrictions on the tolerable local oscillator amplitude modulation.

(2) For line widths between $(\Gamma/2\pi) \simeq 10^7$ cps and $(\Gamma/2\pi) \simeq 10^8$ cps the crossed field photomultipliers represent the best choice of mixer when the relatively low value of ε for the S-1 photosurface is not critical.[§]

(3) The best solid state detector, including those with and without internal current gain, is the Bell Telephone Laboratories point contact germanium photodiode. This mixer achieves its low values of $[P/P_{COH}]$ because of its extremely small junction capacitance, C_j, and dynamic series resistance, R_s. The required local oscillator power exceeds the minimum allowable value $(P = 100P_{COH})$ by a factor that varies between $\simeq 10^4$ for $(\Gamma/2\pi) \simeq 10^6$ cps to $\simeq 10^8$ for $(\Gamma/2\pi) \simeq 2 \times 10^9$ cps. However, since modulation effects become significantly less important with increasing i.f. frequency, these values of $[P/P_{COH}]$ should not place unduly severe limits on the amplitude stability of the local oscillator source.

[§] The values of ε used throughout this thesis refer to $\lambda_{air} = 6328\text{Å}$.

[†] Chapter 3, Section D.2.

5. The Effect of Excess Amplifier Noise

Having dealt with the dark current and thermal noise terms in the expression for F we now turn to an examination of the effects of the unavoidable excess noise that characterizes any practical amplifier. The "amplifier" of interest here is that device which must handle the lowest level signals in the mixing spectrometer electronics and, therefore, which most seriously degrades the pre- and post-detection signal-to-noise ratios. In general this will be the radio frequency amplifier or receiver that is connected to the photomixer output terminals.

The excess noise of an amplifier manifests itself as a current power per unit bandwidth at the device output terminals even under conditions of zero input. Its origin and magnitude may be determined explicitly from the thermal noise and shot-noise characteristics of the amplifier components. However, a much simpler approach which utilizes the concept of an amplifier "noise figure" is sufficient for the present discussion.

Suppose that we consider simultaneously the effects of Johnson noise in the photomixer load and amplifier noise; then the contribution to the signal-to-noise reduction factor F follows from Eq. (3-153) as

$$F_R' = F_R + F_{RA} = \frac{I_R^2(\omega) + I_{RA}^2(\omega)}{I_N^2(\omega)} \qquad (3\text{-}227)$$

The current power spectral densities in Eq. (3-227) are defined as equivalent values referred to the photocathode.* However, as stated above, F may be calculated at any desired point in the signal processing chain by suitably computing the current powers as referred to that point. In the present case it is convenient to work with the currents produced at the photomixer load impedance, that is, at the amplifier input terminals. Using the notation for these currents which was adopted in Eq. (3-176) we have

---

* Chapter 3, Section F.1.

$$F_R' = \frac{I_r^2(\omega) + I_{ra}^2(\omega)}{I_n^2(\omega)} \qquad (3\text{-}228)$$

This relationship may be written in a more interesting form as

$$F_R' = \frac{I_r^2(\omega)}{I_n^2(\omega)} \{1 + \frac{I_{ra}^2(\omega)}{I_r^2(\omega)}\} = F_R\{1 + \frac{I_{ra}^2(\omega)}{I_r^2(\omega)}\} \qquad (3\text{-}229)$$

The quantity

$$1 + \frac{I_{ra}^2(\omega)}{I_r^2(\omega)}$$

when expressed in decibel units is defined as the noise figure (N.F.) of the amplifier.[51] Since this quantity represents the ratio of two powers, rather than two rms currents, we have under the usual conventions[52]

$$\text{N.F.} = 10\, \ell og\{1 + \frac{I_{ra}^2(\omega)}{I_r^2(\omega)}\} \quad \text{db} \qquad (3\text{-}230)$$

The argument of the logarithm in Eq. (3-230)

$$\frac{I_r^2(\omega) + I_{ra}^2(\omega)}{I_r^2(\omega)}$$

is just the ratio of the *total equivalent* noise power per unit bandwidth referred to the amplifier input terminals to the Johnson noise power generated by the resistive component of the amplifier *input impedance*, $\underline{Z}_{in}$. Since an ideal amplifier would have $I_{ra}^2(\omega) = 0$ it follows that the noise figure measures the performance of a real amplifier *relative to that of an inherently noiseless unit* while taking into account the *unavoidable* Johnson noise which will be present in either case.

In general N.F. is a function of both $\underline{Z}_{in}$ and the operating frequency. Since $\underline{Z}_{in}$ for a mixing spectrometer represents a combination of the photodetector internal impedance and the load impedance, the relationship between F_R' and F_R in Eq. (3-229) depends on the exact nature of the mixer, through the value of $\underline{Z}_L$, and on the line width and center frequency of the signal part of the current spectrum. However, under optimized conditions we may regard the noise figure as being independent of $\underline{Z}_L$ and also of the choice of photomixer. This situation is obtained as follows. For most good amplifiers and receivers N.F. is a quite slowly varying function of frequency; however, it is almost always a strong function of the input impedance. As a result an amplifier normally has a *frequency independent optimum* input impedance which will guarantee the minimum possible noise figure. Moreover, this minimum value of N.F. will itself be essentially frequency independent. The problem of transforming the impedance seen at the output of the photomixer-load circuit to the desired value of amplifier input impedance has been treated in detail by Twiss and Beers,[53] and is feasible under certain general restrictions on the impedances to be matched. We assume here that such a transformation is always possible and write F_R' as

$$F_R' = (10)^f F_R \tag{3-231}$$

with

$$f = \frac{(N.F.)_{min} \text{ in db}}{10} \tag{3-232}$$

The quantity $(N.F.)_{min}$ is the noise figure obtained under optimum matching conditions and is a property only of the amplifier under consideration.

Under these circumstances the effect of excess amplifier noise is a quite simple one. The amplifier with a non-zero noise figure can be represented as contributing an additional thermal noise power to the photomixer load circuit. This noise contribution increases the apparent value of F_R by a factor $(10)^f$ with f given by Eq. (3-232). As a result we must require that the photodetector receive a correspondingly increased total optical input power in order to maintain "shot-noise" limited operation, $F_R' \leq (0.1)$. The curves of $\mathcal{P}$ versus Γ and $[\mathcal{P}/\mathcal{P}_{COH}]$ versus Γ which were presented in Figs. 3-29, 3-30, 3-35, 3-36, 3-42, and 3-43 retain their validity if the results read from their ordinate scales are multiplied by the factor $(10)^f$.

Figure 3-44 shows typical values of the noise figure that are encountered in amplifiers or receivers which either (1) are tunable over at least an octave frequency interval or (2) have at least an octave bandwidth. Although narrow band devices can achieve significantly lower noise figures, they are in general unsuitable for use in

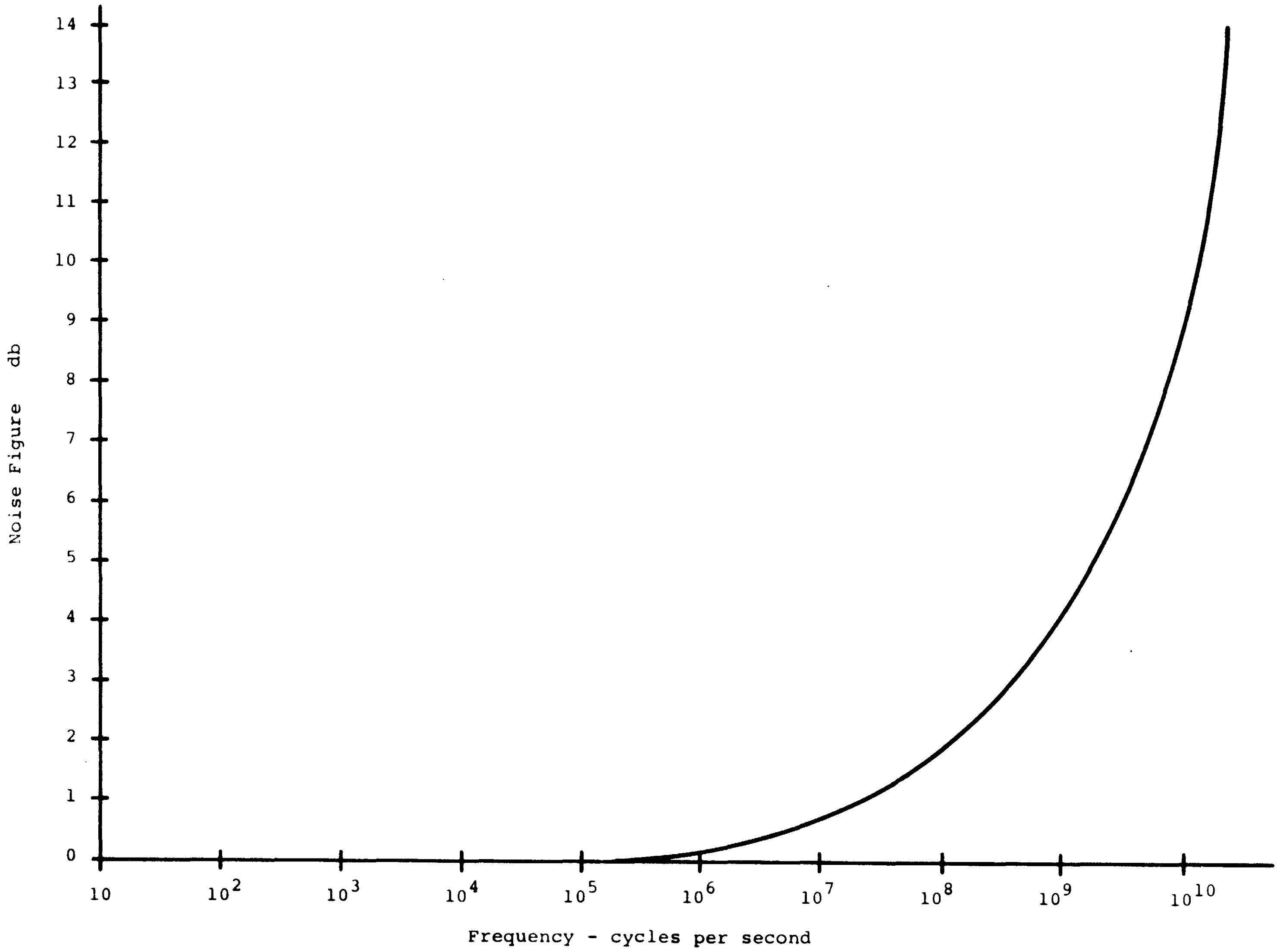

Figure 3-44 Typical noise figures for radio frequency amplifiers useful in optical mixing spectrometers.

light mixing spectrometers. The data presented in Fig. 3-44 indicates that in the range $(\omega/2\pi) = 0$ to $(\omega/2\pi) \simeq 250$ Mc/sec amplifier noise will result in less than a factor of two increase in F_R. For frequencies below $(\omega/2\pi) = 10^5$ cps this excess noise is negligible. However, for frequencies above $(\omega/2\pi) \simeq 5 \times 10^8$ cps the noise figure grows sharply and represents an increase in F_R by a factor of 12 at the highest usable mixer frequencies encountered in Section F.4.

As a result, the curves for P and $[P/P_{COH}]$ versus Γ which were given for $F_R \leq 0.1$ remain essentially unaltered except for large Γ and high intermediate frequencies. For the photosurface type mixers which are capable of operating in the regime $\Gamma > 5 \times 10^8$ cps, namely the crossed-field photomultipliers,* the ratio $[P/P_{COH}]$ for large values of Γ is already being controlled solely by dark current considerations. Therefore, the apparent increase in F_R has no effect on the minimum required optical input power. However, in the case of the solid state mixers it is precisely in the range $\Gamma > 5 \times 10^8$ cps that P and $[P/P_{COH}]$ are dominated by Johnson noise considerations and P approaches the maximum input rating of the detector. For these devices we conclude that observations on line widths greater than $(\Gamma/2\pi) \simeq 10^8$ cps will in general be degraded by Johnson noise and excess amplifier noise simply because of the limited power input capability of the photomixer.

---

* Chapter 3, Section F.2

6. Summary

In the preceding sections we have analyzed the importance of practical noise sources in reducing the pre- and post-detection signal-to-noise ratios of an optical mixing spectrometer. The surprising result is that none of these effects alter the basic sensitivity of the instrument. This sensitivity is specified in terms of a minimum detectable power per coherence area in the input optical signal while the importance of the detrimental effects of dark current shot-noise, thermal noise, and amplifier noise depends only on the total optical power falling on the photomixer. As a result a light mixing spectrometer can achieve its theoretical sensitivity over a range of line widths which is limited solely by the transit time cutoff frequency of the photodetector and its maximum permissible input power. The combination of the effects is such as to place an upper limit on $(\Gamma/2\pi)$ of about 10^9 cps for either the self-beat or superheterodyne spectrometer.

The data on the state-of-the-art capabilities of optical mixing spectrometers is summarized in Fig. 3-45 for three instruments: (1) a self-beat spectrometer, (2) a superheterodyne spectrometer with a zero intermediate frequency, and (3) a superheterodyne spectrometer with $(\omega_1 = 10\Gamma)$. For each of these Fig. 3-45 gives the "sensitivity curve" as a function of the optical line width Γ, that is the minimum power per coherence area necessary to achieve the condition $(S/N)_{OUT} = 1$. The detectors which are represented here were chosen on the basis of best quantum efficiency consistent with the desired frequency response and a tolerable value of $[P/P_{COH}]$. This ratio, $[P/P_{COH}]$, is indicated on each

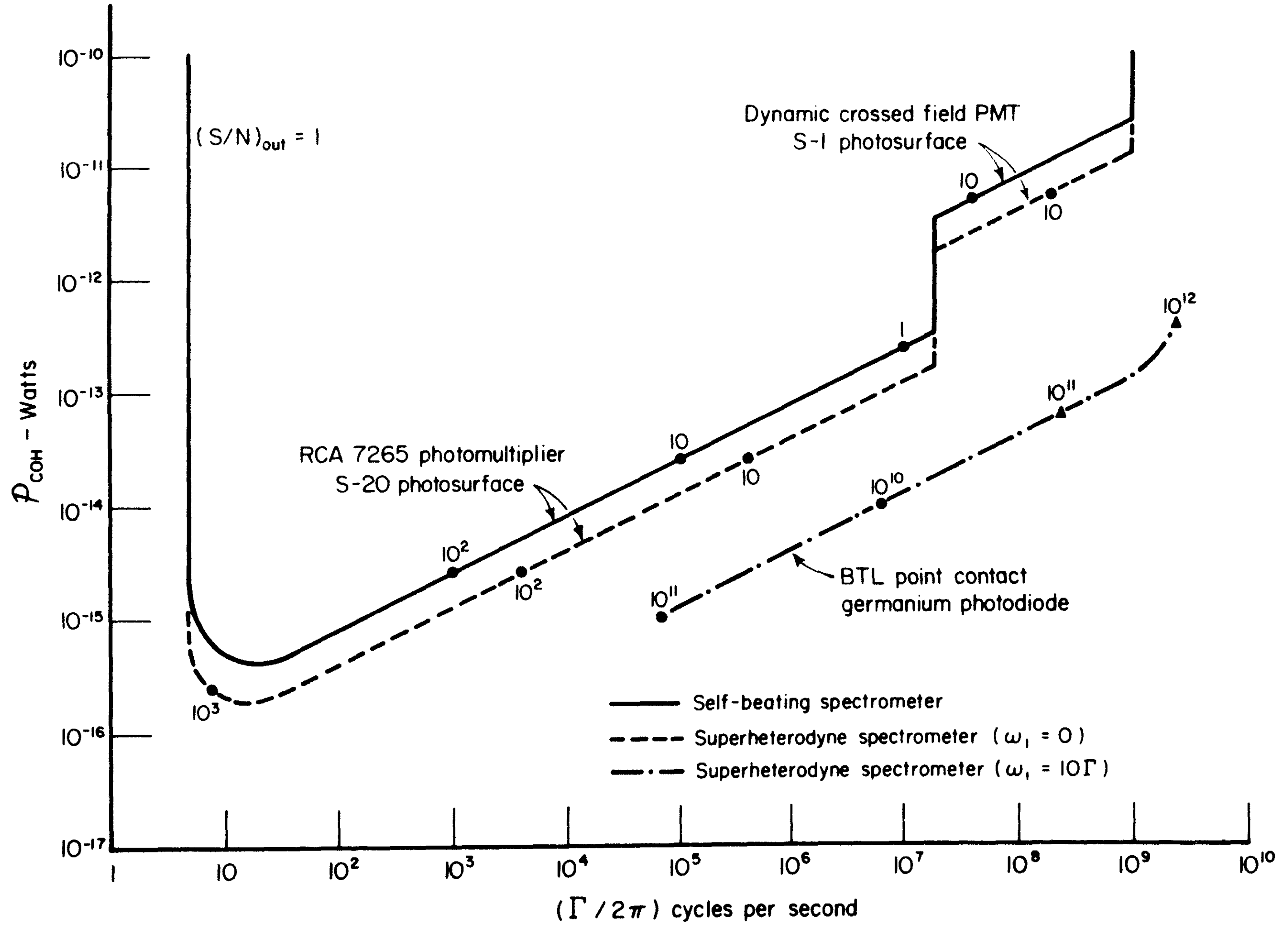

Figure 3-45 The power per coherence area required to achieve unity output signal-to-noise ratio for optical mixing spectrometers employing the best state-of-the-art photo-mixers. The power is given versus the half-width $(\Gamma/2\pi)$ of the Lorentzian spectrum being investigated.

of the curves with the following notation: points denoted by a solid dot correspond to a value of $[P/P_{COH}]$ set by dark current considerations only, solid triangles indicate that $[P/P_{COH}]$ is fixed by thermal noise and amplifier noise.

These results represent the sensitivity achieved under the following conditions:

(1) The tunable filter used to examine the photocurrent spectrum has a fractional resolution $a = (\Delta\omega_f/\Gamma) = (0.1)$.

(2) The output filter[§] time constant is $\tau = 1$ sec.

(3) The heterodyning[†] efficiency for the superheterodyne spectrometer is $[B] = 1$.

G. A Comparison Between Optical Mixing and Conventional Spectrometers

Although Sections E and F present a quantitative analysis of the theoretical and practical sensitivities of optical mixing spectrometers, the numerical results obtained there can be put into proper perspective only with the answers to the following qualitative questions. How do these sensitivity results for light mixing spectrometers compare to similar calculations for conventional optical dispersing instruments such as grating spectrographs and Fabry-Pérot etalons? Are there any fundamental differences between the two spectroscopic methods? In this section we discuss this problem in terms of a comparison between the ideal sensitivity curves for a self-beat optical spectrometer and those for a Fabry-Pérot spectrometer of the same resolution.

[§] Chapter 3, Section C.2.b.4

[†] Chapter 3, Section D.3.c

1. The Fabry-Pérot Etalon Spectrometer

A block diagram of a typical Fabry-Pérot etalon spectrometer is shown in Fig. 3-46. The operation of such an instrument in measuring the spectrum of the incident field, $S_E(\omega)$, was described briefly in Section A. The action of the etalon itself is completely analogous to that of the simple tuned filter shown in Fig. 3-1; its purpose is to examine the incident power spectrum by passing to a photodetector only that portion of the spectrum which lies inside its "bandpass." The desired information on the spectrum of the incident light, $S_E(\omega)$, is contained in the total power getting through the etalon as a function of its center transmission frequency, ω_f. This power is measured by an ordinary photodetector.

a. The Signal Processing

The details of the filtering process may be specified in terms of a system or filter function $|H(\omega)|^2$ as introduced in Section C.2.b.1. In this case we have for the power spectral density of the field reaching the photodetector

$$S_f(\omega) = |H(\omega)|^2 S_E(\omega) \tag{3-233}$$

The system function that describes the frequency transmission characteristics of a Fabry-Pérot etalon is ideally a Lorentzian[54]

$$|H(\omega)|^2 = \frac{(\Delta\omega_f)^2}{(\omega-\omega_f)^2 + (\Delta\omega_f)^2} \tag{3-234}$$

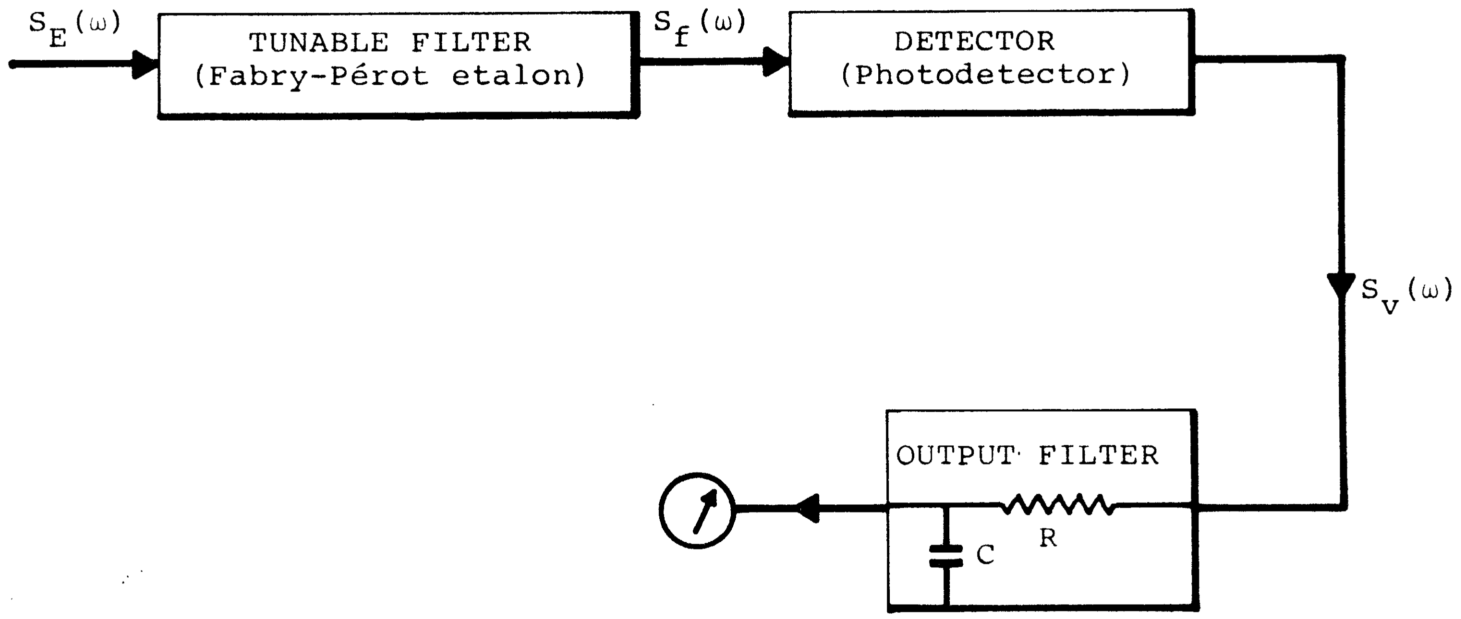
$S_E(\omega)$
TUNABLE FILTER
(Fabry-Pérot etalon)
$S_f(\omega)$
DETECTOR
(Photodetector)
$S_v(\omega)$
OUTPUT FILTER
R
C

Figure 3-46 Block diagram of a conventional Fabry-Pérot spectrometer.

having unity response at the center frequency of its bandpass ($\omega = \omega_f$). The ratio of ω_f to the full-width at half-transmission $2\Delta\omega_f$ is normally referred to as the resolving power of the etalon.

Suppose that the power spectral density of the incident field is a Lorentzian centered at the optical frequency ω_o and having a half-width at half-height of Γ rad/sec. Then from Eq. (3-54) we have

$$\underset{(\omega\geq 0)}{S_E(\omega)} = \frac{\left\langle |\vec{E}(\vec{r}_o,t)|^2 \right\rangle (\Gamma/\pi)}{(\omega-\omega_o)^2 + \Gamma^2} \tag{3-235}$$

Using Eq. (3-234) for $|H(\omega)|^2$ yields $S_f(\omega)$ as

$$\underset{(\omega\geq 0)}{S_f(\omega)} = \frac{\left\langle |\vec{E}(\vec{r}_o,t)|^2 \right\rangle (\Gamma/\pi)}{(\omega-\omega_o)^2 + \Gamma^2} \; \frac{(\Delta\omega_f)^2}{(\omega-\omega_f)^2 + (\Delta\omega_f)^2} \tag{3-236}$$

If the effective area of the etalon-detector combination is A, it follows that the total power falling on the photodetector is given by

$$P_f = (A/\mu_o c_m) \int_0^\infty S_f(\omega)\, d\omega \tag{3-237}$$

In the limit in which the "bandpass" of the etalon, $\Delta\omega_f$, is small compared to the optical line width, Γ, we have immediately from Eq. (3-236)

$$P_f = \frac{(A/\mu_o c_m) \left\langle |\vec{E}(\vec{r}_o,t)|^2 \right\rangle \Gamma(\Delta\omega_f)}{(\omega_f-\omega_o)^2 + \Gamma^2} = \frac{P_o \Gamma(\Delta\omega_f)}{(\omega_f-\omega_o)^2 + \Gamma^2} \tag{3-238}$$

where $P_o = (A/\mu_o c_m)\left\langle|\vec{E}(\vec{r}_o,t)|^2\right\rangle$ is the total optical signal power collected by the etalon. Clearly as ω_f is tuned through its range P_f simply traces out the spectrum of the incident light.

Allowing the filtered optical field to fall on a photodetector produces the usual three components* in the power spectral density of the photocurrent; a dc current given by

$$i_p = (\varepsilon e/\hbar\omega_o)P_f \tag{3-239}$$

a uniform shot-noise background term

$$I_N^2(\omega) = (e/\pi)i_p \tag{3-240}$$

$$(\omega \geq 0)$$

and a self-beat term

$$I_S^2(\omega) = i_p^2 \left\{\begin{matrix} 1 \\ \\ (A_{COH}/A) \end{matrix}\right\} \frac{(2\Delta\omega_f/\pi)}{\omega^2 + (2\Delta\omega_f)^2} \tag{3-241}$$

The upper line in the braces of Eq. (3-241) applies when the etalon area is small compared to the coherence area of the signal field, $A << A_{COH}$, while the lower line holds for $A >> A_{COH}$. Because the desired information in the photocurrent is present as the dc current component, the self-beat part of the detector output represents an additional noise power per unit bandwidth around $(\omega = 0)$ which will tend to obscure a determination of i_p. This situation is completely equivalent to the condition encountered at the detector output of a light mixing spectrometer.[*] However, for practical applications involving conventional spectrometers we usually have $[I_S^2(0) << I_N^2(0)]$ and, therefore, the primary source of noise in the measurement of i_p is the ac shot-noise power, $I_N^2(\omega)$. If these ac noise currents reach the output meter they cause the meter reading to fluctuate and hence make the determination of i_p uncertain. To block a majority of the ac currents from the output indicator the photodetector output is passed through a suitable RC filter as indicated in Fig. 3-46.

---

* Chapter 3, Sections C.1 and C.2.

b. The Output Signal-to-Noise Ratio

The description of this post-detection filtering process and the definition of an output signal-to-noise ratio proceed exactly as in Section C.2.b and yield the result

$$(S/N)_{OUT} = \sqrt{\left(\frac{\varepsilon}{\hbar\omega_o}\right)\mathcal{P}_f\tau} \qquad (3\text{-}242)$$

where $(\tau = RC)$. The quantity $(\varepsilon/\hbar\omega_o)\mathcal{P}_f\tau$ is just the number of photoelectrons ejected from the photocathode during one "response time" of the output filter, τ; that is, Eq. (3-242) reflects the intuitive result that the numerical counting of N uncorrelated[**] photo-events is uncertain by an amount $\sqrt{N}$.

Equation (3-242) may be written in a form that can be compared with the analogous results for a light mixing spectrometer by evaluating P_f at the point of peak etalon transmission, $\omega_f = \omega_o$, and taking $\tau = (1/\Delta\omega_T)$. In this case we have

---

[*] Chapter 3, Section C.2.b.2.

[**] Chapter 3, Section B.2.

$$(S/N)_{OUT} = \sqrt{\left(\frac{\varepsilon}{\hbar\omega_o}\right)\left(\frac{\Delta\omega_f}{\Gamma}\right)\frac{P_o}{\Delta\omega_T}} \qquad (3\text{-}243)$$

c. The Effects of Spatial Coherence

The most striking feature of Eq. (3-243) is that the output (S/N) ratio for a conventional optical spectrometer is unaffected by the coherence properties of the incident electric field and has a sensitivity specified in terms of the total available optical power. Therefore, in a situation in which it is feasible to collect light from a large number of coherence areas in the signal beam the Fabry-Pérot spectrometer has an initial advantage in minimum detectable power that is related to the ratio $[P_o/P_{COH}]$.

2. The Intrinsic Difference Between Conventional and Light Mixing Spectroscopy

Suppose, however, that we arbitrarily restrict the Fabry-Pérot to accepting light only from a single coherence area. How does the sensitivity of such an instrument then compare with the sensitivity of an ideal self-beat spectrometer? For purposes of comparison we will assume that the following conditions hold for both spectrometers: (1) the normalized resolution in each case is $(\Delta\omega_f/\Gamma) = 0.1$, (2) both photodetectors have unit quantum efficiency ($\varepsilon = 1$), and (3) the outputs are filtered by identical RC circuits with a time constant $\tau = 1$ sec. Furthermore, the effects of dark current, thermal noise, and amplifier noise are to be neglected in both cases. Under these circumstances we find the sensitivity curves shown in Fig. 3-47. The results give the optical signal power per single coherence area which the corresponding spectrometer requires in order to achieve a unity output signal-to-noise ratio. Clearly the ideal Fabry-Pérot etalon instrument is capable of examining the spectrum of a much smaller amount of optical power than the ideal self-beating spectrometer. This discrepancy is an indication that an inherent difference exists between the physical processes by which the two methods obtain spectral information on the incident field. In fact, the explanation of this difference is to be found in a fundamental limit on the amount of information which any device may extract from the electromagnetic field; a limit set by quantum mechanical uncertainty considerations.

Any amplifier or detector of electromagnetic radiation produces an output which is some representation of the intensity and possibly also the phase of the input wave. It is possible then, that such a device may obtain, simultaneously, information on the number of quanta in the incident field and also a measurement of its phase. If so, its performance must be limited[55] by the uncertainty relation between these two conjugate quantities. That is, a single measurement at the output of an amplifier or detector from which we can deduce both the phase and the number of quanta in the incoming beam implies an uncertainty in these quantities which must satisfy the inequality

$$\Delta n \Delta \phi \geq \frac{1}{2} \tag{3-244}$$

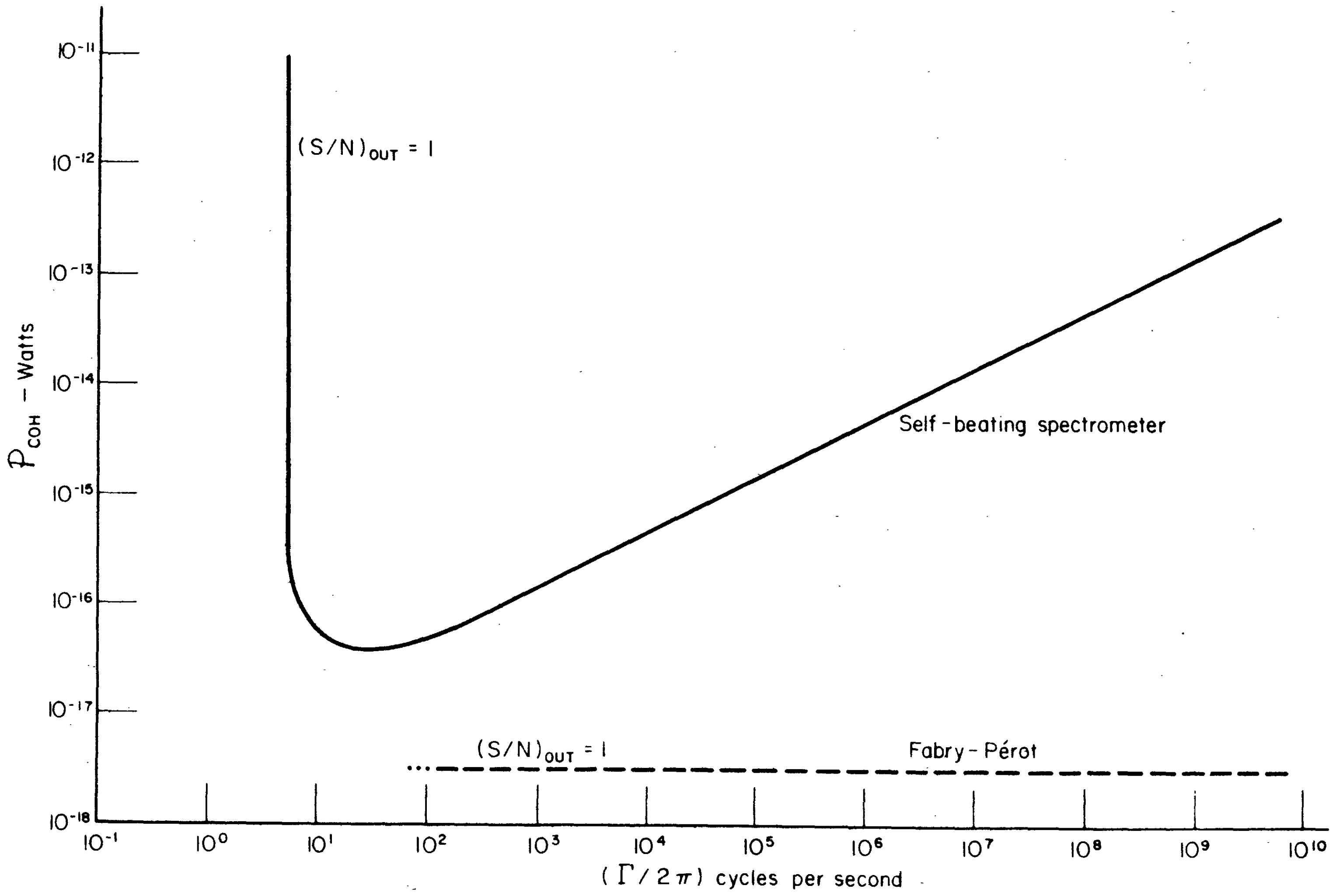

Figure 3-47 A comparison of the sensitivity curves for a self-beat optical spectrometer and a conventional Fabry-Pérot etalon spectrometer.

The factors (Δn) and ($\Delta\phi$) are the rms uncertainties in the number of incident photons, n, and the phase of the incoming field, ϕ, respectively.

This uncertainty principle also places a fundamental lower limit on the amount of optical power which the detector or amplifier requires in order to extract information from the field. In particular, if the sensing apparatus is capable of fixing the phase of the input wave within an error $\Delta\phi$, then during the measuring period this apparatus must receive at least n_{MIN} photons, where

$$n_{MIN} \geq \Delta n = \frac{1}{2\Delta\phi} \tag{3-245}$$

Equation (3-245) states that the number of photons at the input must exceed the inherent uncertainty in n if a measurement is to determine whether the output data in fact represents an input signal. The equality ($n_{MIN} = \Delta n$) is equivalent to a unity value of output signal-to-noise ratio, the rms uncertainty in the desired quantity being equal to the value of the quantity itself.

Suppose that a single "experiment" involves N independent measurements of the type described above. Then Δn, and therefore n_{MIN}, are reduced by the factor $\sqrt{N}$, yielding a detectability condition

$$n_{MIN} \geq \Delta n = \frac{1}{2\Delta\phi\sqrt{N}}$$

We now proceed to determine the values of $\Delta\phi$ and N which characterize light mixing and conventional spectroscopy.

First consider a self-beat spectrometer which is providing information on the spectrum of an incident light beam having the usual Lorentzian power spectral density with a half-width at half-height of Γ rad/sec. This spectral information is present at the photodetector output as the signal part of the photocurrent spectrum shown in Fig. 3-48. The amount of phase data which we gather by examining this beat note spectrum can be calculated as follows. The phase advance of the incident optical field in a measuring time δt is simply

$$\phi = \omega_o \delta t$$

However, if the optical frequency is uncertain by an amount $\Delta\omega$ then at the end of the measurement the phase is also uncertain, namely

$$\Delta\phi = \Delta\omega \cdot \delta t \tag{3-247}$$

From the information available in the self-beat current spectrum we may conclude that the spectral width of the input field is Γ and, hence, during the time δt the exact incident frequency was uncertain by an amount ($\Delta\omega = \Gamma$). Furthermore, the time required for the photomixer to provide one independent determination of $S_i(\omega)$ is just the correlation time of the photocurrent*, $\delta t = (1/2\Gamma)$. Thus a self-beat spectrometer makes a phase measurement on the incoming signal field having an uncertainty

$$\Delta\phi = \Gamma(1/2\Gamma) = \frac{1}{2} \text{ radian}$$

This result in combination with Eq. (3-245) implies that in a time $\delta t = (1/2\Gamma)$ the mixer must receive at least

---

* Chapter 3, Section C.1, Eq. (3-58).

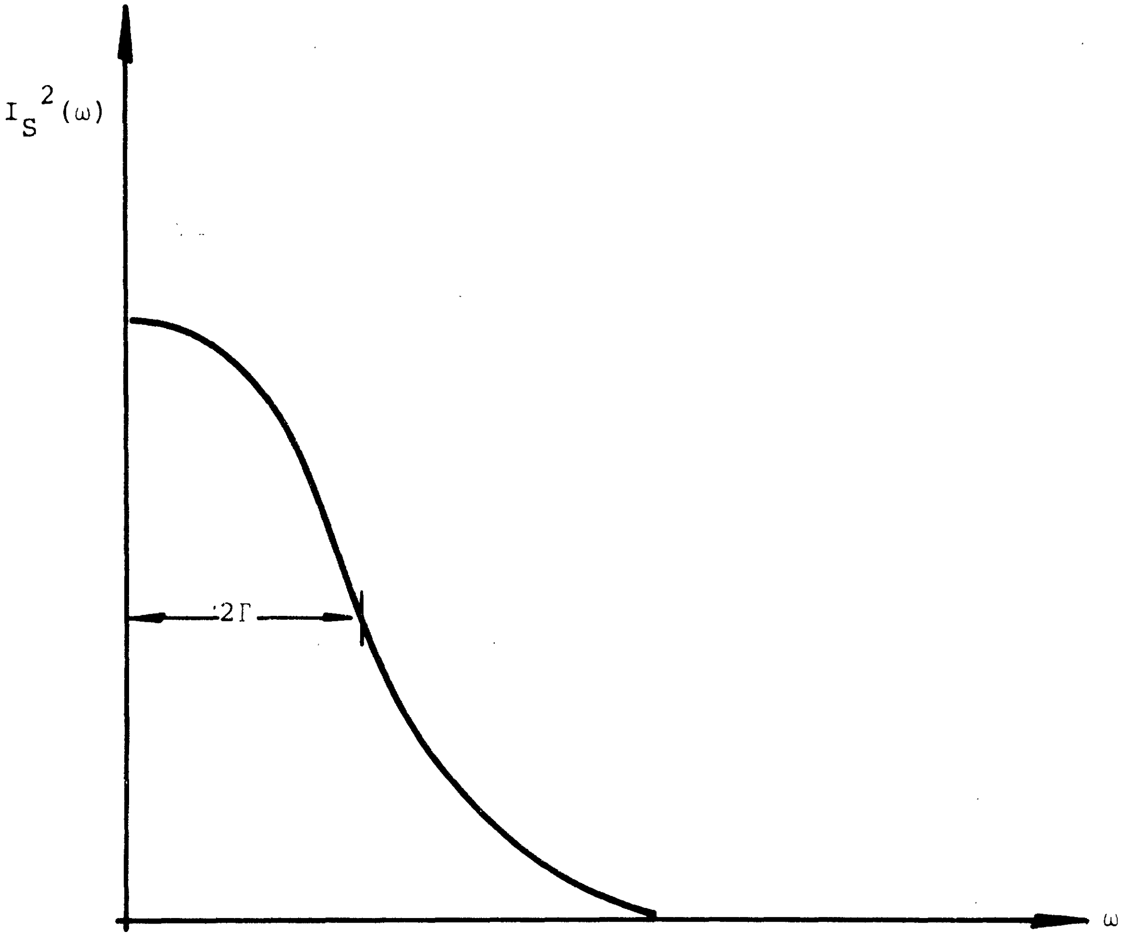

Figure 3-48 The spectral information available at the photodetector output of a self-beating optical spectrometer.

($n_{MIN} \geq 1$) quanta. If the incident power is denoted as P then an equivalent statement is

$$\left(\frac{P}{\hbar\omega_o}\right)\frac{1}{2\Gamma} \geq 1 \tag{3-248}$$

This condition refers to a single elementary determination of $S_i(\omega)$ as made in a time $\delta t = (1/2\Gamma)$. Suppose, however, that we detect the presence of the beat signal by passing the photocurrent through an electrical filter of the type considered in Section C.2.b.1. This filter has the rectangular frequency response shown in Fig. 3-11 and a response time $\tau_f = (\pi/\Delta\omega_f)$ as calculated from its impulse response,* $h(\tau)$. If we have $\tau_f > \delta t$, that is $\Delta\omega_f < (2\Gamma/\pi)$, then in a time ($\tau > \tau_f$) this filter will make

$$N = \tau/\tau_f$$

independent determinations of the possible presence of a beat signal. Writing $\Delta\omega_T = (1/\tau)$ we find the minimum required input power from Eq. (3-246) as

$$\left(\frac{P}{\hbar\omega_o}\right)\frac{1}{2\Gamma} \geq \frac{1}{\sqrt{N}}$$

that is

$$\left(\frac{P}{\hbar\omega_o}\right)\cdot\frac{1}{2\Gamma}\sqrt{\frac{\Delta\omega_f}{\pi\Delta\omega_T}} \geq 1 \tag{3-249}$$

Comparing this result with Eq. (3-140) and employing the assumption $\varepsilon = 1$ shows that Eq. (3-249) is identically the condition which yields $(S/N)_{OUT} \geq 1$ for the ideal self-beat spectrometer. Therefore, we come to the following important conclusion. An ideal optical mixing spectrometer operating at its limit of sensitivity, $(S/N)_{OUT} = 1$, is extracting from the incident field the maximum amount of information allowed by the uncertainty principle. An argument similar to the one presented above shows that this conclusion is equally valid for both self-beat and superheterodyne instruments.

---

* Chapter 3, Section C.2.b.1.

Let us now ask what amount of phase data is present at the detector output of the Fabry-Pérot etalon spectrometer. In this case the desired information is contained in the dc component of the photocurrent. However, since a determination of the dc photocurrent contains no phase information on the incident field, a conventional spectrometer has a characteristic value of $\Delta\phi$ given by

$$\Delta\phi = \infty \qquad (3\text{-}250)$$

This result, together with the minimum input power condition in Eq. (3-245), implies that a single, elementary determination of the presence of an input signal can be made with an arbitrarily small number of incoming quanta. Of course, since the dc photocurrent represents the infinite time average of the incident light intensity

$$i_p = \alpha A \left\langle |\vec{E}(\vec{r}_o,t)|^2 \right\rangle = \alpha A \lim_{T\to\infty} \frac{1}{2T} \int_{-T}^{T} |\vec{E}(\vec{r}_o,t)|^2 dt$$

the time interval required for the detector to produce such a single measurement is $\delta t = \infty$. For the conventional optical spectrometer then, the condition $(S/N)_{OUT} = 1$ implies a minimum detectable optical power which is set simply by the requirement of having at least one photoelectron ejected during the measurement interval, not by the uncertainty principle.

In view of this result perhaps a more revealing comparison between optical mixing and conventional spectroscopy than that illustrated in Fig. 3-47 is contained in the ratio of minimum detectable signal powers in the limit $\tau = (1/\Delta\omega_T) \rightarrow \infty$. Again confining the Fabry-Pérot to gathering light from a single coherence area we have from Eqs. (3-243) and (3-140)

$$\frac{P_{MIN}(\text{self-beat})}{P_{MIN}(\text{Fabry-Pérot})} = \sqrt{\frac{\pi\Delta\omega_f}{\Delta\omega_T}} \tag{3-251}$$

In the limit $(\tau \rightarrow \infty)$ this ratio increases as $\sqrt{\tau}$ and becomes infinitely large. That is the inherent sensitivity of a conventional optical spectrometer is infinitely greater than that of an optical mixing spectrometer. Furthermore, the origin of this advantage lies in the amount of phase information which is obtained by each method in the process of examining the spectrum of the input optical field.

Table V gives a list of some common detecting schemes classified according to their characteristic values of $\Delta\phi$.

Table V THE UNCERTAINTIES Δn AND $\Delta\phi$ FOR VARIOUS MEASUREMENT TECHNIQUES

Measurement Technique	$\Delta\phi$
Quantum Counters[a] (Particle Detectors)	∞
Optical Mixing Spectrometers	$\frac{1}{2}$
Optical Mixing Receiver[b] (detecting an unmodulated carrier)	$\frac{1}{2\sqrt{n}}$
Ideal Maser Amplifier[a]	$\frac{1}{2\sqrt{n}}$
Ideal Phase Detector[a]	$\frac{1}{2n}$

---

[a] R. Serber and C. H. Townes, in Quantum Electronics, edited by C. H. Townes (Columbia University Press, New York, 1960), p. 233.

[b] B. M. Oliver, Proc. IRE 49, 1960 (1961).

H. A. Haus and C. H. Townes, Proc. IRE 50, 1544 (1962).

B. M. Oliver, Proc. IRE 50, 1545 (1962).

BIBLIOGRAPHY: Chapter 3

1. G. W. Stroke, J. Opt. Soc. Am. 51, 1321 (1961).
2. T. J. Greytak and G. B. Benedek, Phys. Rev. Letters 17, 179 (1966).
3. T. J. Greytak, Ph.D. thesis, Massachusetts Institute of Technology, 1967 (unpublished).
4. R. W. Landee, D. C. Davis, and A. P. Albrecht, Electronic Designer's Handbook (McGraw-Hill Book Company, Inc., New York, 1957), Section 7.8.
5. Reference 4; Section 7.3.
6. A. T. Forrester, J. Opt. Soc. Am. 51, 253 (1961).
7. S. S. Alpert, Y. Yeh, and E. Lipworth, Phys. Rev. Letters 14, 486 (1965).
8. H. Z. Cummins, N. Knable, and Y. Yeh, Phys. Rev. Letters 12, 150 (1964).
9. J. B. Lastovka and G. B. Benedek, in Physics of Quantum Electronics, edited by P. L. Kelly, B. Lax, and P. E. Tannenwald (McGraw-Hill Book Company, Inc., New York, 1966), p. 231.
10. J. B. Lastovka and G. B. Benedek, Phys. Rev. Letters 17, 1039 (1966).
11. S. S. Alpert, D. Balzarini, R. Novick, L. Seigel, and Y. Yeh, in Physics of Quantum Electronics, edited by P. L. Kelly, B. Lax, and P. E. Tannenwald (McGraw-Hill Book Company, Inc., New York, 1966), p. 253.
12. Reference 4; Section 7.9.
13. A. T. Forrester, J. Opt. Soc. Am. 51, 253 (1961).
14. N. C. Ford, Jr., and G. B. Benedek, in Critical Phenomena, edited by M. S. Green and J. V. Sengers (United States Government Printing Office, Washington, 1966), p. 150.
15. N. C. Ford, Jr., and G. B. Benedek, Phys. Rev. Letters 15, 649 (1965).

16. J. A. White, J. S. Osmundson, and B. H. Ahn, Phys. Rev. Letters 16, 639 (1966).

17. B. Chu, Phys. Rev. Letters 18, 200 (1967).

18. A. T. Forrester, W. E. Parkins, and E. Gerjouy, Phys. Rev. 72, 728 (1947).

19. W. B. Davenport, Jr., and W. L. Root, An Introduction to the Theory of Random Signals and Noise (McGraw-Hill Book Company, Inc., New York, 1958), pp. 101 ff.

20. L. Mandel, E. C. G. Sudarshan, and E. Wolf, Proc. Phys. Soc. (London) 84, 435 (1964).

21. P. L. Kelly and W. H. Kleiner, Phys. Rev. 136, A316 (1964).

22. R. J. Glauber, in Quantum Optics and Electronics, edited by C. DeWitt, A. Blandin, and C. Cohen-Tannoudji (Gordon and Breach Science Publishers, Inc., New York, 1964), p. 63.

23. Reference 4; pp. (7-9) ff.

24. Reference 19; Article 4-8.

25. Reference 19; Problem 2, p. 168.

26. M. J. Beran and G. B. Parrent, Jr., Theory of Partial Coherence (Prentice-Hall, Inc., Englewood Cliffs, New Jersey, 1964), p. 165.

27. Reference 19; Chapter 9.

28. Reference 19; Article 9.5.

29. R. Bracewell, The Fourier Transform and Its Applications (McGraw-Hill Book Company, Inc., New York, 1965), pp. 112-113.

30. Monte Ross, Laser Receivers (John Wiley and Sons, Inc., New York, 1966).

31. A. T. Forrester, R. A. Gudmundsen, and P. O. Johnson, Phys. Rev. 99, 1691 (1955).

32. A. T. Forrester, Am. J. Phys. 24, 192 (1956).

33. *Spectra-Physics Laser Technical Bulletin Number 1, Spectra-Physics Incorporated*, Mountain View, California.

34. Reference 19; pp. 160-161.

35. C. Freed and H. A. Haus, Phys. Rev. 141, 287 (1966).

36. A. W. Smith and J. A. Armstrong, Phys. Rev. Letters 16, 1169 (1966).

37. G. W. Stroke, J. Opt. Soc. Am. 47, 1097 (1957).

38. E. B. Brown, *Modern Optics* (Reinhold Publishing Corporation, New York, 1965), pp. 464 ff.

39. R. W. Engstrom, J. Opt. Soc. Am. 37, 420 (1947).

40. H. Z. Cummins, N. Knable, L. Gampel, and Y. Yeh, in *Columbia Radiation Laboratory Quarterly Report*, June 15, 1963; pp. 39-46. (AD 418 059).

41. G. B. Benedek, Lectures on the *Theory of the Scattering of Light from Thermal Fluctuations*, Brandeis Summer Institute for Theoretical Physics, 1966 (to be published).

42. Data Sheet, 9558B EMI Photomultiplier, Whittaker Corporation, Plainview, Long Island, New York.

43. G. Lucovsky, M. E. Lasser, and R. B. Emmons, Proc. IEEE 51, 166 (1963).

44. W. H. Middendorf, *Analysis of Electric Circuits* (John Wiley & Sons, Inc., New York, 1956), Chapter 6.

45. J.C. Hancock, *An Introduction to the Principles of Communication Theory* (McGraw-Hill Book Company, Inc., New York, 1961), Section 6.3.

46. Reference 19; pp. 185 ff.

47. Reference 44; Section 18.08.

48. Reference 4; Section 3.11.

49. *RCA Phototubes and Photocells, Technical Manual PT-60* (Radio Corporation of America, Lancaster, Pennsylvania, 1963), pp. 165 ff.

50. L. K. Anderson, P. G. McMullin, L. A. D'Asaro, and A. Goetzberger, App. Phys. Letters 6, 62 (1965).

51. H. T. Friis, Proc. IRE 32, 419 (1944).

52. W. G. Dow, Fundamentals of Engineering Electronics (John Wiley & Sons, Inc., New York, 1952), Section 10.1.

53. R. Q. Twiss and Y. Beers, in Vacuum Tube Amplifiers, edited by G. E. Valley, Jr. and H. Wallman (McGraw-Hill Book Company, Inc., New York, 1948), 1st ed., Volume 18, Chapter 13.

54. K. W. Meissner, J. Opt. Soc. Am. 31, 405 (1941).

55. R. Serber and C. H. Townes, in Quantum Electronics, edited by C. H. Townes (Columbia University Press, New York, 1960), p. 233.

Chapter 4

THE EXPERIMENTAL APPARATUS EMPLOYED IN THE STUDY OF THE BRILLOUIN-MANDEL'SHTAM AND CENTRAL COMPONENTS IN THE LIGHT SCATTERED FROM TOLUENE LIQUID

A. Introduction

This chapter describes the important features of two superheterodyne optical mixing spectrometers which were used to detect the Brillouin-Mandel'shtam and central components respectively in the light scattered from toluene liquid. The discussion of the experimental apparatus and techniques that were employed in these two experiments can be conveniently divided into four major sections.

The first section is concerned with the physical and operational characteristics of the helium-neon gas laser which is used to illuminate the scattering medium and also acts as the source of an optical local oscillator field. We examine in some detail two particularly important properties of this light source: (1) the intensity distribution in its electric field as measured at points both inside the laser resonator and in the laser output beam, and (2) the shape of the constant phase surfaces of this electric field. A knowledge of these wavefront characteristics is essential to a calculation of the intensity and spatial coherence properties of the scattered field* as well as to an understanding of the operation of the mixing spectrometer optical systems. Special attention is also given to a discussion of the precautions which were required to suppress excessive amplitude modulation of the laser output.*

---

* Chapter 2, Section E.4.a.

The second section presents a physical description of the scattering cell and emphasizes the special features that permit this cell to be used inside the laser resonator. A simple geometrical optics approach serves to analyze the trajectories of rays leaving the cell and to express the externally measured scattering angle and ray divergence angles in terms of their values inside the scattering medium. We also examine here the novel technique that was used to accurately fix and measure the rather small ($\Theta < 3°$) scattering angles to which the present observations were confined.

The third and fourth sections analyze the optical systems, electronic detection apparatus, and alignment procedures of two optical superheterodyne spectrometers: one used to detect the presence of the Brillouin-Mandel'shtam doublet in the light scattered from toluene at $\Theta = 0.547°$, the second used to obtain the natural width of the central component in the same sample over the range ($0.31° \leq \Theta \leq 2.83°$).

---

* Chapter 3, Section F.3.b.

B. The Laser

1. General Features

The light source which was used in the measurements presented in this thesis is a conventional helium-neon gas discharge laser oscillating on the $\lambda_{air} = 6328.2$ Å[1] visible transition of neon.

The gas mixture is contained in a Brewster angle terminated, quartz plasma tube from a Spectra-Physics Model 112 laser.[2] This tube is of the so called "dual bore" variety with a total length of 115 cm made up of two equal length sections having inner diameters of 8 mm and 5 mm respectively. The required current discharge is maintained by rf energy coupled in capacitively through the tube walls. As indicated schematically in Fig. 4-1 the large electrical impedance (∿200 kΩ) of the tube is lowered by dividing up the discharge path into a number of parallel connected segments. An inverted pi-network[3] matches the resulting impedance to a standard 50Ω transmission line.

The rf driving power necessary to saturate[4] the 6328Å transition was approximately 50-75 watts. In order to minimize amplitude modulation of the optical output, this power was supplied from the highly regulated, crystal controlled rf transmitter whose schematic diagram is given in Fig. 4-2. The total rms noise and ripple on the rf output voltage of this device was less than 0.01% under typical operating conditions. In addition, the efficiency of the residual noise in producing a laser power output fluctuation was reduced substantially by operating the laser near its saturation point[4] where to first order the laser power output becomes independent of the discharge current. These two precautions were sufficient to guarantee

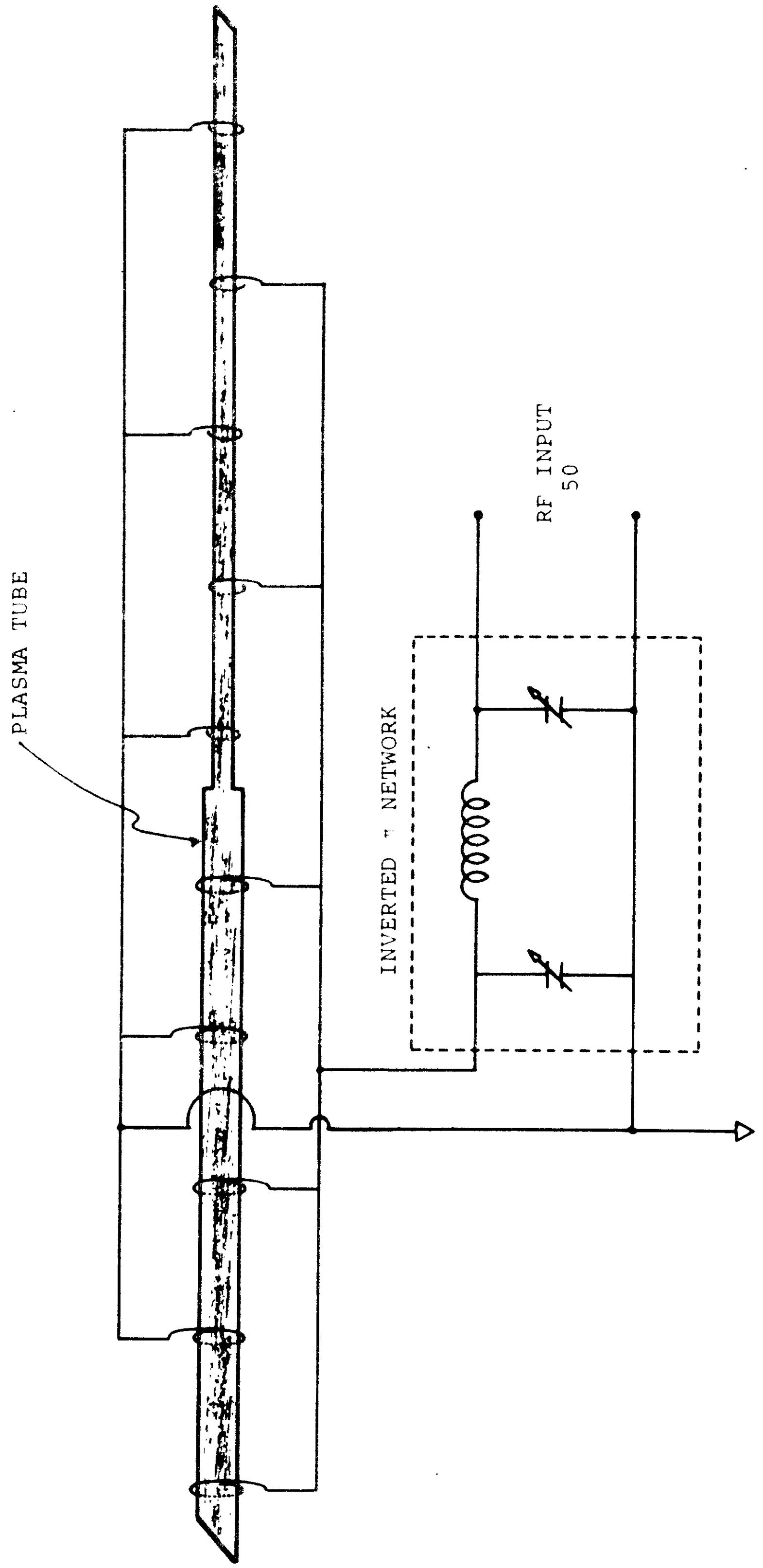
PLASMA TUBE
INVERTED π NETWORK
RF INPUT
50

Figure 4-1 Laser plasma tube and rf excitation geometry.

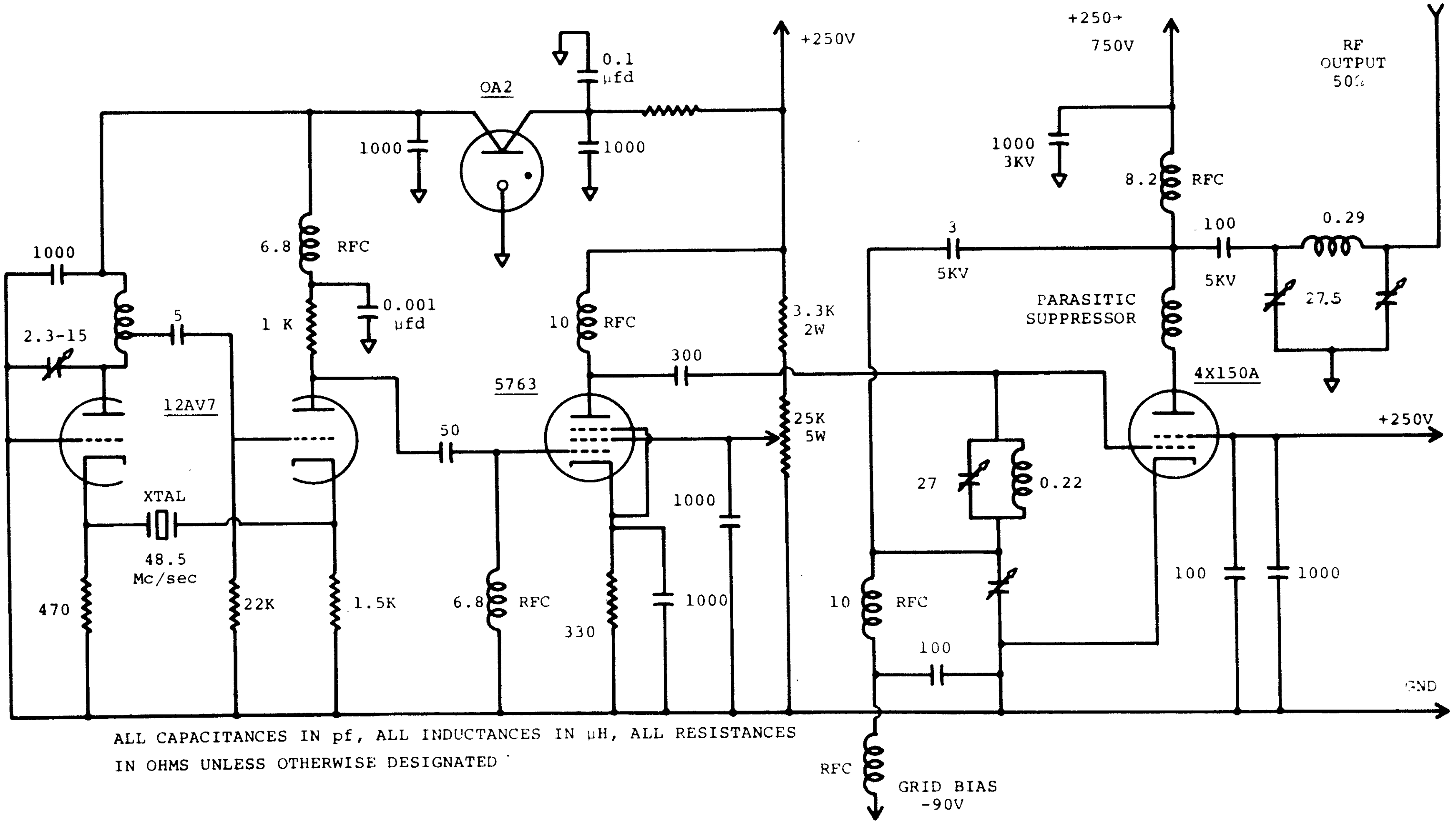
+250V
+250→
750V
RF
OUTPUT
50Ω
0.1
μfd
OA2
1000
1000
1000
3KV
8.2
RFC
1000
6.8
RFC
3
5KV
100
5KV
0.29
2.3-15
5
1 K
0.001
μfd
10
RFC
3.3K
2W
PARASITIC
SUPPRESSOR
27.5
12AV7
300
5763
4X150A
50
25K
5W
+250V
XTAL
48.5
Mc/sec
1000
27
0.22
470
22K
1.5K
6.8
RFC
330
1000
10
RFC
100
100
1000
GND
RFC
GRID BIAS
-90V

ALL CAPACITANCES IN pf, ALL INDUCTANCES IN μH, ALL RESISTANCES IN OHMS UNLESS OTHERWISE DESIGNATED

Figure 4-2 The schematic diagram of the rf laser exciter.

that noise from the rf power supply contributed negligibly to both the short and long term instabilities in laser output.

2. The Phase and Intensity Profiles of the Laser Electric Field

The plasma tube is mounted inside a cavity resonator formed by two high reflectivity dielectrically coated mirrors placed in a hemispherical[5] configuration. For the present experiments these are: (1) a spherical mirror with a radius of curvature of $r_s = 200$ cm and a reflection coefficient $R \geq (0.999)$; and (2) a flat mirror with a reflection coefficient $R \simeq (0.98)$. For hemispherical operation the mirror spacing ℓ is adjusted to be slightly less than the radius of curvature of the spherical reflector, r_s. The simple physical argument given below serves to explain the intensity and phase patterns that are normally generated by a laser with this particular mirror arrangement.

Since the laser output represents an oscillation on one or more of the normal modes (resonances) of the cavity, the resulting intensity and phase distributions inside the resonator will in general be characteristic of its lowest loss resonances. A normal mode of the cavity may be defined[6,7,8] as an electric field disturbance that reproduces itself in spatial distribution and phase, although not in amplitude, as the wave bounces back and forth between the two reflectors. Suppose we consider a hypothetical "normal mode" having a uniform phase and intensity over the surface of a spherical reflector. In this case the trajectory and intensity profile of the field that propagates away from the mirror can be described simply in analogy with the problem of focussing by an ideal lens. Figure 4-3 illustrates the equivalence between the proposed "normal mode" field pattern and that produced by a lens of focal length ($f = r_s$) illuminated by a uniform intensity, parallel light beam.

The solution to the problem of the diffraction limited focussing of parallel light is well known.[9] For our purposes one of the most useful results of this analysis shows that the focal plane, the plane normal to the axis of the lens and containing the geometrical focal point, F, is a plane of inversion symmetry for both the phase and intensity profiles of the focussed beam. It follows that the proposed electric field disturbance can be made into a normal mode of a resonant cavity by placing a flat mirror so that its reflecting surface is coincident with the focal plane. This situation, in fact, represents the condition of exact hemispherical[5] operation. Moreover, the "constant phase" normal modes represent the lowest loss resonances of the system.[8]

The rigorous solutions describing the complete set of normal modes of the hemispherical resonator have been given by Boyd and Kogelnik.[8] The important features of their results are summarized below.

The modes may be designated by the usual microwave convention, TEM_{mnq}, where TEM indicates that the normal mode disturbance is a transverse electromagnetic wave. The mode designations m and n give the number of phase reversals, $(0 \rightarrow \pi)$ or $(\pi \rightarrow 0)$, encountered while traversing the reflector surface in two orthogonal directions (x,y), (r,θ), etc. The mode designation q gives the number of half-wavelengths which are contained in the resonator. The self-reproducing condition demands that q be integral.

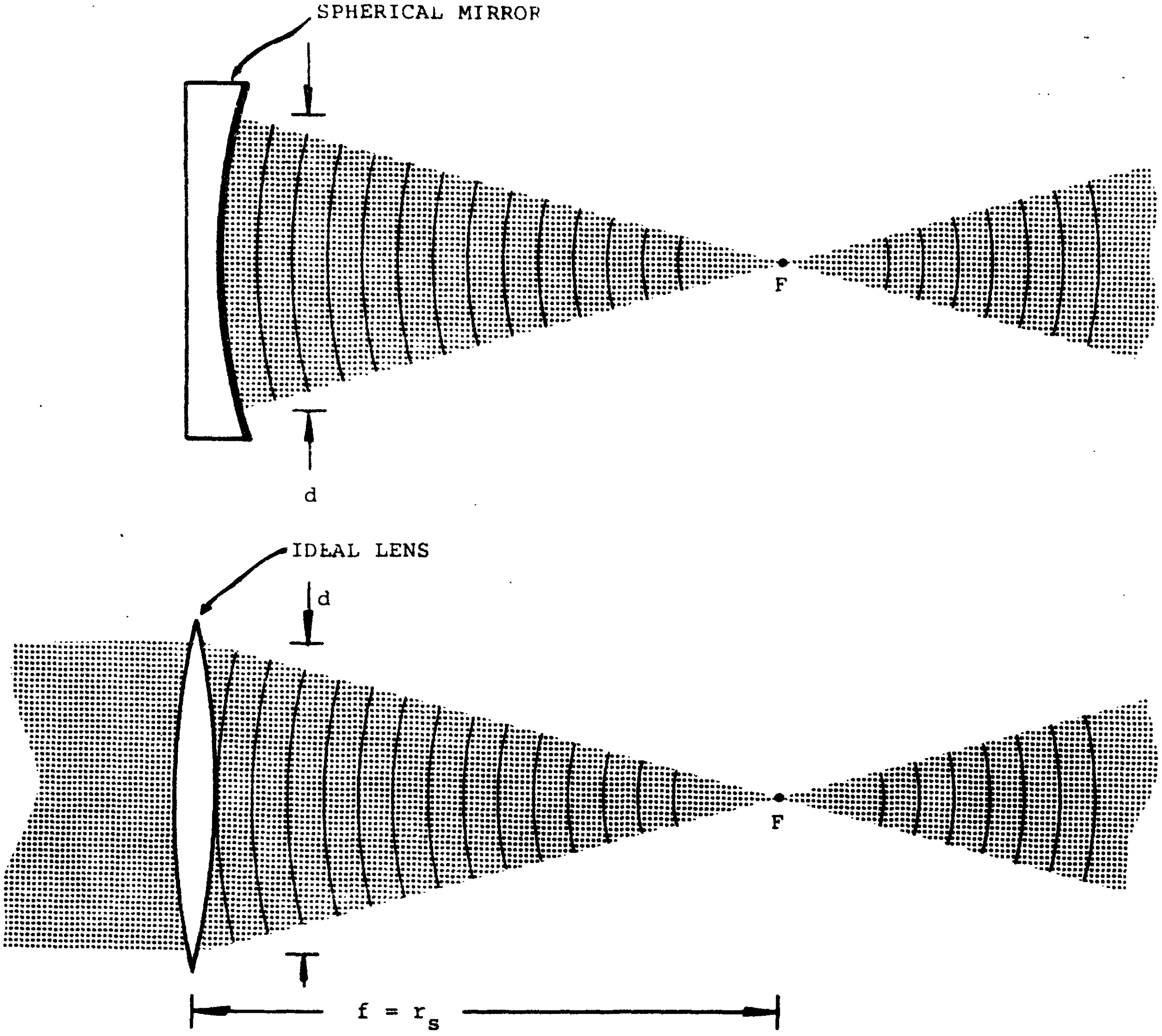
SPHERICAL MIRROR
d
F
d
IDEAL LENS
d
F
d
f = r_s

Figure 4-3 A comparison between the intensity profiles for the uni-phase modes of a spherical mirror and for the light focussed by an ideal lens.

Based on this notation the "constant phase" normal modes which we described above are given the designation TEM_{ooq} and are commonly referred to as "uni-phase," "longitudinal," or "axial" modes. Those cavity resonances that have (n > 0) or (m > 0) are generally called "transverse modes."

The uni-phase modes exhibit a number of important properties that make them especially useful in light scattering experiments. The first is their distribution of intensity and phase near the resonator "focus."

For a hemispherical cavity having azimuthal symmetry about the axis of the resonator, the uni-phase modes have an electric field amplitude distribution on both reflectors which is Gaussian,[8] viz.

$$E(r) = E_o e^{-4r^2/D^2} \tag{4-1}$$

where r is the radial distance from the cavity axis. The quantity (D/2) is the value of r at which the field amplitude falls to (1/e) of its central (r = 0) value; we will refer to D as the spot diameter. Integrating the square of Eq. (4-1) over the reflector surfaces shows that 86.5% of the power reaching the reflector is contained within these spot diameters. Taking ℓ as the mirror spacing in a hemispherical system and r_s as the radius of curvature of the spherical mirror we find for the spot diameters[8]

$$D_f' = 2\left\{\left(\frac{r_s - \ell}{r_s}\right)(r_s\ell)^{\frac{1}{2}}\right\}^{\frac{1}{2}} \sqrt{\frac{\lambda}{\pi}} \tag{4-2}$$

$$D_s' = 2\left\{\left(\frac{r_s}{r_s - \ell}\right)(r_s\ell)^{\frac{1}{2}}\right\}^{\frac{1}{2}} \sqrt{\frac{\lambda}{\pi}} \tag{4-3}$$

on the flat and spherical reflectors respectively.

For the usual condition of hemispherical operation, ($\ell \simeq r_s = f$), D_f' can be written in terms of D_s' as

$$D_f' = 1.27\left(\frac{f}{D_s'}\right)\lambda_{air} \tag{4-4}$$

This is almost precistly the relation[10] between lens aperture diameter ($d \equiv D_s'$) and the diameter of the first Airy disk in the image formed by an ideal lens of focal length f. We may again use the focussing analogy to advantage in discussing the intensity distribution between the two reflectors. Except near the focal point F, which in this case is at the flat mirror, the mode phase-fronts remain spherical and the majority of the power in the beam is concentrated inside the geometrical ray cone drawn from F to a circle of diameter D_s' on the spherical mirror. This ray cone is shown in Fig. 4-4. On the other hand, the effects of diffraction become severe at the focal plane where instead of a geometrical point focus we have the total power smeared out over a disk of diameter D_f'. It is useful to define the focal region as that cylindrically shaped volume with diameter D_f' and length L

$$L = 6.770\left(\frac{f}{D_s'}\right)^2 \lambda \tag{4-5}$$

whose cylindrical axis is collinear with the resonator axis and centered at the geometrical focus F. Approximately 85% of the total power reaching the focal plane passes through this tubular region. Furthermore, Farnell[11] has shown that the wavefronts in the focal region are planes normal to the resonator axis. Figure 4-5 schematically illustrates a cross section of the focal

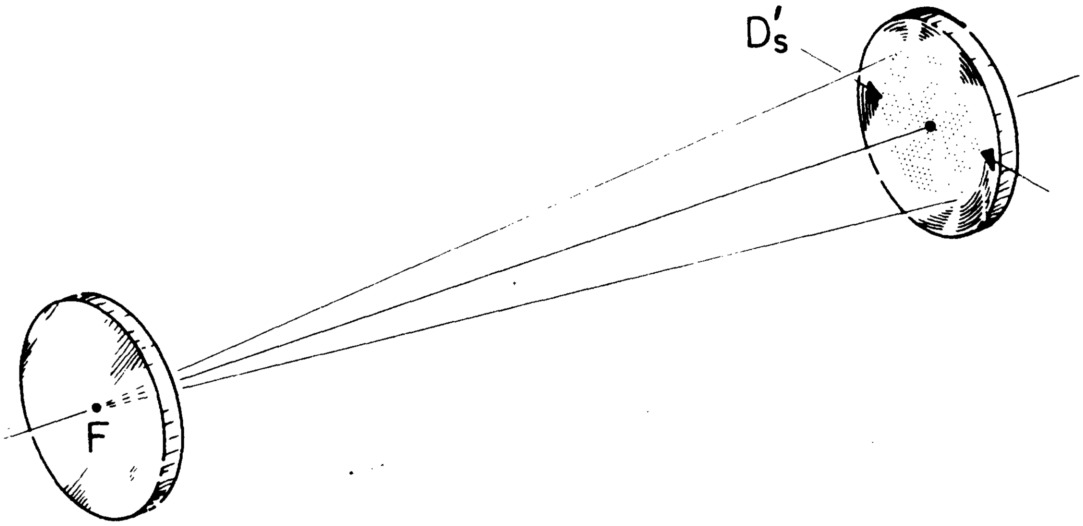

Figure 4-4 The geometrical ray cone of the constant phase normal modes of a near-hemispherical resonator.

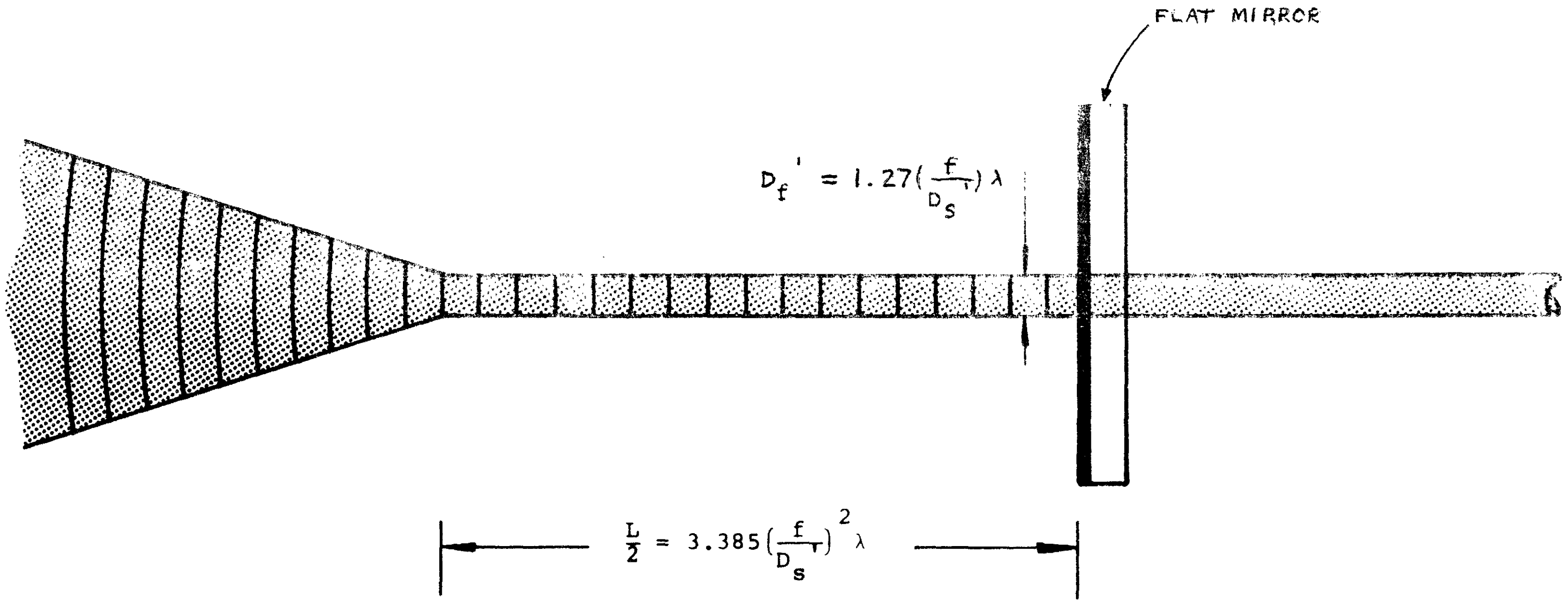
FLAT MIRROR
$D_f' = 1.27(\frac{f}{D_s})\lambda$
$\frac{L}{2} = 3.385(\frac{f}{D_s})^2\lambda$

Figure 4-5 A model of the intensity and phase profiles in the focal region of a hemispherical resonator.

region showing the general shape of the high intensity region and the wavefront behavior. The important conclusion is that the focal region of the hemispherical resonator operating in a uni-phase, TEM_{ooq}, mode consists essentially of a plane parallel pencil of light collimated to the diffraction limit.

The discussion presented in Section E.6 of Chapter 2 showed that such a plane wave, narrow pencil illumination of the scattering volume results in a maximum value of the scattered power per coherence area, P_{COH}. Therefore, the hemispherical resonator provides two regions, one inside and one outside the flat mirror, which are ideal for scattering purposes.* Furthermore, because the focussed beam is obtained without the use of auxiliary lenses, this system avoids an added source of wavefront distortion and consequent loss in heterodyning efficiency.**

Although Eqs. (4-2), (4-3), and (4-4) would indicate that the mirror spacing ℓ can be used to control the diameter of the focal region, in general D_s' and, therefore, D_f' are fixed by a second consideration. In the exactly hemispherical configuration the natural mode diameter on the spherical mirror approaches infinity and D_f' tends to zero. This situation is one of extremely high losses[6,7,8] since the aperture of the system is restricted to the inside dimensions of the plasma tube. The laser can be allowed to oscillate in the uni-phase modes by decreasing the mirror spacing until the geometrical ray cone of the mode fits inside the plasma tube.

---

* Chapter 3, Sections C.2.a.2 and D.3.a.

** Chapter 3, Section D.3.b.3.

At this point the losses are minimal and these modes oscillate strongly. By reducing ℓ further we can decrease D_s' and increase D_f'; however, this also allows oscillation on transverse modes, which in general have somewhat larger spot diameters and, therefore, larger losses than the uni-phase modes.[7,8,9]

In the present case the resonator length was adjusted to maximize the uni-phase power while suppressing all tendency for oscillation on transverse modes. Under these conditions with

$$r_s = 200 \text{ cm}$$

ℓ was approximately

$$\ell \simeq 199 \text{ cm}.$$

The spot diameter on the spherical mirror was estimated as

$$D_s' \simeq 0.53 \text{ cm} \tag{4-6}$$

Using Eqs. (4-4) and (4-5) we have for the dimensions of the focal region

$$D_f' = 0.030 \text{ cm} \tag{4-7}$$

and

$$(L/2) \simeq 30 \text{ cm} \tag{4-8}$$

The predicted value of D_f' was checked by direct observation of the beam diameter at the flat mirror using a 20X power microscope. This measurement gave $D_f' \simeq 0.01"$ $= 0.025$ cm.

The uniphase laser power output in the hemispherical configuration was

$$P_{\text{OUTPUT}} \simeq 25 \text{ milliwatts}$$

continuous output at $\lambda_{air} = 6328.2$ Å, and was avilable through the flat mirror ($R \approx 0.98$). Assuming a negligible loss coefficient* in the mirror coating this corresponds to a cavity power of

$$\frac{P_{OUTPUT}}{T} = 1.25 \text{ watts}$$

where T is the reflector transmission coefficient.

A second important advantage of the hemispherical uni-phase mode of operation is that the available laser output consists of a spherically spreading wave emanating from a diffraction limited point source. As we saw in Section E.4.c of Chapter 2 the wavefronts of the scattered field in the Fraunhofer region are also spheres. Therefore, if the laser output is used as the local oscillator source, the necessary wavefront matching** can be accomplished with a minimum of difficulty.

The points in favor of the hemispherical resonator can be summarized as follows:

(1) It provides a collimated, plane wave beam without the use of additional optics. This collimated beam is avilable both inside and outside the resonator.

(2) It is a structure in which the lowest loss resonances are the desired uni-phase TEM_{ooq} modes.

(3) Its uni-phase output is a simple spherically spreading wave.

---

* The loss coefficient of good dielectric coatings is typically less than (0.002).

** Chapter 3, Section D.3.b.2.

3. Amplitude Modulation Effects

Operation of the laser under varying conditions revealed that serious amplitude modulation of the laser output, corresponding to rms power fluctuations of a few percent, were traceable to four primary sources.

a. Mechanical Stability

The first is any mechanical instability which can modulate the positions of the resonator reflectors. In the present system an angular misalignment of the spherical reflector by about (0.3) minutes of arc can completely stop the laser action.[5] This represents a tilting of the mirror surface from exact alignment by approximately one wavelength of light over the spot diameter.

The following steps were taken to minimize the mechanical instability problem. The reflectors were held in a pair of precision gimbal suspensions (GS-253) manufactured by the Lansing Research Corporation. Although capable of (0.1) second of arc resolution[12] these mirror mounts proved barely adequate from the standpoint of both rigidity and adjustability. The resonator itself was formed by attaching these mounts to a (3" × 6" × 8') solid piece of stress relieved aluminum jig plate. This base exhibited excellent thermal stability, showing only the expected linear change in length with varying temperature. However, it did have serious acoustic resonances. For this reason the experiments described here were carried out in the "40 foot room" facility of the M.I.T. Spectroscopy Laboratory. The floor of this room is acoustically isolated and effectively damped except for extremely low frequencies (≃3 cps). In addition, the room ambient audio noise level is exceptionally low under optimum conditions. Even with these precautions, the lower lower limit on laser amplitude modulation was, in fact, set by mechanical microphonics.* The modulation spectrum was peaked at zero frequency with a modulation index** of

$$2\pi[m(30\ \text{cps})] \simeq 10^{-6}\ \text{cps}^{-1}$$

at $(\omega/2\pi) \simeq 30$ cps which rapidly declined to better than $10^{-8}\ (\text{cps})^{-1}$ at $(\omega/2\pi) \simeq 1000$ cps.

b. Discharge Current Noise

The second source of amplitude instability was noise in the plasma tube discharge power supply. This problem was eliminated by the methods discussed at the beginning of this section.

c. Dust

The presence of dust inside the resonator provided a third source of power fluctuations. In a hemispherical resonator this problem is seriously enhanced by the small diameter of the laser beam in the focal region. In fact, a single dust particle located at the center of the focal region in some cases caused sufficient loss to stop the laser oscillation completely. This extraneous modulation was eliminated by sealing the open portions of the resonator in Plexiglas enclosures. The dust remaining inside the cavity was then electrostatically precipitated to the walls by rubbing the Plexiglas with a dry cotton cloth. After a few hours only one or two dust particles per second could be seen crossing a 30 cm length of beam near the resonator focus.

---

* Chapter 5, Section C.

** Chapter 3, Section F.3.b.

d. Axial Mode Locking

The fourth source of amplitude noise resulted from a weak interaction between the various longitudinal modes which were in simultaneous oscillation at maximum laser power output. Although the point was not stressed above, in fact, the uniphase modes correspond to an infinite number of resonances, TEM_{ooq}, which differ only in the value of their axial mode number q. The frequency difference between two adjacent resonances, TEM_{ooq} and $\mathrm{TEM}_{oo(q\pm1)}$ is called the axial mode spacing $\Delta\omega_{\mathrm{axial}}$ and is given by

$$\frac{\Delta\omega_{\mathrm{axial}}}{2\pi} = \frac{c}{2\ell} \tag{4-9}$$

where c is the velocity of light in the resonator. For $\ell \simeq 200$ cm we have

$$\frac{\Delta\omega_{\mathrm{axial}}}{2\pi} \simeq 75 \text{ Mc/sec}$$

Since the Doppler-broadened gain profile of the 6328 Å neon transition has a full-width at half-height of approximately 1.5 kMc/sec,[13] there are about 20 such

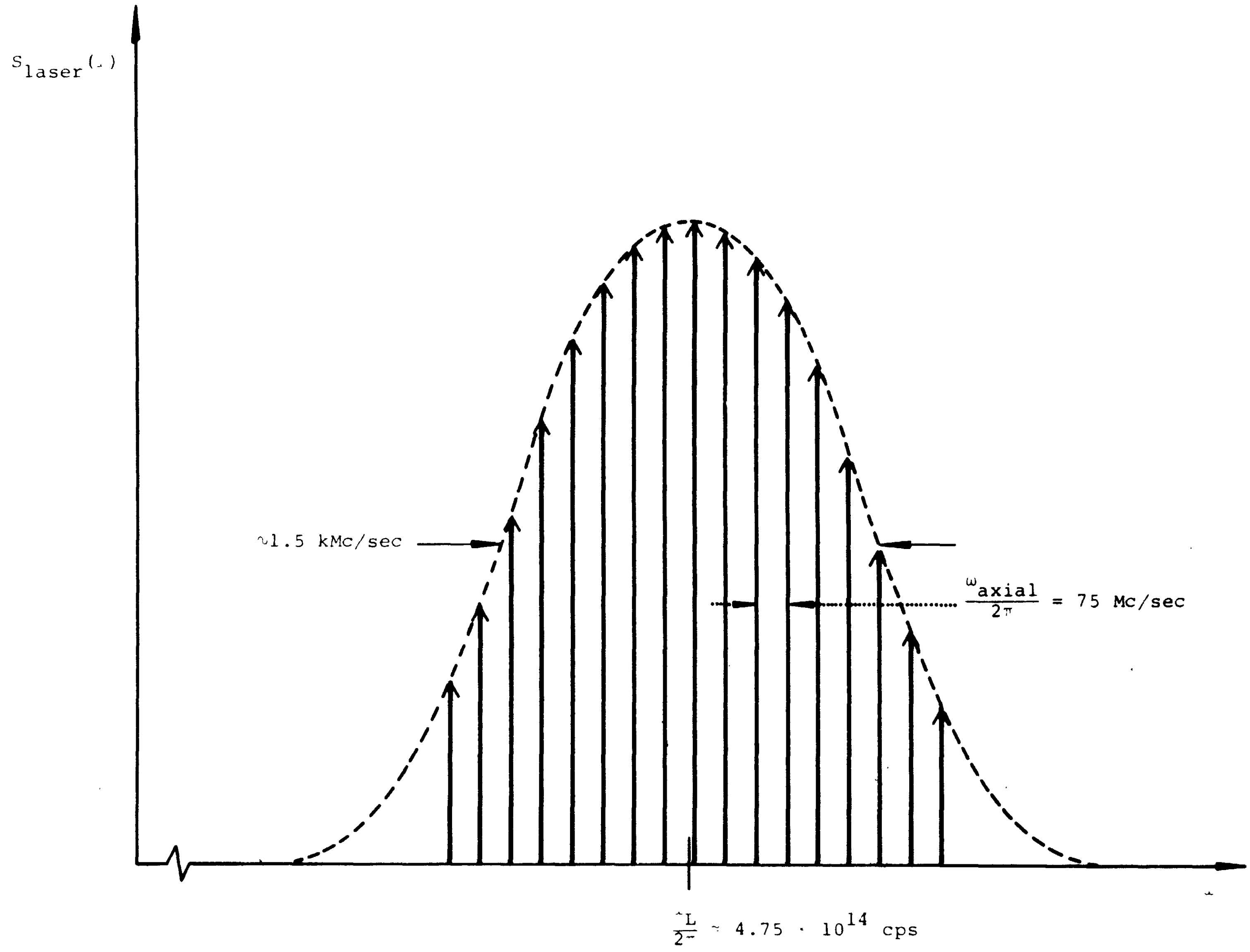

Figure 4-6 A typical laser power output spectrum.

modes in simultaneous oscillation at any given time. Figure 4-6 illustrates the corresponding power spectrum of the laser, $S_{LASER}(\omega)$.

In the absence of any non-linearity in the optical properties of the medium these modes are uncoupled and, therefore, would oscillate with random relative phases. However, Lamb[14] has shown that the reaction of the plasma to the process of oscillation is such as to result in a resistive as well as reactive coupling mechanism between modes. If this coupling is sufficiently weak the modes still oscillate with random phase; however, the resonance frequencies are slightly "pulled" from their uncoupled values. This pulling lifts the degeneracy of the axial mode spacing, $\Delta\omega_{axial}$. As the coupling strength is increased[15] a point is reached at which the modes spontaneously "phase lock" to one another; under these conditions the relative phases of the oscillating modes are exactly defined and time independent. In this case $S_{LASER}(\omega)$ as shown in Fig. 4-6 represents a time function which is a sine wave "carrier" at a frequency $\omega \simeq \omega_L$ being pulse modulated at the frequency of the unperturbed axial mode spacing. Recently, McClure[16] has observed that this "mode locking" will tend to occur naturally in sufficiently long cavities.

This natural locking tendency was found to be rather strong in the laser used for the present measurements. However, it was not sufficiently strong to keep the modes permanently locked as the length of the cavity varied due to thermal expansion. The observed result was a transition from locked to unlocked operation and a consequent return to lock as the cavity length changed by $(\lambda/2)$. Unlocked operation and particularly the transitions in either direction were always accompanied by a large amount of broadband audio ($\sim$2000 cps) amplitude modulation of the laser output. On the other hand, operation in the locked condition resulted in an undetectably small noise modulation.

The following method was used to observe and correct the cavity length in order to maintain the situation of maximum laser output stability. The degree of locking was continuously monitored by detecting beat-notes between the axial-modes with a high frequency photodiode and displaying the resulting current spectrum on a panoramic spectrum analyzer. The monitoring system is shown schematically in Fig. 4-7. A small amount of laser power available through the spherical mirror is focussed onto an EG&G SD-100 silicon photodiode. The resulting self-beat current is examined by a Singer-Metrics Division model SPA-4a Panoramic spectrum analyzer which is tuned to display approximately a 200 kc/sec wide band of frequencies centered at the axial mode spacing, $(\omega_{axial}/2\pi) \simeq$ 75 Mc/sec. The interpretation of the characteristic behavior of this spectrum as a function of cavity length can be summarized as below.

(1) The changing pattern of the beat spectrum repeated itself at regular intervals as the cavity length increased due to heat flow from the plasma tube to the resonator base. Since the operation of the laser should be identical whenever the axial mode resonances assume equivalent positions relative to the laser gain curve, this interval corresponds to a resonator length change $\Delta\ell = (\lambda/2)$. The time necessary for one such complete cycle was generally 30-100 sec.

(2) The laser operated in the locked condition during approximately 70% of one cycle. During this period the axial mode beat note was extremely narrow,

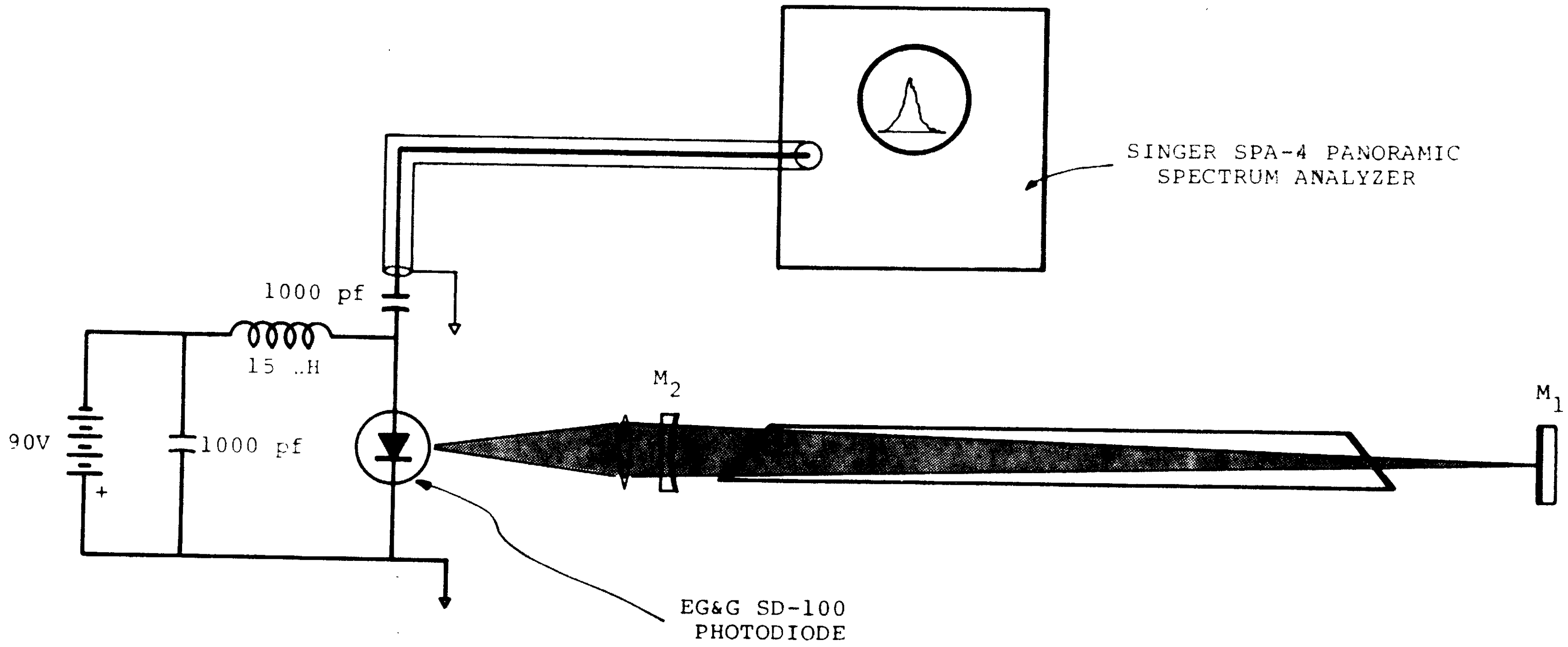
SINGER SPA-4 PANORAMIC
SPECTRUM ANALYZER
1000 pf
15 ..H
90V
+
1000 pf
M_2
M_1
EG&G SD-100
PHOTODIODE

Figure 4-7 Photodiode monitoring circuit used to observe changes in the axial mode beat pattern of the laser source.

having a width which was undetectable even at the minimum available analyzer resolution $(\Delta\omega/2\pi) \simeq 1$ kc/sec. Furthermore, the short term (< 1 sec) amplitude stability of the beat note was as good as the output stability of a good rf signal generator. The first condition indicates that the frequency spacing between all pairs of adjacent axial modes is degenerate, while the observed amplitude stabilization implies that the relative phases of these pairs is indeed constant with time.

(3) The power in the beat note as seen during the "locked" portion of the cycle executed a single maximum. The points of transition into and out of lock occurred at roughly 75% of this peak value.

(4) Operation in the unlocked condition produced a rather broad ($\simeq$ 150 Kc/sec) axial mode beat note spectrum which was composed of many closely spaced, barely resolvable contributions. Moreover, there was no detectable amplitude stabilization; the observed spectrum resembles that of a narrow band random noise generator.

In order to allow for small adjustments $(\pm\,\lambda)$ in the cavity length to one of the regions of stable, locked operation the spherical resonator mirror is mounted on a piezoelectric cylinder whose length is a function of the applied voltage. The "servo" system used to control this voltage is shown in Fig. 4-8. The battery voltage V_o is adjusted such that the range $V = 0$ to $V = V_o$ corresponds to a $(\lambda/2)$ length change of the piezoelectric element. The single turn potentiometer R_1 is made continuously rotatable so that V can be made to go "discontinuously" from $V = V_o$ to $V = 0$ or vice versa. In this way the continuous expansion of the resonator base caused by heating need be counteracted only over a range $\Delta\ell = (\lambda/2)$. Suppose,

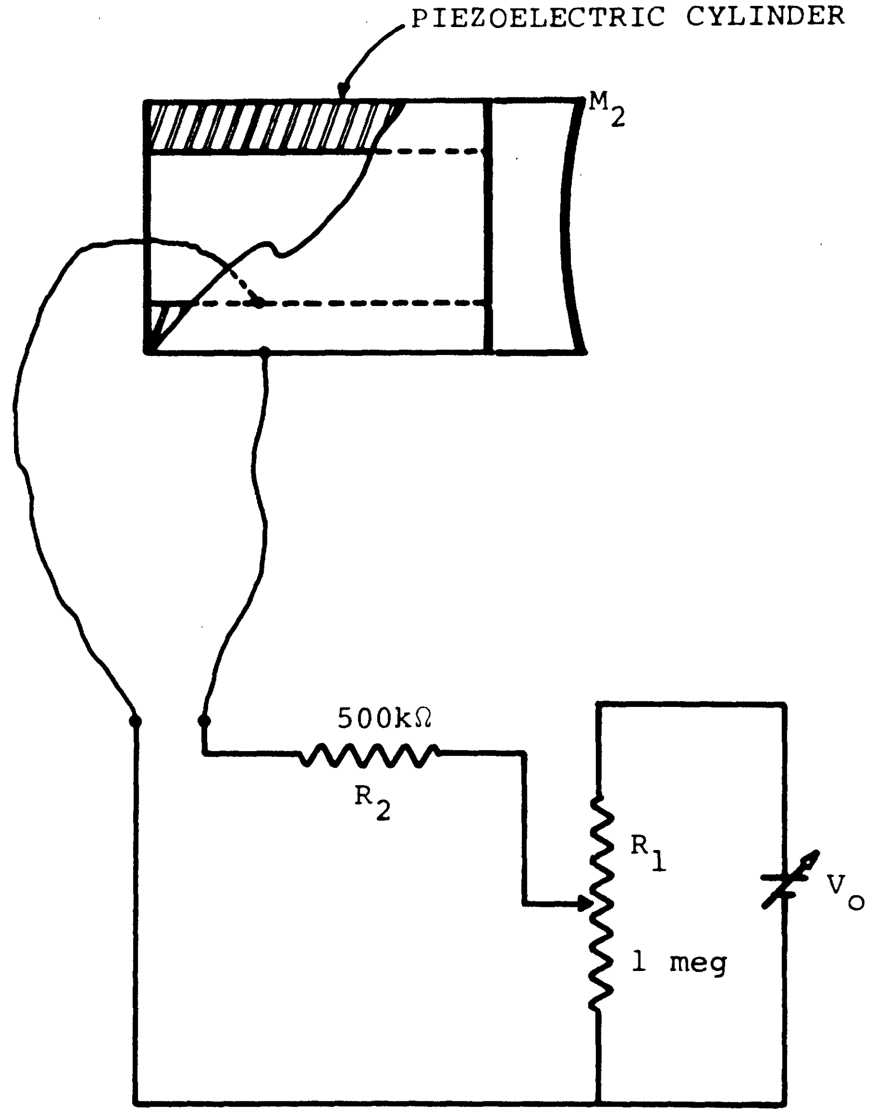
PIEZOELECTRIC CYLINDER
M_2
500kΩ
R_2
R_1
1 meg
V_o

Figure 4-8 Servo system used to control the laser cavity length.

for example, that the length of the piezoelectric element increases with increasing applied voltage. As the resonator base expands, V is increased to keep ℓ constant; however, when $V = V_o$ no further correction is avilable. At this point V is made to go "discontinuously" to V = 0, increasing the cavity length ℓ to $[\ell + (\lambda/2)]$. Since $\ell' = [\ell + (\lambda/2)]$ is also a region of stability the process repeats as before starting with V = 0. The RC network formed by resistor R_2 and the capacitance of the piezoelectric element guarantees that the change in applied voltage across the element occurs slowly enough to avoid transients in the laser output.

The servo loop is completed manually by visually observing the beat note power on the spectrum analyzer; R_1 is then rotated to keep this power near its peak value. Under these conditions the total rms noise modulation on the laser power output due to the locking phenomenon was less than (0.005%). In terms of the modulation index $m(\omega)$ this implies the result

$$\int_0^\infty m(\omega)d\omega < 5 \times 10^{-5}$$

e. Importance of the Modulation Effects

For measurements on the spectrum of the central component, which were made using a zero intermediate frequency ($\omega_1 = 0$), all four of the above precautions were necessary to insure that the self-beat between the local oscillator and its own modulation spectrum did not swamp the desired heterodyne signal. On the other hand, the intermediate frequency for detection of the Brillouin components was $(\omega_1/2\pi) = 30$ Mc/sec.

In this case no dust shielding or cavity length control were required even though* very large local oscillator powers were necessary to overcome the photomixer dark current.

C. The Scattering Cell

The cell which contains the liquid sample was designed specifically to be placed in the focal region inside the laser resonator. As stated in the previous section, the optical power available in the cavity was approximately fifty times greater than the actual laser output. However, if intra-cavity operation is to result in an enhanced incident power, the cell design must meet three criteria. First, because the amplitude of the laser oscillation can be seriously reduced even by very small losses (0.1%) introduced into the resonator, special precautions are necessary to keep these losses to an absolute minimum. Second, the allowed tolerance on the cell dimensions must be small enough to guarantee that the cell may be adjusted inside the cavity without causing an apparent misalignment of the resonator mirrors due to wedge angle effects. Third, the non-uniformity in optical thickness of cell windows and fluid combined should not appreciably warp the wavefronts of the incoming beam. If possible, the apparent optical length of the cell should be uniform to within ($\lambda/20$) over the beam diameter.

---

* Chapter 3, Section F.3.b.

1. General Description

A sectional view of the cell used in the present experiments is shown in Fig. 4-9. With the cell properly oriented in the laser cavity the plane of this drawing contains the resonator axis, $\overline{AB}$, and also coincides with the plane of polarization of the incident electric field.

The cell is basically a cylindrical bar of stainless steel, C, with an axially bored hole S serving as the sample chamber.

a. Reflection Losses

In order to minimize reflection losses at the outer window surfaces, the faces of the cell are cut at an angle such that a ray which travels along the cell axis enters and leaves the windows at the Brewster angle, Θ_B. In actual use the cell is rotated about an axis normal to the plane of Fig. 4-9 in order to obtain the exact Brewster angle condition. At optimum alignment the total reflection loss at both windows is less than (0.1%). In general the window-liquid interface would represent a serious loss problem since ordinarily it will not have the same Brewster angle as the outer air-glass interface. In the present case, however, the index of refraction of the toluene sample ($n = 1.4925$) so closely matches the index of the window ($n = 1.52$) that this reflection is less than (0.002%) as calculated from the Fresnel equations.[17] Since the transmission of the flat mirror represents a (2%) cavity loss the Brewster angle cell design was quite adequate from the standpoint of reflection losses.

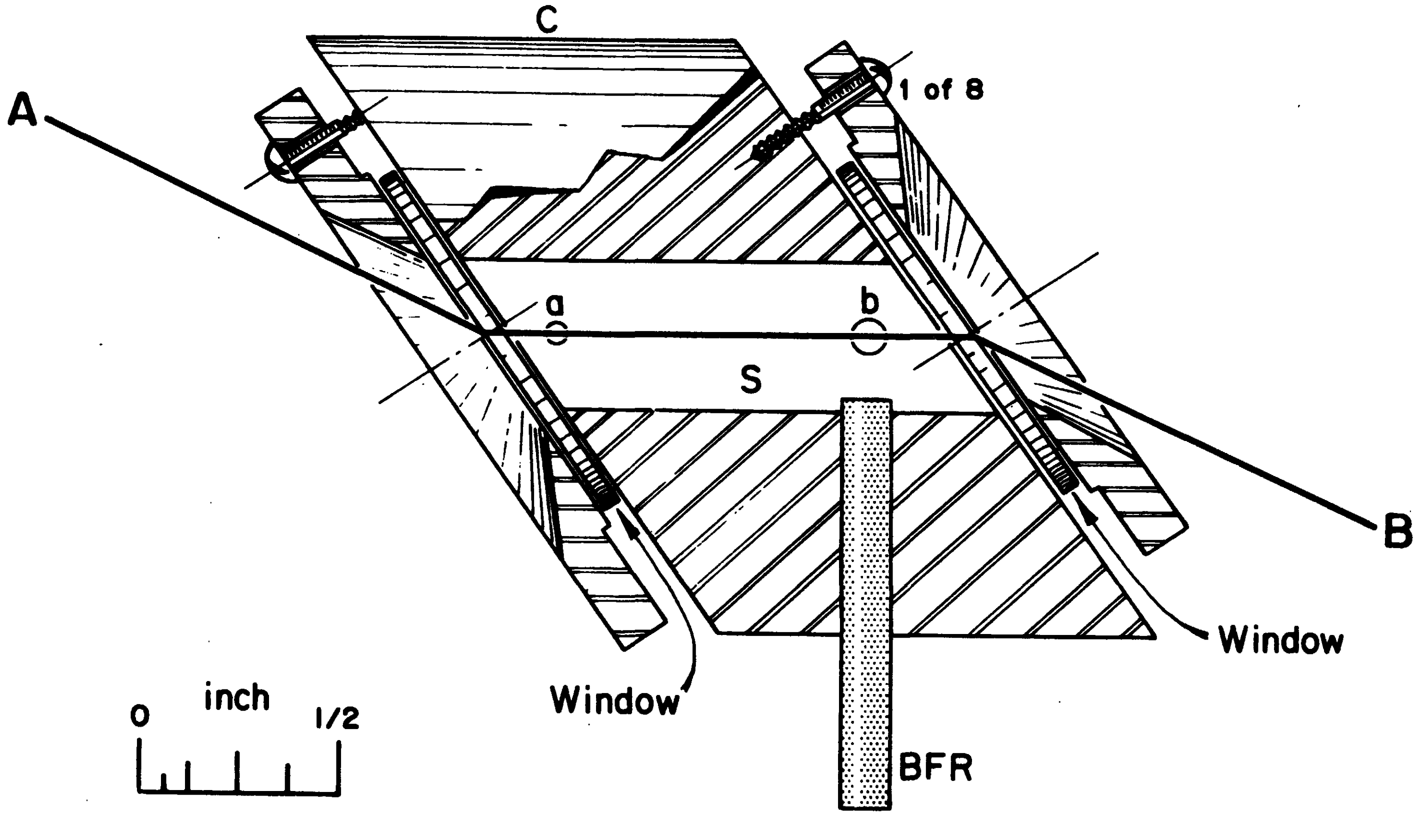
C
A
1 of 8
a
b
S
B
Window
Window
0
inch
1/2
BFR

Figure 4-9 A cross sectional view of the scattering cell.

b. Wedge Angle

Figure 4-10 illustrates the fact that inserting the cell into the laser resonator will result in a rather large (≃0.4") translation of the apparent cavity axis as seen by the nearest reflector, M_1. However, in the hemispherical resonator employed here, the desired position of the cell is inside the focal region; therefore, M_1 is a flat mirror. In this case, cavity alignment will be maintained automatically if the cell does not change the angular direction of the beam. The allowable wedge angle in the windows and cell body can be calculated easily in terms of the angular alignment sensitivity[5] of mirror M_1. Using the values of D_s', D_f', ℓ, and r_s given in the preceding section we find a maximum permissible wedge angle, α, as

$$\alpha \simeq 0.02 \text{ radians} \simeq 1^\circ$$

This large tolerance reflects the characteristic alignment insensitivity of the flat mirror in a hemispherical system and is quite easily satisfied.

For the cell shown in Fig. 4-9 there are two contributions to α, the wedge angles of the windows and the cell body respectively. The cell windows are standard reticle blanks[18] having a quoted wedge angle of less than 10^{-5} rad. Typical machining tolerance (±0.0001") on the thickness variation of the cell body contributed $\alpha \simeq 10^{-4}$ rad to the overall wedge. Experimental observations showed, in fact, that the angular readjustment of the flat mirror which was required to peak the laser output power once the cell was in the cavity generally amounted to less than 10^{-3} radians.

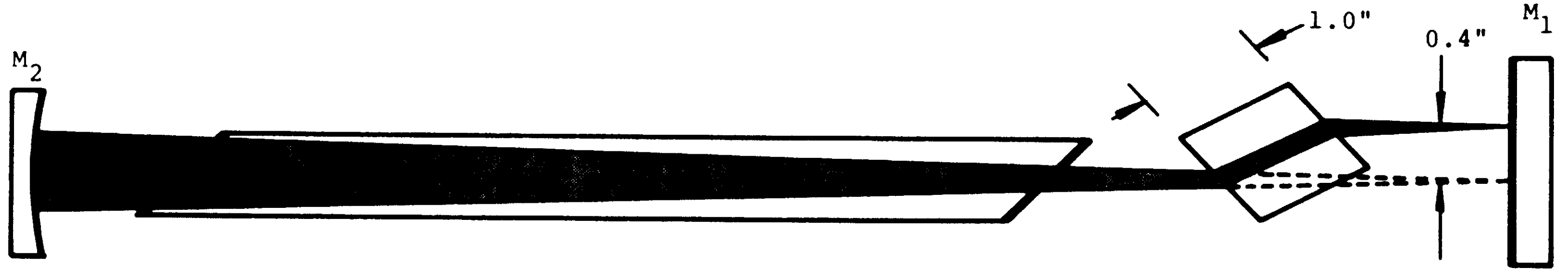

Figure 4-10 The geometrical effects of an intracavity scattering cell on the laser axis orientation in a hemispherical system.

c. Optical Thickness Distortion

The most serious problem encountered with intra-cavity operation was a severe wavefront distortion due to random variations in the apparent optical thickness of the cell. Assuming that the scattering liquid has a uniform temperature and hence index of refraction we may conclude that the problem originates entirely at the windows. Three principal sources of distortion were observed: (1) actual physical warpage of the windows induced by the stress of clamping, (2) poor surface flatness of the window blanks even in an unstressed condition, and (3) optical inhomogeneities in the window material.

The reticle blank windows employed here were circular disks 1.2 mm thick and 22 mm in diameter. The quoted surface flatness was $\pm(\lambda/4)$ over the central 10 mm diameter area. These windows were thin enough to introduce a negligible wavefront distortion from the viewpoint of inherent inhomogeneities; however, this thinness made them easily susceptible to bending. The following steps were taken to lower the clamping pressure necessary to join the windows to the cell body. First, the cell faces were fine ground to a flatness better than (±0.0001") using a conventional surface grinder. This figure was then improved to about $(\pm 3\lambda)$ by hand lapping in a slurry of Lava soap and water. Finally the faces were optically polished using chromium oxide on paper.[19] With this surface preparation a direct glass-to-metal optical contact could be achieved between the cell body and the windows using only minimal clamping pressure.

Based on the measured surface figure of the cell faces and the value quoted for the windows by the manufacturer we may estimate the optical thickness variation of the cell as ($\pm\lambda$) over a usable aperture of 1 cm. This represents a distortion of $\pm(\lambda/30)$ over the laser beam diameter ($D_f' = 0.030$ cm) in the focal region.

The above cell design proved to be entirely adequate for operation inside the cavity from the standpoint of optical quality. If could be inserted, translated, and rotated inside the resonator with only a small loss in alignment. This fact permitted adjustment of the cell to the exact Brewster angle and lateral positioning for minimum window scattering without the need for continuously retuning mirror M_1 to maximum laser output.

2. The Thermal Lens Effect

Although a factor of 50 enhancement in incident power was expected with intra-cavity operation, the gain obtained experimentally was between 2 and 4. With the cell in position the cavity power dropped from 1.25 watts to (50-100) milliwatts and the laser output correspondingly decreased from 25 milliwatts to (1-2) milliwatts.

The origin of this large unexpected loss of power was traced to a local heating of the fluid due to *absorption* of the laser radiation. This phenomenon has been observed and explained by Gordon and his co-workers[20] as a "thermal lens effect" resulting from gradients in the index of refraction of the medium induced by the heating. Although the absorption coefficient, A, of "optically clear" liquids is quite small[21] at $\lambda_{air} = 6328$ Å, $A \simeq 5 \times 10^{-4}\,\mathrm{cm}^{-1}$, a very slight temperature rise at the center of the illuminated region is sufficient to destroy the apparent optical homogeneity of the sample. The result is a large effective cavity loss due to distortion of the mode wavefronts.

Gordon et al.[20] have solved the required heat flow problem to determine the sample temperature distribution for a uni-phase laser beam having a Gaussian intensity profile. They find for the temperature rise on the beam axis

$$\Delta T(r=0) = \frac{0.06\mathcal{A}\mathcal{P}_{\text{cavity}}}{\Lambda} \ell n\left[\frac{2\gamma a^2}{D^2}\right] \tag{4-10}$$

$\mathcal{P}_{\text{cavity}}$ - the incident laser power

$\mathcal{A}$ - optical absorption coefficient of the sample at the laser frequency; in cm^{-1}

Λ - thermal conductivity of the sample

a - diameter of the sample chamber

D - spot size of the incident beam

γ - Euler's constant ($\gamma = 1.781\ldots$)

Using the following values for the quantities appearing in Eq. (4-10)

$\mathcal{P}_{\text{cavity}} = 100$ mW

$\mathcal{A} = 4.7 \times 10^{-4}\ \text{cm}^{-1}$ [21]- toluene

$\Lambda = 1.38$ mW/cm °C [22]- toluene

$a = 1$ cm

$D_f' = 0.030$ cm

we find

$$\Delta T(r=0) \simeq 17 \text{ millidegrees}$$

This temperature rise was sufficient to produce an apparent shortening* of the optical path along the beam axis; however, it has a negligible effect on the measurements of the properties of the fluid as deduced from the spectrum of the scattered light.

3. Refractive Corrections to the Scattering Angle

We turn now to a description of the scattering geometry as seen from outside the cell. Specifically we will consider three effects of refraction at the cell windows: (1) the change in the dimensions of the incident beam, (2) the alteration in the divergence angle between two rays from its value measured inside the scattering chamber S, and (3) the change in the apparent scattering angle.

The scattering plane, that is the plane containing the axes of the incident and scattered beams, was chosen as the plane of Fig. 4-9. Therefore, it coincides with the plane of Brewster angle incidence for the incoming beam. Figure 4-11 illustrates the trajectories of the incident beam and of two rays scattered from an arbitrary point inside the illuminated region as viewed in this scattering plane. For reference purposes we also show the cartesian co-ordinate system which was used to orient

---

* Toluene has a negative value of (dn/dT).

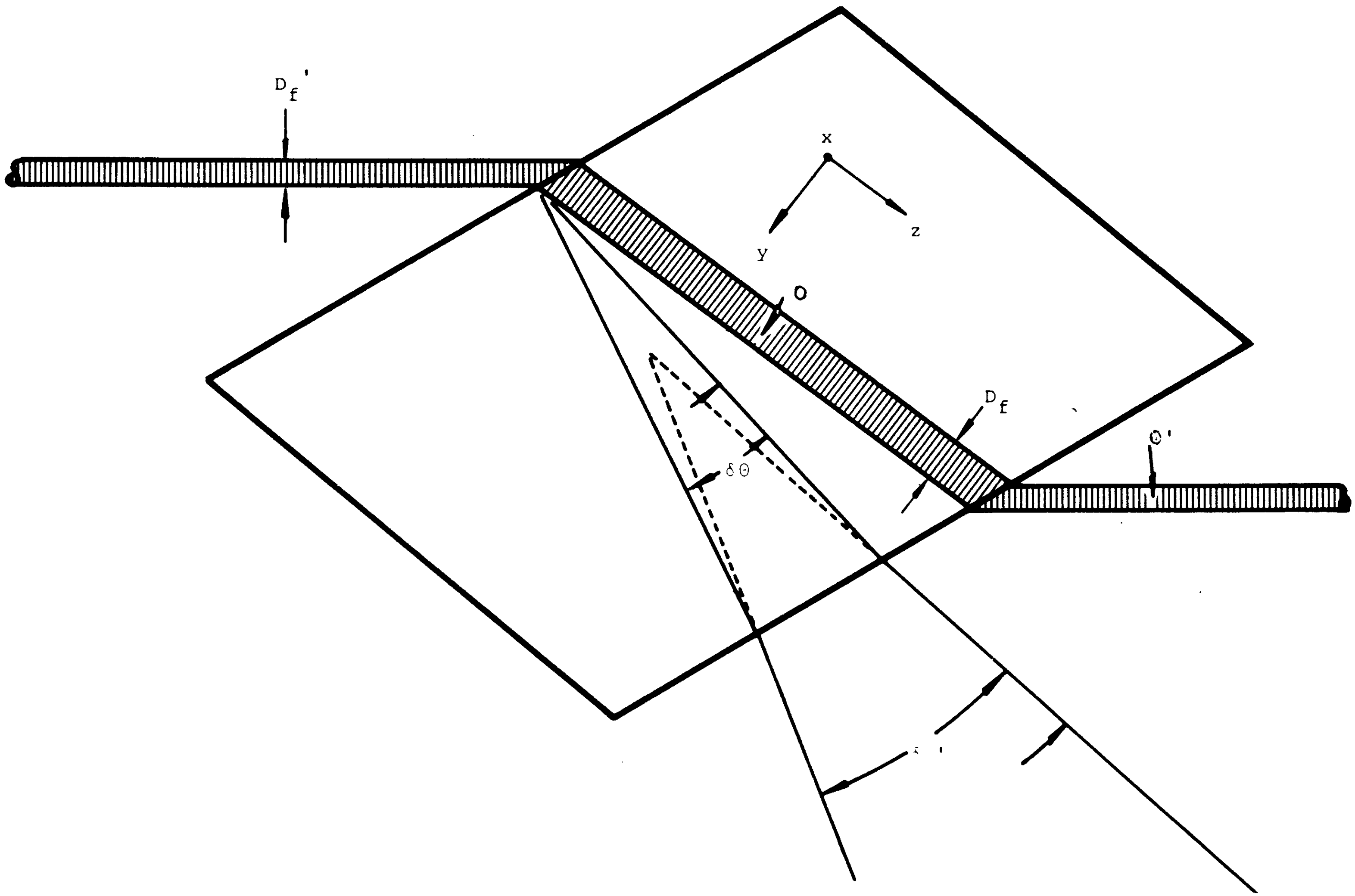

Figure 4-11 The relationship between the internal and external scattering angles, Θ and Θ' , as measured in the (y,z) plane of the scattering volume.

the scattering angles Θ and Φ introduced in Chapter 2.[*] Figure 4-11 corresponds to the situation $\Phi = 90°$.

The first effect of refraction is to increase the actual incident beam diameter D_f' to a larger value D_f as measured along the y direction inside the illuminated region. Using Snell's law and the Brewster angle[23] condition we find easily

$$D_f = nD_f' \tag{4-11}$$

where n is the index of refraction. We assume throughout that the indices of refraction of the toluene and the windows are the same and equal to n = (1.5). The resulting increase in the y dimension of the beam has a direct effect on the size of the coherence solid angle of the illuminated region.[**]

The second effect of refraction is to alter the true scattering angle, Θ, as observed from outside the cell. Calling the external angle Θ' and again applying Snell's law and the Brewster angle condition yields the exact relation

$$n\{\cos \Theta - n \sin \Theta\} = n \cos \Theta' - \sin \Theta' \tag{4-12}$$

For the small angles ($\Theta < 3°$) used in the present experiments we may to good approximation take $\sin \Theta \simeq \Theta$, $\sin \Theta' \simeq \Theta'$, and $\cos \Theta \simeq \cos \Theta' \simeq 1$. In this case we have from Eq. (4-12)

$$\Theta' = n^2\Theta \tag{4-13}$$

which is the desired result.

---

[*] Chapter 2, Section E, Fig. 2-4.

[**] Chapter 2, Section E.5.

The third effect of refraction is to modify the divergence angle $\delta\Theta$ between two rays leaving any given point in the scattering volume. This effect is extremely important since it directly modifies the coherence solid angle of the scattered light. Differentiating Eq. (4-13) gives the result

$$\delta\Theta' = n^2(\delta\Theta) \tag{4-14}$$

where $\delta\Theta'$ is the angular divergence of the rays as viewed from outside the cell.

The geometry in the direction perpendicular to the scattering plane can be handled in a similar manner. Figure 4-12 shows a cut through the illuminated region in the xz plane of Fig. 4-11. Since the beam enters the cell at normal incidence in this plane its lateral dimension is unaltered. A single application of Snell's law gives the desired relation between the internal angle Ψ and the external angle Ψ' as

$$n \sin \Psi = \sin \Psi' \tag{4-15}$$

For small Ψ this may be approximated as

$$\Psi' = n\Psi \tag{4-16}$$

The relationship between the internal and external divergence angles, $\delta\Psi$ and $\delta\Psi'$ respectively, follows directly from differentiating Eq. (4-16), namely

$$\delta\Psi' = n(\delta\Psi) \tag{4-17}$$

The results outlined above may be summarized as follows. As a result of refraction at the cell windows the incident beam has an elongated spot diameter with imensions D_f' and nD_f' in the x and y directions respectively.

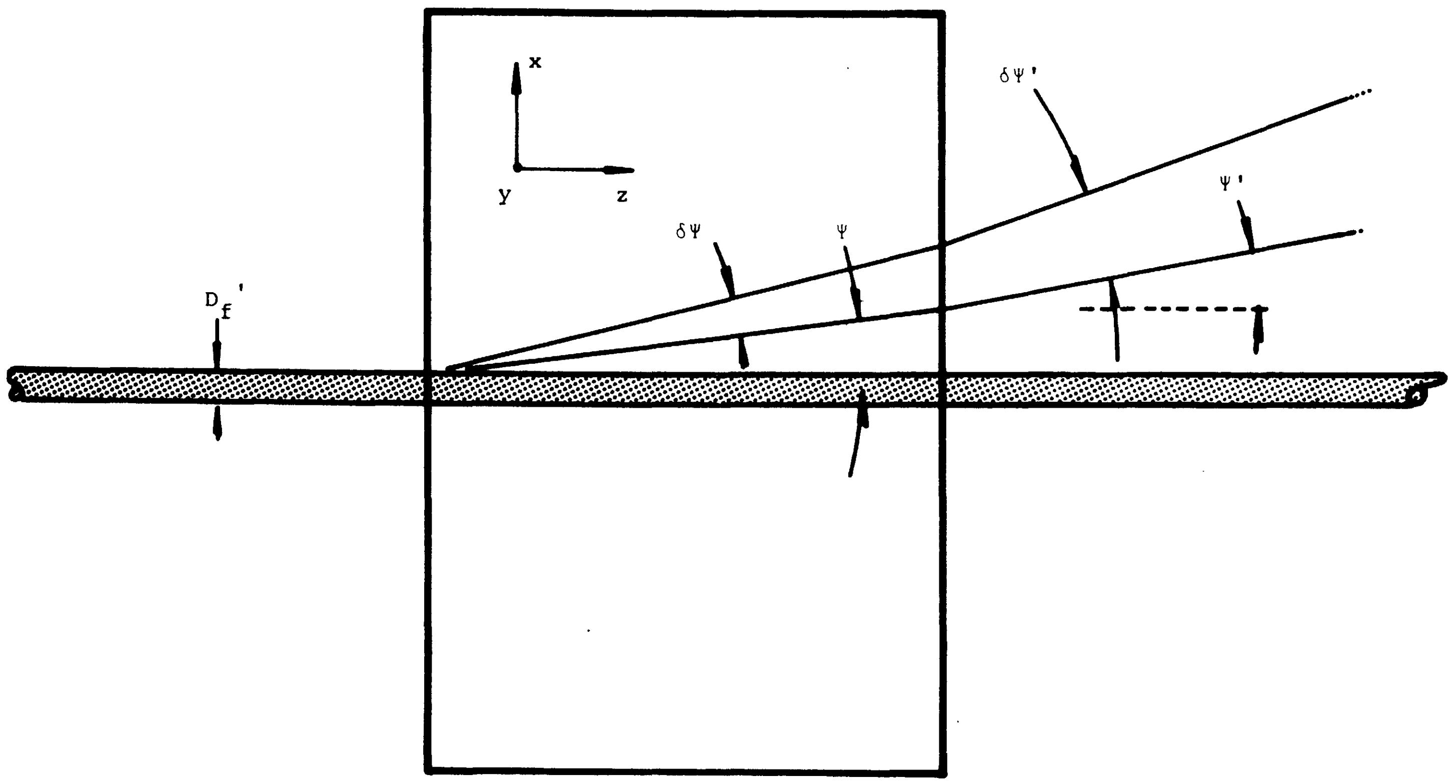

Figure 4-12 The relationship between the internal and external scattering angles, Ψ and Ψ', as measured in the (x,z) plane of the scattering volume.

Secondly, the light scattered into an angle Θ from the forward direction leaves the cell at an angle $n^2\Theta$ to the incident beam. Finally, since the true coherence solid angle, Ω_{COH}, may be written as a product of two coherence angles* as

$$\Omega_{COH} = 4\ \overline{\Delta\Psi}\cdot\overline{\Delta\Theta} \qquad (4\text{-}18)$$

it follows that the refraction corrections increase the apparent coherence solid angle by a factor n^3, i.e.

$$\Omega'_{COH} = n^3\Omega_{COH} \qquad (4\text{-}19)$$

where Ω'_{COH} is the coherence solid angle as measured outside the scattering cell.

4. The Dimensions of the Illuminated Region

Since the scattering cell was used inside the focal region of the laser described in Section B, the beam passing through the sample may be described as a collimated pencil of light with a cross-sectional intensity distribution given by**

$$I(x,y) = I(0,0)\ \exp -\left[\frac{8x^2}{(D_f')^2}\right]\ \exp -\left[\frac{8y^2}{(nD_f')^2}\right] \qquad (4\text{-}20)$$

The coordinates (x,y) are measured from the beam axis in the cartesian system of Fig. 4-11. For purposes of calculating the spatial coherence solid angle of the illuminated

---

[*] Chapter 2, Section E.5.

[**] Chapter 4, Section B.2.

region it is convenient to approximate this Gaussian distribution by the uniform intensity distribution

$$I^*(x,y) = \begin{cases} I(0,0) & ; \begin{cases} -\frac{L_x}{2} \le x \le \frac{L_x}{2} \\ -\frac{L_y}{2} \le y \le \frac{L_y}{2} \end{cases} \\ 0 & ; \text{otherwise} \end{cases} \tag{4-21}$$

Equating the total incident power for each case we find

$$L_x = \frac{D_f'}{\sqrt{(8/\pi)}} = \frac{D_f'}{1.596}$$

$$L_y = \frac{nD_f'}{\sqrt{(8/\pi)}} = \frac{nD_f'}{1.596} \tag{4-22}$$

where L_x and L_y will be called the lateral dimensions of the illuminated region. Using the measured value of D_f' and $(n=1.5)$ we have

$$L_x = 0.019 \text{ cm}$$

$$L_y = 0.028 \text{ cm} \tag{4-23}$$

$$L_z = 2.54 \text{ cm}$$

where L_z is the axial length of the scattering chamber.

5. Measurement of the Scattering Angle

There are a number of experimental factors which combine to preclude the use of a purely geometric procedure for fixing the scattering angle Θ and achieving the necessary alignment* between the scattered light and the local oscillator.

Firstly, for the small angles involved in the present measurements ($\Theta < 3°$) no simple geometrical method is capable of determining Θ to good fractional accuracy. Moreover, such a measurement would imply extremely precise knowledge of the direction of the resonator axis inside the scattering chamber.

Secondly, to achieve good heterodyning efficiency the wavefronts of the scattered light must be aligned with those of the local oscillator source to interferometric accuracy.* This is an extremely difficult condition to meet using a non-interferometric alignment technique.

Thirdly, even the exact relationship between the observed and true scattering angles as given in Eq. (4-12) assumes that the cell is set precisely at the Brewster angle relative to the resonator axis. In practice the laser power is rather insensitive to a rotation of the cell by as much as a few degrees. Therefore, unless the angle of incidence can also be determined directly, the calculation of Θ from a measurement of Θ' is uncertain.

To avoid these difficulties a simple trick was used to obtain an intense beam originating in the scattering volume and leaving the illuminated region at a precisely defined scattering angle, Θ. This technique utilizes the fact that the intensity of the light which is spontaneously Brillouin scattered from a sound wave of a particular wave vector K can be enhanced 8-9 orders of magnitude by launching an *externally generated* sound wave of the proper frequency and direction into the illuminated region. The result is a "Bragg reflected" or Brillouin scattered *beam* leaving the cell at an angle determined by the condition

---

* Chapter 3, Section D.3.b.

$$K = \frac{\bar{\omega}}{v_s} = 2k_o \sin\frac{\Theta}{2} \tag{4-24}$$

which was derived in Chapter 2.

K - the wave vector of the scattering sound wave

$\bar{\omega}$ - the angular sound wave frequency

v_s - the phase velocity of sound in the medium

$k_o = \left(\frac{2\pi}{\lambda_{air}}\right)n$ - the wave vector of the incident light in the medium.

Therefore, by measuring the frequency of the injected sound wave we may *compute* the scattering angle, Θ.

This method of angle measurement had a number of distinct advantages. One, it determined the quantity K directly by producing a beam which is scattered from a particular wavelength fluctuation. From Section D of Chapter 2 it is clear that K rather than Θ is of fundamental importance; for example, the splitting of the B-M doublet and the width of the central component are given by

$$\varpi = v_s K \tag{2-102}$$

and

$$\Gamma = (\Lambda/\rho c_p)K^2 \tag{2-82}$$

respectively. Since the purpose of measuring ϖ and Γ is to determine the sound velocity and thermal diffusivity respectively, the specification of the alignment of the spectrometer in terms of K circumvents the necessity for a precise determination of the scattering angle.

Secondly, having an intense (1 mW) beam coming *from the scattering region* at the desired *internal* angle Θ we can *visually* align the optical system of the spectrometer without explicitly calculating the refractive effects at the cell windows.

Finally, by observing the *beat note* between the Bragg beam and the local oscillator we can effectively bring the wavefronts of the scattered light into *interferometric alignment* with the local oscillator simply by adjusting the optical system for maximum beat note amplitude and, hence, maximum heterodyning efficiency. With approximately 1 milliwatt of power in each of these beams the detection of the beat note becomes quite easy even when the system is in only crude alignment.

Fluid contamination and the necessity of placing a sound wave transducer inside the sample chamber were eliminated by injecting the sound waves into the cell through the fused quartz buffer rod, BFR, shown in Fig. 4-9. The transducer is an X-cut crystal quartz disk having a 10 Mc/sec fundamental thickness resonance and co-axially plated gold-platinum contacts. The disk is bonded onto the end of the buffer rod using a thin film of crystalline salol (salicylic acid, phenyl ester) or a high viscosity silicon grease.

An rf voltage applied between the transducer contacts generates a longitudinal sound wave travelling along the axis of the buffer rod. In the limit of small Θ, $\Theta < 5°$, the wave vectors of the sound waves responsible for Brillouin scattering are very nearly perpendicular to $\vec{k}_o$, the wave vector of the incident light. Therefore, the required orientation between $\vec{k}_o$ and $\vec{K}$ is achieved by having the buffer rod axis at right angles to the length of the illuminated region as is indicated in Fig. 4-9.

Figure 4-13 gives a pictorial-schematic diagram of the apparatus used to drive the transducer. For the angles involved here $(0.3° \leq \Theta \leq 2.8°)$ the required sound wave frequency ϖ was in the range 16.7 Mc/sec $\leq (\varpi/2\pi) \leq 153.5$ Mc/sec. The rf driving signal is obtained from a Hewlett-Packard Model 608D V.H.F. signal generator and amplified to approximately 15 volts rms by a Boonton Model 230A RF power amplifier. This output is then stepped up to approximately 150 volts rms by an inverted π network[3] and applied to the transducer electrodes. A Hewlett-Packard Model 5245L electronic counter measures the signal generator frequency to an accuracy of one part in 10^6.

For frequencies below 100 Mc/sec a driving voltage of 150 volts was sufficient to scatter approximately 2% of the incident power into the "Bragg" beam. In this case the power in the scattered beam was equal to the laser output power. At higher sound wave frequencies the attenuation between the end of buffer rod and the illuminated region due to acoustic absorption in the sample became serious and appreciably more voltage was required to maintain a sufficient amount of scattered power.

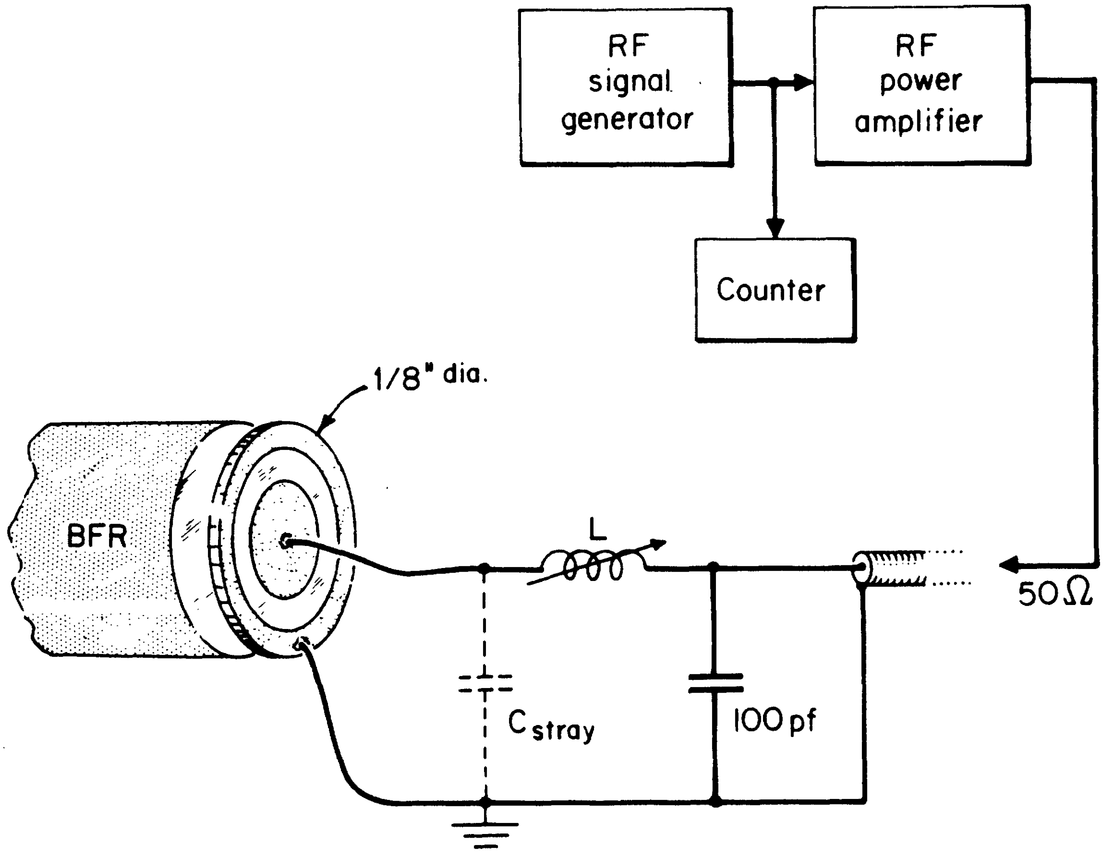
RF signal generator
RF power amplifier
Counter
1/8" dia.
BFR
L
C_{stray}
100 pf
50Ω

Figure 4-13 Pictorial and block diagram of the quartz transducer and associated electronics used to inject sound waves into the scattering cell.

Using the above technique K could be determined with an accuracy varying from (1.2%) at ($\Theta \simeq 0.3°$) to (0.7%) at ($\Theta \simeq 2.8°$). These quoted errors include a (0.6%) uncertainty in the velocity of sound in toluene. The remaining error originates entirely in the alignment procedure discussed in Section E.

6. Sample Preparation

After careful cleaning and assembly the sample cell was filled by a continuous flushing procedure which served to eliminate all foreign particles left inside the sample chamber. Baker reagent grade toluene entered the cell through the radial hole a shown in Fig. 4-9 after passing through a Millipore[24] 25 mm diameter micro-syringe filter holder equipped with a (0.22μ) filter disk. Approximately 1000 cc of fluid were necessary to completely flush the 2 cc sample chamber. This cleaning procedure was found to be extremely important in eliminating fluctuations in laser output power caused by particles that slowly drifted through the illuminated region.

D. The Optical and Electronic System for Detection of the Brillouin Components

1. The Optical System

Figure 4-14 shows the basic optical system of the superheterodyne spectrometer which was used to detect the Brillouin-Mandel'shtam components in the light scattered from toluene at ($\Theta \simeq 0.5°$). The light coming from the Brewster angle cell C at the appropriate external

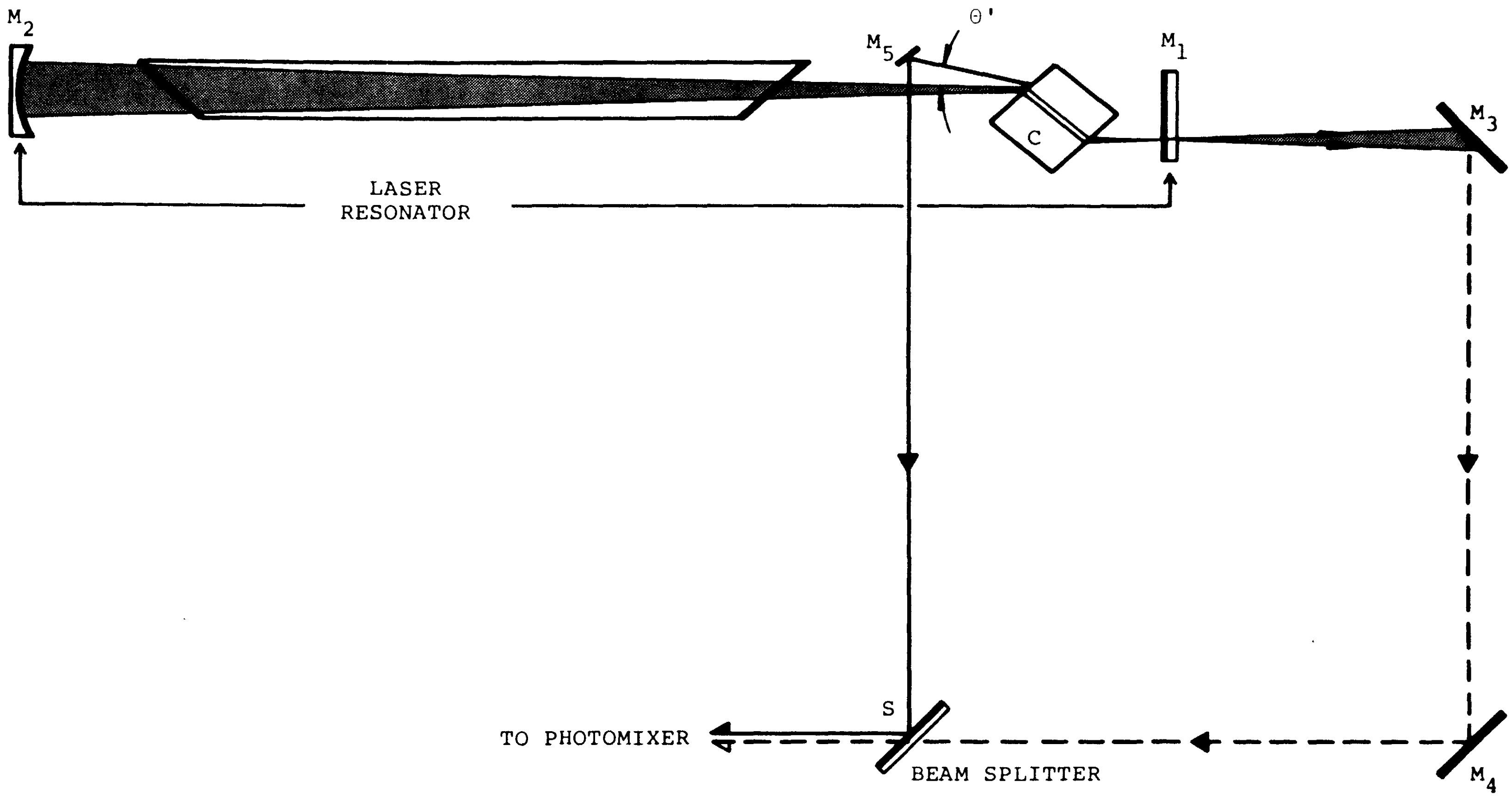
M_2
M_5
θ'
M_1
M_3
C
LASER
RESONATOR
S
TO PHOTOMIXER
BEAM SPLITTER
M_4

Figure 4-14 Basic Mach-Zehnder optical system used as a superheterodyne mixing spectrometer.

scattering angle Θ' is collected by a small mirror M_5 and sent to a beam splitter, S, where approximately one-half of the collected power is reflected in the direction of the photomixer. The local oscillator of the spectrometer is the laser output beam exiting through the flat resonator mirror M_1; it combines with the scattered light via mirrors M_3 and M_4, and the beam splitter.

The light gathering system composed of M_5, M_3, M_4, and S forms a classic 4-element Mach-Zehnder interferometer.[25] The approximate path lengths involved are:

$$\begin{aligned} \overline{CM_1} &= 6 \text{ cm} & \overline{M_1M_3} &= 25.4 \text{ cm} \\ \overline{CM_5} &= 33 \text{ cm} & \overline{M_3M_4} &= 38 \text{ cm} \\ \overline{M_5S} &= 38 \text{ cm} & \overline{M_4S} &= 64.4 \text{ cm} \end{aligned} \qquad (4\text{-}25)$$

Since M_1 is the flat reflector of a hemispherical resonator the local oscillator beam is a spherically spreading wave originating from a diffraction limited point source* located on mirror M_1. Thus the local oscillator wavefronts at the beam splitter are spheres of radius R_{LO}, where

$$R_{LO} = \overline{M_1M_3} + \overline{M_3M_4} + \overline{M_4S} = 127.8 \text{ cm} \qquad (4\text{-}26)$$

In addition, since the total signal path length to the beam splitter $\overline{CM_5} + \overline{M_5S} = 71$ cm is large compared to the maximum dimension of the illuminated region** $L_z = 2.54$ cm, the wavefronts of the scattered light at S are also spheres†

---

[*] Chapter 4, Section B.2.

[**] Chapter 4, Section C.4.

[†] Chapter 2, Section E.4

with a radius of curvature R_S given by

$$R_S = \overline{CM_5} + \overline{M_5S} = 71 \text{ cm} \tag{4-27}$$

Comparing R_S and R_{LO} indicates a sizable difference in the wavefront curvature of the two mixing fields. The maximum radius mismatch which can be tolerated if we permit a 40% loss in heterodyning efficiency $[B]_{\Delta\text{-RADIUS}}$ follows from Appendix D as

$$|R_{LO} - R_S| = (\lambda)(2R_{LO}R_S/d^2) \tag{4-28}$$

where d is either the local oscillator beam diameter at S or the characteristic dimension of one coherence area of the signal field at S, whichever is smaller.* In the present case we find

$$d = d_{COH} \simeq 0.2 \text{ cm} \tag{4-29}$$

as calculated below in Section E. This yields the condition

$$|R_{LO} - R_S| \leq 28 \text{ cm} \tag{4-30}$$

as compared to the actual difference

$$|R_{LO} - R_S| = 56.8 \text{ cm}$$

To avoid a serious loss in heterodyning efficiency because of this large mismatch, the real local oscillator source point at M_1 is imaged to a virtual focus at the required distance (71 cm) behind S by means of a simple negative

---

* Chapter 4, Section E.

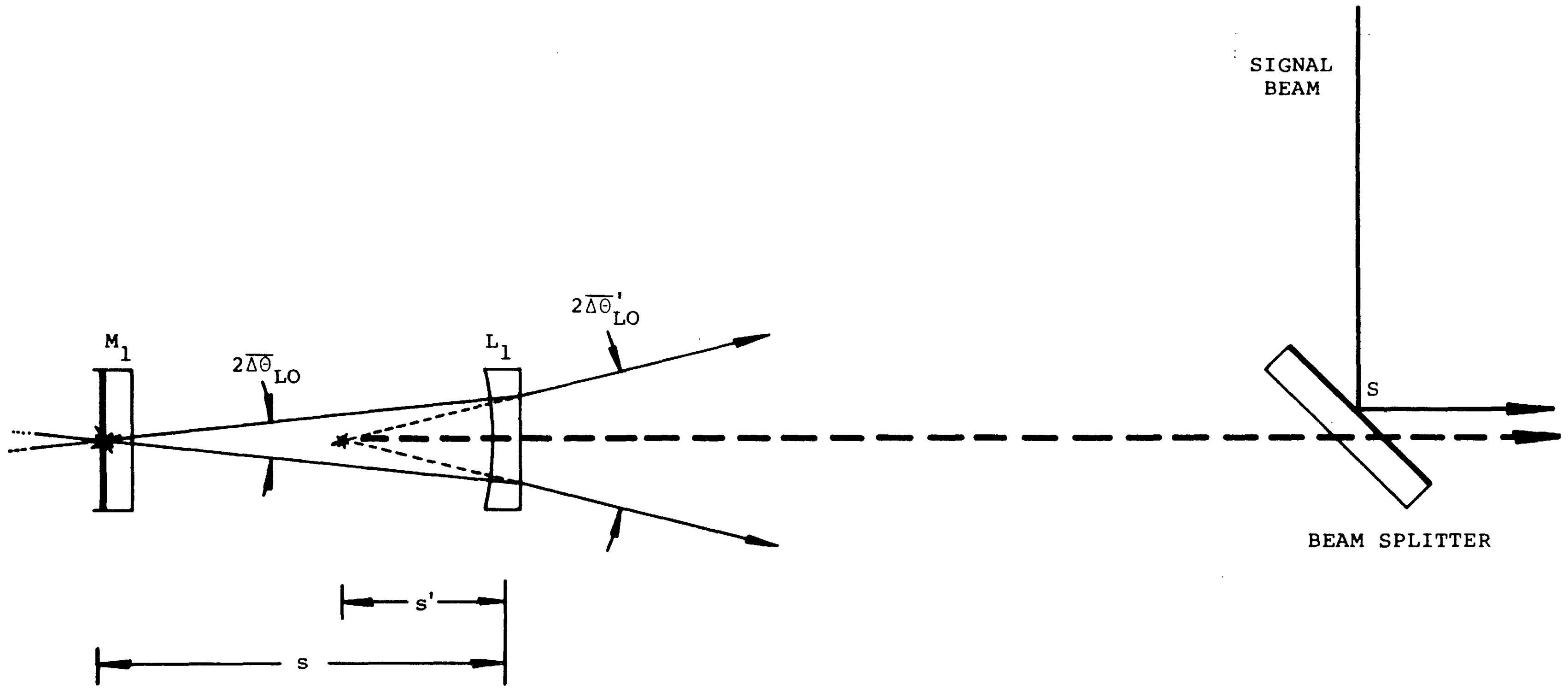
SIGNAL
BEAM
S
BEAM SPLITTER
M_1
$2\overline{\Delta\Theta}_{LO}$
L_1
$2\overline{\Delta\Theta}'_{LO}$
s'
s

Figure 4-15 The effect of a diverging lens on the apparent local oscillator source point and divergence angle.

lens. This lens alters the observed position and divergence of the local oscillator beam as illustrated in Fig. 4-15.

The distance between the lens and the virtual source point s' is given by the thin lens formula as

$$\frac{1}{s} - \frac{1}{s'} = \frac{1}{f} \qquad (4\text{-}31)$$

where f is the focal length (f < 0) and both s and s' are taken as positive quantities. Solving Eq. (4-31) for the apparent reduction in the local oscillator path length (s - s') yields the result

$$s - s' = \frac{s^2}{s + |f|} \qquad (4\text{-}32)$$

The lens also increases the observed local oscillator divergence angle $\overline{\Delta\Theta}_{LO}$ to an apparent value $\overline{\Delta\Theta}'_{LO}$ given by

$$\overline{\Delta\Theta}'_{LO} = \overline{\Delta\Theta}_{LO}(s/s') \qquad (4\text{-}33)$$

In the present system L_1 had a focal length of

$$|f| = 100 \text{ cm}$$

and the desired path length reduction of (s - s') = 56.8 cm was obtained with

$$s = 108.9 \text{ cm}$$

The corresponding increase in local oscillator divergence angle was

$$\frac{\overline{\Delta\Theta}_{LO}}{\overline{\Delta\Theta}_{LO}} \quad \frac{s}{s'} = \frac{108.9}{52.1} = 2.1 \qquad (4\text{-}34)$$

The layout of the complete optical system including the negative lens L_1 and a focussing lens L_2 is shown in Fig. 4-16.

For the experiment described here, mirrors M_1, M_2, and M_5 were held in Lansing Research Corporation Model GS-253 precision gimbal suspensions which were attached directly to the resonator base. Mirrors M_3 and M_4, the beam splitter S, and negative lens L_1 were also held in GS-253 mounts; in addition, L_1 had an intermediate translational stage which allowed it to be moved a distance of approximately 3 cm along the local oscillator beam axis. For stability reasons the four mounts were attached to large brass blocks which rested on a soapstone slab that also supported the laser base. The mechanical stability of this system is described below in the discussion of the optical alignment procedure.

In calculating the expected efficiency of the spectrometer is is important to include the effects of reflection and transmission losses in both the local oscillator and signal arms of the interferometer. The reflection and transmission coefficients of the beam splitter S were experimentally determined at $\lambda_{air} = 6328$ Å to be ($\mathcal{R} = 0.49$) and ($\mathcal{T} = 0.45$) respectively. The value of $\mathcal{R}$ for mirrors M_3, M_4, and M_5, which are all first surface aluminum coated reflectors, was measured as ($\mathcal{R} = 0.89$) at a 45° angle of incidence. The reflection losses at lenses L_1 and L_2, and at the rear surface of S may be taken as the usual (0.04) per surface.[26] The combined effects give a local oscillator power at the detector of approximately 29% of the laser output at M_1,

$$\mathcal{P}_{LO} \simeq 0.29\mathcal{P}_{LASER} \qquad (4\text{-}35)$$

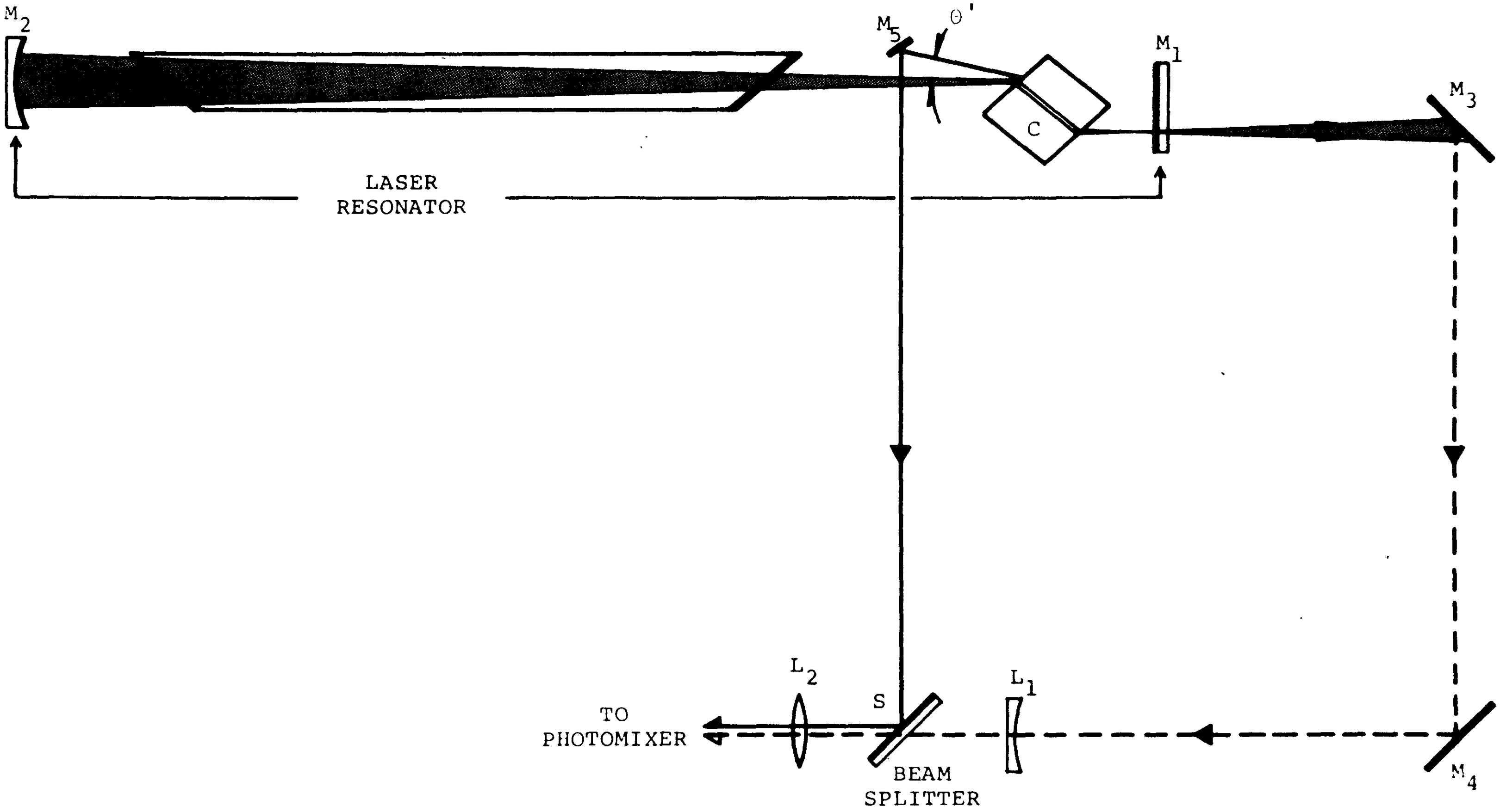
M_2
M_5
Θ'
M_1
M_3
C
LASER
RESONATOR
L_2
S
L_1
TO
PHOTOMIXER
BEAM
SPLITTER
M_4

Figure 4-16 Complete optical system of the superheterodyne spectrometer employed in measurements on the Brillouin components of the light scattered from toluene liquid.

The combined losses in the path of the scattered light give a detected signal power of

$$P_S \simeq 0.38 P_{SCATTERED} \qquad (4\text{-}36)$$

2. The Alignment Procedure

The systematic technique required to bring the optical system of Fig. 4-16 into interferometric alignment at some specific scattering angle, which in the present measurement was $\Theta = 0.547°$, is most easily described by giving the detailed steps of a typical alignment procedure.

We assume a starting point at which the laser reflectors are accurately aligned for maximum power in the absence of the scattering cell.

(1) The cell is then inserted and adjusted to the Brewster angle by minimizing the intensity of the specular reflections from the windows.

(2) At this point the cell may also be translated back and forth across the beam to avoid any window scattering that may be present.

(3) Mirror M_1 is now used to repeak the laser power and, if necessary, steps (1) and (2) are repeated to optimize the output.

(4) The exact positions of the beam splitter S and mirrors M_3 and M_4 are unimportant except that the final location of lens L_1 must fall at some available location in the $(M_1M_3M_4S)$ leg of the interferometer. Once some convenient position has been chosen for the beam splitter, M_3 and M_4 are simply aligned visually to

reflect the local oscillator beam through the approximate center of S.

(5) Sound waves of the appropriate frequency,* namely

$$\left(\frac{\overline{\omega}}{2\pi}\right) = \frac{v_s|\vec{K}|}{2\pi} = \frac{k_o}{\pi} \sin(\theta/2)$$

are now injected into the illuminated region using the system described in Section C.5 of this chapter. The sound wave amplitude is generally increased until the power in the Brillouin scattered beam exiting toward M_5 is approximately (0.5 mW). Mirror M_5 is then visually centered on this beam and its angles are adjusted until the reflected rays strike the reflecting surface of S at the same point as the local oscillator beam. The latter adjustment centers the two beams on each other at S to an accuracy of about (±0.5 mm).

(6) The locations of M_3, M_4, M_5, and S are now final; only the angular positioning of S and a slight angular readjustment of M_5 are necessary to complete their alignment. Therefore, the distances $\overline{CM_5}$, $\overline{M_1M_3}$, $\overline{M_5S}$, $\overline{M_3M_4}$, and $\overline{M_4S}$ are also fixed. These lengths are now measured to (±1 mm) accuracy and the results, together with Eqs. (4-26), (4-27), and (4-32), are used to determine the position of L_1. Lens L_1 is inserted at the appropriate point, visually centered on the local oscillator beam, and adjusted in angle until the rays which it reflects back toward M_1 are within a few beam diameters of retracing the local oscillator axis. The condition of exact back reflection results in the formation of a parasitic cavity between

---

* Chapter 4, Section C.5, Eq. (4-24)

$\underline{M_1}$ and $\underline{L_1}$ and leads to unstable laser operation.

(7) Mirror M_5 is now realigned, if necessary, to again center the two beams on each other at S as described in Step (5).

(8) With the beam axes in rough coincidence at S the directions of these two axes are now made approximately parallel by superimposing the two beam spots at another point about 3 meters from S in the direction of the photomixer. The beam splitter angles are set to make the centers of the two spots coincide to (±2 mm). This step yields an angular misalignment* $|\varepsilon|$ which is smaller than

$$|\varepsilon| \leq 10^{-3} \text{ radians} = 5 \times 10^{-2} \text{ degrees}$$

and completes the visual portion of the alignment procedure.

(9) The maximum tolerable angle between the two beams that still allows good mixing efficiency can be calculated from the "diameter" of the coherence area of the scattered field and the alignment criterion given in Eq. (3-118). Using d_{COH} as quoted in Eq. (4-29) we find

$$|\varepsilon| \leq 8 \times 10^{-5} \text{ radians} = 4.5 \times 10^{-3} \text{ degrees}$$

which is approximately 20 seconds of arc. The beam splitter angles are now set to this accuracy by focussing the two beams coming from S onto an auxiliary photomixer and searching for a beat note at the sound wave frequency $(\varpi/2\pi)$ due to mixing between the enhanced Brillouin beam and the local oscillator. The electronic system employed for this purpose was illustrated in Fig. 4-7. With approximately (0.5 mW) in each of the two beams even this simple system can detect a beat note which is a factor of 10^5 below its value at optimum alignment. Because of this sensitivity the coarse visual adjustment scheme given in steps (1) through (8) always resulted in an easily observed beat note and no "blind" searching was required.

---

* Chapter 3, Section D.3.b.

(10) The beam splitter S is now set to maximize the beat note amplitude; this adjustment results in a final misalignment angle $|\varepsilon|$ of less than 0.5 seconds of arc. At this point the negative lens L_1 may also be moved along the local oscillator beam axis to optimize the wavefront curvature; however, as would be expected from Eq. (4-30) this is an extremely non-critical adjustment. This step completes the interferometer alignment.

The availability of a strong, readily detected beat note between the "enhanced" Brillouin scattered light and the local oscillator also made possible a rather simple evaluation of the spectrometer stability and efficiency under actual operating conditions. Some of the more important observations are given below.

The Mach-Zehnder interferometer system proved to be extremely microphonic, a common problem with long path length instruments such as the one used here. This vibration sensitivity seemed to originate to a large degree in the rather poor mechanical stability of the mirror mounts, although some distortion of the soapstone interferometer table was also detected.

The modulation effects of dust inside the laser resonator and in the interferometer arms were negligible at the beat frequency of the experiment ($\varpi/2\pi$) = 30 Mc/sec. Furthermore, the mode locking phenomenon described in Section B.3.d of this chapter had an undetectably small effect on beat notes at this frequency. As a result, no dust shielding or cavity length control were found necessary in this portion of the experiment.

A semi-quantitative check was made on the actual heterodyning efficiency factor $[B_{COH}]$ by simply removing lens L_1 from the optimally aligned system. Using the values of R_{LO}, R_S and d_{COH} given in Eqs. (4-26), (4-27) and (4-29) respectively we find with the help of Appendix D that this should result in a decrease in the beat note power by a factor of approximately W = (6.3). The observed reduction was $W \approx 2$ indicating sufficient wavefront warpage* over d_{COH} to substantially offset the effect of L_1. An estimate of $[B_{COH}]$ with L_1 in position gives

$$[B_{COH}] \leq 0.3 \qquad (4\text{-}37)$$

3. The Electronic Detection System

a. General Discussion

The choice of the photomixer and electronic detection apparatus to be used with the optical system described above was made on the basis of one criterion: to provide a simple, low noise system which could detect the beat note between the local oscillator beam and the light spontaneously Brillouin scattered from toluene at a single angle ($\Theta = 0.547°$) where the Brillouin-Mandel'shtam shift

---

* Chapter 3, Section D.3.b.3.

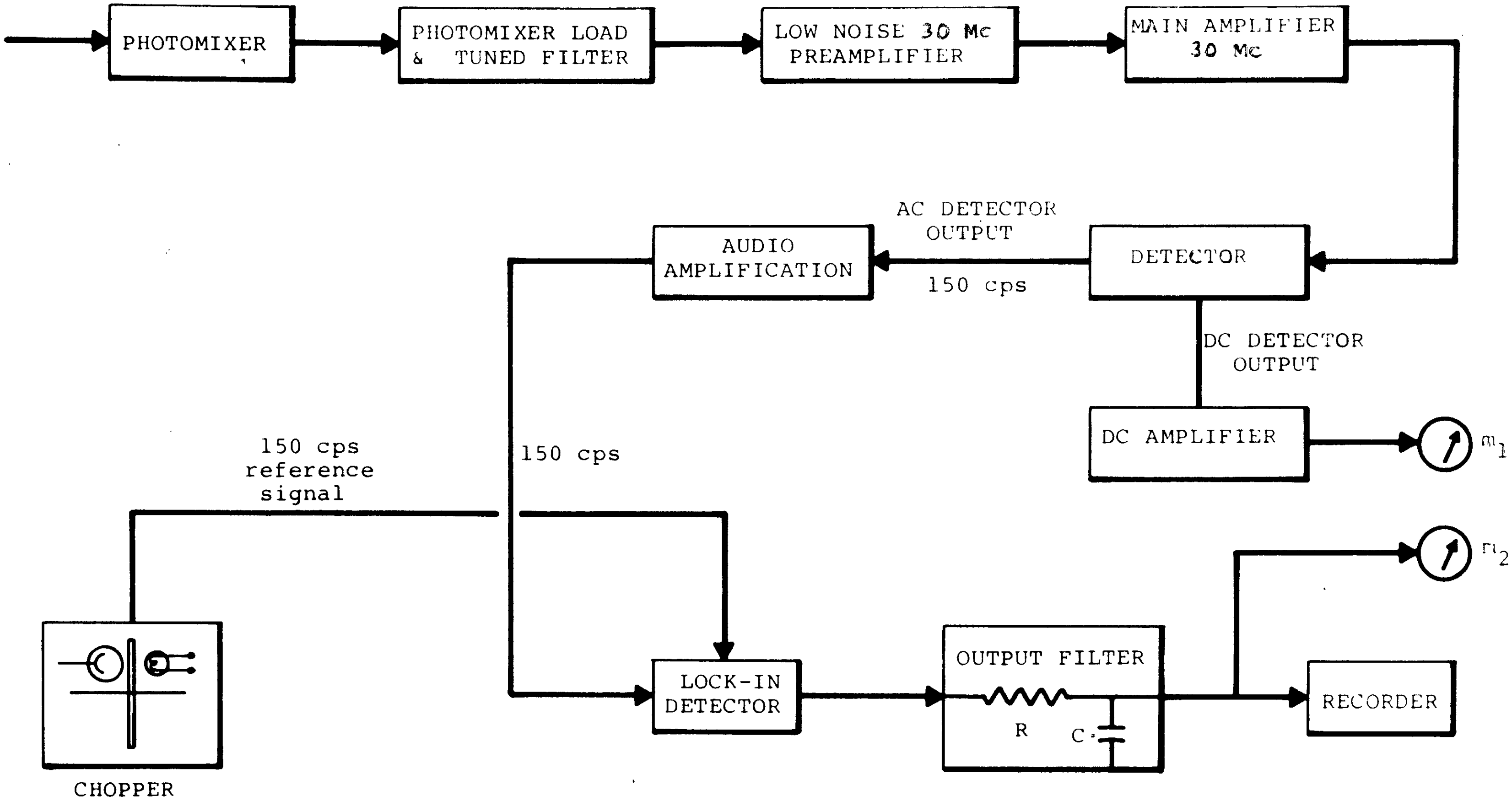
PHOTOMIXER
PHOTOMIXER LOAD & TUNED FILTER
LOW NOISE 30 Mc PREAMPLIFIER
MAIN AMPLIFIER 30 Mc
DETECTOR
AC DETECTOR OUTPUT
150 cps
AUDIO AMPLIFICATION
DC DETECTOR OUTPUT
DC AMPLIFIER
m_1
150 cps
150 cps reference signal
m_2
CHOPPER
LOCK-IN DETECTOR
OUTPUT FILTER
R
C
RECORDER

Figure 4-17 Block diagram of the superheterodyne spectrometer used in detecting the Brillouin components.

was $(\varpi/2\pi) = 30$ Mc/sec. Figure 4-17 shows a block diagram of the major components of this system.

The "tunable filter" which examines the photocurrent spectrum is simply a high-Q resonant circuit that also serves as the photomixer load impedance. The filtered current is amplified directly at the i.f. frequency and then sent to a square-law detector. Meter m_1 monitors the dc detector output voltage $\langle\!\langle v_D(t)\rangle\!\rangle$; its deflection is proportional to the total power in the filtered current including the beat note, shot-noise, Johnson noise, and excess amplifier noise contributions.* It was found experimentally that the pre-detection signal-to-noise ratio was rather poor; the filtered beat note power per unit bandwidth contributed only a very small fraction (≤ 0.01) of the total detector output. The following technique was used to prevent slow drifts in $\langle\!\langle v_D(t)\rangle\!\rangle$ from completely masking this small "signal." A chopping wheel inserted in the $\overline{CM_5S}$ arm of the interferometer interrupted the scattered light at a 150 cps rate; the "signal" part of the detector output is therefore a 150 cps ac signal whose amplitude can be measured by a conventional lock-in detector. Since the shot-noise, Johnson noise, and amplifier noise signals are unmodulated, meter m_2 responds only to the power in the signal component of the total filtered current. The desired heterodyne signal spectrum is then obtained by recording the lock-in output as the center frequency of the tuned filter is swept through its range.

The following sections describe some of the important features of the electronics from the "practical sensitivity" viewpoint which was adopted in Section F of Chapter 3. In particular, we discuss the experimentally measured values of the resolution and the quantities F_R and F_D which determine the degradation of the pre-detection (S/N) ratio from its ideal value.*

---

* Chapter 3, Sections C.2.b.2 and F.1.

b. The Photodetector

The photomixer which detected the 30 Mc/sec beat signal was an Edgerton, Germeshausen, and Grier model SD-100 silicon photodiode operating with 90V of reverse bias.[27] The principal advantages of this detector over the other devices listed in Table IV are: (1) its good quantum efficiency, (2) fast response, (3) a relatively large active area (0.073 cm^2), and (4) commercial availability. The dark current (20°C), quantum efficiency, and equivalent circuit parameters of the particular SD-100 used in this experiment were experimentally measured as

$$\begin{aligned} i_D &= 0.3\ \mu\text{amps} \qquad (T = 20°\text{C}) \\ \varepsilon &= 0.59 \\ C_j &= 7\ \text{pf} \\ R_s &= 220\ \Omega \end{aligned} \tag{4-38}$$

---

* Chapter 3, Section F.1.

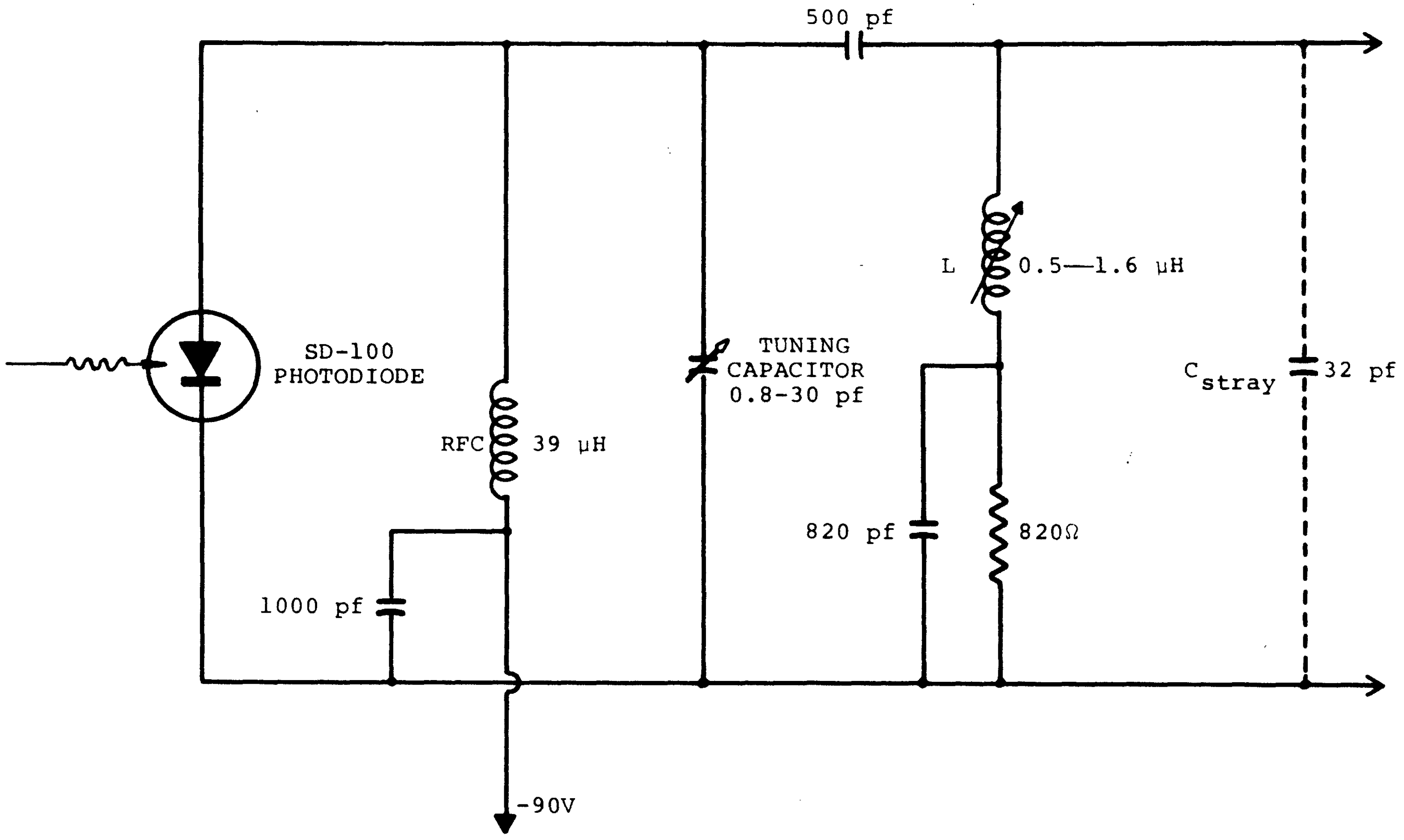
500 pf
SD-100
PHOTODIODE
RFC
39 μH
1000 pf
-90V
TUNING
CAPACITOR
0.8-30 pf
L
0.5—1.6 μH
820 pf
820Ω
C_{stray}
32 pf

Figure 4-18 The SD-100 photodiode load circuit.

c. The Tunable Filter and Photomixer Load Circuit

Figure 4-18 shows the circuit diagram of the combination photomixer load impedance and tuned filter element.

The parallel combination of L, C, C_{STRAY}, and the diode impedance form a resonant circuit whose center frequency can be swept from 26 Mc/sec to 34 Mc/sec via tuning capacitor C. A parallel equivalent representation of detector and load as drawn in Fig. 4-19 shows that the large amount of capacitance added to the circuit by C and C_{STRAY} has the effect of increasing the Q of the load resonance from

$$Q_o(30\ \text{Mc/sec}) = \frac{R_p}{X(C_j)} = 3.6$$

to

$$Q_1(30\ \text{Mc/sec}) = \frac{R_p}{X(C_j + C + C_{STRAY})} = 27 \qquad (4\text{-}39)$$

This method of Q increase was essential in obtaining a filter bandwidth ($\Delta\omega_f$) which was smaller than the line width of the signal part of photocurrent spectrum.*

Unfortunately, the circuit of Fig. 4-18 cannot be transformed to a simple frequency independent series equivalent of the type analyzed in Section F.4.c of Chapter 3. However, an explicit numerical calculation of the load impedance $\underline{Z}_L$ seen by the mixer at $(\omega/2\pi) = 30$ Mc/sec gives the circuit of Fig. 4-20a as compared

---

* Chapter 5, Section B.2.d.

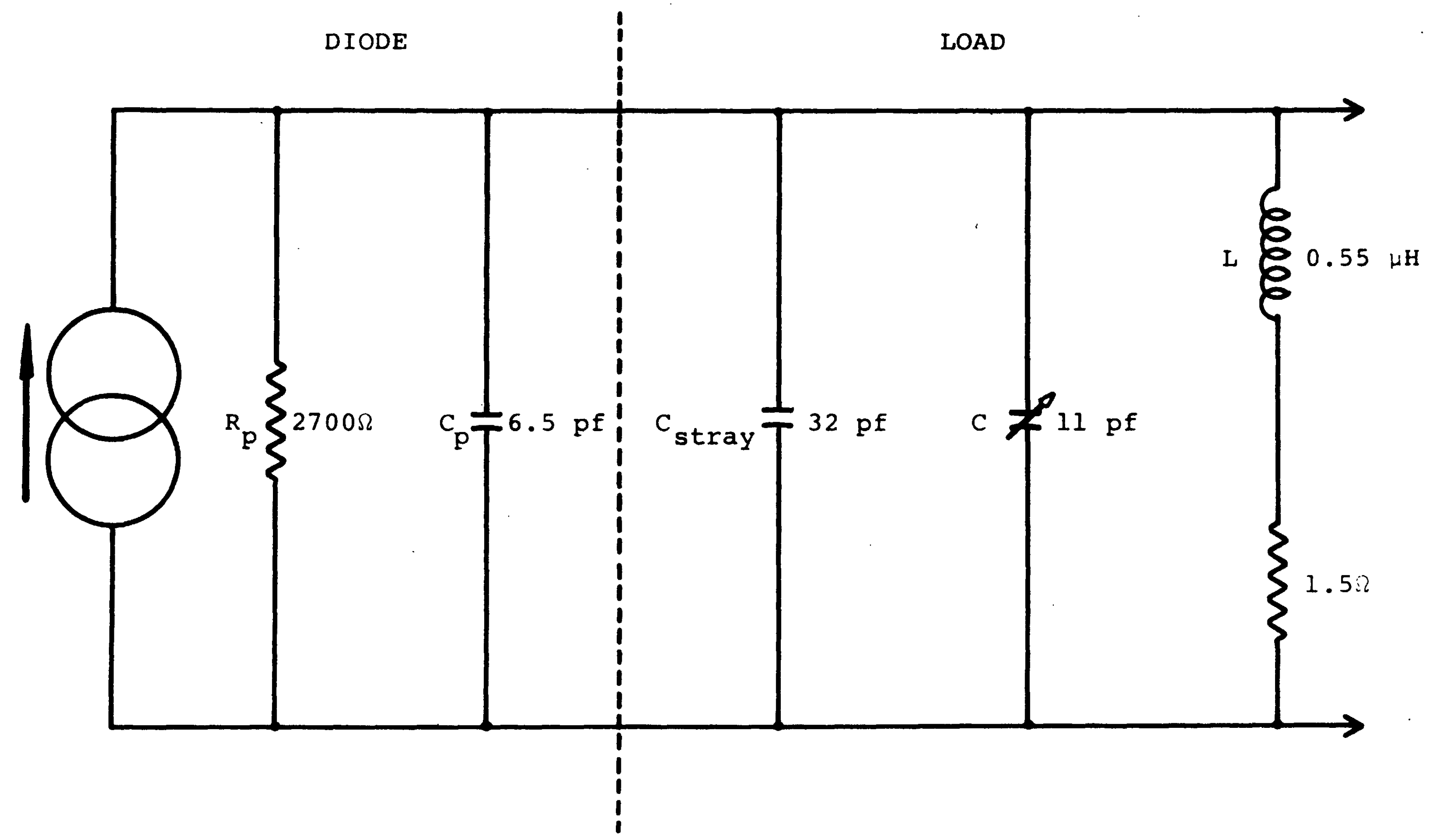
DIODE
LOAD
R_p 2700Ω
C_p 6.5 pf
C_{stray} 32 pf
C 11 pf
L 0.55 μH
1.5Ω

Figure 4-19 Equivalent parallel circuit for the photomixer and its load impedance.

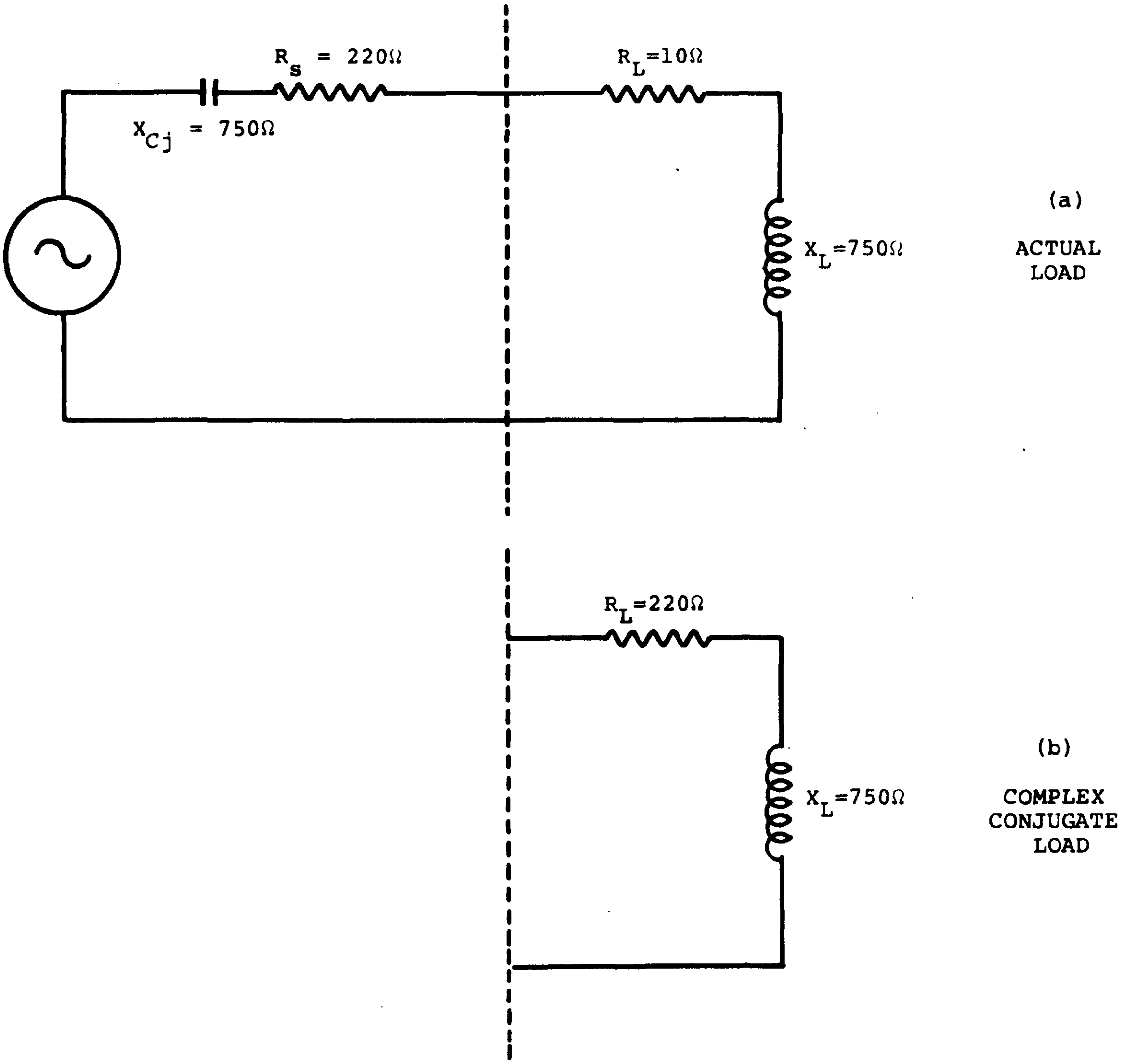
R_s = 220Ω
X_{Cj} = 750Ω
R_L=10Ω
X_L=750Ω
(a)
ACTUAL LOAD
R_L=220Ω
X_L=750Ω
(b)
COMPLEX CONJUGATE LOAD

Figure 4-20 Equivalent series circuit of the photomixer and load as compared to the ideal complex conjugate load.

to the ideal complex conjugate load shown in Fig. 4-20b. The consequence of the Q increase is a sacrifice in the efficiency of power transfer to the load and, therefore, a corresponding boost in the minimum optical local oscillator power required to achieve shot-noise limited operation.* The local oscillator power available at the detector was**

$$P_{LO} \simeq 0.29\ P_{LASER} \simeq \frac{1}{3}\ \text{milliwatt}$$

yielding a dc photocurrent of

$$i_p = 100\ \mu\text{amps} \qquad (4\text{-}40)$$

The thermal noise part of the signal-to-noise reduction factor F can be calculated from Eqs. (3-175) and (3-219) and the observed dc photocurrent. The predicted value of F_R is

$$F_R(30\ \text{Mc/sec}) = \frac{2kT}{ei_p}\ \frac{\omega^2 C_j^{\,2}(R_s + R_L)}{R_L} = 4.8 \qquad (4\text{-}41)$$

not including the effects of excess amplifier noise. Under the same conditions the complex conjugate load would lead to ($F_R = 0.81$). Equation (4-41) implies† that the actual pre-detection (S/N) ratio for this spectrometer must be at least five times smaller than the ideal. This prediction is contradicted by the experimentally observed value of F reported in Section D.4.

---

[*] Chapter 3, Section F.4.c.

[**] Chapter 4, Sections B.2 and D.1.

[†] Chapter 3, Section F.1, Eq. (3-152).

d. The Pre-Amplifier and Main Amplifier

The filtered beat note signal and various noise currents are amplified directly at the intermediate frequency, rather than heterodyned to a new i.f. frequency, since excellent gain and low noise figures are readily obtained at 30 Mc/sec. Figures 4-21 and 4-22 present the schematic diagrams of the pre-amplifier and main amplifier respectively; both devices are broadband units capable of amplifying all frequencies falling within the range of the tunable filter (26-34 Mc/sec).

The pre-amplifier is a modified LEL (-3) series intermediate frequency mixer preamp[25] having the following characteristics:

CENTER FREQUENCY = 30.0 Mc/sec
BANDWIDTH (3 db) = 8±1 Mc/sec
N.F. ≃ 3 db
GAIN = 46 db

The main amplifier is a variable gain unit with 10 Mc/sec bandwidth (3 db) and a maximum voltage gain of 10^4 (80 db).

e. The Detector

A detector with small signal square-law characteristics was obtained by operating a 6AL5 vacuum diode at low forward currents in the full-wave circuit shown in Fig. 4-22.

The total dc detector output $\langle\!\langle v_D(t) \rangle\!\rangle$ is amplified and then read out by meter m_1. Equations (3-73) and (3-149) show that this dc voltage is proportional to the

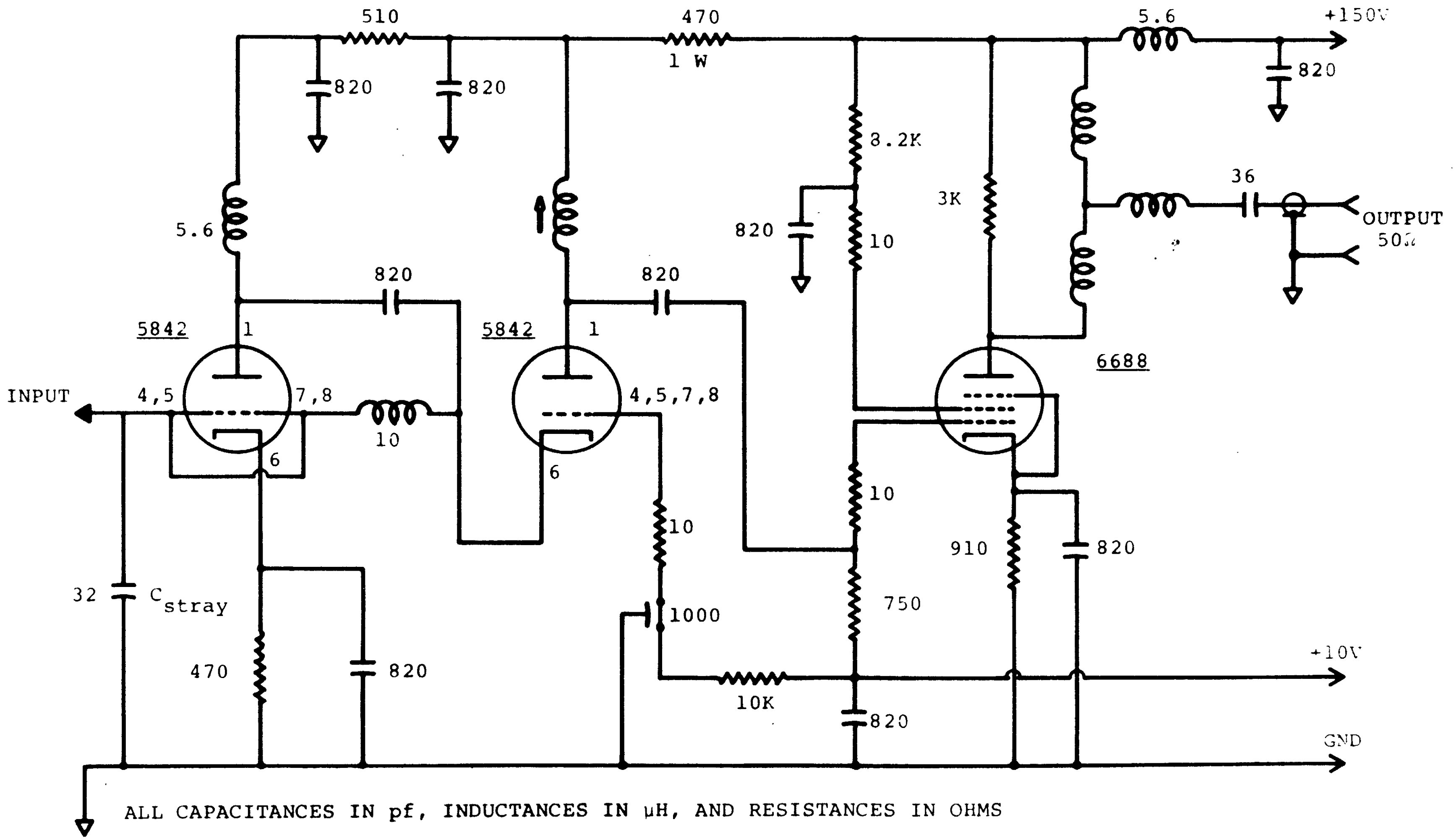
510
470
1 W
5.6
+150V
820
820
820
8.2K
3K
36
5.6
820
10
OUTPUT
50Ω
820
820
5842
1
5842
1
6688
INPUT
4,5
7,8
10
4,5,7,8
6
6
10
10
910
820
32
C_{stray}
1000
750
470
820
+10V
10K
820
GND

ALL CAPACITANCES IN pf, INDUCTANCES IN μH, AND RESISTANCES IN OHMS

Figure 4-21 The schematic diagram of the 30 Mc/sec preamplifier.

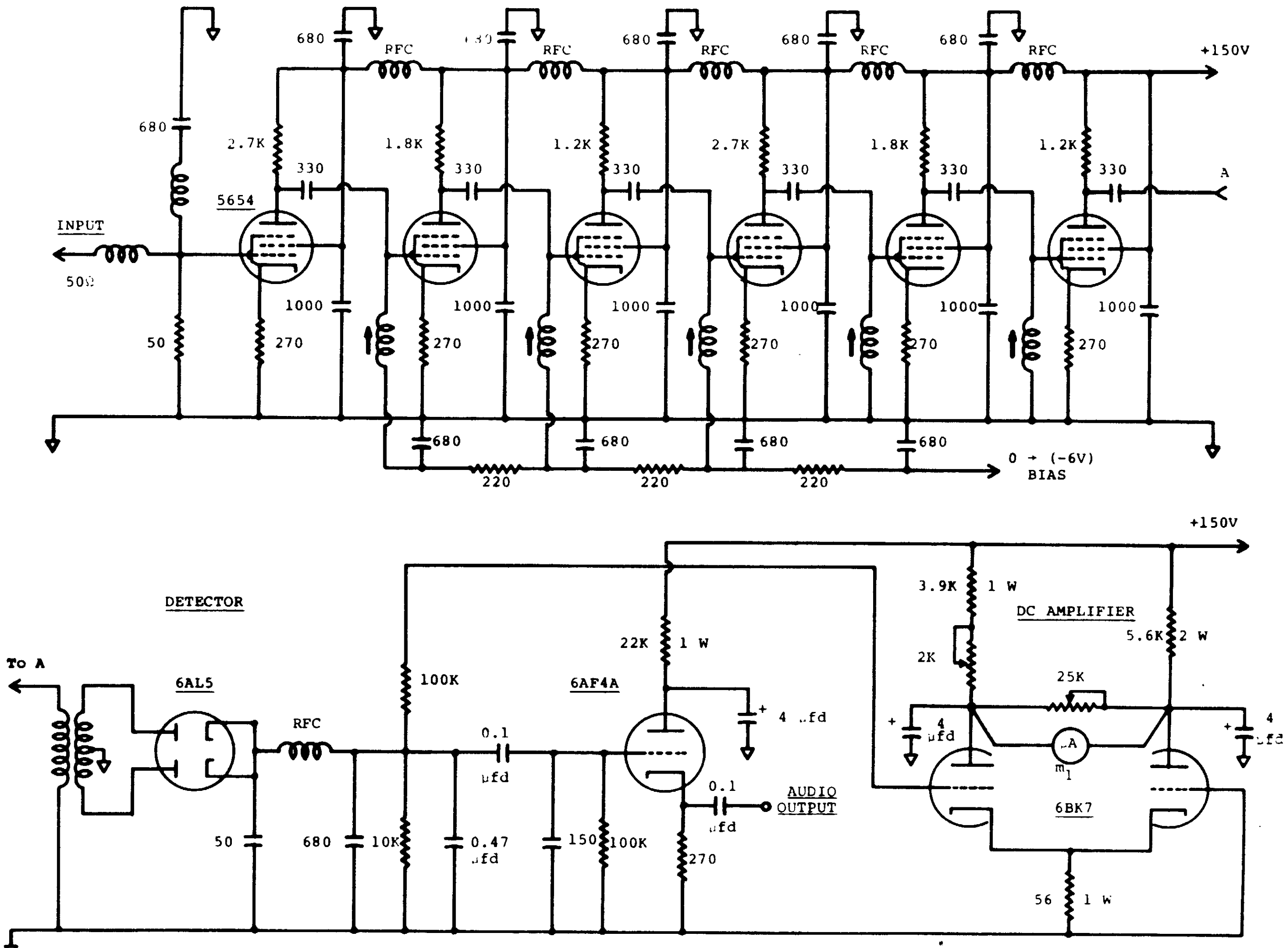
680
680
RFC
680
RFC
680
RFC
680
RFC
680
RFC
+150V
2.7K
1.8K
1.2K
2.7K
1.8K
1.2K
330
330
330
330
330
330
A
5654
INPUT
50Ω
1000
1000
1000
1000
1000
1000
50
270
270
270
270
270
270
680
680
680
680
220
220
220
0 → (-6V)
BIAS
+150V
3.9K
1 W
DC AMPLIFIER
5.6K
2 W
DETECTOR
22K
1 W
2K
To A
6AL5
100K
6AF4A
25K
RFC
4 μfd
4 μfd
4 μfd
0.1 μfd
μA
m_1
0.1 μfd
AUDIO OUTPUT
6BK7
50
680
10K
0.47 μfd
150
100K
270
56
1 W

ALL CAPACITANCES ARE IN pf AND ALL RESISTANCES IN OHMS UNLESS OTHERWISE NOTED

Figure 4-22 The schematic diagram of the 30 Mc/sec main amplifier, detector, and dc detector output monitoring circuits.

total filtered current power, including the signal, shot-noise, thermal noise, dark noise, and amplifier noise contributions. In terms of the relevant power spectral densities we have

$$\langle\langle v_D(t)\rangle\rangle = M(\Delta\omega_f)[I_S{}^2(\omega_f) + I_N{}^2(\omega_f) + I_R{}^2(\omega_f) + I_D{}^2(\omega_f) + I_{RA}{}^2(\omega_f)] \tag{4-42}$$

where $\Delta\omega_f$ is the tunable filter bandwidth and M is a constant.[†] The deflection of meter m_1 can be used to measure two important characteristics of the spectrometer; the modified pre-detection signal-to-noise ratio,[§] $(S/N)^*_{PRE}$, and the total signal-to-noise degradation factor,[¶] F, as follows. By reading m_1 with the path of the scattered light blocked (1) and then open (2) we obtain $(S/N)^*_{PRE}$ directly from the ratio

$$\frac{\langle\langle v_D(t)\rangle\rangle_1}{\langle\langle v_D(t)\rangle\rangle_2} = \frac{I_N{}^2(\omega_f) + I_R{}^2(\omega_f) + I_D{}^2(\omega_f) + I_{RA}{}^2(\omega_f)}{I_S{}^2(\omega_f) + I_N{}^2(\omega_f) + I_R{}^2(\omega_f) + I_D{}^2(\omega_f) + I_{RA}{}^2(\omega_f)} = 1 - (S/N)^*_{PRE} \tag{4-43}$$

the last equality following from the definition given in Eq. (3-151). Furthermore, by temporarily interrupting the local oscillator beam with the signal path blocked we can also determine the experimental value of F as

---

[†] Chapter 3, Section C.2.b.2, Eq. (3-68).

[§] Chapter 3, Section F.1, Eq. (3-151).

[¶] Chapter 3, Section F.1, Eqs. (3-152) and (3-153).

$$\frac{\langle\langle v_D(t)\rangle\rangle_3}{\langle\langle v_D(t)\rangle\rangle_4} = \frac{I_R^2(\omega_f) + I_D^2(\omega_f) + I_{RA}^2(\omega_f)}{I_N^2(\omega_f) + I_R^2(\omega_f) + I_D^2(\omega_f) + I_{RA}^2(\omega_f)}$$

$$= \frac{F}{1 - F} \qquad (4\text{-}44)$$

Where F is given by Eq. (3-153). The voltage ratio in Eq. (4-44) simply measures the ability of the photocurrent shot-noise to dominate all the "extraneous" noise sources in the spectrometer.

In principle, if the output signal-to-noise ratio is sufficiently large, then a plot of the desired spectrum can be obtained by recording $\langle\langle v_D(t)\rangle\rangle$ as the tuned filter frequency ω_f is swept over its range. However, in the present case, the observed pre-detection signal-to-noise ratio $(S/N)^*_{PRE}$ was considerably less than one. This result implies that the filtered signal power satisfied the inequality

$$I_S^2(\omega_f) << I_N^2(\omega_f) + I_R^2(\omega_f) + I_D^2(\omega_f) + I_{RA}^2(\omega_f)$$

$$= [I_N^2(\omega_f)]_{eff}$$

In this case Eq. (4-42) shows that slow changes in $[I_N^2(\omega_f)]_{eff}$ caused by drifts in amplifier gain and by the variation in amplifier frequency response with ω_f will combine to completely mask the small change in $\langle\langle v_D(t)\rangle\rangle$ due to the beat signal. For this reason the scattered light and, therefore, $I_S^2(\omega_f)$ is chopped at 150 cps and the resulting ac component of $v_D(t)$ measured by a synchronous (lock-in) detector. A straightforward analysis shows that this 150 cps signal in $v_D(t)$ has an amplitude

$$[v_D(t)]_{150} \propto I_S^2(\omega_f)$$

which is determined only by the signal component of the filtered current. Thus a plot of the lock-in output versus ω_f reproduces the desired beat note spectrum without interference from drifts in the large "effective" shot-noise level.

The addition of synchronous detection to the signal processing chain discussed in Section C.2 of Chapter 3 does not produce any drastic alteration in the output signal-to-noise ratio of the spectrometer. In fact, if the chopping is a square wave modulation and both systems employ final RC filters with identical time constants then we find

$$(S/N)_{\mathrm{OUT}}^{\mathrm{synchronous}} = (0.90)(S/N)_{\mathrm{OUT}}^{\mathrm{dc}} \qquad (4\text{-}45)$$

representing a slight overall decrease in sensitivity.

4. The Resolution and Sensitivity of the Spectrometer

The basic resolving power of the present spectrometer is fixed entirely by the frequency response characteristics of the tuned circuit photomixer load. This response was determined experimentally by using the optical system of Fig. 4-16 and the complete electronic system illustrated in Fig. 4-17 to detect the beat note between the local oscillator beam and the "enhanced" Brillouin scattered beam produced by injecting 30 Mc/sec sound waves into the scattering cell. Since the spectrum of this beat note is a delta function at the sound wave frequency, a plot of lock-in output versus filter frequency ω_f gives what might be called the "instrumental profile" of the spectrometer. Figure 4-23 shows this instrumental profile for the case $(\omega_{sound}/2\pi) = 30.20$ Mc/sec; the dotted curve includes the correction for rolloff in the preamplifier and main amplifier frequency response.[*] A fit of the observed profile to the expected[**] Lorentzian shape gives the results shown in heavy dots and a measured fill-width at half-response of

$$\frac{\Delta\omega_f}{2\pi} = 2.35 \text{ Mc/sec} \tag{4-46}$$

The corresponding resonant circuit Q

$$Q_1 = \frac{2\omega_{sound}}{\Delta\omega_f} = 25.5$$

is in excellent agreement with the value Q = 27 calculated in Eq. (4-39) on the basis of the load and photodetector circuit parameters.

The equivalent instrumental resolving power of the spectrometer at an optical frequency of $(\omega_o/2\pi) = 4.74 \times 10^{14}$ cps $(\lambda_{air} = 6328$ Å) is

$$\text{RESOLVING POWER} = \frac{\omega_o}{\Delta\omega_f} = 2.2 \times 10^8 \tag{4-47}$$

and the resolution

---

[*] Chapter 4, Section D.3.d.

[**] Chapter 3, Section F.4.c.

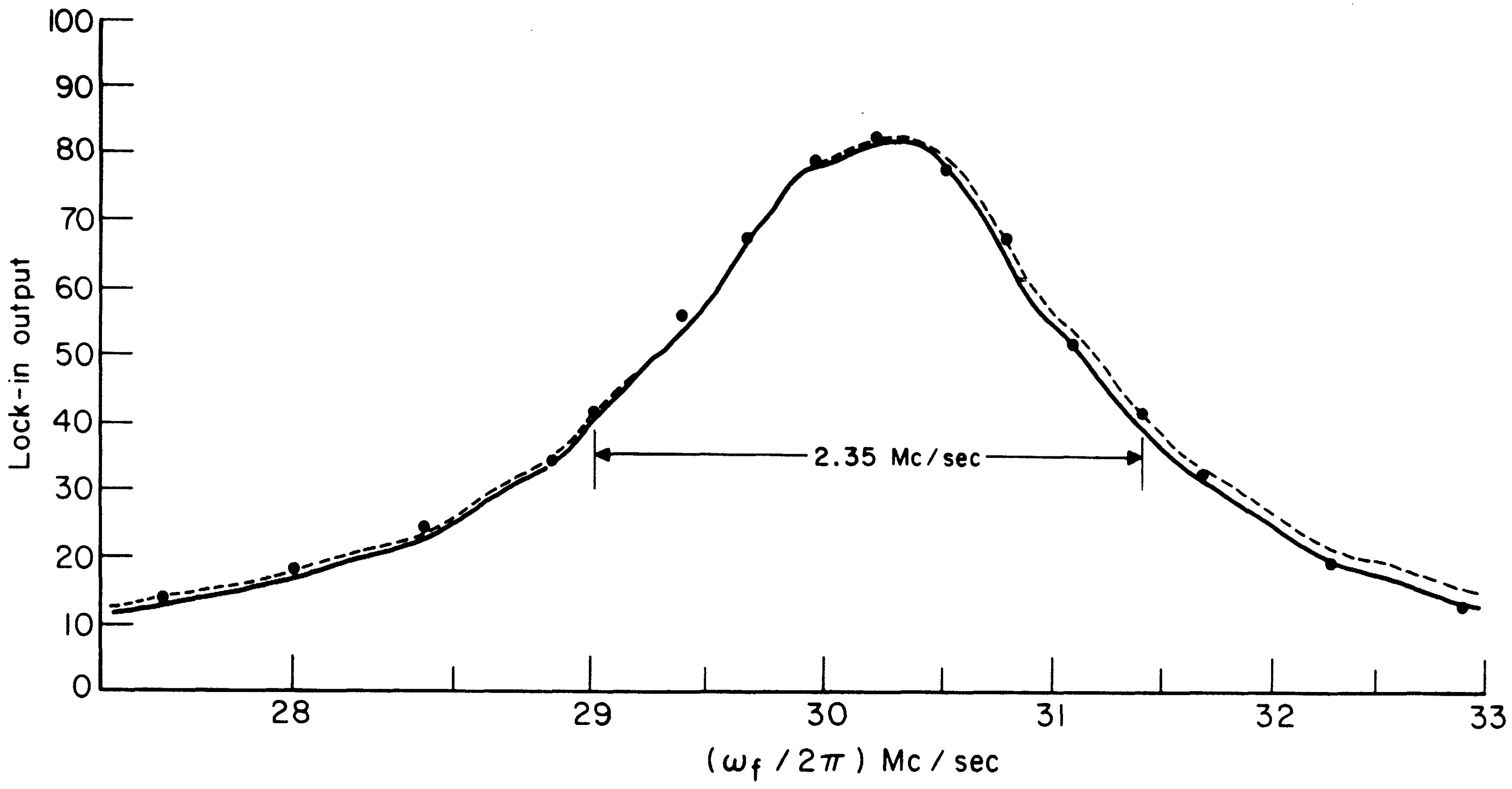

Figure 4-23 The instrumental profile for the superheterodyne optical spectrometer used to detect the Brillouin doublet in the light scattered from toluene liquid.

$$\text{RESOLUTION} = \frac{\Delta\omega_f}{\omega_o} = 4.4 \times 10^{-9} \tag{4-48}$$

This resolving power may be compared to the value 5×10^7 attainable with ultra-high resolution Fabry-Pérot etalons.

In the process of measuring the practical sensitivity of the spectrometer a serious contradiction arose in the form of a large discrepancy between the theoretical and experimental values of the signal-to-noise reduction factor F. The calculation of Eq. (4-41) and the pre-amplifier noise figure quoted in Section 3.d combine with Eqs. (3-227), (3-231), and (3-232) to give

$$F \geq F_R' = \frac{I_R^2(\omega) + I_{RA}^2(\omega)}{I_N^2(\omega)} = 9.6$$

On the other hand the value measured by observing the change in meter reading m_1 on interrupting the local oscillator beam was

$$F(\text{Measured}) = 1.66$$

The possibility that this result was due to laser amplitude modulation at 30 Mc/sec was ruled out by illuminating the mixer with a sufficient amount of white light to give the required dc photocurrent of $i_p = 100$ μamps. It follows from the definition of F that this result must originate from an experimental shot-noise current power per unit bandwidth $I_N^2(\omega)$ which is approximately 5.8 times as large as its theoretically expected value. There are two possible explanations for this excess noise. The first is that the photomixer has a gain G greater than unity due to avalanche effects,[29] and that the quantum efficiency ($\varepsilon = 0.59$) quoted in Eq. (4-38) is actually in error.

Writing the mixer dc output current as I_{OUT} we have

$$I_{OUT} = Gi_p = (G\varepsilon)(eP/\hbar\omega_o)$$

and a shot-noise level given by

$$I_N^2(\omega) = G^2[(e/\pi)i_p] = G(e/\pi)I_{OUT}$$

Since I_{OUT} depends only on the product $(G\varepsilon)$ we may resolve the discrepancy in F_R' by taking $G = 5.8$ and $\varepsilon = 0.10$. This interpretation was further supported by measuring the fraction of the total light incident on the photodiode which was lost because of specular reflection from the silicon chip; this fraction was observed to be greater than (0.5) at $\lambda_{air} = 6328$ Å. Therefore, a quantum efficiency $\varepsilon = 0.59$ is clearly inconsistent with the number of photons actually available at the junction region.

A second possible explanation is that the photocarrier production process in this type of diode is intrinsically more noisy than would be predicted by simple shot-noise theory. At present there is no evidence to firmly contradict or support this possibility.

Since the reflection data proves conclusively that the SD-100 detector had greater than unity gain, we will here adopt the following self-consistent set of diode parameters:

$$\begin{aligned} G &= 5.8 \\ \varepsilon &= 0.1 \end{aligned} \tag{4-49}$$

Furthermore, we assume that simple shot-noise theory adequately describes the noise characteristics of the mixer at $(\omega/2\pi) \simeq 30$ Mc/sec. In this case the modified pre-detection (S/N) ratio in Eq. (3-152) has the simple form

$$(S/N)^*_{PRE} = \frac{(S/N)_{PRE}}{1 + F' + F_D} \tag{4-50}$$

Using the measured values

$F' = 1.66$

$F_D = 0.003$

we have

$$(S/N)^*_{PRE} = \frac{(S/N)_{PRE}}{2.66} \tag{4-51}$$

Equation (4-51), the detector parameters given in Eq. (4-49), and the estimated value of $[B_{COH}]$ in Eq. (4-37) completely determine the sensitivity of the spectrometer. These results will be used in Chapter 5 in order to compare the values of $(S/N)_{OUT}$ and $(S/N)^*_{PRE}$ observed in the detection of the Brillouin-Mandel'shtam components with values determined from the signal-to-noise curves of Fig. 3-19 and the known scattering cross section.

E. The Optical and Electronic System for Superheterodyne Detection of the Central Component

1. General Discussion

The overall objective which determined the basic features of the mixing spectrometer used in this part of the experimental investigation was to obtain measurements of the natural line width of the central or Rayleigh component* in the light scattered from toluene. The calculations presented in Section D.4 of Chapter 2 gave the predicted spectrum of this component as a Lorentzian

$$S_E(\omega) = \left\langle |\vec{E}_s(\vec{r}_o,t)|^2 \right\rangle \frac{(\Gamma/\pi)}{(\omega-\omega_o)^2 + \Gamma^2}$$
$$(\omega \geq 0)$$

whose half-width at half-height Γ

$$\Gamma = [(\Lambda/\rho c_p) 4k_o^2] \sin^2(\Theta/2)$$

is a function of the scattering angle but whose center frequency is the frequency of the incident light, ω_o. The measurements reported in this thesis were confined to scattering angles near the forward direction ($0.3° \leq \Theta \leq 2.8°$) where the narrow line widths [$75 \text{ cps} \leq (\Gamma/2\pi) \leq 7500 \text{ cps}$] led to large values of the scattered optical power per unit frequency interval, per unit coherence area [P_{COH}/Γ] and consequently** to good pre- and post-detection signal-to-noise ratios.

---

* Chapter 2, Section D.4.

** Chapter 3, Section E.3.

Since the desired information is contained only in the line width of the spectrum, either type of light mixing spectrometer can be used to obtain the necessary resolving power. In the present case, because of serious problems with stray light which are discussed below, a superheterodyne method was chosen over the simpler self-beating technique. Since the central component is not shifted away from the frequency of the laser source a superheterodyne spectrometer which uses the direct laser output as a local oscillator, such as the one illustrated in Fig. 4-16, produces a heterodyne signal whose spectrum is peaked at the intermediate frequency ($\omega_1 = 0$).

However, some preliminary measurements pointed out a modulation-like effect that made width measurements on narrow lines $(\Gamma/2\pi) \leq 10$ kc/sec incompatible with the Mach-Zehnder optical system shown in Fig. 4-16. The effect was a random noise, time dependent disturbance of the interferometer alignment brought about by the sensitivity of the system to acoustic noise. The depth of this "modulation" was essentially 100%, the rms amplitude of the fluctuations in angle between the local oscillator and signal beam axes being sufficiently large to vary the beat note amplitude between zero and its maximum value. If the time dependence of this noise is described quantitatively by specifying the correlation function of the alignment fluctuations, $R_M(\tau)$, then the signal part of the photocurrent correlation function given in Eq. (3-106) takes the form

$$[R_i(\tau)]_{SIGNAL} \propto R_M(\tau)[R_E(\tau)R_{LO}(\tau)] \qquad (4\text{-}52)$$

where $R_{LO}(\tau)$ and $R_E(\tau)$ are the correlation functions of the local oscillator and the scattered fields respectively. It follows from Eq. (4-52) that regardless of the intermediate frequency the observed "signal" part of the photocurrent spectrum will be the convolution of the spectrum of the incident field

$$S_E(\omega) = (1/2\pi) \int_{-\infty}^{\infty} R_E(\tau) \cos \omega\tau \, d\tau$$

with the spectrum of the alignment modulation

$$S_M(\omega) = (1/2\pi) \int_{-\infty}^{\infty} R_M(\tau) \cos \omega\tau \, d\tau$$

Because $S_M(\omega)$ tends to be extremely irregular and irreproducible, in addition to having a "half-width" ($\approx$2kc/sec) which is comparable to the line widths of interest here, it is impossible to separate out the two spectra by a de-convolution procedure.

The most direct way of eliminating the alignment noise is to have both the local oscillator and signal beams follow identical paths from the scattering cell to the photomixer. However, this requires (1) that the local oscillator beam originate somewhere in or extremely near the illuminated region and (2) that it leave the cell at the desired angle. Both of these conditions can be met by the enhanced Brillouin scattered beam which is generated by injecting the appropriate frequency sound waves into the medium. Of course this scheme results in an intermediate frequency which is simply the frequency of the sound wave

$$\omega_1 = \varpi = 2k_o v_s \sin(\Theta/2) \tag{4-53}$$

$k_o = (2\pi/\lambda_{air})n$ - the wave vector of the incident light in the medium

v_s - the phase velocity of sound in the medium

ϖ - the angular frequency of the sound wave

Θ - the scattering angle as measured inside the cell

For the angles of interest here in the scattering from toluene we find* the limiting values of ω_1 and Γ tabulated below.

	Θ	$(\omega_1/2\pi)$	$(\Gamma/2\pi)$
Toluene	0.3°	16.5 Mc/sec	85 cps
T = 20°C	3.0°	165 Mc/sec	8500 cps

Although ideal from the standpoint of alignment modulation this method has a number of undesirable features: first, the intermediate frequency changes with scattering angle so that the electronic detection system must be capable of operating over a rather wide frequency range. Secondly, the intermediate frequency is much larger than the ideal value $\omega_1 = 10\Gamma$. As described in Section F.4.c of Chapter 3 the situation $\omega_1 >> 10\Gamma$ will be accompanied by a sacrifice of power transfer between the mixer and its load and correspondingly enhanced thermal noise problems. Thirdly, the high i.f. frequencies require the use of high speed, no gain photomixers, further exaggerating the thermal noise problem. Finally, practical difficulties make it virtually impossible to achieve the necessary filter bandwidths ($\Delta\omega_f \simeq 0.1\Gamma$) at the resulting i.f. frequencies; a further heterodyning process is necessary before the central component spectrum can be scanned with sufficient resolution.

---

* Chapter 5, Section B.1.

An attempt to use the sound wave injection technique to obtain a local oscillator beam at $\Theta = 0.547°$ with $(\omega_1/2\pi) = 30$ Mc/sec gave an extremely strong beat-note at the sound wave frequency. This signal was traced to mixing between the enhanced Brillouin scattered beam and the light which was elastically scattered in all directions from "dust" or grinding imperfections located at the two points where the laser beam strikes the outer surfaces of the cell windows. The wavefronts of this "stray" light and those of the light scattered from the illuminated volume were evidently sufficiently collinear to allow mixing between the two fields.

The elastically scattered light provided a convenient source of light at the laser frequency; and, for all the central component line width measurements reported here, the stray light was used as the local oscillator beam of the spectrometer. The resulting optical system exhibited the following important features.

(1) It yields a zero intermediate frequency independent of the scattering angle. For the range of line widths investigated here the choice $\omega_1 = 0$, in fact, offered some very attractive advantages. First, since the signal information in the photocurrent will be located at relatively low frequencies, in the present case $10(\Gamma/2\pi) < 100$ kc/sec, we can take advantage of high gain but slow speed photomultiplier mixers, and broadband resistive mixer loads.* Secondly, commercial spectrum analyzers with a convenient range of filter bandwidths,

---

* Chapter 3, Section F.

excellent sensitivity, and low noise figures are readily available for these frequencies. Thirdly, the combination of high gain mixers and low noise receivers make it simple to achieve the theoretical ideal pre- and post-detection (S/N) ratios.

On the other hand, the spurious beat-notes produced in the photocurrent by local oscillator amplitude modulation* also tend to become seriously large in the range of frequencies below a few kc/sec. This modulation must be eliminated if meaningful spectral measurements are to be taken near $\omega_1 = 0$.

(2) The intensity of the elastically scattered light was typically 10^5 times the intensity in the central component so that no interference arises from the self-beat part of the photocurrent spectrum.**

(3) Since the two beams travel the same optical path, acoustic noise does not introduce alignment modulation; however,

(4) the source points of the local oscillator and signal beams are not exactly coincident; as a result some loss in heterodyning efficiency† is to be expected.

A detailed analysis of the operation and sensitivity of this spectrometer is presented below.

---

* Chapter 3, Section F.3.b.

** Chapter 3, Section D.2.

† Chapter 3, Section D.3.

It should be pointed out that the presence of the stray light also made it impossible to use the simpler self-beat detection system. The amount of elastically scattered light reaching the detector was so much greater than that coming from the liquid sample that it produced sufficient dc photocurrent shot-noise to completely overwhelm the desired self-beat signal.

2. The Optical System

a. General Features

Figure 4-24 shows the complete optical system of the superheterodyne spectrometer which was used to make measurements of the central component line width. The scattering plane is the same one illustrated in Figs. 4-11 and 4-14 and corresponds to the plane of Brewster angle incidence at the scattering cell, C.

The scattered light coming from the cell at the desired external scattering angle Θ' is collected by mirror M_5 and sent via mirror M_3, aperture A, and focussing lens L_2 to the surface of the photomixer. Some of the elastically scattered light produced at the cell windows is also collected by M_5 and reaches the photodetector via the same optical path as the signal beam.

The distance between the source points of the signal and local oscillator beams and the limiting aperture A is

$$\overline{CM_5} + \overline{M_5M_3} + \overline{M_3A} \simeq 100 \text{ cm}$$

Since this distance is large compared to the maximum

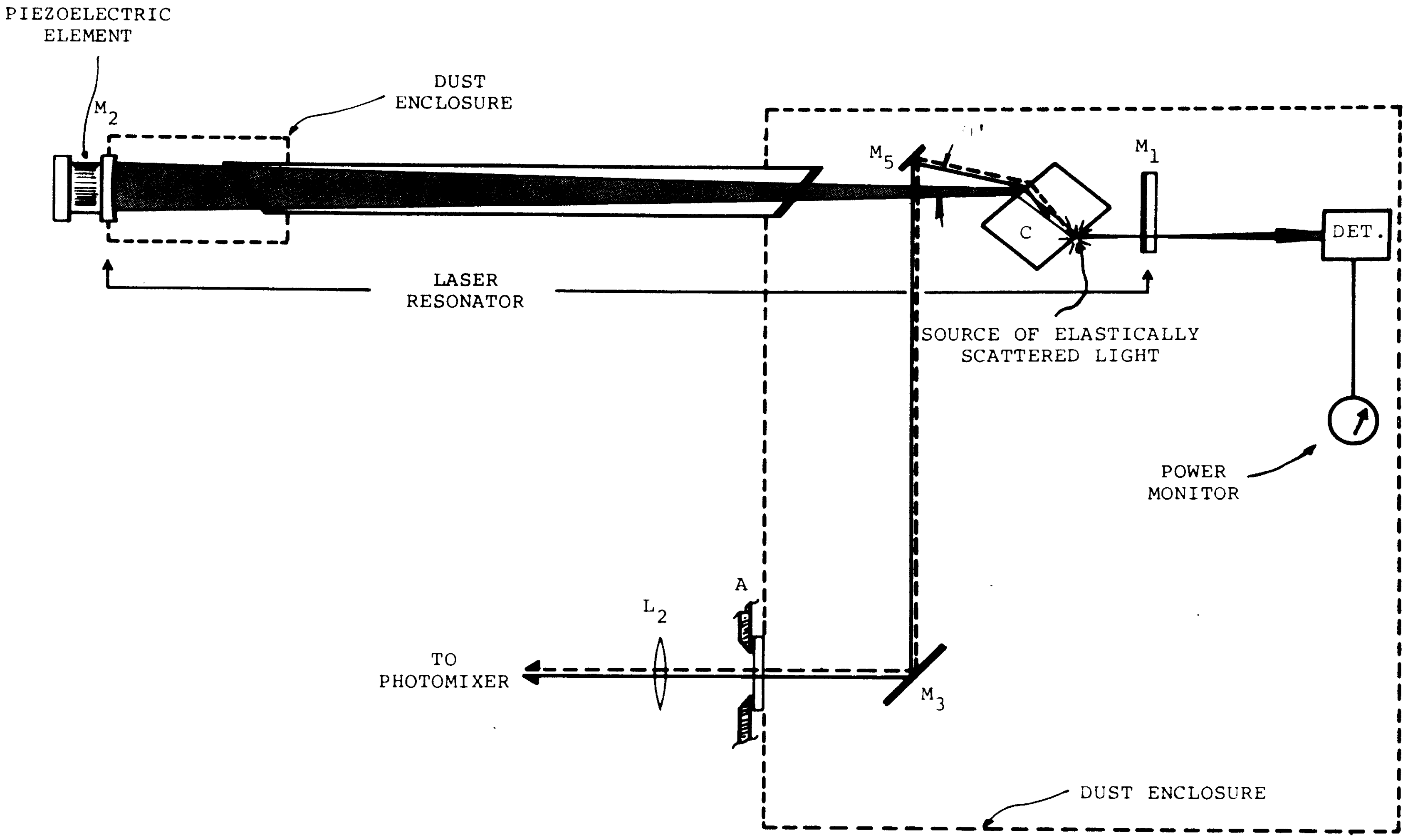
PIEZOELECTRIC ELEMENT
M_2
DUST ENCLOSURE
M_5
M_1
C
DET.
LASER RESONATOR
SOURCE OF ELASTICALLY SCATTERED LIGHT
POWER MONITOR
A
L_2
TO PHOTOMIXER
M_3
DUST ENCLOSURE

Figure 4-24 Optical system for the superheterodyne spectrometer used to observe the central component line width.

dimension of the illuminated volume* (L_z = 2.54 cm) the wavefronts of the signal field at A are spherical with a radius of curvature $R_S \simeq 100$ cm. Furthermore, since the imperfection which scatters the local oscillator field must be small compared to the incident beam diameter* ($D_f{}' = 0.030$ cm), and hence much smaller than R_S, the local oscillator also has spherical wavefronts at A. Clearly efficient mixing can take place between the two fields if the angular alignment** and wavefront radius mismatch† criteria are satisfied. In the Mach-Zehnder interferometer of Fig. 4-16 these conditions were easily fulfilled since the wavefront radius of curvature and the axis of the local oscillator beam were both continuously variable. However, in the optical system of Fig. 4-24 the two fields cannot be affected individually since they follow identical paths to the detector. As a result the mixing efficiency of this spectrometer is fixed *a priori* by the geometry of the scattering cell and the scattering angle.

In calculating the expected signal-to-noise ratios from the known laser power and the scattering cross sections it is important to specify the amount of power which is lost in the light gathering system. Using the measured reflection and transmission of M_5, M_3, and L_2, we find for the scattered power reaching the photodetector

$$\mathcal{P}_S = 0.73\ \mathcal{P}_{\text{SCATTERED}} \qquad (4\text{-}54)$$

---

* Chapter 4, Section C.4.

** Chapter 3, Section D.3.b.1.

† Appendix D.

b. The Wavefront Radius Mismatch Heterodyning Efficiency

The effect of wavefront radius mismatch can be determined from Appendix D which gives the appropriate heterodyning efficiency factor $[B_{COH}]$ in the form

$$[B_{COH}]_{\Delta\text{-RADIUS}} = \frac{\sin w_1}{w_1} \tag{4-55}$$

where

$$w_1 = \left[\left(\frac{\pi}{4\lambda_{air}}\right) d^2\right]\left[\frac{R_{LO} - R_S}{R_{LO}R_S}\right] \tag{4-56}$$

R_{LO} - the radius of curvature of the local oscillator beam at some convenient reference point H in the optical system.

R_S - the radius of curvature of the local oscillator beam at H.

d - the smallest of the following dimensions as measured at H: (1) the diameter of the coherence area of the scattered light, (2) the diameter of the local oscillator coherence area, or (3) the limiting aperture diameter of the light collection system set either by the aperture or the size of the photodetector.

In order to apply this result to the present system we may choose the reference point as the aperture and calculate the sizes of the local oscillator and signal field coherence areas at A.

The coherence half-angles of the light coming from the scattering volume were calculated in Section E.5 of Chapter 2 as

$$\overline{\Delta\Theta} = \frac{\lambda}{2[L_z \sin\Theta + L_y \cos\Theta]} \qquad (4\text{-}57)$$

$$\overline{\Delta\Psi} = \frac{\lambda}{2L_x} \qquad (4\text{-}58)$$

λ - wavelength of the incident light in the scattering medium.

L_x, L_y, L_z - the dimensions of the illuminated volume measured in the cartesian coordinate system of Figs. (4-11) and (4-12)

Θ - the scattering angle as in Fig. (4-11)

Ψ - the angle measured normal to the scattering plane as in Fig. (4-12)

Equations (4-57) and (4-58) give the "internal" coherence angles as seen from inside the cell. Correcting for the refractive effects at the cell windows with the help of Eqs. (4-14) and (4-17) we have for the externally observed coherence angles, $\Delta\Theta'$ and $\Delta\Psi'$

$$\begin{aligned} \overline{\Delta\Theta}' &= n^2\overline{\Delta\Theta} \\ \overline{\Delta\Psi}' &= n\overline{\Delta\Psi} \end{aligned} \qquad (4\text{-}59)$$

where n is the index of refraction of the scattering medium. Therefore, the coherence area of the scattered field in the plane of the aperture can be described as a rectangle whose dimensions in the Θ' and Ψ' directions are

$$[d_{COH}]_{\Theta'} = 2R_S\overline{\Delta\Theta}' = \frac{n^2 R_S \lambda}{L_z \sin\Theta + L_y \cos\Theta} \tag{4-60}$$

and

$$[d_{COH}]_{\Psi'} = 2R_S\overline{\Delta\Psi}' = \frac{nR_S\lambda}{L_x} \tag{4-61}$$

respectively. The dimensions of the illuminated region were given in Eq. (4-23) as

$$\begin{aligned} L_x &= 0.019 \text{ cm} \\ L_y &= 0.028 \text{ cm} \\ L_z &= 2.54 \text{ cm} \end{aligned} \tag{4-62}$$

Combining these results with the quantities

$$\begin{aligned} R_S &= \overline{CM_5A} \simeq 100 \text{ cm} \\ n &\simeq 1.5 \\ \lambda &= (\lambda_{air}/n) = 4220 \text{ Å} \end{aligned} \tag{4-63}$$

we find the numerical values of $\overline{\Delta\Theta}$, $\overline{\Delta\Theta}'$, $\overline{\Delta\Psi}$, $\overline{\Delta\Psi}'$, $[d_{COH}]_{\Theta'}$ and $[d_{COH}]_{\Psi'}$ which are plotted in Figs. 4-25 and 4-26.

A calculation of the local oscillator coherence area at A follows an identical procedure. For our purposes it is sufficient to note from Eqs. (4-57) and (4-58) that $\overline{\Delta\Theta}$ and $\overline{\Delta\Psi}$ are both inversely proportional to the dimensions

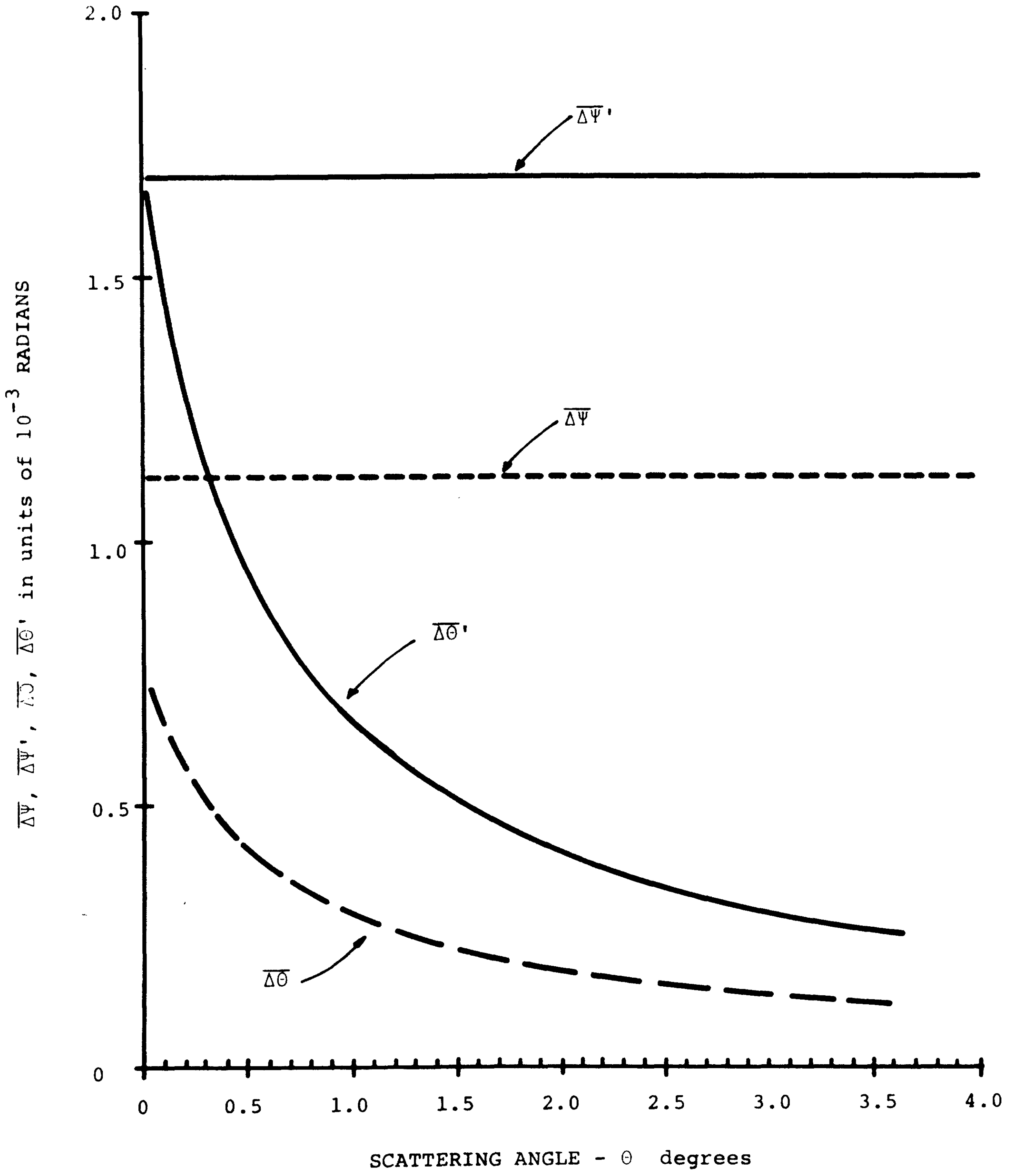

Figure 4-25 The coherence angles for the experimental scattering geometry.

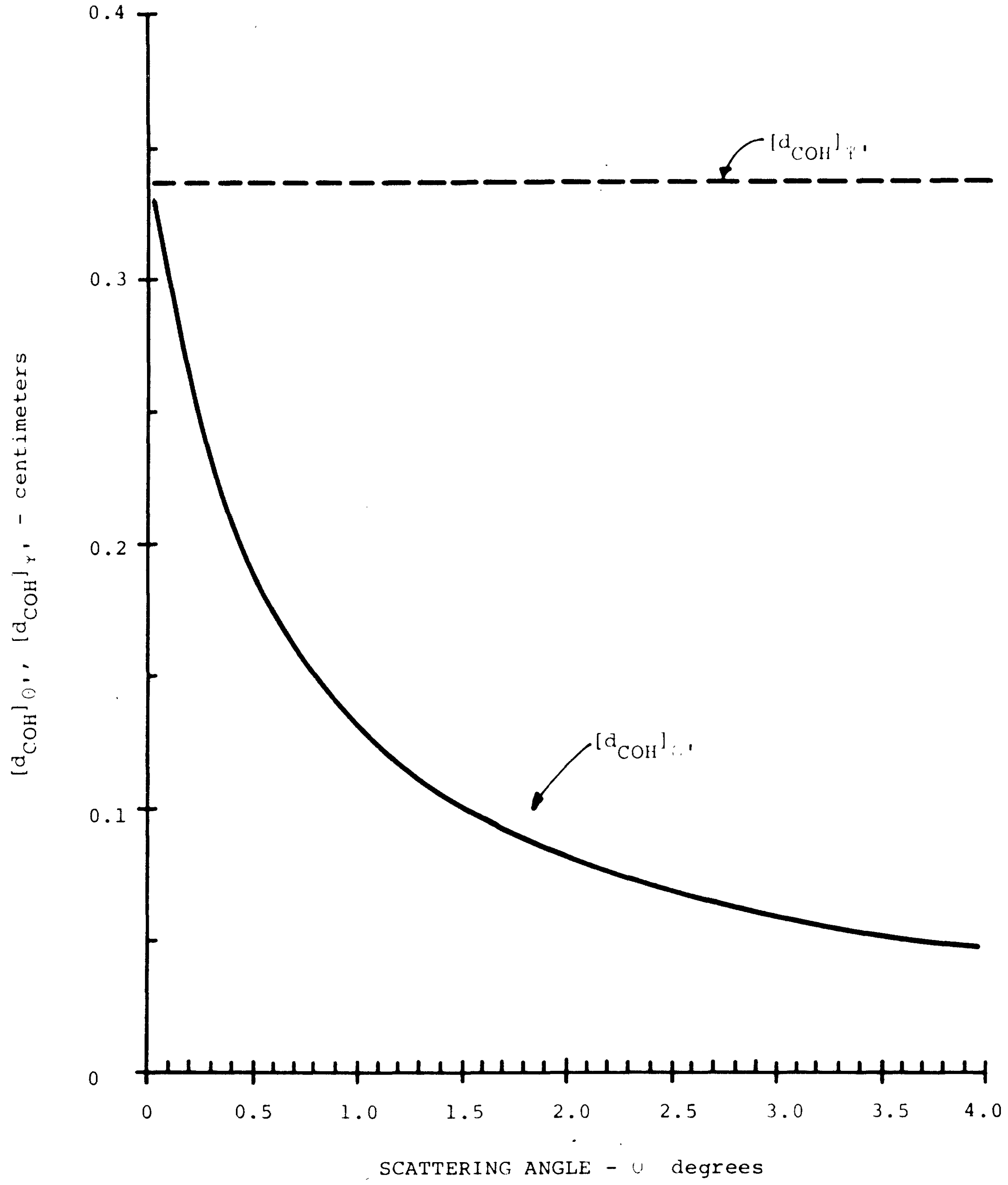

Figure 4-26 The Θ and Ψ dimensions of the scattered field coherence area at the beam splitter of the Mach-Zehnder spectrometer.

of the scatterer. However, the dust particle or scratch which acts as the local oscillator source has a maximum dimension D that satisfies the inequality $D << (L_x, L_y, L_z)$; therefore, the size of the local oscillator coherence area is large compared to $[d_{COH}]_{\Theta', \Psi'}$. It follows that, regardless of the aperture size, the maximum possible value of d appearing in Eq. (4-56) is just $[d_{COH}]_{\Psi'} \simeq 0.4$ cm.

The important factor in w_1 yet to be determined is the difference between the optical path lengths $(R_{LO} - R_S)$ from the signal and local oscillator source points to the aperture. This quantity can be calculated on the basis of Fig. 4-27 which shows the effective positions of these two points in relation to the illuminated volume and the light collection system. The difference $R_{LO} - R_S$ follows directly as

$$(R_{LO} - R_S) = (L_z/2) \cos \Theta \tag{4-64}$$

Taking $\cos \Theta \simeq 1$ in Eq. (4-64) and $d \leq [d_{COH}]_{\Psi'}$ yields an upper limit on the factor w_1 given by

$$w_1 \leq \left\{ \left(\frac{4\pi}{\lambda_{air}}\right) [d_{COH}]^2_{\Psi'} \right\} \frac{(L_z/2)}{R_{LO} R_S} \tag{4-65}$$

$$\leq 0.08\pi$$

We immediately find from Eq. (4-55) that the wavefront radius mismatch part of the heterodyne efficiency factor has a minimum value

$$[B]_{\Delta\text{-RADIUS}} \geq 0.99 \tag{4-66}$$

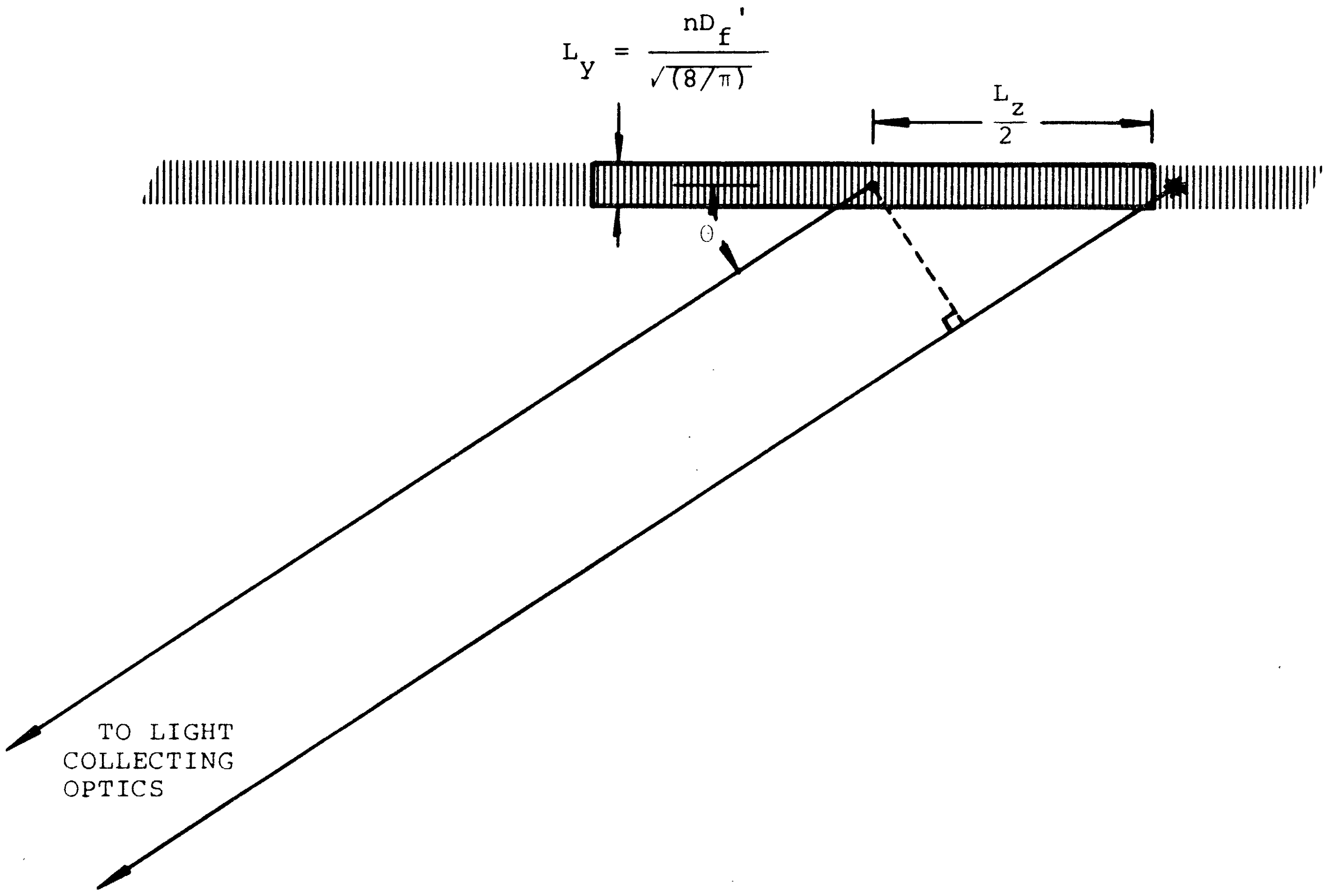
$L_y = \frac{nD_f'}{\sqrt{(8/\pi)}}$
$\frac{L_z}{2}$
θ
TO LIGHT
COLLECTING
OPTICS

Figure 4-27 The geometrical positions of the local oscillator and effective signal source points in relation to the light collection system.

Since the ideal value of [B] is [B] = 1, this result shows that the spectrometer exhibits a negligible loss of mixing efficiency due to wavefront curvature differences.

c. The Angular Misalignment Heterodyning Efficiency

The heterodyning efficiency factor due to an angular misalignment of the two mixing fields was calculated in Section D.3 of Chapter 3 as

$$[B]_{\Delta\text{-ANGLE}} = \frac{\sin w_2}{w_2} \qquad (4\text{-}67)$$

with

$$w_2 = \left[\left(\frac{2\pi}{\lambda_{air}}\right) d\right] \varepsilon \qquad (4\text{-}68)$$

ε - the angle between the axes of the two beams at the mixing surface

d - the smallest of the following dimensions measured at the photodetector in the plane defined by the two beam axes: (1) width of the mixer active area, (2) the width of the local oscillator coherence area, (3) the width of the coherence area of the scattered light, or (4) the limiting aperture dimension as seen at the photomixer.

Because of the effects of the imaging optics between the mixer surface and the cell it is more convenient to express Eq. (4-68) in a form which allows d and ε to be determined at some arbitrary reference point in the optical system.

Such a reformulation must always be possible on general grounds since once the two fields have been combined the mixing efficiency cannot be altered by any optical processing which affects them both in the same manner. This statement can be proved rigorously by examining the free space propagation characteristics of the two spatial coherence functions, $T_{LO}(\vec{r},\vec{\rho})$ and $T_E(\vec{r},\vec{\rho})$, that enter* into the calculation of [B].

Figure 4-28 illustrates the origin of the angle ε between the local oscillator and signal beam axes as seen from some arbitrary point H. Calling the lateral separation of the two source points as observed from outside the cell W' we have

$$\varepsilon = (W'/R) \tag{4-69}$$

in the usual small angle approximation. The externally observed W' is related to the internal separation W by

$$W' = (W/n)$$

as follows from Snell's law and the Brewster angle condition. Expressing W in terms of L_z and Θ from the geometry of Fig. 4-27 gives

$$\varepsilon = \left(\frac{L_z}{2nR}\right) \sin \Theta \tag{4-70}$$

which depends explicitly on the choice of the point H through the factor R. However, d also depends on the location of the reference point. In fact, in the present

---

* Chapter 3, Section D.3.b.

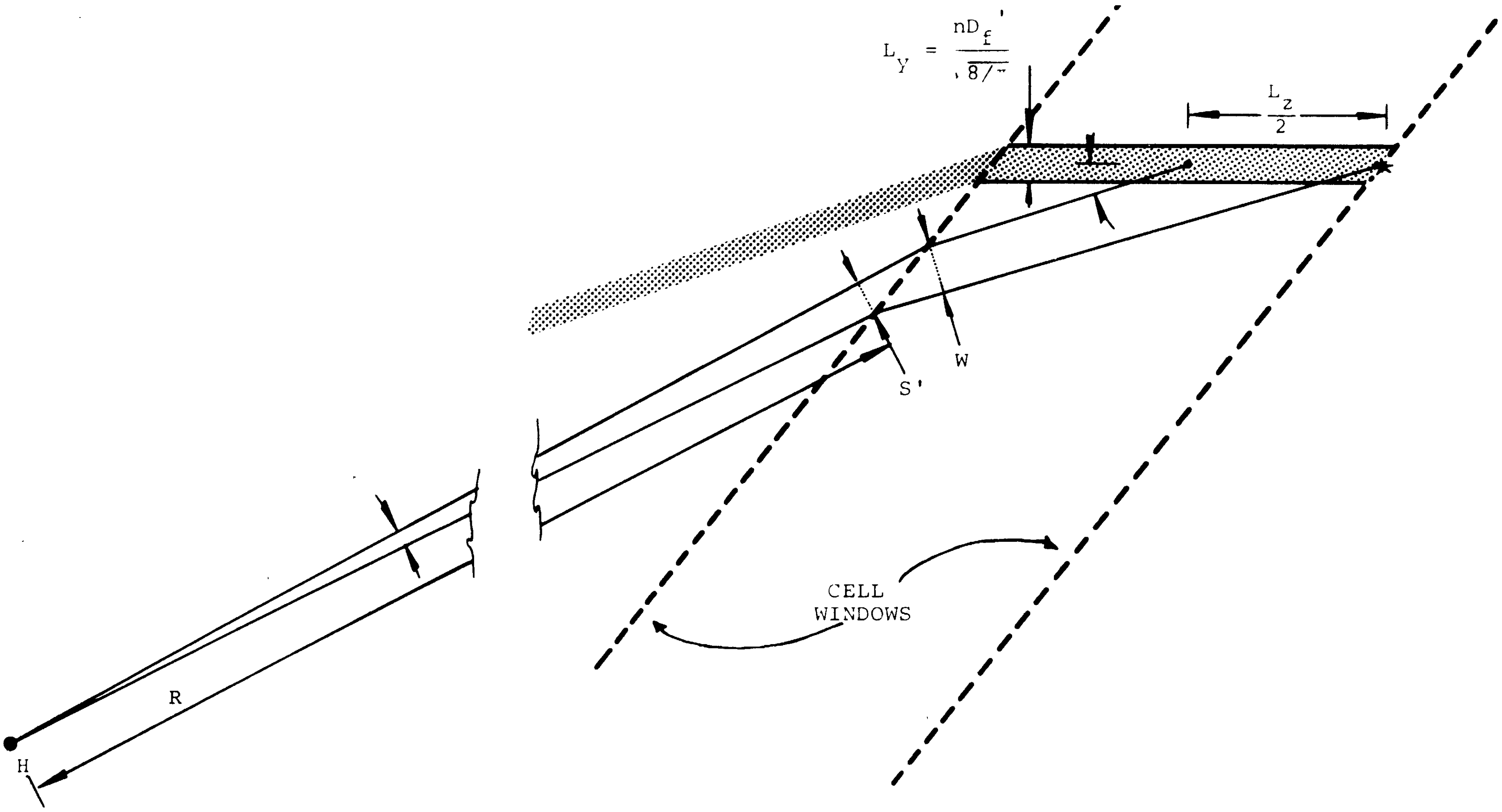
$L_y = \frac{nD_f'}{\sqrt{8/\pi}}$
$\frac{L_z}{2}$
W
S'
CELL WINDOWS
R
H

Figure 4-28 The origin of the angular misalignment between the local oscillator and signal fields.

case d is the Θ' dimension of the scattered field coherence area and Eq. (4-63) gives

$$d = [d_{COH}]_{\Theta'} = 2R_S\overline{\Delta\Theta}' = 2R_S n^2\overline{\Delta\Theta} \qquad (4\text{-}71)$$

$\overline{\Delta\Theta}$ being the coherence half-angle as defined in Eq. (4-57) and R_S the total optical path length between the apparent source point of the field and the point H. As would be expected intuitively for a spherically spreading wave $[d_{COH}]_{\Theta'}$ simply increases linearly with R_S. If we neglect the cell dimensions relative to the distance R, so that we have approximately $R \simeq R_S$, then w_2 takes the form

$$w_2 = \left[\left(\frac{2\pi}{\lambda_{air}}\right)L_z\right] n\overline{\Delta\Theta} \sin\Theta \qquad (4\text{-}72)$$

This expression includes all the effects of refraction at the cell windows and is independent of the location of the point H as desired.

The factor $[B]_{\Delta\text{-ANGLE}}$ can now be calculated from Eq. (4-72) using the numerical data given in Eq. (4-62) and Fig. 4-25. The results are plotted in Fig. 4-29 for the range $(0° \le \Theta \le 4°)$. In obtaining $[B]_{\Delta\text{-ANGLE}}$ from the value of w_2 for $w_2 \ge 0.69$ radians it was assumed that slight irregularities in the mixing wavefronts would wash out the zero crossings of the function $(\sin w_2)/w_2$ and give an rms [B] value which was approximately

$$[B]_{\Delta\text{-ANGLE}} \simeq \frac{\frac{1}{2\pi}\int_0^{2\pi} |\sin w_2|\, dw_2}{w_2} = \frac{0.637}{w_2} \qquad (4\text{-}73)$$

For $w_2 \le 0.69$ radians $(\Theta \le 0.177°)$ the curve shown in Fig. 4-29 is that calculated from the exact expression presented in Eq. (4-67).

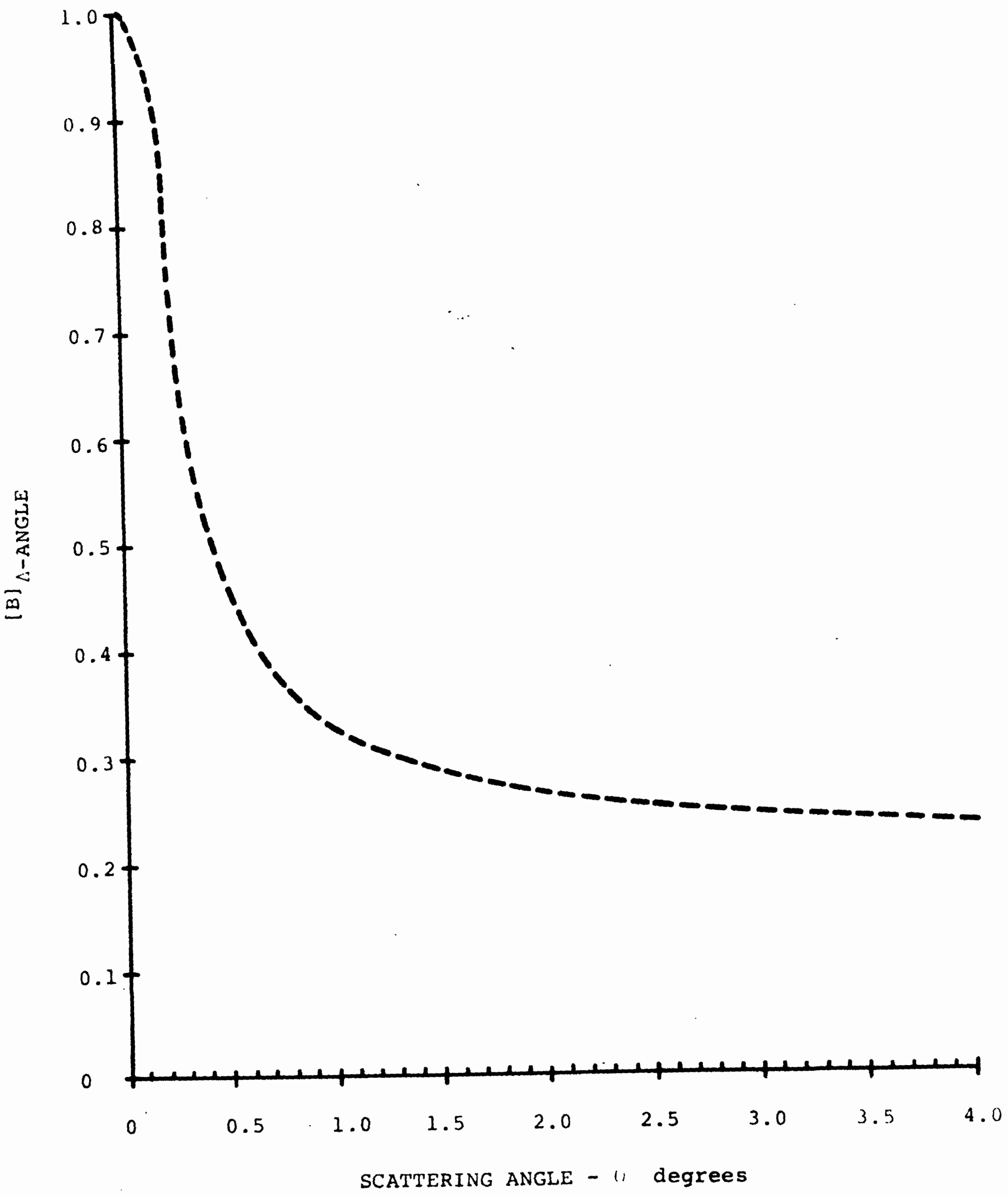

Figure 4-29 The angular misalignment contribution to the heterodyning efficiency for the superheterodyne spectrometer used to detect the width of the central component.

These results demonstrate that the angular misalignment caused by having the local oscillator source point outside the scattering volume produces a moderate loss in the heterodyning efficiency except for very small scattering angles. For the range of Θ covered here ($0.30° \leq \Theta \leq 2.8°$) $[B]_{\Delta\text{-ANGLE}}$ varies from (0.63) to (0.25).

For the purpose of deciding whether a particular local oscillator source position will result in a good heterodyning efficiency it is interesting to note that the "radius" and "angle" criteria of Eqs. (4-55), (4-56), (4-67), and (4-68) depend respectively on the depth and lateral separations of the two sources. That is, for good mixing efficiency the origin of the local oscillator beam should be confined to a specified rectangular region whose dimensions are fixed by the scattering angle and the geometrical shape of the scattering volume. In fact, the size of this region has a rather simple physical interpretation in terms of the spatial "resolving power" of a circular aperture with diameter d. Suppose we express the factors w_1 and w_2 in terms of the depth and lateral separations between the sources, namely $(R_{LO}-R_S)$ and W'. Then writing $(R_{LO} \simeq R_S \simeq R) \equiv f$ we have

$$w_1 = \frac{\pi}{4} \frac{R_{LO}-R_S}{(f/d)^2\lambda}$$

and

$$w_2 = (2\pi)\frac{W'}{(f/d)\lambda}$$

But the quantities $(f/d)\lambda$ and $(f/d)^2\lambda$ are respectively nothing but the usual Rayleigh resolution criterion and the resolvable depth of field that apply to two sources located a distance f from an optical system with a limiting circular aperture of diameter d. Or viewing the reverse process, as we did in Section B.2, they represent the diameter and length of the focal region which is produced by spherical wavefronts leaving the same aperture with a radius of curvature f. These two situations are illustrated in Fig. 4-30; in the first the "observer" is unable to resolve the two sources because the wavefronts passing through d produce overlapping diffraction patterns in his optical system. Although the resolution criteria are not usually presented in these terms, two sources which lie within the Rayleigh limit, or equivalently within the diffraction limit, generate wavefronts at d which are collinear to within $(\lambda/4)$ over the aperture area. In the reverse process the observer is incapable of deciding where he is in the focal region because of the uniformity of the intensity and phase distributions.* He is therefore unable to detect differences in direction and radius of curvature between two different spherical waves reaching the aperture unless their focal regions are clearly separated. Again this resolution limit implies that the two wavefronts at the aperture are collinear to within $(\lambda/4)$ over its entire area.

From this viewpoint the condition for good mixing efficiency over a single coherence area, or over the limiting aperture of the system if it is smaller, is that the local oscillator and signal source points must be unresolvable when viewed through this area. The data given in Fig. 4-29 expresses the physically plausible result that in the optical system of Fig. 4-24 the two sources are unresolvable only when viewed from the extreme forward direction $(\theta < 0.1°)$.

---

* Chapter 4, Section B.2.

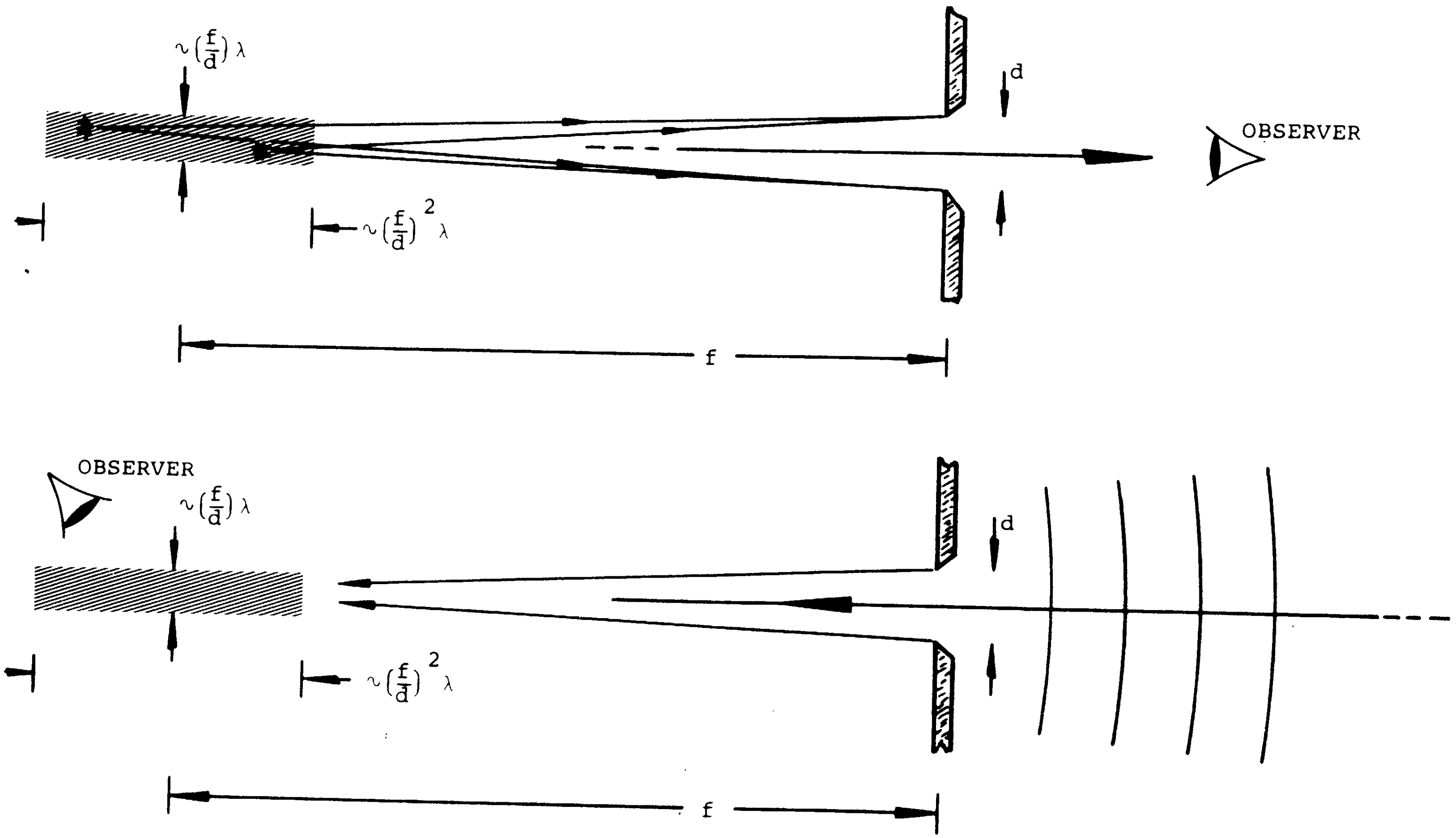
$\sim(\frac{f}{d})\lambda$
d
OBSERVER
$\sim(\frac{f}{d})^2\lambda$
f
OBSERVER
$\sim(\frac{f}{d})\lambda$
d
$\sim(\frac{f}{d})^2\lambda$
f

Figure 4-30 The two possible interpretations of the wavefront alignment criteria in terms of resolution limits.

d. Determining the Scattering Angle and the Instrumental Acceptance Angle

The limiting aperture A has three important functions in the spectrometer optical system. Unlike the Mach-Zehnder system shown in Fig. 4-16 the spectrometer of Fig. 4-24 cannot rely on the excellent directivity of a local oscillator beam to result in a heterodyne signal at the mixer only from those rays which leave the scattering cell at some fixed angle. The intensity pattern of the elastically scattered local oscillator field is almost isotropic, allowing it to mix to an extent determined by $[B_{COH}]_{\Delta\text{-ANGLE}}$ with light leaving the cell at an arbitrary angle. Therefore, the first purpose of the aperture is to define the mean scattering angle Θ_m. A ray leaving the illuminated region at the angle Θ_m passes through the center of the aperture. Secondly, the aperture size can be chosen to accept only a single coherence area of the scattered field, thereby minimizing the effects of laser amplitude modulation.* Thirdly, its Θ' dimension also controls the range of scattering angles which simultaneously contribute to the light reaching the detector. If the full range in Θ' collected by the detector is designated the acceptance angle, $\Delta\Theta'_{acc}$, we have

$$\Delta\Theta'_{acc} = (D_{\Theta'}/R) \qquad (4\text{-}74)$$

where $D_{\Theta'}$ is the Θ' dimension of the aperture and R is the optical path length between the aperture plane and the scattering cell. The acceptance angle measured inside* the cell is

---

* Chapter 3, Section F.3.b.

** Chapter 4, Section C.3, Eq. (4-14).

$$\Delta\Theta_{acc} = (D_{\Theta'}/n^2R) \qquad (4\text{-}75)$$

Since Eq. (2-82) shows that the line width of the central component will be a function of the scattering angle, $\Delta\Theta_{acc}$ must be small enough to avoid a distortion of the actual spectrum which is characteristic of the mean scattering angle $\Theta = \Theta_m$. If the light leaving the illuminated volume at the angle Θ has a Lorentzian spectrum whose half-width at half-height increases as $\sin^2 (\Theta/2)$ as predicted by Eq. (2-87) then, for small ratios of $(\Delta\Theta_{acc}/\Theta_m)$ the spectrum of the total field reaching the detector is to first order also Lorentzian. However, this latter spectrum has a half-width Γ which is larger than the half-width at the mean angle Θ_m by the fractional amount

$$\left(\frac{\Delta\Gamma}{\Gamma_m}\right) \simeq \left(\frac{\Delta\Theta_{acc}}{\Theta_m}\right)^2 \qquad (4\text{-}76)$$

For the measurements reported here $(\Delta\Theta_{acc}/\Theta_m)$ was adjusted to satisfy the inequality $(\Delta\Theta_{acc}/\Theta_m) < 0.1$ leading to an extraneous line width increase of less than 1%.

3. The Alignment Procedure

The techniques that were found to be useful in optimizing the performance of the spectrometer at some predetermined scattering angle can be most easily described by giving the detailed steps of a typical alignment procedure. We assume a starting point at which the laser reflectors are accurately aligned for maximum laser output power in the absence of the scattering cell.

(1) The cell is then inserted into the resonator and adjusted to the Brewster angle by minimizing the intensity of the specular reflections from the windows.

(2) Choosing the wave vector K of the entropy fluctuations whose spectrum are to be determined, indirectly fixes the scattering angle via Eq. (2-31).

$$K = 2k_o \sin(\Theta/2)$$

Sound waves of the identical wave vector are now injected into the cell using the technique discussed in Section C.5. The result is an "enhanced" Brillouin beam leaving the illuminated region at the appropriate value of Θ given by Eq. (2-31).

(3) The cell is now translated back and forth in the incident laser beam to locate a scratch or dust particle on one of the windows which scatters a significant amount of light in the direction of the Brillouin beam. The cell position is locked at the point which maximizes the intensity of this scattering.

(4) With the injected sound waves turned off, mirror M_1 is adjusted to repeak the laser output power. At this point step (3) may also be repeated to optimize the intensity of the elastically scattered light.

(5) The sound wave amplitude is now increased to give about (0.5 mW) of power in the Brillouin scattered light. Mirrors M_5 and M_3 are then visually positioned to reflect this beam in the direction of the photomixer.

(6) In order to check and optimize the heterodyning efficiency of the spectrometer, the beat-note between the enhanced Brillouin beam and the superimposed elastically scattered "local oscillator" field is detected by the auxiliary photodiode and spectrum analyzer system shown in Fig. 4-7. The amplitude of the beat-note is then maximized by repositioning the cell as described in step (3). This procedure, in addition to peaking up the intensity of the local oscillator, also serves to minimize the relative warpage between the wavefronts of the elastically scattered light and the light coming from the scattering volume. The alignment of the optical system is now complete except for the insertion of aperture A.

(7) The size of the rectangular aperture A is now selected on the basis of the dimensions of the scattered field coherence area at the aperture plane and the maximum allowable acceptance angle. For the angles involved here ($0.30° \leq \Theta \leq 2.8°$), taking the aperture to be the size of a single coherence area, $D_{\Theta'} = [d_{COH}]_{\Theta'}$ and $D_{\Psi'} = [d_{COH}]_{\Psi'}$, gives from Eqs. (4-75), (4-60), and (4-59)

$$\left(\frac{\Delta\Theta_{acc}}{\Theta_m}\right) = \left\{\frac{[d_{COH}]_{\Theta'}}{n^2 R}\right\}\left(\frac{1}{\Theta_m}\right) = \frac{2\overline{\Delta\Theta}}{\Theta_m}$$

In the extreme cases $\Theta = 0.3°$ and $\Theta = 2.8°$ we would find from Fig. 4-25

$$\left.\frac{\Delta\Theta_{acc}}{\Theta_m}\right|_{0.3°} = 0.2 \qquad \left.\frac{\Delta\Theta_{acc}}{\Theta_m}\right|_{2.8°} = 0.005$$

In order to maintain the condition $(\Delta\Theta_{acc}/\Theta_m) \leq 0.1$, $D_{\Theta'}$ was stopped down to be smaller than $[d_{COH}]_{\Theta'}$ for scattering angles in the range $(\Theta < 1°)$ and was made correspondingly larger than $[d_{COH}]_{\Theta'}$ for larger angles.

(8) The final position of the aperture is now fixed by visually centering it on the enhanced Brillouin scattered beam. For the typical aperture size $D_{\Theta'} \simeq 0.4$ cm the tolerance in placement was (±0.2 mm) and represents a possible error in the mean scattering angle of

$$\delta\Theta_m = \pm 0.005°$$

The result is an uncertainty in the square of the wave vector of the scattering fluctuation

$$\frac{\delta(K^2)}{K^2} = \frac{2\delta\Theta_m}{\Theta_m} = \begin{cases} \pm 0.033 & \Theta_m = 0.3° \\ \\ \pm 0.004 & \Theta_m = 2.8° \end{cases} \tag{4-77}$$

Step (8) completes the alignment of the optical system.

4. The Electronic System

Figure 4-31 presents a block diagram of the electronic detection apparatus which was combined with the optical system of Fig. 4-24 to obtain measurements of the central component line width. The mixer is a conventional photomultiplier whose output is terminated in an untuned broadband resistive load. The spectrum of the ac part of the mixer output is examined by a commercial audio wave analyzer having a bandwidth which is small compared to

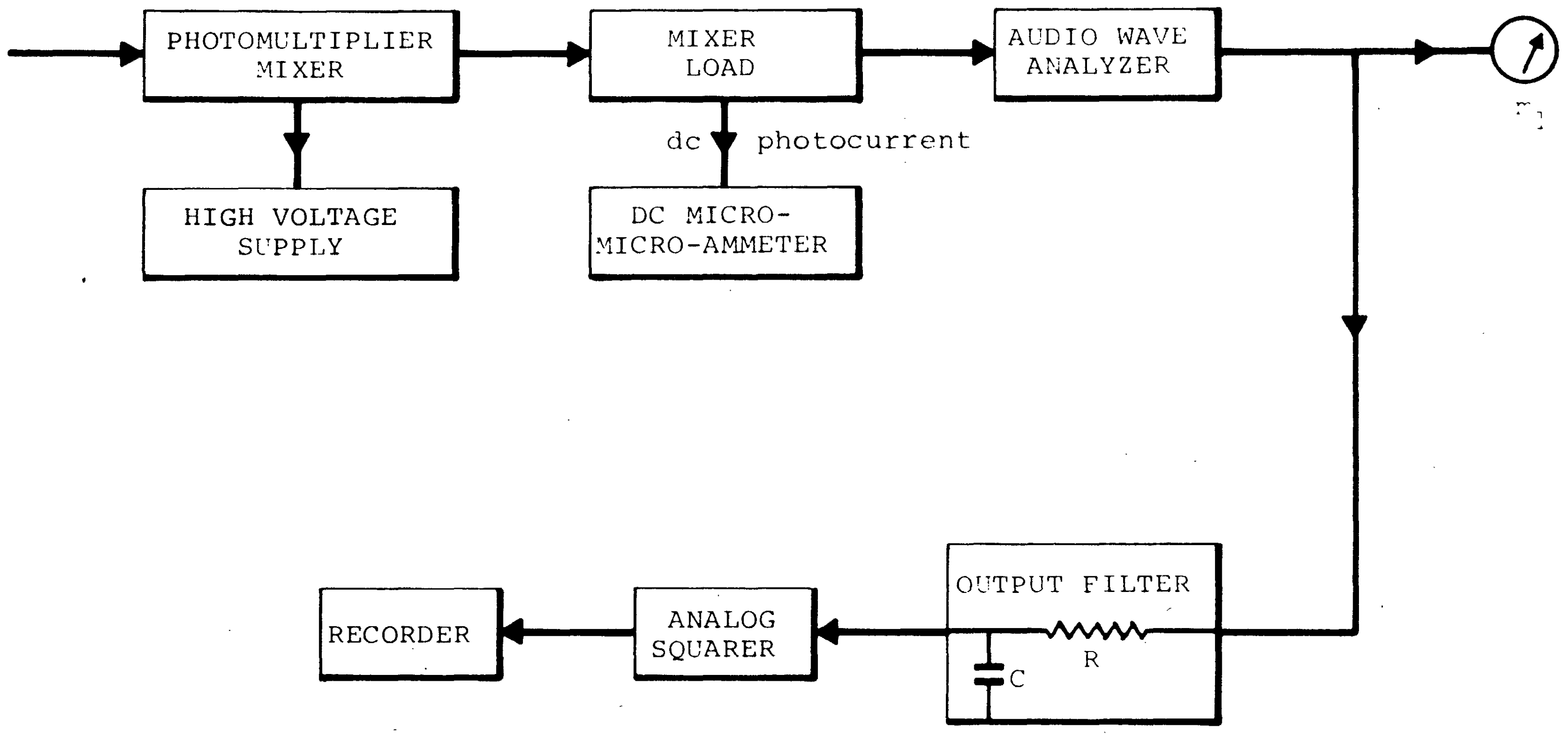
PHOTOMULTIPLIER MIXER
HIGH VOLTAGE SUPPLY
MIXER LOAD
dc photocurrent
DC MICRO-MICRO-AMMETER
AUDIO WAVE ANALYZER
OUTPUT FILTER
R
C
ANALOG SQUARER
RECORDER

Figure 4-31 Block diagram of the superheterodyne spectrometer used to observe the width of the central component.

the line width ($\Gamma/2\pi$) of the signal part of the photocurrent spectrum, $I_S^2(\omega)$. The wave analyzer acts as a narrow band tuned filter whose center frequency can be swept over the range of frequencies of interest in the beat-note spectrum. The analyzers which were used for the present measurements incorporated their own internal detectors. However, these detectors were linear-law devices[30] rather than the square-law variety whose rectification properties were analyzed in Section C.2.b.2 of Chapter 3. The linear rectifier produces a dc detector output voltage $\langle\langle v_D(t)\rangle\rangle$ that is proportional to the root-mean-square current at its input.[31] As a result the analyzer output is a dc voltage which is proportional to the square root of total power passed to the detector by the narrow band filter. Thus as the filter frequency, ω_f, is tuned over its range, the deflection of meter m_1 traces out the square root of the desired photocurrent spectrum, i.e. $\sqrt{S_i(\omega_f)}$. In order to generate a plot of $S_i(\omega)$ directly, the dc detector output is "squared" by a simple analog "computer" prior to recording.

a. The Photomixer

The photodetector-mixer used in this experiment was an RCA 7326 multiplier phototube having an S-20 type photosurface. This tube is a lower gain version of the RCA 7265 whose features were discussed in Section F of Chapter 3; it has the following typical characteristics:[32]

$$
\begin{aligned}
&\varepsilon(\lambda_{air} = 6328\ \text{Å}) \simeq 0.05 \\
&P_{DARK}(T = 20°C) = 2.5 \times 10^{-13}\ \text{watts} \\
&G_{DC} = G_{AC} \simeq 1.5 \times 10^{5} \\
&R_j = \infty \\
&R_s = 0 \\
&C_j = 7\ \text{pf.}
\end{aligned}
\qquad (4\text{-}78)
$$

Although this detector has a lower quantum efficiency than is available with a solid-state junction device, it exhibits three important advantages in the present system. First its dark equivalent input power P_{DARK} is approximately 9 orders of magnitude smaller than that typical of solid state junction detectors. The amount of optical local oscillator power necessary to overcome the dark current is correspondingly reduced, thereby decreasing the effects of local oscillator amplitude modulation[*] to a tolerable level. Secondly, the large internal gain available in a photomultiplier allows the amplified photocurrent shot-noise to overwhelm both the thermal noise in the load and any excess amplifier noise, again with an absolute minimum of local oscillator power input.[**] These first two features were essential considerations since measurements were made near ($\omega_1 = 0$) where the problems with laser modulation are most severe.

---

[*] Chapter 3, Section F.3.b.

[**] Chapter 3, Section F.4.b.

Thirdly, a photosurface type detector does not exhibit the troublesome "one-over-f" type excess noise which characterizes semi-conductor devices.[33] This feature was indispensable in obtaining reliable, undistorted spectra in the range of line widths below $(\Gamma/2\pi) < 1000$ cps.

The photomultiplier high voltage requirements were supplied by a well regulated, highly stable (0.01% per hour) Northeast Scientific Corporation[34] model RE-3002 power supply capable of delivering up to 3 kV to the multiplier dynode chain. The dc anode current of the detector was monitored by a Hewlett-Packard model 425A DC Microvolt-Ammeter.

b. The Mixer Load Circuits

The mixer terminations employed here were in essence untuned, broadband, resistive loads of the type discussed in Section F.4.a of Chapter 3. However, the large internal mixer gain which was available made it unnecessary to choose the load resistance R_L as the recommended optimum value corresponding to the line width being measured.* Negligibly small values of the signal-to-noise reduction factor F_R were obtained even with R_L selected on the basis of the total circuit capacitance to provide a flat response over the entire useful frequency range of a particular wave analyzer.

Figure 4-32 shows the equivalent mixer and load circuit used in conjunction with a General Radio Model 1900A wave analyzer capable of tuning the frequency range

---

* Chapter 3, Sections F.4.a and F.4.b, Eq. (3-185).

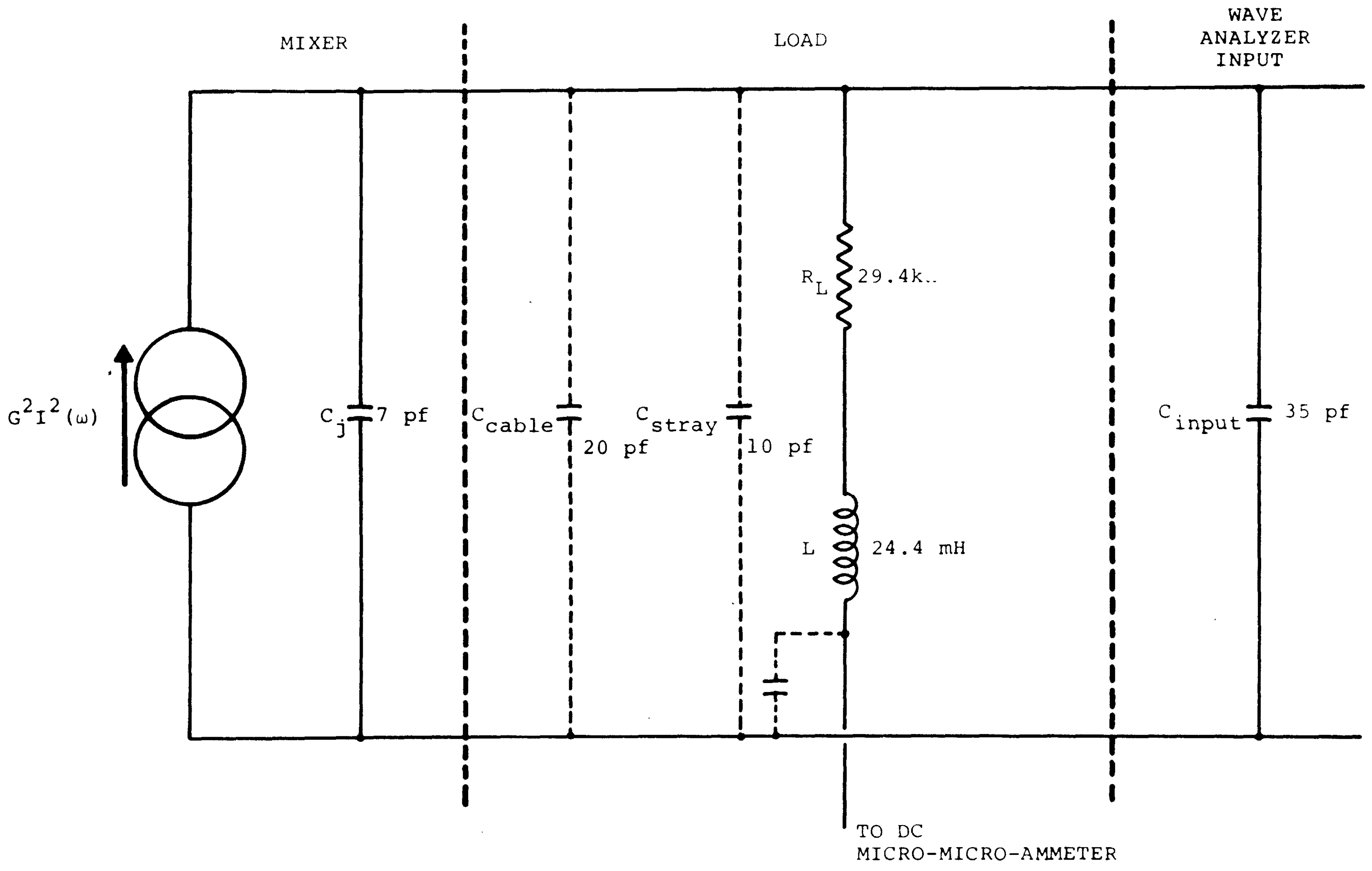
MIXER
LOAD
WAVE
ANALYZER
INPUT
$G^2I^2(\omega)$
C_j 7 pf
C_{cable} 20 pf
C_{stray} 10 pf
R_L 29.4k..
L 24.4 mH
C_{input} 35 pf
TO DC
MICRO-MICRO-AMMETER

Figure 4-32 Compensated photomixer load used with a General Radio 1900A wave analyzer.

$0 \leq (\omega_f/2\pi) \leq 60$ kc/sec. The parallel combination of $R_L = 29.4$ kΩ and the total circuit capacitance $C = 72$ pf would comprise an equivalent load whose power response dropped to one-half of its zero frequency value at $(\omega_{RC}/2\pi) \simeq 75$ kc/sec. However, the expected rolloff is counteracted to a large degree by inductance L which introduces a moderate amount of shunt compensation[35] in order to increase the apparent load resistance at high frequencies. The compensated network achieves an overall power response which is flat to within +0% and -3% between $(\omega_f/2\pi) = 0$ and $(\omega_f/2\pi) = 58$ kc/sec respectively.

The pre-detection signal-to-noise reduction factors F_R and F_D that describe the detector-load-analyzer combination of Fig. 4-32 are given by Eqs. (3-193) and (3-163) as

$$F_R = \frac{2\underline{k}T}{G_{AC}{}^2 eR_L i_p} \qquad (3\text{-}193)$$

$$F_D = (P_{DARK}/P_{LO}) \qquad (3\text{-}163)$$

Typical values of the local oscillator power P_{LO} and mixer gain $G = G_{DC} = G_{AC}$ for the measurements reported here were

$$P_{LO} \simeq 2 \times 10^{-8} \text{ watts}$$
$$G \simeq 6.5 \times 10^4 \qquad (4\text{-}79)$$

yielding from Eqs. (4-78), (3-193), and (3-163)

$$i_p = \left(\frac{\varepsilon e}{\hbar\omega_o}\right) P_{LO} = 4.6 \times 10^{-10} \text{ amps}$$

$$I_{OUT} = G i_p = 0.03 \text{ ma}$$

$$F_R = 9 \times 10^{-7} \qquad (4\text{-}80)$$

$$F_D = 1.2 \times 10^{-5}$$

The resulting F factors indicate that the effects of both thermal and dark current noise are completely negligible; therefore, apart from the question of heterodyning efficiency, this spectrometer will achieve the ideal pre- and post-detection signal-to-noise ratios predicted by Fig. 3-19.

Figure 4-33 illustrates the combined mixer and load circuit used at the input of a Hewlett Packard Model 310A wave analyzer which has a tuning range of 1 kc/sec $\leq (\omega_f/2\pi) \leq$ 1.5 Mc/sec. The half-power frequency of the uncompensated network consisting of R_L = 10 kΩ and a total shunt capacitance C = 57 pf was $(\omega_{RC}/2\pi)$ = 280 kc/sec. For the present measurements, which extended out to $(\omega_f/2\pi) \simeq$ 100 kc/sec, the undesirable rolloff in load response was corrected by a combination of shunt (L_1) and series (L_2 and L_3) compensating inductors.[35] The overall power response of this circuit was flat to within ±1.8% for filter frequencies in the range 1 kc/sec $\leq (\omega_f/2\pi) \leq$ 75 kc/sec.

The expected F factors for the above detector-load-analyzer system follow directly from Eqs. (3-193), (3-163), and (4-80) as

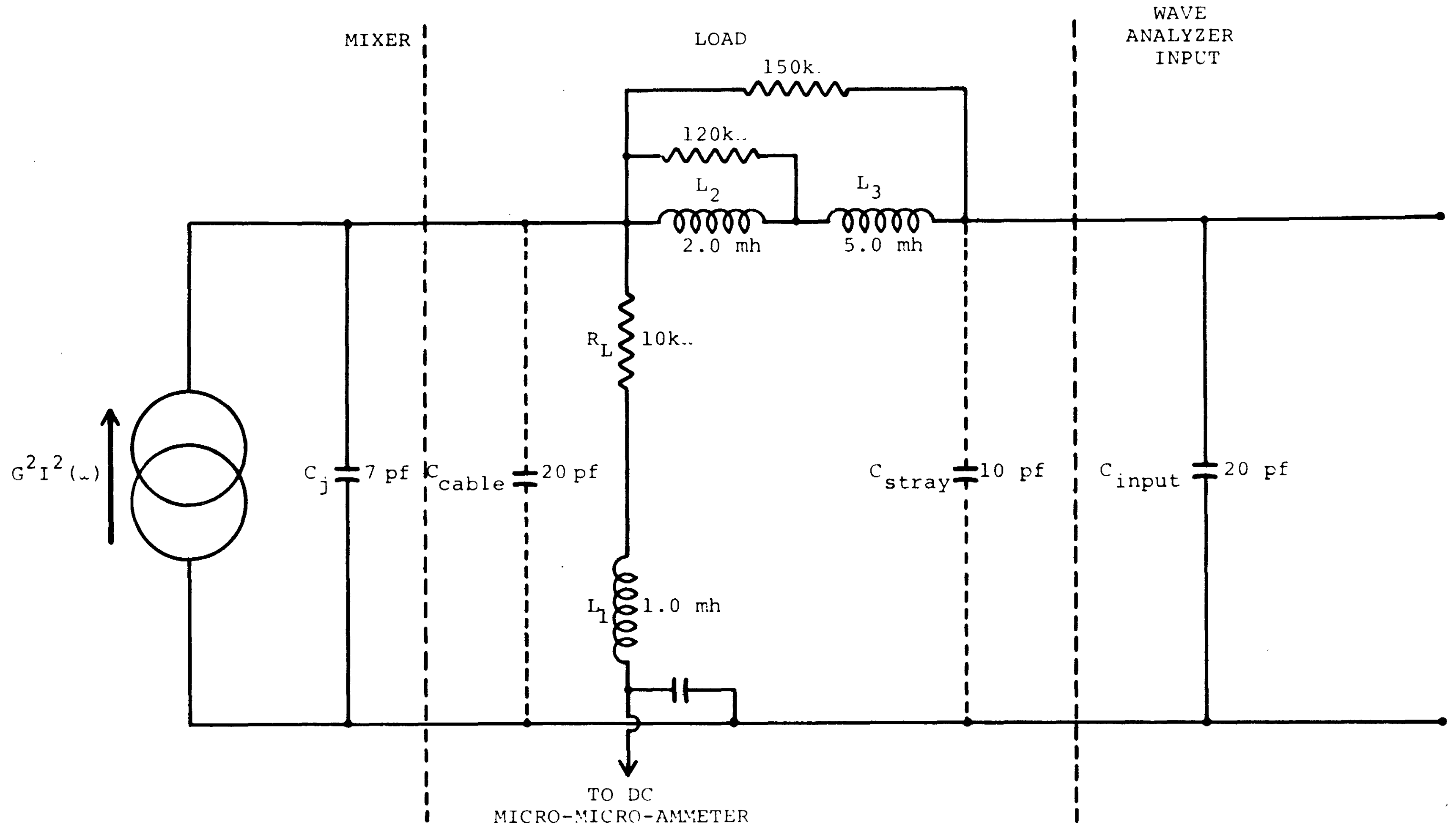

MIXER
LOAD
WAVE ANALYZER INPUT
150k
120k
L2
2.0 mh
L3
5.0 mh
RL
10k
L1
1.0 mh
G2I2(ω)
Cj 7 pf
Ccable 20 pf
Cstray 10 pf
Cinput 20 pf
TO DC MICRO-MICRO-AMMETER

Figure 4-33 Compensated photomixer load used with a Hewlett-Packard 310A wave analyzer.

$$F_R = 2.7 \times 10^{-6}$$

$$F_D = 1.2 \times 10^{-5} \qquad (4\text{-}81)$$

We again find that the amplified photocurrent shot-noise is sufficiently large to completely swamp both dark current shot-noise and Johnson noise effects. Thus the expected pre- and post-detection (S/N) ratios are the ideal values given in Fig. 3-19.

c. Wave Analyzers

The mixer current power spectral density, $S_i(\omega)$, was examined by one of two wave analyzers: a General Radio Model 1900A for measurements on line widths less than $(\Gamma/2\pi) \simeq 2500$ cps, and a Hewlett-Packard Model 310A for larger half-widths.

The 1900A has a tuning range of $0 \leq (\omega_f/2\pi) \leq 60$ kc/sec and selectable filter bandwidths of

$$(\Delta\omega_f/2\pi) = 3,\ 10,\ 50 \text{ cps}$$

These bandwidths represent effective resolving powers $(\omega_o/\Delta\omega_f)$ and resolutions $(\Delta\omega_f/\omega_o)$ at the incoming light wave frequency as tabulated below.

BANDWIDTH	3 cps	10 cps	50 cps
RESOLVING POWER	1.6×10^{14}	4.75×10^{13}	9.5×10^{12}
RESOLUTION	6.25×10^{-15}	2.1×10^{-14}	1×10^{-13}

The quoted resolving powers are typically 10^5 to 10^8 times larger than those obtainable by conventional spectroscopic techniques.

The Hewlett-Packard Model 310A analyzer can be tuned over the range 1 kc/sec $\leq (\omega_f/2\pi) \leq$ 1.5 Mc/sec with filter bandwidths of

$$(\Delta\omega_f/2\pi) = 300,\ 1000,\ 3000 \text{ cps}$$

The corresponding resolving powers and resolutions attained at the light wave frequency are given below.

BANDWIDTH	300 cps	1000 cps	3000 cps
RESOLVING POWER	1.6×10^{12}	4.75×10^{11}	1.6×10^{11}
RESOLUTION	6.25×10^{-13}	2.1×10^{-12}	6.25×10^{-12}

Both of these wave analyzers incorporate linear full-wave detectors to rectify the ac current passed by the narrow band filter. If the instantaneous input current from the filter is designated as $i_f(t)$ then this type of detector yields an output voltage given by

$$v_D(t) = M|i_f(t)| \tag{4-82}$$

where M is a constant. An analysis similar to the one presented in Section B.2 Chapter 3 for the square-law photodetector shows[36,37] that the dc detector output calculated by taking the appropriate time and statistical averages of $v_D(t)$ has the form

$$\left\langle\!\left\langle v_D(t) \right\rangle\!\right\rangle = (2/\pi)^{\frac{1}{2}} M \sqrt{\int_{-\infty}^{\infty} S_f(\omega)\, d\omega} \tag{4-83}$$

$$= (2/\pi)^{\frac{1}{2}} M \sqrt{\left\langle |i_f(t)|^2 \right\rangle}$$

in which $S_f(\omega)$ is the power spectral density of the filtered current $i_f(t)$. Thus the dc output of a linear detector measures the root-mean-square current at its input terminals.

If the narrow band filter has the rectangular system function shown in Fig. 3-11 and a bandwidth $\Delta\omega_f$ which is small compared to the line width of the heterodyne signal spectrum, then $S_f(\omega)$ takes the simple form given in Eq. (3-67). In this case we have for $\left\langle\!\left\langle v_D(t) \right\rangle\!\right\rangle$

$$\left\langle\!\left\langle v_D(t) \right\rangle\!\right\rangle = M'(\Delta\omega_f)^{\frac{1}{2}}\{I_S{}^2(\omega_f) + [I_N{}^2(\omega_f)]_{eff}\}^{\frac{1}{2}}$$

$$= M'(\Delta\omega_f)^{\frac{1}{2}}[I_S{}^2(\omega_f) + I_N{}^2(\omega_f) + I_R{}^2(\omega_f) + I_D{}^2(\omega_f) + I_{RA}{}^2(\omega_f)]^{\frac{1}{2}} \tag{4-84}$$

where $I_S{}^2(\omega_f)$ is the signal part of the photocurrent power spectral density and $[I_N{}^2(\omega_f)]_{eff}$ is the "effective shot-noise current power per unit bandwitch" defined in Eq. (3-149). For the spectrometer described here, where $I_R{}^2(\omega)$, $I_D{}^2(\omega)$, and $I_{RA}{}^2(\omega)$ (the equivalent thermal noise, dark noise, and amplifier noise respectively) are all negligible compared to the photocurrent shot-noise $I_N{}^2(\omega)$, Eq. (4-84) becomes simply

$$\langle\!\langle v_D(t) \rangle\!\rangle = M'(\Delta\omega_f)^{\frac{1}{2}}[I_S{}^2(\omega_f) + I_N{}^2(\omega_f)]^{\frac{1}{2}} \tag{4-85}$$

Therefore, as ω_f is tuned over an appropriate frequency range $\langle\!\langle v_D(t) \rangle\!\rangle$ traces out the square-root of the sum of the desired beat-note spectrum, $I_S{}^2(\omega)$, and a constant, $I_N{}^2(\omega)$.

d. The Squarer

In order to obtain a convenient plot of the signal spectrum directly, the analyzer output voltage was first passed through the post-detection RC filter shown in Fig. 4-31 and then "squared" by a slow speed analog squaring machine prior to recording. A block-diagram schematic circuit of this device is shown in Fig. 4-34.

In this case the recorded data trace has an amplitude proportional to the square of the dc detector output, namely

$$\begin{aligned}\langle\!\langle v_o(t) \rangle\!\rangle &\propto [\langle\!\langle v_D(t) \rangle\!\rangle]^2 \\ &= M'(\Delta\omega_f)[I_S{}^2(\omega_f) + I_N{}^2(\omega_f)]\end{aligned} \tag{4-86}$$

A plot of $\langle\!\langle v_o(t) \rangle\!\rangle$ versus the filter frequency ω_f yields the desired heterodyne signal spectrum $I_S{}^2(\omega)$ superposed on a shot-noise level $I_N{}^2(\omega)$ which is independent of ω_f.

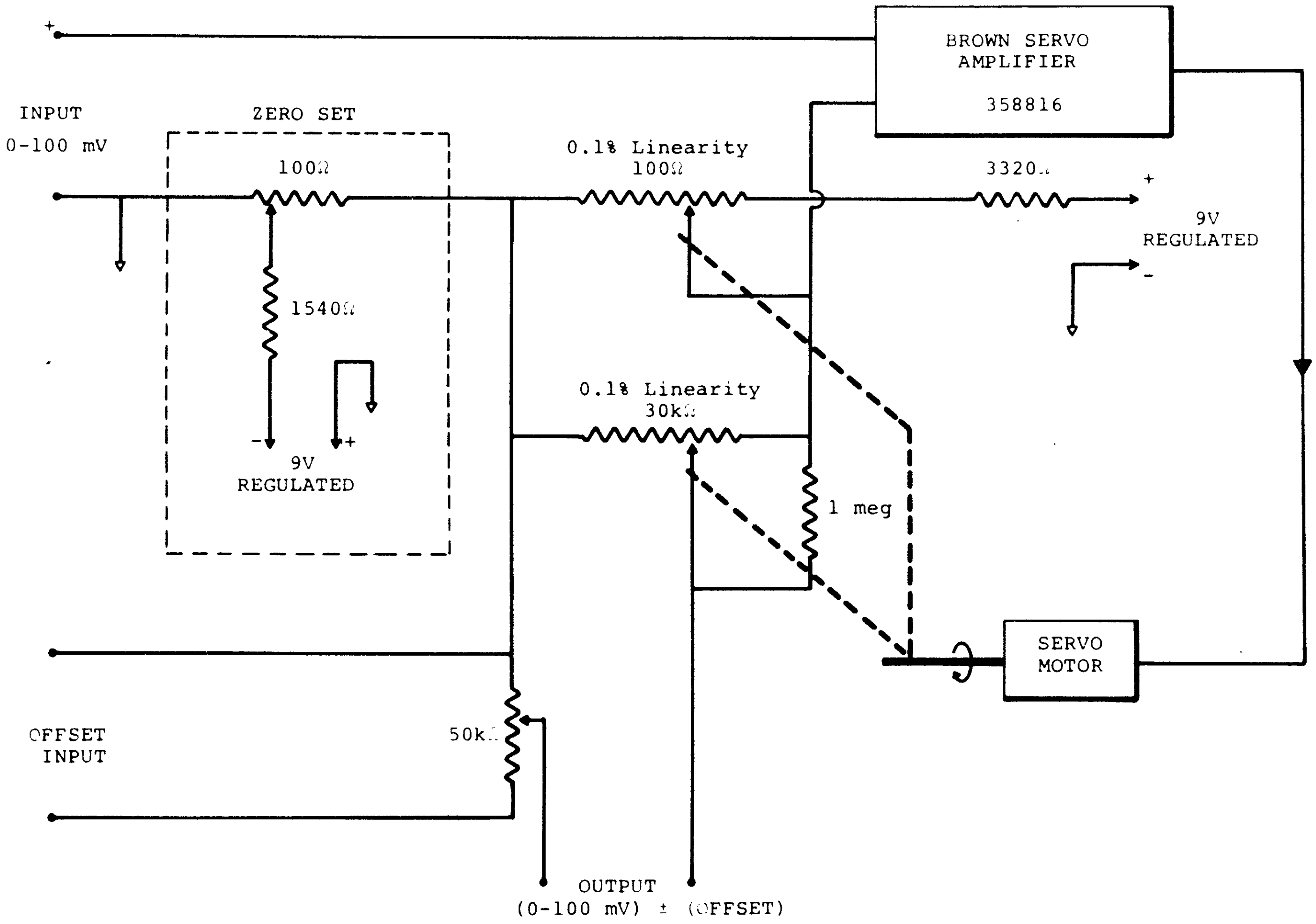

+
INPUT
0-100 mV
ZERO SET
100Ω
1540Ω
-
+
9V
REGULATED
0.1% Linearity
100Ω
0.1% Linearity
30kΩ
1 meg
BROWN SERVO
AMPLIFIER
358816
3320Ω
+
9V
REGULATED
-
SERVO
MOTOR
OFFSET
INPUT
50kΩ
OUTPUT
(0-100 mV) ± (OFFSET)

Figure 4-34 Block and schematic diagram of the analog squaring device.

e. The Effect of a Finite Bandwidth on the Recorded Heterodyne Spectrum

Equations (4-84) and (4-85) which relate the detector output to the power spectral density of the mixer current are valid only when $(\Delta\omega_f)$ is small compared to the line width of the signal spectrum $I_S{}^2(\omega_f)$. In this case the change in $I_S{}^2(\omega)$ over the filter bandpass is neglected; if the input optical field has a Lorentzian spectrum of half-width Γ, the recorded spectrometer output is simply

$$\langle\langle v_o(t)\rangle\rangle = \frac{A\Gamma^2}{\omega_f{}^2 + \Gamma^2} + B \tag{4-87}$$

where A and B are constants. However, for the line widths measured here the ratio $(\Delta\omega_f/\Gamma)$ fell in the range $0.02 \leq (\omega_f/\Gamma) \leq 0.15$ while the output signal-to-noise ratio was sufficient to establish the half-width to typically ±3% accuracy. Under these circumstances it becomes important to determine the influence of the finite bandwidth on the shape and width of the recorded spectra.

The exact relationship between the output voltage, the filter frequency, the filter bandwidth, and the photocurrent spectrum has the form

$$\langle\langle v_o(t)\rangle\rangle = A'\Gamma^2 \int_{\omega_f - \frac{\Delta\omega_f}{2}}^{\omega_f + \frac{\Delta\omega_f}{2}} \frac{d\omega}{\omega^2 + \Gamma^2} + B \tag{4-88}$$

The evaluation of this integral is straightforward and gives

$$\left\langle\!\left\langle v_o(t) \right\rangle\!\right\rangle = \frac{A'\Gamma^3}{\Delta\omega_f} \tan^{-1} \left[\frac{(\Delta\omega_f/\Gamma)}{1 + \left(\frac{\omega_f}{\Gamma}\right)^2 \left[1 - \left(\frac{\Delta\omega_f}{2\omega_f}\right)^2\right]} \right] + B \qquad (4\text{-}89)$$

By using the condition $(\Delta\omega_f/\Gamma) < 1$ and the series expansion of the inverse tangent we have to second order in $(\Delta\omega_f/\Gamma)$

$$\left\langle\!\left\langle v_o(t) \right\rangle\!\right\rangle = \frac{A'\Gamma^2}{[1 - (\Delta\omega_f/2\Gamma)^2]} \frac{1}{1 + \left[\frac{(\omega_f/\Gamma)^2}{1 - (\Delta\omega_f/2\Gamma)^2}\right]} \qquad (4\text{-}90)$$

Therefore, in the approximation $(\Delta\omega_f/\Gamma) < 1$ we find that the recorded spectrometer output is also a Lorentzian; however, the observed half-width has the value

$$\Gamma_{obs} \simeq \Gamma[1 + (\Delta\omega_f/2\Gamma)^2] \qquad (4\text{-}91)$$

For the largest ratio of $(\Delta\omega_f/\Gamma)$ used here this correction represented an apparent line width increase of only (0.5%).

5. Operating Characteristics of the Spectrometer

The superheterodyne spectrometer described above showed several undesirable effects which were not evident in the spectrometer used for the detection of the Brillouin-Mandel'shtam components. Most of these difficulties appeared only because the system was inherently capable of attaining excellent signal-to-noise ratios and, therefore, of providing spectral measurements with exceptional accuracy. The following paragraphs discuss some of the more important features that influenced the actual operation of the instrument and the interpretation of the resulting data.

Even with the extensive dust shielding pictured in Fig. 4-24 and with manual control of the cavity length as described in Section B.3.c, fluctuations in laser output were still evident. The increase of the power per unit bandwidth in the laser amplitude modulation spectrum* near $\omega \simeq 0$ was sufficiently rapid that spurious signals in the photocurrent were easily detectable above the shot-noise level at frequencies below $(\omega/2\pi) \simeq 30$ cps. Because of this effect most of the data traces exhibit a sharp increase in amplitude as the filter frequency ω_f is tuned to within a few filter bandwidths of $\omega = 0$. In general, points belonging to these values of ω_f were discarded in the analysis of the experimental spectra.

Since the recorded output of the spectrometer is the sum of a signal term

$$\left\langle\!\left\langle v_o(t) \right\rangle\!\right\rangle \Big|_{\text{signal}} = M''(\Delta\omega_f)\,[I_S{}^2(\omega_f)]$$

porportional to $I_S{}^2(\omega_f)$ and a shot-noise background level

$$\left\langle\!\left\langle v_o(t) \right\rangle\!\right\rangle \Big|_{\text{shot}} = M''(\Delta\omega_f)\,[I_N{}^2(\omega_f)]\,,$$

poor pre-detection signal-to-noise ratios,

$$(S/N)_{PRE} = [I_S{}^2(\omega_f{=}0)/I_N{}^2(\omega_f{=}0)] << 1,$$

imply that small uncertainties in the total output $\left\langle\!\left\langle v_o(t) \right\rangle\!\right\rangle$ may lead to rather large errors in the amplitude of the signal component. For example, with $(S/N)_{PRE} = 0.2$ a ±3% non-uniformity in the overall frequency response of the electronic detection apparatus represents a possible error in $\langle\langle v_o(t)\rangle\rangle|_{signal}$ which is ±15% of its peak value $M''(\Delta\omega_f)I_S^2(0)$. When necessary this source of error was eliminated by correcting the experimentally recorded spectrum to a normalized response curve of the system. This standard curve was generated by illuminating the photomixer with an extremely stable white light source and recording the supposedly uniform shot-noise spectrum as a function of the filter frequency ω_f.

---

* Chapter 3, Section F.3.b.

The effects of long term drift in laser power output on the uncertainty in $\langle\langle v_o(t)\rangle\rangle|_{signal}$ are similarly enhanced by small values of $(S/N)_{PRE}$. To avoid this error the power output was continuously monitored and manually corrected by changing the rf drive power to the plasma tube.

It was also observed that slow drifts in the alignment of the laser resonator mirrors tended to change the local oscillator power as the laser beam altered its position slightly with respect to the scattering imperfection on the cell window. Again in the limit of small $(S/N)_{PRE}$ the apparent effect on the signal part of the recorded output is exaggerated by the relatively large change in shot-noise level. This power drift was monitored during the course of a data run by simultaneously recording both the spectrometer output and the dc mixer output current (Gi_p). Since both $I_S^2(\omega_f)$ and $I_N^2(\omega_f)$ are proportional* to i_p, we have $\langle\langle v_o(t)\rangle\rangle \propto i_p$ and the experimental spectrum can be corrected to "constant local oscillator power" by using the recorded behavior of i_p.

---

* Chapter 3, Section D.4, Eq. (3-129).

As a result of these corrections it is estimated that the signal spectra obtained after subtraction of the shot-noise level reproduced the actual heterodyne beat-note spectrum $I_S^2(\omega)$ to within 1% of its peak value.

BIBLIOGRAPHY: Chapter 4

1. K. D. Mielenz, H. D. Cook, K. E. Gillilland, and R. B. Stephans, Science 146, 1672 (1964).

2. Spectra-Physics Incorporated, 738 Terra Bella Avenue, Mountain View, California.

3. The Radio-Amateur's Handbook, edited by Byron Goodman (The American Radio Relay League, Newington, Connecticut, 1966), 43rd ed.

4. A. D. White and E. I. Gordon, Appl. Phys. Letters 2, 91 (1963).

5. Spectra-Physics Laser Technical Bulletin Number 2, Spectra-Physics Incorporated, Mountain View, California.

6. A. G. Fox and T. Li, Bell System Tech. J. 40, 453 (1961).

7. G. D. Boyd and J. P. Gordon, Bell System Tech. J. 40, 489 (1961).

8. G. D. Boyd and H. Kogelnik, Bell System Tech. J. 41, 1347 (1962).

9. M. Born and E. Wolf, Principles of Optics (The Macmillan Company, New York, 1964), 2nd ed., pp. 435 ff.

10. Reference 9; pp. 395 ff.

11. G. W. Farnell, Can. J. Phys. 35, 780 (1957).

12. Product Catalog, The Lansing Research Corporation; Ithaca, New York.

13. Spectra-Physics Laser Technical Bulletin Number 1, Spectra Physics Incorporated, Mountain View, California.

14. W. E. Lamb, Jr., Phys. Rev. 134, 1429 (1964).

15. L. E. Hargrove, R. L. Fork, and M. A. Pollack, Appl. Phys. Letters 5, 4 (1964).

16. R. E. McClure, Appl. Phys. Letters 7, 148 (1965).

17. Reference 9, p. 42.

18. A. D. Jones Optical Works, Burlington, Massachusetts.

19. J. Strong, Procedures in Experimental Physics (Prentice-Hall, Inc., New York, 1945), p. 33.

20. J. P. Gordon, R. C. C. Leite, R. S. Moore, S. P. S. Porto, and J. R. Whinnery, J. Appl. Phys. 36, 3 (1965).

21. R. C. C. Leite, R. S. Moore, and J. R. Whinnery, Appl. Phys. Letters 5, 141 (1964).

22. American Institute of Physics Handbook, edited by D. E. Gray (McGraw-Hill Book Company, Inc., New York, 1963), 2nd ed.

23. Reference 9; p. 43.

24. Millipore Filter Corporation, Bedford, Massachusetts.

25. Reference 9; pp. 312 ff.

26. F. A. Jenkins and H. E. White, Fundamentals of Optics (McGraw-Hill Book Company, Inc., New York, 1957), pp. 511, 513.

27. SD-100 Data Sheet, Edgerton, Gerheshausen, and Grier Inc., Boston, Massachusetts.

28. LEL, Division of VARIAN Associates, Copiague, Long Island, New York.

29. L. K. Anderson, P. G. McMullin, L. A. D'Asaro, and A. Goetzberger, Appl. Phys. Letters 6, 62 (1965).

30. N. C. Ford, Jr., and G. B. Benedek, in Critical Phenomena, edited by M. S. Green and J. V. Sengers (United States Government Printing Office, Washington, 1966), p. 150.

31. W. B. Davenport, Jr., and W. L. Root, An Introduction to the Theory of Random Signals and Noise (McGraw-Hill Book Company, Inc., New York, 1958), pp.267 ff.

32. RCA Phototubes and Photocells, Technical Manual PT-60 (Radio Corporation of America, Lancaster, Pennsylvania, 1963), pp. 165 ff.

33. M. Ross, Laser Receivers (John Wiley and Sons, Inc., New York, 1966), pp.58 ff.

34. Northeast Scientific Corporation, Acton, Massachusetts.

35. R. W. Landee, D. C. Davis, and A. P. Albrecht, *Electronic Designers' Handbook* (McGraw-Hill Book Company, Inc., New York, 1957), pp. *3*-40 ff.

36. S. O. Rice, Bell System Tech. J. *23*, 282 (1944).

37. R. E. Burgess, Phil. Mag., Ser. 7 *42*, 475 (1951).

Chapter 5

EXPERIMENTAL RESULTS

A. Introduction

This chapter presents a discussion and an analysis of the experimental results obtained on the spectrum of light scattered from toluene liquid at room temperature and atmospheric pressure. The results may be grouped conveniently into two sections.

The first describes the observation of the Brillouin-Mandel'shtam components of the spectrum at a single scattering angle, $\Theta = 0.547°$. The frequency splitting of the doublet is found to be $(\bar{\omega}/2\pi) = 30.0 \pm 0.3$ Mc/sec, in agreement with the frequency of the sound waves which were used in aligning the optical system.[§] The measured half-width at half-height of the spectrum is approximately 2.2 Mc/sec and is determined primarily by the acceptance angle of the spectrometer. The natural broadening[†] due to the finite lifetime of 30 Mc/sec thermal sound waves (16 kc/sec) was undetectable.

In analyzing the observed spectra we also calculate the values of $(S/N)^*_{PRE}$ and $(S/N)_{OUT}$ predicted on the basis of the known Brillouin scattering coefficient for toluene, the theoretical sensitivity results which were derived in Chapter 3, and the characteristic parameters of the spectrometer. The experimentally measured signal-to-noise ratios are in substantial agreement with these theoretical values.

[§] Chapter 4, Section D.2

[†] Chapter 2, Section D.

The second section presents and analyzes the data obtained on the line shape and natural line width of the central component for scattering angles between $\Theta = 0.3°$ and $\Theta = 2.8°$. The spectrum in this range was found to be accurately Lorentzian with a half-width at half-height varying from $(\Gamma/2\pi) \simeq 75$ cps to $(\Gamma/2\pi) \simeq 7500$ cps. The line width data accurately follow the K^2 dependence predicted in Section D of Chapter 2 and yield a measured thermal diffusivity of

$$(1/2\pi)(\Lambda/\rho c_P)_{\text{exptl.}} = (1.38 \pm 0.05) \times 10^{-4} \text{ cm}^2/\text{sec}$$

after correction to T = 20.0°C. This result is in good agreement with the thermodynamically determined value

$$(1/2\pi)(\Lambda/\rho c_P)_{\text{static}} = (1.52 \pm 0.09) \times 10^{-4} \text{ cm}^2/\text{sec}$$

The central component spectra also yielded important quantitative data on the behavior of the pre- and post-detection signal-to-noise ratios over a rather wide dynamic range of the ratio (P_{COH}/Γ) and hence* of $(S/N)_{PRE}$. This information is used (1) to verify the calculations of the heterodyning efficiency factors which were presented in Section E.2 of Chapter 4, (2) to test the spatial coherence and signal-to-noise theories given in Chapter 3, and (3) to confirm the expected operating characteristics of the spectrometer optical system.

---

* Chapter 3, Section D.5.a.

B. The Brillouin-Mandel'shtam Components

1. The Frequency Shift

Figures 5-1 and 5-2 show typical Brillouin spectra recorded with the heterodyne spectrometer of Figs. 4-16 and 4-17 when the instrument was aligned* by injecting 30.0 Mc/sec and 27.5 Mc/sec sound waves respectively into the scattering cell. The corresponding experimentally measured frequency shifts are

$$(\varpi/2\pi) = 30.0 \pm 0.1 \text{ Mc/sec}$$

and

$$(\varpi/2\pi) = 27.5 \pm 0.2 \text{ Mc/sec}$$

Since an independent determination of the scattering angle Θ was not made, these splittings cannot be used to obtain a value for the phase velocity v_s of the thermal pressure fluctuations.** However, the agreement between the observed splitting and the frequency of the injected ultrasonic wave confirm the fact that v_s is the ordinary phase velocity of sound in the medium.

Taking $(\varpi/2\pi) = 30.0$ Mc/sec and using an average[1] of the ultrasonically measured values of v_s

---

* Chapter 4, Section D.2.

** Chapter 2, Section D.5.

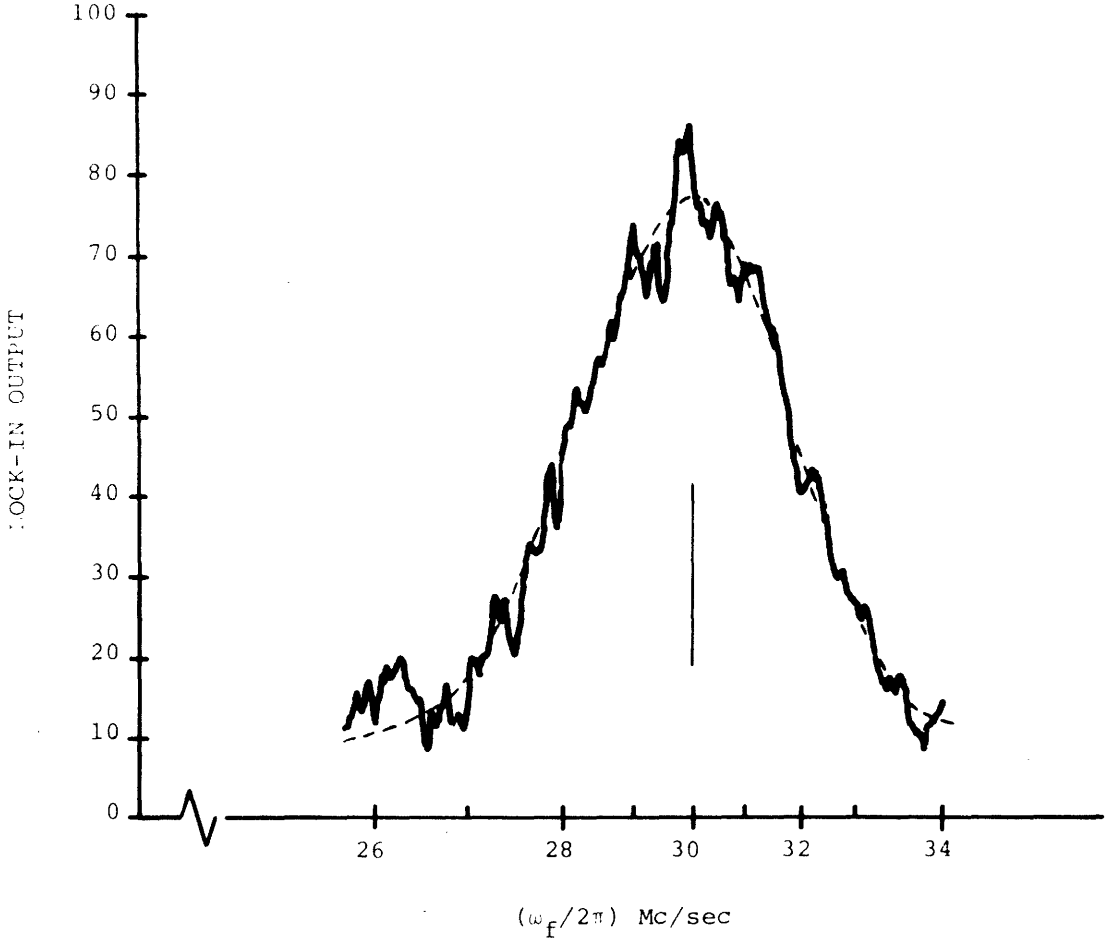

Figure 5-1 Typical Brillouin spectrum. This spectrum was obtained with the spectrometer optical system aligned by injection of 30.0 Mc/sec sound waves. The lock-in output time constant was $\tau = 10$ sec. This spectrum was recorded in about 1 hour.

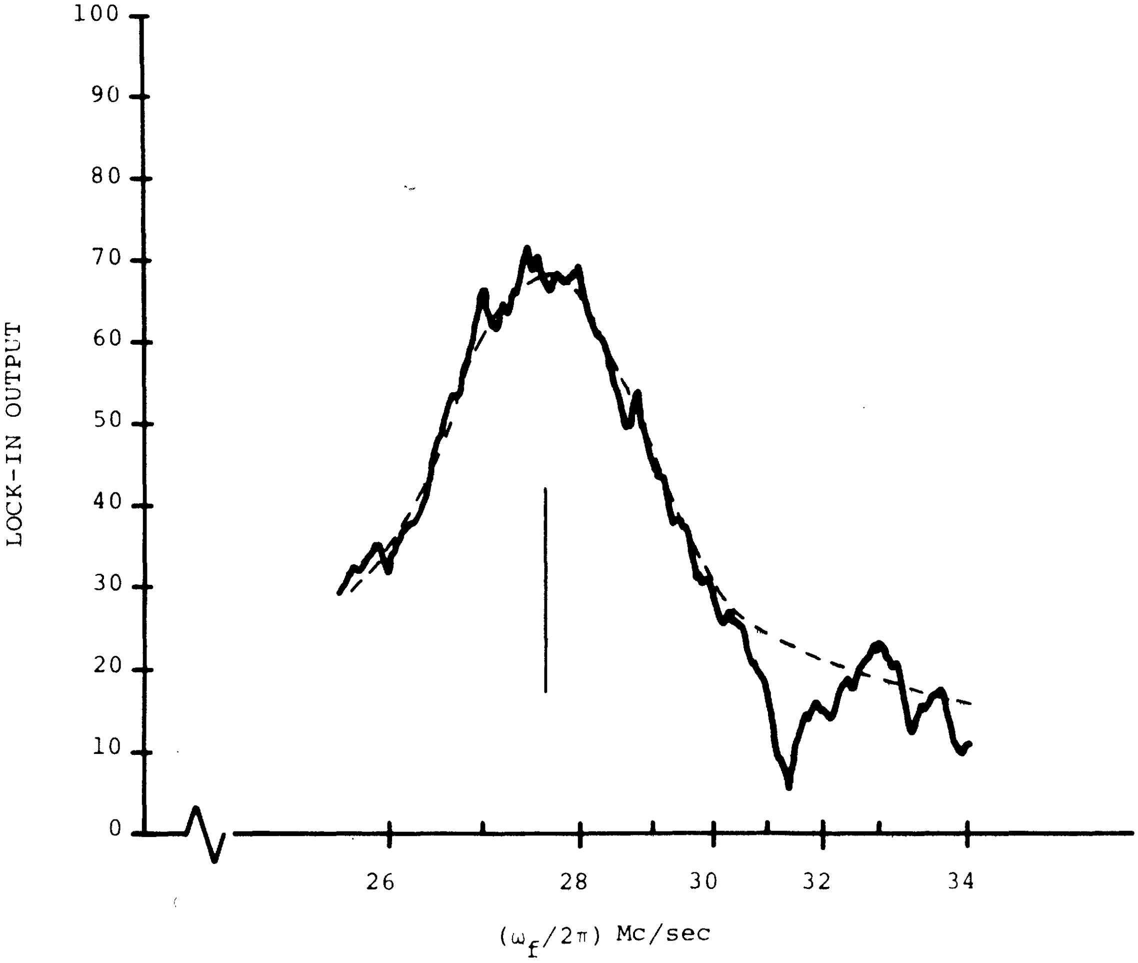

Figure 5-2 Typical Brillouin spectrum. This spectrum was obtained with the spectrometer optical system aligned by injection of 27.5 Mc/sec sound waves. The lock-in output time constant was $\tau = 10$ sec. This spectrum was recorded in about 1 hour.

$$v_s = 1332 \pm 13 \text{ meters/sec} \tag{5-1}$$

we may calculate the wave vector and wavelength of the scattering fluctuation at T = 20.0°C as

$$\begin{aligned} K &= (\overline{\omega}/v_S) = 1.4\bar{1}5 \times 10^{3} \text{ cm}^{-1} \\ \lambda_f &= 4.4 \times 10^{-3} \text{ cm} \end{aligned} \tag{5-2}$$

The internal scattering angle Θ can be determined from Eq. (2-32) with the quantities

$$\begin{aligned} \lambda_{air} &= 6328 \text{ Å} \\ n(T = 20.0°\text{C}) &= 1.4925 \end{aligned} \tag{5-3}$$[2]

as

$$\Theta = 0.5\bar{4}7° = 0.00954 \text{ rad} \tag{5-4}$$

2. The Line Width

The half-width at half-height of the spectrum recorded in Fig. 5-1 is approximately 2.2 Mc/sec while the spectrometer "instrumental profile" determined by the tuned filter response* has a half-width at half-power of $(1/2)(\Delta\omega_f/2\pi) = 1.17$ Mc/sec. This rather substantial broadening reflects the natural width of the photocurrent power spectral density $S_i(\omega)$. There are three factors that contribute to the overall line shape and line width of the current spectrum.

---

* Chapter 4, Section D.4.

a. The Natural Broadening

First, the Brillouin-Mandel'shtam components of the scattered light have an intrinsic width due to the finite lifetime of the scattering sound wave.* The effect of this damping, assuming a monochromatic incident beam, is to give the light scattered into an infinitesimally small angle $d\Theta$ around $\Theta = \Theta_m$ a Lorentzian spectrum with a half-width at half height of

$$(\gamma_K/2\pi) = (\alpha_K v_s/2\pi) \quad ; \tag{5-5}$$

the quantity α_K is the amplitude attenuation coefficient of a sound wave having wave vector

$$K = 2k_o \sin(\Theta_m/2)$$

and, therefore, a frequency

$$\nu = (\overline{\omega}/2\pi) = (1/2\pi)v_s K$$

Heasell and Lamb[3] give the ultrasonically determined ratio (α_K/ν^2) as

$$(\alpha_K/\nu^2) = 85.5 \times 10^{-17} \text{ sec}^2/\text{cm}$$

---

[*] Chapter 2, Section D.5.

independent of frequency* for $\nu < 200$ Mc/sec. From this result and the value of v_S given in Eq. (5-1) we compute

$$(\gamma_K/2\pi) = 16.4 \text{ kc/sec} \tag{5-6}$$

for $(\overline{\omega}/2\pi) = 30.0$ Mc/sec. Clearly this intrinsic width is negligible compared to the observed broadening.

b. The Effect of Finite Sample Dimensions

The spectrum of the light collected in some infinitesimally small range of scattering angle is also broadened by a second effect. Because of the finite dimensions of the scattering volume and the resultant uncertainty in the conservation of momentum condition**, the light scattered into a particular angle Θ is contributed simultaneously by fluctuations having a finite range in wave vector ΔK around the value

$$K = 2k_o \sin (\Theta/2)$$

Appendix E shows that for the light source and the scattering cell geometries and scattering angles involved here the light collected at the angle Θ_o has a spectrum given by

$$\overline{\overline{S_E(\omega;\Theta_o)}} = \frac{L_Y}{\pi} \int_{K=-\infty}^{\infty} S_E(\omega,K)\, e^{-\frac{L_Y^2}{\pi}(K - K_o)^2}\, dK \tag{5-7}$$

---

* Chapter 2, Section D.5.

** Chapter 2, Section E.4.e.

$K_o = 2k_o \sin(\Theta_o/2)$

L_y - the width of the illuminated volume measured in the scattering plane; Chapter 4, Section C.4.

where $S_E(\omega,K)$ is the spectrum of the light scattered by a single fluctuation having wave vector K. Eq. (2-101) gives the power spectral density of the light scattered by pressure fluctuations of wave vector K as

$$S_E(\omega,K) = \left\langle|\vec{E}_S(\vec{r},t)|^2\right\rangle \left[\frac{(1/2)(\gamma_K/2\pi)}{[\omega - (\omega_o + \overline{\omega}_K)]^2 + \gamma_K^2} + \frac{(1/2)(\gamma_K/2\pi)}{[\omega - (\omega_o - \overline{\omega}_K)]^2 + \gamma_K^2}\right] \qquad (2\text{-}101)$$

In the limit of negligible attenuation ($\gamma_K \to 0$), which is valid here, $S_E(\omega,K)$ takes the simple form

$$S_E(\omega,K) = \left\langle|\vec{E}_S(\vec{r},t)|^2\right\rangle\left\{\tfrac{1}{2}\delta[\omega - (\omega_o + v_S K)] + \tfrac{1}{2}\delta[\omega - (\omega_o - v_S K)]\right\} \qquad (5\text{-}8)$$

where ω_o is the incident light frequency. We then find easily

$$\overline{\overline{S_E(\omega,\Theta)}} = \frac{L_y}{2\pi v_s}\left\langle|\vec{E}_S(\vec{r},t)|^2\right\rangle e^{-\frac{L_y^2}{\pi v_s^2}[\omega - (\omega_o \pm v_S K)]^2} \qquad (5\text{-}9)$$

That is, in the limit $\gamma_K \to 0$ the uncertainty in the condition $\vec{K} = \pm(\vec{k}_s - \vec{k}_o)$ caused by the finite size of the illuminated region results in an artificial broadening of each of the B-M doublet components into a Gaussian spectrum with an effective half-width at half-height of

$$(\gamma_1/2\pi) = \left(\frac{0.693}{4\pi}\right)^{\frac{1}{2}} \frac{v_s}{L_y} \qquad (5\text{-}10)$$

From the data given in Eqs. (4-23) and (5-1) we obtain for the present geometry

$$(\gamma_1/2\pi) = 1.12 \text{ Mc/sec} \qquad (5\text{-}11)$$

c. The Acceptance Angle Contribution

The third factor that contributes to the observed shape and width of $S_i(\omega)$ is the finite range of Θ over which mixing takes place between the scattered light and the local oscillator field. In the present system this acceptance angle is fixed solely by the intensity distribution in the local oscillator beam.

Consider the fields falling on a plane screen H inserted to the left of the beam splitter in Fig. 4-16 and positioned to be normal to the signal and local oscillator beam axes. Figure 5-3 shows the surface of H and a local cartesian coordinate system having its origin at the center of the local oscillator beam spot and its x axis lying in the scattering plane, i.e. the plane of Fig. 4-16. A ray of the scattered light passing through the point (x,y) = (0,0) leaves the cell at the external angles* Θ_o' and $\Psi_o' = 0$ for which the system

---

* Chapter 4, Section C.5.

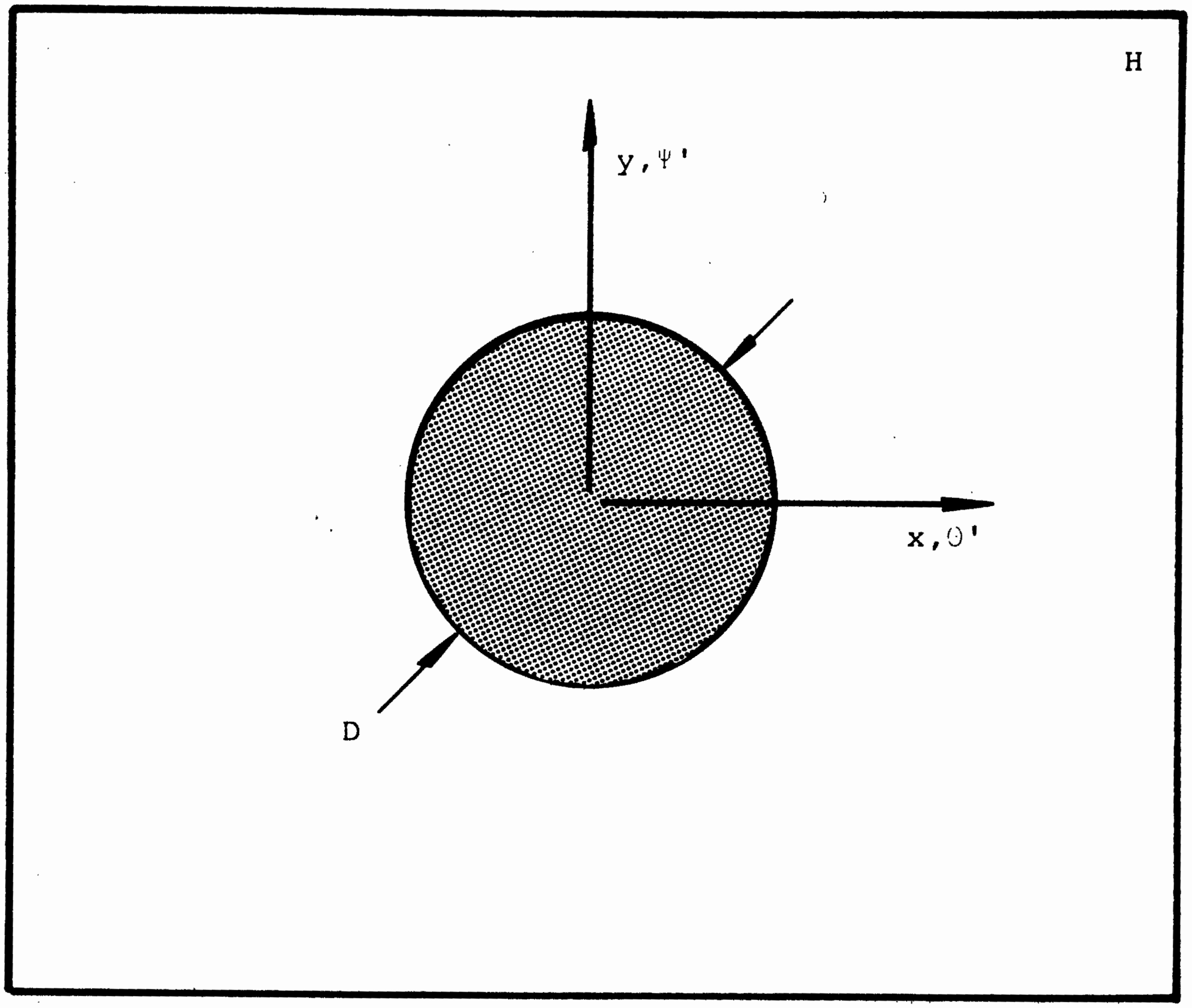

Figure 5-3 The geometry of the plane H used to calculate the instrumental acceptance angle of the superheterodyne Mach-Zehnder spectrometer.

was originally aligned. If the total optical path length from the cell to the plane H is R_H then scattered rays reaching the general point (x,y) have external scattering angles given by

$$\Theta' = \Theta_o' + (x/R_H) \tag{5-12}$$

and

$$\Psi' = \Psi_o' + (y/R_H) \tag{5-13}$$

in the usual small angle approximation. Equations (4-13) and (4-16) give the corresponding internal scattering angles as

$$\Theta = \Theta_o + (x/n^2 R_H) \tag{5-14}$$

and

$$\Psi = \Psi_o + (y/nR_H) \tag{5-15}$$

respectively.

Suppose that the power spectral densities of the two fields present at the point (x,y) are designated as $\overline{\overline{S_E(\omega;x,y)}}$ and $S_{LO}(\omega;x,y)$, the scattered and local oscillator spectra respectively. Then if H were a photosurface the beat note part of the photocurrent density generated at (x,y) would have a power spectrum

$$S_j(\omega;x,y) \propto \int_{-\infty}^{\infty} S_E(\omega';x,y) S_{LO}(\omega'-\omega;x,y)\,d\omega' \tag{5-16}$$

as follows directly from Eq. (3-126). Integrating this current density spectrum over the entire H plane gives the desired power per unit bandwidth in the total photocurrent as

$$S_i(\omega) \propto \int_{x=-\infty}^{\infty} dx \int_{y=-\infty}^{\infty} dy \int_{\omega'=-\infty}^{\infty} \overline{\overline{S_E(\omega';x,y)}}\; S_{LO}(\omega'-\omega;x,y)\,d\omega' \tag{5-17}$$

Of course, the two power spectral densities $\overline{\overline{S_E}}$ and S_{LO} can be functions of x and y for two distinct reasons; the intensity and/or the spectral shape of the corresponding field component may depend on the observation position.

The mean-square amplitude of the scattered field received at H is independent* of (x,y); however, its spectrum is a function of the observation point via the scattering angle Θ. For the small scattering angles involved here, the mean wave vector of the fluctuations that scatter the light observed at the angle Θ may be approximated as

$$K = 2k_o \sin(\Theta/2) \simeq k_o\Theta \tag{5-18}$$

In this case we have immediately from Eqs. (5-9) and (5-14)

$$\overline{\overline{S_E(\omega;x,y)}} = \frac{L_y}{2\pi v_s}\left\langle|\vec{E}_S(\vec{r},t)|^2\right\rangle \times$$

$(\omega \geq 0)$

$$\exp - \frac{L_y^2}{\pi v_s^2}\left\{\omega - \left[\omega_o \pm v_s k_o\left(\Theta_o + \frac{x}{n^2 R_H}\right)\right]\right\}^2 \tag{5-19}$$

In contrast, the spectrum of the local oscillator field is independent of (x,y); however, its intensity has an axially symmetric Gaussian profile* centered around $(x,y) = (0,0)$. Using Eqs. (3-83) and (4-1) we have

---

* Chapter 2, Section C.

$$S_{LO}(\omega;x,y) = \left\langle |\vec{E}_{LO}(\vec{r},t)|^2 \right\rangle \delta(\omega - \omega_{LO})$$

$$(\omega \geq 0)$$

$$= E_o^{\,2}(\vec{r}_o)\, e^{-\frac{8}{D^2}(x^2 + y^2)}\, \delta(\omega - \omega_{LO}) \qquad (5\text{-}20)$$

The spot diameter D is the radial distance from the beam axis $(x,y) = (0,0)$ at which the field falls to $(1/e)$ of its maximum value.

Since an observer to the left of the beam splitter sees the source points of the local oscillator and scattered fields in apparent exact superposition and there is no limiting aperture in the optical system it is only the "beam" characteristic of the local oscillator field which delimits the range of scattering angles over which perfect mixing between the two fields will take place.

With Eqs. (5-19) and (5-20) for $\overline{\overline{S_E}}$ and S_{LO}, Eq. (5-17) takes the form of a convolution of two Gaussians and gives the photocurrent power spectral density as

$$S_i(\omega) \propto \exp -\left[\frac{(\omega - v_s k_o \Theta_o)^2}{\dfrac{\pi v_s^{\,2}}{L_y^{\,2}} + \dfrac{v_s^{\,2} k_o^{\,2} D^2}{8 n^4 R_H^{\,2}}} \right] \qquad (5\text{-}21)$$

$$(\omega \geq 0)$$

The result is a Gaussian centered at the sound wave frequency for which the system was aligned, $\varpi_o = v_s k_o \Theta_o$, and having a half-width at half-height

---

* Chapter 4, Section B.2.

$$\frac{"\gamma"}{2\pi} = \frac{(0.693)^{\frac{1}{2}}}{2\pi} \sqrt{\frac{\pi v_s^2}{L_y^2} + \frac{v_s^2 k_o^2 D^2}{8n^4 R_H^2}} \qquad (5\text{-}22)$$

This effective half-width is made up of two contributions: (1) an "intrinsic" broadening γ_1 due to the K vector uncertainty effect discussed above

$$(\gamma_1)^2 = \frac{(0.693)\pi v_s^2}{L_y^2} \qquad (5\text{-}23)$$

and an instrumental width γ_2 due to the finite acceptance angle of the optical system

$$(\gamma_2)^2 = \frac{(0.693)v_s^2 k_o^2 D^2}{8n^4 R_H^2} \qquad (5\text{-}24)$$

The instrumental width factor can be written in a more transparent form as follows. From Fig. 4-15 the ratio (D/R_H) is simply the apparent full opening angle of the local oscillator beam as seen "outside" the negative lens L_1

$$\frac{D}{R_H} = 2\overline{\Delta\Theta}'_{LO} \qquad (5\text{-}25)$$

Equation (4-34) relates the $\overline{\Delta\Theta}'_{LO}$ to the real opening angle of the laser beam as

$$2\overline{\Delta\Theta}'_{LO} \simeq 4\overline{\Delta\Theta}_{LO} = 2(D_s'/r_s) \qquad (5\text{-}26)$$

where D_s' is the spot diameter on the spherical resonator mirror and r_s is the radius of curvature of this mirror. Using Eq. (5-26) and the relation $\bar{\omega}_o = v_s k_o \Theta_o$ we have

$$\gamma_2 = (1.386)^{\frac{1}{2}}\, \bar{\omega}_o \left(\frac{\overline{\Delta\Theta}_{LO}}{\Theta_o}\right) \frac{1}{n^2} \tag{5-27}$$

This expression confirms the expected intuitive result that γ_2 must be some fraction α of the frequency shift, $\bar{\omega}_o$, where α is determined by the ratio of the acceptance angle to the scattering angle. Furthermore, the acceptance angle is fixed completely by the opening angle of the local oscillator beam.

With the help of the quantities

$$\begin{aligned} (\bar{\omega}_o/2\pi) &= 30.0 \text{ Mc/sec} \\ \Theta_o &= 0.00954 \text{ radians} \\ 2\overline{\Delta\Theta}_{LO} &= (D_s'/r_s) = 0.00267 \text{ radians} \\ n &\simeq 1.5 \end{aligned} \tag{5-28}$$

we compute the numerical result

$$(\gamma_2/2\pi) = 2.2 \text{ Mc/sec} \tag{5-29}$$

It follows that $S_i(\omega)$ has an effective half-width at half-height given by

$$\frac{"\gamma"}{2\pi} = \sqrt{\left(\frac{\gamma_1}{2\pi}\right)^2 + \left(\frac{\gamma_2}{2\pi}\right)^2} = 2.25 \text{ Mc/sec} \tag{5-30}$$

d. The Observed Half-Width

The spectrometer output which is recorded as a function of the tuned filter frequency ω_f is the convolution of the photocurrent power spectral density $S_i(\omega)$ with the system function of the filter $|H(\omega)|^2$. In the present case then, the observed output should be the folding of a Gaussian and a Lorentzian having half-widths at half-heights of 2.25 Mc/sec and 1.17 Mc/sec respectively. The required convolution, which gives rise to the so-called Voigt function, cannot be carried out in analytical form; however, Rautian[4] has presented numerical data on the width of the resulting spectrum from which we find

$$2(\gamma_{\text{recorded}}/2\pi) = 5.9 \text{ Mc/sec} \tag{5-31}$$

Figure 5-4 shows a typical spectrum obtained at $(\varpi_o/2\pi) \simeq 30$ Mc/sec including correction for rolloff in the response of the signal processing amplifiers. The measured full-width at half-height is

$$2(\gamma_{\text{measured}}/2\pi) = 4.45 \text{ Mc/sec} \tag{5-32}$$

The discrepancy between this result and the predicted value of 5.9 Mc/sec indicates a probable overestimate of the spot diameter D_s' and hence of the laser opening angle $\overline{\Delta\Theta}_{LO}$. The theoretical and measured widths could be brought into agreement by a 30% reduction in D_s'.

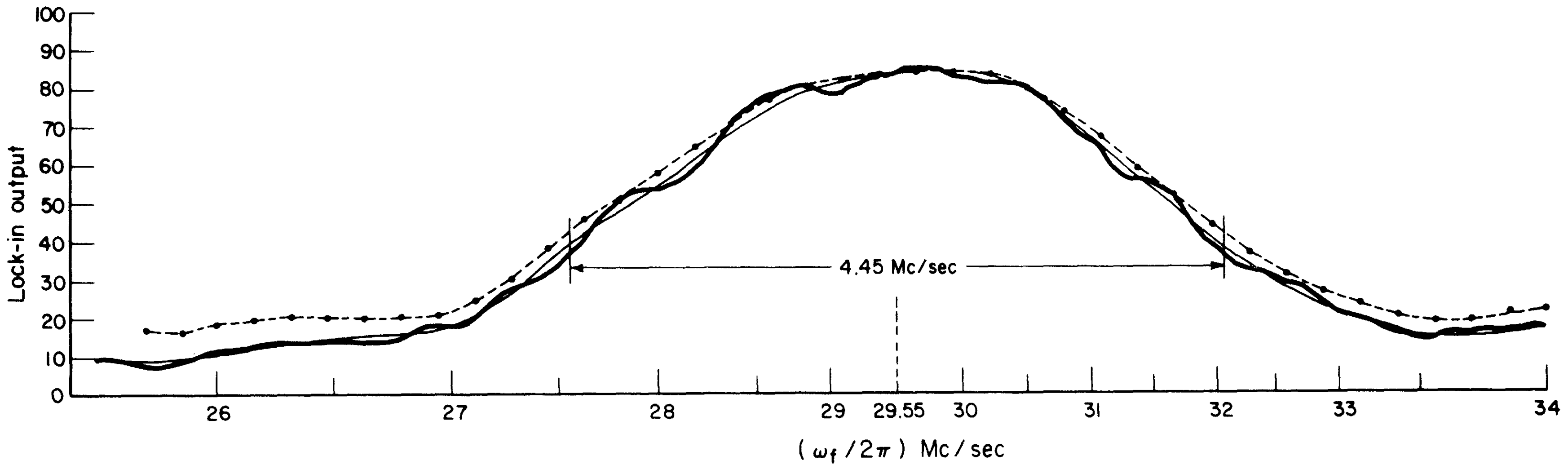

Figure 5-4 Data trace showing the natural width of the photocurrent spectrum for the beat note between the laser local oscillator and the Brillouin components of the light scattered from toluene at $\theta = 0.547^{\circ}$. The major contributions to the natural width are, (1) the instrumental profile of the heterodyne spectrometer and, (2) the finite acceptance angle of the optical system.

3. The Signal-to-Noise Ratios

The theoretical pre- and post-detection signal-to-noise ratios are most easily obtained by calculating the scattered power per coherence area available at the detector and then using the (S/N) curves presented in Fig. 3-19. From Eqs. (2-55) and (2-166) we have

$$\mathcal{P}_{COH} = 2\mathcal{P}_o \mathbf{R}_p L_z (\sin^2 \phi) \Omega_{COH}$$

where

$$\Omega_{COH} = 4\overline{\Delta\Theta}\cdot\overline{\Delta\Psi} = \frac{\lambda^2}{L_x[L_z \sin\Theta + L_y \cos\Theta]}$$

$\mathcal{P}_o$ - the power incident on the scattering volume

$\mathbf{R}_p$ - the pressure fluctuation contribution to the Rayleigh ratio

ϕ - the angle between the polarization vector of the incident field and the direction of observation

L_x, L_y, L_z - the dimensions of the illuminated volume as in Eq. (4-23)

For $\Theta = 0.547°$ we find from Fig. 4-25

$$\begin{aligned} \overline{\Delta\Theta} &= 3.95 \times 10^{-4} \text{ radians} \\ \overline{\Delta\Theta}' &= 8.95 \times 10^{-4} \text{ radians} \\ \overline{\Delta\Psi} &= 1.12 \times 10^{-3} \text{ radians} \\ \overline{\Delta\Psi}' &= 1.685 \times 10^{-3} \text{ radians} \end{aligned} \qquad (5\text{-}33)$$

the primed and unprimed quantities corresponding to values of the coherence angles as measured inside and outside the cell respectively. A comparison of these results to the "external" half-opening angles of the laser source

$$\overline{\Delta\Theta}'_{LO} = \overline{\Delta\Psi}'_{LO} = 2.67 \times 10^{-3} \text{ radians} \tag{5-34}$$

indicates that the spectrometer accepts light from approximately five coherence areas in the scattered signal beam.

For toluene, Fabelinskii[5] quotes the value of $\mathbf{R}_P$ at $\lambda_{air} = 4358$ Å as $\mathbf{R}_P = 9.66 \times 10^{-6}$ /cm. Scaling this result to $\lambda_{air} = 6328$ Å assuming an ω_o^4 dependence gives

$$\mathbf{R}_P = 2.18 \times 10^{-6} \text{ /cm } (6328\text{Å}) \tag{5-35}$$

It is worthwhile to point out that $\mathbf{R}_P$ represents the fraction of the incident power scattered into both Brillouin-Mandel'shtam components. In the present spectrometer, where the local oscillator frequency is the frequency of the incident light $\omega_{LO} = \omega_o$, the signal portion of the photocurrent spectrum results from simultaneous mixing between the local oscillator and both the up and down shifted components of the doublet. Therefore $\mathbf{R}_P$ is, in fact, the appropriate measure of the scattering cross section.

In estimating the factor $\sin^2 \phi$ we may note from Fig. 4-16 that the polarization vector of the laser beam lies in the plane of scattering; it follows that ϕ can be expressed in terms of the scattering angle Θ as $\phi = [(\pi/2) - \Theta]$. In the range $\Theta \leq 3°$, then, we have $\sin^2 \phi = 1$ to excellent approximation. In this case taking

$$\begin{aligned} P_o &= 100 \text{ milliwatts} \\ L_z &= 2.54 \text{ cm} \\ L_x &= 0.019 \text{ cm} \\ L_y &= 0.028 \text{ cm} \end{aligned} \tag{5-36}$$

yields immediately

$$P_{COH} = 2.05 \times 10^{-12} \text{ watts} \tag{5-37}$$

Before being plotted on Fig. 3-19, P_{COH} must be adjusted for the following factors:

(1) Transmission and reflection in the light collection system. Equation (4-36) gives the detected signal power as $P_S = 0.38\ P_{scattered}$.

(2) The difference between the actual photodetector quantum efficiency $\varepsilon = 0.10$ given in Eq. (4-49) and the value $\varepsilon = 0.05$ for which Fig. 3-19 was constructed.

(3) The heterodyning efficiency factor estimated in Eq. (4-37) as $[B_{COH}] \leq (0.3)$.

(4) The pre-detection signal-to-noise ratio degradation factor $(1 + F)$ whose experimentally measured value is given in Eq. (4-51) as $(1 + F) = (2.66)$.

The combination of these effects yields the power to be plotted as

$$P_{PLOT} = (0.38)\left[\frac{\varepsilon}{0.05}\right] \frac{[B_{COH}]}{1 + F} P_{COH} = 1.75 \times 10^{-13} \text{ watts} \tag{5-38}$$

Combining this result with the effective half-width of $(\text{"}\gamma\text{"}/2\ ) = 2.25$ Mc/sec yields from Fig. 3-19

$$(S/N)^*_{PRE} \simeq 2.0 \times 10^{-3}$$

$$(S/N)^2_{OUT} \simeq 2.0 \left[\begin{array}{l} \tau = 1.0 \text{ sec} \\ a = (\Delta\omega_f/\gamma) = 0.1 \end{array}\right. \tag{5-39}$$

When $(S/N)^2_{OUT}$ is corrected[§] for the increased values of the fractional resolution $a = (\Delta\omega_f/\gamma)$ and of the final filter time constant τ with which Figs. 5-1 and 5-2 were obtained we find

$$(S/N)^2_{OUT} \simeq 200 \left[\begin{array}{l} \tau = 10 \text{ sec} \\ a = (\Delta\omega_f/\gamma) \simeq 1.0 \end{array}\right.$$

$$(S/N)_{OUT} \simeq 14 \tag{5-40}$$

An attempt to determine the experimental value of $(S/N)^*_{PRE}$ by observing the change in dc detector output[†] as the signal path of the spectrometer was alternately opened and blocked produced a null result. The sensitivity of this measurement placed an upper limit on $(S/N)^*_{PRE}$ of

$$(S/N)^*_{PRE}\Big|_{\text{exptl.}} < 0.01 \tag{5-41}$$

which is consistent with the expected value

$$(S/N)^*_{PRE} = 2 \times 10^{-3} \ .$$

[§] Chapter 3, Section E.4.

[†] Chapter 4, Section D.3.e.

From Fig. 5-1 we may estimate the measured output signal-to-noise ratio as

$$(S/N)_{OUT}\Big|_{\text{exptl.}} \simeq 15 \tag{5-42}$$

in excellent agreement with the theoretically predicted value.

C. The Central (Rayleigh) Component

The thermodynamic calculations of Chapter 2 Section D yielded the predicted spectrum of the central component as a Lorentzian centered at the incident light frequency ω_o and having a half-width at half-height Γ given by

$$\Gamma = (\Lambda/\rho c_p)K^2, \tag{2-82}$$

where

$$K = 2k_o \sin(\Theta/2) \tag{2-31}$$

is the wave vector of the entropy fluctuation responsible for the observed scattering. The results presented here are sufficient to test all three basic predictions of this theory: (1) the Lorentzian line shape, (2) the K^2 dependence of the line width, and (3) the quantitative relation between Γ, K, and the thermal diffusivity. The experimental data available to test the theory are confined to scattering angles in the range $(0.3° \le \Theta < 2.8°)$ where the small line widths 75 cps $\le (\Gamma/2\pi) \lesssim$ 7500 cps lead to a scattered power per coherence area per unit spectral interval which is within the detection capabilities of the superheterodyne spectrometer.

The central component spectra also yielded important quantitative measurements of both the pre-detection and post-detection signal-to-noise ratios over a rather wide dynamic range of the ratio ($\mathcal{P}_{COH}/\Gamma$). This information is used to confront theoretically predicted values of $(S/N)_{PRE}$ and $(S/N)_{OUT}$ which are calculated from (1) the known scattering coefficient for toluene[5], (2) the coherence solid angle[§], (3) the heterodyning efficiency factor of the spectrometer[†], and (4) the signal-to-noise theory presented in Chapter 3.

1. The Line Shape

The observed central component line shape was in all cases found to be Lorentzian within an experimental accuracy limited only by the output signal-to-noise ratio. Figures 5-5, 5-6, and 5-7 illustrate typical spectra obtained at $\Theta \simeq 0.31°$, $\Theta \simeq 1.72°$, and $\Theta \simeq 2.8°$ respectively. In each case the dashed curves correspond to the actual spectrometer output after corrections are made for local oscillator power drift[*] and the non-uniform frequency response[*] of the electronic detection system. This correction is negligible in Fig. 5-5 where the pre-detection signal-to-noise ratio is high,[*] while in Fig. 5-7 it approaches 10% of the peak signal amplitude, $I_S{}^2(0)$.

The heavy triangles superimposed on each trace are the results of a least-squares fit of the corrected curve to a Lorentzian heterodyne signal spectrum $I_S{}^2(\omega)$ plus a constant frequency independent shot-noise level $I_N{}^2(\omega)$.

[§] Chapter 2, Section E.

[†] Chapter 4, Sections E.2.b and E.2.c.

[*] Chapter 4, Section E.5.

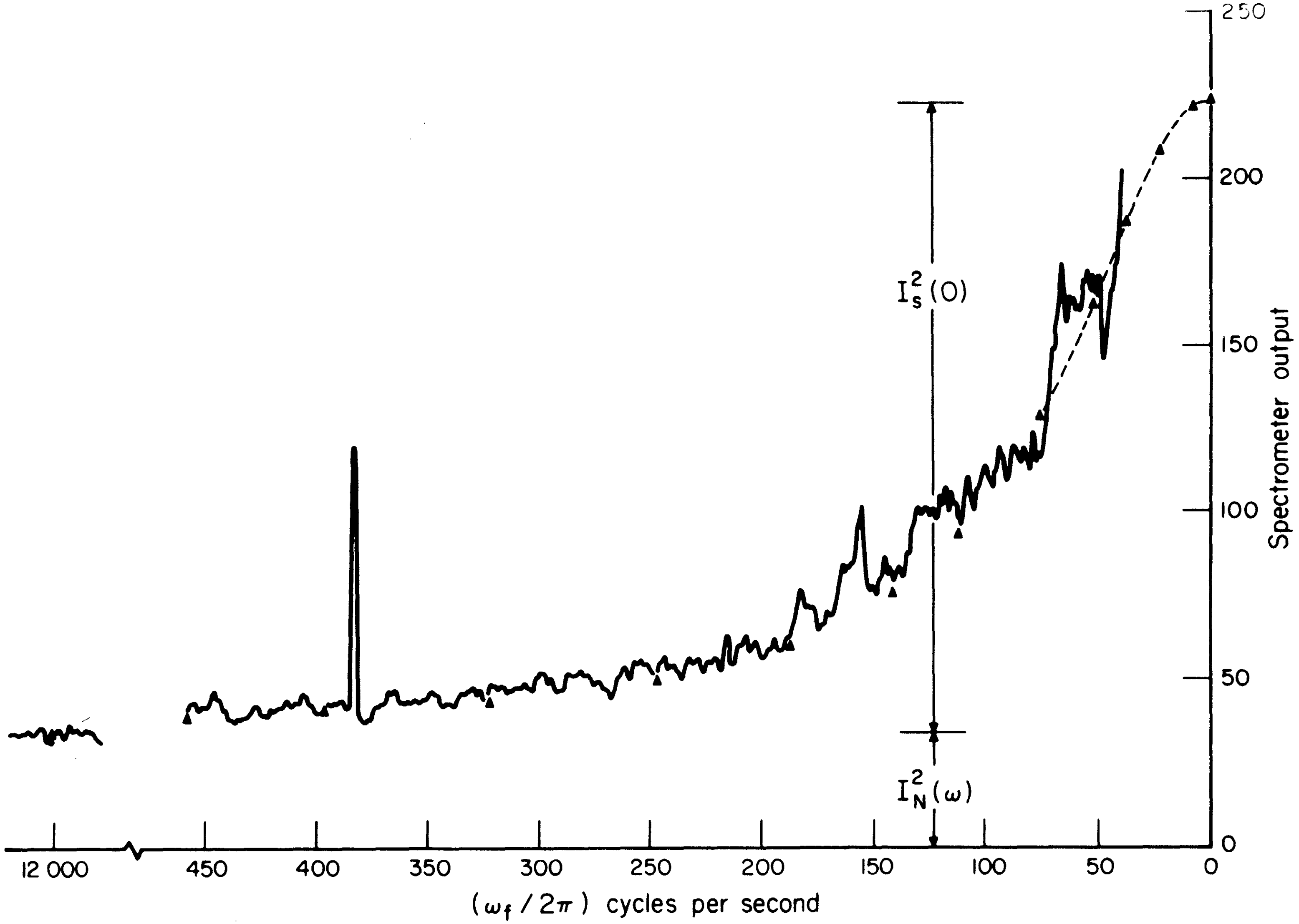

Figure 5-5 A typical central component spectrum obtained at $\Theta \simeq 0.31^\circ$. The measured line width of this trace is $(\Gamma/2\pi) = (75 \pm 5)$ cps. The large spike at $(\omega_f/2\pi) \simeq 380$ cps is due to a momentary failure of the laser mode locking control system.

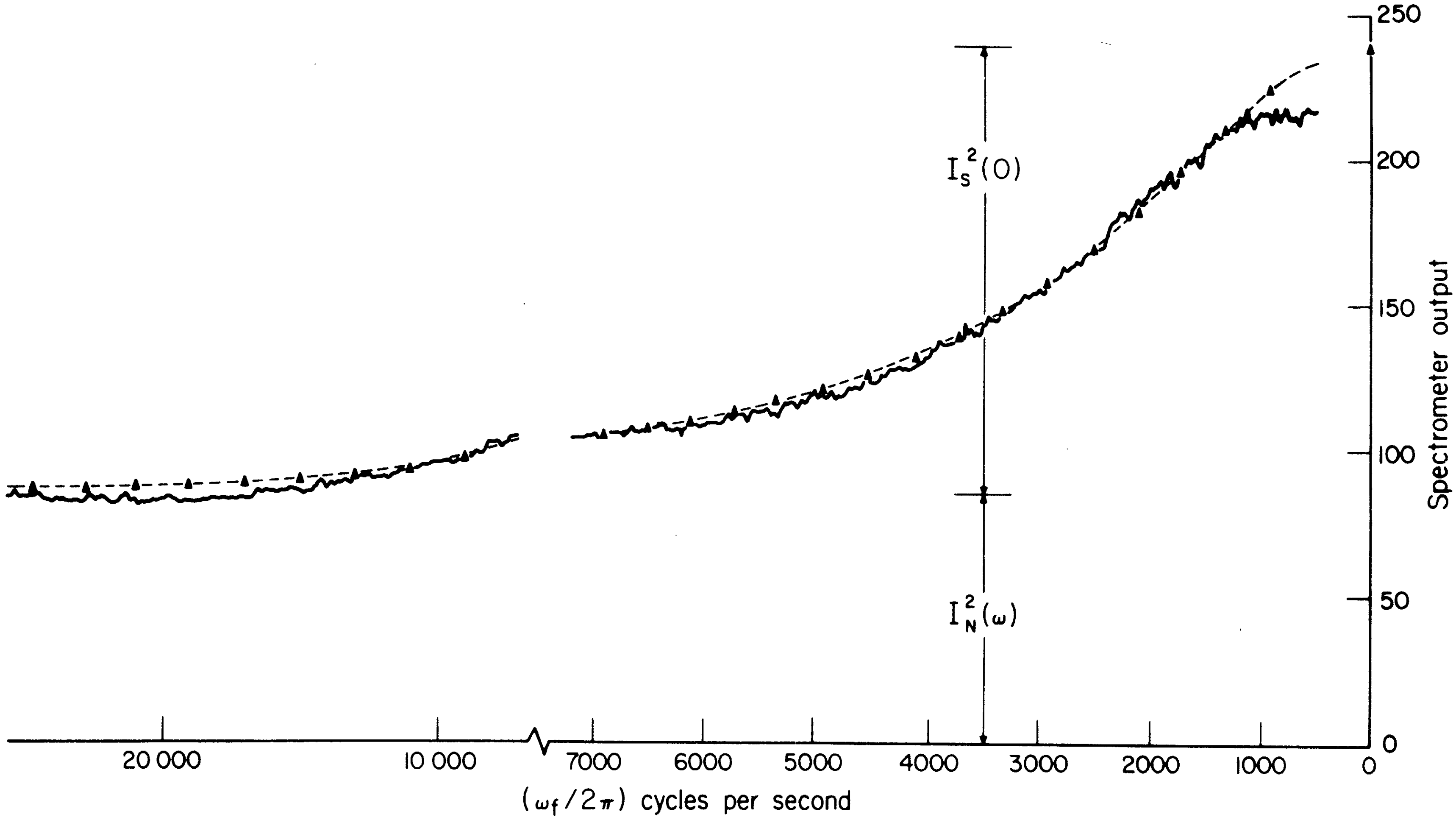

Figure 5-6 A typical central component spectrum obtained at $\theta \approx 1.72^\circ$. The measured line width of this trace is $(\Gamma/2\pi) = (2725 \pm 30)$ cps. The spectrum was plotted out using a post-detection time constant of 7 seconds and required approximately 1.5 hours to record.

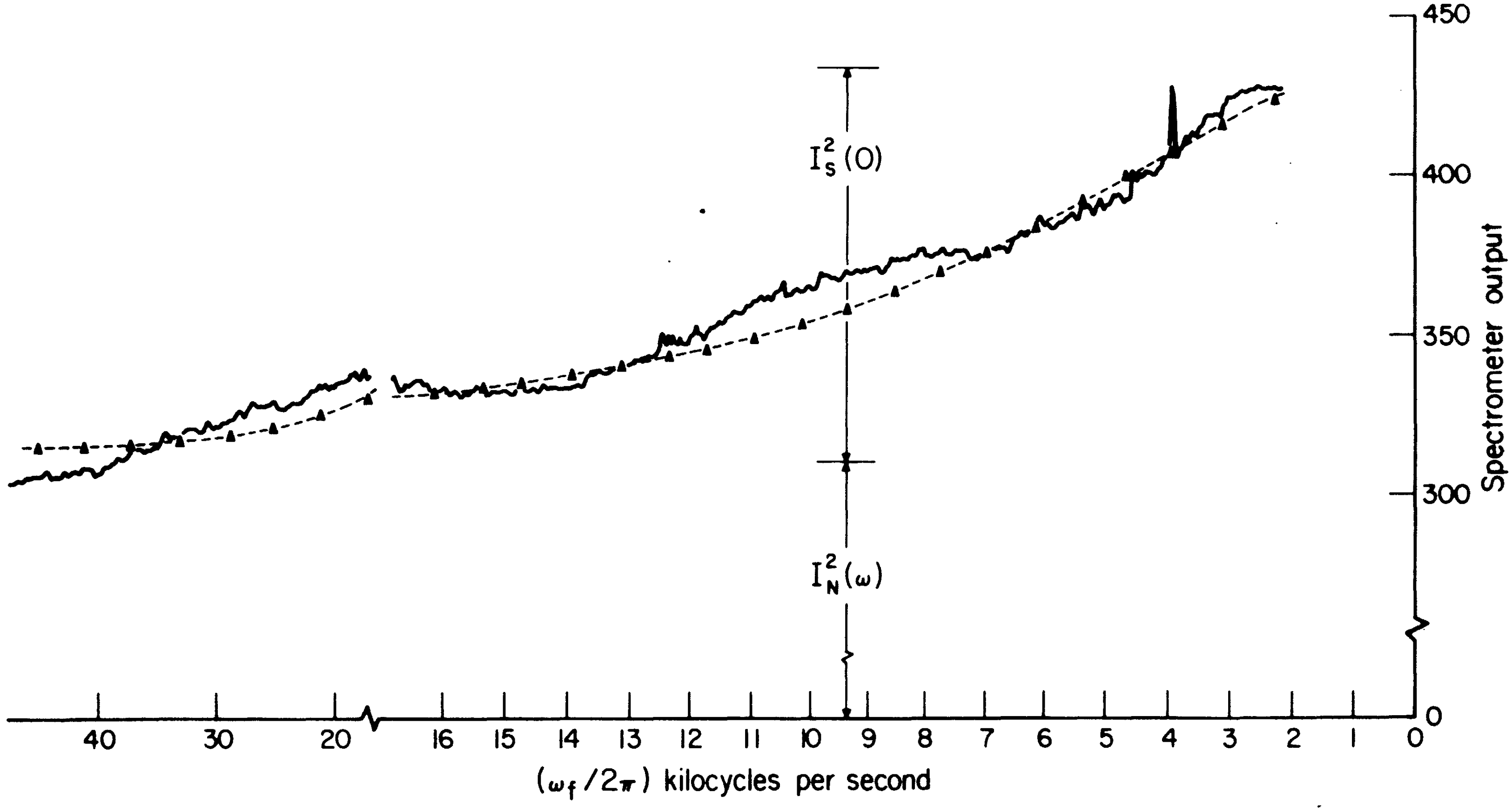

Figure 5-7 A typical central component spectrum obtained at $\Theta \simeq 2.8^{\circ}$. The dotted curve represents the data trace after correction to constant local oscillator power and uniform filter (ω_f) response. The measured half-width was $(\Gamma/2\pi) = (7240 \pm 100)$ cps.

This least-squares analysis procedure involved curve fitting to the corrected trace at approximately fifty values of $(\omega_f/2\pi)$ between zero and ten times the half-width of the beat note spectrum. As indicated by Figs. 5-5, 5-6, and 5-7, the fits obtained by this technique generally fell well within the noise present on the spectrometer output.

An estimate of the quantitative accuracy with which the observed spectra can be assigned a Lorentzian line shape is obtained as follows. The amplitude differences between the corrected data and the "best fit" Lorentzian are measured at the values of $(\omega_f/2\pi)$ used in the least-squares analysis, are squared, and then summed. The square-root of this result divided by the number of points measures the root-mean-square amplitude uncertainty of the fit. Figure 5-8 shows a plot of this uncertainty as a function of the observed half-width of the signal spectrum; the calculated rms deviation is presented as a percentage of the peak signal amplitude $I_S^2(0)$. As is evident from a comparison of Figs. 5-5 and 5-7, the increase in line shape uncertainty for small half-widths reflects a decrease in the output signal-to-noise ratio.

2. The Line Width

The natural line width of the central component was measured for entropy fluctuations whose wave vector fell in the range

$$795 \text{ cm}^{-1} \leq K \leq 7333 \text{ cm}^{-1} \tag{5-43}$$

The corresponding limits on the wavelength of the scattering fluctuations $\lambda_f = (2\pi/K)$ are

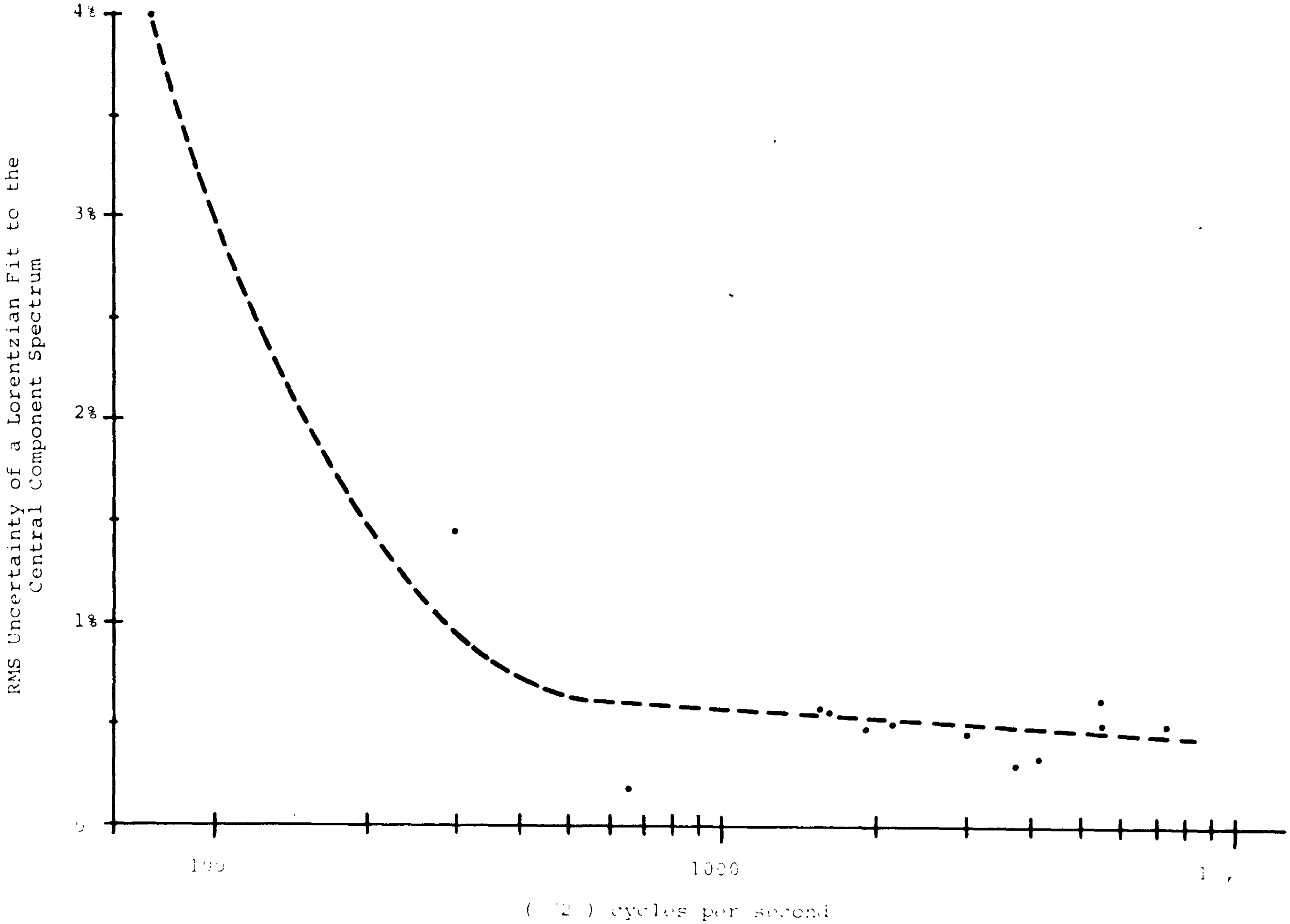

Figure 5-8 The rms uncertainty of a Lorentzian fit to the central component spectrum.

$$0.008 \text{ cm} \geq \lambda_f \geq 0.00085 \text{ cm} \qquad (5\text{-}44)$$

respectively. Since the sound wave injection technique used to align the spectrometer[*] fixes the value of K, rather than the scattering angle, the desired experimental relationship between Γ and K is obtained directly without a knowledge of the scattering angle, the index of refraction of the scattering medium, or its temperature dependence. However, the approximate range in scattering angle can be calculated from Eqs. (2-31) and (5-43) as

$$0.31° \leq \Theta \leq 2.83° \qquad (5\text{-}45)$$

In order to check the predicted K^2 dependence of the half-width and obtain an experimental determination of the thermal diffusivity, $(\Lambda/\rho c_p)$, the measured half-widths were corrected to T = 20.0°C by the following method. For fixed K, Eq. (2-82) relates the half-widths measured at the temperatures T_1 and T_2 as

$$\Gamma(T_2) = C(T_2,T_1)\Gamma(T_1) \qquad (5\text{-}46)$$

where

$$C(T_2,T_1) = \frac{\Lambda(T_2)}{\Lambda(T_1)} \cdot \frac{\rho(T_1)}{\rho(T_2)} \cdot \frac{c_p(T_1)}{c_p(T_2)} \qquad (5\text{-}47)$$

The correction factor $C(20.0°C, T_1)$ was calculated for toluene using the known temperature dependences of the statically measured thermal conductivity and specific heat at constant pressure. Over the temperature range involved here ($20.0°C \leq T_1 \leq 24.0°C$) the change in density was negligible. The largest required correction factor C(20°C, 24°C) yielded a 1.6% increase in the observed half-width.

---

[*] Chapter 4, Section D.2.

Table VI and Fig. 5-9 present the line width data after reduction to T = 20.0°C. The quoted error limits on each half-width measurement represent that range of $(\Gamma/2\pi)$ over which the least-squares "Lorentzian" analysis of the data trace produced a fit that remained within the noise on the recorded spectrum.

Figure 5-9 shows that the observed half-width at half-height $(\Gamma/2\pi)$ is linearly proportional to K^2 over the entire range of K to within the accuracy of the measurements. As discussed in Section C.3, this result indicates that the simple heat flow equation with wavelength independent thermal conductivity and specific heat correctly describes the damping of entropy fluctuations in toluene over the range $0.001 \text{ cm} < \lambda_f < 0.01 \text{ cm}$. An extension of the data to even smaller values of λ_f and, consequently, larger half-widths has been made by Greytak[8] using a single frequency helium-neon laser and an ultra-high resolution spherical Fabry-Pérot interferometer. At $\Theta = 173^\circ$

$$K = 2.94 \times 10^5 \text{ cm}^{-1}$$

he finds $(\Gamma/2\pi) = (10.5 \pm 2)$ Mc/sec. A K^2 extrapolation of the present small-K results to this value of K yields a half-width of $(\Gamma/2\pi) = (12.0 \pm 0.35)$ Mc/sec. This result suggests that the simple heat flow approach is valid in toluene for entropy fluctuations whose wavelength is as small as $\lambda_f = 2.1 \times 10^{-5}$ cm.

The slope of the best straight line fit to the data, as shown on Fig. 5-9, gives $(1/2\pi)(\Lambda/\rho c_p) = (1.38 \pm 0.04) \times 10^{-4}$

Table VI EXPERIMENTAL RESULTS FOR THE CENTRAL COMPONENT LINE WIDTH

#	K - cm^{-1}	$\frac{\Gamma}{2\pi}(20^\circ C)$ - cps	#	K - cm^{-1}	$\frac{\Gamma}{2\pi}(20^\circ C)$ - cps
1	794.5	75 ± 10	24	4272	2415 ± 100
2	795.4	75 ± 5	25	4283	2545 ± 50
3	1420	250 ± 10	26	4303	2578 ± 50
4	1496	275 ± 15	27	4442	2763 ± 30
5	1498	300 ± 25	28	4610	3030 ± 75
6	2205	650 ± 15	29	4767	3245 ± 100
7	2225.4	700 ± 20	30	4880	3397 ± 100
8	2306.5	700 ± 20	31	4880	3363 ± 100
9	2382	750 ± 15	32	4995	3421 ± 75
10	2385	725 ± 15	33	5120	3623 ± 80
11	2589	925 ± 25	34	5155	3800 ± 200
12	2599	875 ± 15	35	5295	3900 ± 200
13	2998	1185 ± 25	36	5295	3800 ± 100
14	2145	1387 ± 25	37	5320	3850 ± 100
15	3326	1550 ± 50	38	5466	4097 ± 100
16	3331	1513 ± 25	39	5470	4160 ± 50
17	3515	1636 ± 50	40	6060	5400 ± 100
18	3615	1785 ± 50	41	6205	5400 ± 200
19	3817	1917 ± 50	42	6323	5560 ± 200
20	3997	2170 ± 50	43	6466	5944 ± 100
21	4098	2270 ± 25	44	7333	7750 ± 100
22	4190	2522 ± 50	45	7333	7360 ± 100
23	4190	2396 ± 50			

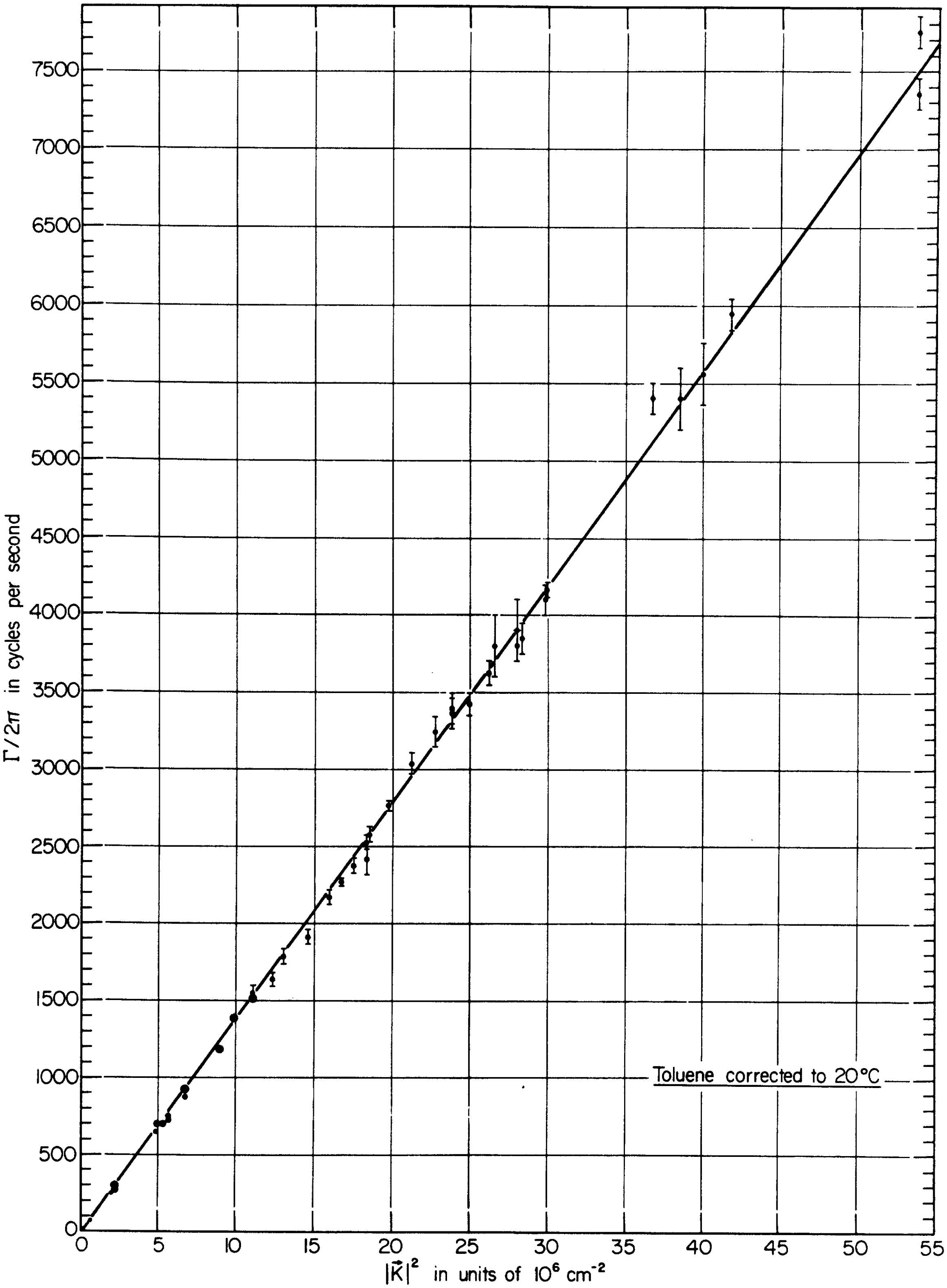

Figure 5-9 Experimental results on the central component line width versus K^2.

cm^2/sec. Including a systematic 2% uncertainty in the determination of K^2 traceable to the quoted error in the velocity of the sound waves used to align the spectrometer and to the alignment procedure itself, we find

$$(1/2\pi)(\Lambda/\rho c_P)_{\text{experimental}} = (1.38 \pm 0.05) \times 10^{-4}\ \text{cm}^2/\text{sec} \tag{5-48}$$

Conventional macroscopic thermodynamic (K = 0) measurements of Λ, ρ, and c_P yield

$$\rho = 0.8669\ \text{g/cc}\ ^{6}$$

$$c_P = (1.6725 \pm 0.016)\text{J/g}\ ^{7} \tag{5-49}$$

$$\Lambda = (1.38 \pm 0.07)\ \text{mW/cm}\ ^\circ\text{C}\ ^{6}$$

from which we can compute the static result

$$(1/2\pi)(\Lambda/\rho c_P)_{\text{static}} = (1.52 \pm 0.09) \times 10^{-4}\ \text{cm}^2/\text{sec} \tag{5-50}$$

The good agreement between Eqs. (5-48) and (5-50) indicates that the thermodynamic heat flow theory quantitatively describes the damping of spontaneous entropy fluctuations in toluene.

3. Discussion of the Results

The central component line shape and line width data confirm the two basic features of the simple thermodynamic treatment of entropy fluctuations; (1) the exponentially damped time behavior which results in a Lorentzian spectrum and (2) the proportionality between the damping rate and the spatial derivative of the entropy gradient, which gives the observed linear dependence of the half-width on K^2. The significance of the present results in relation to this theory and their bearing on the properties of the scattering medium are most easily discussed by examining the restrictions under which the theory is expected to be valid.

The line shape data shows that in toluene the damping of an entropy fluctuation that arises at time $t = 0$ is accurately exponential for times in the range

$$10^{-4} \text{ sec} \leq t \leq \infty \text{ sec} \tag{5-5}$$

However, since the thermodynamic approach assumes that entropy fluctuations occur quasi-statically compared to the equilibration time of the system, t_c, we expect deviations will occur from exponential damping for times that fall in the range $0 < t < t_c$. Equivalently, the central component spectrum should exhibit a non-Lorentzian behavior for frequencies greater than the critical frequency $\omega_c = (1/t_c)$.

Since the generation or decay of an entropy fluctuation is accompanied by a local change in the temperature of the medium, the appropriate equilibration time is the minimum duration necessary to re-establish an equilibrium Boltzmann population of the energy levels of the system. It follows that t_c is fixed by the slowest energy exchange processes in the liquid. For a relatively complicated structure like toluene, these "slow" processes may correspond, for example, to energy transfer between the translational degrees of freedom of the molecule and its internal vibrational, rotational, or structural states.[9]

The study of low frequency ($\leq 10^9$ cps) energy exchange processes in liquids has been pursued extensively using sound wave absorption and velocity measurements[9] and, more recently, using light scattering results based on measurements of the splitting and natural width of the Brillouin-Mandel'shtam components.[10,11,12,13] Typical equilibration or relaxation times have been found throughout the entire experimental range from $t_c \simeq 10^{-5}$ sec to $t_c \simeq 10^{-10}$ sec. For the purpose of describing the behavior of the sound wave absorption and velocity measurements at frequencies near $\omega_c = (1/t_c)$ it is customary to purely formally retain the thermodynamically derived equations of motion by allowing the parameters of the medium, such as its compressibility, specific heat, and viscosity, to become frequency dependent.

The same approach can be adopted in describing the line shape of the central component by formally rewriting the power spectral density of an entropy fluctuation with wave vector K as

$$S_{\text{entropy}}(\omega,K) = \left[\frac{\underline{k}\rho c_p(\omega)}{V}\right] \frac{(2/\pi)\Gamma(\omega)}{\omega^2 + \Gamma^2(\omega)} \qquad (5\text{-}51)$$

where

$$\Gamma(\omega) = [\Lambda/\rho c_p(\omega)]K^2 \qquad (5\text{-}52)$$

The thermal conductivity can normally be assumed to be frequency independent.[14]

An appropriate form for $c_p(\omega)$ can be derived as follows. Since a system will ordinarily approach equilibrium exponentially in time, the frequency dependent components of a particular thermodynamic parameter will in general take the form of a Lorentzian. For example, we may write the specific heat at constant pressure, c_p as

$$c_p(\omega) = c_p^{\infty} + \frac{c_p^{i}}{1 + \omega^2 t_c^{2}} \qquad (5\text{-}53)$$

where t_c is the relaxation time of an internal degree of freedom having a specific heat c_p^{i} and c_p^{∞} is the specific heat at frequencies much larger than $\omega_c = (1/t_c)$. By Fourier transforming Eq. (5-53) we can also give c_p in a form that explicitly displays the time behavior of the equilibration process, namely

$$c_p(t) = \sqrt{2\pi}\, c_p^{\infty}\delta(t) + \frac{1}{2}\sqrt{\frac{\pi}{2}}\, \frac{c_p^{i}}{t_c}\, e^{-t/t_c} \qquad (5\text{-}54)$$

Equation (5-54) may be interpreted as follows: a sudden change in the temperature of the medium at time $t = 0$ results in (1) an instantaneous heat flow into those energy levels of the system that equilibrate "infinitely" rapidly $[c_p^{\infty}]$, and (2) in a delayed heat flow into the level $[c_p^{i}]$. The existence of a molecular or structural energy level having an equilibration time t_c gives $c_p(t)$ a non-local dependence on time; the rate of heat transfer in such a system depends on its past history over the duration $t \approx t_c$.

From Eqs. (5-51), (5-52), and (5-53) and from the toluene line shape data we may conclude that if any toluene molecular or structural energy levels have $t_c > 10^{-4}$ sec, then they must contribute only a small fraction ∿2% of the zero frequency (thermodynamic) specific heat

$$c_p(\omega{=}0) = c_p^{\infty} + c_p^{i} .$$

It appears that the line shape of the central component will provide an accurate and powerful tool for examining "thermal" relaxations at very low frequencies < 10 kc/sec where the ultrasonic technique becomes impossibly difficult.

The central line width behavior in toluene versus the scattering wave vector K shows that the linear relationship predicted by the heat flow equation between the damping rate of an entropy fluctuation and the spatial derivative of the entropy gradient is valid in toluene at room temperature and atmospheric pressure for entropy fluctuations whose wavelengths fall in the range $(2 \times 10^{-5}\ \text{cm} \leq \lambda_f \leq \infty)$. However, the validity of the thermodynamic theory must break down at sufficiently small wavelengths. This fact may be predicted qualitatively as follows. Consider the explicit form of the heat flow differential equation for the thermodynamic entropy $\bar{s}$

$$\frac{\Lambda}{\rho c_p} \nabla^2 \bar{s}(\vec{r},t) = \frac{\partial \bar{s}(\vec{r},t)}{\partial t} \tag{2-71}$$

and its complete Fourier transform

$$\frac{\Lambda}{\rho c_p} K^2 \underline{\bar{s}}(\vec{K},\omega) = i\omega \underline{\bar{s}}(\vec{K},\omega) \tag{5-55}$$

The transform $\underline{\bar{s}}(\vec{K},\omega)$ is given by

$$\underline{\bar{s}}(\vec{K},\omega) = \frac{1}{(2\pi)^2} \int_r \int_t \bar{s}(\vec{r},t)\, e^{i(\vec{K}\cdot\vec{r} - \omega t)}\, d^3\vec{r}\, dt \tag{5-56}$$

If Λ and c_P are *constants* then Eq. (2-71) shows that the heat flow approach is a *completely local* theory; the damping of an entropy fluctuation at $(\vec{r},t)$ is controlled by the properties of the medium at position and time coordinates that differ only *infinitesimally* from $(\vec{r},t)$. As we saw above, the assumption of a local time dependence must break down for times small compared to some characteristic time for energy transfer in the system. Similarly, the assumption of a local space dependence must fail for distances which are comparable to the distances over which the molecular motions exhibit strong correlation.

That is, we may expect[15,16] a deviation from the K^2 behavior of the half-width when the wavelength of the fluctuation $\lambda_f = (2\pi/K)$ approaches the range of the molecular pair-correlation function. This range is determined by the strength and range of the intermolecular potential; for normal liquids it usually does not exceed a few molecular diameters.[17,18]

The problem of calculating the effect of a non-zero correlation range on the K dependence of the central component half-width has received considerable attention recently. In particular, Fixman[16] and Felderhof[15] have considered the departure from K^2 behavior as one approaches the liquid-gas critical point where the pair-correlation function range is known to diverge.

In order to maintain the equilibrium thermodynamics equation of motion given in Eq. (5-55) we may express their results in a purely formal way by allowing the specific heat c_P to become *wave vector dependent*. Felderhof finds the first order result

$$c_P(K) = \frac{c_P(K=0)}{1 + K^2 r^2} \qquad (5\text{-}57)$$

where r is the range of the pair correlation function. The fact that Eq. (5-57) actually introduces a non-local spatial dependence into the equations of motion can be displayed explicitly by taking the Fourier spatial transform of $c_p(K)$, namely

$$c_p(\vec{r}) = \frac{1}{(2\pi)^{\frac{3}{2}}} \int_K c_p(\vec{K})\, e^{-i\vec{K}\cdot\vec{r}}\, d^3\vec{K}$$

from which we find

$$c_p(\vec{r}) = \sqrt{\frac{\pi}{2}}\, \frac{1}{r^2}\cdot \frac{c_p(K=0)}{|\vec{r}|}\, e^{-|\vec{r}|/r} \tag{5-58}$$

It follows that a heat pulse applied at the point $\vec{r} = 0$ in the medium will produce an increase in temperature throughout a sphere of radius r surrounding that point.

Equation (5-57) predicts an increase in half-width over the extrapolated K^2 value for wave vectors approaching the inverse of the correlation distance r. For toluene at room temperature and atmospheric pressure r can be estimated from x-ray scattering data as $r \simeq 6$ Å.[17,18] Therefore, the accurate K^2 dependence of the observed central component half-width in toluene for entropy fluctuations with inverse wave vectors as small as $(1/K) \simeq 3.4 \times 10^{-6}$ cm = 340 Å is consistent with the known pair-correlation range in this liquid.

In general c_p may be regarded as being both wave vector and frequency dependent, namely

$$c_p(K,\omega) = \frac{c_p(0,\infty)}{1 + K^2 r^2} + \frac{c_p{}^i(0,0)}{(1 + K^2 r^2)(1 + \omega^2 t_c{}^2)} \tag{5-59}$$

Therefore, in favorable cases the central component spectrum can yield information on two independent properties of the molecular system; (1) the characteristic rate of slow energy transfer processes, and (2) the range of the pair-correlation function.

4. The Observed Signal-to-Noise Ratios

The equations given below summarize the results obtained in Chapters 2 and 3 from which we can compute the expected pre- and post-detection signal-to-noise ratios for superheterodyne detection of the central component.

$$(S/N)_{PRE} = (2)2\left(\frac{\varepsilon}{\hbar\omega_o}\right)\frac{\mathcal{P}_{COH}}{\Gamma}\,[B_{COH}] \tag{3-133}$$

$$(S/N)_{OUT} = \frac{1}{(\pi)^{\frac{1}{2}}}\sqrt{\frac{\Delta\omega_f}{\Delta\omega_T}}\;\frac{(S/N)_{PRE}}{(S/N)_{PRE}+1} \tag{3-135}$$

$$\mathcal{P}_{COH} = 2\mathcal{P}_o\mathbf{R}_S L_z \Omega_{COH} \tag{2-55}$$

$$\Omega_{COH}(\Theta,\Phi=90°) = \frac{\lambda^2}{L_xL_z\sin\Theta + L_xL_y\cos\Theta} \tag{2-166}$$

$$\Gamma = (\Lambda/\rho c_p)K^2 \tag{2-82}$$

$$K = 2k_o\sin(\Theta/2) \tag{2-31}$$

ε - quantum efficiency of the photodetector

ω_o - angular frequency of the incident light beam

$\mathcal{P}_{COH}$ - the available scattered power per coherence solid angle

Γ - the half-width at half-height of the central component spectrum, in radians/sec

$[B_{COH}]$ - the heterodyning efficiency factor

$\Delta\omega_f$ - bandwidth of the tuned filter used to examine the photocurrent spectrum

$\Delta\omega_T$ - bandwidth of the final post-detection filter

$\mathcal{P}_o$ - the incident power

$\mathbf{R}_S$ - the entropy fluctuation contribution to the Rayleigh coefficient

L_z - the length of the illuminated region

$\Omega_{COH}(\Theta,\Phi)$ - the coherence solid angle for a rectangular parallelopiped scattering volume having dimensions L_x, L_y, and L_z in the coordinate system of Fig. 2-10

λ - the wavelength of the incident light in the scattering medium

K - the wave vector of the entropy fluctuation responsible for the observed scattering

$k_o = (2\pi/\lambda)$ - the wave vector of the incident light measured in the scattering medium

The additional factor of two multiplying Eq. (3-133) appears only for the special case of a zero intermediate frequency.

a. The Pre-Detection (S/N) Ratio

The predicted values of $(S/N)_{PRE}$ may be obtained as a function of the observed half-width Γ from the plot of $[B_{COH}]$ shown in Fig. 4-29; from Eqs. (3-133), (2-55), (2-166), (2-31), and (2-82) and from the numerical quantities

$\varepsilon = 0.05$ [*]

$\lambda_{air} = 6328$ Å

$(1/2\pi)(\Lambda/\rho c_p) = 1.38 \times 10^{-4}$ cm²/sec [**]

$\mathbf{R}_S = 0.93 \times 10^{-6}$ cm^{-1} [5]

$L_x = 0.019$ cm [§]

$L_y = 0.028$ cm [§]

$L_z = 2.54$ cm [§]

$P_o = 50$ milliwatts [†]

---

[*] Chapter 4, Section E.4.a.

[**] Chapter 5, Section C.2, Eq. (5-48).

[§] Chapter 4, Section C.4.

[†] Chapter 4, Section C.2.

The results of this calculation are displayed in Fig. 5-10 in two forms: (1) the maximum value of $(S/N)_{PRE}$ which would be achieved with a spectrometer having a unity heterodyning efficiency, $[B_{COH}] = 1$, and (2) the expected pre-detection (S/N) ratio for the actual spectrometer optical system used in these measurements. However, both of these theoretical curves include the effect of the 27% power loss in the light collection optics.*

The dramatic decrease in $(S/N)_{PRE}$ with increasing line width is due primarily to its dependence on the scattered power per unit spectral interval $(\mathcal{P}_{COH}/\Gamma)$ rather than on the explicit variation of $\mathcal{P}_{COH}$ with Θ via the coherence solid angle $\Omega_{COH}(\Theta,\Phi)$ or on the decrease in $[B_{COH}]$. Fig. 2-20 shows that Ω_{COH} decreases by less than a factor of five between $\Theta = 0.33°$ and $\Theta = 3.3°$ while the line width increases by a factor of 100 from $(\Gamma/2\pi) \simeq 100$ cps to $(\Gamma/2\pi) \simeq 10^4$ cps.

Figure 5-10 also presents the experimentally measured values of $(S/N)_{PRE}$ that were obtained from the recorded spectra by applying the fundamental definition of $(S/N)_{PRE}$ given in Eq. (3-132), namely,

$$(S/N)_{PRE} \equiv [I_S^2(\omega_1)/I_N^2(\omega_1)] \tag{3-132}$$

Here $I_S^2(\omega_1)$ is the peak amplitude of the signal component of the spectrum, which in the present case occurs at $\omega_1 = 0$, and $I_N^2(\omega)$ is the uniform shot-noise level. The agreement between experiment and theory is considered to be excellent, especially in view of the number of approximations which are involved in the derivation of the coherence solid angle.**

---

* Chapter 4, Section E.2.a.

** Chapter 2, Section E.

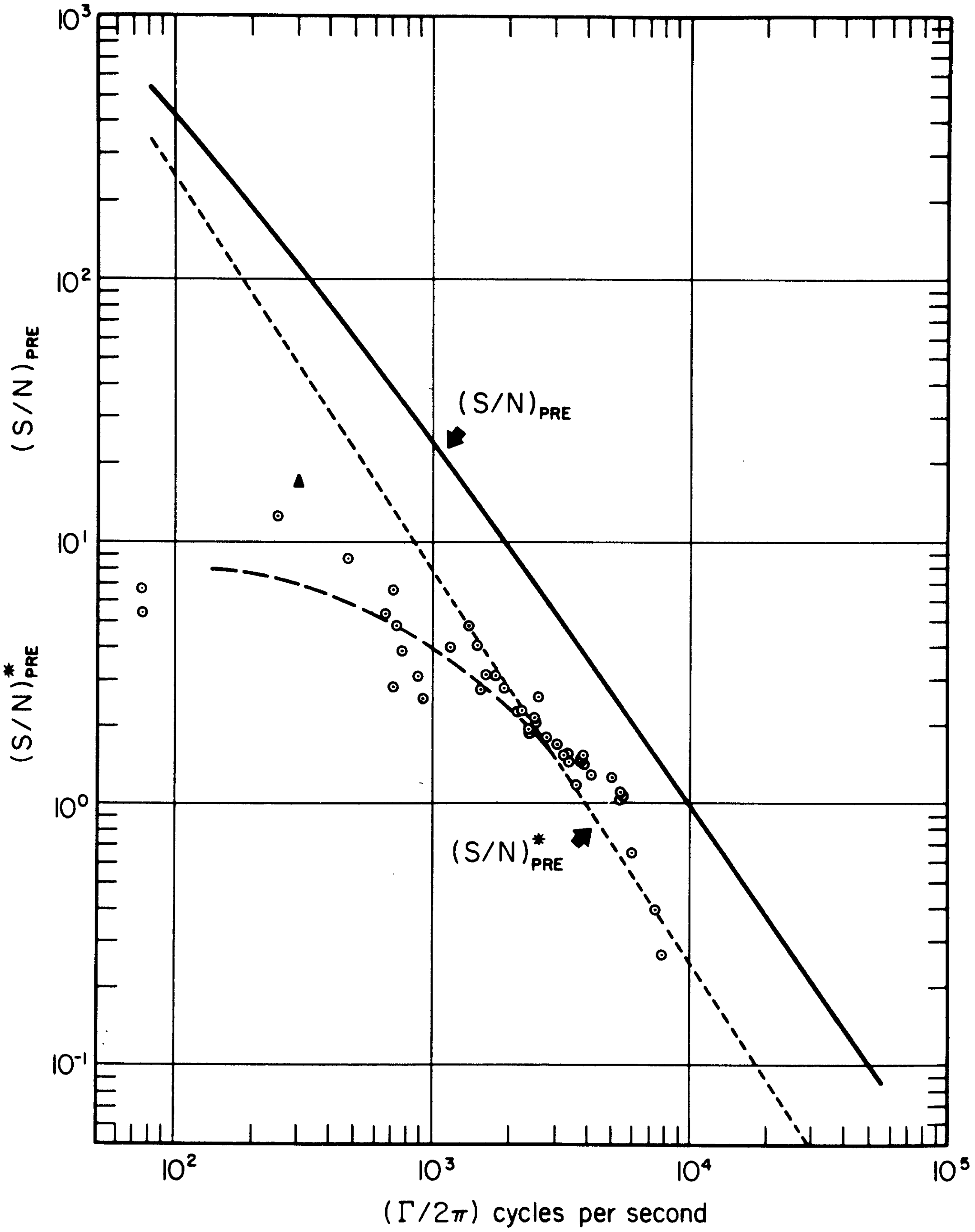

Figure 5-10 The experimentally observed values of the pre-detection signal-to-noise ratio for the measurements on the central component in the light scattered from toluene.

The measurements on half-widths greater than $(\Gamma/2\pi) \simeq 1000$ cps, where the limiting acceptance aperture of the optical system* becomes large compared to the size of a single coherence area, clearly show that $(S/N)_{PRE}$ is indeed proportional to P_{COH} rather than to the total collected power. For $\Theta = 2.83°$, where we have $(\Gamma/2\pi) \simeq 7500$ cps, the number of coherence areas received by the aperture is $N \simeq 12$. The poor agreement at small half-widths can be explained in terms of two effects. First, as we approach $\Theta = 0°$ the coherence angle in the scattering plane $\overline{\Delta\Theta}'$ is increasing toward its maximum value while the Θ' dimension of the limiting acceptance aperture is being decreased to avoid an unnatural broadening of the observed spectrum.* In the regime $(\Gamma/2\pi) < 300$ cps the acceptance solid angle of the spectrometer was considerably less than the coherence solid angle Ω_{COH}; therefore, the power used to calculate $(S/N)_{PRE}$ should be taken as the total power reaching the detector rather than P_{COH} as is assumed in Fig. 5-10. For example, compare the measurement of $(S/N)_{PRE}$ at $(\Gamma/2\pi) = 300$ cps, shown as a heaving triangle in Fig. 5-10, to that at the neighboring point $(\Gamma/2\pi) = 275$ cps; the former was obtained with an aperture size of approximately on coherence area while the latter was taken with $N \simeq (0.2)$. Secondly, for scattering angles smaller than $\Theta \simeq 0.5°$ a large amount of stray light scattered by resonator mirror** M_1 was able to reach the photomixer and produce an increase in the dc photocurrent and hence in the shot-noise level. Both of these effects contribute to the observed reduction in the pre-detection signal-to-noise ratio.

---

* Chapter 4, Section E.2.d.

** Chapter 4, Section E.2.a, Fig. 4-24.

b. The Output (S/N) Ratio

Although the derivation of Eq. (3-135) for $(S/N)_{OUT}$

$$(S/N)_{OUT} = \frac{1}{(\pi)^{\frac{1}{2}}} \sqrt{\frac{\Delta\omega_f}{\Delta\omega_T}} \frac{(S/N)_{PRE}}{1 + (S/N)_{PRE}} \qquad (3\text{-}135)$$

depends only on the characteristics of the electronic detection system, rather than on the properties of the scattered light or the details of the photomixing process, it is interesting to make a comparison between Eq. (3-135), the usual expression that is given for the output signal-to-noise ratio

$$\overline{(S/N)}_{OUT} = \frac{1}{(\pi)^{\frac{1}{2}}} \sqrt{\frac{\Delta\omega_f}{\Delta\omega_T}} (S/N)_{PRE}, \qquad (5\text{-}60)$$

and the experimental results. As was pointed out in Section E.3.b of Chapter 3, Eq. (5-60) is valid only in the limit $(S/N)_{PRE} << 1$ where the primary source of fluctuation in the spectrometer output is the photocurrent shot-noise. Since most of the measurements taken here corresponded to the case $(S/N)_{PRE} \geq 1$, the experimental data provides a pertinent test of the theory.

Figure 5-11 presents the experimental results as a plot of the ratio

$$\sigma = \frac{\overline{(S/N)}_{OUT}}{(S/N)^{observed}_{OUT}} \qquad (5\text{-}61)$$

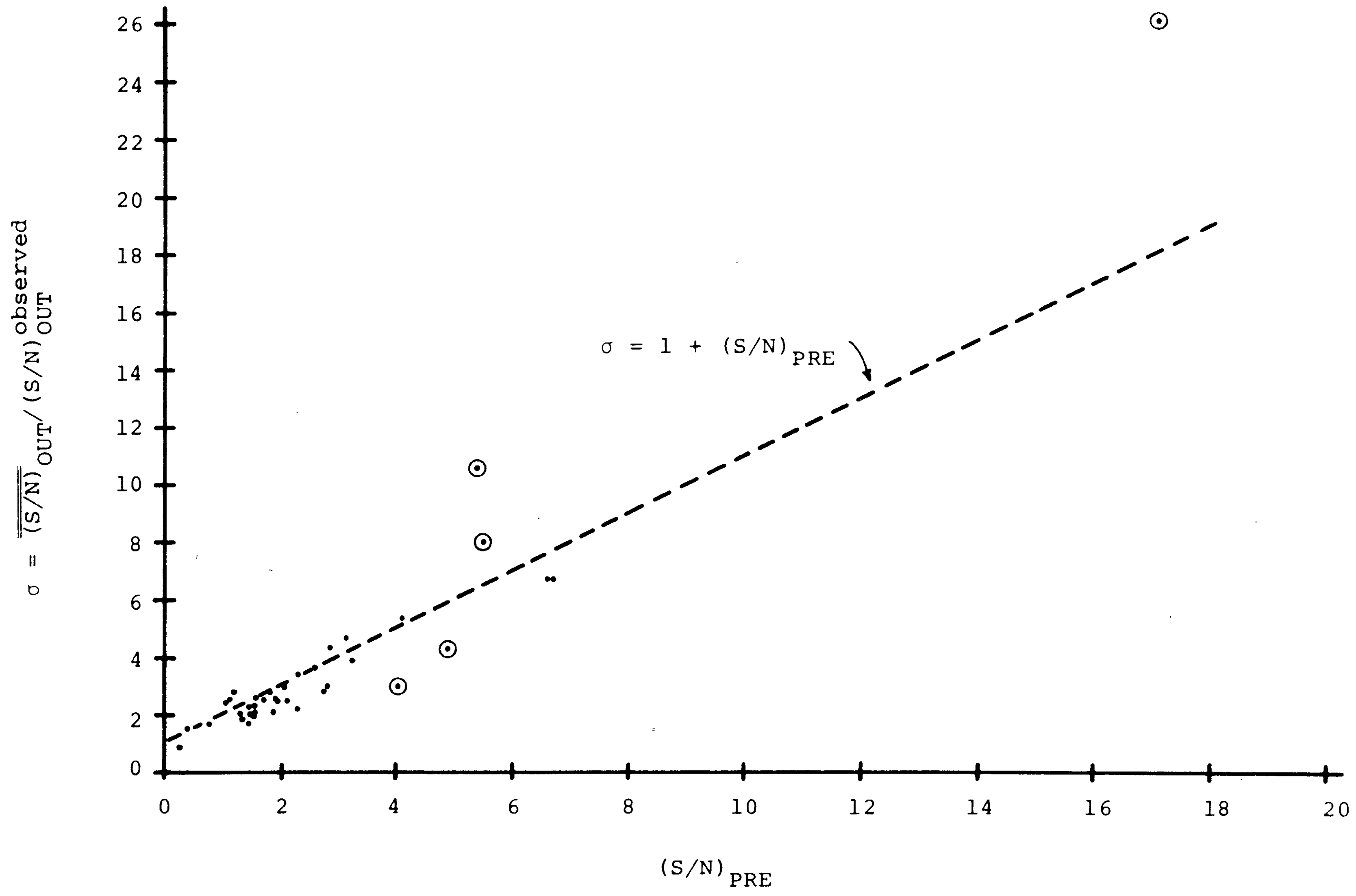

Figure 5-11 Experimental results on the output signal-to-noise ratio for detection of the central component.

versus $(S/N)_{PRE}$. If the observed output signal-to-noise ratio is described by Eq. (3-135) then this plot should yield a straight line $\sigma = 1 + (S/N)_{PRE}$ while if $(S/N)_{OUT}^{observed}$ follows Eq. (5-60) then the result should be the straight line $\sigma = 1$. Figure 5-11 shows that the data are, in fact, in good quantitative agreement with the former behavior.

A striking example of the difference between Eqs. (5-60) and (3-135) that occurs at large pre-detection signal-to-noise ratios is provided by the typical data spectrum presented in Fig. 5-5. The tuned and post-detection filter bandwidths for this trace are $(\Delta\omega_f/2\pi) = 10$ cps and $(\Delta\omega_T/2\pi) = 0.015$ cps respectively. From these constants and the measured value of $(S/N)_{PRE}$, $(S/N)_{PRE} = 5.5$, we find

$$\overline{\overline{(S/N)}}_{OUT} \simeq 80$$

$$(S/N)_{OUT} = \frac{\overline{\overline{(S/N)}}_{OUT}}{(S/N)_{PRE} + 1} \simeq 12$$

The observed output signal-to-noise ratio on the recorded spectrum is $(S/N)_{OUT}^{observed} \simeq 10$.

BIBLIOGRAPHY: Chapter 5

1. S. Parthasarathy, M. Pancholy, and A. F. Chhapgar, Nuovo Cimento 10, 118 (1958).

2. International Critical Tables, E. W. Washburn editor-in-chief (McGraw-Hill Book Company, Inc., New York, 1929), 1st ed., Volume 7.

3. E. L. Heasell and J. Lamb, Proc. Phys. Soc. 69B, 869 (1956).

4. S. G. Rautian, Usp. Fiz. Nauk 66, 475 (1958) [English transl.: Soviet Phys.—Usp. 1, 245 (1959)].

5. I. L. Fabelinskii, Usp. Fiz. Nauk 63, 355 (1957) [English transl.: AEC Translation 3973, Part I, Advan. Phys. Sci. 63, 474 (1957)].

6. American Institute of Physics Handbook, edited by D. E. Gray (McGraw-Hill Book Company, Inc., New York, 1963), 2nd ed., p. 4-86.

7. International Critical Tables, E. W. Washburn editor-in-chief (McGraw-Hill Book Company, Inc., New York, 1929), 1st ed., Volume 5.

8. T. J. Greytak, Bull. Am. Phys. Soc. 11, 404 (1966); and private communication.

9. K. F. Herzfeld and T. A. Litovitz, Absorption and Dispersion of Ultrasonic Waves (Academic Press, Inc., New York, 1959).

10. D. I. Mash, V. S. Starunov, and I. L. Fabelinskii, Zh. Eksperim. i Teor. Fiz. 47, 783 (1964) [English transl.: Soviet Phys.—JETP 20, 523 (1965)].

11. R. Y. Chiao and P. A. Fleury, in Physics of Quantum Electronics, edited by P. L. Kelley, B. Lax, and P. E. Tannenwald (McGraw-Hill Book Company, Inc., New York, 1966), p. 241.

12. G. Benedek and T. Greytak, Proc. IEEE 53, 1623 (1965).

13. D. I. Mash, V. S. Starunov, E. V. Tiganov, and I. L. Fabelinskii, Zh. Eksperim. i Teor. Fiz. 49, 1764 (1965) [English transl.: Soviet Phys.—JETP 22, 1205 (1966)].

14. T. Litovitz, private communication.

15. B. U. Felderhof, J. Chem. Phys. 44, 602 (1966).

16. M. Fixman, J. Chem. Phys. 33, 1357 (1960).

17. C. M. Sogani, Indian J. Phys. 1, 357 (1927).

18. C. M. Sogani, Indian J. Phys. 2, 97 (1927).

Appendix A

THE GENERAL EXPRESSION FOR THE SCATTERED ELECTRIC FIELD

In this appendix we show that the general expression for the scattered field may be given in terms of the fluctuating part of the optical susceptibility $\chi(\vec{r},t)$.

In the illuminated region V the total fields, incident plus scattered, must satisfy Maxwell's equations

$$\vec{\nabla}\cdot\vec{B} = 0 \qquad \text{(A-1)} \qquad\qquad \vec{\nabla}\times\vec{E} = -\partial\vec{B}/\partial t \qquad \text{(A-2)}$$

$$\vec{\nabla}\cdot\vec{D} = 0 \qquad \text{(A-3)} \qquad\qquad \vec{\nabla}\times\vec{H} = \partial\vec{D}/\partial t \qquad \text{(A-4)}$$

where we have assumed that ρ and $\vec{j}$, the free charge and current densities respectively, are both zero.

Writing $\vec{D} = \varepsilon_o\vec{E} + \vec{P}$ and assuming that the scattering medium has unit magnetic permeability gives $\vec{B} = \mu_o\vec{H}$ and yields Eqs. (A-1) through (A-4) as

$$\vec{\nabla}\cdot\vec{B} = 0 \qquad \text{(A-1)} \qquad\qquad \vec{\nabla}\times\vec{E} = -\partial\vec{B}/\partial t \qquad \text{(A-2)}$$

$$\vec{\nabla}\cdot\vec{E} = -(1/t_o)(\vec{\nabla}\cdot\vec{P}) \qquad \text{(A-5)} \qquad\qquad \vec{\nabla}\times\vec{B} = \mu_o\varepsilon_o(\partial\vec{E}/\partial t) + \mu_o(\partial\vec{P}/\partial t) \qquad \text{(A-6)}$$

If the scattering medium is characterized by a scalar optical electric susceptibility $\chi(\vec{r},t)$ the polarization vector $\vec{P}(\vec{r},t)$ has the form

$$\vec{P}(\vec{r},t) = \varepsilon_o \chi(\vec{r},t)\vec{E}(\vec{r},t) \tag{A-7}$$

and Eqs. (A-5) and (A-6) become

$$\vec{\nabla}\cdot\vec{E} = -(1/\varepsilon_o)(\vec{\nabla}\cdot\varepsilon_o\chi\vec{E}) \tag{A-8}$$

and

$$\vec{\nabla}\times\vec{B} = \varepsilon_o\mu_o\{(\partial\vec{E}/\partial t) + \partial/\partial t[\chi\vec{E}]\} \tag{A-9}$$

respectively. The function $\chi(\vec{r},t)$ may be decomposed into a time average and a fluctuating component

$$\chi(\vec{r},t) = \langle\chi\rangle + \Delta\chi(\vec{r},t) \tag{A-10}$$

so that we have finally

$$\vec{\nabla}\cdot\vec{E} = -\langle\chi\rangle(\vec{\nabla}\cdot\vec{E}) - \vec{\nabla}\cdot[\Delta\chi\cdot\vec{E}] \tag{A-11}$$

$$\vec{\nabla}\times\vec{B} = \mu_o\varepsilon_o\{(\partial\vec{E}/\partial t) + \langle\chi\rangle(\partial\vec{E}/\partial t) + (\partial/\partial t)(\Delta\chi\cdot\vec{E})\} \tag{A-12}$$

The effects of the time average susceptibility may be removed from explicit consideration by the following procedure. The results in Eqs. (A-11) and (A-12) may be reexpressed as

$$\vec{\nabla}\cdot\vec{E} = -\frac{\vec{\nabla}\cdot(\Delta\chi\cdot\vec{E})}{1+\langle\chi\rangle} \tag{A-13}$$

and

$$\vec{\nabla}\times\vec{B} = \mu_o\varepsilon_o(1+\langle\chi\rangle)\{\frac{\partial\vec{E}}{\partial t} + \frac{\partial/\partial t[\Delta\chi\cdot\vec{E}]}{1+\langle\chi\rangle}\} \tag{A-14}$$

Let us define the quantities $\vec{P}'(\vec{r},t)$ and c_m as

$$\vec{P}'(\vec{r},t) = \frac{\varepsilon_o \Delta\chi(\vec{r},t)\vec{E}(\vec{r},t)}{1 + \langle\chi\rangle} \qquad \text{(A-15)}$$

and

$$c_m^{\ 2} = \frac{1}{\mu_o \varepsilon_o (1 + \langle\chi\rangle)} \qquad \text{(A-16)}$$

where $\vec{P}'$ represents the polarization field associated with the fluctuations, and c_m is the velocity of light in the scattering medium. It follows that $\langle\chi\rangle$ is related to the index of refraction of the medium n as

$$\langle\chi\rangle = n^2 - 1 \qquad \text{(A-17)}$$

In terms of $\vec{P}'$ and c_m we obtain a set of modified Maxwell's equations

$$\vec{\nabla}\cdot\vec{B} = 0 \qquad \text{(A-1)}$$

$$\vec{\nabla}\cdot\vec{E} = (1/\varepsilon_o)(\vec{\nabla}\cdot\vec{P}') \qquad \text{(A-18)}$$

$$\vec{\nabla}\times\vec{E} = -\ \partial\vec{B}/\partial t \qquad \text{(A-2)}$$

$$\vec{\nabla}\times\vec{B} = (1/c_m^{\ 2})[\partial\vec{E}/\partial t + (1/\varepsilon_o)(\partial\vec{P}'/\partial t)] \qquad \text{(A-19)}$$

in which the effect of $\langle\chi\rangle$ appears simply as a modification in the velocity of propagation.

The solutions for the total fields $\vec{B}$ and $\vec{E}$ may be written in terms of the usual vector and scalar potentials, $\vec{A}$ and ϕ, as

$$\vec{B} = \vec{\nabla}\times\vec{A} \qquad \text{(A-20)}$$

$$\vec{E} = -\vec{\nabla}\phi - \partial\vec{A}/\partial t \qquad \text{(A-21)}$$

We will take $\vec{A}$ and ϕ to satisfy the modified Lorentz gauge

$$\vec{\nabla}\cdot\vec{A} + (1/c_m^2)(\partial\phi/\partial t) = 0 \qquad \text{(A-22)}$$

If $\vec{B}$ and $\vec{E}$ are defined as in Eqs. (A-20) and (A-21), then the Maxwell equations in Eq. (A-1) and (A-2) are automatically satisfied and Eqs. (A-18) and (A-19) become

$$-\nabla^2\phi - \partial/\partial t(\vec{\nabla}\cdot\vec{A}) = -(1/t_o)(\vec{\nabla}\cdot\vec{P}') \qquad \text{(A-23)}$$

$$\vec{\nabla}\times(\vec{\nabla}\times\vec{A}) = \frac{1}{c_m^2}\{-\frac{\partial}{\partial t}(\vec{\nabla}\phi) - \frac{\partial^2 A}{\partial t^2} + \frac{1}{\varepsilon_o}\cdot\frac{\partial P'}{\partial t}\} \qquad \text{(A-24)}$$

Using the gauge condition and the vector identity $\vec{\nabla}\times(\vec{\nabla}\times\vec{A}) = \vec{\nabla}(\vec{\nabla}\cdot\vec{A}) - \nabla^2\vec{A}$ yields

$$\nabla^2\phi - \frac{1}{c_m^2}\left(\frac{\partial^2\phi}{\partial t^2}\right) = \frac{1}{\varepsilon_o}(\vec{\nabla}\cdot\vec{P}') \qquad \text{(A-25)}$$

and

$$\nabla^2\vec{A} - \frac{1}{c_m^2}\left(\frac{\partial^2 A}{\partial t^2}\right) = -\frac{1}{\varepsilon_o c_m^2}\left(\frac{\partial P'}{\partial t}\right) \qquad \text{(A-26)}$$

Thus we find that $\vec{A}$ and ϕ represent solutions to the usual wave equations in a medium where the velocity of light is c_m and where there are effective charge and current distributions given by

$$\rho_{eff} = -(\varepsilon/\varepsilon_o)(\vec{\nabla}\cdot\vec{P}') \qquad \text{(A-27)}$$

$$\vec{J}_{eff} = (c_o/c_m)^2(\partial\vec{P}'/\partial t) \qquad \text{(A-28)}$$

The quantities $\varepsilon = (1 + \langle\chi\rangle)\varepsilon_o$ and c_o are the optical susceptibility of the scattering medium and the velocity of light in free space respectively.

The two wave equations for the potentials $\vec{A}$ and ϕ can be solved[§] most easily in terms of a "superpotential." Let us set

$$\vec{A} = (1/c_m^2)(\partial\vec{Z}/\partial t) \qquad \text{(A-29)}$$

and

$$\phi = -(\vec{\nabla}\cdot\vec{Z}) \qquad \text{(A-30)}$$

In this case $\vec{A}$ and ϕ automatically satisfy the gauge condition and the $\vec{A}$ wave equation becomes

$$\frac{1}{c_m^2}\nabla^2\left(\frac{\partial Z}{\partial t}\right) - \frac{1}{c_m^2}\frac{\partial^2}{\partial t^2}\left(\frac{1}{c_m^2}\cdot\frac{\partial Z}{\partial t}\right) = -\frac{1}{\varepsilon_o c_m^2}\left(\frac{\partial\vec{P}'}{\partial t}\right) \qquad \text{(A-31)}$$

Removing one $\partial/\partial t$ by integration yields

$$\nabla^2\vec{Z} - \frac{1}{c_m^2}\frac{\partial^2\vec{Z}}{\partial t^2} = -\frac{\vec{P}'}{\varepsilon_o} \qquad \text{(A-32)}$$

The integration constant, which would be a function of position coördinates only, can be shown to be zero by noting that $\vec{Z}$ must satisfy the free field wave equation when $\vec{P}' = 0$.

Straightforward substitution of Eqs. (A-29) and (A-30) into the ϕ wave equation yield a wave equation for $\vec{Z}$ which is identical to Eq. (A-32). Therefore the problem of calculating the fields is reduced to finding the solution to the wave equation

$$\nabla^2\vec{Z} - (1/c_m^2)(\partial^2\vec{Z}/\partial t^2) = -(\vec{P}'/\varepsilon_o) \qquad \text{(A-33)}$$

Equation (A-33) is of the general form

$$\nabla^2\vec{G} - (1/c_m{}^2)(\partial^2\vec{G}/\partial t^2) = -4\pi f(\vec{r},t) \qquad \text{(A-34)}$$

which has a Green's function[†] solution

$$\vec{G}(\vec{r},t) = \int_{\vec{r}_1}\int_{t_1} \frac{f(\vec{r}_1,t_1)\,\delta\left[t_1 - t + \frac{|\vec{r}-\vec{r}_1|}{c_m}\right]d^3\vec{r}_1 dt_1}{|\vec{r}-\vec{r}_1|} \qquad \text{(A-35)}$$

Therefore, the desired solution for the superpotential $\vec{Z}$ (also called the Hertz vector) is

$$\vec{Z}(\vec{r},t) = \frac{1}{4\pi\varepsilon_o}\int_{\vec{r}_1}\int_{t_1} \frac{\vec{P}'(\vec{r}_1,t_1)\,\delta\left[t_1 - t + \frac{|\vec{r}-\vec{r}_1|}{c_m}\right]d^3\vec{r}_1 d^3 t_1}{|\vec{r}-\vec{r}_1|}$$

(A-36)

The fields $\vec{B}$ and $\vec{E}$ can be obtained from the Hertz vector as follows. From Eqs. (A-20), (A-21), (A-29), and (A-30) we have

$$\vec{B} = \vec{\nabla}\times\vec{A} = \frac{1}{c_m{}^2}\frac{\partial}{\partial t}(\vec{\nabla}\times\vec{E}) \qquad \text{(A-37)}$$

and

$$\vec{E} = -\vec{\nabla}\phi - (\partial\vec{A}/\partial t) = \vec{\nabla}(\vec{\nabla}\cdot\vec{Z}) - \frac{1}{c_m{}^2}\left(\frac{\partial^2 Z}{\partial t^2}\right) \qquad \text{(A-38)}$$

The result for $\vec{E}$ in terms of $\vec{Z}$ can be simplified with the help of the identity $\vec{\nabla}\times(\vec{\nabla}\times\vec{Z}) = \vec{\nabla}(\vec{\nabla}\cdot\vec{Z}) - \nabla^2\vec{Z}$ to the form

$$\vec{E} = \vec{\nabla}\times(\vec{\nabla}\times\vec{Z}) + \{\nabla^2\vec{Z} - (1/c_m^{\,2})(\partial^2 Z/\partial t^2)\} \qquad \text{(A-39)}$$

It follows that if the observation point is outside the illuminated region so that $\vec{P}' \equiv 0$ we have simply

$$\vec{E} = \vec{\nabla}\times(\vec{\nabla}\times\vec{Z}) \qquad \text{(A-40)}$$

[§] W. K. H. Panofsky and M. Phillips, Classical Electricity and Magnetism (Addison-Wesley Publishing Co., Inc., Reading, Mass., 1955), p. 254.

[†] J. D. Jackson, Classical Electrodynamics (John Wiley and Sons, Inc., New York, 1962), p. 183 ff.

Appendix B

THE EVALUATION OF THE SUSCEPTIBILITY DERIVATIRES $(\partial\chi/\partial s)_P$ AND $(\partial\chi/\partial P)_s$ IN TERMS OF THE PRESSURE AND TEMPERATURE DEPENDENCES OF THE INDEX OF REFRACTION

Consider the two derivatives $(\partial\chi/\partial s)_P$ and $(\partial\chi/\partial P)_s$ which determine the scattered intensity. The optical susceptibility, χ, is related to the index of refraction, n, by the result* $n^2 = 1 + \langle\chi\rangle$ so that the required thermodynamic derivatives can be written as

$$(\partial\chi/\partial s)_P = (\partial n^2/\partial s)_P \qquad \text{(B-1)}$$

and

$$(\partial\chi/\partial P)_s = (\partial n^2/\partial P)_s \qquad \text{(B-2)}$$

respectively.

Static measurements on the index of refraction are usually performed as a function of pressure and temperature, and yield the quantities $(\partial n/\partial P)_T$ and $(\partial n/\partial T)_P$. The desired entropy and pressure derivatives can be given in terms of the known pressure and temperature dependences as follows. Writing $n = n(P,T)$ gives Eq. (3-1) in the form

---

* Appendix A.

$$(\partial n^2/\partial s)_P = 2n(\partial n/\partial s)_P$$

$$= 2n[(\partial n/\partial T)_P(\partial T/\partial s)_P + (\partial n/\partial P)_T(\partial P/\partial s)_P] \quad \text{(B-3)}$$

The last term vanishes identically leaving

$$(\partial n^2/\partial s)_P = 2n(T/\rho c_P)(\partial n/\partial T)_P \quad \text{(B-4)}$$

$c_P = (T/\rho)(\partial s/\partial T)_P$ - the specific heat at constant pressure per unit mass

s - the entropy per unit volume

T - the absolute temperature

Similarly we find from Eq. (B-2)

$$(\partial n^2/\partial P)_s = 2n(\partial n/\partial P)_s$$

$$= 2n[(\partial n/\partial T)_P(\partial T/\partial P)_s + (\partial n/\partial P)_T(\partial P/\partial P)_s] \quad \text{(B-5)}$$

In terms of the thermodynamic equality $(\partial T/\partial P)_s = T\alpha/\rho c_P$, where α is the volume expansivity, $\alpha = -(1/V)(\partial V/\partial T)_P$, we have

$$(\partial n^2/\partial P)_s = 2n[(T\alpha/\rho c_P)(\partial n/\partial T)_P + (\partial n/\partial P)_T] \quad \text{(B-6)}$$

A tabulation of the thermodynamic parameters appearing in Eqs. (B-4) and (B-6) is given in Table B-I for some typical liquids and isotropic solids; all are measured at a temperature of 20°C and a pressure of 760 mm of mercury. These tabulated results were used to calculate the Rayleigh ratios which are quoted in Table I of Chapter 2.

Table B-1 USEFUL THERMODYNAMIC PARAMETERS FOR SOME TYPICAL SCATTERING MEDIA

Material	ρ - gms/cm^3	c_P - joules/gm °C	n^*
CS_2	1.263	0.994	1.6232
Benzene	0.879	1.699	1.4975
Toluene	0.867	1.673	1.4925
H_2O	1.0	4.185	1.3318
Glycerol	1.260	2.30	1.4723
CCl_4	1.595	0.841	1.458
Acetone	0.792	2.210	1.3577
Methanol	0.792	2.511	1.3278
Fused Quartz	2.22	0.761	1.457
KCl	1.984	0.684	1.488
NaCl	2.165	0.864	1.542

---

[*] Measured at $\lambda_{air} = 6328$ Å.

Table B-I (continued)

Material	$(\partial n/\partial T)$ [†] $(°C)^{-1}$	B_s dyne/cm^2	α $(°C)^{-1}$	$(\partial n/\partial P)_T$ [§] cm^2/dyne	$(T\alpha/\rho c_P)(\partial n/\partial T)_P$ cm^2/dyne
CS_2	-8.0×10^{-4}	1.69×10^{10}	1.218×10^{-3}	650×10^{-13}	-233×10^{-13}
Benzene	-6.45 ×	1.52 ×	1.237 ×	503 ×	-160 ×
Toluene	-5.8 ×	1.503 ×			
H_2O	-0.79 ×	2.23 ×	0.207 ×	150 ×	-1.2 ×
Glycerol	-2.0 ×	4.62 ×	0.505 ×	108 ×	-10.5 ×
CCl_4	-5.0 ×	1.41 ×	1.236 ×		
Acetone	-5.3 ×	1.12 ×	1.487 ×		
Methanol	-3.6 ×	0.829 ×	1.199 ×		
Fused Quartz	+0.102 ×		0.00126 ×		
KCl	-0.36 ×	39.8 ×			
NaCl	-0.36 ×	48.7 ×	0.1212 ×		

[†] measured at λ_{air} = 5893 Å

[§] measured at λ_{air} = 5893 Å

Appendix C

THE PROBABILITY DISTRIBUTIONS FOR THE ENTROPY AND PRESSURE FLUCTUATIONS OF WAVE VECTOR K

In order to calculate the probability densities $\mathbf{P}[\Delta s_K(0)]$ and $\mathbf{P}[\Delta P_K(0)]$ we make use of the statistical mechanical derivation for the probability of locating a system in a specified non-equilibrium configuration. The probability for finding the system in a state which may be reached reversibly from the equilibrium state by performing an amount of work ΔW is simply*

$$\mathbf{P}(\text{state}) = e^{-\frac{\Delta W(\text{state})}{\underline{k}T}} \qquad \text{(C-1)}$$

where $\underline{k}$ is Boltzmann's constant and T is the absolute temperature. A straightforward expansion* of ΔW in terms of the variables s and P leads to

$$\mathbf{P}[\Delta s_P, \Delta P_s] = \mathbf{N} \exp\{-\frac{\beta_s}{2\underline{k}T} V_o(\Delta P_s)^2 - \frac{1}{2\underline{k}\rho c_P} V_o(\Delta s_P)^2\} \qquad \text{(C-2)}$$

where $\mathbf{N}$ is a normalizing factor and β_s is the adiabatic compressibility

$$\beta_s = -\frac{1}{v}\left(\frac{\partial v}{\partial P}\right)_s$$

Equation (C-2) assumes that ΔP_s and Δs_P are uniform over the volume V_o and zero elsewhere. The joint probability $\mathbf{P}[\Delta s_P, \Delta P_s]$ may be factored into two simple probability functions

$$\mathbf{P}[\Delta P_s] = \mathbf{N}_P \, e^{-\frac{\beta_s}{2kT} V_o (\Delta P_s)^2} \tag{C-3}$$

$$\mathbf{P}[\Delta s_P] = \mathbf{N}_s \, e^{-\frac{1}{2k\rho c_P} V_o (\Delta s_P)^2} \tag{C-4}$$

Let us consider $\mathbf{P}[\Delta P_s]$ first. In a real system ΔP_s will be a function of both position in the medium and time, i.e. $\Delta P_s = \Delta P_s(\vec{r},t)$. It follows that the product $V_o(\Delta P_s)^2$ is really the integral

$$\int_{V_o} \Delta P_s^{\,2}(\vec{r},t)\, d^3\vec{r}$$

which is obtained by letting $V_o \rightarrow dV_o$ and summing over all elementary volumes. This result can also be obtained directly by computing the adiabatic reversible work ΔW required to produce a system whose pressure deviation from equilibrium is given by $\Delta P_s(\vec{r},t)$. Therefore, we have

$$\mathbf{P}[\Delta P_s(\vec{r},t)] = \mathbf{N}_P \, \mathbf{e}^{-\frac{s}{2kT} \cdot \int_{V_o} \Delta P_s^{\,2}(\vec{r},t)\, d^3\vec{r}} \tag{C-5}$$

and a similar result for the entropy fluctuation term, namely

$$\mathbf{P}[\Delta s_P(\vec{r},t)] = \mathbf{N}_s \, \mathbf{e}^{-\frac{1}{2\underline{k}\rho c_P} \int_{V_o} \Delta s_P{}^2(\vec{r},t)\, d^3\vec{r}} \qquad \text{(C-6)}$$

Let the volume V_o refer to the illuminated volume V. In this region we have expressed the fluctuations $\Delta P_s(\vec{r},t)$ and $\Delta s_P(\vec{r},t)$ in terms of a spatial Fourier series as

$$\Delta P_s(\vec{r},t) = \sum_K \underline{\Delta P}_K(t)\, e^{i\vec{K}\cdot\vec{r}} \qquad \text{(C-7)}$$

$$\Delta s_P(\vec{r},t) = \sum_K \underline{\Delta s}_K(t)\, e^{i\vec{K}\cdot\vec{r}} \qquad \text{(C-8)}$$

where the Fourier amplitudes $\underline{\Delta P}_K(t)$ and $\underline{\Delta s}_K(t)$ are given by

$$\underline{\Delta P}_K(t) = \frac{1}{V} \int_V \Delta P_s(\vec{r},t)\, e^{-i\vec{K}\cdot\vec{r}}\, d^3\vec{r} \qquad \text{(C-9)}$$

$$\underline{\Delta s}_K(t) = \frac{1}{V} \int_V \Delta s_P(\vec{r},t)\, e^{-i\vec{K}\cdot\vec{r}}\, d^3\vec{r} \qquad \text{(C-10)}$$

The integral appearing in Eq. (C-5) can now be expressed in terms of the corresponding Fourier amplitudes as follows. Expanding

$$\int_V \Delta P_s{}^2(\vec{r},t)\, d^3\vec{r}$$

with the help of the Fourier series in Eq. (C-7) we have

$$\int_V \Delta P_s{}^2(\vec{r},t)\,d^3\vec{r} = \sum_K \sum_{K'} \underline{\Delta P}_K(t)\,\underline{\Delta P}_{K'}(t) \int_V e^{i(\vec{K}+\vec{K}')\cdot\vec{r}}\,d^3\vec{r}$$

Since $e^{i\vec{K}\cdot\vec{r}}$ and $e^{i\vec{K}'\cdot\vec{r}}$ are chosen[**] to be orthonormal over V, the remaining volume integral yields

$$\int_V e^{i(\vec{K}+\vec{K}')\cdot\vec{r}}\,d^3\vec{r} = V\delta_{\vec{K},-\vec{K}'} \qquad \text{(C-11)}$$

Using the identity $\underline{\Delta P}_{-K}(t) = \underline{\Delta P}_K^*(t)$ we find

$$\int_V \Delta P_s{}^2(\vec{r},t)\,d^3\vec{r} = V\sum_K \underline{\Delta P}_K(t)\,\underline{\Delta P}_K^*(t) = V\sum_K |\underline{\Delta P}_K(t)|^2 \qquad \text{(C-13)}$$

which is simply Parseval's theorem[†] as applied to the real space and $\vec{k}$-space representations of the zero mean function $\Delta P_s(\vec{r},t)$. With the help of Eq. (C-13), Eq. (C-5) becomes

$$\mathbf{P}[\Delta P_s(\vec{r},t)] = \mathbf{N}_P \exp\left\{-\frac{\beta_s V}{2\underline{k}T}\sum_K |\underline{\Delta P}_K(t)|^2\right\} \qquad \text{(C-14)}$$

This is a separable extended product[§] of Gaussians, indicating that the $\underline{\Delta P}_K(t)$ are statistically independent quantities each having a probability distribution

$$\mathbf{P}[\underline{\Delta P}_K(t)] = \mathbf{N}' \exp\left\{-\frac{\beta_s V}{2\underline{k}T}|\underline{\Delta P}_K(t)|^2\right\} \qquad \text{(C-15)}$$

The corresponding result for $\underline{\Delta s}_K(t)$ follows immediately from Eq. (C-6) as

$$\mathbf{P}[\underline{\Delta s}_K(t)] = \mathbf{N}' \exp\left\{- \frac{V}{2\underline{k}\rho c_P} |\underline{\Delta s}_K(t)|^2\right\} \qquad \text{(C-16)}$$

---

[*] L. D. Landau and E. M. Lifshitz, *Statistical Physics* (Pergamon Press Ltd., London; Addison-Wesley Publishing Co., Inc., Reading, Mass., 1958), p. 344 ff.

[**] Chapter 2, Section E.4.f.

[†] R. Bracewell, *The Fourier Transform and Its Applications* (McGraw-Hill Book Company, Inc., New York, 1965), pp. 112-113.

[§] G. B. Benedek, Lectures on the *Theory of the Scattering of Light from Thermal Fluctuations*, Brandeis Summer Institute for Theoretical Physics, 1966 (to be published).

Appendix D

THE EFFECT OF WAVEFRONT CURVATURE MISMATCH ON THE HETERODYNING EFFICIENCY

This appendix describes the efficiency of mixing [B] between two spherically spreading waves having radii of curvature r_1 and r_2 and falling on a photodetector of diameter d. Both incoming beams are assumed to be monochromatic, non-stochastic fields with coherence areas much larger than the detector aperture.

We will assume that the source points of both spherical waves lie on a line perpendicular to the photosurface and passing through its geometrical center. This situation avoids the added effect of angular misalignment which was treated in Section D.3.b.1 of Chapter 3. The orientation between the two beam axes and the circular detector aperture is illustrated in Fig. D-1.

From Eq. (3-107) we have [B] in the form

$$[B] = \frac{1}{A} \int_A T_1(\vec{r}_o,\vec{\rho})T_2(\vec{r}_o,\vec{\rho})d^2\vec{\rho} \qquad (3\text{-}107)$$

where $\vec{\rho}$ ranges over the surface of the detector, A. As before, $T_1(\vec{r}_o,\vec{\rho})$ and $T_2(\vec{r}_o,\vec{\rho})$ are normalized descriptions of the amplitude and phase behavior of the two incoming fields as a function of position $\vec{\rho}$ relative to the fixed point $\vec{r}_o$. To simplify the evaluation of the integral we assume that the photomixer has a spherical surface with

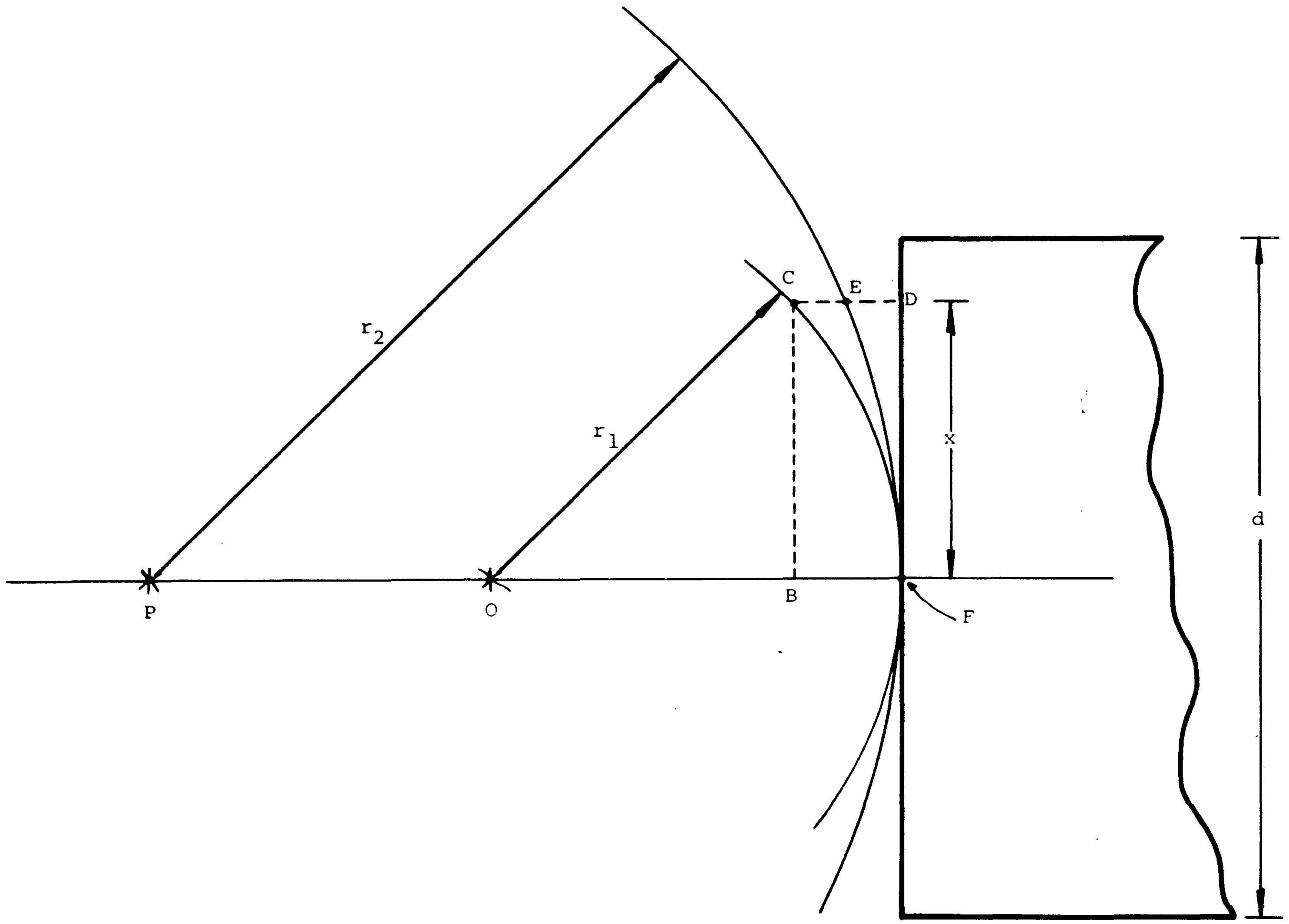
r_2
r_1
C
E
D
x
d
P
O
B
F

Figure D-1 Two spherically spreading waves of different radius of curvature incident collinearly on a circular, plane photocathode.

a radius of curvature $R = \sqrt{r_1 r_2}$ oriented as shown in Fig. D-2. For $r_1 \approx r_2$ it follows that both beams have constant intensity on A and Eq. (3-107) may be simplified to

$$[B] = (1/A) \int_A \cos\,[\Delta\phi(\vec{\rho})]\, d^2\vec{\rho} \qquad \text{(D-1)}$$

where $\Delta\phi(\vec{\rho})$ is the phase difference between the incoming fields as a function of position on the photosurface. Assuming that the mixing geometry is azimuthally symmetric it follows that $\Delta\phi(\vec{\rho})$ depends only on the polar angle θ shown in Fig. D-2. In this case we have immediately

$$[B] = \frac{\int_{\theta=0}^{\theta_{MAX}} \cos\,[\Delta\phi(\theta)]\, 2\pi R^2 \sin\theta\, d\theta}{\int_{\theta=0}^{\theta_{MAX}} 2\pi R^2 \sin\theta\, d\theta} \qquad \text{(D-2)}$$

where

$$\sin\theta_{MAX} = (d/2R)$$

The spatial separation and phase difference between two wavefronts that coincide on the detector axis at F are most easily obtained as a function of the radial distance off axis, x, shown in Fig. D-1. Calculating the lengths of the perpendiculars $\overline{CD}$ and $\overline{ED}$ dropped to the plane tangent to the wavefronts at F we find

$$\overline{CD} = \overline{BF} = r_1 - \sqrt{r_1^2 - x^2} \qquad \text{(D-3)}$$

$$\overline{ED} = r_2 - \sqrt{r_2^2 - x^2} \qquad \text{(D-4)}$$

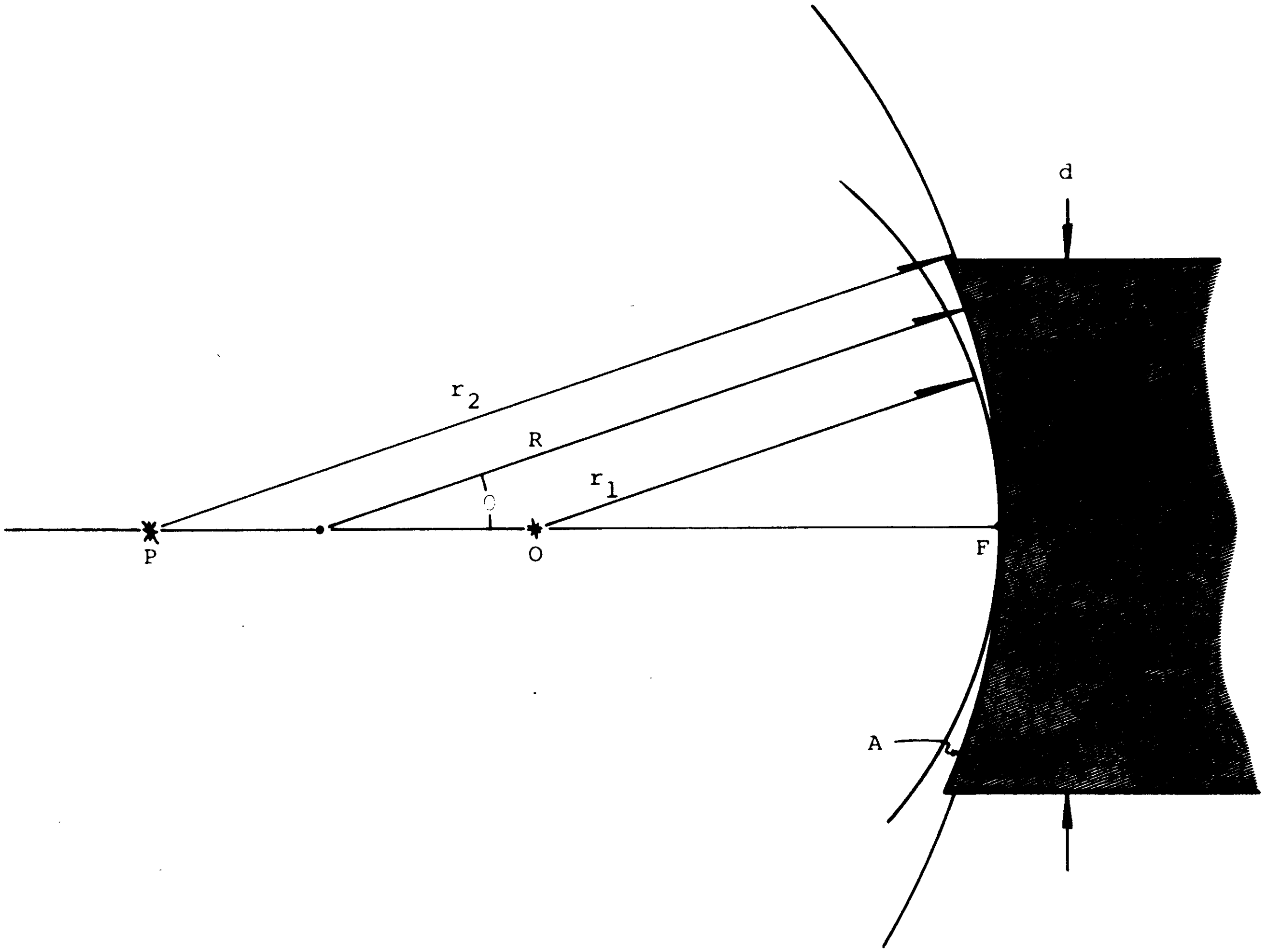

Figure D-2 The assumed photocathode geometry used to compute the wavefront radius mismatch heterodyning efficiency.

The resulting phase difference between the waves is

$$\Delta\phi(x) = (2\pi/\lambda)[\overline{CD} - \overline{ED}] \tag{D-5}$$

where λ is the average wavelength of the two fields. In the limit $x << R$, which holds for all the cases considered here, we have approximately

$$\overline{CD} = (x^2/2r_1) \tag{D-6}$$

and

$$\overline{ED} = (x^2/2r_2) \tag{D-7}$$

Equations (D-5), (D-6), and (D-7) give $\Delta\phi$ as

$$\Delta\phi(x) = \frac{\pi x^2}{\lambda}\left(\frac{r_2 - r_1}{r_1 r_2}\right) \tag{D-8}$$

Writing $x = R \sin\theta$ gives the desired integral for [B] as

$$[B] = \frac{\displaystyle\int_{\theta=0}^{\theta_{MAX}} \cos\left\{\frac{\pi \sin^2\theta}{\lambda}(r_2 - r_1)\right\} \sin\theta \, d\theta}{\displaystyle\int_{\theta=0}^{\theta_{MAX}} \sin\theta \, d\theta} \tag{D-9}$$

Equation (D-9) may be integrated in the usual limit of $(d/2R) = \sin\theta_{MAX} << 1$ with the approximation $\sin\theta \simeq \theta$. This procedure yields the final result

$$[B] = \frac{\sin w}{w} \tag{D-10}$$

where

$$w = \left(\frac{\pi}{4\lambda}\right)\left(\frac{r_2 - r_1}{r_1 r_2}\right)d^2 \qquad \text{(D-11)}$$

A detailed analysis of the behavior of the function $g = (\sin w)/w$ may be found in Section D.3.b.1 of Chapter 2.

Appendix E

THE EFFECT OF THE FINITE SIZE OF THE ILLUMINATED REGION ON THE SPECTRUM OF THE SCATTERED LIGHT

In this Appendix we examine the relationship between an uncertainty in the "momentum conservation" condition[*]

$$\vec{k}_s = \vec{k}_o + \vec{K}$$

resulting from the finite dimensions of the illuminated volume and the spectrum of the light scattered into a particular angle, Θ_o, away from the incident beam direction.

For an incident beam having an arbitrary cross sectional amplitude variation, i.e.

$$\underline{\vec{E}}_{INC} = \vec{E}_o(\vec{r})\, e^{i(\vec{k}_o \cdot \vec{r} - \omega_o t)} \tag{E-1}$$

it is convenient to allow the sample volume[**] V to become infinite, and to describe the size of the illuminated region simply in terms of the intensity distribution of the source

---

[*] Chapter 2, Section E.4.e.

[**] Chapter 2, Section B.1.

$$I_o(\vec{r}) = (1/2)\sqrt{\varepsilon\varepsilon_o/\mu_o}\ |\vec{E}_o(\vec{r})|^2 \tag{E-2}$$

In this case, the spatial Fourier series expansion of the susceptibility fluctuations which was introduced in Chapter 2* becomes a Fourier integral,

$$\Delta\chi(\vec{r},t) = \frac{1}{(2\pi)^3}\int_{\vec{K}} \underline{\Delta\chi_K}(t)\ e^{i\vec{K}\cdot\vec{r}}\ d^3\vec{K} \tag{E-3}$$

and Eq. (2-18) gives the scattered field as

$$\underline{\vec{E}_S}(\vec{r},t) = \frac{\vec{\mathbf{f}}(\vec{r})}{(2\pi)^3}\ e^{i\omega_o t}\int_{\vec{K}}\int_{\vec{r}_1} E_o(\vec{r}_1)\underline{\Delta\chi_K}(t)\ e^{i(\vec{k}_o-\vec{k}_s+\vec{K})\cdot\vec{r}_1}\ d^3\vec{r}_1 \tag{E-4}$$

The time independent factor $\vec{\mathbf{f}}(\vec{r})$ and the wave vector of the scattered light $\vec{k}_s$ are defined as

$$\vec{\mathbf{f}}(\vec{r}) = \frac{1}{4\pi r}\left(\frac{\varepsilon_o}{\varepsilon}\right)\vec{\nabla}_r\times[\vec{\nabla}_r\times\hat{E}_o e^{ik_s r}] \tag{E-5}$$

and

$$\vec{k}_s = (\omega_o/c_m)\hat{r}$$

respectively.

Equation (E-4) shows that the light observed at $\vec{r}$ is contributed by a single spatial Fourier component of the fluctuations, $\underline{\Delta\chi_K}(t)$, only when the electric field amplitude

---

* Chapter 2, Section B.3, Eq. (2-22).

$E_o(\vec{r}_1)$ is uniform throughout all space. In this case, the interference integral

$$\int e^{i(\vec{k}_o-\vec{k}_s+\vec{K})\cdot\vec{r}_1}\, d^3\vec{r}_1 \tag{E-6}$$

picks out only that particular $\underline{\Delta\chi}_K(t)$ whose wave vector satisfies the condition

$$\vec{K} = \vec{k}_o - \vec{k}_s \tag{E-7}$$

In general, however, $\vec{E}_S(\vec{r},t)$ is contributed simultaneously by all Fourier components whose wave vectors fall within an amount[*]

$$\Delta\vec{k} = [\hat{x}\Delta k_x + \hat{y}\Delta k_y + \hat{z}\Delta k_z] \simeq [\hat{x}(2\pi/L_x) + \hat{y}(2\pi/L_y) + \hat{z}(2\pi/L_z)]$$

of satisfying Eq. (E-7). The uncertainties Δk_x, Δk_y, and Δk_z give the range of wave vectors that would be present in a spatial Fourier decomposition of the incident field amplitude variation, $E_o(\vec{r}_1)$. The quantities L_x, L_y, and L_z are the dimensions of the illuminated region in the cartesian coordinate system of Fig. 2-10.

For the source and scattering cell geometries used in this thesis, $E_o(\vec{r}_1)$ has the form[**]

$$E_o(\vec{r}_1) = \begin{cases} E_o \exp[-\dfrac{\pi x_1^2}{2L_x^2}]\ \exp[-\dfrac{\pi y_1^2}{2L_y^2}] & ;\ -(L_z/2) \le z_1 \le (L_z/2) \\ 0 & ;\ \text{otherwise} \end{cases} \tag{E-8}$$

---

[*] Chapter 2, Section E.4.e.

[**] Chapter 4, Section B.2; Chapter 4, Section C.4.

and we have $\underline{\vec{E}}_S(\vec{r},t)$ from Eq. (E-4) as

$$\underline{\vec{E}}_S(\vec{r},t) = \frac{\vec{\mathbf{f}}(\vec{r})}{(2\pi)^3} E_o e^{i\omega_o t} \int_{\vec{K}} \underline{\Delta\chi}_K(t) \int_{x_1=-\infty}^{\infty} \int_{y_1=-\infty}^{\infty} \int_{z_1=-(L_z/2)}^{(L_z/2)}$$

$$\times e^{-\frac{\pi x_1^2}{2L_x^2}} e^{-\frac{\pi y_1^2}{2L_y^2}} e^{-i(\vec{k}_o-\vec{k}_s+\vec{K})\cdot\vec{r}_1} d^3\vec{r}_1 \, d^3\vec{K} \qquad \text{(E-9)}$$

Taking $\hat{k}_s$ to lie in the (x,z) plane of Fig. 2-10 and restricting our attention to scattering angles in the range $\Theta \leq 5°$ gives*

$$\vec{k}_s - \vec{k}_o \equiv \vec{K}_o \simeq 2k_o \sin(\Theta_o/2)\hat{y} \qquad \text{(E-10)}$$

from which we find

$$\underline{\vec{E}}_S(\vec{r},t) = \frac{\vec{\mathbf{f}}(\vec{r})}{(2\pi)^3} E_o e^{i\omega_o t} \int_{\vec{K}} \underline{\Delta\chi}_K(t) \int_{x_1=-\infty}^{\infty} e^{-\frac{\pi x_1^2}{2L_x^2} + i(K_x)x_1} dx_1$$

$$\times \int_{y_1=-\infty}^{\infty} e^{-\frac{\pi y_1^2}{2L_y^2} + i(K_y-K_o)y_1} dy_1 \int_{z_1=-(L_z/2)}^{(L_z/2)} e^{i(K_z)z_1} dz_1 \, d^3\vec{K}$$

(E-11)

---

* Chapter 2, Section B.3, Fig. 2-5.

The (x_1,y_1,z_1) integrals are straightforward and yield

$$\underline{\vec{E}}_S(\vec{r},t) = L_xL_yL_z \frac{2\vec{\mathbf{f}}\,(\vec{r})}{(2\pi)^3} E_o\, e^{i\omega_o t} \tag{E-12}$$

$$\int_{\vec{K}} \underline{\Delta\chi_K}(t)\, \exp\left[-\frac{L_x^{\,2}K_x^{\,2}}{2\pi}\right] \exp\left[-\frac{L_y^{\,2}(K_y-K_o)^2}{2\pi}\right] \frac{\sin\,(K_zL_z/2)}{(K_zL_z/2)}\, d^3\vec{K}$$

This result shows that the spatial Fourier components of $\Delta\chi(\vec{r},t)$ within a range

$$(\Delta K_x, \Delta K_y, \Delta K_z) \simeq \left[\pm\frac{\sqrt{2\pi}}{L_x},\ \pm\frac{\sqrt{2\pi}}{L_y},\ \pm\frac{\pi}{L_z}\right] \tag{E-13}$$

of $\vec{K} = \vec{K}_o$ will contribute a significant portion of the scattered field observed at $\vec{r}$. The power spectral density of this field may be found via the time correlation function $R_E(\tau)$. Equations (2-61) and (E-12) combine to give

$$R_E(\tau) = \frac{1}{2}\left\langle \underline{\vec{E}}_S(\vec{r},t)\cdot\underline{\vec{E}}_S^{\,*}(\vec{r},t+\tau)\right\rangle \tag{E-14}$$

$$= 2(L_xL_yL_z)^2 \frac{|\vec{\mathbf{f}}\,(\vec{r})|^2 E_o^{\,2}}{(2\pi)^6} e^{-i\omega_o\tau} \int_{\vec{K}}\int_{\vec{K}'} \left\langle \underline{\Delta\chi_K}(t)\,\underline{\Delta\chi_K}^*(t+\tau)\right\rangle$$

$$\times \exp\left[-\frac{L_x^{\,2}K_x^{\,2}}{2\pi}\right] \exp\left[-\frac{L_x^{\,2}(K_x')^2}{2\pi}\right] \exp\left[-\frac{L_y^{\,2}(K_y-K_o)^2}{2\pi}\right]$$

$$\times \exp\left[-\frac{L_y^{\,2}(K_y'-K_o)^2}{2\pi}\right] \frac{\sin\,(K_zL_z/2)}{(K_zL_z/2)}\,\frac{\sin\,(K_z'L_z/2)}{(K_z'L_z/2)}\, d^3\vec{K}\, d^3\vec{K}'$$

For the range of $\vec{K}$ vectors of interest here, two distinct Fourier amplitudes $\underline{\Delta\chi}_K(t)$ and $\underline{\Delta\chi}_{K'}(t)$ are statistically independent.[§] As a result the time average in Eq. (E-14) will vanish unless $\vec{K} = \vec{K}'$, i.e.

$$\left\langle \underline{\Delta\chi}_K(t)\,\underline{\Delta\chi}_{K'}(t+\tau)\right\rangle = [R_{\Delta\chi}(\tau)]_K\,\delta(\vec{K}-\vec{K}') \qquad \text{(E-15)}$$

This simplification yields $R_E(\tau)$ in the form

$$R_E(\tau) = 2(L_xL_yL_z)^2\,\frac{|\vec{\mathbf{f}}\,(\vec{r})|^2E_o^{\,2}}{(2\pi)^6}\,e^{-i\omega_o\tau}\int_{\vec{K}}[R_{\Delta\chi}(\tau)]_K$$

$$\times\,\exp\left[-\,\frac{L_x^{\,2}K_x^{\,2}}{\pi}\right]\exp\left[-\,\frac{L_y^{\,2}(K_y-K_o)^2}{\pi}\right]\frac{\sin^2\,(K_zL_z/2)}{(K_zL_z/2)^2}\;d^3\vec{K}$$

$$\text{(E-16)}$$

Equations (2-62), (2-81), (2-82), and (2-99) show that for thermal fluctuations in liquids $[R_{\Delta\chi}(\tau)]_K$ is a function only of the magnitude of $\vec{K}$. Since $\vec{K}_o$ has been assumed to be collinear with the y axis, the x and z terms in Eq. (E-16) have only a second order effect on $R_E(\tau)$; to first order $[R_{\Delta\chi}(\tau)]$ may be removed from these integrations to yield

$$R_E(\tau) = (L_xL_yL_z)\,\frac{|\vec{\mathbf{f}}\,(\vec{r})|^2E_o^{\,2}}{2(2\pi)^3}\,e^{-i\omega_o\tau}$$

$$\times\,\frac{L_y}{\pi}\int_K[R_{\Delta\chi}(\tau)]_K\,\exp\left[-\,\frac{L_y^{\,2}(K-K_o)^2}{\pi}\right]dK \qquad \text{(E-17)}$$

[§] Chapter 2, Section E.4.b.

The corresponding power spectral density of the observed field may be written as

$$\overline{\overline{S_E(\omega;\Theta_o)}} = \frac{L_y}{\pi} \int_{K=-\infty}^{\infty} S_E(\omega,\vec{K})\, e^{-\frac{L_y^2}{\pi}(K-K_o)^2}\, dK \qquad \text{(E-18)}$$

where

$$S_E(\omega,K) = (L_x L_y L_z)\, \frac{|\vec{f}(\vec{r})|^2 E_o^2}{2(2\pi)^3}\, \frac{1}{2\pi} \int_{\tau=-\infty}^{\infty} e^{-i\omega_o\tau}\, [R_{\Delta\chi}(\tau)]_K \cos\omega\tau\, d\tau$$

$$\text{(E-19)}$$

is the spectrum of the light scattered by a single Fourier component of the fluctuations; and Θ_o is related to $\vec{K}_o$ via Eq. (E-10).

BIOGRAPHICAL NOTE

Joseph Benedict Lastovka was born in Cleveland, Ohio on June 8, 1940. He received his primary and secondary school education at the Blessed Sacrament parochial school and St. Ignatius High School. From 1958 to 1962 he attended John Carroll University in University Heights, Ohio, majoring in physics. He was graduated *magna cum laude* in June, 1962 with the degree of Bachelor of Science.

From July, 1962 to the present the author has been a graduate student in the Physics Department of the Massachusetts Institute of Technology.

ACKNOWLEDGEMENTS

In thanking those who have contributed to the growth of my professional and personal maturity during the course of this thesis, I would particularly acknowledge a debt to my thesis supervisor, Professor George B. Benedek, whose patience, encouragement, and dynamic involvement in physics have guided me through the many difficulties encountered in thesis research.

I would also express a deeply felt through usually unmentioned gratitude to all my associates here at M.I.T. for their genuine concern and constructive criticism in every phase of my graduate career. In particular, I would like to thank by name Professor Peter Heller for the many hours of stimulating discussion that he generously engaged in.

I am grateful to the American Can Company for their financial help in the form of a full tuition and stipend scholarship which extended over two years of this thesis.

The presentation of this thesis would not be complete without a mention of the able typing skill and personal kindness of Mr. and Mrs. Ernest Ford who prepared the manuscript.

Lastly, in place, though certainly not in importance, I would acknowledge the greatest favor given to me during the past five years by simply saying that without the grace of God this thesis would not have been completed.